Ph.D. report:

Secular theories and orbital dynamics beyond Neptune

Melaine Saillenfest

supervised by Marc Fouchard
and Giacomo Tommei

Oral defense:

3rd July 2017

Examining committee:

Anne Lemaître – *reviewer*
Tabaré Gallardo – *reviewer*
Andrea Milani – *inspector*
Giovanni Valsecchi – *inspector*
Nicolas Rambaux – *inspector*
Bruno Sicardy – *president*

Università di Pisa

last modification: 7th July 2017

— Abstract —

Théories séculaires et dynamique orbitale au-delà de Neptune

La structure dynamique de la région transneptunienne est encore loin d'être entièrement comprise, surtout concernant les objets ayant un périhélie très éloigné. Dans cette région, les perturbations orbitales sont très faibles, autant de l'intérieur (les planètes) que de l'extérieur (les étoiles de passage et les marées galactiques). Pourtant, de nombreux objets ont des orbites très excentriques, ce qui indique qu'ils ne se sont pas formés tels qu'on les observe actuellement. De plus, certaines accumulations dans la distribution de leurs éléments orbitaux ont attiré l'attention de la communauté scientifique, conduisant à de nombreuses conjectures sur l'origine et l'évolution du Système Solaire externe.

Avant d'envisager des théories plus "exotiques", une analyse exhaustive doit être menée sur les différents mécanismes qui peuvent reproduire les trajectoires observées à partir de ce qui est jugé "certain" dans la dynamique du Système Solaire, à savoir les perturbations par les planètes connues et par les marées galactiques. Cependant, nous ne pouvons pas nous fier uniquement aux simulations numériques pour explorer efficacement l'espace des comportements possibles. Dans ce contexte, notre objectif est de dégager une vision globale de la dynamique entre Neptune et le nuage de Oort, y compris les orbites les plus extrêmes (même si elles sont peut-être improbables).

Teorie secolari e dinamica orbitale oltre Nettuno

La struttura dinamica della regione trasnettuniana è ancora lontana dall'essere interamente capita, soprattutto per ciò che concerne gli oggetti che hanno un perielio molto distante. In questa regione le perturbazioni orbitali sono molto deboli, sia dall'interno (i pianeti) che dall'esterno (le stelle di passaggio e le maree galattiche). Eppure, numerosi oggetti hanno delle orbite molto eccentriche, il che dimostra che non si sono formati così come li osserviamo ora. Inoltre, alcune accumulazioni nella distribuzione dei loro elementi orbitali hanno attratto l'attenzione della comunità scientifica, producendo innumerevoli congetture sull'origine e l'evoluzione del Sistema Solare esterno.

Prima di considerare teorie più "esotiche", un'analisi completa deve essere condotta sui diversi meccanismi che possono produrre le traiettorie osservate partendo da quello che è considerato "certo" nella dinamica del Sistema Solare, cioè le perturbazioni dai pianeti conosciuti e dalle maree galattiche. Tuttavia, non ci si può fidare solo delle simulazioni numeriche per esplorare efficacemente lo spazio dei comportamenti possibili. In tale contesto, il nostro obbiettivo è di sviluppare una visione globale della dinamica tra Nettuno e la Nube di Oort, comprese le orbite più estreme (anche se sono forse improbabili).

Le orbite completamente esterne alla regione planetaria possono essere divise in due macroclassi: da una parte gli

Secular theories and orbital dynamics beyond Neptune

The dynamical structure of the trans-Neptunian region is still far from being fully understood, especially concerning high-perihelion objects. In that region, the orbital perturbations are very weak, both from inside (the planets) and from outside (passing stars and galactic tides). However, numerous objects have very eccentric orbits, which indicates that they did not form in their current orbital state. Furthermore, some intriguing clusters in the distribution of their orbital elements have attracted attention of the scientific community, leading to numerous conjectures about the origin and evolution of the external Solar System.

Before thinking of "exotic" theories, an exhaustive survey has to be conducted on the different mechanisms that could produce the observed trajectories involving only what we take for granted about the Solar System dynamics, that is, the orbital perturbations by the known planets and/or by galactic tides. However, we cannot rely only on numerical integrations to efficiently explore the space of possible behaviours. In that context, we aim at developing a general picture of the dynamics between Neptune and the Oort Cloud, including the most extreme orbits (even if they are maybe improbable).

The orbits entirely exterior to the planetary region can be divided into two broad classes: on the one hand, the objects undergoing a diffusion of semi-major

bables).

Les orbites entièrement extérieures à la région planétaire peuvent être divisées en deux classes générales : d'un côté, les objets soumis à une diffusion du demi grand-axe (ce qui empêche toute variation importante du périhélie) ; de l'autre côté les objets qui présentent une dynamique intégrable à court terme (ou quasi-intégrable). La dynamique de ces derniers peut être décrite par des modèles séculaires. Il existe deux sortes d'orbites régulières : les orbites non résonnantes (demi grand-axe fixe) et celles piégées dans une résonance de moyen mouvement avec une planète (demi grand-axe oscillant).

La majeure partie de ce travail de thèse se concentre sur le développement de modèles séculaires pour les objets transneptuniens, dans les cas *non résonnant* et *résonnant*. Des systèmes à un degré de liberté peuvent être obtenus, ce qui permet de représenter chaque trajectoire par une courbe de niveau du hamiltonien. Ce type de formalisme est très efficace pour explorer l'espace des paramètres. Il révèle des trajectoires menant à des périhélies éloignés, de même que des "mécanismes de captures", capables de maintenir les objets sur des orbites très distantes pendant des milliards d'années. L'application du modèle séculaire résonnant aux objets connus est également très instructive, car elle montre graphiquement quelles orbites observées nécessitent un scénario complexe (comme la migration planétaire ou un perturbateur extérieur), et lesquelles peuvent être expliquées par l'influence des planètes connues. Dans ce dernier cas,

oggetti sottoposti a una diffusione del semiasse maggiore (che impedisce una variazione importante del perielio); dall'altra gli oggetti che presentano una dinamica integrabile a breve termine (o quasi-integrabile). La dinamica di questi ultimi può essere descritta con modelli secolari. Ci sono due tipi di orbite regolari: le orbite non risonanti (semiasse maggiore fisso) e quelle intrappolate in una risonanza di moto medio con un pianeta (semiasse maggiore oscillante).

La maggior parte di questo lavoro di dottorato si concentra sullo sviluppo di modelli secolari per gli oggetti trasnettuniani relativi ai due casi *non risonante* e *risonante*. Sistemi con un grado di libertà possono essere ottenuti in modo tale che ogni traiettoria sia rappresentata da una curva di livello dell'Hamiltoniana. Questo tipo di formalismo è molto efficace per esplorare lo spazio dei parametri. Esso rivela traiettorie che conducono a perieli lontani, insieme a dei "meccanismi di cattura", in grado di mantenere questi oggetti su delle orbite molto distanti per miliardi di anni. L'applicazione del modello secolare risonante agli oggetti conosciuti fornisce inoltre molte informazioni, dato che mostra graficamente quali orbite osservate necessitano di uno specifico scenario (come la migrazione planetaria o un perturbatore esterno) e quali possono essere spiegate mediante l'azione dei pianeti conosciuti. In quest'ultimo caso, la storia dinamica dei piccoli corpi può essere tracciata fin dalla loro cattura in risonanza.

L'ultima parte di questo lavoro è dedicata all'utilizzo del modello secolare non risonante esteso al caso di un perturbatore esterno massivo. Se esso ha una eccentricità e/o inclinazione sostanziale, introduce uno o due gradi di libertà in più

axis (which prevents any large variation of the perihelion distance); on the other hand, the objects which present an integrable (or quasi-integrable) dynamics on a short timescale. The dynamics of the latter can be described by secular models. There are two kinds of regular orbits: the non-resonant ones (fixed semi-major axis) and those trapped in a mean-motion resonance with a planet (oscillating semi-major axis).

The major part of this Ph.D. work is focussed on the development of secular models for trans-Neptunian objects, both in the non-resonant and resonant cases. One-degree-of-freedom systems can be obtained, which allows to represent any trajectory by a level curve of the Hamiltonian. Such a formalism is pretty efficient to explore the parameter space. It reveals pathways to high perihelion distances, as well as "trapping mechanisms", able to maintain the objects on very distant orbits for billions of years. The application of the resonant secular model to the known objects is also very informative, since it shows graphically which observed orbits require a complex scenario (as the planetary migration or an external perturber), and which ones can be explained by the influence of the known planets. In this last case, the dynamical history of the small bodies can be tracked back to the resonance capture.

The last part of this work is devoted to the extension of the non-resonant secular model to the case of an external massive perturber. If it has a substantial eccentricity and/or inclination, it introduces one or two more degrees of freedom in the

l'histoire dynamique des petits corps peut être retracée depuis leur capture en résonance.

La dernière partie de ce travail est consacrée à l'extension du modèle séculaire non résonnant au cas d'un perturbateur extérieur massif. S'il est doté d'une excentricité et/ou d'une inclinaison non négligeable, cela introduit un, voire deux degrés de liberté supplémentaires dans le système, d'où une dynamique en général non intégrable. Dans ce cas, l'analyse peut être réalisée à l'aide de sections de Poincaré, qui permettent de distinguer les régions chaotiques et régulières de l'espace des phases. Pour des demi grands-axes croissants, le chaos se propage très rapidement. Les structures les plus persistantes sont des résonances séculaires produisant des trajectoires alignées ou anti-alignées avec la planète distante.

Le développement des modèles séculaires est décrit dans Saillenfest et al. (2016), et l'exploration de l'espace des paramètres dans Saillenfest et al. (2017a). L'application aux objets transneptuniens connus, incluant les corps au périhélie distant récemment découverts, est présentée dans Saillenfest and Lari (2017). Finalement, l'extension du modèle non résonnant au cas d'un perturbateur extérieur est décrite et explorée dans Saillenfest et al. (2017b).

batore esterno massiccio. Se questo presenta un'eccentricità e/o un'inclinazione significativa, introduce uno o persino due gradi di libertà aggiuntivi nel sistema, dando luogo, in generale, ad una dinamica non integrabile. In tal caso, l'analisi si può condurre mediante sezioni di Poincaré, che permettono di differenziare le regioni caotiche e regolari dello spazio delle fasi. Aumentando il semiasse maggiore, il caos si estende molto rapidamente. Le strutture più persistenti sono risonanze secolari che conducono a traiettorie allineate o anti-allineate col pianeta esterno.

Lo sviluppo dei modelli secolari è descritto in Saillenfest et al. (2016), e l'esplorazione dello spazio dei parametri in Saillenfest et al. (2017a). L'applicazione agli oggetti trasnettuniani conosciuti, che includono i corpi con perielio distante scoperti di recente, è presentata in Saillenfest and Lari (2017). Infine, l'estensione del modello non risonante al caso di un perturbatore esterno è descritta in Saillenfest et al. (2017b).

system, so the secular dynamics is non integrable in general. In that case, the analysis can be realised by Poincaré sections, which allows to distinguish the chaotic regions of the phase space from the regular ones. For increasing semi-major axes, the chaos spreads very fast. The most persistent structures are secular resonances producing trajectories aligned or anti-aligned with the orbit of the distant planet.

The development of the secular models is described in Saillenfest et al. (2016), and the exploration of the parameter space in Saillenfest et al. (2017a). The application to the known trans-Neptunian objects, including recently discovered high-perihelion bodies, is presented in Saillenfest and Lari (2017). Finally, the extension of the non-resonant model to the case of an external perturber is described and explored in Saillenfest et al. (2017b).

— Remerciements/Ringraziamenti —

Cette thèse est l'aboutissement de mon cursus universitaire, c'est pourquoi je souhaite rendre hommage aux professeurs qui ont marqué mon parcours et qui m'ont guidé dans mes choix. Chacun à sa manière, ils ont participé à ce travail. Je remonterai même jusqu'au collège et au lycée, en remerciant Madame Chenu (Mathématiques) et Monsieur Bradesi (Physique, en particulier la partie Mécanique). Mes années de Licence à l'Université de Tours ont été particulièrement marquées par le cours de Noureddine Mohammedi (Mécanique analytique) et celui de Stam Nicolis (Modélisation numérique), pour lesquels je garde une grande estime. Je remercie également Amaury Mouchet : enseignant de plusieurs cours tout au long de ma Licence, il m'a transmis un intérêt général porté vers les mécanismes de la physique, empreint d'imagination et de poésie ; qu'il sache que je lui réservais la place de mon "parrain de thèse" même si les circonstances en ont décidé autrement. Durant mes années de Master à l'Observatoire de Paris, j'ai été particulièrement influencé par les cours de Jean Souchay (Gravitation), Philippe Robutel (Mécanique hamiltonienne), Nicolas Rambaux (Rotation des corps) et Jacques Féjoz (Géométrie des systèmes hamiltoniens). Enfin, j'adresse une pensée toute particulière à Alain Vienne : notre travail sur les satellites de Saturne m'a énormément apporté et j'espère que nous aurons de nouveau l'occasion de travailler ensemble.

Plus directement impliqués dans mon travail de thèse, je remercie chaleureusement mes deux directeurs de thèse, notamment pour avoir réussi à trouver un équilibre qui corresponde à ma façon de travailler. Ringrazio in particolare Giacomo Tommei per l'accoglienza a Pisa e per avermi liberato di quasi tutto il lato amministrativo italiano, che ho intravisto come molto complicato. Inoltre, esprimo la mia gratitudine a Giovanni Valsecchi: anche se non è stato ufficialmente un mio relatore, mi ha spesso ascoltato e aiutato durante il mio lavoro di tesi.

Je passe maintenant aux contributions plus personnelles, mais dont la place dans ce travail est indiscutable. Du côté français, je remercie Sophia, dont la présence et le soutien sont toujours d'un grand réconfort. Je remercie également Benoît et Étienne pour leur dynamisme et leur curiosité sans limite. À quand l'article en commun sur le modèle EBM ? Dal lato italiano, ringrazio Giacomo e Francesco. Il loro contributo, sia personale che scientifico, è stato importantissimo. Sono molto felice di averli incontrati. Pour finir, je n'oublie évidemment pas ma famille.

À Paris, Pise et ailleurs, dans le cadre professionnel et en dehors, de nombreuses autres personnes ont joué un rôle important pour moi pendant ces trois ans. Je ne les nomme pas individuellement car j'oublierais certainement du monde. Je les invite à se reconnaître dans ces lignes et je les remercie de tout cœur !

To Anna.

Contents

Introduction

This Ph.D. project focusses on the development of secular theories for the orbital dynamics beyond Neptune and on their application to the known population of trans-Neptunian objects. Chapter 1 presents a brief overview of the history of celestial mechanics and its major issues, in particular concerning the external regions of the Solar System. The present work can be considered as a straight continuation of numerous previous studies, and the most recent and influential ones are also introduced. Then, Chapter 2 exposes most of the theoretical tools and concepts used throughout this report. (Readers already familiar with the two-body problem and perturbation theories in Hamiltonian systems can safely skip this chapter.) The essence of the problem is addressed in Chp. 3, where we introduce both the non-resonant and resonant secular models designed to describe the long-term orbital dynamics beyond Neptune. Since the resonant dynamics was found extremely rich, the whole Chapter 4 is dedicated to the exploration of the possible types of trajectories driven by a mean-motion resonance with Neptune. The confrontation to observed trans-Neptunian objects is also realised, as well as to a large simulated sample. In Chp. 5, we study the influence of a distant massive planet on the non-resonant secular dynamics by the means of Poincaré sections. Finally, Chp. 6 summarises our results and highlights some points which should be further explored in future works.

In appendix, Chp. A presents the general principle of the frequency analysis of J. Laskar, along with some arguments (both theoretical and numerical) about its implementation. This tool, introduced in Laskar (1988, 1990), allows to study any integrable or weakly-chaotic dynamical system by tracking its main frequencies from numerical solutions. The work presented in this chapter was mainly realised for my Master thesis, but it was reused during this Ph.D. and it led in particular to the published paper by Renner et al. (2016).

Chapter 1

Statement of the problem

Starting this chapter, Sect. 1.1 presents a brief overview of celestial mechanics from the oldest records found by archaeologists until the present day. Once the historical background is set, Sect. 1.2 particularises the current state of research about the region of interest in the scope of this work, namely, the external Solar System. Finally, Sect. 1.3 introduces our objectives and specific approach.

1.1 Historical context

Various references were used to build that section, among them *Les comètes et les astéroïdes* by A.-C. Levasseur-Regourd (in particular the part by P. de La Cotardière); *Gravitation Classique* by J. Perez; *Solar System Dynamics* by C. D. Murray and S. F. Dermott.

1.1.1 The birth of astronomy

The first evidence of astronomical activities is reported in the Sumerian civilisation, 5000 years ago, developing in parallel with astrology (these two activities were indissociable at the time). From about 750 BC, the Babylonians instigated systematic observations and measures of the positions of celestial bodies, recorded on clay tablets engraved with cuneiform writing. The complete set of records is thought to have covered a period extending to AD 75, but numerous tablets were lost. Considered as "science", the beginning of occidental astronomy can be placed in the sixth century BC, when philosophers of Ancient Greece and Rome began to reflect upon the essence of the world in their will to understand natural phenomena.

The most developed and longest-lived theory from that time is attributed to Aristotle (384-322 BC). It states that the sublunary world, imperfect and corrupted by nature (because stemming from inhomogeneous mixtures of the different elements) is to be opposed to the cosmos, perfect and immutable (because constituted of pure essences). In that context, Plato formulates the problem raised by the motion of celestial bodies, as considered in Ancient Greece: since the cosmos is defined as perfect, it can be

composed only of the purest geometrical objects, that is, spheres rotating with constant velocities. Therefore, in what way can such spheres be arranged to "save face" and account for the seemingly erratic motions of the planets? This question was disconnected from the observed motions of comets, which were considered as atmospheric phenomena and thus placed on the "impure" side. The remarkable discernment of Seneca in the first century, who considered the comets as celestial bodies possibly returning on very long periods, remained quite unnoticed in his time. The Aristotelian conception of the world was rethought and enriched by Ptolemy in the second century, leading to intricate planetary spheres with increasing complexity. Ptolemy gathered the work of his predecessors in an incredibly rich and complete master work, the *Almagest*, in which the Earth is considered spherical and at the centre of the world. From the support of the Christian Church, the picture of Aristotle got deeply rooted in occidental science and philosophy, and remained virtually untouched for fourteen centuries. In parallel, the cometary astrology grew to such extent that even astronomers associated comets with misfortune and disasters.

1.1.2 From Copernicus to Newton

In 1543, though, the work of Copernicus *De revolutionibus orbium coelestium* achieved an extraordinary revival. In his conception of the world, the Earth appeared as a planet just like the other ones, all of them following circular trajectories around the Sun. Some heliocentric (or partly heliocentric) theories were also reported from Ancient Greece, but none of them managed to destabilise the views of Aristotle. One can be impressed, for instance, by the simplicity and ingenuity of the consideration by Aristarchus of Samos, comparing the relative sizes of the Earth and the Sun: "Why make the fly turn around the torch?" (quoted from J. Perez's book). The breakthrough of Copernicus could be partly due to his very cautious behaviour: indeed, he accepted to publish his work only under the pressure of his young assistant, starting from a careful extract. His overall work was finally published shortly before his death. Intentionally or not, Copernicus did not underline any of the fundamental consequences implied by his model to the very conception of the world. He did not address the question of *infinity*, either, though inherent to his theory. From his work, it simply appeared that some astronomical phenomena (as the temporary retrograde motion of planets as seen from the Earth) could be described in terms of simple geometrical effects. This left the possibility for the Church to consider the work of Copernicus as an elegant mathematical formulation, with no link to the physical world.

Meanwhile, the Aristotelian conception of comets was known to be in contradiction with observations, and their nature and their origin (extra or sublunary) were open problems. However, during the 1500-year period extending from Seneca to Copernicus, the historical mentions of comets were almost exclusively related to portents or evil signs, with no new scientific interpretation. In that context, Tycho Brahe, a Danish astronomer, was convinced that information about the nature and motion of celestial bodies could only be obtained from accurate and repeated observations. He accumu-

lated an enormous amount of measures of the positions of stars, comets and planets, with an unprecedented precision for naked eyes. In 1577, a very bright comet appeared in the sky and he charged one of his colleagues to measure its position simultaneously from Prague, at about 1000 km from his observatory. The very small parallax obtained with respect to the background stars made them deduct that comets are astronomical objects, located way beyond the Moon. From his observations, Tycho Brahe even considered the possibility that comets follow "oval" orbits with non-uniform velocity. In 1600, he employed the young and skilled Kepler as assistant but died a year later, leaving to him his incredible observational records.

Kepler had a complicated life, constrained notably to interrupt his works to save his mother from being burned as a witch (he did not manage to save his aunt from the same fate). His studies were themselves distributed between superstitions and science: he wrote down horoscopes and he was convinced that the dynamical properties of the planets (as the sizes of their orbits or their velocities) were not accidental. Consequently, Kepler looked empirically for laws governing their motions, constants linking their characteristics, or the geometrical figures their trajectories could form. Thanks to the remarkable observations by Tycho Brahe and after many years of work (1600-1619), Kepler found the three laws that made him famous, distributed among complex theories involving geometric figures, music and astrology:

1. The planets move in ellipses in which the Sun occupies one focus.

2. The line connecting the Sun to a planet sweeps out equal areas in equal durations.

3. The square of the orbital period of a planet is proportional to the cube of its semi-major axis.

The planetary model of Kepler, based exclusively on observations, included thus non-circular orbits (ellipses), followed with non-uniform velocities (the second law implies a higher velocity when the planet is closer to the focus occupied by the Sun). These were other arguments against the perfection of the cosmos inherited from Aristotle, more than 2000 years before. Thanks to Copernicus, though, new ideas had begun to spread.

Contemporaneous to Kepler, Galileo was a precursor of the modern scientific methods, based on observation and experimentation. His works on the falling bodies (partly conducted when he was professor of mathematics in the University of Pisa) would turn out to be of great importance in the history of science. In 1609, his revolutionary use of the refracting telescope for sky observations[1] had a tremendous effect on the scientific community and the general public: indeed, the Moon proved to be covered with mountains and "seas"! Galileo even proposed that the tenuous light coming from the dark part of the Moon could be due to the "earthshine" as seen from the Moon. He also discovered Jupiter's satellites (appearing as small luminous points moving around

[1]It is too bad that English does not make as clear a distinction as the French words "lunette" and "télescope" (or in Italian "cannocchiale" and "telescopio")!

Jupiter just like the Moon around the Earth), and phases on Venus. Finally, the diffuse regions of the Milky Way proved to be constituted of a gigantic amount of stars. Such discoveries gave rise to very audacious ideas for that time, such as the possibility of other worlds or the notion of infinity. Despite Galileo's pretentious and ironic attitude when presenting his results, his discoveries did not suffer much from the Inquisition, maybe partly because of his relations with the Medici family (it took some time, though, to convince people that his observations were not due to artefacts coming from the telescope).

After the success of Kepler and Galileo, some astronomers began to think that comets, which were known from Tycho Brahe to evolve beyond the Moon, could also verify Kepler's laws. They could follow indeed very large elliptic orbits, bringing them back after long periods of time, such that their tiny paths in the vicinity of the Earth would seem rectilinear (which was the theory often admitted at the time). In 1668, the visionary Hevelius envisaged also parabolic or hyperbolic trajectories.

More generally, the very existence of Kepler's laws, based on strong observational evidence, was addressed by researchers. How could they be explained? Newton, a distinguished mathematician from Cambridge university, started to work on that question in 1666, with already the idea that the Moon could fall toward the Earth just as an apple does. His interest was reinforced by two very bright comets (1680 and 1682), and he soon verified that the accelerations of the Moon and the apple were inversely proportional to the square of their distance to the Earth, making an audacious link between Galileo's experiments of falling bodies and planetary motions. The genius of Newton led him actually to much more: after having developed the required formalism (the infinitesimal calculus, the ancestor of derivatives and integrals), he applied his inverse-square law to two isolated massive bodies, which is known today as the "two-body problem". Despite the complexity of the question (even addressed with modern tools, see Sect. 2.1), he succeeded in demonstrating which types of trajectories obey to such dynamics... which were nothing else than Kepler's ellipses, followed at velocities implying the two other laws as natural consequences!

Contemporaneously, Halley, another English astronomer, was also eager to link Kepler's empirical relations to mathematical proofs. The idea of an inverse-square law had already been suggested by some scientists, but without any conclusive proof. In 1684, Halley visited Newton for advice, and asked him which would be, in his opinion, the trajectories obeying such a law. Newton answered immediately: *ellipses, I have calculated that!* A few months later, Newton sent him some of his works, in which he showed that the first law of Kepler is actually generalised to all conics (not only ellipses), and he detailed the proofs for the two other laws. Very enthusiastic, Halley encouraged him to pursue his work, and above all to publish it. Newton, mainly interested by the results (and not by their possibly controversial exposure), finally accepted Halley's request, and in 1686, he presented his work to the Royal Society. As feared by Newton, this immediately produced quite hostile reactions from other mathematicians,

who claimed (incorrectly) the priority on some results[2]. In reaction, Newton considered the option of removing a large part of his manuscript before publication. Only the great diplomacy used by Halley allowed to bypass Newton's unwillingness (he even provided himself the money for the first edition of the works). In 1687, the *Philosophiae naturalis principia mathematica* were finally published, presenting the unified version of Kepler's and Galileo's results in a new conception of astronomical and terrestrial dynamics, both subject to the "universal attraction". Newton detailed also the context of application of this law, namely his three principles on the motions of bodies:

1. Any isolated body remains at rest or in a uniform motion of translation (principle of inertia).

2. The mass-acceleration product of a body is equal to the total external force acting on it (fundamental principle of dynamics).

3. Any object exerting a force on another object is in return subject to an equal force with opposite direction (action-reaction principle).

Incidentally, the reader will note that the very same laws, along with Newton's gravitation theory, are used all along this Ph.D. work: we will simply study their implication for the trans-Neptunian objects. The Newtonian gravitation solved also the problem of cometary trajectories (even if himself still spoke of rectilinear motions): they are subject to the same law as the planets and should thus follow indeed very elongated ellipses, or even parabolas or hyperbolas which are also conic sections. Newton described his conception on the nature of comets as solid bodies from which emanate streams of vapour when they are close to the Sun (what a remarkable intuition!). He even proposed methods to compute the orbital elements of celestial bodies from three observations. Finally, from his studies on the light, Newton invented the reflecting telescope, allowing the use of an instrument much more compact that Galileo's refracting telescope for the same precision. Very modestly, he wrote in a 1676 famous letter to Hooke: "If I have seen further, it is by standing on the shoulders of giants", referring to his predecessors. History would reveal, though, that Newton has himself his place among the tallest giants.

1.1.3 Perturbation methods and predictions

From 1695 on, Halley relied on the published works of Newton to renew the idea of periodical returns of comets, and tried to apply his method of orbit determination to the comets observed during long-enough periods of time. In 1705, he published an application to 24 comets, and most of all, he postulated that the historical comets of 1531, 1607 and 1682, recorded as different objects, could actually be several passages

[2]It should be noted that Hooke, one of the greatest rivals of Newton, had already proposed the inverse square law. However, his claim of priority was unjustified since he did not draw any valuable conclusion from it, contrary to the extremely rich work of Newton.

of one single comet. On this hypothesis, the fact that its orbital elements seemed to be slightly different at each passage could be explained by the planetary perturbations (since the system is not strictly a Sun-comet two-body problem). Consequently, he predicted the return of that comet around the year 1758, but he died in 1742 at the age of 85. Since then, astronomers tackled the task to calculate precisely the date of the new return of this comet (supposing that the observations came indeed from a single comet), taking into account the planetary perturbations. Their goal was to get a prediction accurate enough to prevent a mistaken conclusion that the comet had not returned. Clairaut, a French mathematician, developed the appropriate formulas using successive approximations, more or less equivalent to the temporal steps of our modern numerical integrators. The problem was that without a computer, every single step had to be computed by hand. The extremely laborious work was realised by his young colleague Lalande, with the help of the mathematician Nicole-Reine Lepaute. In 1758, after months of uninterrupted calculus, they finally announced their prediction for the next perihelion passage of the comet: April 1759 with a error bar of a month (the comet had been delayed by 618 days due to the perturbations from Jupiter and Saturn). And indeed, the comet was observed from the end of December 1758, passed its perihelion a month before the prediction, and remained visible until the end of June 1759: it became *Halley's comet*. This was a tremendous success for Newton's theory of gravitation, which was still questioned by numerous scientists. Comets lost also some credibility as occult phenomena, since they obeyed to universal laws and their returns could be predicted.

The scope of Newton's theories was extremely vast, and besides the trajectories of comets, astronomers began to develop accurate ephemeris of the Moon and the planets, taking into account their mutual perturbations. A lot of famous mathematicians were involved in that period, very rich in theoretical discoveries (with among them Euler, D'Alembert, Laplace, Lagrange...), leading to always finer verifications of Newton's laws. Indeed, after Herschel discovered the planet Uranus in 1781 (by telescopic observations), Gauss showed in 1801 that they could have predicted its presence from the observed trajectories of the other planets. Thereafter, Adams (1841) and Le Verrier (1845) conjectured, from the orbital perturbations undergone by Uranus, that an eighth massive planet should evolve in the external Solar System. Their prediction proved to be correct (despite erroneous calculations), since Neptune was discovered in 1846.

1.1.4 Planets, asteroids and trans-Neptunian objects

Similarly to Kepler and his three laws (preceding their demonstration by Newton), the searches for simple ratios between astronomical quantities were frequently conducted, leading to as many theoretical discoveries as tenacious misconceptions. Let us recall, for instance, the Titius-Bode relation, published by Titius and renewed by Bode in 1772. They presented that, taking as unit of length the average distance between the Earth and the Sun, the average distances of the others planets can be obtained by the

sequence:

$$D_n = 0.4 + 0.3 \times 2^n \quad \text{with} \quad n = -\infty, 0, 1, 2, 4, 5 \tag{1.1}$$

This relation accounts for the distances of Mercury, Venus, the Earth, Mars, Jupiter and Saturn, but with an intriguing "absence of planet" for $n = 3$. This questioning was reinforced by the discovery of Uranus, which had an orbit compatible with $n = 6$. On the basis of the empirical rule by Titius, Bode became the instigator of a search for the missing planet. Organised groups of observers were formed, each of them with the task to monitor an assigned portion of the sky. In 1801, an observer discovered indeed a small body having the required distance to the Sun, to which the name of Ceres was given. However, between 1802 and 1807, three other bodies were observed, and then plenty of others from 1845, reaching the number of 300 in 1890. They had a clearly different status than the previously known planets, so they were called *asteroids* (or more generically *minor planets*). Their orbital region, stretching between the orbits of Mars and Jupiter, is nowadays called the *Main Belt*. The Titius-Bode relation, though totally empirical with no physical nor mathematical foundation, opened thus a large field of research still relevant today[3]. It was however definitively abandoned after the discovery of Neptune, which has an average distance to the Sun quite different from the value obtained by putting $n = 7$ (the existence of Neptune was in turn predicted from consistent mathematical calculations). Actually, a small number of bodies with random spacings have a quite large probability to present a sequence similar to the Titius-Bode relation (Murray and Dermott, 1999).

In 1906, the American astronomer Lowell found some unexplained features in the orbits of Uranus and Neptune, and by the same argument as Le Verrier in his time, he attributed them to another, more distant, still unobserved planet[4]. He immediately started a large search campaign, realised by comparing photographic plates and locating by eye any moving point, but he remained unable to locate his "Planet X". After his death in 1916, the Lowell Observatory pursued the researches, and in 1930 Tombaugh found a body in the vicinity of the predicted position. This ninth planet, named Pluto, appeared as a confirmation of Lowell's predictions. However, further observations of Pluto always tended to decrease its mass estimate, until in 1978, its mass could be precisely measured thanks to the discovery of its satellite Charon. The very low value obtained (0.2% of the mass of the Earth, smaller than the Moon) made it unable to perturb substantially the motion of Uranus and Neptune. The anomalies in their observed positions were later understood to result from a slight error in the estimates of Neptune's mass. From 1992 on, many other objects were found with orbits beyond Neptune (whence their denomination of *trans-Neptunian objects*). In particular, Eris, discovered in 2005, was announced by NASA as the tenth planet of the Solar System. Its mass could be estimated thanks to its small satellite, revealing that it is more massive than Pluto. Moreover, numerous smaller objects were found to follow orbits

[3]More than 700 000 asteroids are known today and they allow the study of very deep questions about the formation and evolution of the Solar System.

[4]Lowell is also known for his conviction that artificial canals were visible on the surface of Mars, popularising the idea of an intelligent Martian life.

similar to that of Pluto (called *Plutinos*). This raised the same controversy that had followed the discovery of Ceres and the asteroids two hundred years before: if Pluto and Eris were classified as planets, what strong argument could be used to justify that other large trans-Neptunian objects were not, nor the largest asteroids? The question was addressed in 2006 by the International Astronomical Union. It was agreed that the denomination of "planet" should be given only to objects having: *i*) an orbit around the Sun; *ii*) a rounded shape due to hydrostatic equilibrium; *iii*) a large-enough gravitational influence such that no other body can share their orbits. Objects fulfilling only *i* and *ii* were thus downgraded to *dwarf planets* (as Pluto, Eris and Ceres), whereas the ones fulfilling only *i* were called generically *small Solar System objects*.

1.1.5 From Poincaré to modern celestial mechanics

Despite the fast progress of perturbation methods in the 19th century, the dynamical properties of the N-body problem (with an implicit $N > 2$) remained badly understood. In particular nobody knew whether an analytical solution existed in the general case, which could be expressed generically as a convergent series of usual functions. This became the subject of an international mathematical challenge organised in 1887 in honour of the king of Sweden. The prize was won by Poincaré, although he only partially answered the question. The revision of his work (which actually contained a now famous mistake), made him conclude that such a convergent series does not exist in the general case: indeed, extremely small changes of initial conditions were found to lead to completely different solutions (whereas absolutely deterministic). This opened a new area in the study of dynamical systems: the theory of chaos. Poincaré is often considered as one of the last "generalist" scientists, since he addressed successfully a very broad range of questions from theoretical physics, mathematics and philosophy. After him, the study of dynamical systems became a whole field of mathematics, and moved away somehow from physics and celestial mechanics (though related to them). A major breakthrough in this field was realised by the so-called *KAM theorem* (named after Kolmogorov, Arnold and Moser), developed from 1954 to 1962. It deals with the general case of a perturbed Hamiltonian (that is conservative) system, which is integrable when the perturbation is set to zero. Under some conditions, it was shown that some sets of integrable quasi-periodic[5] trajectories do persist (while being more or less distorted) for non-zero but small-enough perturbations. In simple words, KAM theorem gave the conditions for the convergence of the perturbation method presented in Sect. 2.3.2. Please note that Poincaré worked on the same type of system (namely the integrable two-body problem perturbed by a third perturbing mass), but the scope of KAM theorem stretches well beyond celestial mechanics. Though extremely powerful from a mathematical point of view, it is besides not directly applicable to Solar System dynamics: using the original form of the theorem, Hénon (1966) remarked that integrable trajectories are proved to persist for planet masses smaller than $\sim 10^{-320}$ times

[5]A trajectory is said to be *quasi-periodic* when it is composed of several non-commensurable fixed frequencies. It thus never returns exactly to its initial position, but it can pass arbitrarily close to it.

the mass of the Sun (versus $\sim 10^{-3}$ for Jupiter)! The development of new versions of KAM theorem, restricted for instance to finite timescales, are an active field of modern research in mathematics. On the other hand, the increasing power of computers, at the end of the twentieth century, allowed astronomers to study the stability of the Solar System from more physicist-like approaches, based on semi-analytical models or purely numerical experiments. It was notably proved that it is unstable in general (Laskar, 1989), with possible ejections or collisions of inner planets over a few hundred million years, even if some components, such as the orbits of the giant planets, are indeed stable. This chaotic nature prevents from predicting the precise position of the inner planets after about 100 Myrs, since tiny imprecisions in their initial conditions lead to errors larger that the sizes of their orbits. Moreover, even if the initial conditions were known to arbitrary precision and the numerical integrations were *exact*, the uncertainty would anyway be brought by the approximations of the dynamical model itself, since it is impossible to take every effect into account (as mutual interactions between asteroids).

Even if the problem is now known to be chaotic, we saw that approximate (but accurate) solutions can be obtained on relatively short timescales by analytical series and/or successive approximations. In 1859, a fundamental problem was raised by Le Verrier, who showed that the predicted orbital variations of Mercury due to the other planets and a possible flattening of the Sun were notably different from the observed ones. Far from questioning the very validity of Newton's laws, a series of hypotheses were proposed, including the existence of a planet "Vulcan" orbiting very close to the Sun. As we can imagine, planet hunters were moreover misled by various round sunspots which seemed to "orbit" the Sun. The definitive answer was brought by Einstein in 1915 and his theory of General Relativity. Indeed, he had the intuition that if the inertial mass (measuring the difficulty to set an object in motion) and the gravitational mass (measuring the mutual attractions of the planets) were indeed equal, they should not appear in an independent way as in Newton's theory. General Relativity describes the gravitation as a curvature of the space-time itself, which contrasts singularly with a force-like conception of the gravitational interaction. It led people to rethink the world, and in particular the absolute nature of time-spans and lengths. However, despite its very important implications in fields like signal propagation, galaxy dynamics, cosmology or particle physics, General Relativity cannot be said to have brought a "revolution" in the Solar System dynamics. In such weak gravitational fields, it diverges only very slightly from the Newtonian theory, so that its orbital effects are only detectable for objects very close to the Sun (as Mercury). Moreover, the use of Einstein's equations is very cumbersome compared to the simple laws of Newton. Consequently, General Relativity, when it has indeed notable effects, is usually introduced as additional perturbative terms in Newton's equations: this allows to keep their convenient structure. More subtle effects of General Relativity are completely negligible at the level of the Solar System. Hence, its very intricate dynamical structure can be essentially described by the simple inverse-square law, and this makes it even more fascinating. In the trans-Neptunian region, very far from the Sun, perturbations issued from General

Relativity or non-gravitational forces can be safely ignored (we will not even mention them anymore).

1.2 The dynamics of the Solar System

1.2.1 The formation scenario

The shapes and dynamics of the planets and small Solar System bodies are qualitatively well explained by the currently accepted formation scenario of the Solar System. The Solar System is nowadays considered to have been formed about 4.6 billion years ago[6], from the gravitational collapse of a giant molecular cloud. The instability initiating this collapse could have been produced by the nearby explosion of a supernova. The compression of the solar nebula, constituted of gas and dust, made drastically increase the temperature in its centre. Starting from a very low residual rotation, the contraction made it spin rapidly from the conservation of angular momentum. This rotation caused the nebula to flatten naturally into a *protoplanetary disk*, surrounding the central denser region constituting the *protosun*. By direct contact, particles of the disk stuck together and formed grains. Some of them grew enough to exert a substantial gravitational influence on their neighbourhood and accreted more and more material from the nebula (this is indeed what is observed around young stars, see Fig. 1.1). The complex interaction between the planets and the disk are also known to result in the migration of the planets themselves inside the disk.

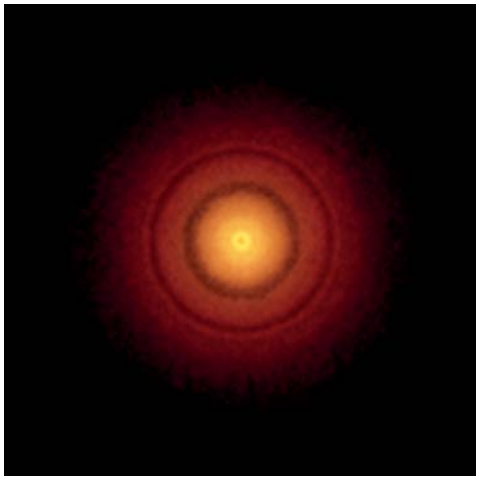

Figure 1.1 – Image of the young star TW Hydrae surrounded by its protoplanetary disk. It is located at about 180 light-years from the Solar System. The circular gaps in the disk are thought to be created by forming planets, accreting and sweeping particles away. This image was taken in 2016 by the Atacama Large Millimeter Array (ALMA).

The gradient of temperature in the protoplanetary disk caused different compositions of the bodies formed: rocky near the hot star and icy beyond some distance called the *frost line*. Then, the strong and irregular solar wind coming from the young Sun

[6]The age of the Solar System can be estimated by dating the earliest formed components of meteorites and asteroids, by the relative abundance of radioactive isotopes. It corresponds thus to the time-span from the formation of the first solid grains until today.

(in its so-called T Tauri phase) swept away the remaining gas and dust, and some remained only trapped around the massive-enough bodies, that is, the giant planets Jupiter, Saturn, Uranus and Neptune. The telluric planets, on the contrary, were left only with their rocky core. They were probably more numerous than today, occasioning various collisions (as the one thought to have created the Moon). From the solar nebula, no large bodies could have formed just beyond the orbit of Mars because of the strong disrupting gravitational influence of Jupiter and Saturn: this formed the Main Asteroid Belt, only constituted of relatively small rocky bodies. Beyond Uranus and Neptune, on the contrary, the density of the solar nebula was too weak to form large bodies: this resulted in the Kuiper Belt objects, constituted of small icy bodies.

According to recent theories, the four giant planets underwent several migration phases across the Solar System during its early stages. This is necessary to match both the formation mechanisms deduced from observed exoplanetary systems and the size and distribution of Solar System objects. At first, Jupiter and Saturn are thought to have migrated inward due to the action of the protoplanetary gas, but they subsequently drifted back again to larger heliocentric distances because of their mutual perturbations (Walsh et al., 2011). This explains the characteristics of the Main Asteroid Belt and of the terrestrial planets, as well as the current position of Jupiter and Saturn compared to the numerous "hot Jupiter" exoplanets found very close to their host star. Moreover, Uranus, Neptune and the trans-Neptunian objects were probably located initially much closer to the Sun, just beyond Jupiter and Saturn (Tsiganis et al., 2005). The interaction of the four giant planets with the numerous smaller bodies made them slowly migrate, until Jupiter and Saturn passed the $2:1$ mean-motion resonance[7]. This had very important consequences on the whole dynamical structure of the Solar System, driving Uranus and Neptune inside the Kuiper Belt up to their current orbits, and projecting many small rocky and icy bodies in every direction. That mechanism can explain the Late Heavy Bombardment, which is a resurgence of cratering events observed on the Moon (Gomes et al., 2005a). It predicts also the existence of the Oort Cloud, constituted of the icy bodies ejected very far but still bound to the gravitational attraction of the Solar System.

1.2.2 The dynamics beyond Neptune

The dynamical structure of the Solar System as it is observed now is represented schematically on Fig. 1.2. Please note that the axis ticks are not regular, and that they refer to the semi-major axes of the orbits followed by the objects. The trajectories of the planets and of the Main Belts asteroids are quite circular, so the scale gives an idea of their mutual distances. On the contrary, the orbits of the trans-Neptunian objects and of the comets can be very eccentric, so their trajectories in the physical space span a

[7] A mean-motion resonance occurs when two or more bodies follow orbits of commensurable periods, which make them always "meet" in the same configuration. Instead of cancelling out, their mutual perturbations become organised and pile up, producing important effects (stabilising or destabilising). This will be more detailed in the following.

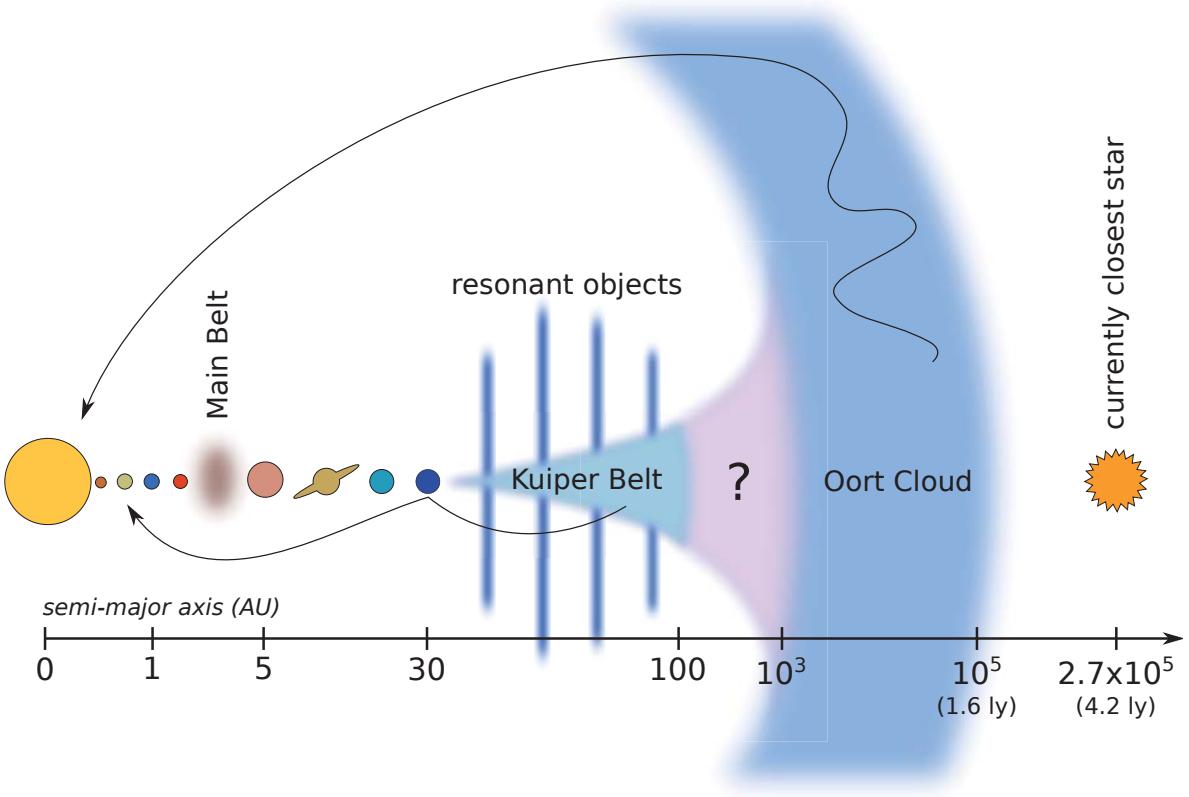

Figure 1.2 – Current dynamical structure of the Solar System as it is considered today. The bodies sizes are not to scale. The horizontal axis represents the semi-major axes of the orbits, and the vertical placement gives an idea of the inclinations. The arrows symbolise the creation of long-period comets, Centaurs and Halley-type comets. The latter two are produced from trans-Neptunian and Oort Cloud objects through close encounters with the planets.

very large range of distances (from the Sun to very remote regions). In the figure, objects as Centaurs and Halley-type comets[8] are not represented as "populations", since they are usually considered as unstable transitional orbital states.

Bodies of the Oort Cloud have so large semi-major axes that they are affected by galactic tides (that is, an acceleration from the whole Galaxy which is slightly different that the one felt by the barycentre of the Solar System). Passing stars can also have a strong influence on them, creating sporadic "comets showers" toward the planetary region if they pass close enough. As a result of these perturbations, the Oort Cloud is thought to be quite spherical, at least beyond 10^4 AU. Oort Cloud comets that have a perihelion inside the planetary region spend almost all their orbital period away, near aphelion (from Kepler's second law).

The trans-Neptunian region is usually decomposed into three main components: *i*) the Kuiper Belt, formed of objects with small inclinations and eccentricities (thus re-

[8]Centaurs and Halley-type comets can have any eccentricity and inclination but only moderate semi-major axes.

sembling the primordial population); *ii*) the Scattered Disk, composed of objects which "diffuse" chaotically in the orbital elements space due to the effect of the planets; *iii*) the resonant objects, locked in mean-motion resonances with Neptune, which can raise their inclinations to high values. Whereas the shape of the Kuiper Belt component is quite well explained by the admitted formation scenario of the Solar System (Sect. 1.2.1), the overall dynamics and past evolution of the trans-Neptunian region is still poorly understood. This holds, especially at high-perihelion distances, where it connects the Oort Cloud. This is firstly due to the lack of observational data (since it is very difficult to observe such distant objects), but also because the few observed objects have orbits which are incompatible with the formation scenario of the Solar System detailed in Sect. 1.2.1. Indeed, objects as Sedna or $2012\,VP_{113}$ have very eccentric orbits (0.85 and 0.69) but also very high perihelion distances (76 and 80 AU), which indicates that: *i*) they cannot have been formed in their current state, otherwise their orbits would be quite circular; *ii*) they are too far to have been scattered in their current position by the planets; *iii*) they are not far enough to be substantially affected by the galactic tides. Various numerical experiments showed that mean-motion resonances are also unlikely to be able to produce such orbits (Morbidelli and Levison, 2004). However, it is known from a long time by numerical ways that the secular dynamics in a mean-motion resonance can produce high-amplitude oscillations of the perihelion distance and of the inclination (see for example Gomes et al., 2005b). Consequently, the main goal of this work is to characterize and quantify that kind of mechanism by other means than statistics on the output of numerical simulations. The quite smooth nature of the numerical solutions in case of mean-motion resonance should allow the development of analytical or semi-analytical models, which could reveal, at least qualitatively, what types of trajectories are allowed.

During the course of this work, some authors put forward again the hypothesis of a still undiscovered planet orbiting in the far trans-Neptunian region (Batygin and Brown, 2016a). Indeed, the six most distant objects known appear to have roughly aligned orbits, and numerical simulations show that a distant Neptune-mass planet could produce such an accumulation. This would also explain their unexpectedly distant and eccentric orbits (though the problem would be moved toward the origin of this planet itself!). This new study, published a few days before the submission of our first paper (Saillenfest et al., 2016), caused great bustle in the planetary science community. Tens of articles about this "Planet 9" were published during the following months, dealing with its formation or capture, its effects on the known planets, its orbital stability, its current probable position, its physical characteristics, its observability... Alternative journals even discussed its astrological effects on mankind! A year later, as I am writing these lines, the initial exaltation has calmed down, but various observation campaigns are being organised to locate this hypothetical ninth planet. Even if the results were negative, this search will probably lead to the discovery of numerous trans-Neptunian objects, allowing in any case a deeper knowledge of the external Solar System. Whereas Adams and Le Verrier did predict the existence of Neptune, please remember that the Titius-Bode relation led to the discovery of the asteroids (with Ceres as false positive),

and the calculations of Lowell led to the discovery of the trans-Neptunian objects (with Pluto as a false positive).

Despite tremendous announcements made by some media, the results by Batygin and Brown (2016a) remain sufficiently vague and hypothetical (because of the scarce dataset available) to legitimate further studies of the external Solar System *without* unknown perturber. We thus used the model introduced in our first article to explore the resonant dynamics only driven by the known planets (Saillenfest et al., 2017a), and to discuss the long-term evolution of some recently-discovered trans-Neptunian objects (Saillenfest and Lari, 2017). The introduction of an external perturber, leading to a very different dynamical system, was then discussed in Saillenfest et al. (2017b).

1.3 Secular models

Several methods can be used to investigate the dynamics in a whole region of the Solar System. Even if there is no analytical representation in the general case, accurate numerical integrations (analogous to the method of Clairaut, applied by hand to compute the return date of Halley's comet) can give an insight of the solution for given initial conditions. The confrontation between the real equations and their numerical solutions, however, is always a very subtle problem... On the other hand, some suitable approximations, valid for very specific cases, are sometimes able to give good analytical representations of the solutions and lead to a deeper understanding of the problem. When the dynamics is highly chaotic, however, the numerical integration is often unavoidable, associated with stability studies (frequency analysis, Lyapounov exponents, statistical estimators, etc.). The two approaches are complementary: numerical integrations can provide an insight of the different types of possible trajectories, guiding the development of analytical theories, explaining in turns the forms of the trajectories obtained numerically (which are only discrete examples of whole varieties of orbits revealed by the analytical approach).

Secular theories are kinds of "simplified models" (introduced in Chp. 2). They are widely used in celestial mechanics because in some cases they allow to study graphically in a glance a large variety of trajectories (see for instance Morbidelli, 2002). We give here a succinct context of their applications to trans-Neptunian objects. In 1962, Kozai developed an analytical secular model for asteroids with arbitrary inclination and eccentricity. His model is designed for an external perturbing planet (namely Jupiter) and the article presents the dynamics given by the first terms of the analytical expansion. Then, Kozai (1985) added the possibility of a mean-motion resonance between the particle and its perturber and turned to semi-analytical methods. As it assumes a fixed value of the resonant angle, that second model can only be used as a rough insight of the true resonant dynamics. Thanks to the increasing power of computers, Thomas and Morbidelli (1996) used a semi-analytical approach to generalise the non-resonant model of Kozai for several planets. They presented a collection of secular level curves for semi-major axes larger than 30 AU with a special attention given to perihelion dis-

tances inside the planetary region (the collision curves appear as pinch lines). Lastly, Gallardo et al. (2012) made a thorough review of the variety of trajectories beyond Neptune. They adapted the analytical model of Kozai (1962) to a set of internal perturbing planets and used it, as well as semi-analytical methods, to describe qualitatively the non-resonant dynamics for a perihelion outside the planetary region. They also modified the semi-analytical resonant model of Kozai (1985) to deal with a more realistic sinusoidal evolution of the resonant angle. As we will see, their method is however still unsatisfactory, since the evolution of mean-motion-resonance angles in that region can actually undergo strong variations during the dynamics (centre, amplitude, frequency). Besides, these variations are unknown *a priori*. Some improvements had thus to be realised in order to take into account the precise variation of the resonant angle, so as to get accurate representations of the dynamics.

To sum up, the background for secular dynamics beyond Neptune is now well established but the analyses found in the literature remained vague and qualitative. Since quasi-integrable motions beyond Neptune are known to be responsible for large variations of orbital elements (through mean-motion resonances and Kozai mechanism), a special effort has to be deployed to construct secular models, designed to explore in a straightforward way all the possible regular orbits. For instance, it could help to determine in a categorical way how far the known planets can raise the perihelion distances of small bodies, or if that kind of dynamics could explain the distribution of the observed distant objects. In this line of thinking, our first goals were to provide a thorough analysis of the non-resonant case and to develop an accurate resonant secular model[9]. In the non-resonant case, the introduction of a distant massive planet will be presented in Chp. 5.

[9]To prevent any confusion in the following, please note that we will not deal with so-called "secular resonances". What we call here a "resonant secular model" is a secular model that takes into account a mean-motion resonance between the particle and one of the planets.

Chapter 2

Theoretical background

This chapter is designed to get that work as self-explanatory as possible and readable also by non-specialists. Any required theoretical concept is thus introduced briefly, from the two-body problem (Sect. 2.1) to Hamiltonian systems (Sect. 2.2) and the Lie-series formalism (Sect. 2.3). These notes can also be used as a memory aid throughout the reading. Naturally, the reader only interested by "new" results can directly jump to Chp. 3.

This chapter is based mainly on my master courses, in particular in Paris Observatory: *Gravitation* by J. Souchay, *Systèmes hamiltoniens* by P. Robutel, *Géométrie des systèmes hamiltoniens* by J. Féjoz, and in Pisa University: *Dinamica del sistema solare* by A. Milani. The lessons by L. Duriez and A. Milani in the book *Modern methods in celestial mechanics* (Éditions Frontières 1990) allowed to add complementary explanations.

2.1 The two-body problem

That problem was stated and solved by Newton around 1680. It gave a mathematical justification of Kepler's empirical laws and led to a revolution of celestial mechanics (see Sect. 1.1). The classic method of resolution and the corresponding set of variables are widely used throughout this work, so it seems necessary to recall them succinctly.

2.1.1 Analytical solution

We consider two isolated point bodies[1], with masses (m_1, m_2) and positions $(\mathbf{r}_1, \mathbf{r}_2)$ in a three-dimensional inertial reference system. Their respective accelerations are governed by the gravitational force only, leading to the equations of motion (fundamental

[1] As long as there is no contact between them, two homogeneous (or layered) spherical bodies can be considered as well, since they produce the same external gravitational field as a point gathering all the mass (as shown by Newton in 1685).

principle of dynamics):

$$m_1\ddot{\mathbf{r}}_1 = -\mathcal{G}m_1m_2\frac{\mathbf{r}_1-\mathbf{r}_2}{|\mathbf{r}_1-\mathbf{r}_2|^3} \quad \text{and} \quad m_2\ddot{\mathbf{r}}_2 = -\mathcal{G}m_2m_1\frac{\mathbf{r}_2-\mathbf{r}_1}{|\mathbf{r}_2-\mathbf{r}_1|^3} \tag{2.1}$$

where $\mathcal{G}$ is the gravitational constant. Knowing the positions and velocities of the two particles at a given time t_0, we are looking for the expression of $\mathbf{r}_1$ and $\mathbf{r}_2$ as functions of the time t. This is a Cauchy problem with 12 dimensions. The classical resolution consists in using the constants of motion, also called *first integrals*, to reduce the number of dimensions of the problem. By definition, the barycentre $\mathbf{r}_0$ of the two bodies writes:

$$(m_1+m_2)\mathbf{r}_0 = m_1\mathbf{r}_1 + m_2\mathbf{r}_2 \tag{2.2}$$

and from (2.1) we get $\ddot{\mathbf{r}}_0 = \mathbf{0}$. Hence, the barycentre $\mathbf{r}_0$ follows a rectilinear motion with constant velocity:

$$\mathbf{r}_0 = \mathbf{a}\,t + \mathbf{b} \tag{2.3}$$

where $\mathbf{a}$ and $\mathbf{b}$ are two constant vectors directly obtained from the initial conditions. We can take advantage of these 6 first integrals by considering only the *relative* position of the two bodies $\mathbf{r} = \mathbf{r}_2 - \mathbf{r}_1$ (or equivalently $\mathbf{r}_1 - \mathbf{r}_2$). Indeed, $(\mathbf{r}_0, \mathbf{r})$ is equivalent to $(\mathbf{r}_1, \mathbf{r}_2)$ from the equation (2.2) and $\mathbf{r}_0$ is a known function of the time. By (2.1), we obtain straightforwardly:

$$\ddot{\mathbf{r}} = -\mu\frac{\mathbf{r}}{|\mathbf{r}|^3} \tag{2.4}$$

where $\mu = m_1+m_2$. This new problem has 6 dimensions, that is 6 less than the original system.

Another way to reduce the system is to use a barycentric reference frame, that is the new coordinates $(\mathbf{q}_1, \mathbf{q}_2) = (\mathbf{r}_1 - \mathbf{r}_0\,, \mathbf{r}_2 - \mathbf{r}_0)$. From the equation (2.3), such a reference frame is *inertial*, so the equations of motion in the new coordinates remain unchanged. This time, though, the direct link:

$$\mathbf{q}_1 = -\frac{m_2}{m_1}\mathbf{q}_2 \tag{2.5}$$

implies that it is enough to study the motion of only one particle, say $\mathbf{q}_2$. Introducing (2.5) in (2.1), we obtain:

$$\ddot{\mathbf{q}}_2 = -\mu_b\frac{\mathbf{q}_2}{|\mathbf{q}_2|^3} \tag{2.6}$$

with $\mu_b = \mathcal{G}\,m_1^3/(m_1+m_2)^2$. This equation is the same as in the case of the relative motion (2.4), so the resolution is generic. In the following, $(\mathbf{r}, \mu)$ could thus be replaced by $(\mathbf{q}_2, \mu_b)$. Please note that if one mass (say m_2) is negligible with respect to the other, the barycentric and relative motions are equivalent ($\mathbf{q}_2 = \mathbf{r}$ and $\mu = \mu_b = \mathcal{G}m_1$).

From the equation of motion (2.4), we get:

$$\dot{\mathbf{r}}\cdot\ddot{\mathbf{r}} + \mu\frac{\mathbf{r}}{|\mathbf{r}|^3}\cdot\dot{\mathbf{r}} = 0 \iff \frac{\mathrm{d}}{\mathrm{d}t}\left(\frac{1}{2}\,\dot{\mathbf{r}}^2 - \frac{\mu}{|\mathbf{r}|}\right) = 0 \tag{2.7}$$

thus revealing a new constant of motion, namely the energy per unit of mass. It writes:

$$h = \frac{1}{2}\,\dot{\mathbf{r}}^2 - \frac{\mu}{|\mathbf{r}|} \tag{2.8}$$

and is determined by the initial conditions. In order to go further in the resolution, let us introduce the angular momentum per unit of mass $\mathbf{C} = \mathbf{r} \times \dot{\mathbf{r}}$. This is a constant vector, since from (2.4):

$$\dot{\mathbf{C}} = \dot{\mathbf{r}} \times \dot{\mathbf{r}} + \mathbf{r} \times \left(-\mu \frac{\mathbf{r}}{|\mathbf{r}|^3}\right) = \mathbf{0} \tag{2.9}$$

Given that $\mathbf{C}$ is perpendicular to $\mathbf{r}$ and $\dot{\mathbf{r}}$ (by the definition of the cross product), its constancy implies that the motion takes place in a plane[2]. Consequently, we can use a system of coordinates such that the third component of $\mathbf{r}$ is always zero. Starting from an arbitrary system of coordinates, this is realised by a simple rotation (see the following section). Using polar coordinates (r, θ) for the first two components of $\mathbf{r}$, the energy integral becomes:

$$h = \frac{1}{2}\,\dot{r}^2 + \frac{1}{2}\,r^2\dot{\theta}^2 - \frac{\mu}{r} \tag{2.10}$$

Considering that the (conserved) norm of $\mathbf{C}$ writes $C = r^2\dot{\theta}$, we can now reduce the system to only one degree of freedom:

$$h = \frac{1}{2}\,\dot{r}^2 + \frac{1}{2}\,\frac{C^2}{r^2} - \frac{\mu}{r} \tag{2.11}$$

Incidentally, one can note that the conservation of C implies naturally the second law of Kepler[3]. The geometry of the trajectory, dropping for now the temporal information, would be given by r as a function of θ. At this point a famous trick consists in replacing r in (2.11) by the variable:

$$u = \frac{C^2}{\mu}\frac{1}{r} - 1 \tag{2.12}$$

assuming that C is different from 0. Indeed we have:

$$\frac{\mathrm{d}u}{\mathrm{d}\theta} = \frac{\mathrm{d}u}{\mathrm{d}r}\frac{\mathrm{d}r}{\mathrm{d}t}\frac{\mathrm{d}t}{\mathrm{d}\theta} = -\frac{C^2}{\mu}\frac{\dot{r}}{r^2\dot{\theta}} = -\frac{C}{\mu}\dot{r} \tag{2.13}$$

such that the equation (2.11) becomes:

$$\left(\frac{\mathrm{d}u}{\mathrm{d}\theta}\right)^2 + u^2 = 1 + 2\frac{C^2 h}{\mu^2} \tag{2.14}$$

[2]We will not consider the case $\mathbf{C} = \mathbf{0}$. It corresponds to a degenerate rectilinear motion.

[3]Indeed, the area swept out by $\mathbf{r}$ in a duration $\Delta t = t_2 - t_1$ is equal to $\mathcal{A} = \int_{t_1}^{t_2} r \cdot r\dot{\theta}\,\mathrm{d}t = \int_{t_1}^{t_2} C\,\mathrm{d}t = C\Delta t$. For a same time span Δt, the area $\mathcal{A}$ is thus the same.

in which the right-hand term is non-negative. The equation (2.14) has the obvious general solution $u(\theta) = e\cos(\theta - \theta_0)$, where the constant θ_0 is given by the initial conditions and with:

$$e = \sqrt{1 + 2\frac{C^2 h}{\mu^2}} \tag{2.15}$$

Noting $\nu = \theta - \theta_0$, the expression of r is finally obtained from (2.12):

$$r(\nu) = \frac{p}{1 + e\cos\nu} \tag{2.16}$$

where $p = C^2/\mu$ and the angle ν is called the "real anomaly". This is the polar equation of a conic, with parameter p and eccentricity e. The value of e governs the geometric type of the trajectory, namely a circle ($e = 0$), an ellipse ($0 < e < 1$), a parabola ($e = 1$) or a hyperbola ($e > 1$). This proves the first law of Kepler.

In the following, we will consider the bounded case ($e < 1$), that is when the two bodies cannot go to infinity with respect to each other. We can note that in (2.16), the origin of the coordinate system (that is, the body 1 or the barycentre) is located at one of the two focusses of the conic. In celestial mechanics, it is more common to parametrise the ellipse by its semi-major axis a, given by the relation $p = a(1 - e^2)$. It is directly linked to the energy integral, since from (2.15) we get:

$$C^2/\mu = a(1 - e^2) \iff h = -\frac{\mu}{2a} \tag{2.17}$$

The semi-major axis being defined positive (as $p > 0$ and $0 \leqslant e < 1$), we see that the energy integral is negative in the bounded case. Along the trajectory, the points of the closest and farthest approaches of the two bodies are called the "pericentre" and "apocentre" (or perihelion and aphelion for a motion relative to the Sun). They are reached respectively for $\nu = 0$ and π. The corresponding distances, generally noted q and Q, can be directly obtained from $r(\nu)$:

$$q = a(1 - e) \qquad \text{and} \qquad Q = a(1 + e) \tag{2.18}$$

Although (2.16) gives the *shape* of the trajectories, we still do not have the solution as a function of the time. The next step is thus to determine an expression for the real anomaly $\nu(t)$. This is realised through an intermediary angle called the "eccentric anomaly" E. Let us consider the circle of radius a with the same centre as the ellipse, such that their only contact points are q and Q. Let $P = (r(\nu), \nu)$ be a point on the ellipse. Then, the eccentric anomaly of P is defined as the polar angle measured around the *centre* of the ellipse (instead of its focus) of the vertical projection of P on the circle[4]. That projection is obtained in a natural way by considering that the circle is a vertical dilation of the ellipse by a factor $1/\sqrt{1 - e^2}$. We show easily that:

$$r = a\,(1 - e\cos E) \tag{2.19}$$

[4]The introduction of the angle E is not as far-fetched as it could appear. Indeed, the description of a point moving on a circle *should be* simpler than on an ellipse. Moreover, it corresponds to the real motion of the particle if $e = 0$, since in that case $\nu = E$.

and by mixing (2.16) and (2.19) we get:

$$\frac{\mathrm{d}\nu}{\mathrm{d}E} = \frac{a}{r}\sqrt{1-e^2} \tag{2.20}$$

This is also recoverable from the direct relation between E and ν:

$$\tan\left(\frac{\nu}{2}\right) = \sqrt{\frac{1+e}{1-e}}\tan\left(\frac{E}{2}\right) \tag{2.21}$$

The temporal information can be introduced by the conservation of the angular momentum, since:

$$C = r^2\dot{\theta} = r^2\dot{\nu} = r^2\frac{\mathrm{d}\nu}{\mathrm{d}E}\dot{E} = a^2\sqrt{1-e^2}(1-e\cos E)\dot{E} \tag{2.22}$$

That expression can be integrated to give:

$$Ct = a^2\sqrt{1-e^2}(E - e\sin E) + const. \iff E - e\sin E = n(t-t_0) \tag{2.23}$$

where t_0 is function of the initial conditions and corresponds to the instant of the last passage at pericentre. The constant n is called the "mean motion" and it writes:

$$n = \frac{C}{a^2\sqrt{1-e^2}} = \sqrt{\frac{\mu}{a^3}} \tag{2.24}$$

This expression naturally implies the third law of Kepler[5]. The mean motion represents the constant frequency of the angle:

$$M = E - e\sin E \tag{2.25}$$

known as the "mean anomaly". The expression of M in terms of E is historically called "Kepler's equation". Its gives in particular the useful relations:

$$\frac{\mathrm{d}M}{\mathrm{d}E} = \frac{r}{a} \quad \text{and thus} \quad \frac{\mathrm{d}M}{\mathrm{d}\nu} = \frac{r^2}{a^2\sqrt{1-e^2}} \tag{2.26}$$

Through (2.25) and (2.21), the explicit expression of the mean anomaly $M(t) = n(t-t_0)$ allows to obtain the true anomaly ν at any time t (the equation 2.25 is implicit, though, and requires an iterative procedure, see appendix C.1). This closes the resolution of the bounded two-body problem.

[5]Indeed, the rotation period of the body is given by $T = 2\pi/n = (2\pi/\sqrt{\mu})a^{3/2}$. Considering that the masses of the planets are negligible compared to the Sun's (the difference was undistinguishable given the precision of the observations used by Kepler), their heliocentric two-body motion is obtained using $\mu = \mathcal{G}(m_p + m_\odot) \approx \mathcal{G}m_\odot$, leading to a constant quantity T^2/a^3 among the planets.

2.1.2 The Keplerian elements

We saw that the trajectories in the bounded two-body problem are ellipses, and we obtained the position of the considered body along its ellipse as a function of time. Hence, the motion in the plane of the trajectory is entirely determined. It writes $(r(\nu)\cos\nu,\ r(\nu)\sin\nu,\ 0)$ in Cartesian coordinates. However, it is more useful in practice to describe it in an arbitrarily oriented reference frame. Since the two coordinate systems have the same origin, the passage from one to the other is a rotation, decomposable as three elementary rotations. Several combinations of angles are possible. The most commonly used in celestial mechanics is presented in Fig. 2.1 and corresponds to the 313 combination.

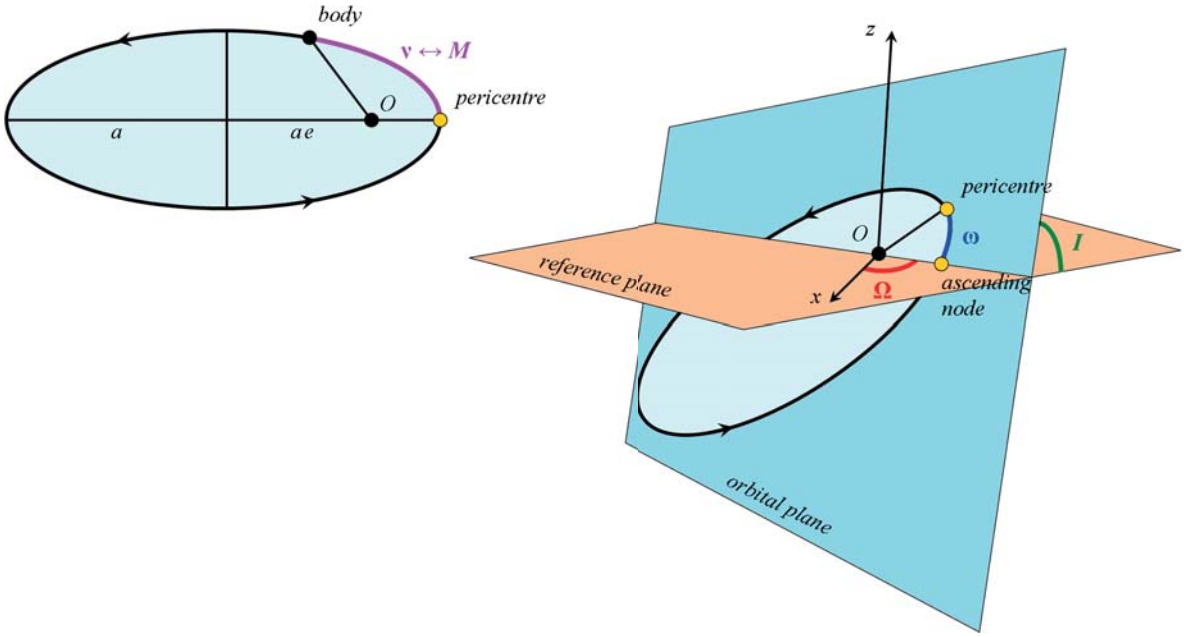

Figure 2.1 – Traditional orbital elements in the mutual or barycentric reference frame (in which the focal point O of the ellipse is the position of the second body, or the position of the mutual barycentre of the two bodies, respectively). Two parameters describe the shape of the ellipse: the semi-major axis a and the eccentricity e. One angle gives the position of the particle *on* the ellipse (the true anomaly ν, related to the mean anomaly M), and three angles represent the position *of* the ellipse in a three-dimensional reference frame centred on O (the inclination I, the longitude of ascending node Ω and the argument of pericentre ω).

The angle I is called the "inclination", whereas Ω and ω are respectively the "longitude of ascending node" and the "argument of pericentre". They cover all the possible configurations by setting $I \in [0, \pi]$ and $\Omega, \omega \in [0, 2\pi]$. In the arbitrarily oriented reference frame, the position of the body writes finally:

$$\mathbf{r} = \mathrm{R}_3(\Omega)\,\mathrm{R}_1(I)\,\mathrm{R}_3(\omega) \begin{pmatrix} r(\nu)\cos\nu \\ r(\nu)\sin\nu \\ 0 \end{pmatrix} \tag{2.27}$$

By computing explicitly the products of the three rotation matrices, we obtain:

$$\mathbf{r} = r(\nu) \begin{pmatrix} \cos(\omega+\nu)\cos\Omega - \sin(\omega+\nu)\sin\Omega\cos I \\ \cos(\omega+\nu)\sin\Omega + \sin(\omega+\nu)\cos\Omega\cos I \\ \sin(\omega+\nu)\sin I \end{pmatrix} \tag{2.28}$$

with:

$$|\mathbf{r}| = r(\nu) = \frac{a\,(1-e^2)}{1+e\cos\nu} \tag{2.29}$$

The complete set of orbital elements, defining unequivocally the position of the two bodies at a time t in an arbitrary reference frame centred on the second body (or on the two-body barycentre), is finally given by $(a, e, I, \omega, \Omega, M)$. Here, the real anomaly is seen as an implicit function $\nu(E(M,e), e)$ of the mean anomaly M via (2.21) and (2.25). Of course, the mean anomaly can be equivalently replaced by E or ν, or by the time t_0 of last passage at perihelion (see Sect. 2.1.1).

This set of orbital elements is singular for $I = 0$ (Ω and ω are ill-defined) and for $e = 0$ (ω and M are ill-defined). They are only singularities of the coordinates used, though, with no dynamical meaning. In the zero-inclination case, Ω and ω bring a redundant information, so they can be replaced by the angle $\varpi = \omega + \Omega$ called the "longitude of pericentre". This removes the singularity. In the same way, M and ω can be replaced by $M + \omega$ in the circular case. Finally, Ω, ω and M should be replaced by the "mean longitude" $\lambda = \omega + \Omega + M$ in the zero-inclination circular case. In order to allow a generic treatment, a complete non-singular set of coordinates is sometimes required, such as the "equinoctial elements":

$$a \quad ; \quad \lambda \quad ; \quad z = e\exp(i\,\varpi) \quad ; \quad \zeta = \sin\frac{I}{2}\exp(i\,\Omega) \tag{2.30}$$

In that formulation, z and ζ are complex numbers ($i = \sqrt{-1}$). The equinoctial elements are regular whatever the bounded orbit considered. They are useful for instance to deal with a large number of orbits without the necessity to study particular cases. For a generic orbit, though, they are much less self-explanatory than the classic Keplerian elements.

2.1.3 Osculating elements

In Sect. 2.1.1, we presented the analytical solution of the two-body problem. Numerous integration constants appeared through the successive steps of the resolution and were structured in the form of the Keplerian elements (Sect. 2.1.2). However, their link toward the initial conditions $(t, \mathbf{r}, \dot{\mathbf{r}})$ is still far from obvious. Following Duriez (1990), we summarise here the general procedure. Each step can be recovered from the resolution presented above.

The position and velocity are supposed already written in the suitable reference frame (relative or barycentric, with the corresponding μ constant). As before, we will

consider here only the bounded non-collisional case ($h < 0$ and $C \neq 0$). We will also suppose that I and e are different from zero (to avoid the singularities of the usual Keplerian elements). From the energy and angular momentum integrals:

$$h = \frac{1}{2}\,\dot{\mathbf{r}}^2 - \frac{\mu}{r} \quad ; \quad \mathbf{C} = \mathbf{r} \times \dot{\mathbf{r}} \tag{2.31}$$

we get the semi-major axis $a = -\mu/(2h)$ and the eccentricity $e = \sqrt{1 - C^2/(\mu a)}$. If it is small, the numerical errors of cancellation can be reduced by using the equivalent form:

$$e = \sqrt{\left(1 - \frac{r}{a}\right)^2 + \frac{(\mathbf{r} \cdot \dot{\mathbf{r}})^2}{\mu a}} \tag{2.32}$$

Since $\mathbf{C}$ is perpendicular to the plane of the trajectory, its direction gives directly the longitude of ascending node Ω and the inclination I. Indeed, it writes:

$$\mathbf{C} = \begin{pmatrix} C_x \\ C_y \\ C_z \end{pmatrix} = C \begin{pmatrix} \sin\Omega \sin I \\ -\cos\Omega \sin I \\ \cos I \end{pmatrix} \tag{2.33}$$

which gives $\Omega = \text{atan2}(-C_y, C_x)$ and $I = \text{acos}(C_z/C)$. If it is near 0 or π, the inclination is better computed numerically by the equivalent form:

$$I = \text{atan2}\left(\sqrt{C_x^2 + C_y^2}\,,\, C_z\right) \tag{2.34}$$

On the other hand, the argument of perihelion ω can be obtained by using the "eccentricity vector", which is another constant vector intrinsic to the two-body problem, pointing towards the pericentre of the trajectory. It writes:

$$\mathbf{e} = \frac{1}{\mu}\dot{\mathbf{r}} \times \mathbf{C} - \frac{\mathbf{r}}{r} \tag{2.35}$$

and its norm is equal to the eccentricity e. Expressed in Keplerian elements, its components are thus:

$$\mathbf{e} = \begin{pmatrix} e_x \\ e_y \\ e_z \end{pmatrix} = e \begin{pmatrix} \cos\omega\cos\Omega - \sin\omega\sin\Omega\cos I \\ \cos\omega\sin\Omega + \sin\omega\cos\Omega\cos I \\ \sin\omega\sin I \end{pmatrix} \tag{2.36}$$

which gives $\omega = \text{atan2}(Ce_z\ ,\ C_x e_y - C_y e_x)$. To complete the set of Keplerian elements, it only remains to compute the mean anomaly M. It is given via the eccentric anomaly:

$$\begin{cases} e\cos E = 1 - \dfrac{r}{a} \\ e\sin E = \dfrac{\mathbf{r}\cdot\dot{\mathbf{r}}}{\sqrt{\mu a}} \end{cases} \implies E = \text{atan2}\left(\frac{\mathbf{r}\cdot\dot{\mathbf{r}}}{\sqrt{\mu a}}\ ,\ 1 - \frac{r}{a}\right) \tag{2.37}$$

and through Kepler's equation: $M = E - e \sin E$. At the time t considered, we have thus finally the orbital elements $(a, e, I, \omega, \Omega, M)$ which are equivalent to the Cartesian vectors $(\mathbf{r}, \dot{\mathbf{r}})$.

Naturally, these elements are only valid in the strict two-body problem, which could appear of little interest in celestial mechanics. However, a large variety of gravitational systems are hierarchical, either in terms of the masses or of the distances involved. The more obvious example is the case of the Solar System, in which the Sun gathers about 99.9% of the total mass. The trajectories of the other bodies, as planets and asteroids, are thus largely dominated by a "two-body component" with the Sun. In that case, we can still use the previous equations (that is, putting aside the contribution of other bodies), but considering the Keplerian elements as *instantaneous quantities* instead of integration constants. Indeed, the vectors $\mathbf{r}$ and $\dot{\mathbf{r}}$ define unequivocally the six Keplerian elements of a two-body problem, even if there are actually more bodies in the system. Such elements are called "osculating" because, strictly speaking, they represent the true motion of the particle only in a vanishingly small interval of time around the instant t considered. Nevertheless, if the system is indeed a weakly-perturbed two-body problem, the osculating Keplerian elements still give a plain approximation of the trajectory in a close past or future. They are thus much more meaningful than a set of Cartesian coordinates $(\mathbf{r}, \dot{\mathbf{r}})$. The time evolution of the vector of orbital elements $(a, e, I, \omega, \Omega, M)$ can be obtained directly from the dynamical equations, using the planetary equations of Lagrange (for a force deriving from a potential) or Gauss (directly in terms of the force). Another approach, using the Hamiltonian formalism, is described in Sect. 2.2.6.

Osculating Keplerian elements can also be used in a very perturbed problem, in which the trajectories have nothing in common with ellipses. In that case, though, they loose their principal virtue and they may even be very misleading. Consider for instance a trajectory for which the mean anomaly M oscillate around 0 instead of being linear with time: this means that the two bodies stay always at pericentre!

2.2 Notions of Hamiltonian formalism

2.2.1 Hamilton's equations

A Hamiltonian system with n degrees of freedom is a dynamical system entirely described by a function:

$$\mathcal{H} \ : \ \mathbf{Q}, \mathbf{q}, t \in \mathbb{R}^n \times \mathbb{R}^n \times \mathbb{R} \ \longmapsto \ \mathbb{R} \tag{2.38}$$

at least of class $\mathcal{C}^2$, called the *Hamiltonian*[6]. In that expression, $\mathbf{Q}$ and $\mathbf{q}$ are said to be "canonical coordinates" if their evolution is governed by Hamilton's equations:

$$\begin{cases} \dfrac{\mathrm{d}\mathbf{Q}}{\mathrm{d}t} = -\dfrac{\partial \mathcal{H}}{\partial \mathbf{q}}(\mathbf{Q}, \mathbf{q}, t) \\ \dfrac{\mathrm{d}\mathbf{q}}{\mathrm{d}t} = \dfrac{\partial \mathcal{H}}{\partial \mathbf{Q}}(\mathbf{Q}, \mathbf{q}, t) \end{cases} \tag{2.39}$$

where $\partial\mathcal{H}/\partial\mathbf{q}$ stands for the column vector $(\,\partial\mathcal{H}/\partial q_1\,,\,\partial\mathcal{H}/\partial q_2 \,...\, \partial\mathcal{H}/\partial q_n\,)^{\mathrm{T}}$. At a time t, the state of the system is completely determined by $\mathbf{q}(t) \in \mathbb{R}^n$ (the position) and $\mathbf{Q}(t) \in \mathbb{R}^n$ (the vector of conjugate momenta). The power of the Hamiltonian formalism is that $\mathbf{q}$ and $\mathbf{Q}$ can be very distant from conventional coordinates (say the Cartesian position and velocity), but allow a description of the dynamics in a much simpler form. In simple words, the resolution of a Hamiltonian system consists in finding the coordinates in which it is "trivially" solvable (or at least, in which some information on the dynamics can be obtained).

In a Hamiltonian system, the time derivative of any function of the coordinates $f(\mathbf{Q}, \mathbf{q}, t)$ can be written in terms of Hamilton's equations, since by using the chain rule:

$$\begin{aligned} \frac{\mathrm{d}f}{\mathrm{d}t} &= \frac{\partial f}{\partial \mathbf{q}} \cdot \frac{\mathrm{d}\mathbf{q}}{\mathrm{d}t} + \frac{\partial f}{\partial \mathbf{Q}} \cdot \frac{\mathrm{d}\mathbf{Q}}{\mathrm{d}t} + \frac{\partial f}{\partial t} \\ &= \frac{\partial f}{\partial \mathbf{q}} \cdot \frac{\partial \mathcal{H}}{\partial \mathbf{Q}} - \frac{\partial f}{\partial \mathbf{Q}} \cdot \frac{\partial \mathcal{H}}{\partial \mathbf{q}} + \frac{\partial f}{\partial t} \\ &= \{f, \mathcal{H}\} + \frac{\partial f}{\partial t} \end{aligned} \tag{2.40}$$

where we introduced the Poisson's brackets $\{\,,\}$. For the Hamiltonian itself, in particular, we have $\{\mathcal{H}, \mathcal{H}\} = 0$, so that:

$$\frac{\mathrm{d}\mathcal{H}}{\mathrm{d}t} = \frac{\partial \mathcal{H}}{\partial t} \tag{2.41}$$

The Poisson's bracket gives another definition of canonical coordinates, as verifying:

$$\{q_i, Q_j\} = \delta_{ij} \quad ; \quad \{Q_i, Q_j\} = 0 \quad ; \quad \{q_i, q_j\} = 0 \qquad \text{for each } i, j = 1, 2...n \tag{2.42}$$

which is equivalent to satisfy (2.39).

A Hamiltonian system is called "autonomous" if the Hamiltonian does not depend explicitly on the time t. Any non-autonomous Hamiltonian system with n degrees of freedom can be written in terms of an autonomous Hamiltonian system with $n + 1$ degrees of freedom. Indeed, starting from a Hamiltonian $\mathcal{H}(\mathbf{Q}, \mathbf{q}, t)$, we can use the new set of canonical coordinates:

$$\mathbf{Q}' = \begin{pmatrix} \mathbf{Q} \\ T \end{pmatrix} \quad ; \quad \mathbf{q}' = \begin{pmatrix} \mathbf{q} \\ t \end{pmatrix} \tag{2.43}$$

[6]It is often written $\mathcal{H}$, following Lagrange who used that character in honour of the Dutch astronomer Huygens.

and the new Hamiltonian function:

$$\mathcal{H}'(\mathbf{Q}', \mathbf{q}') = \mathcal{H}(\mathbf{Q}, \mathbf{q}, t) + T \tag{2.44}$$

The momentum $Q'_{n+1} = T$ is conjugate to $q'_{n+1} = t$, such that:

$$\frac{\mathrm{d}Q'_{n+1}}{\mathrm{d}t} = -\frac{\partial \mathcal{H}}{\partial t} \quad \text{and} \quad \frac{\mathrm{d}q'_{n+1}}{\mathrm{d}t} = 1 \tag{2.45}$$

This results in the constancy of $\mathcal{H}'$ along the trajectory (since its partial derivative with respect to the time is zero, see Eq. 2.41). The initial condition of T is arbitrary, but, considering an initial condition $(\mathbf{Q}_0, \mathbf{q}_0, t_0)$ of the original system, a usual choice is to take $T(t_0) = \mathcal{H}(\mathbf{Q}_0, \mathbf{q}_0, t_0)$ which gives zero for the constant value of $\mathcal{H}'$.

Depending on the problem under study, a more sophisticated expression for q'_{n+1} can be chosen, in order to allow a simpler expression of $\mathcal{H}'$. Later in this work, for instance, we will use a linear function of the time.

2.2.2 Time regularisation

The basic principle of time-regularisation methods is to replace the time t by a pseudo time τ, expressed in terms of the dynamical variables, with the aim of getting simpler equations of motion. For an initial set of canonical coordinates $(\mathbf{Q}, \mathbf{q}) \in \mathbb{R}^n \times \mathbb{R}^n$ with the general Hamiltonian $\mathcal{H}(\mathbf{Q}, \mathbf{q}, t)$, the chosen definition of the new time τ has the form:

$$\frac{\mathrm{d}t}{\mathrm{d}\tau} = \kappa(\mathbf{Q}, \mathbf{q}) \tag{2.46}$$

in which the function κ is at least $\mathcal{C}^2$ in its variables (as the Hamiltonian). If κ does not depend on the coordinates (so that it is a constant scaling factor), the Hamiltonian giving rise to equivalent dynamical equations as the initial system, but using the regularised time τ, is simply:

$$\mathcal{M}(\mathbf{Q}, \mathbf{q}) = \kappa \mathcal{H}(\mathbf{Q}, \mathbf{q}) \tag{2.47}$$

Indeed, we have:

$$\begin{cases} \dfrac{\mathrm{d}\mathbf{q}}{\mathrm{d}\tau} = \dfrac{\partial \mathcal{M}}{\partial \mathbf{Q}} \\ \dfrac{\mathrm{d}\mathbf{Q}}{\mathrm{d}\tau} = -\dfrac{\partial \mathcal{M}}{\partial \mathbf{q}} \end{cases} \quad \text{with} \quad \begin{cases} \dfrac{\mathrm{d}\mathbf{q}}{\mathrm{d}\tau} = \dfrac{\mathrm{d}\mathbf{q}}{\mathrm{d}t}\dfrac{\mathrm{d}t}{\mathrm{d}\tau} = \kappa \dfrac{\mathrm{d}\mathbf{q}}{\mathrm{d}t} \\ \dfrac{\mathrm{d}\mathbf{Q}}{\mathrm{d}\tau} = \dfrac{\mathrm{d}\mathbf{Q}}{\mathrm{d}t}\dfrac{\mathrm{d}t}{\mathrm{d}\tau} = \kappa \dfrac{\mathrm{d}\mathbf{Q}}{\mathrm{d}t} \end{cases} \tag{2.48}$$

so that, as expected:

$$\begin{cases} \dfrac{\mathrm{d}\mathbf{q}}{\mathrm{d}t} = \dfrac{1}{\kappa}\dfrac{\partial \mathcal{M}}{\partial \mathbf{Q}} = \dfrac{1}{\kappa}\dfrac{\partial(\kappa\mathcal{H})}{\partial \mathbf{Q}} = \dfrac{\partial \mathcal{H}}{\partial \mathbf{Q}} \\ \dfrac{\mathrm{d}\mathbf{Q}}{\mathrm{d}t} = -\dfrac{1}{\kappa}\dfrac{\partial \mathcal{M}}{\partial \mathbf{q}} = -\dfrac{1}{\kappa}\dfrac{\partial(\kappa\mathcal{H})}{\partial \mathbf{q}} = -\dfrac{\partial \mathcal{H}}{\partial \mathbf{q}} \end{cases} \tag{2.49}$$

Much more interesting transformations, of course, are obtained when κ depends on the coordinates $\mathbf{Q}$ and/or $\mathbf{q}$. In that case, the classic method, in order to obtain an equivalent dynamical system in the regularised time τ, is to firstly add the time t as a new canonical coordinate along with its conjugate momentum T. That method was introduced in Sect. 2.2.1 to deal with non-autonomous systems: here it is required *even if* the system is autonomous. Instead of $\mathcal{H}$, we thus initially consider the Hamiltonian:

$$\mathcal{K}(\mathbf{Q}, T, \mathbf{q}, t) = \mathcal{H}(\mathbf{Q}, \mathbf{q}, t) + T \tag{2.50}$$

in which, for now, the initial value of T is arbitrary. It produces the same dynamical equations as $\mathcal{H}$ (see Sect. 2.2.1). As before, the dynamical system using the regularised time τ is obtained by using the Hamiltonian:

$$\mathcal{M}(\mathbf{Q}, T, \mathbf{q}, t) = \kappa(\mathbf{Q}, \mathbf{q})\, \mathcal{K}(\mathbf{Q}, T, \mathbf{q}, t) = \kappa(\mathbf{Q}, \mathbf{q}) \left(\mathcal{H}(\mathbf{Q}, \mathbf{q}, t) + T \right) \tag{2.51}$$

This time, though, the equivalence of this dynamical system and the initial one is not guaranteed in the general case. Indeed, we have:

$$\begin{cases} \dfrac{\mathrm{d}\mathbf{q}}{\mathrm{d}t} = \dfrac{1}{\kappa}\dfrac{\partial \mathcal{M}}{\partial \mathbf{Q}} = \dfrac{1}{\kappa}\dfrac{\partial(\kappa\mathcal{K})}{\partial \mathbf{Q}} = \dfrac{1}{\kappa}\left(\dfrac{\partial \kappa}{\partial \mathbf{Q}}\mathcal{K} + \kappa \dfrac{\partial \mathcal{K}}{\partial \mathbf{Q}} \right) = \dfrac{\partial \mathcal{K}}{\partial \mathbf{Q}} + \dfrac{1}{\kappa}\dfrac{\partial \kappa}{\partial \mathbf{Q}}\mathcal{K} \\ \dfrac{\mathrm{d}\mathbf{Q}}{\mathrm{d}t} = -\dfrac{1}{\kappa}\dfrac{\partial \mathcal{M}}{\partial \mathbf{q}} = -\dfrac{1}{\kappa}\dfrac{\partial(\kappa\mathcal{K})}{\partial \mathbf{q}} = -\dfrac{1}{\kappa}\left(\dfrac{\partial \kappa}{\partial \mathbf{q}}\mathcal{K} + \kappa \dfrac{\partial \mathcal{K}}{\partial \mathbf{q}} \right) = -\dfrac{\partial \mathcal{K}}{\partial \mathbf{q}} - \dfrac{1}{\kappa}\dfrac{\partial \kappa}{\partial \mathbf{q}}\mathcal{K} \end{cases} \tag{2.52}$$

Using the expression (2.50) of $\mathcal{K}$, we thus obtain:

$$\begin{cases} \dfrac{\mathrm{d}\mathbf{q}}{\mathrm{d}t} = \dfrac{\partial \mathcal{H}}{\partial \mathbf{Q}} + \dfrac{1}{\kappa}\dfrac{\partial \kappa}{\partial \mathbf{Q}}(\mathcal{H} + T) \\ \dfrac{\mathrm{d}\mathbf{Q}}{\mathrm{d}t} = -\dfrac{\partial \mathcal{H}}{\partial \mathbf{q}} - \dfrac{1}{\kappa}\dfrac{\partial \kappa}{\partial \mathbf{q}}(\mathcal{H} + T) \end{cases} \tag{2.53}$$

Here, the crucial introduction of the variable T becomes obvious. Indeed, we retrieve the original equations only if at any time t (or pseudo time τ), we have the relation:

$$\mathcal{K} = \mathcal{H} + T = 0 \tag{2.54}$$

In the new coordinates, the evolution of the real time and its conjugate momentum is governed by:

$$\begin{cases} \dfrac{\mathrm{d}t}{\mathrm{d}\tau} = \dfrac{\partial \mathcal{M}}{\partial T} = \kappa \quad \text{(definition of the pseudo time)} \\ \dfrac{\mathrm{d}T}{\mathrm{d}\tau} = -\dfrac{\partial \mathcal{M}}{\partial t} = -\kappa \dfrac{\partial \mathcal{H}}{\partial t} \end{cases} \tag{2.55}$$

showing that the value of $\mathcal{K}$ is conserved also in the new coordinates:

$$\begin{aligned}\frac{\mathrm{d}\mathcal{K}}{\mathrm{d}\tau} &= \frac{\mathrm{d}\mathcal{H}}{\mathrm{d}\tau} + \frac{\mathrm{d}T}{\mathrm{d}\tau} \\ &= \frac{\partial\mathcal{H}}{\partial\mathbf{q}}\cdot\frac{\mathrm{d}\mathbf{q}}{\mathrm{d}\tau} + \frac{\partial\mathcal{H}}{\partial\mathbf{Q}}\cdot\frac{\mathrm{d}\mathbf{Q}}{\mathrm{d}\tau} + \frac{\partial\mathcal{H}}{\partial t}\frac{\mathrm{d}t}{\mathrm{d}\tau} + \frac{\mathrm{d}T}{\mathrm{d}\tau} \\ &= \frac{\partial\mathcal{H}}{\partial\mathbf{q}}\cdot\frac{\partial\mathcal{M}}{\partial\mathbf{Q}} - \frac{\partial\mathcal{H}}{\partial\mathbf{Q}}\cdot\frac{\partial\mathcal{M}}{\partial\mathbf{q}} + \frac{\partial\mathcal{H}}{\partial t}\frac{\partial\mathcal{M}}{\partial T} - \frac{\partial\mathcal{M}}{\partial t} \\ &= \frac{\partial\mathcal{H}}{\partial\mathbf{q}}\cdot\left(\kappa\frac{\partial\mathcal{H}}{\partial\mathbf{Q}} + \frac{\partial\kappa}{\partial\mathbf{Q}}(\mathcal{H}+T)\right) - \frac{\partial\mathcal{H}}{\partial\mathbf{Q}}\cdot\left(\kappa\frac{\partial\mathcal{H}}{\partial\mathbf{q}} + \frac{\partial\kappa}{\partial\mathbf{q}}(\mathcal{H}+T)\right) + \kappa\frac{\partial\mathcal{H}}{\partial t} - \kappa\frac{\partial\mathcal{H}}{\partial t} \\ &= 0\end{aligned} \tag{2.56}$$

Consequently, if the value of $\mathcal{K}$ is zero at the initial instant $\tau = \tau_0$, it remains zero all along the solution. Moreover, one can remember that the initial value of T was so far considered arbitrary. Writing $(\mathbf{Q}_0, \mathbf{q}_0, t_0)$ the initial conditions, the regularised system defined by (2.51) is equivalent to the original one only if we set:

$$T(\tau = 0) = T_0 = -\mathcal{H}(\mathbf{Q}_0, \mathbf{q}_0, t_0) \tag{2.57}$$

Of course, if the initial system is autonomous $\mathcal{H}$ and T are both constant quantities, but their sum is still required to be zero. Actually, the regularisation method introduced in this section is only one particular example of a more general family of transformations (see Mikkola and Wiegert, 2002).

2.2.3 The integral flow

Since it results in simpler formulas, we will now consider an autonomous system (if necessary, the time should have been introduced among the canonical coordinates). We will also gather the position and conjugate momenta in a single vector $\mathbf{z} = (\mathbf{Q}, \mathbf{q}) \in \mathbb{R}^{2n}$. The Hamiltonian function writes thus $\mathcal{H}(\mathbf{z})$ and it is a constant of motion. With these notations, the equations of Hamilton write:

$$\dot{\mathbf{z}} = J\,(\mathrm{D}\mathcal{H})^{\mathrm{T}} \tag{2.58}$$

where $(\mathrm{D}\mathcal{H})^{\mathrm{T}}$ is the gradient of $\mathcal{H}$ as a column vector and J is the fundamental symplectic matrix. It writes:

$$J = \begin{pmatrix} \mathbb{0} & -\mathbb{1} \\ \mathbb{1} & \mathbb{0} \end{pmatrix} \tag{2.59}$$

where $\mathbb{0}$ and $\mathbb{1}$ are the $n \times n$ zero and identity matrices. The equation (2.58) is thus strictly equivalent to (2.39). Finally, the Poisson's brackets of two functions $f(\mathbf{z})$ and $g(\mathbf{z})$ rewrite:

$$\{f, g\} = \mathrm{D}f\, J\,(\mathrm{D}g)^{\mathrm{T}} \tag{2.60}$$

This formalism is much more convenient when speaking of integral flows and canonical changes of coordinates.

The "integral flow" $\Phi^t_{\mathcal{H}}(\mathbf{z}_0)$ of the Hamiltonian system is the unique solution of the system of differential equations (2.58) starting from $\mathbf{z}_0$ at $t = 0$. It is a function of both the time and the initial conditions:

$$\Phi_{\mathcal{H}} \ : \ t, \mathbf{z}_0 \in \mathbb{R} \times \mathbb{R}^{2n} \ \longmapsto \ \Phi^t_{\mathcal{H}}(\mathbf{z}_0) \in \mathbb{R}^{2n} \tag{2.61}$$

and verifies by definition $\Phi^0_{\mathcal{H}}(\mathbf{z}_0) = \mathbf{z}_0$. By the regularity theorem for solutions of ordinary differential equations, $\Phi^t_{\mathcal{H}}$ is at least as smooth as $\mathcal{H}$. Moreover, it has the semigroup property:

$$\Phi^{t_2}_{\mathcal{H}} \circ \Phi^{t_1}_{\mathcal{H}} = \Phi^{t_1+t_2}_{\mathcal{H}} \tag{2.62}$$

In particular, the mapping $\Phi^t_{\mathcal{H}} : \mathbb{R}^{2n} \mapsto \mathbb{R}^{2n}$ is a bijection with inverse $\Phi^{-t}_{\mathcal{H}}$ (which is also equivalent to $\Phi^t_{-\mathcal{H}}$).

2.2.4 Canonical changes of coordinates

A diffeomorphism $\phi : \mathbf{z} \in \mathbb{R}^{2n} \mapsto \tilde{\mathbf{z}} \in \mathbb{R}^{2n}$ of class at least $\mathcal{C}^2$ is said to be a "canonical change of coordinates with valence α" if for any Hamiltonian $\mathcal{H}(\mathbf{z})$, the function:

$$\tilde{\mathcal{H}} = \alpha \, \mathcal{H} \circ \phi^{-1} \ , \ \ \alpha \in \mathbb{R} \tag{2.63}$$

can be used as a Hamiltonian in the $\tilde{\mathbf{z}}$ space. In other words, the structure of the equations remains unchanged, that is:

$$\dot{\mathbf{z}} = J \, (\mathrm{D}\mathcal{H})^{\mathrm{T}} \iff \dot{\tilde{\mathbf{z}}} = J \, (\mathrm{D}\tilde{\mathcal{H}})^{\mathrm{T}} \tag{2.64}$$

It implies also that the integral flows $\Phi^t_{\mathcal{H}}$ and $\Phi^t_{\tilde{\mathcal{H}}}$ commute by ϕ:

$$\phi \circ \Phi^t_{\mathcal{H}} = \Phi^t_{\tilde{\mathcal{H}}} \circ \phi \tag{2.65}$$

The condition for ϕ to be a canonical transformation can be derived by the chain rule:

$$\dot{\tilde{\mathbf{z}}} = \frac{\mathrm{d}\, \phi(\mathbf{z})}{\mathrm{d}t} = \mathrm{D}\phi(\mathbf{z}) \, \dot{\mathbf{z}} = \mathrm{D}\phi(\mathbf{z}) \, J \, (\mathrm{D}\mathcal{H})^{\mathrm{T}}(\mathbf{z}) \tag{2.66}$$

and from (2.63) we have:

$$\alpha \, \mathcal{H} = \tilde{\mathcal{H}} \circ \phi \implies (\mathrm{D}\mathcal{H})^{\mathrm{T}} = \left(\frac{1}{\alpha} \, \mathrm{D}\tilde{\mathcal{H}} \, \mathrm{D}\phi \right)^{\mathrm{T}} = \frac{1}{\alpha} \, (\mathrm{D}\phi)^{\mathrm{T}} \, (\mathrm{D}\tilde{\mathcal{H}})^{\mathrm{T}} \tag{2.67}$$

so, finally:

$$\dot{\tilde{\mathbf{z}}} = \left[\frac{1}{\alpha} \, \mathrm{D}\phi(\mathbf{z}) \, J \, (\mathrm{D}\phi)^{\mathrm{T}}(\mathbf{z}) \right] \, (\mathrm{D}\tilde{\mathcal{H}})^{\mathrm{T}} \tag{2.68}$$

By identification with (2.64), the diffeomorphism ϕ is a canonical change of coordinates if and only if:

$$\mathrm{D}\phi \, J \, (\mathrm{D}\phi)^{\mathrm{T}} = \alpha \, J \tag{2.69}$$

If that relation holds, we will say that the matrix $\mathrm{D}\phi$ is *symplectic*. For one-degree-of-freedom systems, this is equivalent to the simple condition $\det(\mathrm{D}\phi) = \alpha$. One can note that a coefficient α different from 1 corresponds to a change of unit and/or dimension. A different way to present a canonical change of coordinates is to write every component of $\tilde{\mathbf{z}} = (\tilde{\mathbf{Q}}, \tilde{\mathbf{q}})$ as a function of $\mathbf{z}$. Then, the transformation is canonical if and only if the components of $\tilde{\mathbf{z}}$ verify (2.42). Various other definitions of canonical transformations exist, for instance using generating functions, or such as conserving the symplectic 2-form. A more exhaustive presentation, though, would be out of the scope of this introduction. Throughout this work, some usual canonical transformations are frequently used, so it is worth to present them here:

- A typical case is when a transformation $\tilde{\mathbf{q}} = f(\mathbf{q})$ is made to the positions and we look for an expression $\tilde{\mathbf{Q}} = F(\mathbf{Q}, \mathbf{q})$ making canonical the overall change of coordinates. The matrix $\mathrm{D}\phi$ can be written in four blocks of $n \times n$ matrices:

$$\mathrm{D}\phi = \begin{pmatrix} \mathrm{D}_{\mathbf{Q}} F & \mathrm{D}_{\mathbf{q}} F \\ \mathbb{0} & \mathrm{D}f \end{pmatrix} \tag{2.70}$$

  and choosing $\alpha = 1$, the condition (2.69) writes:

$$\begin{cases} \mathrm{D}f \left(\mathrm{D}_{\mathbf{Q}} F\right)^{\mathrm{T}} = \mathbb{1} \\ \mathrm{D}_{\mathbf{q}} F \left(\mathrm{D}_{\mathbf{Q}} F\right)^{\mathrm{T}} = \mathrm{D}_{\mathbf{Q}} F \left(\mathrm{D}_{\mathbf{q}} F\right)^{\mathrm{T}} \end{cases} \tag{2.71}$$

  Obviously, the simplest choice is to define F linear with respect to the momenta. In that case, the change of coordinates is made canonical by putting (from the first equation):

$$\tilde{\mathbf{Q}} = F(\mathbf{Q}, \mathbf{q}) = \left(\mathrm{D}f(\mathbf{q})^{-1}\right)^{\mathrm{T}} \mathbf{Q} \tag{2.72}$$

  This function verifies also automatically the second equation (see appendix B.1.1). In particular, when f is a linear transformation with matrix A, the change of coordinates can be made canonical simply by applying its inverse transposed to the momenta.

- Another useful example is the construction of polar coordinates in the phase space spanned by one couple of conjugate coordinates (Q, q). The coordinates Q and q can be one component of $\mathbf{Q}$ and $\mathbf{q}$ or the overall coordinates for a one-degree-of-freedom system. We call *canonical polar coordinates* a couple (R, θ) such that:

$$\begin{cases} Q = f(R)\cos\theta \\ q = f(R)\sin\theta \end{cases} \tag{2.73}$$

  where $R > 0$ is the momentum conjugate to θ. The determinant of the Jacobian of $\phi : (R, \phi) \mapsto (Q, q)$ writes $f'(R)f(R)$, so the transformation is canonical with valence 1 if and only if:

$$f'(R)f(R) = 1 \iff \frac{\mathrm{d}f(R)^2}{\mathrm{d}R} = 2 \tag{2.74}$$

Hence, the simplest choice is $f(R) = \sqrt{2R}$. If $R < 0$, the transformation (2.73) with $f(R) = \sqrt{-2R}$ would result in a canonical change of coordinates with valence $\alpha = -1$. In order to avoid the change of sign of the Hamiltonian, there are two analogous canonical transformations with valence 1, namely:

$$\begin{cases} Q = \sqrt{-2R}\cos(-\theta) \\ q = \sqrt{-2R}\sin(-\theta) \end{cases} \quad \text{or} \quad \begin{cases} Q = \sqrt{-2R}\sin\theta \\ q = \sqrt{-2R}\cos\theta \end{cases} \tag{2.75}$$

- Now, let us consider a Hamiltonian system with conjugate coordinates $\mathbf{r}, \mathbf{p} \in \mathbb{R}^3 \times \mathbb{R}^3$. The position $\mathbf{r}$ can be also described by generalised spherical coordinates, that is a set of two rotations plus a function of $\mathbf{r}$ and/or $\mathbf{p}$. We can show that the momentum conjugate to any rotation angle in the position space is equal to the projection of $\mathbf{r} \times \mathbf{p}$ on the axis around which it rotates. In the same way, the momentum conjugate to any position along one axis is the projection of $\mathbf{p}$ on this axis. This is easily verified for the classic spherical coordinates, in which the position is described by the angles $(\theta, \varphi) \in]0, \pi[\times [0, 2\pi]$ and the radial distance r through:

$$\mathbf{r} = \begin{pmatrix} x \\ y \\ z \end{pmatrix} = r \begin{pmatrix} \cos\varphi\sin\theta \\ \sin\varphi\sin\theta \\ \cos\theta \end{pmatrix} \quad \text{that is} \quad \begin{pmatrix} r \\ \theta \\ \varphi \end{pmatrix} = \begin{pmatrix} \sqrt{x^2+y^2+z^2} \\ \operatorname{acos}(z/r) \\ \operatorname{atan2}(y,x) \end{pmatrix} \tag{2.76}$$

This transformation implies only the position, so the first example of canonical transformation given above can be applied to deduce the expression of the new momenta. Calling $f(\mathbf{r})$ the transformation applied to the position, we get:

$$\mathrm{D}f(\mathbf{r}) = \begin{pmatrix} x/r & y/r & z/r \\ \frac{xz}{r^2\sqrt{x^2+y^2}} & \frac{yz}{r^2\sqrt{x^2+y^2}} & -\frac{\sqrt{x^2+y^2}}{r^2} \\ -\frac{y}{x^2+y^2} & \frac{x}{x^2+y^2} & 0 \end{pmatrix} \tag{2.77}$$

which has the determinant $1/(r^2\sin\theta)$. Provided that $r \neq 0$ and $\sin\theta \neq 0$, its inverse transposed gives the transformation to be applied to $\mathbf{p}$ to obtain the momenta $(P_r, P_\theta, P_\varphi)$ in terms of $\mathbf{r}$ and $\mathbf{p} = (p_x, p_y, p_z)^{\mathrm{T}}$:

$$\begin{aligned} \begin{pmatrix} P_r \\ P_\theta \\ P_\varphi \end{pmatrix} &= \begin{pmatrix} x/r & y/r & z/r \\ \frac{xz}{\sqrt{x^2+y^2}} & \frac{yz}{\sqrt{x^2+y^2}} & -\sqrt{x^2+y^2} \\ -y & x & 0 \end{pmatrix} \begin{pmatrix} p_x \\ p_y \\ p_z \end{pmatrix} \\ &= \begin{pmatrix} \mathbf{p}\cdot\mathbf{r}/r \\ \frac{-y}{\sqrt{x^2+y^2}}(y\,p_z - z\,p_x) + \frac{x}{\sqrt{x^2+y^2}}(z\,p_x - x\,p_z) \\ x\,p_y - y\,p_x \end{pmatrix} \end{aligned} \tag{2.78}$$

We see that P_φ is indeed the projection of $\mathbf{r} \times \mathbf{p}$ on the z-axis, whereas P_θ is the projection of $\mathbf{r} \times \mathbf{p}$ on the axis generated by $(-y, x, 0)$, around which rotates the

angle θ. In the same way, P_r is the projection of $\mathbf{p}$ on the axis generated by $\mathbf{r}$ itself. In the particular case in which $(p_x, p_y, p_z) = (\dot{x}, \dot{y}, \dot{z})$, the vector $\mathbf{r}\times\mathbf{p}$ is the angular momentum and we retrieve the classic result $(P_r, P_\theta, P_\varphi) = (\dot{r}\,,\, r^2\dot{\theta}\,,\, r^2\sin^2\theta\,\dot{\varphi})$.

In a more general spherical coordinate system (as the one presented in Sect. 2.2.6), the rotation axes can be functions of both $\mathbf{r}$ and $\mathbf{p}$.

- The last case is a bit more subtle. Actually, what could be a better example of canonical transformation than the integral flow of a Hamiltonian system itself? Let us consider an auxiliary Hamiltonian function $\mathcal{X}(\mathbf{z})$. The associated integral flow (solving the equations of Hamilton) writes $\Phi^\tau_\mathcal{X}(\mathbf{z}_0)$, where the independent variable τ should not be necessary interpreted as "time". Then, for a given τ, the transformation $\Phi^\tau_\mathcal{X} : \mathbf{z} \mapsto \tilde{\mathbf{z}}$ can be interpreted as a canonical change of coordinates. The fact that the matrix $\mathrm{D}\Phi^\tau_\mathcal{X}$ is symplectic whatever the value of τ considered is given by Liouville's theorem. Indeed, by definition of the flow, we have:
$$\frac{\mathrm{d}\Phi^\tau_\mathcal{X}(\mathbf{z})}{\mathrm{d}\tau} = J(\mathrm{D}\mathcal{X})^{\mathrm{T}}(\Phi^\tau_\mathcal{X}(\mathbf{z})) \tag{2.79}$$
By taking the derivative with respect to $\mathbf{z}$ we get:
$$\frac{\mathrm{d}\,\mathrm{D}\Phi^\tau_\mathcal{X}(\mathbf{z})}{\mathrm{d}\tau} = J\,\mathrm{D}^2\mathcal{X}(\Phi^\tau_\mathcal{X}(\mathbf{z}))\,\mathrm{D}\Phi^\tau_\mathcal{X}(\mathbf{z}) \tag{2.80}$$
where $D^2\mathcal{X}$ is the Hessian matrix of $\mathcal{X}$. The fact that $\mathrm{D}\Phi^\tau_\mathcal{X}$ verifies (2.69) is finally obtained by studying the τ-evolution of the matrix $C^\tau = \mathrm{D}\Phi^\tau_\mathcal{X}\,J\,(\mathrm{D}\Phi^\tau_\mathcal{X})^{\mathrm{T}}$. By definition of the flow, $\Phi^0_\mathcal{X}(\mathbf{z}) = \mathbf{z}$, which gives $\mathrm{D}\Phi^0_\mathcal{X} = \mathbb{1}$ and thus $C^0 = J$. Then, its τ-derivative writes:
$$\begin{aligned}\frac{\mathrm{d}C^\tau}{\mathrm{d}\tau} &= \frac{\mathrm{d}\,\mathrm{D}\Phi^\tau_\mathcal{X}}{\mathrm{d}\tau}\,J\,(\mathrm{D}\Phi^\tau_\mathcal{X})^{\mathrm{T}} + \mathrm{D}\Phi^\tau_\mathcal{X}\,J\left(\frac{\mathrm{d}\,\mathrm{D}\Phi^\tau_\mathcal{X}}{\mathrm{d}\tau}\right)^{\mathrm{T}} \\ &= (J\,\mathrm{D}^2\mathcal{X}\,\mathrm{D}\Phi^\tau_\mathcal{X})\,J\,(\mathrm{D}\Phi^\tau_\mathcal{X})^{\mathrm{T}} + \mathrm{D}\Phi^\tau_\mathcal{X}\,J\,(J\,\mathrm{D}^2\mathcal{X}\,\mathrm{D}\Phi^\tau_\mathcal{X})^{\mathrm{T}} \\ &= J\,\mathrm{D}^2\mathcal{X}\,C^\tau - C^\tau\,\mathrm{D}^2\mathcal{X}\,J\end{aligned} \tag{2.81}$$
using the identity $J^{\mathrm{T}} = -J$ and the fact that the Hessian is symmetric. The unique solution of (2.81) starting from $C^0 = J$ is the constant function $C^\tau = J$, which proves that $\Phi^\tau_\mathcal{X}$ is indeed a canonical change of coordinates.

2.2.5 The action-angle coordinates

Let us consider an integrable Hamiltonian system with n degrees of freedom, represented by the Hamiltonian function $\mathcal{H}$. If the system evolves on a compact and connected manifold, then the theorem of Arnold-Liouville[7] implies the existence of *action-angle*

[7]The scope of Arnold-Liouville's theorem is actually much larger, since it encompasses also the notion of *integrability* of the system, namely if there exist n functions (including the Hamiltonian) with zero mutual Poisson brackets. See Arnold (1989) for a complete formulation and the demonstration.

coordinates $(I, \theta) \in \mathbb{R}^n \times \mathbb{T}^n$ in which the dynamics writes in a very simple way:

$$\mathcal{H}(I,\theta) = \mathcal{H}_0(I) \implies \begin{cases} \dfrac{\mathrm{d}I_i}{\mathrm{d}t} = -\dfrac{\partial \mathcal{H}}{\partial \theta_i} = 0 \\ \dfrac{\mathrm{d}\theta_i}{\mathrm{d}t} = \dfrac{\partial \mathcal{H}}{\partial I_i} = \omega_i(J) = const. \end{cases} \tag{2.82}$$

In other words, the motion takes place on an n-dimensional torus with radii $\{J_i\}_{i=1,2...n}$ and at the constant angular velocities $\{\omega_i\}_{i=1,2...n}$. Such coordinates are very convenient to study the slightly perturbed case, in which this torus is deformed (the problem is still integrable) or even destroyed (the problem becomes non-integrable).

These variables are not uniquely defined: any canonical change of coordinates leaving the structure of n constant momenta and n angles with linear time-evolution would result in suitable action-angle coordinates. Consider for instance the transformation $(J_i, J_j) \mapsto (J_i + J_j, J_j)$ along with $(\theta_i, \theta_j) \mapsto (\theta_i, \theta_j - \theta_i)$.

2.2.6 Application to the two-body problem

A conservative system always admits a Hamiltonian formulation with the conserved total energy taken as Hamiltonian function. Indeed, with the force written as the negative gradient of a potential $V(\mathbf{r})$, it is immediate to verify that the Hamiltonian system defined by:

$$\mathcal{H}(\mathbf{p}, \mathbf{r}) = \frac{1}{2m}\mathbf{p}^2 + V(\mathbf{r}) \tag{2.83}$$

is equivalent to Newton's equations of the dynamics, taking the linear momentum $\mathbf{p} = m\,\dot{\mathbf{r}}$ as vector of momenta conjugate to the position $\mathbf{r}$. Of course, a more rigorous approach consists in using the Lagrangian formalism as an auxiliary between Newton's and Hamilton's equations. Similarly, in the case of the two-body problem written in relative (or barycentric) coordinates, the total energy by unit of mass can be used as Hamiltonian function:

$$\mathcal{H}(\mathbf{p}, \mathbf{r}) = \frac{1}{2}\mathbf{p}^2 - \frac{\mu}{|\mathbf{r}|} \tag{2.84}$$

taking $\mathbf{p} = \dot{\mathbf{r}}$. In terms of the Keplerian elements, the constant value of $\mathcal{H}$ writes thus $-\mu/(2a)$. The two-body problem being integrable and fulfilling the conditions of Arnold-Liouville's theorem, it admits action-angle coordinates. We will look for a set of coordinates (L, G, H, ℓ, g, h) as close as possible to the easy-to-use Keplerian elements. Our task is greatly facilitated since we already know the analytical solution from Sect. 2.1.1. In particular, the angle M is an obvious choice for the first angular coordinate ℓ. Indeed, it has already a linear evolution so it can be used as it is. Its conjugate momentum can be deduced from the expression of $\mathcal{H}$ in terms of the Keplerian elements, which includes only the semi-major axis a. The constant frequency of M is $n = \sqrt{\mu/a^3}$ which gives:

$$\sqrt{\frac{\mu}{a^3}} = \dot{\ell} = \frac{\partial \mathcal{H}}{\partial L} = \frac{\partial \mathcal{H}}{\partial a}\frac{\partial a}{\partial L} = \frac{\mu}{2a^2}\frac{\partial a}{\partial L} \iff \frac{\partial L}{\partial a} = \frac{1}{2}\sqrt{\frac{\mu}{a}} \tag{2.85}$$

which has the simplest solution $L = \sqrt{\mu a}$, setting the integration constant (function of e, I, ω, Ω) to zero. This gives the Hamiltonian system:

$$\mathcal{H}(L, G, H, \ell, g, h) = -\frac{\mu^2}{2L^2} \tag{2.86}$$

which is in accordance with the resolution from Sect. 2.1.1: even if the initial problem has three degrees of freedom, the solution is characterised by only one varying angle (namely ℓ). The corresponding action-angle variables should thus contain two angles with a zero frequency (g and h). The set of angles must be completed by two angles giving the orientation of the ellipse in the three-dimensional reference frame. This can be seen as the switch from $(\mathbf{r}, \mathbf{p})$ to generalised spherical coordinates. From Sect. 2.2.4, we know that their respective conjugate momenta are the projections of the angular momentum $\mathbf{C}$ on the axes around which they rotate. As such, the inclination I cannot be used, since by definition it rotates around an axis perpendicular to $\mathbf{C}$ (this would result in a momentum identically equal to zero, leading to no further information about the system). Hence, the classic choice is to set $g = \omega$ and $h = \Omega$. Using the expression of $\mathbf{C}$ in terms of the Keplerian elements (Sect. 2.1.3), we obtain finally:

$$G = \|\mathbf{C}\| = \sqrt{\mu a(1-e^2)} \quad \text{and} \quad H = C_z = \sqrt{\mu a(1-e^2)}\cos I \tag{2.87}$$

This complete set of action-angles coordinates:

$$\begin{cases} \ell = M \\ g = \omega \\ h = \Omega \end{cases} \quad \text{and} \quad \begin{cases} L = \sqrt{\mu a} \\ G = \sqrt{\mu a\,(1-e^2)} \\ H = \sqrt{\mu a\,(1-e^2)}\,\cos I \end{cases} \tag{2.88}$$

is usually called the "Delaunay coordinates". Written in function of the initial variables $(\mathbf{r}, \mathbf{p})$ with the expressions given in Sect. 2.1.3, we can show that they respect indeed all the conditions (2.42) of canonical coordinates. A more rigorous introduction of these variables can be found in Brouwer and Clemence (1961), or see Floría (1995) for a review.

Naturally, the Delaunay coordinates are singular where the Keplerian elements are, that is for $e = 0$ and $\sin I = 0$. In order to get coordinates which are smooth also in these cases, we need a canonical analogous to the equinoctial elements (see Sect. 2.1.2). The first step consists in replacing ℓ and g, which are undefined for $e = 0$, by λ and ϖ. This is realised by a linear transformation on the Delaunay angles:

$$\begin{pmatrix} \lambda \\ u \\ v \end{pmatrix} = \begin{pmatrix} 1 & 1 & 1 \\ 0 & 1 & 1 \\ 0 & 0 & 1 \end{pmatrix} \begin{pmatrix} \ell \\ g \\ h \end{pmatrix} = \begin{pmatrix} \ell + g + h \\ g + h \\ h \end{pmatrix} \tag{2.89}$$

which is extended to the momenta by applying its inverse transposed (see Sect. 2.2.4), leading to:

$$\begin{pmatrix} \Lambda \\ U \\ V \end{pmatrix} = \begin{pmatrix} 1 & 0 & 0 \\ -1 & 1 & 0 \\ 0 & -1 & 1 \end{pmatrix} \begin{pmatrix} L \\ G \\ H \end{pmatrix} = \begin{pmatrix} L \\ G - L \\ H - G \end{pmatrix} \tag{2.90}$$

The singularities when $e = 0$ and $I = 0$ are analogous to the singularity at the origin for polar coordinates. This leads to define Cartesian-like coordinates (which thus includes also the origin) by a polar canonical change of coordinates with "negative radius" (see Sect. 2.2.4):

$$\begin{cases} A = \sqrt{-2U}\,\sin u \\ \alpha = \sqrt{-2U}\,\cos u \end{cases} \quad ; \quad \begin{cases} B = \sqrt{-2V}\,\sin v \\ \beta = \sqrt{-2V}\,\cos v \end{cases} \tag{2.91}$$

The complete set of coordinates is still action-angle for the two-body problem, and the corresponding Hamiltonian writes:

$$\mathcal{H}(\Lambda, A, B, \lambda, \alpha, \beta) = -\frac{\mu^2}{2\Lambda^2} \tag{2.92}$$

They are called the "Poincaré coordinates" and are smooth functions of the Cartesian position and velocity (except for $e = 1$ and/or $I = \pi$). Their link to the Keplerian elements, though, is more tortuous than for Delaunay coordinates.

Naturally, these coordinates can be used for dynamical systems with a Hamiltonian function different than (2.84), in particular if it contains additional perturbing terms in $\mathbf{r}$ and/or $\mathbf{p}$. In that case, the coordinates of Delaunay (or Poincaré) will not be action-angle, but the canonical analogue to the *osculating* coordinates (Sect. 2.1.3). The corresponding equations of Hamiltonian, will thus be equivalent to the planetary equations of Lagrange or Gauss.

2.2.7 Naive picture of the long-term evolution

Actually, the two-body problem is not only integrable, but also *degenerate*, in the sense that there is only one varying angle among the three ones used to describe the dynamics in action-angle coordinates. In Delaunay coordinates, this writes:

$$\dot{M} = \sqrt{\frac{\mu}{a^3}} \quad ; \quad \dot{\omega} = 0 \quad ; \quad \dot{\Omega} = 0 \tag{2.93}$$

In practice, this means that any quantity representative of the system (as the Cartesian position and velocity) is constituted of one single frequency. In other words, its Fourier spectrum is only composed of multiple of this "proper" frequency. If we now perturb slightly this periodic orbit, it is pretty intuitive that it will give rise to two very separated timescales, since we will have this time:

$$\dot{M} = \sqrt{\frac{\mu}{a^3}} + \mathcal{O}(\varepsilon) \quad ; \quad \dot{\omega} = \mathcal{O}(\varepsilon) \quad ; \quad \dot{\Omega} = \mathcal{O}(\varepsilon) \tag{2.94}$$

If the problem is still integrable (which is often questionable), the perturbed system will thus admit in general three non-zero proper frequencies, related more or less closely to the evolution of M, ω and Ω. Any dynamical quantity will thus contain a fast varying component (associated to the orbital period) and a slow *secular* one (associated to

the precession of the orbit). Fig. 2.2 gives an example of such dynamics for a trans-Neptunian object orbiting around the Sun and perturbed by the planets. On a short timescale (here some hundreds of years), the motion of the particle essentially amounts to a Keplerian orbit. On a long timescale, on the contrary, the Keplerian elements undergo wide modulations. In a study of the long-term evolution of the Solar System, that is on a Giga-year timescale, only the low-frequency part is dynamically interesting. This leads use to define the concept of "secular theory", which deals only with the slow component of the dynamics (blue curve on Fig. 2.2), significantly simpler than the overall one. In other words, the goal of a secular theory is not to describe the motion of the particle *on* its orbit, but to describe the deformation and the rotation of the orbit *itself*. Naturally, that kind of description is only possible if the particle follows indeed a slowly deforming Keplerian orbit, that is without catastrophic close encounters or other chaotic phenomena.

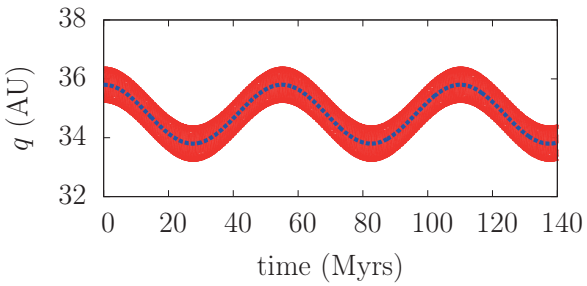

Figure 2.2 – Typical evolution of a dynamical quantity (here the perihelion distance) in a quasi-integrable perturbed two-body problem. The red curve represents the osculating trajectory obtained by numerical integration. Its "thickness" is made of fast small-amplitude oscillations. The blue curve is the corresponding secular trajectory.

2.3 Toward action-angle coordinates

2.3.1 Near-identity transformations

Let us consider a generic Hamiltonian function $\mathcal{H}(\mathbf{z})$ with $\mathbf{z} = (\mathbf{Q}, \mathbf{q}) \in \mathbb{R}^n \times \mathbb{R}^n$ or $\mathbb{R}^n \times \mathbb{T}^n$, and a small parameter $\varepsilon \ll 1$. According to the last example of Sect. 2.2.4, a near-identity canonical change of coordinates can be seen as the flow at time $\tau = 1$ associated to a "small" Hamiltonian function $\varepsilon\mathcal{X}(\mathbf{z})$ (or equivalently, the flow at time $\tau = \varepsilon$ associated to the Hamiltonian $\mathcal{X}$). The new coordinates write then:

$$\tilde{\mathbf{z}} = \Phi^1_{\varepsilon\mathcal{X}}(\mathbf{z}) \tag{2.95}$$

Let $f(\mathbf{z})$ be a real function of the initial coordinates, at least of class $\mathcal{C}^2$. Its evolution along the flow $\Phi^\tau_{\varepsilon\mathcal{X}}$ is governed by:

$$\frac{\mathrm{d}}{\mathrm{d}\tau} f = \{f, \varepsilon\mathcal{X}\} = -L_{\varepsilon\mathcal{X}} f \tag{2.96}$$

where we write $L_{\varepsilon\mathcal{X}}$ the linear operator associated to the Poisson brackets:

$$L_{\varepsilon\mathcal{X}} = \varepsilon \{\mathcal{X}, \, . \} = \varepsilon \sum_{i=1}^{n} \left(\frac{\partial \mathcal{X}}{\partial q_i} \frac{\partial .}{\partial Q_i} - \frac{\partial \mathcal{X}}{\partial Q_i} \frac{\partial .}{\partial q_i} \right) \tag{2.97}$$

Evaluated in the new coordinates, the function f can be written using the so-called Lie-series formalism (by integration of 2.96 and putting $\tau = 1$):

$$\begin{aligned} f(\tilde{\mathbf{z}}) &= \exp(-L_{\varepsilon\mathcal{X}}) f(\mathbf{z}) \\ &= \left(\sum_{n=0}^{\infty} \frac{1}{n!} (-L_{\varepsilon\mathcal{X}})^n \right) f(\mathbf{z}) \\ &= \left(1 - L_{\varepsilon\mathcal{X}} + \frac{1}{2} L_{\varepsilon\mathcal{X}}^2 - \frac{1}{6} L_{\varepsilon\mathcal{X}}^3 + \dots \right) f(\mathbf{z}) \\ &= \left(f - \varepsilon\{\mathcal{X}, f\} + \frac{\varepsilon^2}{2}\{\mathcal{X}, \{\mathcal{X}, f\}\} - \frac{\varepsilon^3}{6}\{\mathcal{X}, \{\mathcal{X}, \{\mathcal{X}, f\}\}\} + \dots \right) (\mathbf{z}) \end{aligned} \tag{2.98}$$

By definition of the flow, the inverse transformation is simply given by:

$$\tilde{\mathbf{z}} = \Phi_{\varepsilon\mathcal{X}}^{1}(\mathbf{z}) \iff \mathbf{z} = \Phi_{\varepsilon\mathcal{X}}^{-1}(\tilde{\mathbf{z}}) \tag{2.99}$$

and thus, for a generic function f we have also:

$$\begin{aligned} f(\mathbf{z}) &= \exp(L_{\varepsilon\mathcal{X}}) f(\tilde{\mathbf{z}}) \\ &= \left(f + \varepsilon\{\mathcal{X}, f\} + \frac{\varepsilon^2}{2}\{\mathcal{X}, \{\mathcal{X}, f\}\} + \frac{\varepsilon^3}{6}\{\mathcal{X}, \{\mathcal{X}, \{\mathcal{X}, f\}\}\} + \dots \right) (\tilde{\mathbf{z}}) \end{aligned} \tag{2.100}$$

Now, by choosing $f = \mathcal{H}$ and imposing $\mathcal{H}(\mathbf{z}) = \tilde{\mathcal{H}}(\tilde{\mathbf{z}})$, we deduce directly the expression of the Hamilonian function in the new coordinates:

$$\tilde{\mathcal{H}} = \mathcal{H} + \varepsilon \{\mathcal{X}, \mathcal{H}\} + \frac{\varepsilon^2}{2} \{\mathcal{X}, \{\mathcal{X}, \mathcal{H}\}\} + \frac{\varepsilon^3}{6} \{\mathcal{X}, \{\mathcal{X}, \{\mathcal{X}, \mathcal{H}\}\}\} + \dots \tag{2.101}$$

In the same way, considering this time $f = \Pi_j$ (function j^{th} component), we get an explicit expression of the component z_j in terms of the new coordinates $\tilde{\mathbf{z}}$.

2.3.2 Suppressing the angles dependency

Let us consider a Hamiltonian function $\mathcal{H}(I, \theta)$ with $(I, \theta) \in \mathbb{R}^n \times \mathbb{T}^n$ (we now splits $\mathbf{z}$ in momenta/positions and we drop the bold notations). According to Arnold-Liouville theorem, if the dynamical system associated to $\mathcal{H}$ is integrable, there exists a set of coordinates in which the Hamiltonian function is independent of the angles θ (see Sect. 2.2.5). In these action-angle coordinates, the system evolves on an n-dimensional torus and the resolution is trivial. Supposing that the dynamics is integrable or quasi-integrable (that is tightly trapped between KAM tori), an idea of resolution is to look

for such coordinates. In the particular case where $\mathcal{H}$ is already "almost" expressed in actions-angles variables, it can write generically:

$$\mathcal{H}(I,\theta) = \mathcal{H}_0(I) + \varepsilon\,\mathcal{H}_1(I,\theta) + \varepsilon^2\,\mathcal{H}_2(I,\theta) + \dots \tag{2.102}$$

and the actions-angles coordinates, if they indeed exist, can be obtained by a near-identity canonical change of coordinates. All the problem consists in finding a suitable auxiliary Hamiltonian function $\varepsilon\mathcal{X}$. Replacing $\mathcal{H}$ by its expression (2.102) in the equation (2.101), we get:

$$\tilde{\mathcal{H}} = \mathcal{H}_0 + \varepsilon\Big(\mathcal{H}_1 + \{\mathcal{X},\mathcal{H}_0\}\Big) + \varepsilon^2\Big(\mathcal{H}_2 + \{\mathcal{X},\mathcal{H}_1\} + \frac{1}{2}\{\mathcal{X},\{\mathcal{X},\mathcal{H}_0\}\}\Big) + \dots \tag{2.103}$$

We can also rewrite the auxiliary Hamiltonian $\varepsilon\mathcal{X}$ in a series of ε:

$$\mathcal{X}(I,\theta) = \mathcal{X}_1(I,\theta) + \varepsilon\,\mathcal{X}_2(I,\theta) + \cdots \tag{2.104}$$

which gives finally:

$$\begin{aligned}\tilde{\mathcal{H}} &= \mathcal{H}_0 \\ &\quad + \varepsilon\Big(\mathcal{H}_1 + \{\mathcal{X}_1,\mathcal{H}_0\}\Big) \\ &\quad + \varepsilon^2\Big(\mathcal{H}_2 + \{\mathcal{X}_2,\mathcal{H}_0\} + \{\mathcal{X}_1,\mathcal{H}_1\} + \frac{1}{2}\{\mathcal{X}_1,\{\mathcal{X}_1,\mathcal{H}_0\}\}\Big) + \dots \\ &= \tilde{\mathcal{H}}_0 + \varepsilon\,\tilde{\mathcal{H}}_1 + \varepsilon^2\,\tilde{\mathcal{H}}_2 + \dots\end{aligned} \tag{2.105}$$

From now on, the problem is to determine every function $\mathcal{X}_j$ such as $\tilde{\mathcal{H}}$ is independent of the angles at every order. In order to suppress the angular dependency at order 1, let us write the $\mathcal{X}_1$ in terms of an n-dimensional Fourier series of the angles θ:

$$\mathcal{X}_1(I,\theta) = \sum_{\mathbf{k}\in\mathbb{Z}^n} \mathcal{X}_{1\mathbf{k}}(I)\exp(i\,\mathbf{k}\cdot\theta) \tag{2.106}$$

with:

$$\mathcal{X}_{1\mathbf{k}}(I) = \left(\frac{1}{2\pi}\right)^n \int_0^{2\pi}\!\!\int_0^{2\pi}\!\!\dots\; \mathcal{X}_1(I,\theta)\exp(-i\,\mathbf{k}\cdot\theta)\,\mathrm{d}^n\theta \tag{2.107}$$

Its Poisson brackets with $\mathcal{H}_0$ write then:

$$\begin{aligned}\{\mathcal{X}_1,\mathcal{H}_0\} &= \sum_{j=1}^{n} \frac{\partial\mathcal{H}_0}{\partial I_j}(I)\,\frac{\partial\mathcal{X}_1}{\partial\theta_j}(I,\theta) = \sum_{j=1}^{n}\omega_j(I)\sum_{\mathbf{k}\in\mathbb{Z}^n}\mathcal{X}_{1\mathbf{k}}(I)\,i\,k_j\exp(i\,\mathbf{k}\cdot\theta) \\ &= \sum_{\mathbf{k}\in\mathbb{Z}^n} i\,\mathbf{k}\cdot\omega(I)\,\mathcal{X}_{1\mathbf{k}}(I)\exp(i\,\mathbf{k}\cdot\theta)\end{aligned} \tag{2.108}$$

where $\omega(I)$ represents the vector of unperturbed frequencies $\omega \equiv \partial\mathcal{H}/\partial I$. Now if we develop also the functions $\mathcal{H}_1$ and $\tilde{\mathcal{H}}_1$ in Fourier series:

$$\begin{cases}\mathcal{H}_1(I,\theta) = \displaystyle\sum_{\mathbf{k}\in\mathbb{Z}^n}\mathcal{H}_{1\mathbf{k}}(I)\exp(i\,\mathbf{k}\cdot\theta) \\ \tilde{\mathcal{H}}_1(I,\theta) = \displaystyle\sum_{\mathbf{k}\in\mathbb{Z}^n}\tilde{\mathcal{H}}_{1\mathbf{k}}(I)\exp(i\,\mathbf{k}\cdot\theta)\end{cases} \tag{2.109}$$

the equation (2.105) gives the equality term by term:

$$\tilde{\mathcal{H}}_{1\mathbf{k}}(I) = \mathcal{H}_{1\mathbf{k}}(I) + i\,\mathbf{k}\cdot\omega(I)\,\mathcal{X}_{1\mathbf{k}}(I) \tag{2.110}$$

We finally deduce the equations which must be verified to suppress the angular dependency of the Hamiltonian at order 1:

$$\mathcal{X}_{1\mathbf{k}}(I) = \frac{-\mathcal{H}_{1\mathbf{k}}(I)}{i\,\mathbf{k}\cdot\omega(I)} \quad \text{, for } \mathbf{k}\neq\mathbf{0} \tag{2.111}$$

The function $\mathcal{X}_{1\mathbf{k}}(I)$ can be anything for $\mathbf{k}=\mathbf{0}$, so we will choose the null function $\mathcal{X}_{1\mathbf{0}}(I)\equiv 0$. There are now different cases:

- If the vector $\omega(I)$ is non-resonant, that is if:

$$\mathbf{k}\cdot\omega(I) = 0 \iff \mathbf{k}=\mathbf{0} \tag{2.112}$$

  then Eq. (2.111) has a unique solution for all $\mathbf{k}\in\mathbb{Z}^n$ and the angular dependency can by entirely suppressed. The Hamiltonian $\mathcal{X}_1$ being fixed, we can look for $\mathcal{X}_2$ from Eq. (2.105) using the same method, and so on for every relevant order. In particular, at first order the new Hamiltonian turns out to be simply the term $\mathbf{k}=\mathbf{0}$ of the Fourier series of $\mathcal{H}_1$ (since the choice of $\mathcal{X}_1$ cancelled every other term):

$$\tilde{\mathcal{H}}_1 = \tilde{\mathcal{H}}_{1,\mathbf{0}}(I) = \left(\frac{1}{2\pi}\right)^n \int_0^{2\pi}\!\!\int_0^{2\pi}\!\!\dots\; \mathcal{H}_1(I,\theta)\,\mathrm{d}^n\theta \tag{2.113}$$

  that is its average upon the angles θ.

- On the other hand, if $\omega(I)$ presents one or several resonance relations (even approximate), the auxiliary Hamiltonian $\mathcal{X}$ will not be defined for all $\mathbf{k}$, which denotes the impossibility to totally suppress the angular dependency by a perturbative method. Nevertheless, if the vector $\omega(I)$ presents only a single resonance relation (or a few isolated ones):

$$\mathbf{k}_{res}\cdot\omega \approx 0 \quad , \quad \mathbf{k}_{res}\neq\mathbf{0} \tag{2.114}$$

  the suppression of every other term in the Fourier series will still greatly simplify the system. In this case, the new Hamiltonian $\tilde{\mathcal{H}}$ will just contain some supplementary oscillating terms, with the resonant angle:

$$\sigma = \mathbf{k}_{res}\cdot\theta \tag{2.115}$$

  as argument. If such a resonant combination is known *a priori*, an effective method to study the dynamics is to take the resonant angle as a new independent coordinate (by a linear canonical transformation, see Sect. 2.2.4), and then remove all the *other* angles by the perturbation method. By doing so, the coordinates obtained are not action-angle, because it remains a single angular dependency,

but the Hamiltonian can become sufficiently "simple" to be solved (for instance, it can be of type *pendulum*). If the dynamics is integrable, though, action-angle coordinates do exist, but the required canonical transformation is not close to identity.

In that work, actually, we will never try to obtain action-angles coordinates, but just *secular* ones (see Sect. 2.2.7). Indeed, they can be seen as a first step towards the action-angles coordinates (if they actually exist). In the context of a secular theory in celestial mechanics, the only angles to be suppressed are the so-called *fast angles* (the mean anomalies or the mean longitudes) given that the non-perturbed part of the Hamiltonian function, written in action-angle coordinates, depends only on their conjugate momenta (see the equations 2.86 or 2.92). For such a change of coordinates, the non-resonant condition (2.112) implies only the so-called *mean-motion resonances* between the bodies involved, that is commensurable ratios between the orbital periods.

Chapter 3

Secular models beyond Neptune

Most of the results detailed in this chapter are more succinctly presented in Saillenfest et al. (2016).

This chapter is devoted to the development of secular theories, in order to describe the long-term orbital dynamics of trans-Neptunian objects. Section 3.1 presents the planetary model used and the resulting osculating Hamiltonian function, starting point for any secular representation. In Sect. 3.2, we revisit Kozai's non-resonant secular model in the trans-Neptunian region. Its general form is detailed and an analysis of the lowest-order terms is conducted to get general information about the dynamics. Moreover, semi-analytical methods are used to explore systematically the space of parameters. Then, Sect. 3.3 presents the construction of a "resonant secular model". The adiabatic invariant theory is used to get a one-degree-of-freedom system: all the possible orbits are described by the level curves of the Hamiltonian. Finally, Sect. 3.4 presents some illustrations of the resonant model, along with detailed explanations about its use for the various types of dynamics we can be confronted with. As the variety of trajectories is found to be very rich, the exhaustive exploration of the parameter space is left for Chp. 4.

We are interested in the long-term orbital evolution of trans-Neptunian objects, that is, asteroidal-sized bodies that have a negligible mass compared to the planets. Along this work, we focus only on planetary perturbations: the galactic tides, effective for very high semi-major axes (see for instance Fouchard et al., 2006), can be introduced in a second step. We will further restrict the study to perihelion distances greater than the orbit of Neptune, that is, to trajectories completely out of the planetary region. This is the less known dynamical region of the Solar System, since, because of the distance to Earth, its population is very difficult to observe. Such orbits can be divided into two broad classes:

- The first class, called generically the Scattered Disc, contains the objects undergoing a diffusion of semi-major axis. It denotes a chaotic short-timescale dynamics, so these orbits are unstable by essence. It has been shown that a diffusive process

is unable to produce a substantial variation in perihelion distance (see Gallardo et al., 2012, for a thorough review).

- The second class contains the objects with integrable (or quasi-integrable) short-timescale dynamics. As such, their orbits can be described by *secular models*. Such models can exhibit stable equilibrium points and libration zones for the secular argument of perihelion ω and perihelion distance q. If a particle follows such a kind of orbit, we say that it experiences "Lidov-Kozai mechanism" in reference to the pioneer papers of Kozai (1962, 1985) and to the independent study by Lidov (1962) about the motion of artificial satellites. That class can be further divided into two kinds of objects: the non-resonant ones (fixed secular semi-major axis) and those trapped in a mean-motion resonance with a planet (oscillating secular semi-major axis). To prevent any scattering, the non-resonant objects need a sufficiently high perihelion distance, the limit being estimated by Gallardo et al. (2012) as roughly $q_{\min} = a/27.3+33.3$ AU (where a stands for the semi-major axis expressed in AU). The resonant orbits are much more permissive because the forced link with one of the planets can act as a protective mechanism against diffusion. However, the resonance overlapping and, of course, the close encounters with Neptune, are still well-known sources of chaos for perihelion distances very close to the planetary region. A secular model is thus never relevant in all the parameter space.

This classification is based on the dynamics of the objects rather than on their observed orbits, so it is slightly different from the one introduced in Sect. 1.2.2. These two broad classes are somehow permeable: a diffusion of semi-major axis can stop abruptly because of a resonance capture, or on the contrary, a quasi-integrable secular motion can lead the perihelion distance to decrease toward a diffusive region. We will come back to that point later.

3.1 A simple planetary model

We write μ the product of the gravitational constant and the mass of the Sun, and μ_i the product of the gravitational constant and the mass of the i^{th} planet. According to Newton's law of motion, the acceleration of a massless body affected by the gravitational attraction of the Sun and N planets writes:

$$\ddot{\mathbf{x}} = -\mu \frac{\mathbf{x} - \mathbf{x}_\odot}{|\mathbf{x} - \mathbf{x}_\odot|^3} - \sum_{i=1}^{N} \mu_i \frac{\mathbf{x} - \mathbf{x}_i}{|\mathbf{x} - \mathbf{x}_i|^3} \tag{3.1}$$

where $\mathbf{x}$, $\mathbf{x}_\odot$ and $\mathbf{x}_i$ are the positions of the particle, of the Sun and of the i^{th} planet in an inertial reference frame. In order to present the system as a perturbed two-body problem with the Sun, we must switch to the relative reference frame[1] (see Sect. 2.1).

[1] A reference frame centred on the mutual barycentre would be equivalent since the small body is considered massless.

Using the notations $\mathbf{r} \equiv \mathbf{x} - \mathbf{x}_\odot$ and $\mathbf{r}_i \equiv \mathbf{x}_i - \mathbf{x}_\odot$, the equation (3.1) becomes:

$$\ddot{\mathbf{r}} + \ddot{\mathbf{x}}_\odot = -\mu \frac{\mathbf{r}}{|\mathbf{r}|^3} - \sum_{i=1}^{N} \mu_i \frac{\mathbf{r} - \mathbf{r}_i}{|\mathbf{r} - \mathbf{r}_i|^3} \tag{3.2}$$

Since the Sun is affected only by the massive planets, its acceleration in the inertial reference frame writes:

$$\ddot{\mathbf{x}}_\odot = -\sum_{i=1}^{N} \mu_i \frac{\mathbf{x}_\odot - \mathbf{x}_i}{|\mathbf{x}_\odot - \mathbf{x}_i|^3} = \sum_{i=1}^{N} \mu_i \frac{\mathbf{r}_i}{|\mathbf{r}_i|^3} \tag{3.3}$$

which gives finally the equations of motion of the small body in the heliocentric reference frame:

$$\ddot{\mathbf{r}} = -\mu \frac{\mathbf{r}}{|\mathbf{r}|^3} - \sum_{i=1}^{N} \mu_i \left(\frac{\mathbf{r} - \mathbf{r}_i}{|\mathbf{r} - \mathbf{r}_i|^3} + \frac{\mathbf{r}_i}{|\mathbf{r}_i|^3} \right) \tag{3.4}$$

This acceleration is the negative gradient of the potential:

$$V(\mathbf{r}) = -\frac{\mu}{|\mathbf{r}|} - \sum_{i=1}^{N} \mu_i \left(\frac{1}{|\mathbf{r} - \mathbf{r}_i|} - \mathbf{r} \cdot \frac{\mathbf{r}_i}{|\mathbf{r}_i|^3} \right) \tag{3.5}$$

As explained in Sect. 2.2.6, the total energy per unit of mass can be taken as Hamiltonian, the vector $\mathbf{p} = \dot{\mathbf{r}}$ being the momentum conjugate to the position $\mathbf{r}$. It writes thus:

$$\mathcal{H}(\mathbf{p}, \mathbf{r}, t) = \frac{1}{2}\mathbf{p}^2 - \frac{\mu}{|\mathbf{r}|} - \sum_{i=1}^{N} \mu_i \left(\frac{1}{|\mathbf{r} - \mathbf{r}_i|} - \mathbf{r} \cdot \frac{\mathbf{r}_i}{|\mathbf{r}_i|^3} \right) \tag{3.6}$$

Written in that form, $\mathcal{H}$ is time-dependent through the planetary positions, supposed known functions of the time: $\mathbf{r}_i \equiv \mathbf{r}_i(t)$. Let us now switch to Delaunay heliocentric elements (Eq. 2.88). The new Hamiltonian, equal to (3.6) by value, will still be noted $\mathcal{H}$. It writes:

$$\mathcal{H}(L, G, H, \ell, g, h, t) = -\frac{\mu^2}{2L^2} - \sum_{i=1}^{N} \mu_i \left(\frac{1}{|\mathbf{r} - \mathbf{r}_i|} - \mathbf{r} \cdot \frac{\mathbf{r}_i}{|\mathbf{r}_i|^3} \right) \tag{3.7}$$

As before, we write $\{a, e, I, \omega, \Omega, M\}$ the heliocentric Keplerian elements, appearing in $\mathbf{r}$ though (2.28). In order to apply a perturbative method, we split $\mathcal{H}$ into its Keplerian part $\mathcal{H}_0$ and the planetary perturbations $\varepsilon\,\mathcal{H}_1$, where the size ε of the perturbation is proportional to $\max\{\mu_i/\mu\}$:

$$\mathcal{H}(L, G, H, \ell, g, h, t) = \mathcal{H}_0(L) + \varepsilon\,\mathcal{H}_1(L, G, H, \ell, g, h, t) \tag{3.8}$$

with:

$$\begin{cases} \mathcal{H}_0 = -\dfrac{\mu^2}{2L^2} \\ \varepsilon\,\mathcal{H}_1 = -\displaystyle\sum_{i=1}^{N} \mu_i \left(\frac{1}{|\mathbf{r} - \mathbf{r}_i|} - \mathbf{r} \cdot \frac{\mathbf{r}_i}{|\mathbf{r}_i|^3} \right) \end{cases} \tag{3.9}$$

That Hamiltonian is written in *osculating* coordinates, defining the instantaneous motion of the small body. This is the starting point of every secular model presented in this work, for both different types of dynamics (resonant or non-resonant) and different forms of the planetary orbits (the known functions $\mathbf{r}_i(t)$). All the problem is to define rigorously, in the form of a canonical change of coordinates, the transformation leading from the osculating coordinates (red curve of Fig. 2.2) to the secular ones (blue curve).

In order to study the specific role of each planet, we must choose a planetary model, that is an explicit formulation of the $\{\mathbf{r}_i(t)\}$ functions to be put in (3.7). This can be done either by a synthetic representation (see appendix A), or by analytical expansions as in Lemaître and Morbidelli (1994) or Moons et al. (1998). We will opt for the very simple planetary model used by Kozai (1962), in which the N planets evolve on circular and coplanar orbits. As recalled by Thomas and Morbidelli (1996), such a model can be seen as the dominant term of an expansion in powers of the planetary eccentricities and inclinations. Anyway, that approximation seems quite viable, given that the only relevant planetary perturbations in the region under study come from the four giant planets (eccentricities < 0.1 and inclinations $< 3°$), on relatively stable orbits from the end of the planetary migration (see for instance Laskar, 1988, 1990; Tsiganis et al., 2005). This approximation is even more accurate when choosing the invariant plane of the planetary system as reference plane (instead of the ecliptic). Thanks to that planetary model, it is straightforward to disentangle the effect of each planet, since:

$$\mathbf{r}_i(t) = a_i \begin{pmatrix} \cos\lambda_i(t) \\ \sin\lambda_i(t) \\ 0 \end{pmatrix} \quad ; \quad \lambda_i(t) = n_i\, t + \lambda_{i0} \tag{3.10}$$

where the heliocentric semi-major axis a_i is constant and $n_i^2\, a_i^3 = \mu + \mu_i$. Then, we get rid of the explicit time dependency by defining the angles $\{\lambda_i\}$ as new canonical coordinates, along with their conjugate momenta $\{\Lambda_i\}$ artificially added to the non-perturbed part $\mathcal{H}_0$:

$$\mathcal{H}_0 = -\frac{\mu^2}{2L^2} + \sum_{i=1}^{N} n_i\, \Lambda_i \tag{3.11}$$

The general form of the Hamiltonian function is finally:

$$\mathcal{H}\Big(\{\Lambda_i\}, L, G, H, \{\lambda_i\}, \ell, g, h\Big) = \mathcal{H}_0\Big(\{\Lambda_i\}, L\Big) + \varepsilon\, \mathcal{H}_1\Big(L, G, H, \{\lambda_i\}, \ell, g, h\Big) \tag{3.12}$$

3.2 Non-resonant case

Let us now switch to secular coordinates. In order to do so, we will use the Lie-series formalism (see Sect. 2.3) applied to the perturbed Hamiltonian system (3.12). In this section, we assume that there is no mean-motion resonance in the system, so the fast angles ℓ and $\{\lambda_i\}$ can be removed by a close-to-identity transformation. In the *secular coordinates*, the Hamiltonian function is then:

$$\mathcal{F} = \mathcal{F}_0 + \varepsilon\, \mathcal{F}_1 + \mathcal{O}(\varepsilon^2) \tag{3.13}$$

where $\mathcal{F}_0$ is *functionally* equal to $\mathcal{H}_0$ and $\varepsilon\,\mathcal{F}_1$ is *functionally* equal to the average of $\varepsilon\,\mathcal{H}_1$ with respect to the independent angles ℓ and $\lambda_1, \lambda_2 ... \lambda_N$. In the region considered here, we judge enough to carry on the transformation up to the first order in ε.

The average of the indirect part of $\varepsilon\,\mathcal{H}_1$ is quite simple, since even for a planet i with non-zero eccentricity and inclination, we have from (2.26):

$$\frac{1}{2\pi}\int_0^{2\pi} \frac{\mathbf{r_i}}{r_i^3}\,\mathrm{d}\lambda_i \;=\; \frac{1}{2\pi}\int_0^{2\pi} \frac{\mathbf{r_i}}{r_i^3}\,\frac{r_i^2\,\mathrm{d}\nu_i}{a_i^2\sqrt{1-e_i^2}} \;=\; \frac{1}{a_i^2\sqrt{1-e_i^2}}\,\frac{1}{2\pi}\int_0^{2\pi} \frac{\mathbf{r_i}}{r_i}\,\mathrm{d}\nu_i \;=\; \mathbf{0} \quad (3.14)$$

This is true *a fortiori* for $e_i = I_i = 0$, so the indirect part of the perturbation cancels out. In order to calculate the average of the direct part, however, a choice has to be made. With $\mathcal{H}$ as described above, it is indeed impossible to compute the required integrals analytically without the use of infinite series. Section 3.2 is thus organised as follows: in Sect. 3.2.1, the analytical model of Kozai (1962) is adapted to the outer Solar System. The dominant terms are then studied in Sect. 3.2.2. Naturally, this will give only a rough picture of the secular dynamics, but some general results will be obtained and guide the construction of an "exact" semi-analytical model in Sect. 3.2.3.

3.2.1 Analytical solution

The possible very large eccentricities and inclinations of the trans-Neptunian objects make inefficient the use of classical expansions around a circular orbit in the planetary plane as in Murray and Dermott (1999). A development centred on some specific values (see for instance Roig et al., 1998) would also be inappropriate because of possible large variations of orbital elements, and because it would imply a loss of generality. Instead, supposing that the heliocentric distance of the small body is always larger than the one of the farthest planet considered (here, Neptune), the idea is to use a development in Legendre Polynomials of the inverse mutual distances, that is in powers of the $\{r_i/r\}$ ratios:

$$\frac{1}{|\mathbf{r}-\mathbf{r}_i|} = \frac{1}{r}\sum_{n=0}^{\infty}\left(\frac{r_i}{r}\right)^n P_n(\cos\psi_i) \quad (3.15)$$

In that expression, the angle ψ_i is defined by:

$$\cos\psi_i = \widehat{(\mathbf{r},\mathbf{r}_i)} = \frac{\mathbf{r}\cdot\mathbf{r}_i}{r\,r_i} \quad (3.16)$$

and the functions $\{P_n\}$ are the Legendre polynomials:

$$\begin{array}{ll} P_0(x) = 1 & P_5(x) = (63\,x^5 - 70\,x^3 + 15\,x)/8 \\ P_1(x) = x & P_6(x) = (231\,x^6 - 315\,x^4 + 105\,x^2 - 5)/16 \\ P_2(x) = (3\,x^2 - 1)/2 & P_7(x) = (429\,x^7 - 693\,x^5 + 315\,x^3 - 35\,x)/16 \\ P_3(x) = (5\,x^3 - 3\,x)/2 & \ldots \\ P_4(x) = (35\,x^4 - 30\,x^2 + 3)/8 & \end{array} \quad (3.17)$$

which can be obtained from Bonnet's recursion formula:

$$(n+1)P_{n+1}(x) = (2n+1)xP_n(x) - nP_{n-1}(x) \ , \ n > 1 \tag{3.18}$$

One can note that any Legendre polynomial of even order involves only even powers of x, and any polynomial of odd order involves only odd powers of x. This can be shown using the recursion formula. Thanks to the planetary model used (3.10), the angle ψ_i writes simply:

$$\begin{aligned} \cos\psi_i = \quad & \big(\cos(\omega+v)\cos\Omega - \sin(\omega+v)\sin\Omega\cos I\big)\cos\lambda_i \\ & + \big(\cos(\omega+v)\sin\Omega + \sin(\omega+v)\cos\Omega\cos I\big)\sin\lambda_i \end{aligned} \tag{3.19}$$

or schematically $\cos\psi_i = \alpha\cos\lambda_i + \beta\sin\lambda_i$. Computing first the average of (3.15) with respect to λ_i, we get a sum of integrals of the different powers of $\cos\psi_i$. The odd-order polynomials all vanish, since they involve only integrals of the form:

$$\chi^{2k+1} = \frac{1}{2\pi}\int_0^{2\pi} (\alpha\cos\lambda_i + \beta\sin\lambda_i)^{2k+1}\,\mathrm{d}\lambda_i \quad , \quad k \in \mathbb{N} \tag{3.20}$$

which are all zero (see the proof in B.2.1). The even-order polynomials, on the contrary, result in terms of the form:

$$\chi^{2k} = \frac{1}{2\pi}\int_0^{2\pi} (\alpha\cos\lambda_i + \beta\sin\lambda_i)^{2k}\,\mathrm{d}\lambda_i \quad , \quad k \in \mathbb{N} \tag{3.21}$$

which can be computed explicitly:

$$\begin{cases} \chi^0 = 1 \\ \chi^{2k} = \dfrac{1\times 3\times ...\times(2k-1)}{2\times 4\times ...\times 2n}(\alpha^2+\beta^2)^k \ , \ k = 1,2,3... \end{cases} \tag{3.22}$$

(see the proof in B.2.2). Consequently, we get:

$$\frac{1}{(2\pi)^N}\int_0^{2\pi}\!\!\int_0^{2\pi}\!\!...\int_0^{2\pi} \varepsilon\mathcal{H}_1 \ \mathrm{d}\lambda_1\mathrm{d}\lambda_2...\mathrm{d}\lambda_N = -\frac{1}{r}\sum_{n=0}^{+\infty}\left(\sum_{i=1}^{N}\mu_i\left(\frac{a_i}{r}\right)^{2n}\right)P_{2n}(\chi) \tag{3.23}$$

which remains to be averaged over ℓ to get the secular Hamiltonian. The integral is more conveniently realised over the real anomaly ν (from Eq. 2.26), appearing in r via (2.29) and in χ through:

$$\alpha^2+\beta^2 = \cos^2(\omega+\nu) + \sin^2(\omega+\nu)\cos^2 I \tag{3.24}$$

Each polynomial $2n$ in (3.23) leads to the computation of $n+1$ integrals of the form:

$$\frac{1}{2\pi}\int_0^{2\pi}\frac{(\alpha^2+\beta^2)^k}{r^{2n+1}}\,\mathrm{d}\ell = \frac{1}{a^2\sqrt{1-e^2}}\,\frac{1}{2\pi}\int_0^{2\pi}\frac{(\alpha^2+\beta^2)^k}{r^{2n-1}}\,\mathrm{d}\nu \quad , \quad k = 0,1,2...n \tag{3.25}$$

These integrals have a well-defined analytical formulation, but their expression becomes quickly very long when n grows. The final result can be concisely written as:

$$\varepsilon\,\mathcal{F}_1 = -\sum_{i=1}^{N}\frac{1}{4\pi^2}\int_0^{2\pi}\!\!\int_0^{2\pi}\frac{\mu_i}{|\mathbf{r}-\mathbf{r}_i|}\,\mathrm{d}\lambda_i\,\mathrm{d}\ell = -\frac{1}{a}\sum_{n=0}^{+\infty}\left(\sum_{i=1}^{N}\mu_i\left(\frac{a_i}{a}\right)^{2n}\right)\mathcal{B}_n(e,I,\omega) \quad (3.26)$$

where $\mathcal{B}_0 = 1$, and for $n > 0$ the $\mathcal{B}_n$ functions are of the form:

$$\mathcal{B}_n(e,I,\omega) = \frac{\alpha_n}{(1-e^2)^{\frac{4n-1}{2}}}\sum_{k=0}^{n-1} P_n^k(e)\times Q_n^k(\cos I)\times\, e^{2k}\,\sin^{2k}(I)\,\cos(2k\,\omega) \quad (3.27)$$

In that expression, α_n is a rational coefficient and P_n^k et Q_n^k are even polynomials of order $2(n-k-1)$ and $2(n-k)$ respectively. The appendix B.2.3 shows the first 8 terms. The variables (a,e,I,ω) should then be replaced by their expressions in Delaunay elements (2.88) to get the Hamiltonian in canonical coordinates. Its general expression is thus (at first order of the planetary masses):

$$\mathcal{F}\Big(\{\Lambda_i\},L,G,H,g\Big) = \mathcal{F}_0\Big(\{\Lambda_i\},L\Big) + \varepsilon\,\mathcal{F}_1\Big(L,G,H,g\Big) \quad (3.28)$$

where $\mathcal{F}_0$ is given by (3.11) and $\varepsilon\,\mathcal{F}_1$ by (3.26). Please note that even if we write the coordinates with the same symbols as before, we now manipulate the *secular* coordinates, related to the osculating ones by a complex canonical transformation (see Sect. 2.3).

One can see that the angle $h = \Omega$ has disappeared during the average over λ_i (see Eq. 3.24). This happened because of the symmetry of rotation implied by the circular and coplanar planetary orbits. Furthermore, the secular Hamiltonian depends only on the magnitude of $H/G = \cos I$ (not its sign), and it is π-periodic in $g = \omega$ and symmetric with respect to $\pi/2$. The non-resonant secular dynamics is rather simple because we are left with only one degree of freedom: the secular momenta L and $\Lambda_1, \Lambda_2 ... \Lambda_N$ are conserved, as well as H thanks to the extra disappearance of h. Hence, all the possible orbits can be described by plotting the level curves of $\mathcal{F}$ in the (G,g) plane, with L and H as free parameters. For a more direct interpretation of the results, we can also use the plane (q,ω), equivalent to (G,g), and the two parameters can be rewritten as:

$$\begin{cases} a = L^2/\mu \\ C_K = (H/L)^2 = (1-e^2)\cos^2 I \end{cases} \quad (3.29)$$

The "Kozai constant" C_K links the secular eccentricity and inclination of the particle. We chose to square the H/L ratio to stress the independence of $\mathcal{F}$ over its sign. The variations allowed by the value of C_K are then:

$$e \in \Big[0\,,\sqrt{1-C_K}\Big] \quad \text{and} \quad \cos^2 I \in \Big[C_K\,,1\Big] \quad (3.30)$$

In order to explore the phase space with respect to the two parameters, let us remark at first that for a circular orbit, the secular Hamiltonian becomes also independent of $g = \omega$. The elements (a,e,I) are thus constant, and the angles Ω and ω (ill-defined in that case) circulate.

3.2.2 Analysis of the lowest-order terms

In the study of a dynamical system, the first step is to look for possible equilibrium points. An insight of the non-resonant secular dynamics can be obtained by truncating the development (3.26). The general form of Eqs. (3.26,3.27) makes obvious that the truncated model will be accurate only for high semi-major axes and small eccentricities (that is, for trajectories always far from Neptune). Dropping the constant parts and carrying the expansion up to the very first term containing the angle $\omega = g$, we get (see appendix B.2.3):

$$\begin{aligned}\mathcal{F} = {} & \delta^2 \frac{1}{8} \frac{1 - 3\cos^2 I}{(1-e^2)^{3/2}} \\ & + \delta^4 \frac{9}{1024} \frac{(-3 + 30\cos^2 I - 35\cos^4 I)(2 + 3\,e^2) + 10\,(1 - 7\cos^2 I)\,e^2\,\sin^2 I \cos(2\,\omega)}{(1-e^2)^{7/2}} \\ & + \mathcal{O}(\delta^6)\end{aligned} \tag{3.31}$$

where we wrote symbolically:

$$\delta^{2n} \equiv \frac{1}{a} \sum_{i=1}^{N} \mu_i \left(\frac{a_i}{a}\right)^{2n} \tag{3.32}$$

In order to write down the dynamical equations, the Hamiltonian (3.31) needs to be expressed in canonical coordinates. Replacing the Keplerian elements by their expression in terms of the Delaunay coordinates, we get:

$$\begin{aligned}\mathcal{F} = {} & \delta^2 \frac{1}{8} \left(\frac{L}{G}\right)^3 \left(1 - 3\left(\frac{H}{G}\right)^2\right) \\ & + \delta^4 \frac{9}{1024} \left(\frac{L}{G}\right)^7 \left[\left(-3 + 30\left(\frac{H}{G}\right)^2 - 35\left(\frac{H}{G}\right)^4\right)\left(5 - 3\left(\frac{G}{L}\right)^2\right)\right. \\ & \qquad \left. + 10\left(1 - 7\left(\frac{H}{G}\right)^2\right)\left(1 - \left(\frac{H}{G}\right)^2\right)\left(1 - \left(\frac{G}{L}\right)^2\right)\cos(2g)\right] \\ & + \mathcal{O}(\delta^6)\end{aligned} \tag{3.33}$$

Up to the lowest order, the equations of motion are thus:

$$\begin{cases} \dot{g} = \dfrac{\partial \mathcal{F}}{\partial G} = \delta^2 \dfrac{3}{8} \dfrac{L^3}{G^6}\left(5\,H^2 - G^2\right) + \mathcal{O}(\delta^4) \\ \dot{G} = -\dfrac{\partial \mathcal{F}}{\partial g} = \delta^4 \dfrac{45}{256} \left(\dfrac{L}{G}\right)^7 \left(1 - 7\left(\dfrac{H}{G}\right)^2\right)\left(1 - \left(\dfrac{H}{G}\right)^2\right)\left(1 - \left(\dfrac{G}{L}\right)^2\right)\sin(2\,g) + \mathcal{O}(\delta^6) \end{cases} \tag{3.34}$$

The condition of stationarity writes:

$$\begin{cases} \dot{g} = 0 + \mathcal{O}(\delta^4) \\ \dot{G} = 0 + \mathcal{O}(\delta^6) \end{cases} \iff \begin{cases} G^2 = 5H^2 \\ \sin(2g) = 0 \end{cases} \quad \text{that is} \quad \begin{cases} \cos^2 I = 1/5 \\ \sin(2\omega) = 0 \end{cases} \tag{3.35}$$

The equilibrium points correspond thus to two very specific values of the inclination (about 63.4° or 116.6°) and of the argument of perihelion (0 or $\pi/2 \mod \pi$). In order to check the stability of the equilibrium points, let us note $\mathbf{z}$ the position $(g, G)^{\mathrm{T}}$ and f the vector field defined in (3.34) by $\dot{\mathbf{z}} = f(\mathbf{z})$. If we consider a small displacement $\Delta\mathbf{z}$ around a solution $\mathbf{z}_0(t)$, we have at first order:

$$\frac{\mathrm{d}\Delta\mathbf{z}}{\mathrm{d}t} = \mathrm{D}f(\mathbf{z}_0)\Delta\mathbf{z} \tag{3.36}$$

This system is autonomous if $\mathbf{z}_0$ is a fixed point, and by using the fixed point expressed in (3.35) we get:

$$Df(\mathbf{z}_0) = \begin{pmatrix} \mathcal{O}(\delta^4) & \frac{-3L^3}{100\sqrt{5}|H|^5}\delta^2 + \mathcal{O}(\delta^4) \\ \eta\,\frac{9L^5(5H^2-L^2)}{10000\sqrt{5}|H|^7}\delta^4 + \mathcal{O}(\delta^6) & \mathcal{O}(\delta^6) \end{pmatrix} \tag{3.37}$$

where the coefficient η is defined as:

$$\eta = \begin{cases} +1 \text{ for the equilibrium point at } g = 0 \mod \pi \\ -1 \text{ for the equilibrium point at } g = \pi/2 \mod \pi \end{cases} \tag{3.38}$$

Since $\mathrm{D}f$ is a constant matrix, the general solution of the variational equations expressed in (3.36) can be written as:

$$\Delta\mathbf{z}(t) = a\exp(\nu_+ t)\,\mathbf{v}_+ + b\exp(\nu_- t)\,\mathbf{v}_- \tag{3.39}$$

where a and b are constants given by the initial conditions, $\mathbf{v}_\pm$ are the eigenvectors of $\mathrm{D}f$ and $\nu_\pm$ are the associated eigenvalues. The expression of the eigenvalues can be directly computed from (3.37):

$$\nu_\pm = \pm\frac{3}{1000}\sqrt{\frac{3}{5}}\frac{L^4}{H^6}\sqrt{\eta\,\delta^2\,\delta^4\,(L^2 - 5H^2)} + \mathcal{O}(\delta^5) \tag{3.40}$$

with $(L^2 - 5H^2) \geqslant 0$ because of (3.35). The equilibrium at $g = 0 \mod \pi$ is a saddle point, since the corresponding eigenvalues $\nu_\pm$ are real (the solution 3.39 has one component exponentially rejoining the equilibrium, and one leaving it). On the other hand, the equilibrium at $g = \pi/2 \mod \pi$ is central, since the corresponding eigenvalues $\nu_\pm$ are pure imaginary (the solution 3.39 has only components oscillating around the equilibrium with frequencies $i\nu_\pm$).

Figure 3.1 gives an example of level curves obtained from the truncated secular Hamiltonian (3.33), taking into account Jupiter, Saturn, Uranus and Neptune ($N = 4$), the mass of the inner planets being added to the Sun. The equilibrium is not located exactly at $I = 63.4°$ because we neglected the term of order δ^4 for $\dot{g}$ in Eq. (3.35). Taking that term into account (or considering the infinite series as in Sect. 3.2.3), the inclination at equilibrium is actually a function of a and C_K. Figure 3.2 shows the period of oscillation (3.40) around the stable equilibrium as a function of the two

parameters. On the red line, the perihelion at equilibrium is equal to the semi-major axis of Neptune (below which the analytical development is not defined). Then, it goes up with C_K, until it reaches a for $C_K = 1/5$. We remark that the secular timescale in that region is almost always larger than a billion years, which prevents probably any occurrence of a secular resonance with the planets. This is a new argument in support of a very simple planetary model (with fixed orbital elements) and is consistent with the results of Knezevic et al. (1991).

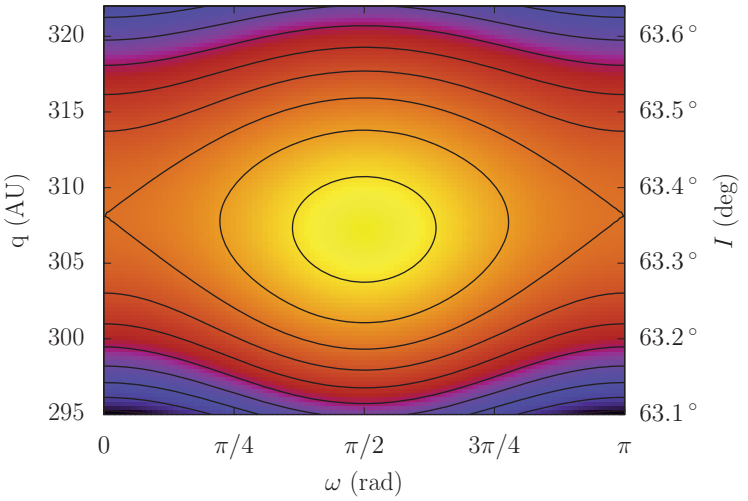

Figure 3.1 – Level curves of the truncated version of $\mathcal{F}$ with terms up to δ^4 (parameters: $a = 400$ AU, $C_K = 0.19$). The inclinations on the right are deduced from q by a and C_K and are equivalent to $(116.9°, 116.8°...116.4°)$, from bottom to top.

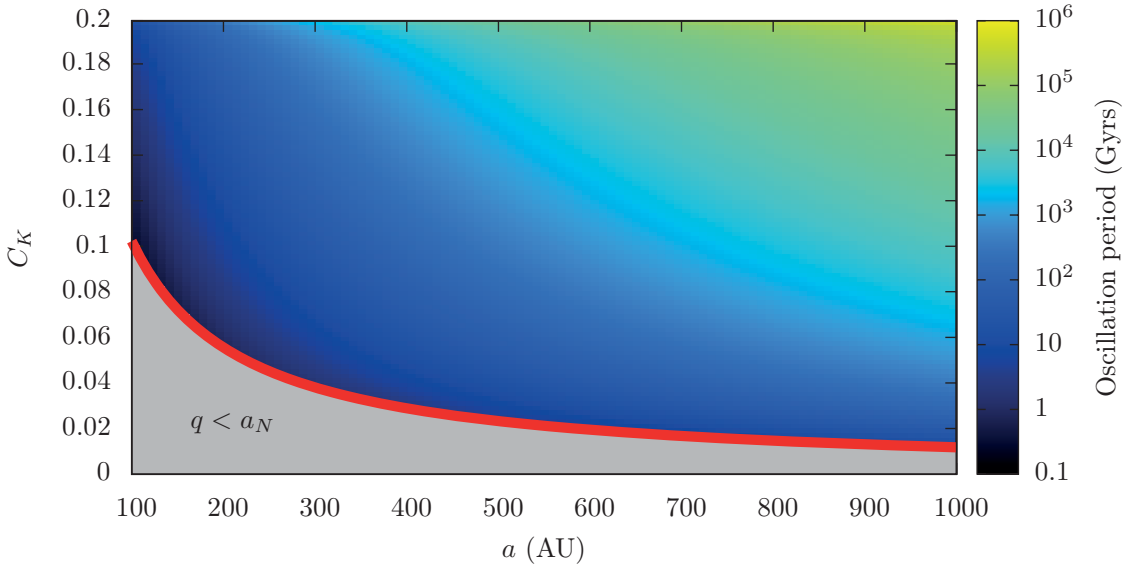

Figure 3.2 – Oscillation period for small oscillations around the stable equilibrium. The red line defines the limit of convergence of the Legendre development (that is $q = a_N$).

3.2.3 Semi-analytical solution

In the previous section, we saw that it is possible to construct an analytical development of the non-resonant secular Hamiltonian in powers of the (r_i/r) ratios. The analysis of the first terms, then, led to qualitative results about the geometry of the phase space. Naturally, these results are asymptotic, accurate only for high semi-major axes and small eccentricities, and are not valid for orbits near or inside the planetary region. In particular, Gallardo et al. (2012) reported that the oscillation island at $\omega = \pi/2$ disappears below some value of the semi-major axis and that the equilibrium at $\omega = 0$ can become stable.

In order to get quantitative and accurate results, one can turn to numerical methods to compute the double average of $\varepsilon\,\mathcal{H}_1$: we thus get its exact value, that is, the value obtained for an infinite number of terms in the Legendre development. In that section and the rest of this work, we will use the integration package of Piessens et al. (1983), already successfully applied to such problems by Thomas and Morbidelli (1996) and Gronchi and Milani (1999). Each evaluation of $\mathcal{F}$ on a point (ω, q) requires the numerical evaluation of the double integral (3.26). The integrand is singular if the orbit of the particle crosses the orbit of one planet, but the integral itself is well-defined and it can be computed numerically by splitting it at the singularities[2] (see appendix B.5.1). Of course, the general properties of the secular Hamiltonian still hold (Eq. 3.28 and comments thereafter) and help us to apprehend the geometry of the phase space. We recall in particular that it is π-periodic with respect to ω. The non-resonant secular regime beyond Neptune is qualitatively known from the work of Gallardo et al. (2012). There are four different cases according to the values of the parameters:

a) no equilibrium point

b) one stable equilibrium point at $\omega = 0 \mod \pi$

c) one stable equilibrium point at $\omega = \pi/2 \mod \pi$

d) stable equilibrium points at both $\omega = 0$ and $\pi/2 \mod \pi$

To fix ideas, Fig. 3.3 gives an example of phase portrait for each case, obtained from the semi-analytical model. When the semi-major axis is out of any mean-motion resonance and not much affected by chaotic diffusion, this semi-analytical model is quite well representative of the true dynamics of the particles. As an example, Fig. 3.4 shows the evolution of a fictitious body obtained by a non-averaged numerical integration. The variations of the semi-major axis are only of second order with respect to the perturbation. The additional oscillations present in q and I are due to the small eccentricities and inclinations of the planets and their variations. They turn the predicted periodic

[2]Even if the semi-analytical model is also valid for a perihelion inside the planetary region, we still limit the study to $q > a_{\mathrm{N}}$ as this is the region of interest in the scope of this work. For details about the non-resonant secular dynamics with a perihelion *inside* the planetary region, see Thomas and Morbidelli (1996) or Gallardo et al. (2012).

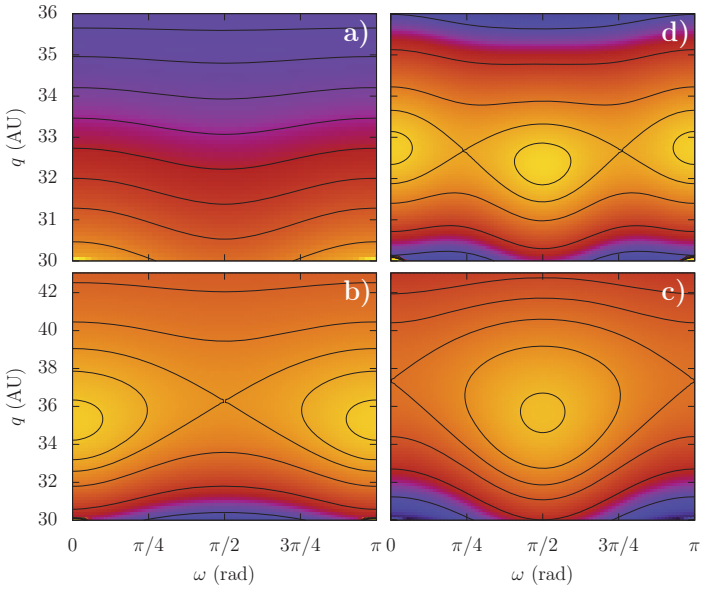

Figure 3.3 – The four possible types of geometry of the phase space for a non-resonant secular dynamics beyond Neptune. The chosen parameters are: **a)** $a = 36$ AU, $C_K = 0.15$; **b)** $a = 46.1$ AU, $C_K = 0.222$; **c)** $a = 80$ AU, $C_K = 0.16$; **d)** $a = 60$ AU, $C_K = 0.184$.

orbit into a quasi-periodic trajectory, which oscillates around the level curve given by the semi-analytical model. Finally, Fig. 3.5 shows that when the semi-major axis diffuses slowly, the trajectory still follows roughly the non-resonant secular dynamics, even if the particle is temporarily locked into some mean-motion resonances. Of course, this is only true if the resonant parts of the trajectory are transient enough. It should also be noted that this particle has a very high inclination, which minimises the effects of the resonances (see Chp. 4).

General results about the non-resonant dynamics can be obtained by a systematic exploration of the parameter space. Figure 3.6 shows that the analysis of the lowest-order terms remains qualitatively relevant for a semi-major axis greater than about 80 AU: the equilibrium point at $\omega = \pi/2$ is the only one to remain stable. In other words, the phase space is filled with circulation zones of ω, where the perihelion oscillates with a very small amplitude. The only substantial variations of q are located around the stable equilibrium at $\omega = \pi/2$, where ω can oscillate (see Sect. 3.2.2).

In order to define "how substantial" it is, we used the semi-analytical approach to determine the exact width of the island with respect to the two parameters. The result is shown in Fig. 3.7: for each value of the parameters (a, C_K), we searched numerically for the position of the saddle point, and then followed the two separatrices until they reached their maximum deployment. In the grey areas, there is no equilibrium point possible for a perihelion beyond the semi-major axis of Neptune: in particular, we note that the upper limit of $C_K = 1/5$ obtained analytically is rather well respected in general, and almost exact for $a > 300$ AU. The important point of Fig. 3.7 is the existence of an *asymptotic maximum width* of the oscillation island of about 16.4 AU. Since this result is only numerical, there is actually no way to determine if it is a true asymptote or if the rate of increase tends to a very small value (but we note that an analytical search for the two separatrices at $\omega = \pi/2$ using an expansion of Eq. 3.33

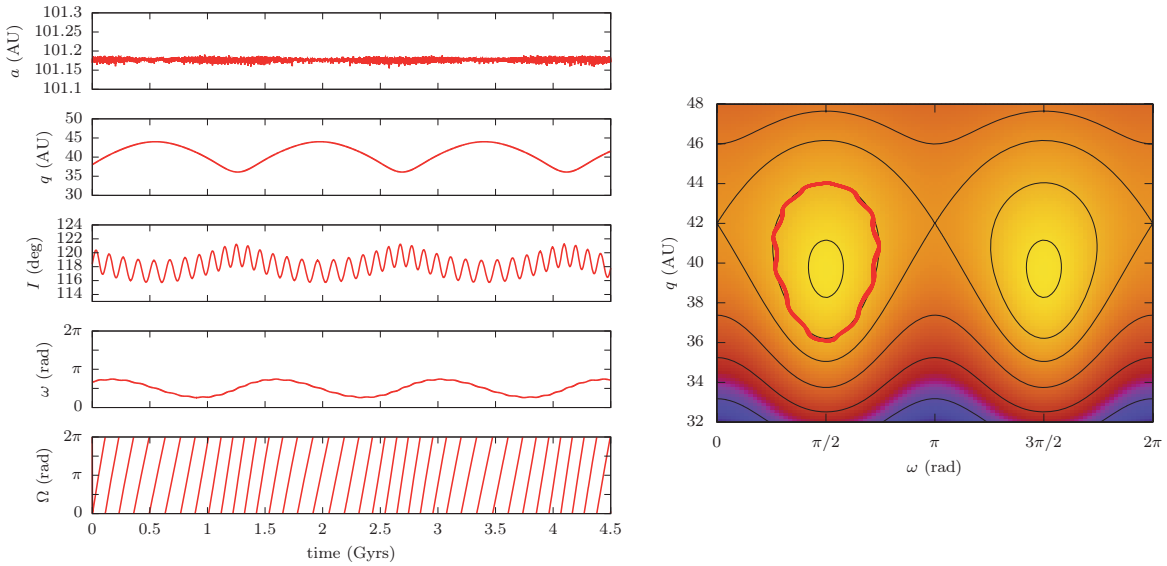

Figure 3.4 – Numerical integration of the non-averaged equations of motions, given by the Hamiltonian (3.9) without any transformation. It includes the four giant planets with the secular variation of their orbital elements (synthetic representation by Laskar, 1990, supposed valid all along the integration span). The mass of the inner planets are added to the Sun. On the left, the Keplerian elements are computed with respect to the barycentre of the Solar System. On the right, the trajectory is projected on the plane (ω, q) in front of the level curves given by the semi-analytical model ($a = 101.18$ AU and $C_K = 0.143$). In that case, we used heliocentric coordinates (for comparison to the secular model), which were filtered to remove the short-period oscillations due to Jupiter.

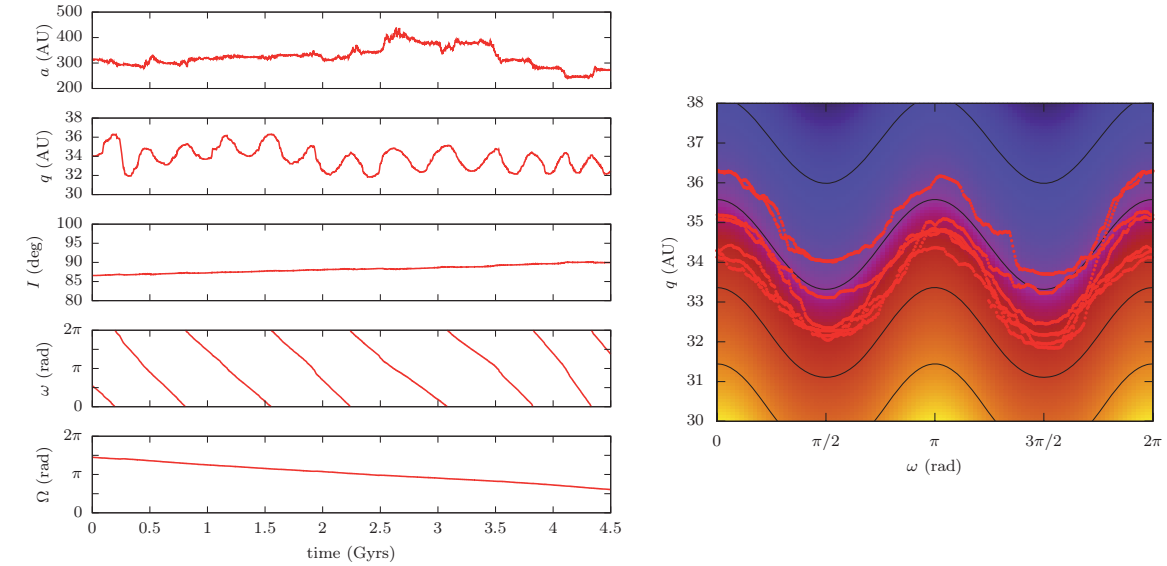

Figure 3.5 – Same as Fig. 3.4 for a particle in the diffusive region (Scattered Disc). Strictly speaking, each new value of the semi-major axis defines another secular model. On the right graph, the parameters chosen for drawing the level curves are $a = 325$ AU and $C_K = 0.00025$.

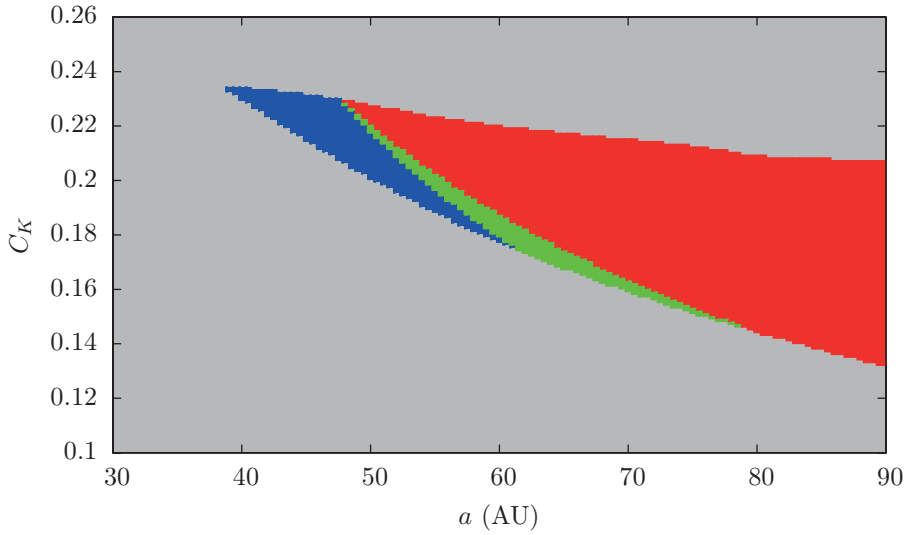

Figure 3.6 – General geometry of the phase space with respect to the two parameters. The grey region denotes the absence of any equilibrium point for a perihelion distance larger than the semi-major axis of Neptune. The blue region stands for the presence of a stable equilibrium point at $\omega = 0$, the red one for a stable equilibrium point at $\omega = \pi/2$, and the green region for the simultaneous existence of both. See Fig. 3.3 for an example of each regime. For higher semi-major axes, the red region fills progressively the graph from $C_K = 0$ to $C_K = 0.2$ (see Fig. 3.7 for a wider scale).

at order 2 of G around the equilibrium does show an asymptotic flat width at about 16.4065975 AU). However, this is not of great concern because a semi-major axis larger than some tens of thousands AU looses obviously its physical meaning (please notice the log-scale in Fig. 3.7). Thus, if a particle begins with an initial perihelion near Neptune (say 35 AU), the very maximum value it could reach in the future with that mechanism would be of about 50 AU. The excursion is consequent but still well below the perihelion distances of Sedna and $2012\mathrm{VP}_{113}$. Furthermore, we saw in Sect. 3.2.2 that the oscillation island is very narrow in terms of inclination (a few degrees near 63° and 117°) which restricts severely the probability for a given object to undergo that kind of process.

For completeness, Fig. 3.8 shows the position of this stable equilibrium point, both in eccentricity and inclination. The inclination at equilibrium is never farther than 3° from the rough analytical value obtained in Sect. 3.2.2 ($I \approx 63.4°$ or 116.6°). As expected, it is more precise for large semi-major axes and small eccentricities. Its position in eccentricity was also well predicted: the perihelion at equilibrium is near the semi-major axis of Neptune for small values of C_K, and near the circular orbit when C_K tends to 1/5.

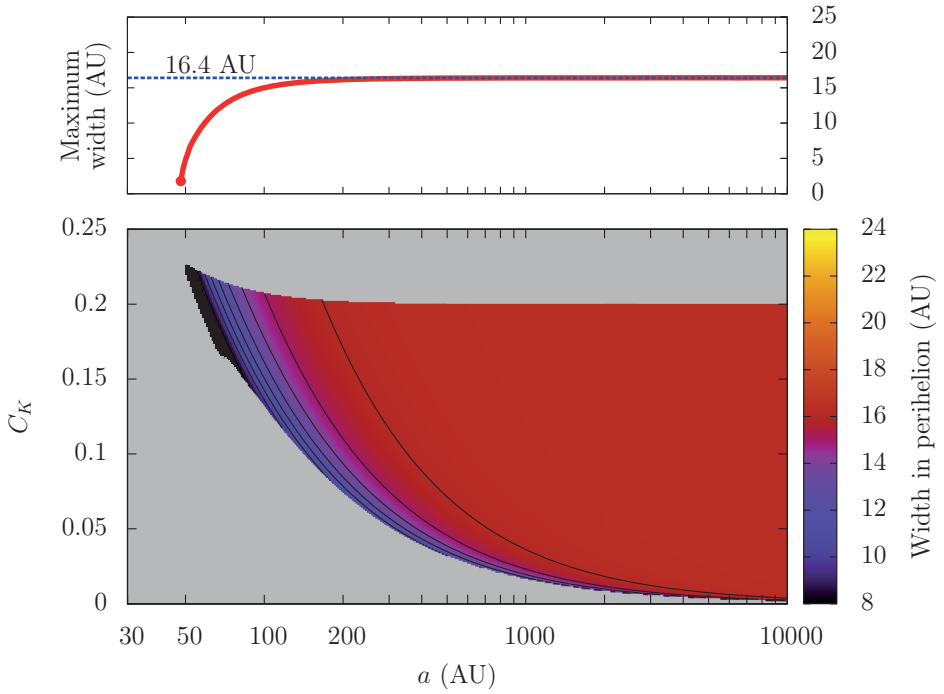

Figure 3.7 – Width of the oscillation island around the stable equilibrium point at $\omega = \pi/2$. On the top graph, only the maximum value for all C_K is retained. The grey region denotes the absence of such equilibrium point for a perihelion distance larger than the semi-major axis of Neptune (or regions where the equilibrium point is so close to it that the lower separatrix ends below). The black lines are iso-width curves, plotted for every integer value (the upper one corresponds to 16 AU). There is an asymptotic value of $q \approx 16.4$ AU, filling progressively all the graph when a increases (the colour shade stops on red). The bump around $a = 70$ AU marks the disappearance of the $\omega = 0$ equilibrium point (see Fig. 3.6).

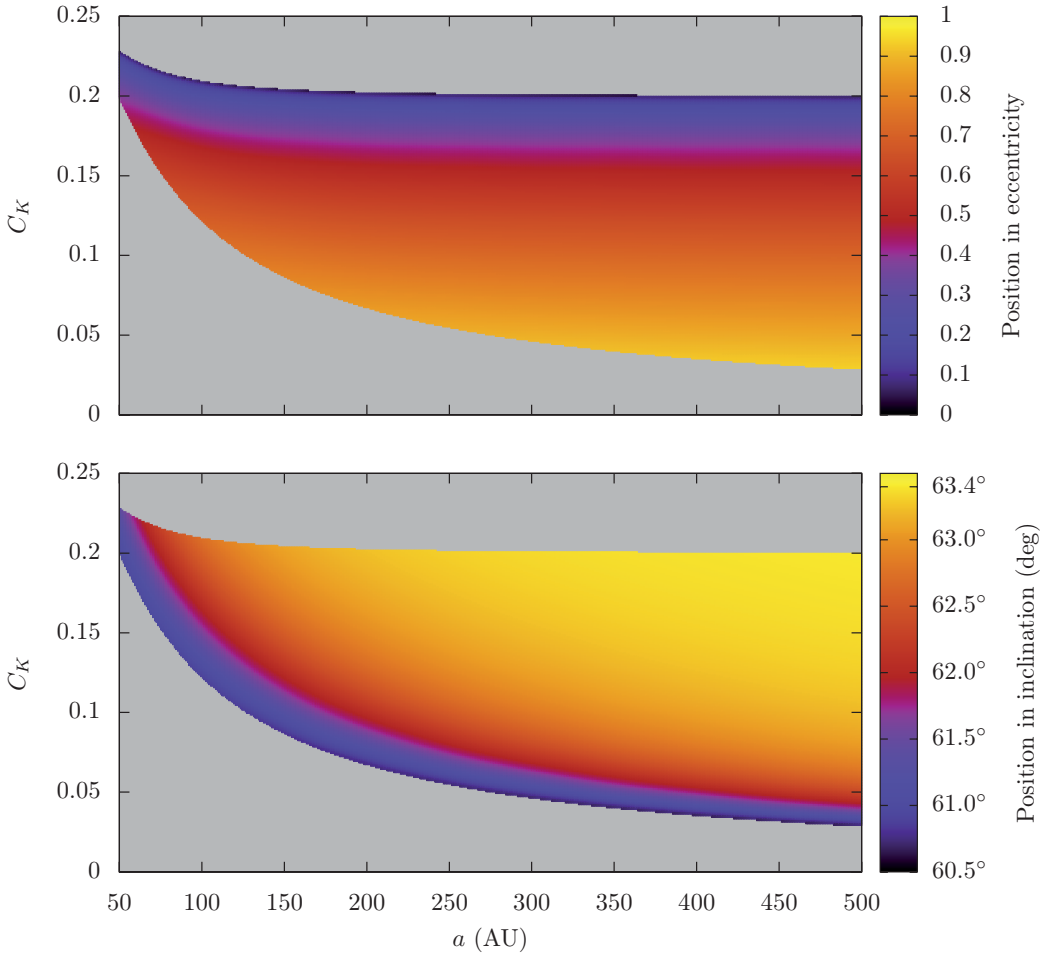

Figure 3.8 – Position of the stable equilibrium point at $\omega = \pi/2$ as given by the semi-analytical model. The grey regions stand for the absence of equilibrium point for a perihelion larger than the semi-major axis of Neptune. Please remember that the eccentricity and the inclination are linked through $C_K = \sqrt{1-e^2}\cos I$. The inclinations shown are equivalent to $180° - I$ (retrograde case).

3.3 Case of a single resonance

If the particle presents a mean-motion resonance with one of the planets, the coordinate change used in Sect. 3.2 in order to get the secular coordinates is not defined any more (some terms explode in the neglected part of the Lie series). A particular treatment for the resonant terms is thus required. Let us consider a single resonance of type $k_p : k$ with a resonant angle of the form:

$$\sigma = k\,\lambda - k_p\,\lambda_p - (k - k_p)\,\varpi \quad , \quad k, k_p \in \mathbb{N} \quad , \quad k > k_p \tag{3.41}$$

In this expression, the angles λ and λ_p are the mean longitudes of the particle and of the planet p involved, and $\varpi = \omega + \Omega$. The integer $k - k_p$ is traditionally called the *resonance order*. In our case, it is directly linked to the magnitude of the semi-major axis a of the particle. Since the planets are supposed on circular and coplanar orbits, no other planetary angle can appear. Resonances of that form are of "eccentricity type". They are by far the most frequent for the observed trans-Neptunian objects, which have eccentricities ranging to very high values (more than 0.9). This could be explained by a very simplified scenario of formation: considering a small body starting with an almost circular and zero-inclination orbit slightly beyond Neptune, the chaotic diffusion due to the planetary perturbations would greatly enlarge its semi-major axis with virtually no variation of its perihelion distance nor its inclination. This objects gets thus a very high eccentricity but an inclination still very small, so it is only affected by eccentricity resonances (which can eventually raise its perihelion distance and/or its inclination, as we will see in Chp. 4). The other possible angles associated with the $k_p : k$ resonance involve both ϖ and Ω (mixed type) or Ω alone (inclination type). They can be studied just as we will show for the angle σ: the method is quite general and can be applied to a large variety of dynamical systems. The only feature we need in order to define a suitable secular Hamiltonian is a clear hierarchy between the timescales. In our case, we have now three of them:

- the short periods (M and $\lambda_1, \lambda_2 ... \lambda_N$)
- the semi-secular periods (oscillation of the resonant angle σ)
- the secular periods (precession of ω and Ω)

Contrary to the non-resonant case, the development of a secular model requires thus a two-step procedure. In Sect. 3.3.1 and 3.3.2, we describe the new canonical coordinates used and the geometrical properties of the Hamiltonian function. Then, Sect. 3.3.3 shows the transformation to an intermediary set of coordinates, referred here as "semi-secular", in which the Hamiltonian is left with two degrees of freedom. The second change of coordinates (equivalent to a second averaging step) is described in Sect. 3.3.4: we finally obtain a one-degree-of-freedom secular system very similar to the non-resonant one. As previously, the phase portraits are preferentially drawn in some kind of secular elliptical elements (defined in Sect. 3.3.5), which are more directly interpretable than their canonical counterparts.

3.3.1 Coordinate change

In order to study the dynamics inside and around the k_p:k resonance, we must at first isolate the resonant angle from the short-period terms, as shown for instance by Milani and Baccili (1998). Basically, this consists in defining the angle σ as a new canonical coordinate. From the Delaunay coordinates used so far (Eq. 2.88), this is done by a linear transformation applied to the angles:

$$\begin{pmatrix} \sigma \\ \gamma \\ u \\ v \end{pmatrix} = A \begin{pmatrix} \ell \\ \lambda_p \\ g \\ h \end{pmatrix} = \begin{pmatrix} k & -k_p & k_p & k_p \\ c & -c_p & c_p & c_p \\ 0 & 0 & 1 & 0 \\ 0 & 0 & 0 & 1 \end{pmatrix} \begin{pmatrix} \ell \\ \lambda_p \\ g \\ h \end{pmatrix} \tag{3.42}$$

where c and c_p are integer coefficients, chosen such that:

$$\det A = c\,k_p - c_p\,k = 1 \tag{3.43}$$

This condition makes the transformation unimodular, so that any 2π-periodic function with respect to the previous angles (as the Hamiltonian), is also 2π-periodic with respect to the new ones. If we assume that σ is a slow angle, this makes γ be the fastest circulating angle possible when λ and λ_p are related through (3.41). In others words, γ makes one revolution during a complete cycle of λ and λ_p (k_p turns of λ and k turns of λ_p). Finally, we kept $\omega = g = u$ and $\Omega = h = v$ as independent coordinates since we are interested in their individual secular evolutions. The transformation is then made canonical by applying $(A^T)^{-1}$ on the conjugate momenta (see Sect. 2.2.4):

$$\begin{pmatrix} \Sigma \\ \Gamma \\ U \\ V \end{pmatrix} = \begin{pmatrix} -c_p & -c & 0 & 0 \\ k_p & k & 0 & 0 \\ 0 & 1 & 1 & 0 \\ 0 & 1 & 0 & 1 \end{pmatrix} \begin{pmatrix} L \\ \Lambda_p \\ G \\ H \end{pmatrix} \tag{3.44}$$

and the coordinates $\{\lambda_{i\neq p}\}$ and $\{\Lambda_{i\neq p}\}$ remain unchanged. In these new variables, the Hamiltonian function $\mathcal{H}$ (Eq. 3.12) rewrites:

$$\begin{aligned} &\mathcal{H}\Big(\{\Lambda_{i\neq p}\},\Sigma,\Gamma,U,V,\{\lambda_{i\neq p}\},\sigma,\gamma,u,v\Big) \\ &\qquad = \mathcal{H}_0\Big(\{\Lambda_{i\neq p}\},\Sigma,\Gamma\Big) + \varepsilon\,\mathcal{H}_1\Big(\Sigma,\Gamma,U,V,\{\lambda_{i\neq p}\},\sigma,\gamma,u,v\Big) \end{aligned} \tag{3.45}$$

where the unperturbed part is:

$$\mathcal{H}_0 = -\frac{\mu^2}{2\,(k\,\Sigma + c\,\Gamma)^2} - n_p\,(k_p\,\Sigma + c_p\,\Gamma) + \sum_{\substack{i=1 \\ i\neq p}}^{N} n_i\,\Lambda_i \tag{3.46}$$

and the perturbation writes formally as in (3.7):

$$\varepsilon\,\mathcal{H}_1 = -\sum_{i=1}^{N} \mu_i \left(\frac{1}{|\mathbf{r} - \mathbf{r}_i|} - \mathbf{r}\cdot\frac{\mathbf{r}_i}{|\mathbf{r}_i|^3} \right) \tag{3.47}$$

However, the resonant part now behaves differently, because $r_p \equiv r_p(\sigma, \gamma, u, v)$ whereas for $i \neq p$ we have simply $r_i \equiv r_i(\lambda_i)$. In these coordinates, γ is a fast angle, and σ evolves with an intermediate (or "semi-secular") timescale.

3.3.2 Analytical development: details about the Hamiltonian function

Before switching to the semi-secular coordinates, some general information can be grabbed about the resonant part of $\varepsilon\,\mathcal{H}_1$. Indeed, if we write the inverse of the mutual distances in terms of the Legendre polynomials (3.15), the angles $u = \omega$ and $v = \Omega$ appear in the perturbations only via the scalar product $\mathbf{r} \cdot \mathbf{r}_i$. With the planets on circular and coplanar orbits, it comes then:

$$\frac{\mathbf{r} \cdot \mathbf{r}_i}{r\, r_i} = \cos(\omega + \nu)\cos(\lambda_i - \Omega) + \sin(\omega + \nu)\sin(\lambda_i - \Omega)\cos I \tag{3.48}$$

For the resonant planet p, that quantity writes in the new coordinates:

$$\frac{\mathbf{r} \cdot \mathbf{r}_p}{r\, r_p} = \cos(u + \nu)\cos(k\gamma - c\,\sigma + u) \;+\; \sin(u + \nu)\sin(k\gamma - c\,\sigma + u)\cos I \tag{3.49}$$

where $\cos I$ should be replaced by:

$$\cos I = \frac{k_p\Sigma + c_p\Gamma + V}{k_p\Sigma + c_p\Gamma + U} \tag{3.50}$$

and where the true anomaly ν is only function of e and M:

$$e = \sqrt{1 - \left(\frac{k_p\Sigma + c_p\Gamma + U}{k\Sigma}\right)^2} \quad \text{and} \quad M = k_p\,\gamma - c_p\,\sigma \tag{3.51}$$

We note here an important point: in the new coordinates, the resonant part of $\varepsilon\,\mathcal{H}_1$ is independent of the angle $v = \Omega$. Once again, this comes from our simple planetary model: in that case, the system "particle + planet p" is invariant by rotation around the vertical axis.

We can go further with some trigonometric identities:

$$\begin{cases} 2\cos(u + \nu)\cos(k\gamma - c\,\sigma + u) = \cos(\nu + c\sigma - k\gamma) + \cos(\nu - c\sigma + k\gamma + 2u) \\ 2\sin(u + \nu)\sin(k\gamma - c\,\sigma + u) = \cos(\nu + c\sigma - k\gamma) - \cos(\nu - c\sigma + k\gamma + 2u) \end{cases} \tag{3.52}$$

which show that the resonant part of $\varepsilon\,\mathcal{H}_1$ is also π-periodic in $u = \omega$ and symmetric with respect to $\pi/2$.

3.3.3 Semi-secular Hamiltonian

Thanks to our new definition of the angles (3.42), we can now safely switch to the "semi-secular coordinates", for which the Hamiltonian is independent of the fast angles. This is done by the same close-to-identity transformation as we used in the non-resonant case. Thus, the semi-secular Hamiltonian writes:

$$\mathcal{K} = \mathcal{K}_0 + \varepsilon\,\mathcal{K}_1 + \mathcal{O}(\varepsilon^2) \tag{3.53}$$

where $\mathcal{K}_0$ is functionally equal to $\mathcal{H}_0$ and $\varepsilon\,\mathcal{K}_1$ is functionally equal to the average of $\varepsilon\,\mathcal{H}_1$ with respect to the independent angles γ and $\{\lambda_{i\neq p}\}$. At this point, it is interesting to note that, by mixing the old and new coordinates we have:

$$\gamma = \frac{1}{k_p}\lambda + \frac{1}{k_p}(c_p\,\sigma - u - v) = \frac{1}{k}\lambda_p + \frac{1}{k}(c\,\sigma - u - v) \tag{3.54}$$

Hence, the average with respect to γ is equivalent to an integral over k_p turns of λ (resp. k turns of λ_p), expressing λ_p (resp. λ) via the resonant angle (3.41). Actually, this is the integral usually given for that kind of resonant problems (see for instance Gallardo, 2006b), in which the coordinate change is just made implicit. Whatever the notation used, the semi-secular Hamiltonian (at first order of the planetary masses) writes formally:

$$\mathcal{K}\Big(\{\Lambda_{i\neq p}\}, \Sigma, \Gamma, U, V, \sigma, u\Big) = \mathcal{K}_0\Big(\{\Lambda_{i\neq p}\}, \Sigma, \Gamma\Big) + \varepsilon\,\mathcal{K}_1\Big(\Sigma, \Gamma, U, V, \sigma, u\Big) \tag{3.55}$$

This time, we will not even try to obtain an analytical expression of $\mathcal{K}$, but the indications obtained from Sect. 3.3.2 are useful to understand its general form. In particular, the angle $v = \Omega$ has disappeared: indeed, the $i \neq p$ parts of $\varepsilon\,\mathcal{H}_1$ behave as in the non-resonant case (see Sect. 3.2) and the $i = p$ part was *already* independent of v. For the same reasons, $\mathcal{K}$ is also π-periodic in $u = \omega$ and symmetric with respect to $\pi/2$.

The semi-secular constants of motion are then V, Γ and the various $\{\Lambda_{i\neq p}\}$, and these lasts will now be omitted since they appear only as a constant term in $\mathcal{K}$. Concerning the Γ momentum, one can notice that:

$$\begin{cases} \Sigma = \dfrac{1}{k}\sqrt{\mu a} - \dfrac{c}{k}\Gamma \\ U = \sqrt{\mu a}\left(\sqrt{1-e^2} - \dfrac{k_p}{k}\right) + \dfrac{1}{k}\Gamma \\ V = \sqrt{\mu a}\left(\sqrt{1-e^2}\cos I - \dfrac{k_p}{k}\right) + \dfrac{1}{k}\Gamma \end{cases} \tag{3.56}$$

Considering that Γ is now a constant, it can by seen as a free parameter of the transformation (3.56) from the semi-secular (a, e, I) elements to the semi-secular (Σ, U, V)

momenta. The choice of Γ being now only a matter of definition[3], we will conveniently choose it equal to 0. Finally, the semi-secular Hamiltonian function used in the following writes:

$$\mathcal{K}\big(\Sigma, U, V, \sigma, u\big) = \mathcal{K}_0\big(\Sigma\big) + \varepsilon\,\mathcal{K}_1\big(\Sigma, U, V, \sigma, u\big) \tag{3.57}$$

where:

$$\mathcal{K}_0\big(\Sigma\big) = -\frac{\mu^2}{2\,(k\Sigma)^2} - n_p k_p \Sigma \tag{3.58}$$

and where $\varepsilon\,\mathcal{K}_1$ is obtained by computing numerically the required integrals, just as we did in Sect. 3.2.3. We are left with a two-degree-of-freedom system (the two angles being σ and $u = \omega$) and several strategies can now be used to study its dynamics. The most general method would be to compute Poincaré maps of the complete semi-secular system, but we did not find any example of this for trans-Neptunian objects in the literature (although it would allow to detect a potential chaotic interaction between the two degrees of freedom). In our particular case, we will see that the intrinsic properties of the system allow to construct a more direct, secular representation.

3.3.4 Secular Hamiltonian

The methods usually used in the literature to construct resonant secular models beyond Neptune are based on the crude model of Kozai (1985). Indeed, in order to get direct estimates of the long-term resonant dynamics, Kozai chose to get rid of the extra degree of freedom by fixing Σ and σ at a supposed libration centre. Some authors, for better estimates, opted later for an assumed sinusoidal evolution of σ with constant centre, frequency and amplitude (Gomes et al., 2005b; Gallardo et al., 2012). Unfortunately, that kind of models is not adapted for the two following reasons: on the one hand, the parameters (centre, frequency, amplitude) have to be known *a priori*. The libration centre cannot be chosen arbitrarily: it must be an equilibrium point of the semi-secular Hamiltonian, otherwise the model is simply wrong... Since it is essential, then, to use a previous numerical integration, the secular model looses its utility as a tool to explore the variety of possible motions. On the other hand, these models just cannot be considered as *secular* at all, because the oscillation parameters of σ can actually vary a lot during the long-term evolution (this is further discussed and explained in Sect. 3.3.6). Therefore, the level curves obtained with such constant parameters are a very poor representation of the real trajectories, since they are valid only in a restricted neighbourhood of each point. That problem was recently mentioned by Brasil et al. (2014): they picked up the oscillation parameters of σ at different times from a numerical integration and plotted a collection of secular level curves, each graph being valid only at a time t and in the very neighbourhood of the considered point. This is quite

[3]We recall that the $\{\Lambda_i\}$ momenta were added artificially to the Hamiltonian to absorb its temporal dependence. Given that $\Gamma = k_p L + k\Lambda_p$, it is not surprising to get an entire liberty concerning its value.

misleading because different classes of dynamics seem to appear (as their "hibernating mode"), whereas they are actually just snapshots of one single secular motion.

On the contrary, we can take advantage of the wide separation between the two timescales associated with the two degrees of freedom in order to reduce the system to an integrable approximation. This technique is called the "adiabatic approximation". Indeed, the oscillation period of σ in that region ranges from a few tens of thousands to some million years (semi-secular timescale), whereas the Lidov-Kozai cycles of ω, as seen in the non-resonant case, are usually completed in more than a billion years (secular timescale)[4]. The method itself is not new: it was traditionally used to compute analytical proper elements for resonant or inclined asteroids, as in Morbidelli (1993), Lemaître and Morbidelli (1994) or Beaugé and Roig (2001). We find it also in a series a paper devoted to the dynamics of asteroids in mean-motion resonance with Jupiter: see for instance Wisdom (1985), Moons and Morbidelli (1995) and Moons et al. (1998). In the following, the procedure is recalled and applied to the semi-secular Hamiltonian. It allows to follow the variations of σ instead of assuming a given evolution.

Our technique is based on two reference works: Henrard (1993) which is a detailed course about the adiabatic invariant theory, and Henrard (1990) which details further the useful transformation to action-angle coordinates. For now, let us suppose that the dynamical system described by the semi-secular Hamiltonian (3.57) is integrable. Let us also forget that it has two degrees of freedom but consider it as two *independent* integrable systems, one for each pair of conjugate coordinates (Σ, σ) and (U, u). We will call ν_σ and ν_u the proper frequencies associated and assume that the resulting evolution of u runs on a timescale much larger than the one of σ, that is:

$$\xi = \frac{\nu_u}{\nu_\sigma} \ll 1 \tag{3.59}$$

If this relation holds, the action-angle coordinates (J, θ) related to the evolution of (Σ, σ) for a fixed value of (U, u) are a good approximation of the related ones in the complete two-degree-of-freedom system. More precisely, J and θ are obtained up to order ξ. In particular, the momentum J is not exactly conserved, but for a sufficiently small value of ξ we can neglect its variations: in that case we say that J is an "adiabatic invariant" of the system. In the new coordinates, that we call *secular*, the Hamiltonian rewrites:

$$\mathcal{F}\big(J, U, V, \theta, u\big) = \mathcal{F}_0(J, U, V, u) + \mathcal{O}(\xi) \tag{3.60}$$

where the new splitting is implicit and has nothing to do with the previous one (Eq. 3.57). Actually, such a change of coordinates could be applied to any two-degree-of-freedom system, but it is of particular interest in the adiabatic regime, that is if (3.59) is verified. Supposing it is, following Wisdom (1985) we will call $\mathcal{F}_0$ a "quasi-integral" of motion. Neglecting the $\mathcal{O}(\xi)$ term, the dynamics can be described by the level curves of $\mathcal{F}$ in the (U, u) plane: each point defines a one-degree-of-freedom subsystem with Hamiltonian $\mathcal{K}$ for (U, u) fixed, and J is the conserved action from the action-angle coordinates of that

[4]That separation prevents probably any occurrence of secondary resonance in our model.

subsystem. In other words, the constant J is related to a specific level curve of $\mathcal{K}$ in the (Σ, σ) plane for (U, u) fixed, called the "guiding trajectory" by Henrard (1993). If we note (Σ_0, σ_0) an arbitrary point of that level curve, the secular Hamiltonian neglecting the $\mathcal{O}(\xi)$ term is simply defined by:

$$\mathcal{F}\big(J, U, V, u\big) = \mathcal{K}(\Sigma_0, U, V, \sigma_0, u) \tag{3.61}$$

One can note that no further averaging is required since the value of $\mathcal{K}$ is by definition the same all along the cycle. Wisdom (1985) used a similar representation to study the resonance 3:1 with Jupiter in the planar problem[5]. In addition, the method of "fixing the slow variables by steps" was employed by Milani and Baccili (1998) to describe the dynamics of Toro-type asteroids, but they did not use it to construct a secular model.

Once the adiabatic invariance is postulated, the tricky part is to determine the action-angle coordinates of the one-degree-of-freedom subsystem. This can be realised by using the semi-analytical method of Henrard (1990), as applied in the following (see also Lemaître, 2010, for an introduction). Except from separatrices or equilibrium points, we can show that all the trajectories $(\Sigma(t), \sigma(t))$ for (U, u) fixed are periodic, with a period T_σ related to the level curve considered. Consequently, $2\pi/T_\sigma$ is the obvious proper frequency of the system, hence the choice of the new angle:

$$\theta = \nu_\sigma\, t + \theta_0 \quad \text{with} \quad \nu_\sigma = \frac{2\pi}{T_\sigma} \tag{3.62}$$

Now, let us search for a complete canonical transformation of the form:

$$\begin{pmatrix} \Sigma \\ V \\ \sigma \\ v \end{pmatrix} = \begin{pmatrix} F(J, V', \theta) \\ V' \\ f(J, V', \theta) \\ v' + \rho(J, V', \theta) \end{pmatrix} \tag{3.63}$$

where F, f and ρ are 2π-periodic functions of θ. We do not apply any change to U and u because they are considered here as *parameters*. In order to make (3.63) a canonical change of coordinates, three equations have now to be verified by the unknown functions F, f and ρ (see Sect. 2.2.4). The first one involves only f and F:

$$1 = \frac{\partial f}{\partial \theta}\frac{\partial F}{\partial J} - \frac{\partial f}{\partial J}\frac{\partial F}{\partial \theta} \tag{3.64}$$

By adding and subtracting terms, we find out that:

$$\frac{\partial f}{\partial \theta}\frac{\partial F}{\partial J} - \frac{\partial f}{\partial J}\frac{\partial F}{\partial \theta} = \frac{1}{2}\left[\frac{\partial}{\partial J}\left(\frac{\partial f}{\partial \theta}F - \frac{\partial F}{\partial \theta}f\right) - \frac{\partial}{\partial \theta}\left(\frac{\partial f}{\partial J}F - \frac{\partial F}{\partial J}f\right)\right] \tag{3.65}$$

When integrating (3.64) with respect to θ, we get then:

$$2\pi = \frac{1}{2}\frac{\partial}{\partial J}\int_0^{2\pi}\left(\frac{\partial f}{\partial \theta}F - \frac{\partial F}{\partial \theta}f\right)\mathrm{d}\theta - \frac{1}{2}\left[\frac{\partial f}{\partial J}F - \frac{\partial F}{\partial J}f\right]_0^{2\pi} \tag{3.66}$$

[5]In Wisdom (1985), please take care that contrary to Henrard (1993) or Milani and Baccili (1998), the "guiding trajectory" refers to the *secular* timescale, that is the level curves of $\mathcal{F}$ in the (U, u) plane.

and the final brackets are zero, since f and F are 2π-periodic with respect to θ. Using the definition (3.62) of θ, we get (apart from an arbitrary constant):

$$4\pi J = \int_0^{2\pi} \left(\frac{\partial f}{\partial \theta} F - \frac{\partial F}{\partial \theta} f \right) \mathrm{d}\theta = \int_0^{T_\sigma} \left(\dot{\sigma}\Sigma - \dot{\Sigma}\sigma \right) \mathrm{d}t \tag{3.67}$$

or equivalently:

$$2\pi J = \frac{1}{2} \oint (\Sigma \, \mathrm{d}\sigma - \sigma \, \mathrm{d}\Sigma) = \oint \Sigma \, \mathrm{d}\sigma = - \oint \sigma \, \mathrm{d}\Sigma \tag{3.68}$$

Except for the 2π factor, the new action J is thus equal to a signed area, positive or negative according to the direction of motion along the level curve. In the case of oscillations around a central equilibrium, $2\pi J$ is the surface enclosed by the trajectory. On the contrary, it represents the area stretched under the curve if σ circulates (see Lemaître, 2010, for a simple example). The two next equations enable to define the function $\rho(J, V', \theta)$:

$$\frac{\partial \rho}{\partial \theta} = \frac{\partial f}{\partial V'} \frac{\partial F}{\partial \theta} - \frac{\partial f}{\partial \theta} \frac{\partial F}{\partial V'} \quad ; \quad \frac{\partial \rho}{\partial J} = \frac{\partial f}{\partial V'} \frac{\partial F}{\partial J} - \frac{\partial f}{\partial J} \frac{\partial F}{\partial V'} \tag{3.69}$$

By direct integration, we obtain the following expression:

$$\begin{aligned} \rho(J, V', \theta) &= \int_0^\theta \frac{\partial \rho}{\partial \theta} \, \mathrm{d}\theta + \int_{J_0}^J \frac{\partial \rho}{\partial J}\Big|_{\theta=0} \mathrm{d}J + g(V') \\ &= \int_0^\theta \left(\frac{\partial f}{\partial V'} \frac{\partial F}{\partial \theta} - \frac{\partial f}{\partial \theta} \frac{\partial F}{\partial V'} \right) \mathrm{d}\theta + \int_{J_0}^J \left(\frac{\partial f}{\partial V'} \frac{\partial F}{\partial J} - \frac{\partial f}{\partial J} \frac{\partial F}{\partial V'} \right) \Big|_{\theta=0} \mathrm{d}J + g(V') \end{aligned} \tag{3.70}$$

where g is some function of V' only. Since the angle θ is always defined apart from an arbitrary constant, we can choose its origin along a curve in the space (Σ, σ) perpendicular to the level curves of $\mathcal{K}$. In that case, the vectors:

$$\left(\frac{\partial F}{\partial J} \, , \, \frac{\partial f}{\partial J} \right) \quad \text{and} \quad \left(\frac{\partial F}{\partial V'} \, , \, \frac{\partial f}{\partial V'} \right) \tag{3.71}$$

are collinear when $\theta = 0$. Choosing $g(V') \equiv 0$, we finally get the simplified expression:

$$\rho(J, V', \theta) = \int_0^\theta \left(\frac{\partial f}{\partial V'} \frac{\partial F}{\partial \theta} - \frac{\partial f}{\partial \theta} \frac{\partial F}{\partial V'} \right) \mathrm{d}\theta \tag{3.72}$$

Concerning the constant frequency of v', it is straightforward to get it from the change of coordinates (3.63):

$$\nu_v = \frac{\mathrm{d}v'}{\mathrm{d}t} = \frac{\mathrm{d}v}{\mathrm{d}t} - \frac{\mathrm{d}\rho}{\mathrm{d}t} \tag{3.73}$$

and by integration between 0 and T_σ we have simply:

$$\nu_v = \frac{v(T_\sigma) - v(0)}{T_\sigma} \tag{3.74}$$

In practice, since the dynamics of $v = \Omega$ is well decoupled from σ (just as for u), the function ρ is only a little correction, that is, $v' \approx v$. Anyway, its calculation is required only if we are interested in the temporal evolution of Ω as a function of the new coordinates.

Naturally, the coordinate change (3.63) is only implicit, since neither F nor f has an explicit definition. Nevertheless, the correspondence between (Σ, V, σ, v) and (J, V', θ, v') can be realised numerically by integrating the equations of motion defined by the semi-secular Hamiltonian $\mathcal{K}$ for (U, u) fixed. Indeed, once we know the period T_σ and the functions $\Sigma(t)$, $\sigma(t)$ and $v(t)$ for a chosen value of J, the link toward $\theta(t)$ and $v'(t)$ is straightforward for all t: the coordinate change is simply defined by identification. In our case, since we are only interested in the value of the secular Hamiltonian $\mathcal{F}(J, U, V, u)$, the procedure is the following:

1. Choose a behaviour for σ: oscillation or circulation (because the definition of J differs from one case to the other).

2. Choose the parameters J and V.

3. For each point (u, U) where we want to compute the value of $\mathcal{F}$, do:

   (a) On the (Σ, σ) plane, look for the equilibrium point(s) of $\mathcal{K}$ with (U, u) fixed. This is done numerically with minimisation/maximisation routines.

   (b) Look also for the position of the separatrix, in order to define the boundaries of the search.

   (c) In the domain of interest (inside or outside the separatrix, see point 1), search for the level curve enclosing (or stretching) the area $A = 2\pi J$. This is done by integrating numerically the semi-secular equations of motion for (U, u) fixed, and applying a Newton algorithm with respect to the initial conditions. Indeed, the surface over time can be added among the dynamical equations:
   $$\dot{A} = \frac{1}{2}\left(\dot{\sigma}\Sigma - \dot{\Sigma}\sigma\right) \tag{3.75}$$
   with another Newton algorithm or the method of Hénon (1982) to stop the integration exactly after a complete cycle.

   (d) If there is no trajectory enclosing/stretching the required area in the domain (for instance if the separatrices are too narrow to contain it), stop with a warning: that combination of parameters is impossible. Conversely if a correct initial condition (Σ_0, σ_0) has been found, pick up the period T_σ associated to verify that it is well below the secular timescale. Some additional output can also be printed (position of the equilibrium point(s), width of the separatrices...).

   (e) The value of the secular Hamiltonian $\mathcal{F}(J, U, V, u)$ is finally given by (3.61).

Practically, the computation of the semi-secular Hamiltonian $\mathcal{K}$ and its partial derivatives (for the iterative numerical integrations) is rather CPU-time consuming because it always implies the numerical averaging over the short periods (see Sect. 3.3.3). Following the idea of Lemaître and Morbidelli (1994), we thus perform a 2D cubic-spline interpolation of $\mathcal{K}$ in the (Σ, σ) plane around the equilibrium point(s), between steps 3b and 3c. The partial derivatives are then calculated by direct derivation of the splines and the numerical integration is performed with virtually no cost (see appendix C.3 for technical details). Besides, the computation of a complete map is easily parallelized since each point is independent of the other ones.

3.3.5 Reference coordinates

We are now able to draw the level curves of the secular Hamiltonian $\mathcal{F}$ in the (U, u) plane with respect to the two fixed parameters V and J. However, it would be convenient to express it with coordinates more directly meaningful, as we did in the non-resonant case. First of all, let us define a reference semi-major axis a_0 (its choice, somewhat arbitrary, is discussed later). Since the momentum V is a secular constant of motion, we have:

$$V = \sqrt{\mu a}\,(\eta - k_p/k) = \text{const.} \tag{3.76}$$

where $\eta = \sqrt{1-e^2}\cos I$. The constant V can then be replaced by the parameter:

$$\eta_0 = \frac{V}{\sqrt{\mu a_0}} + \frac{k_p}{k} \tag{3.77}$$

In the same way, the variable U can be replaced by a reference perihelion distance $\tilde{q} = a_0(1-\tilde{e})$, where the reference eccentricity is defined by:

$$\tilde{e}^{\,2} = 1 - \left(\frac{U}{\sqrt{\mu a_0}} + \frac{k_p}{k} \right)^2 \tag{3.78}$$

At this point, one can remark that a_0 should be chosen large enough to allow a constant $\eta_0 \in [-1, 1]$ and a positive value for (3.78). Finally, we can also define a reference inclination by setting:

$$\sqrt{1-\tilde{e}^{\,2}}\cos\tilde{I} = \eta_0 \tag{3.79}$$

The plane $(\omega, \tilde{q})$ is entirely equivalent to the plane (u, U), and the parameter η_0 is entirely equivalent to the V constant. The point is now to determine if these new quantities have a physical meaning, and to what extend they represent the real secular orbit of the particle. Actually, we can verify (see Sect. 3.4) that the secular variations of the semi-major axis are always rather small, such that it is never far from a central approximate value. If such a value is chosen for a_0, the function $\eta(t)$ will always remain close to the constant η_0, and we will also have $\tilde{e}(t) \approx e(t)$ and $\tilde{q}(t) \approx q(t)$. The parameter η_0 acts then as the Kozai constant of the non-resonant case, linking the inclination and the eccentricity (even if this time, it is only in an approximative way). Consequently, in

all what follows, the level curves of the secular Hamiltonian $\mathcal{F}$ are plotted in the $(\omega, \tilde{q})$ plane with η_0 as parameter. Naturally, the chosen value of a_0 is always given to let us recover the original canonical coordinates U and V.

Concerning the parameter J, its link with the Keplerian elements is so abstract that we will not try to redefine it. Let us just keep in mind that its value is always negative if σ librates (as in our case, the equilibriums are maxima), and that its magnitude is related to the enclosed area in the (σ, Σ) plane, that is to the oscillation amplitudes of a and σ.

3.3.6 Expected geometries of the semi-secular phase space

The above procedure allows to define a secular Hamiltonian in the resonant case. As detailed in Sect. 3.3.4, its value can be computed by searching numerically the required level curve of the averaged Hamiltonian in the plane (σ, Σ). In this section, we present a brief analysis of the geometry of the trajectories in that plane. We will see that it can depart quite substantially from the classic pendulum-like picture.

Even if expansions in inclination and eccentricities were judged inappropriate in our case (see Sect. 3.2.1), they can give a rough idea of the semi-secular dynamics beyond Neptune. In particular, the representation introduced by Ellis and Murray (2000) allows to obtain directly the finite number of terms associated to a given angle, at the chosen order of e and $s = \sin(I/2)$. This is particularly suitable for the study of averaged resonant systems, since the numerous short-period terms are cancelled out under the average, leaving only the resonant terms (containing the angle σ), along with the purely secular ones (containing ω and/or Ω). Using such a type of development, the semi-secular Hamiltonian (3.57) writes analytically as:

$$\mathcal{K} = -\frac{\mu}{2a} - n_p \frac{k_p}{k}\sqrt{\mu a} - \mu_p \left(\frac{1}{a}\mathcal{R}_{\mathrm{D}} + \frac{1}{a_p\,\alpha}\mathcal{R}_{\mathrm{I}} \right) - \frac{1}{a}\mathcal{N} \tag{3.80}$$

in terms of the Keplerian elements, with $\alpha = a_p/a$. In that expression, the resonant parts due to the interaction with the planet p are written $\mathcal{R}_{\mathrm{D}}$ and $\mathcal{R}_{\mathrm{I}}$ (direct and indirect perturbations). As shown in Sect. 3.3.2, they are functions of $(a, e, i, \sigma, \omega)$ but not Ω. On the other hand, the non-resonant part $\mathcal{N}$ contains the perturbations by all the planets $i \neq p$. It is function of (a, e, i, ω) only (see Sect. 3.2). From Ellis and Murray (2000), it is straightforward to get the expression of the lowest-order terms containing the angle σ (defined at Eq. 3.41). They are of order $k - k_p$ that is the order the resonance. The direct part writes[6]:

$$\mathcal{R}_{\mathrm{D}} = \sum_{n=0}^{k-k_p} \frac{(-1)^n}{n!}\alpha^n \frac{\mathrm{d}^n}{\mathrm{d}\alpha^n} b_{1/2}^{(k_p)}(\alpha) \sum_{m=0}^{n} \binom{n}{m} (-1)^m X_k^{-m-1,k_p}(e) \cos\sigma \tag{3.81}$$

[6]The given expansion contains the contribution from both the terms in σ and $-\sigma$, thus the lack of coefficient $1/2$ with respect to the general expansion by Ellis and Murray (2000).

where the functions $b_{1/2}^{(j)}(\alpha)$ and $X_c^{a,b}(e)$ are Laplace and Hansen coefficients, respectively. Naturally, the development should also contain the secular terms (with angles $\sigma + 2\omega$, $\sigma + 4\omega$ etc.) and the purely secular ones (containing only multiples of 2ω, or no angle at all). According to the level of precision requested, higher-order terms can also be added to (3.81), along with the ones with arguments 2σ, 3σ etc. The indirect part behaves differently according to the resonance considered: it is equal to zero at all orders for $k_p > 1$, and for $k_p = 1$, it contains the unique term:

$$\mathcal{R}_{\rm I} = -(1 - s^2) X_k^{1,1}(e) \cos\sigma \tag{3.82}$$

with no secular contribution. Naturally, (3.82) should be truncated to the desired order in e and s. Finally, the analytical expression of the non-resonant part $\mathcal{N}$ can also be taken from Ellis and Murray (2000), or directly from Sect. 3.2.1 (dropping the planet $i = p$) for a development in terms of Legendre polynomials.

Now, let us use these expressions to get an idea of the geometry of the semi-secular phase space. First of all, one can argue that if the particle is close or inside the resonance, the semi-major axis a will not vary much around its nominal value a_0. In such a case, it is usual to take as constants the coefficient α and the various a_i/a appearing in $\mathcal{N}$, such that the only dependence in a is the one expressed explicitly in (3.80). In the same way, we can consider that the variables e and I are equal to their secular reference values $\tilde{e}$ and $\tilde{I}$ (Sect. 3.3.5), which is equivalent to neglect their dependence in Σ. That method was used also in Milani and Baccili (1998), allowing to get a one-degree-of-freedom semi-secular Hamiltonian in (σ, a), in which (e, I, ω) are "varying parameters", changing on a much longer timescale than a and σ. In our case, we have besides the relation $\eta_0 = \sqrt{1 - e^2}\cos I$.

Resonances with $k_p \neq 1$: Let us begin with the simplest case, that is the resonances with $k_p \neq 1$ (no indirect perturbation). Reorganising the terms, the semi-secular Hamiltonian as a function of (σ, a) writes:

$$\mathcal{K}(\sigma, a) = -A_1\sqrt{a} - \frac{1}{a}\big(A_2 + \varepsilon_1\cos\sigma + \varepsilon_2\cos(\sigma + 2\omega) + \varepsilon_3\cos(\sigma + 4\omega) + ...\big) \tag{3.83}$$

in which $A_1, A_2 > 0$. The constant A_2 gathers the Keplerian part and the secular terms, so we have in particular $A_2 \gg |\varepsilon_i|$. According to the rules of D'Alembert, ε_1 is of order e^{k-k_p}, and $\{\varepsilon_2, \varepsilon_3...\}$ are proportional to multiples of e and s (of total order higher or equal to $k - k_p$). From the partial derivatives of $\mathcal{K}$, the conditions of equilibrium write:

$$\begin{cases} \varepsilon_1\sin\sigma + \varepsilon_2\sin(\sigma + 2\omega) + \varepsilon_3\sin(\sigma + 4\omega) + ... = 0 \\ a^{3/2} = \dfrac{2}{A_1}\big(A_2 + \varepsilon_1\cos\sigma + \varepsilon_2\cos(\sigma + 2\omega) + \varepsilon_3\cos(\sigma + 4\omega) + ...\big) \end{cases} \tag{3.84}$$

Since $A_2 \gg |\varepsilon_i|$, the maximum of $\mathcal{K}$ along a is almost independent of σ. Neglecting also the secular terms contained in A_2, we get the usual theoretical value:

$$a \approx \left(2\frac{A_2}{A_1}\right)^{2/3} \approx a_p\left(\frac{k}{k_p}\right)^{2/3} \tag{3.85}$$

On the contrary, the σ-value of the resonance centre strongly depends on the slow parameters (e, I, ω). Let us consider an orbit starting with a near-zero inclination but a high eccentricity. In that configuration, the term ε_1 is much larger than the following ones (proportional to powers of s), so the condition of equilibrium (3.84) leads to $\sigma = 0$ or π. This is the classic pendulum-like picture of the resonant motion, with the saddle point at $\sigma = 0$ and the centre of the resonance at $\sigma = \pi$. If the secular evolution of (e, I, ω) inside the mean-motion resonance leads the orbit towards high perihelion distances, however, the balance is modified. Indeed, since $\eta_0 = \sqrt{1-e^2}\cos I$ is conserved, a decrease of eccentricity implies an increase of inclination, so the term in ε_2 will progressively dominate. The pendulum-like picture is not broken, but its centre depends now on ω: it passes from $\sigma = \pi$ to $\sigma = 0$ for a variation of ω from $\omega = 0$ to $\pi/2$. Still decreasing the eccentricity (and increasing the inclination through η_0), the term in ε_3 will then take over, making the location of the resonance centre even more sensitive to the value of ω: it now passes from $\sigma = \pi$ to $\sigma = 0$ for a variation of ω from $\omega = 0$ to $\pi/4$ only. Going on this way, this period-doubling effect can stop only when a term proportional to the inclination only is reached (possible only for even-order resonances, in which case this term is proportional to s^{k-k_p}).

This is summed up in Fig. 3.9, presenting the location of the resonance centre for $(k_p, k) = (3, 7)$ in function of $\tilde{e}$ (or $\tilde{I}$) and ω. The explicit expansion of the disturbing function for that resonance writes:

$$\begin{aligned}\mathcal{K}(\sigma, a) = &- A_1\sqrt{a} - \frac{1}{a}A_2 \\ &- \frac{\mu_p}{a}\left(e^4 f_{94}\cos\sigma + e^2 s^2 f_{97}\cos(\sigma+2\omega) + s^4 f_{98}\cos(\sigma+4\omega) + ...\right)\end{aligned} \tag{3.86}$$

where the f_i are combinations of Laplace coefficients (see Ellis and Murray, 2000). In the top part of the graphs, at high eccentricities, the term in e^4 dominates. When the eccentricity decreases, on the contrary, the term in $e^2 s^2$, and then s^4 take over successively, producing the period-doubling effect. In order to locate the correct level curve of $\mathcal{K}$, the algorithm developed in Sect. 3.3.4 should thus be able to accurately determine the position of the resonance centre (with minimisation and maximisation routines), whatever the configuration. For completeness, a careful analysis shows that *two* maxima are present at the transition between two regimes (at the tips of the four black zones in the right graph), leading to two distinct resonance islands. However, this happens only in an extremely narrow interval of $\tilde{e}$ and $\tilde{I}$, which can be dismissed. Figure 3.9 shows also the width of the resonance island between the two separatrices: $\Delta\sigma$ is always equal to 2π since there is only one resonance island, and Δa decreases rapidly with the eccentricity.

Resonances with $k_p = 1$: Let us now turn to the particular case in which $k_p = 1$, that is when the indirect part of the resonant perturbation does not vanish. The geometry of the phase space is more complicated, since the direct part (3.81) and the indirect part (3.82) are of the same order in eccentricity and inclination, but have opposite signs.

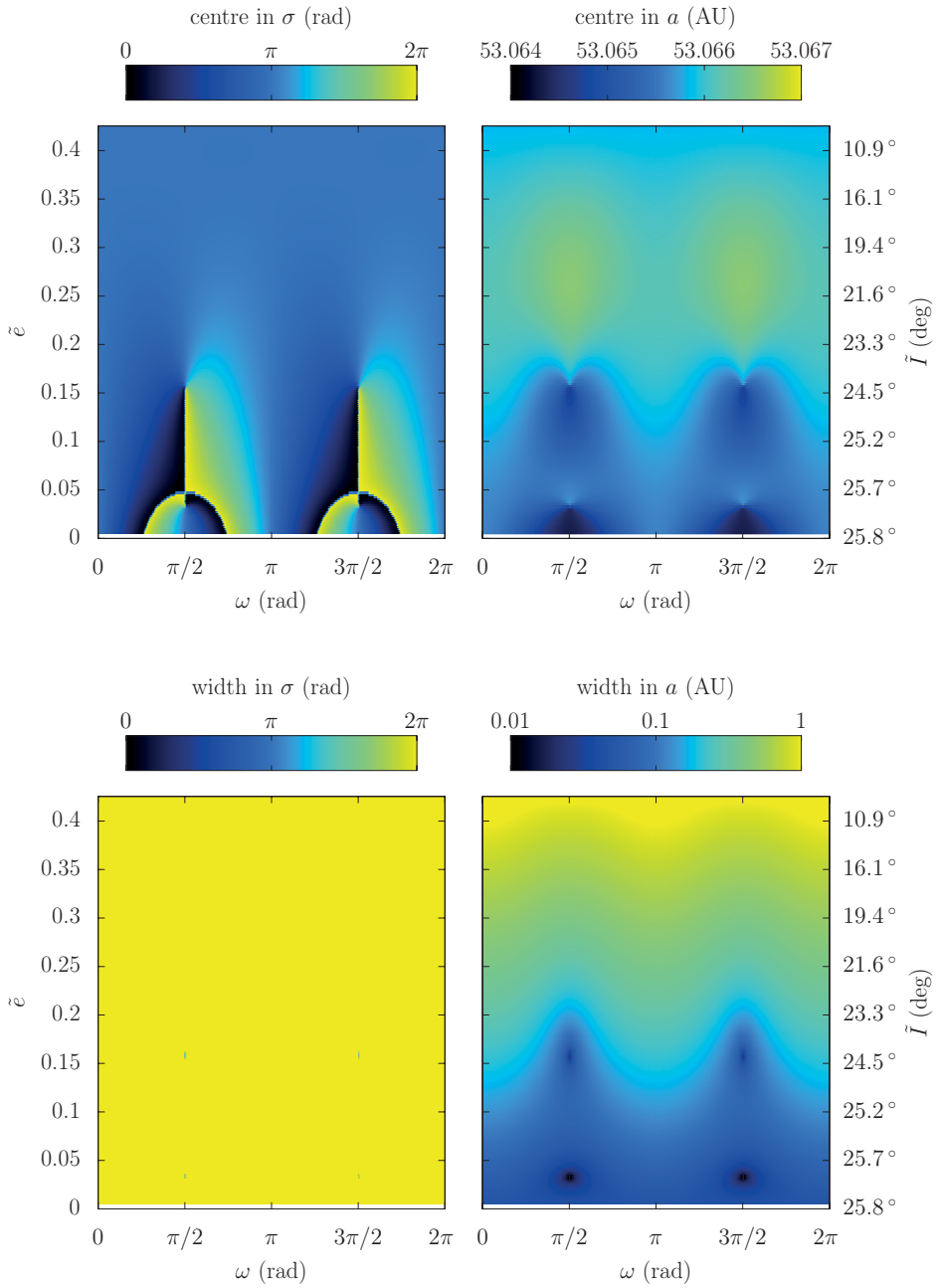

Figure 3.9 – Position and width of the resonance 3 : 7 with Neptune in function of the secular eccentricity and argument of perihelion. These graphs are plotted from the full numerically-averaged Hamiltonian (3.57). The constant η_0 is chosen to 0.9 (for a reference semi-major axis $a_0 = 53.066$ AU). On the right, the inclination is obtained from $\tilde{e}$ through the constant η_0. The particular dependence in ω, qualitatively described in the text, is clearly visible. The small variations of the position in semi-major axis, judged negligible in the text, are also noticeable (top-right graph).

This can be shown be truncating the Hansen coefficients to the lowest order (that is e^{k-1}), which leads to the following results: *i*) all the coefficients considered here are positive; *ii*) the alternate signs of the terms in (3.81) are such that each negative term is compensated by a positive term with larger absolute value. Since the Laplace coefficients are also positive, the lowest-order resonant terms of the Hamiltonian have the general form:

$$\frac{1}{a}\mathcal{R}_{\rm D} = f(\alpha)e^{k-1}\cos\sigma \qquad \text{and} \qquad \frac{1}{a_p\,\alpha}\mathcal{R}_{\rm I} = g(\alpha)e^{k-1}\cos\sigma \tag{3.87}$$

with $f(\alpha) > 0$ and $g(\alpha) < 0$. Moreover, we observe that $f(\alpha)$ and $g(\alpha)$ have the same order of magnitude, and thus partially cancel out[7]. Consequently, the term (3.87) is *not* the leading term of the expansion! More precisely, if we consider as before an orbit starting with a relatively small inclination but a high eccentricity, the dominant term is the *next one* in eccentricity, that is the term in $\cos(2\sigma)$ proportional to $e^{2(k-1)}$. Since that term has no contribution in the indirect part, it cannot be cancelled. Reorganising the terms in the same way as before, the semi-secular Hamiltonian as a function of (σ, a) writes thus generically:

$$\mathcal{K}(\sigma, a) = -A_1\sqrt{a} - \frac{1}{a}\big(A_2 + \varepsilon_1'\cos(2\sigma) + \varepsilon_1\cos\sigma + \varepsilon_2\cos(\sigma + 2\omega) + ...\big) \tag{3.88}$$

In that expression, ε_1' is proportional to $e^{2(k-1)}$, ε_1 is proportional to e^{k-1} (but with a near-zero coefficient), and $\{\varepsilon_2, \varepsilon_3...\}$ are proportional to multiples of e and s (of total order higher or equal to $k-1$). The equilibrium condition for σ writes thus:

$$2\,\varepsilon_1'\sin(2\sigma) + \varepsilon_1\sin(\sigma) + \varepsilon_2\sin(\sigma + 2\omega) + ... = 0 \tag{3.89}$$

Since it has been partially cancelled by the indirect part, the term in ε_1 is much smaller than the term in ε_1' despite the higher power in e. Moreover, if e is sufficiently high with respect to s, the term ε_1' is much larger than the following ones (proportional to powers of s), so the condition of equilibrium (3.89) simplifies to:

$$\varepsilon_1'\sin(2\sigma) \approx 0 \tag{3.90}$$

This leads to $\sigma = \{0, \pi/2, \pi, 3\pi/2\}$, that is *two* equilibrium points (at $\pi/2$ and $3\pi/2$), and *two* saddle points (at 0 and π). As before, however, if the secular evolution of (e, I, ω) inside the mean-motion resonance leads the orbit toward smaller eccentricities, the balance is modified: the term in ε_1 will progressively dominate, producing a change of topology from a double island to a single one. For a small-enough eccentricity, we thus retrieve the classic pendulum. Still decreasing the eccentricity (and increasing the inclination through η_0), the term in ε_2 will then take over, and so on, similarly to resonances with $k_p \neq 1$. In order to locate the correct level curve of $\mathcal{K}$, the algorithm developed in Sect. 3.3.4 should thus be able to determine the position of the

[7]This can probably be proven rigorously, but the complicated expression of the Laplace and Hansen coefficients makes it difficult.

chosen resonance centre even when there are two of them, and locate the corresponding separatrix.

As an example, the explicit four-order expansion for the resonance $(k_p, k) = (1, 3)$ writes:

$$\begin{aligned}\mathcal{K}(\sigma, a) = &- A_1\sqrt{a} - \frac{1}{a}A_2 \\ &- \frac{\mu_p}{a}\Big[(e^2 f_{53} + e^4 f_{55} + e^2 s^2 f_{56})\cos\sigma \\ &\quad + (s^2 f_{57} + e^2 s^2 f_{59} + s^4 f_{60})\cos(\sigma + 2\omega) \\ &\quad + e^4 f_{94}\cos(2\sigma) \\ &\quad + e^2 s^2 f_{97}\cos(2\sigma + 2\omega) \\ &\quad + s^4 f_{98}\cos(2\sigma + 4\omega)\Big] \\ &- \frac{\mu_p}{a_p\alpha}\frac{3}{8}(-e^2 + e^4 + e^2 s^2)\cos\sigma\end{aligned} \tag{3.91}$$

Using the mean semi-major axis of Neptune and the typical semi-major axis of the resonance $\alpha \approx (k_p/k)^{2/3}$, we get the following values of the coefficients (divided by a for the direct part and by $a_p\alpha$ for the indirect part):

term	direct part $\times 10^2$ (AU^{-1})	indirect part $\times 10^2$ (AU^{-1})	total $\times 10^2$ (AU^{-1})
$e^2\cos\sigma$	3.196	-2.582	0.614
$e^4\cos\sigma$	-1.947	2.582	0.635
$e^2 s^2\cos\sigma$	-6.503	2.582	-3.921
$s^2\cos(\sigma + 2\omega)$	0.538	/	0.538
$e^2 s^2\cos(\sigma + 2\omega)$	-1.671	/	-1.671
$s^4\cos(\sigma + 2\omega)$	-3.147	/	-3.147
$e^4\cos(2\sigma)$	11.934	/	11.934
$e^2 s^2\cos(2\sigma + 2\omega)$	8.850	/	8.850
$s^4\cos(2\sigma + 4\omega)$	0.327	/	0.327

In this example, the term in $e^4\cos(2\sigma)$ is the leading term even for eccentricities as small as 0.23 (considering a small-enough inclination). Decreasing the eccentricity (and increasing the inclination through η_0), the next term to dominate can be either $e^2\cos\sigma$ or $s^2\cos(\sigma + 2\omega)$, according to the value of η_0.

That effect is illustrated in Fig. 3.10, presenting the location of the resonance centre for $(k_p, k) = (1, 6)$ in function of $\tilde{e}$ and ω. At high eccentricities, the term in $\cos(2\sigma)$ dominates, producing two resonance islands (with a width $\Delta\sigma < 2\pi$). When the eccentricity decreases, the term in $\cos(\sigma + 2\omega)$, and then $\cos(\sigma + 4\omega)$ take over successively, producing the transition to a single resonance island, followed by the period-doubling effect. As we will see, such a complicated change of geometry can have very important consequences on the dynamics.

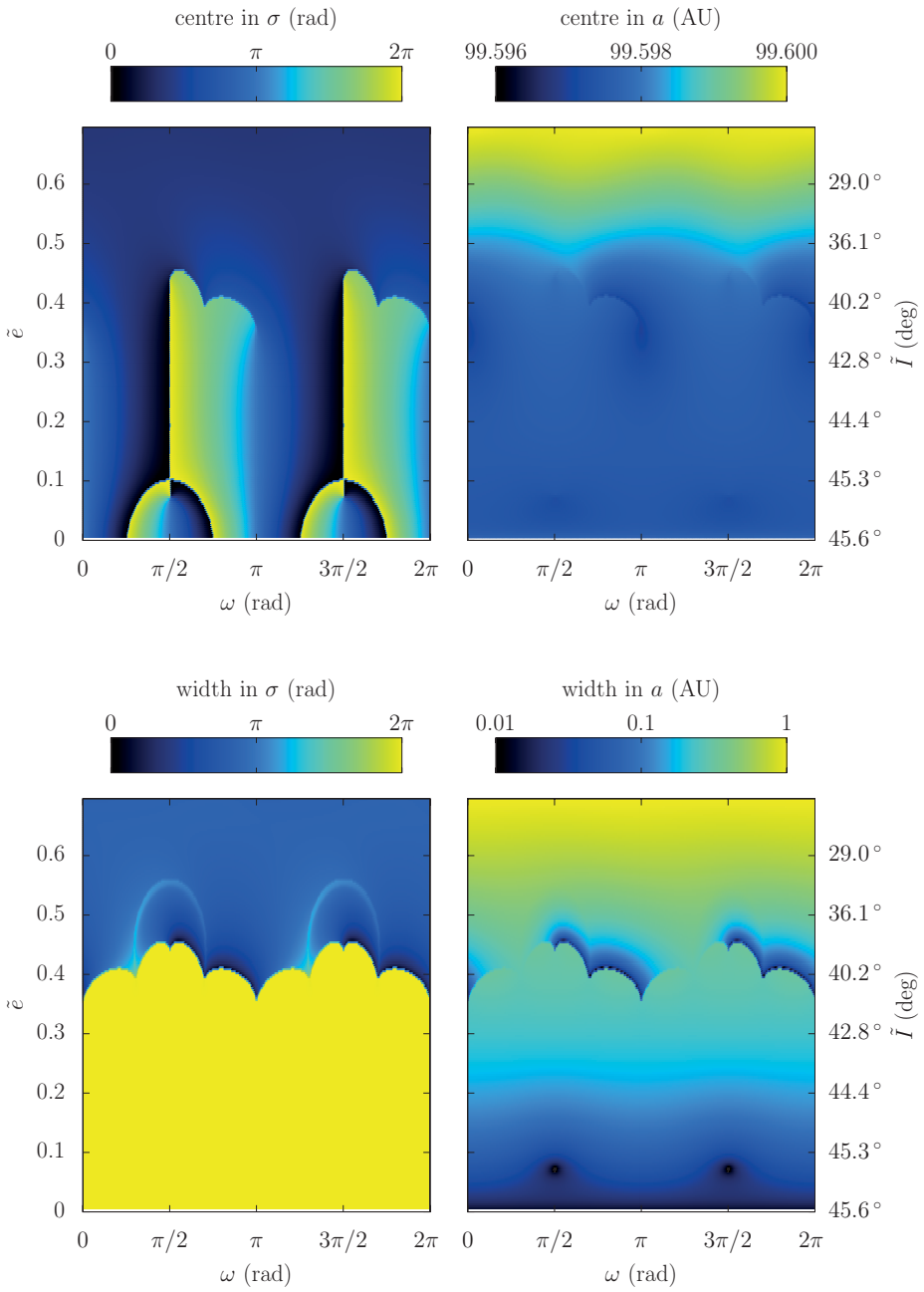

Figure 3.10 – Position and width of the resonance $1:6$ with Neptune in function of the secular eccentricity and argument of perihelion. These graphs are plotted from the full numerically-averaged Hamiltonian (3.57). The constant η_0 is chosen to 0.7 (for a reference semi-major axis $a_0 = 99.598$ AU). On the right, the inclination is obtained from $\tilde{e}$ through the constant η_0. At high eccentricities, there are two resonances islands: we chose to follow the left one. The transition to a single resonance island at $\tilde{e} \approx [0.35, 0.45]$ produces a discontinuity (change of topology). At small eccentricities, the dependence in ω, similar to what was observed for resonances with $k_p \neq 1$, is clearly visible.

3.4 Illustrations of the resonant dynamics

This section presents some examples of use of the resonant secular model. A variety of typical cases are provided to emphasis the main vantages and limitations of the method. As a quick check, the secular model will also be confronted to numerical integrations of the osculating and semi-secular systems. In order to integrate numerically the semi-secular system, the required partial derivatives of $\mathcal{K}$ are obtained by inverting the derivative and integration symbols in the expression of $\varepsilon\mathcal{K}_1$. Some nested derivatives are a bit complex, so the equations of motion are detailed in appendix B.3.3.

Section 3.4.1 presents the ideal case, that is when the adiabatic invariant J is well defined all over the surface $(\omega, \tilde{q})$ considered. In Sect. 3.4.2, we show that a secular description is still possible for higher values of $|2\pi J|$ even if σ switches from oscillation to circulation. Finally, Sect. 3.4.3 illustrates the most complex case in that region, where the existence of two deforming resonance islands leads necessarily to a discontinuity in the secular phase portraits.

3.4.1 Single resonance island and small values of J

Let us begin with the simplest case, that is when the semi-secular plane (Σ, σ) contains a single island of resonance. For resonances with $k_p \neq 1$ and perihelion distances beyond Neptune, this is the case in *almost* all the phase space (see the discussion in Sect. 3.3.6). Of course, that single island will possibly deform and shift a lot during the secular evolution of (U, u), but the secular dynamics is well defined as long as the surface enclosed by the separatrix remains greater than $2\pi J$. Figure 3.11 shows an example of level curves obtained for such a case (black lines). Some extra information is provided to recall the different timescales and appreciate the efficiency of the method:

1. The tiny red dots come from a complete numerical integration (osculating elements): the equations are given by the initial Hamiltonian $\mathcal{H}$ (3.12) without any particular transformation. The fast angles make the plot somewhat messy, mainly because of the shift of the Solar System barycentre.

2. The dashed green line is the result of a numerical integration of the semi-secular system: the equations are given by the two-degree-of-freedom semi-secular Hamiltonian $\mathcal{K}$ (3.57), that is after removing the short-period terms from $\mathcal{H}$. The curve follows very well the average pattern of the red dots and the oscillations due to the second degree of freedom are smaller than the curve width. See Fig. 3.12 for a detailed output of that numerical integration (in particular we can see that the cycle is completed in about 1.12 Gyrs).

3. Finally, the colour shades show the value of the one-degree-of-freedom secular Hamiltonian $\mathcal{F}$ (3.61). Each point is obtained from the action-angle coordinates of $\mathcal{K}$ assuming the adiabatic invariance. The secular dynamics is then given by the level curves of $\mathcal{F}$ (black contours).

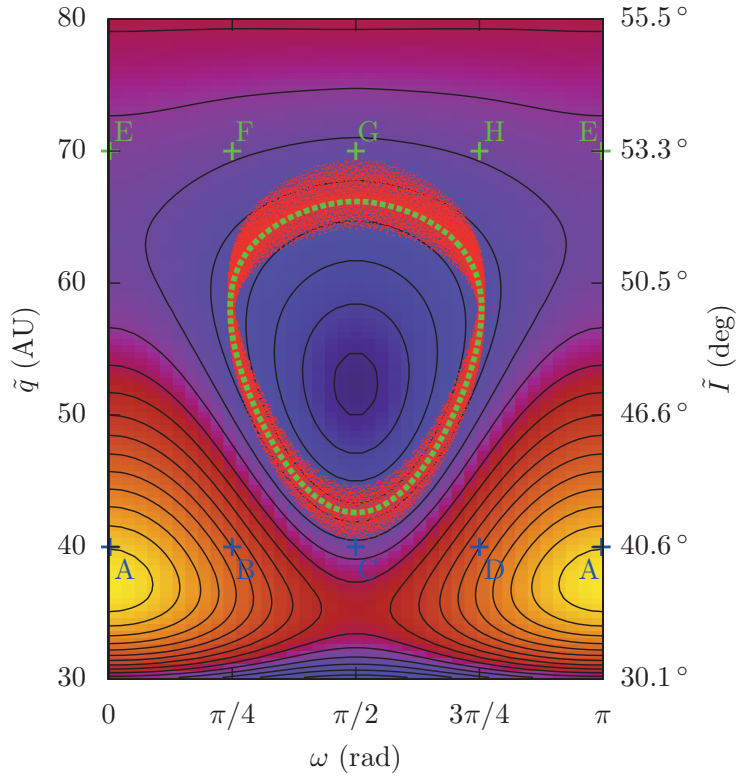

Figure 3.11 – Level curves of the secular Hamiltonian $\mathcal{F}$ for the resonance 2:37 with Neptune. The parameters are $\eta_0 = 0.44$ and $2\pi J = -2.6 \times 10^{-4}$ AU^{2}rad^2/yr. In order to define η_0 and construct the vertical axes, the reference semi-major axis chosen is $a_0 = 210.9944$ AU (see Fig. 3.14 where that value is obvious). The various symbols are detailed in the text.

In order to illustrate the passage from the semi-secular to the secular coordinates, Fig. 3.13 shows the level curves of the semi-secular Hamiltonian $\mathcal{K}$ corresponding to ten points of Fig. 3.11 (letters). The level curve that encloses the required area defines the value of the secular Hamiltonian $\mathcal{F}$. For that set of parameters, the surface $|2\pi J|$ is sufficiently small to fit easily inside the separatrix but its contours can be rather distorted. In particular, the narrowing of the Σ-width of the island, when the perihelion distance increases, forces σ to oscillate with a larger amplitude. The general properties of $\mathcal{K}$ in ω are easily recognizable: π-periodicity and symmetry with respect to $\pi/2$ (see Sect. 3.3.3).

Figure 3.14 presents the same level curves as Fig. 3.11, but with the position of the centre of the resonance island on background shades, as well as the period of oscillation. The amplitudes are not shown here, but Fig. 3.13 gives an idea of their variations. Following a particular level curve, we can see the important changes of the oscillation parameters undergone by the particle (the red line and Fig. 3.12 give a specific example of it). This invalidates any secular model for which the resonance angle is supposed fixed or sinusoidal. Nevertheless, the central value of the semi-major axis is indeed

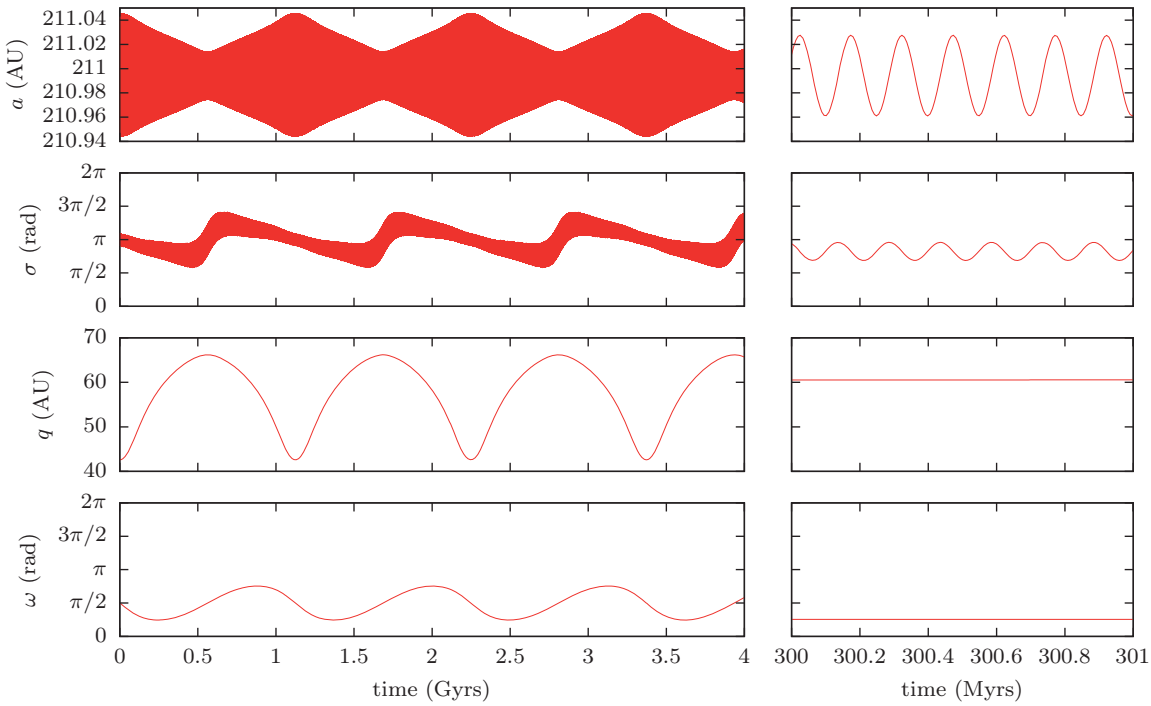

Figure 3.12 – Numerical integration of the two-degree-of-freedom semi-secular system. That trajectory corresponds to the green dashed line of Fig. 3.11 and the red line of Fig. 3.14. The semi-major axis is given instead of Σ and the perihelion distance instead of U (see Eq. 3.56 for the correspondence). On the right, an enlargement underlines the two-timescale dynamics (the small oscillations of q and ω are hidden in the curve width).

rather stable: it is actually imposed by Neptune's semi-major axis. This justifies the use of "reference coordinates" as a short-cut from the secular variable U to the secular orbital elements e and I (see Sect. 3.3.5).

Finally, Fig. 3.15 gives another example of secular dynamics with a small value of $|2\pi J|$. The resonance is the same as Fig. 3.11 but another set of parameters is chosen: one can notice the extreme richness of possible behaviours, with many different ways to raise the perihelion distance. However, it is a general result that the Σ-width of the resonance island becomes much wider when the perihelion gets closer to the orbit of Neptune. Since this is also the case for all neighbouring resonances, we must keep in mind that for small perihelion distances, the overlap of resonances introduces a short-timescale chaos which can push the particle out of the resonance considered. Numerical integrations of the unaveraged system show that this happens at the bottom part of the largest trajectories in Fig. 3.15, but their major portion, though, is perfectly regular. To fix ideas, the biggest cycle represented is completed in about 40 Gyrs, where more than 32 Gyrs are spent with $\tilde{q} > 70$ AU.

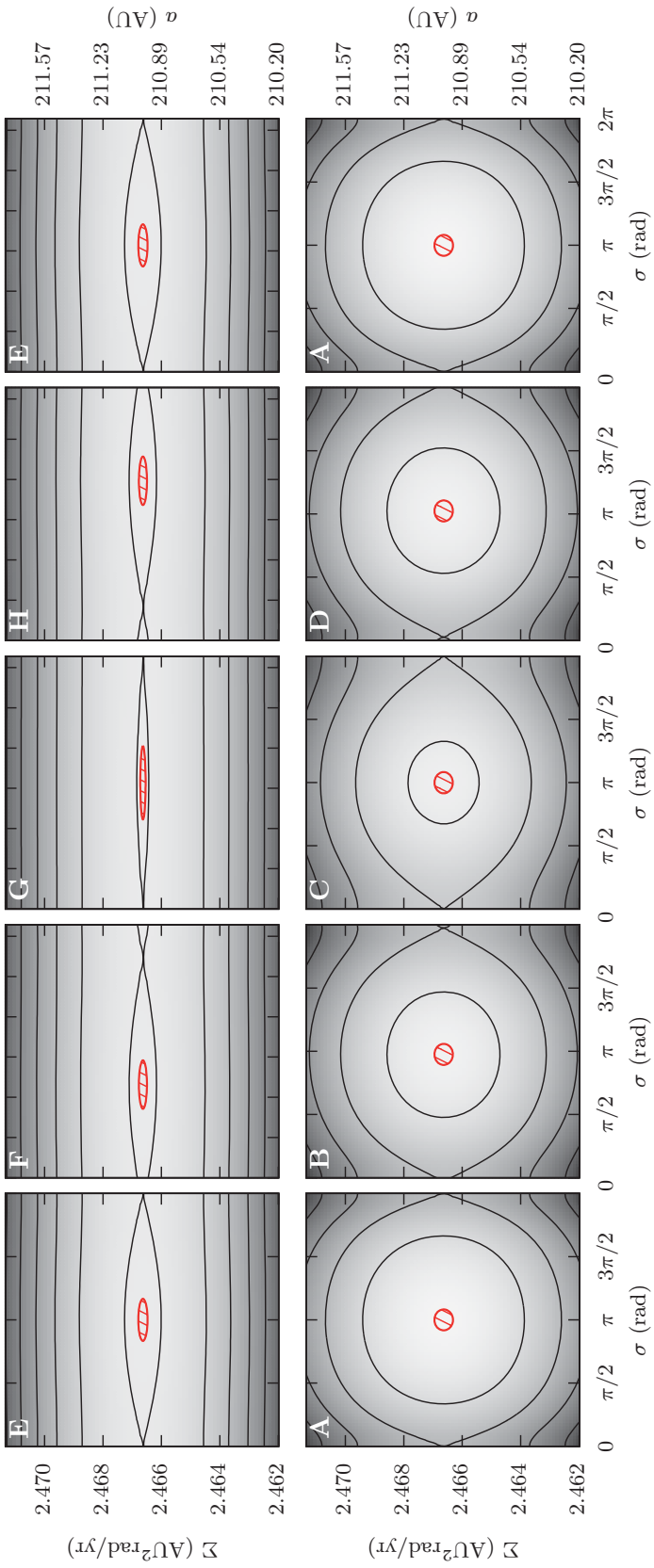

Figure 3.13 – Level curves of the semi-secular Hamiltonian $\mathcal{K}$, for (U, u) fixed according to the points A-H of Fig. 3.11. The trajectory enclosing the surface $2\pi J$ is shown in red and the semi-major axis corresponding to Σ is given on the right. The centre is perfectly at $\sigma = \pi$ for the points (A,C,E,G) but slightly shifted for (B,F) and (D,G) symmetrically on the left and on the right. For the points E-H, the Σ-width of the resonance island is very narrow because of the high perihelion distance (see Fig. 3.11), which makes the red surface to flatten.

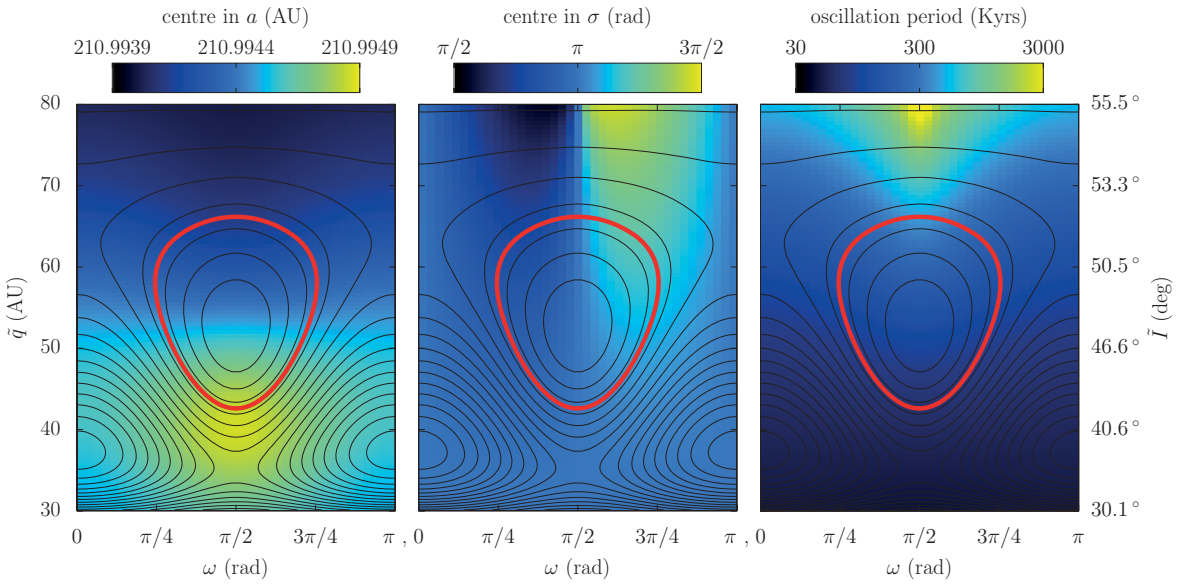

Figure 3.14 – The level curves of Fig. 3.11 are plotted in front of some characteristics of the resonance island in the plane (Σ, σ) used to get the action-angle coordinates of $\mathcal{K}$. On the left graph, the semi-major axis is used instead of Σ for a more direct interpretation. The middle plot shows that in that particular case, the oscillation centre of σ oscillates itself around π (at high perihelion distances, the terms in $\sigma + 2\omega$, described in Sect. 3.3.6, start to be influential). On the right graph, the oscillation period refers to the trajectory enclosing the required area $2\pi J$: even if it varies a lot (note the log-scale), it remains much smaller than the Giga-year secular periods. The red line represents the result of a numerical integration of the semi-secular system (the same as the green dashed line of Fig. 3.11).

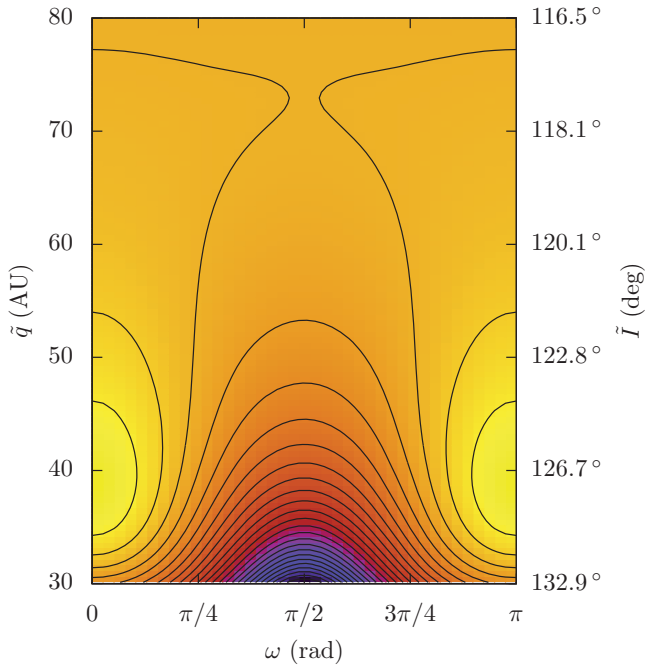

Figure 3.15 – Level curves of the secular Hamiltonian $\mathcal{F}$ for the resonance $2:37$ with Neptune (reference semi-major axis chosen: $a_0 = 210.9944$ AU). The parameters are $\eta_0 = -0.35$ and $2\pi J = -1.7 \times 10^{-5}$ AU^{2}rad^2/yr. Please note that these orbits are retrograde.

3.4.2 Separatrix crossings

For high values of the perihelion distance, we saw that the Σ-width of the resonance island becomes very small (Fig. 3.13). This has a stabilizing effect because the various resonances become very isolated from each other (no overlapping), but what if the island becomes so narrow that the area $|2\pi J|$ cannot fit inside anymore? From a technical point of view, the values of the parameters are simply *incompatible*, so what if a secular level curve *leads* the particle to such a region? The resulting trajectory can be described as follows: the semi-secular separatrices in the (Σ, σ) plane come closer and closer to the trajectory, making raise the amplitude of oscillation of σ, along with a drastic enlargement of its period. Then, the particle can spend some time near the unstable equilibrium point, breaking the adiabatic invariance. Fortunately, this "freeze" is usually quite short because U and u are still evolving. Hence, the particle is simply pushed outside of the resonance island and σ begins to circulate. The method applied in Sect. 3.3.4 is also valid for circulation[8], but the geometrical definition of J has to be changed. Consequently, the only way to handle the crossing in a secular way is to change model: the secular trajectory is then defined by parts, each of them being quasi-integrable. For a given trajectory, the problem is now to link the segments. There is actually no way to deduce the exact value of the new J constant adopted by the system, because it depends of the precise position of the particle when the separatrix crossing occurs. On a secular timescale, this can be seen as a random transition (see Henrard, 1993, and references therein). In particular, since in our case the island is rather symmetric on the Σ-axis, there is roughly 50% of probability to begin circulate toward the left (above the island) or toward the right (under the island). However, if the new secular level curve is periodic the particle is bound to re-enter the resonance in a configuration similar to when it left it. After the new separatrix crossing, the value of J will thus be approximatively restored (apart from some chaotic diffusion).

That mechanism was described thoroughly by Wisdom (1985) in the case of the resonance 3:1 with Jupiter and the associated Kirkwood gap. Near the discontinuities of the secular Hamiltonian (that is when the crossings occur in the semi-secular system), he named "zone of uncertainty" the region in which the adiabatic hypothesis is invalidated. In his model, any passage through this zone produced a jump at possibly planet-crossing eccentricities. Moreover, even if the particle re-entered the resonance afterwards, the value of the adiabatic invariant was not recovered, which produced a large-scale chaotic behaviour. He pointed out that that kind of chaos is *not* due to a mean-motion resonance overlap (that is a short-timescale effect), contrary to many chaotic orbits of asteroids observed in the Solar System. It could be explained, though, by an overlap of secondary resonances between σ and ω which happen to have comparable frequencies of oscillation/circulation in these regions. Subsequently, Neishtadt (1987) developed rather general methods to trace the evolution of the adiabatic invariant near and during such discontinuities. In particular, their application to the problem of Wisdom (1985) results in a probabilistic model governing the new value of

[8]The proximity of the resonance still invalidates a fully non-resonant secular model.

the invariant when the particle re-enters the resonance.

Fortunately, the orbits described here are much more regular and predictable than in the work of Wisdom (1985) because the separation between the two timescales is much larger. This is quite obvious in Fig. 3.12, since it is impossible to resolve the two timescales with a single time unit. This implies that the "zone of uncertainty" is extremely narrow: on a secular timescale, it is crossed quasi-instantaneously. Hence, since there is almost never any interaction between the two degrees of freedom, the new value of J is very predictable for each possible transition.

Figures 3.16 and 3.17 show two examples of such segmented trajectories. Since the diffusion of J is extremely small, we considered only two secular models (one for oscillation, one for circulation), but we must keep in mind that J is actually not exactly retrieved after each circulation phase. It would be erroneous to superimpose the left and right graphs, because the transition from the oscillation value of J to the circulation one is specific to the red trajectory shown. In Fig. 3.16, the circulation phase is rather short and we can easily guess by symmetry the approximative trajectory followed by the particle between the white and black points. This is much less obvious in Fig. 3.17, in which the circulation phase plays an important role in the dynamics. Details of these two semi-secular integrations are given In Fig. 3.18 and 3.19. In particular, one can note the random occurrence of left and right circulation phases with the corresponding central values for the semi-major axis. The secular dynamics is however very similar in both cases: it depends mostly on the amplitude of J and little on its sign. Hence, the right graphs of Fig. 3.16 and 3.17, which are plotted for a right circulation, correspond also roughly to the ones obtained for a left circulation. Since J is almost exactly recovered after each circulation phase, these trajectories are pretty periodic on a secular timescale. The separation of the two timescales can be appreciate in Fig. 3.18 and 3.19: the period of σ and Σ is always much shorter than a secular cycle of q and ω (by more than a factor 1000), even in the neighbourhood of the separatrix crossings.

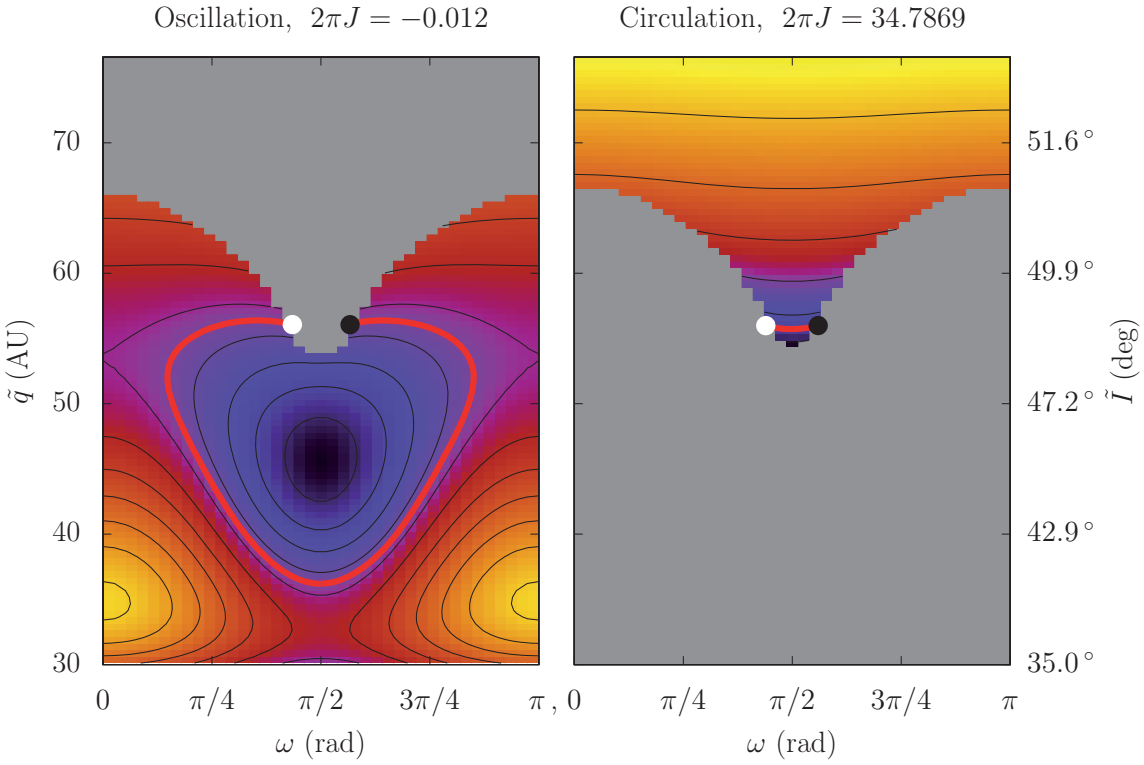

Figure 3.16 – Level curves of the secular Hamiltonian $\mathcal{F}$ for the resonance $2:11$ with Neptune (reference semi-major axis chosen: $a_0 = 93.9872$ AU). The parameter η_0 is equal to 0.6 and J is given above the graphs in $\mathrm{AU}^2\mathrm{rad}^2/\mathrm{yr}$. In the grey region, the area $|2\pi J|$ cannot fit inside the resonance island (left graph), or outside it (right graph). The saw teeth of the background colour are due to the limited resolution. The red trajectory passes from one secular model to the other according to the colour spots (white to white from left to right, black to black from right to left).

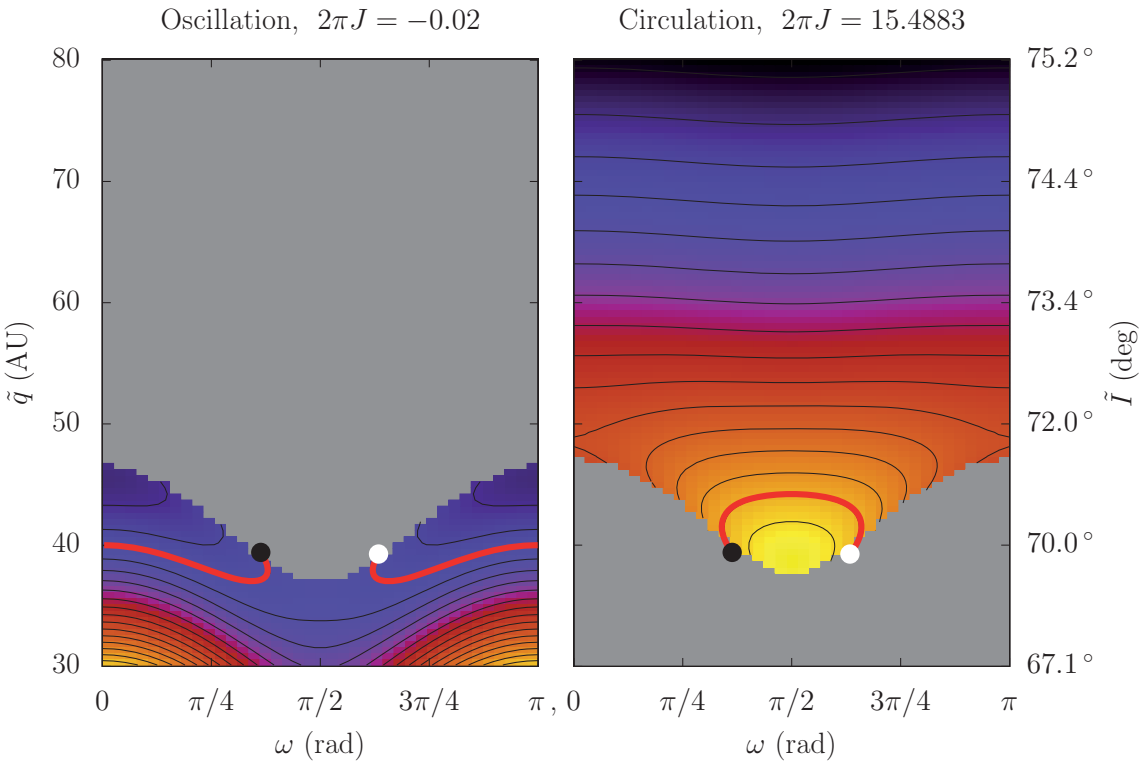

Figure 3.17 – Same as Fig. 3.16 for the resonance 2 : 37 with Neptune (reference semi-major axis chosen: $a_0 = 210.9944$ AU). The parameter η_0 is equal to 0.2 and J is given above the graphs in $\mathrm{AU}^2\mathrm{rad}^2/\mathrm{yr}$.

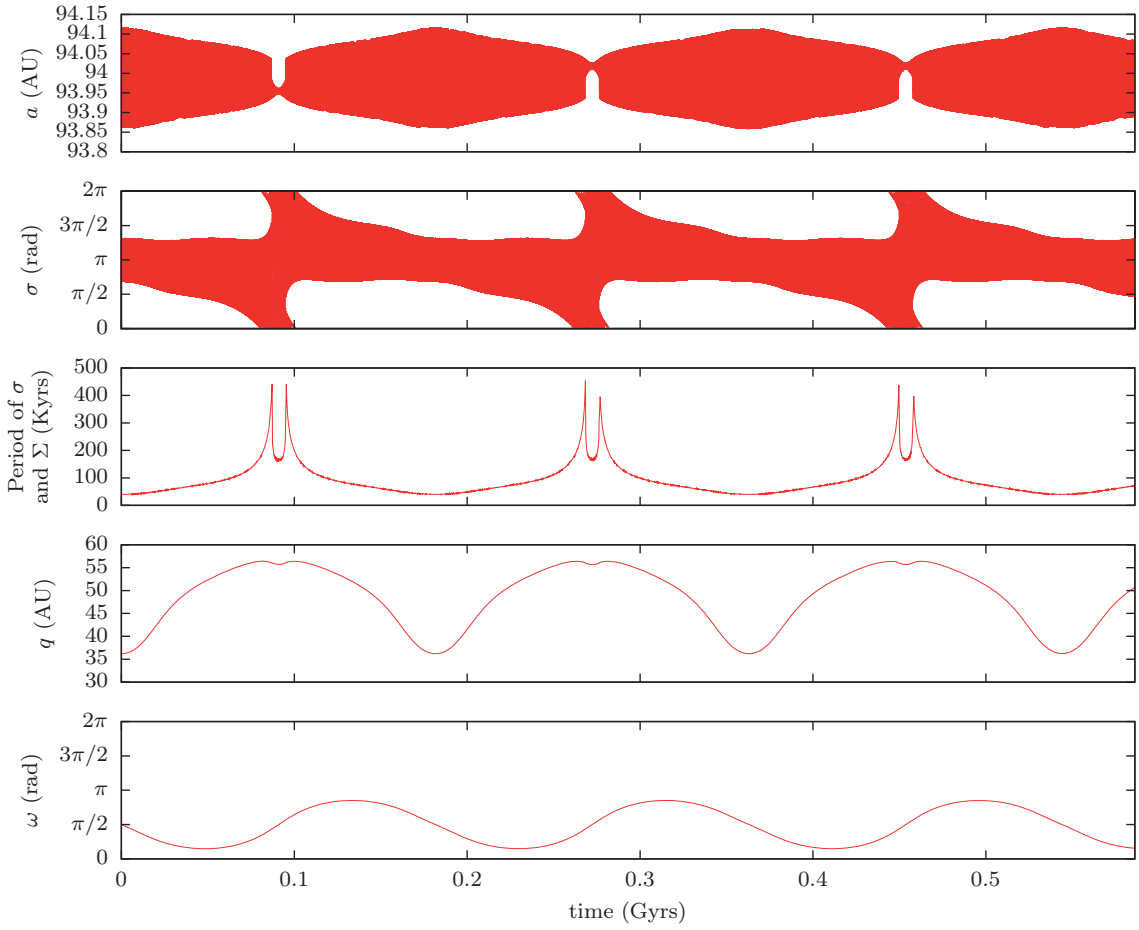

Figure 3.18 – Numerical integration of the two-degree-of-freedom semi-secular system. That trajectory corresponds to the red line of Fig. 3.16. The semi-major axis is given instead of Σ and the perihelion distance instead of U (see Eq. 3.56 for the correspondence). The period of σ (oscillation/circulation) is given in the middle graph, where the separatrix crossings are obvious (the period tends to infinity). The first circulation phase is toward the right (see a and σ) whereas the second and third ones are toward the left.

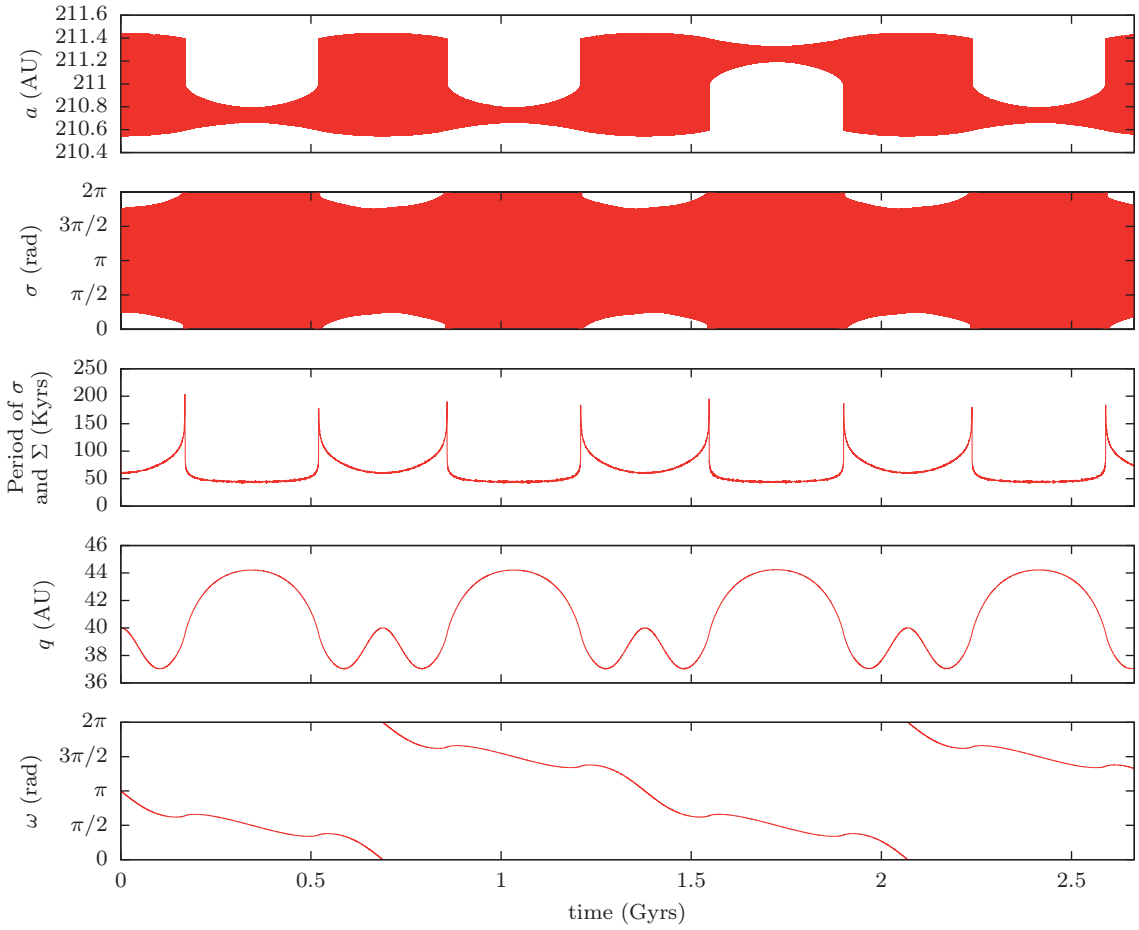

Figure 3.19 – Same as Fig. 3.18 but for the trajectory plotted in Fig. 3.17. The first two and the last circulation phases are toward the right (see a and σ), whereas the third one is toward the left.

3.4.3 Double islands and $1:k$ resonances

In that section, we illustrate the most complex case, that is when there are two resonance islands in the (Σ, σ) plane. According to Gallardo (2006b), this always happens for resonances of type $1:k$ provided that the eccentricity is high enough (see also the discussion in Sect. 3.3.6). Moreover, that specific kind of resonance can also admit horseshoe-type orbits enclosing the two oscillation islands. At this point, we can anticipate a bit and look at Fig. 3.21 for typical examples. The computation of a secular Hamiltonian as defined previously requires thus an additional choice: σ can oscillate around the left centre, around the right one, or around both of them. The method described in Sect. 3.3.4 is valid for each type of trajectories, even if the numerical search for the correct level curve enclosing the required area can become a bit more tricky.

As before, the geometry of the semi-secular level curves evolves during the secular evolution of ω and $\tilde{q}$, and that further complicates the process: the position of the two islands can indeed vary a lot, as well as their sizes. To prevent any erroneous jump from one island to the other during the numerical computation of the secular levels, we adopt the following strategy:

1. Choose the parameters η_0 and J (as before) and an oscillation type for σ (left, right or horseshoe).

2. Start the plot from a particular point $(\omega, \tilde{q})$, typically the lower left corner of the graph. This gives a first value of $\mathcal{F}$.

3. Compute the value for the adjacent points *following* the chosen island in the (Σ, σ) plane. Indeed, since the deformations are continuous, the islands cannot exchange their places between two neighbouring points (assuming a sufficiently fine grid).

4. Go on with the same procedure for the new points.

Naturally, that method is relevant as long as the chosen type of oscillation is allowed by the value of ω and $\tilde{q}$. Indeed, the position of the separatrices can be very different from one point $(\omega, \tilde{q})$ to another, and one of the two inner islands can even vanish (Gallardo, 2006b, defined a critical eccentricity e_a for that). If that phenomenon happens along a secular trajectory, there is necessarily a discontinuity on the plot of $\mathcal{F}$, on which the particle is bound to change its type of trajectory. As in Sect. 3.4.2, the corresponding secular model is defined only by parts.

Figure 3.20 gives an example of level curves for a resonance of type $1:k$. As previously, ten points are marked with letters and refer to semi-secular phase portraits (Fig. 3.21). The semi-secular Hamiltonian $\mathcal{K}$ is still symmetric in ω with respect to $\pi/2$, but this time, the presence of two islands introduces an asymmetry of the secular Hamiltonian $\mathcal{F}$. Indeed, the particle follows one specific island, as shown on Fig. 3.21: the graphs B and D are symmetric but the position of the red trajectory is not. The geometry of the horseshoe-type orbit is even more complicated: from the points B to C, the outer separatrix merges with the inner one, and re-opens shifted by π.

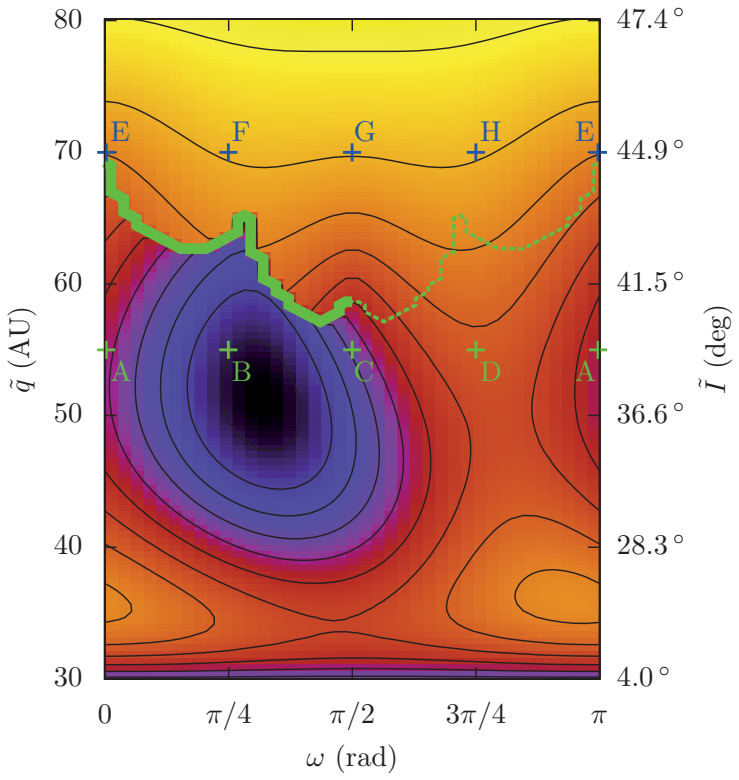

Figure 3.20 – Level curves of the secular Hamiltonian $\mathcal{F}$ for the resonance 1 : 11 with Neptune (reference semi-major axis chosen: $a_0 = 149.1955$ AU). The parameters are $\eta_0 = 0.6$ and $2\pi J = -3 \times 10^{-4}$ AU^{2}rad^2/yr. Here, we chose σ to oscillate inside the "right" island (defined from the lower left point of the graph and followed thereafter). Above the green line, only one resonance island remains: for $\omega \in [0, \pi/2]$ it is the remnant of the left island (thick line, discontinuity), but the remnant of the right one for $\omega \in [\pi/2, \pi]$ (thin dashed line, no discontinuity).

As before, Fig. 3.22 presents the same level curves as Fig. 3.20, but with the position of the centre of the resonance island on background shades, as well as the period of oscillation. Following a particular level curve, we can see the changes of the oscillation parameters undergone by the particle, and we can pick up the "typical" value of the semi-major axis corresponding to that resonance.

The disappearance of one island when the perihelion distance increases deserves further comments. For $\omega = 0$ and $\omega = \pi/2$, it is obvious that the two islands merge into a single one (compare graphs A-E and C-G). On the contrary, for other values of ω, the σ-width of the vanishing island decreases until it merges with the saddle point between the two islands. Hence, the inner separatrix becomes a common periodic trajectory inside the remaining island. The other island remains rather unchanged and passes smoothly from a two-island configuration to a single one. This is detailed in Fig. 3.23, which shows the σ-position of the two resonance centres with respect to the perihelion distance. This explains the structure of the discontinuity line of Fig. 3.20:

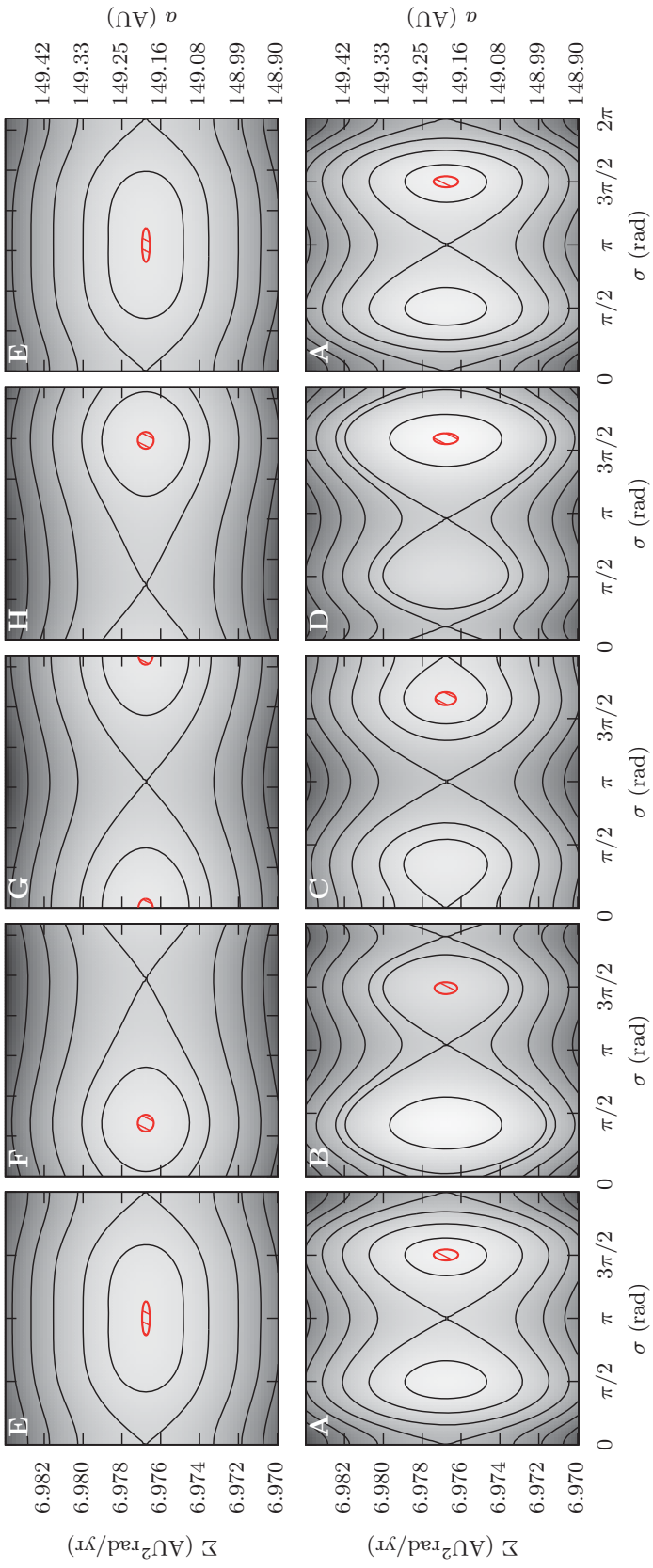

Figure 3.21 – Level curves of the semi-secular Hamiltonian $\mathcal{K}$, for (U, u) fixed according to the points A-H of Fig. 3.20. The trajectory enclosing the surface $2\pi J$ is shown in red, and the semi-major axis corresponding to Σ is given on the right. Only one resonance island is left for the points E-H because they correspond to a high perihelion distance (see Fig. 3.20).

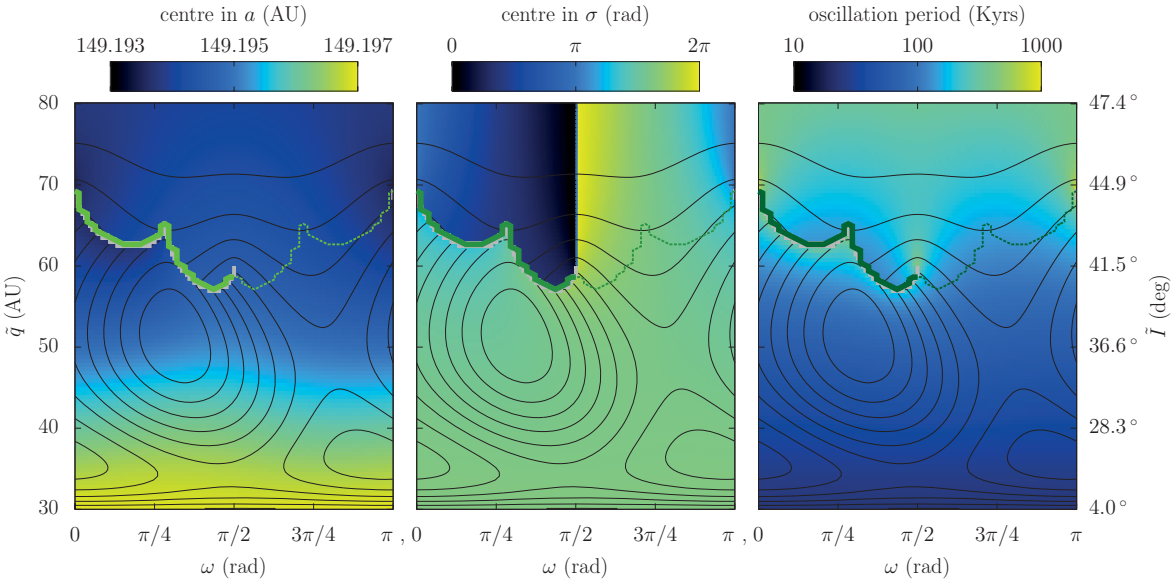

Figure 3.22 – The level curves of Fig. 3.20 are plotted in front of some characteristics of the resonance island in the plane (Σ, σ) used to get the action-angle coordinates of $\mathcal{K}$. The left and middle graphs give the position of the centre around which the particle oscillates: below the discontinuity line, it corresponds to the "right" resonance island; above the discontinuity line, it corresponds to the only resonance island left. When crossing the green line, the continuous or discontinuous transitions are clearly visible in the middle graph.

depending on the oscillation island occupied by the particle, there can be either a smooth transition or a brutal jump to another type of trajectory. In the latter case, the secular model used so far is not relevant anymore for that particle, because the definition of J has to be changed. Notice that Fig. 3.20 is drawn for a very small value of the area $|2\pi J|$. For larger values, the transition happens earlier (before the complete disappearance of the island). After the separatrix crossing (see Sect. 3.4.2), the particle can either oscillate around the other centre, follow a horseshoe-type orbit or circulate. As before, the new trajectory is hard to predict and it can be modelled as a random process.

As an example, Fig. 3.24 presents a numerical integration of the semi-secular system for a specific broken level curve of Fig 3.20. The trajectory begins with the green point, where σ oscillates inside the right island with a small area. On the white point, the right island vanishes, forcing the particle to follow another type of trajectory. For that particular example, it begins to oscillate in the remaining island with a large area (middle graph). The particle crosses the discontinuity at $\omega = \pi/2$ on a safe

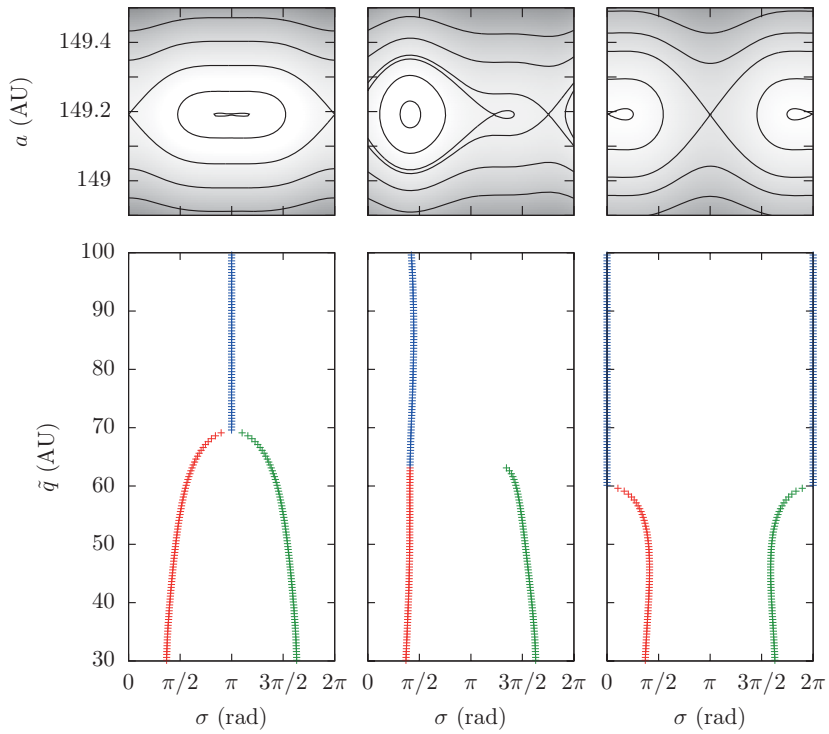

Figure 3.23 – Position of the two resonance centres with respect to the perihelion distance (same resonance and parameters as Fig. 3.20). The left centre is plotted in red, the right one in green, and blue is used when only one resonance centre remains. The fixed value of ω is equal to 0 (left column), $\pi/4$ (middle column) and $\pi/2$ (right column). On the top, the overall phase portrait is shown for a value of $\tilde{q}$ just below the transition ($\tilde{q} = 69$ AU on the left, 63 AU on the middle and 59 on the right). For ω between 0 and $\pi/2$ (middle column), the left resonance island is not affected by the vanishing right island: it becomes smoothly the single remaining resonance island. The roles are exchanged for ω between $\pi/2$ and π (not shown).

horseshoe-type orbit, but hits the growing left island at the black point[9]. For reasons of symmetry, the adopted area inside the left island is very close to the previous one in the right island. After the red point, the particle goes on switching type of trajectory: see Fig. 3.25 for the evolution on a wider timescale. Actually, that kind of behaviour can persist for billion years, as long as the particle does not reach a Neptune-crossing secular trajectory.

We invite the reader to look at Gallardo (2006a) for other examples: his Fig. 12 presents a very similar case (same resonance and nearby values of the parameters). His

[9]Such a symmetrical trajectory was improbable since at the black point the right island is much larger than the left one. A careful analysis of that orbit shows that σ is temporarily trapped around the saddle point and then swallowed by the growing left island. However, other integrations of the osculating and semi-secular systems show various possible behaviours, including further stays in the right island with a large area, or temporary maintenance of a grazing horseshoe-type orbit (see for instance Fig. 3.25 just after 1 Gyr: the double peaks in the period are separatrix approaches without crossing).

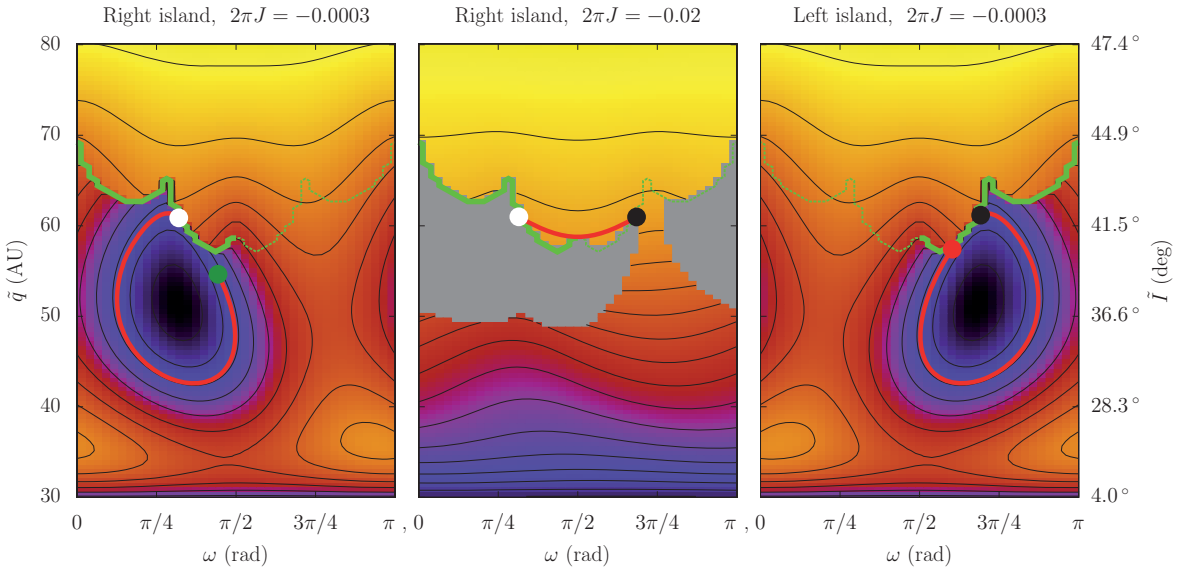

Figure 3.24 – Numerical integration of the two-degree-of-freedom semi-secular system for the resonance $1:11$ with Neptune. The trajectory is plotted by parts in front of the secular level curves: the parameter η_0 is equal to 0.6 and J is given in $\mathrm{AU}^2\mathrm{rad}^2/\mathrm{yr}$ above the pictures. The trajectory begins with the green spot (left graph), ends with the red (right graph), and follows the colour code in between (whit to white and black to black). The middle graph is plotted for oscillations inside the right island, but there is anyway only a single island above the green line. As before, the grey colour denotes regions where the chosen island is too small to contain the area $|2\pi J|$. Since the area is very small for the left and right graphs, the grey region is very thin and hidden under the thick green line.

Fig. 13, on the contrary, shows a steadier evolution without separatrix crossing (the particle is locked indefinitely inside the "right" island). This illustrates how complicated the long-term dynamics inside a $1:k$ resonance can be. A secular model may seem rather cumbersome and ineffective for such "integrable by parts" trajectories, which are chaotic by essence. Indeed, in that case a secular model is more designed for general studies about the dynamics than for following a particular realisation of it. Please note that the chaos invoked here is due to the complex geometries of the $1:k$ resonances, and not to a diffusion of the adiabatic invariant as in the case of Wisdom (1985) discussed above. As seen in Sect. 3.4.2, the two timescales are so well separated that the transition phase at separatrix crossings, during which the adiabatic hypothesis is broken, can be considered as instantaneous. Hence, the uncertainty concerns almost solely the new type of trajectory adopted, rather than the new value of J.

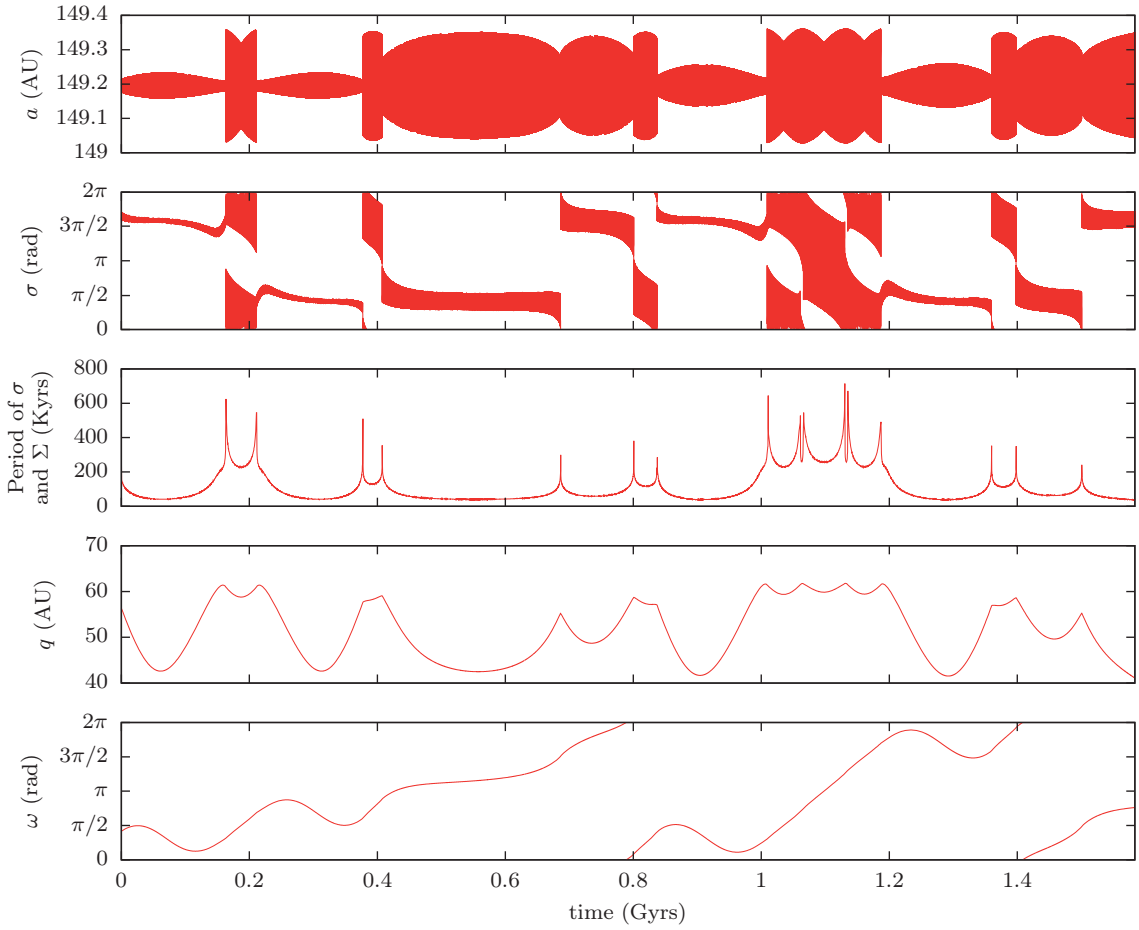

Figure 3.25 – Numerical integration of the two-degree-of-freedom semi-secular system. The semi-major axis is given instead of Σ and the perihelion instead of U (see Eq. 3.56 for the correspondence). The period of σ (central or horseshoe oscillations) is given on the middle graph, where the separatrix crossings are obvious (the period tends to infinity). The first three dynamical regimes (from $t = 0$ to ≈ 0.38 Gyrs) correspond to the trajectory shown on Fig. 3.24.

Chapter 4

The resonant dynamics

Most of the results detailed in this chapter are more succinctly presented in Saillenfest et al. (2017a) and Saillenfest and Lari (2017).

In the previous chapter, we presented the development of secular theories designed to describe the long-term orbital evolution of trans-Neptunian objects. If there is a mean-motion resonance between the particle and one of the planets, a one-degree-of-freedom approximation can be obtained by using the adiabatic approximation. It reveals very rich and complex long-term trajectories, allowing much larger variations of the orbital elements than non-resonant dynamics.

This chapter is devoted to the application of the resonant secular model. In Sect. 4.1, it is used to explore the variety of possible trajectories driven by a mean-motion resonance with Neptune. We show that there is a topological difference between the resonances of type $1 : k$ and other resonances, but no major change of geometry is observed when varying the resonance order. In Sect. 4.2 the model is applied to the trans-Neptunian objects known to be resonant, whereas in Sect. 4.3 we determine to what extent it can apply to the most distant ones, which have generally large orbital uncertainties. The current data is scarce and the resonance captures are hard to detect; however, some general arguments can be used to select the potentially interesting bodies. Of course, it is crucial to establish if these results could imply some selection in the distribution of the trans-Neptunian objects. The confrontation with future observations is indeed the only way to test our knowledge about the distant Solar System. Section 4.4 shows that the long-term resonant dynamics naturally provides a mechanism that can lock bodies at high perihelion distances and maintain them there for billion years. It predicts an accumulation zone in the space of orbital elements. Finally, in Sect. 4.5 we point out that the Oort Cloud is an effective source of Scattered Disc objects and thus contributes to feed this accumulation zone.

4.1 Exploration of the parameter space

To prevent any confusion between the three timescales involved, in the following the terms "resonance island" always refer to the *semi-secular* Hamiltonian $\mathcal{K}$ for (U, u) fixed, that is to the usual oscillations of the semi-major axis and of the resonance angle σ. Regarding the equilibrium points of the *secular* Hamiltonian $\mathcal{F}$, that is in the plane $(\omega, \tilde{q})$, we will speak generically of "libration islands" (because strictly speaking they are not resonant even if some authors call them "Kozai resonances").

In order to determine the influence of the chosen resonance $k_p : k$ and of the parameters (η_0, J) on the phase space, we plotted a vast collection of level curves for various resonances with semi-major axes between 80 and 600 AU. In this section, we describe our results and develop a general picture of the resonant secular dynamics beyond Neptune ($q > a_{\rm N}$). We will see that the geometry of the phase portraits depends mostly on what we call the "resonance type", that is the coefficient k_p involved $(1, 2, 3...)$. Please note that even very high-order resonances can present interesting geometries with wide libration zones. The corresponding probability of capture and stability are of course lower, but these considerations are not studied in this section: here we just suppose that the particle *is* trapped in the chosen resonance and we describe the secular effects that it would produce.

Whatever the resonance considered, we found that for $\eta_0 \approx \pm 1$ or $\eta_0 \approx 0$, that is for orbits nearly circular-coplanar or perpendicular to the planetary plane[1], the level curves of the secular Hamiltonian are very "flat". In these cases, the resonant dynamics is thus very similar to the generic non-resonant one: circulation of ω with very small oscillations of $\tilde{q}$. In particular, the upper features on Fig. 11e by Gallardo et al. (2012) are irrelevant[2]. On the other hand, there is always a range of η_0 both for retrograde ($\eta_0 < 0$) or prograde ($\eta_0 > 0$) orbits, for which the secular Hamiltonian shows equilibrium points for ω and $\tilde{q}$. In the following, we will refer to that interval of η_0 by the "range of interest" because it can allow wide perihelion variations and/or confinement regions for ω.

Additionally, the classic non-resonant Kozai islands show up where the resonant part of the Hamiltonian function weakens[3]. This happens if the corresponding inclination (about 63° or 117°) corresponds to a sufficiently small eccentricity, that is for a parameter η_0 far enough from 0. In the intermediate regime where the non-resonant and resonant parts have comparable strength, the interaction of these islands with the purely resonant features produces complex geometries.

[1] A parameter $\eta_0 = 0$ is also attainable for $e = 1$ (whatever the inclination), but since we are interested in perihelion distances always beyond Neptune, we will not consider this case.

[2] A fixed libration centre is very unsuitable in this region because it varies actually between 0 and 2π. That comment holds also for their Figs. 11f-h beyond about 50 AU. In the lower part, on the contrary, a resonance island centred around 60° does exist (even if it actually shifts and deforms a bit).

[3] Strictly speaking, the non-resonant Hamiltonian is defined with the semi-major axis as a constant parameter. However, the resonant interaction does not cause a to vary enough for the non-resonant Kozai islands to be notably distorted.

4.1.1 Single resonance island for near-zero values of J

Figures 4.1 and 4.2 show the typical evolution of the phase portraits for $k_p \neq 1$ with respect to the parameter η_0. As explained before, such resonances present a single resonance island in all the plane $(\omega, \tilde{q})$, so the corresponding secular phase space is devoid of discontinuity line. Figures 4.3 and 4.4 show further details and comparisons between different resonances of type $k_p \neq 1$ for η_0 in the range of interest. We can make the following general observations:

- Either for prograde or retrograde orbits, some range of η_0 allows a libration island at $\omega = 0$. When η_0 tends to 0 (orbit perpendicular to the planetary plane), that island gets closer to the orbit of Neptune and disappears below it.
- For prograde orbits, a range of η_0 allows an additional island at $\omega = \pi/2$.
- Two resonances of the same "type" (that is with the same coefficient k_p) present very similar geometries, but located in a different range of η_0 (compare Figs. 4.1 and 4.2). Since the features are located both at the same $\tilde{q}$ and $\tilde{I}$, the parameters η_0 giving the same geometries for two different resonances are the ones implying approximatively the same interval of $\tilde{I}$ inside the same interval of $\tilde{q}$ (see the graphs A and B of Fig. 4.3).
- For resonances of type $2:k$, the two respective ranges of η_0 for the existence of the equilibrium points at $\omega = 0$ and $\pi/2$ are rather the same, so the islands can coexist on the same phase portrait (graphs A and B of Fig. 4.3). For $k_p = 3$ and beyond, the $\omega = \pi/2$ island appears at higher inclinations, for which the $\omega = 0$ island is much lower (graph C) or even inside the orbit of Neptune (graph D).
- On some graphs of Figs. 4.3 and 4.4, the classic non-resonant Kozai island is clearly visible. It can either remain isolated (graphs C, D) or interact with the resonant features, to create new islands (graphs E, H at $\omega = 0$ and E, F on both sides of $\omega = \pi/2$) or enlarge the existing ones (graph F, G, H).
- Contrary to the geometry of the phase portraits, the timescale highly depends on the coefficient k, that is on the semi-major axis of the particle (at k_p constant). As an example, numerical integrations of the averaged system show that the biggest loop of the graph A is completed in about 8 Gyrs, whereas the analogous loop takes 16 Gyrs in the graph B.

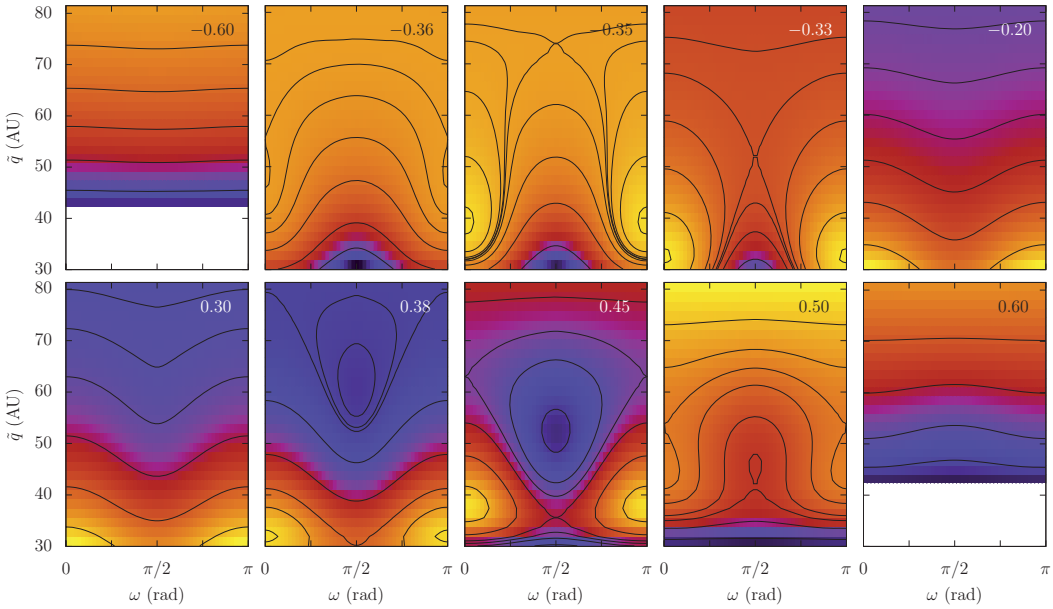

Figure 4.1 – Typical dependence on the parameter η_0 for orbits in resonances of type $k_p \neq 1$ with Neptune. The resonance taken in example here is $2:37$ (reference semi-major axis chosen $a_0 = 210.9911$ AU). All of these graphs are plotted for $J = 0$ and η_0 is indicated in the upper right corners. On the Y-axis of each graph, the reference inclinations can be obtained by $\cos\tilde{I} = \eta_0/\sqrt{1-(1-\tilde{q}/a_0)^2}$. The white regions in the first and last graphs are unreachable with these values of η_0 (they would require a cosine of inclination lower than -1 or higher than 1, respectively).

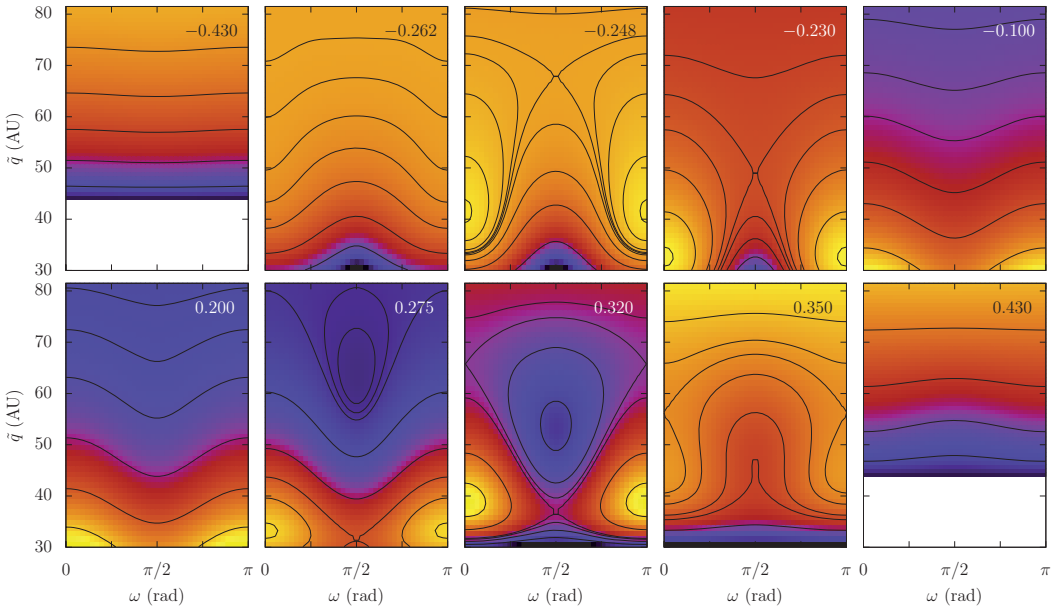

Figure 4.2 – Same as Fig. 4.1 for the resonance $2:115$ (reference semi-major axis chosen $a_0 = 449.3602$ AU). The parameter η_0 has been tuned to give approximatively the same phase portraits as in Fig. 4.1.

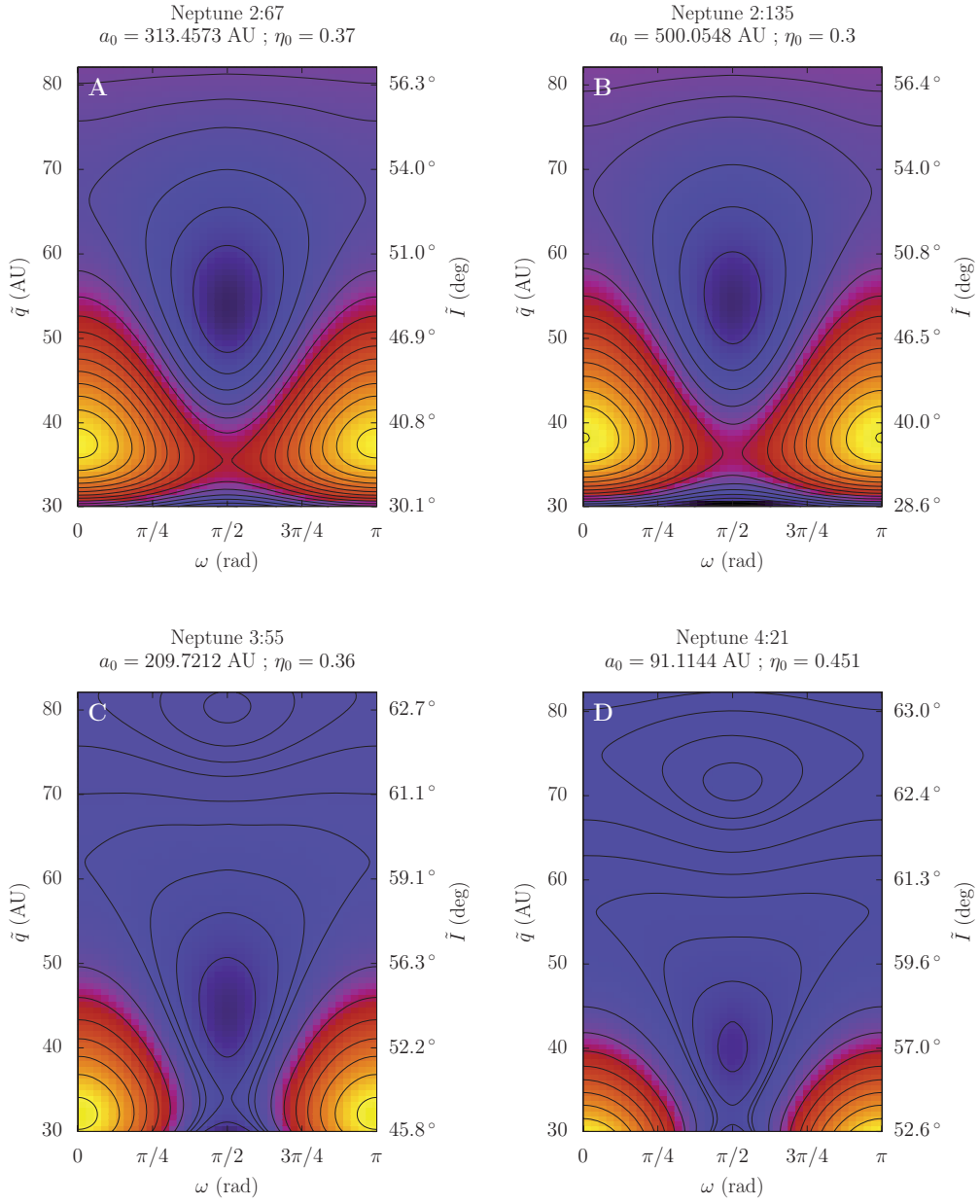

Figure 4.3 – Typical geometries for prograde orbits in resonances of type $k_p \neq 1$ with Neptune, with a parameter $J = 0$. The resonances and corresponding a_0 are indicated above the graphs, as well as the parameter η_0 used. A large variety of semi-major axes are presented to stress that the secular phase space depends little on the resonance order. The graphs A and B are very similar since they have both $k_p = 2$, but correspond to different values of η_0. On the graph C ($3:k$ resonance), the two islands still coexist but a slight increase of η_0, shifting up the $\omega = 0$ island at a perihelion similar to the graphs A and B, would make disappear the island at $\omega = \pi/2$. On the graph D ($4:k$ resonance), the coexistence is even impossible: an increase of η_0 would make disappear the $\omega = \pi/2$ island before the rise of the $\omega = 0$ one. On the graphs C and D, the classic Kozai island is visible at high inclinations.

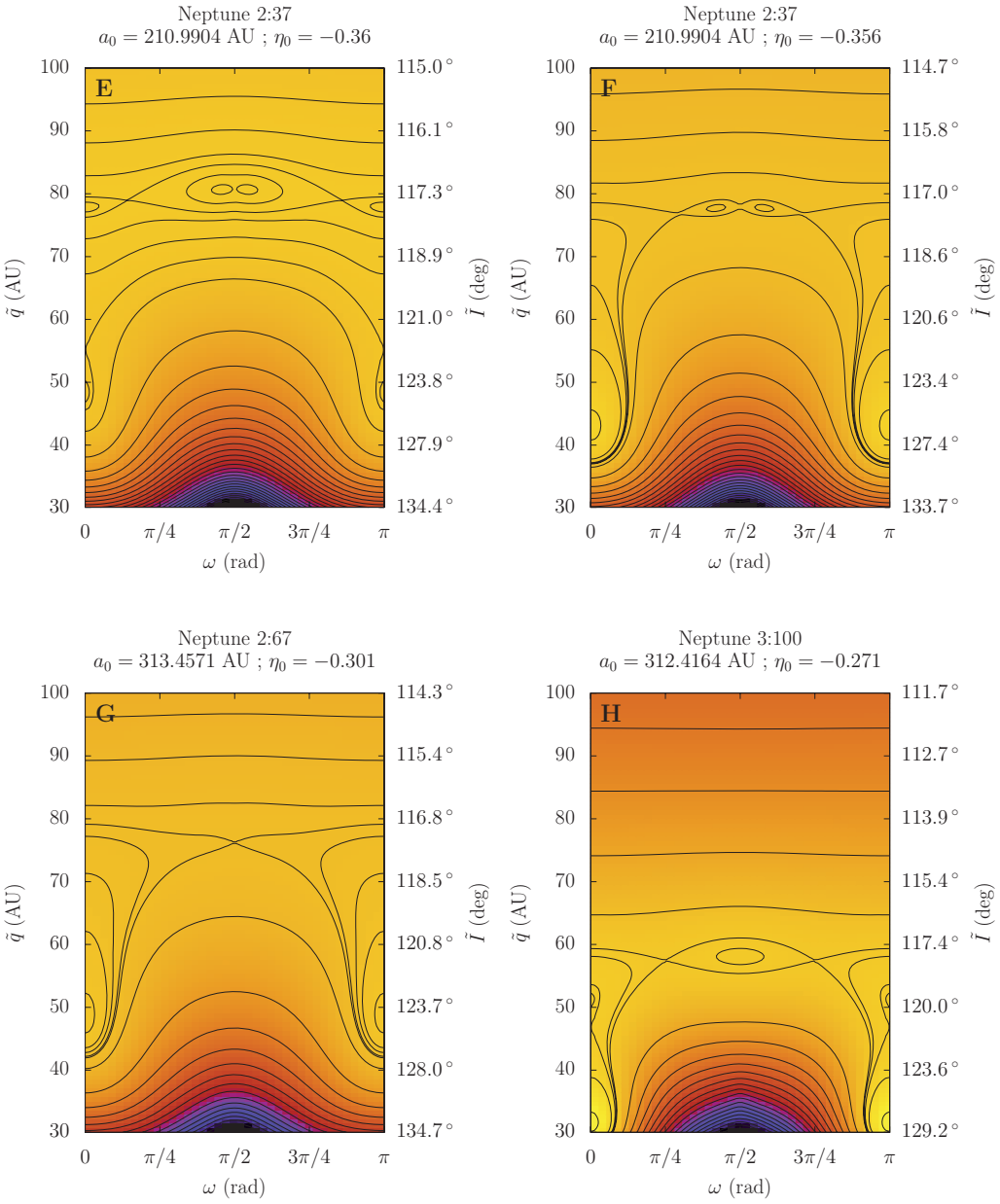

Figure 4.4 – Same as Fig. 4.3 for retrograde orbits. The graphs E and F present the same resonance for a slightly different parameter η_0. Passing in the neighbourhood of the $\omega = 0$ island, the classic Kozai island (at about 117°) deforms and merges to form high-amplitude oscillation zones for the perihelion distance. That enlargement is also clearly visible on the graphs G and H, which present two resonances with neighbour semi-major axes but different types ($2{:}k$ and $3{:}k$). As for prograde orbits, k_p modifies the respective ranges of η_0 for the appearance of the different features, which gives rise to different geometries.

4.1.2 Resonances of type $1:k$ for near-zero values of J

Figure 4.5 presents the typical evolution of the phase portraits for $k_p = 1$ with respect to the parameter η_0. Since this kind of resonance presents two resonance islands in definite regions of the plane $(\omega, \tilde{q})$, we chose to describe the case of σ oscillating inside the "right" island[4]. As before, the green line divides the zones associated with two resonance islands from the zones associated with a single one. If it is crossed, there can be either a discontinuity (if the vanishing island is the very one occupied by the particle), or a soft transition. For particles following a level curve leading to the discontinuity, another secular model is necessary after the crossing, with a different parameter J. Naturally, the discontinuity is only one-way: if the particle comes *from* the one-island side (for prograde orbits, this means from the high-perihelion region), the appearance of the second island does not imply any particular transition (J is continuously conserved). The appropriate secular representation should though be used (σ oscillating in the left or right resonance island). Figure 4.6 shows further details and comparisons between different resonances of type $1:k$ for η_0 in the range of interest. Our general conclusions are listed below:

- For retrograde orbits, there is only one resonance island almost everywhere in the plane $(\omega, \tilde{q})$, which produces symmetric level curves with respect to $\pi/2$ (see Fig. 4.5, upper graphs). The small regions with two resonance islands are located in a small range of perihelion distances at $\omega = \pi/2$ and near the collision points with Neptune ($\omega = 0$ or π and $q = a_{\rm N}$). When η_0 tends to 0, these three regions merge and eventually occupy all the bottom part of the graphs (as for prograde orbits).

- For prograde orbits, the geometries are actually very similar to the ones obtained for $k_p = 2$, apart from the asymmetry and the discontinuity line induced by the two resonance islands. In other words, a range of η_0 allows the same libration islands at $\omega = 0$ and $\pi/2$, which are however shifted and more or less distorted. The $\omega = \pi/2$ island can be besides truncated by the discontinuity line. As before, an increase of η_0 simultaneously shifts up the $\omega = 0$ equilibrium point and down the $\pi/2$ one until they both disappear. The $\pi/2$ island is the last to vanish.

- For retrograde orbits, a range of η_0 allows an equilibrium point at $\omega = 0$. When η_0 tends to zero, that equilibrium shifts toward the orbit of Neptune, but contrary to resonances of type $k_p \neq 1$, it splits in two (see Fig. 4.5 for $\eta_0 = -0.38$). This allows to partially avoid the discontinuity curve (Fig. 4.6, graph A). During this process, a small range of η_0 allows an additional equilibrium point at $\omega = \pi/2$, but the associated libration island is truncated by the discontinuity curve (see Fig. 4.5 for $\eta_0 = -0.36$ and Fig. 4.6, graph A).

[4]Since the semi-secular Hamiltonian $\mathcal{K}$ is symmetric in ω with respect to $\pi/2$, the secular level curves for oscillations inside the left island are obtained by the transformation $\omega \to \pi - \omega$.

- As for other kinds of resonances, the interaction with the classic non-resonant Kozai island can enlarge the resonant features to create spectacular excursions of the perihelion distance. In the graph C of Fig. 4.6, for instance, the classic Kozai island is located at $\tilde{q} = 140$ AU (out of the plot), and produces a possible evolution from $\tilde{q} \approx 41$ AU to 107 AU. A similar kind of enlargement is also visible on Fig. 4.5 for $\eta_0 = 0.45$.

- For small semi-major axes (say < 130 AU), the geometries at high perihelion distances can be more complex because of the proximity of the circular orbit. This can create various new equilibrium points, as on the graph B of Fig. 4.6 (four additional islands). A different behaviour for small semi-major axes was also reported in the non-resonant case (see Sect. 3.2.3, in particular Figs. 3.3 and 3.6).

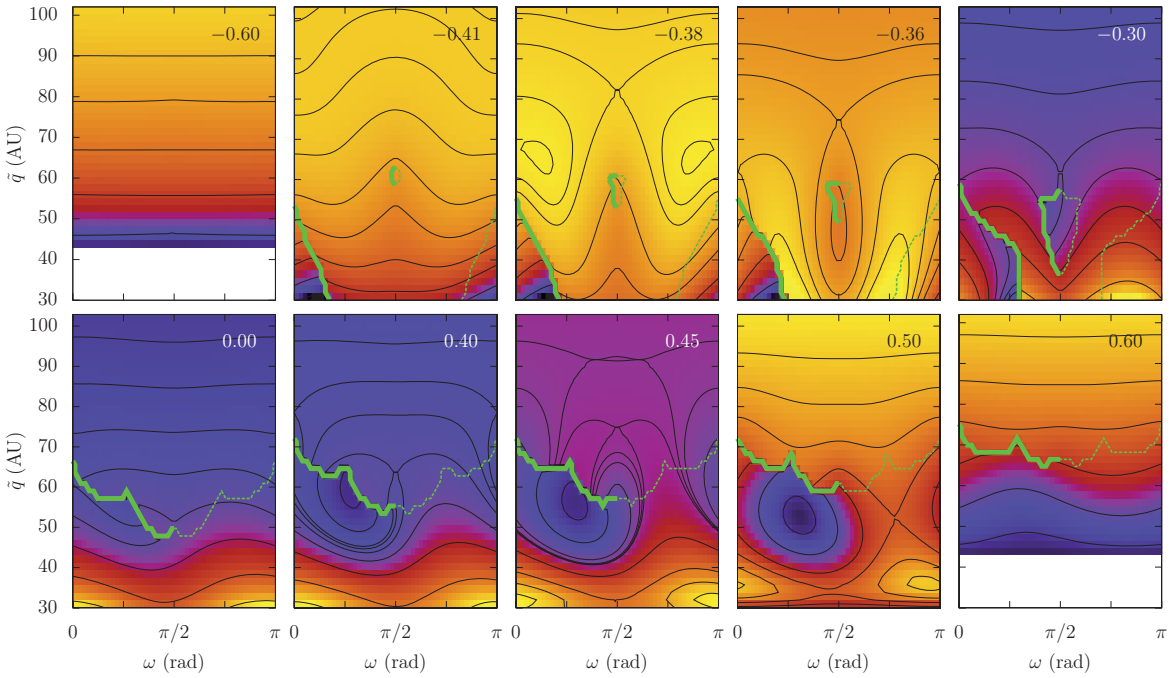

Figure 4.5 – Typical dependence on the parameter η_0 for orbits in resonances of type $1 : k$ with Neptune. The resonance taken in example here is $1 : 19$ (reference semi-major axis chosen $a_0 = 214.7763$ AU). When there is a change of topology in the semi-secular phase space (from a two-resonance-island to a one-resonance-island configuration), the secular phase portrait can either present a discontinuity (thick green line) or a soft transition (thin dashed green line). In the regions where there are two resonance islands (below the green line or inside it when it is closed), we chose σ to oscillate inside the right one. All of these graphs are plotted for $J = 0$ and η_0 is indicated in the upper right corners. On the Y-axis of each graph, the reference inclinations can be obtained by $\cos \tilde{I} = \eta_0 / \sqrt{1 - (1 - \tilde{q}/a_0)^2}$. The white regions in the first and last graphs are unreachable with these values of η_0 (they would require a cosine of inclination lower than -1 or higher than 1, respectively).

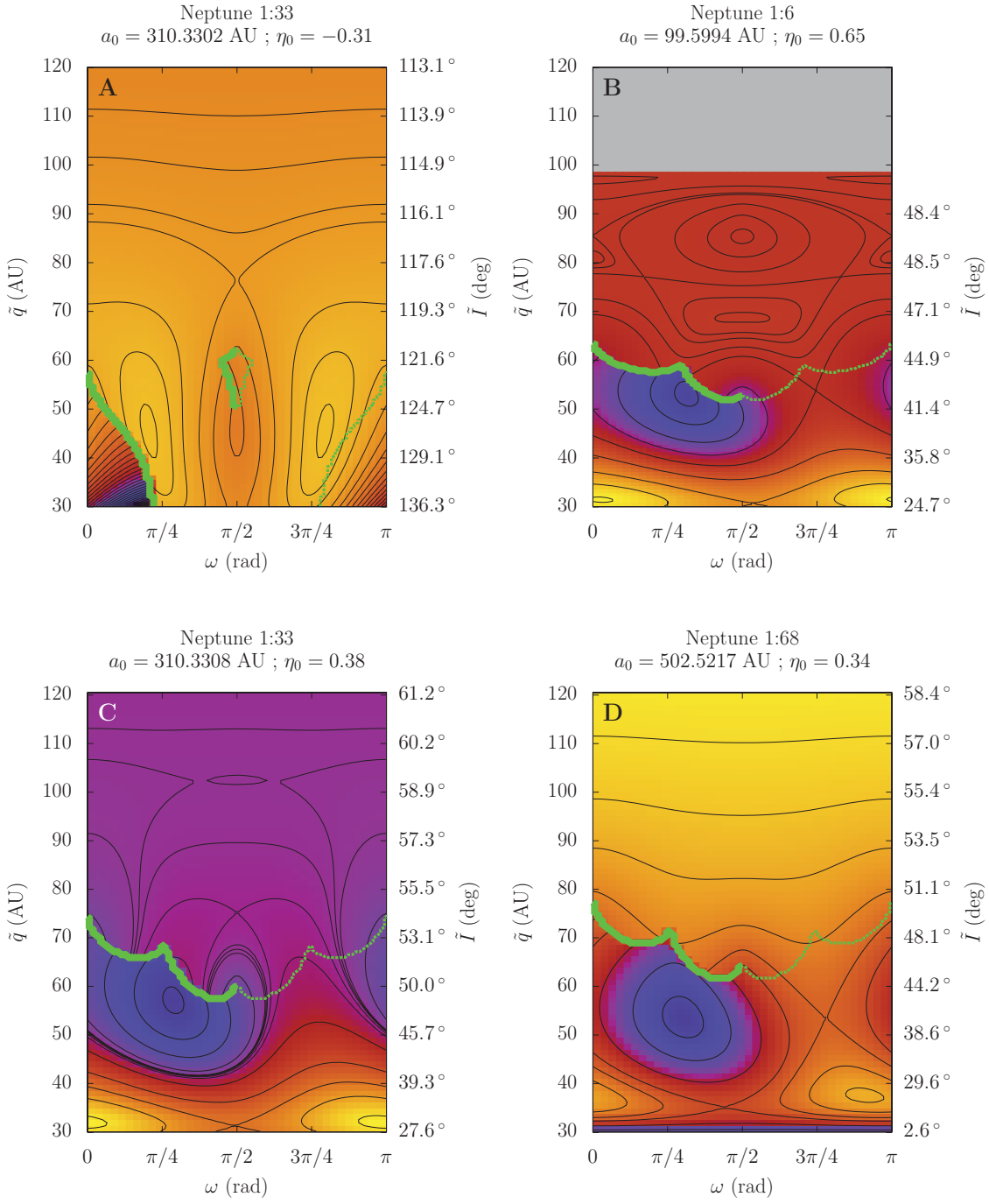

Figure 4.6 – Typical geometries for resonances of type $1:k$ with Neptune, with a parameter $J = 0$ and oscillations of σ inside the right island. The resonances and corresponding a_0 are indicated above the graphs, as well as the parameter η_0 used. These graphs have to be compared and located in Fig. 4.5: note the similar geometries when changing k but for a different scale of the parameter η_0. The graph B shows that for small semi-major axes, the geometry at high perihelion distance is modified by the proximity of the circular orbit. The graph D shows that the interesting trajectories are not restricted to high-inclination regimes and that they can occasion very wide variations of inclination.

4.1.3 Playing with the secular discontinuity line

From Sect. 4.1.2, we know that any secular representation for prograde resonances of type $1:k$ presents a one-way discontinuity line in the plane $(\omega, \tilde{q})$ from low to high perihelion distances. Since that line is only half-width[5], this gives the striking possibility for a particle to pass softly from the left resonance island to the right one, simply by getting *around* the discontinuity line and crossing it in its smooth direction. These trajectories are recognizable in the secular phase portraits as the level curves connected *only* to the *upper side* of the thick green line. Some of them are visible on the graph C of Fig. 4.6 (including the trajectory featuring the largest variations of $\tilde{q}$): when crossing the line from the upper part, the single island in which oscillates σ becomes the left one (the corresponding secular representation is obtained by $\omega \to \pi - \omega$). Since the evolution is not constrained by the discontinuity line, that very particular kind of trajectory allows the largest perihelion variations possible for resonances of type $1:k$.

Figure 4.7 presents an example of such a trajectory obtained by a numerical integration of the unaveraged system (the equations of motion are given by the Hamiltonian from Eq. 3.12 without any transformation). The initial conditions are chosen to match the parameters of Fig. 4.5 for $\eta_0 = 0.45$, where that trajectory is noticeable. Naturally, Fig. 4.5 is plotted for σ oscillating inside the right resonance island, so only the green and red parts of Fig. 4.7 can be represented. Indeed, for these particular trajectories, a secular representation like the one used in this work is necessarily piecewise even if the dynamics is perfectly regular. When the secular discontinuity line is crossed, the particle always occupies the non-vanishing island, which prevents any separatrix crossing. That mechanism is detailed in Fig. 4.8, where the semi-secular geometry is presented.

[5]The discontinuity line spans in $\omega \in [0; \pi/2]$ or $[\pi/2; \pi]$ if the particle occupies the right or the left resonance islands, respectively.

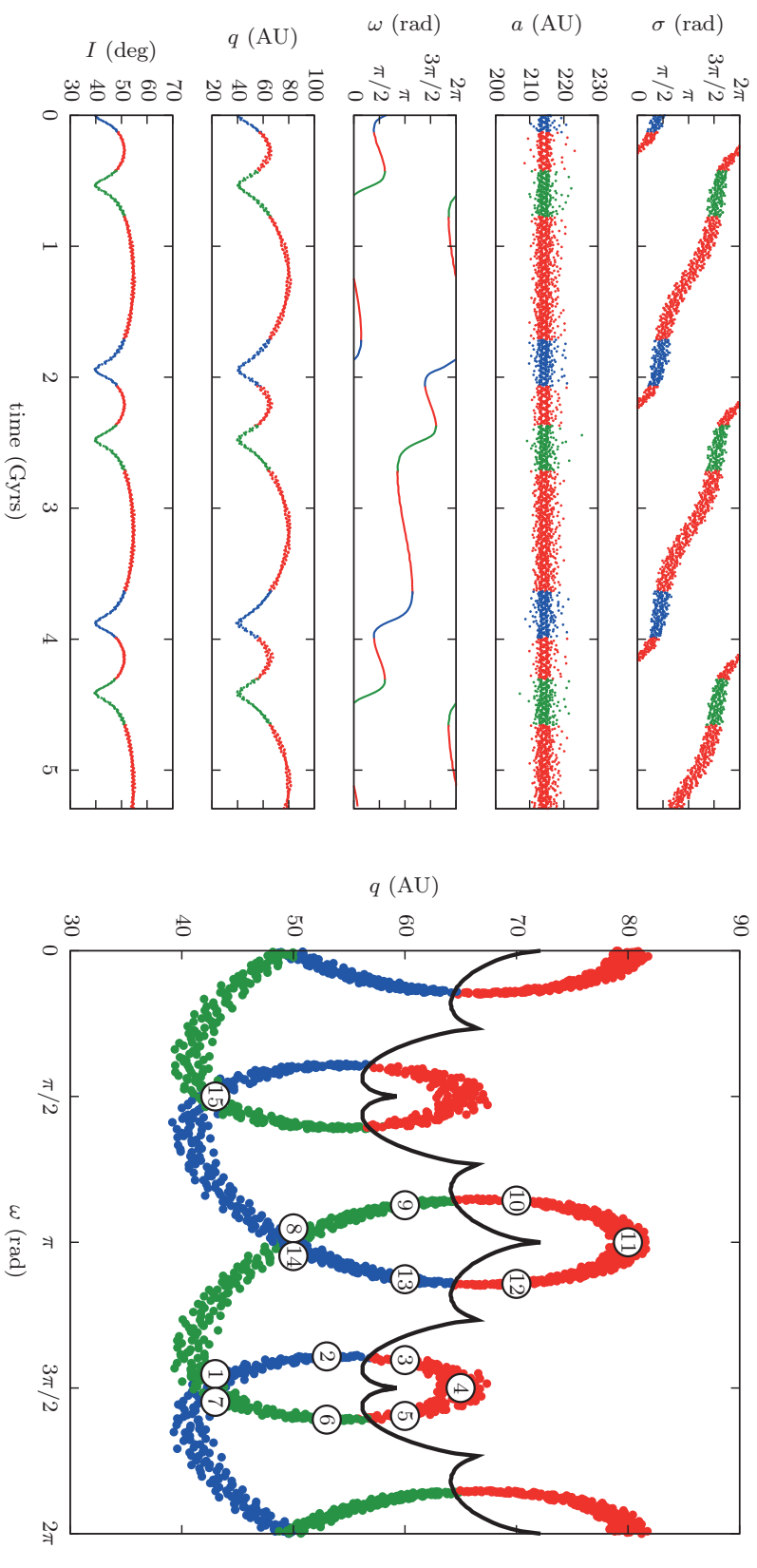

Figure 4.7 – Numerical integration of the unaveraged system for the resonance 1:19 with Neptune. On the right, the trajectory is projected in the plane (ω, q), where the secular discontinuity line is added in black. Visible on the left panel, the oscillations of the semi-major axis are essentially due to the motion of the Sun around the barycentre of the Solar System: in the averaged system, the secular shift of the resonance centre ranges only from 214.775 AU to 214.777 AU. The colour code is chosen according to the geometry of the semi-secular phase space: when it contains two resonance islands, the trajectory is plotted in green (right island) or blue (left island). In the red portions, there is only one resonance island. The numbers refer to Fig. 4.8, where the geometry of the semi-secular phase space is shown.

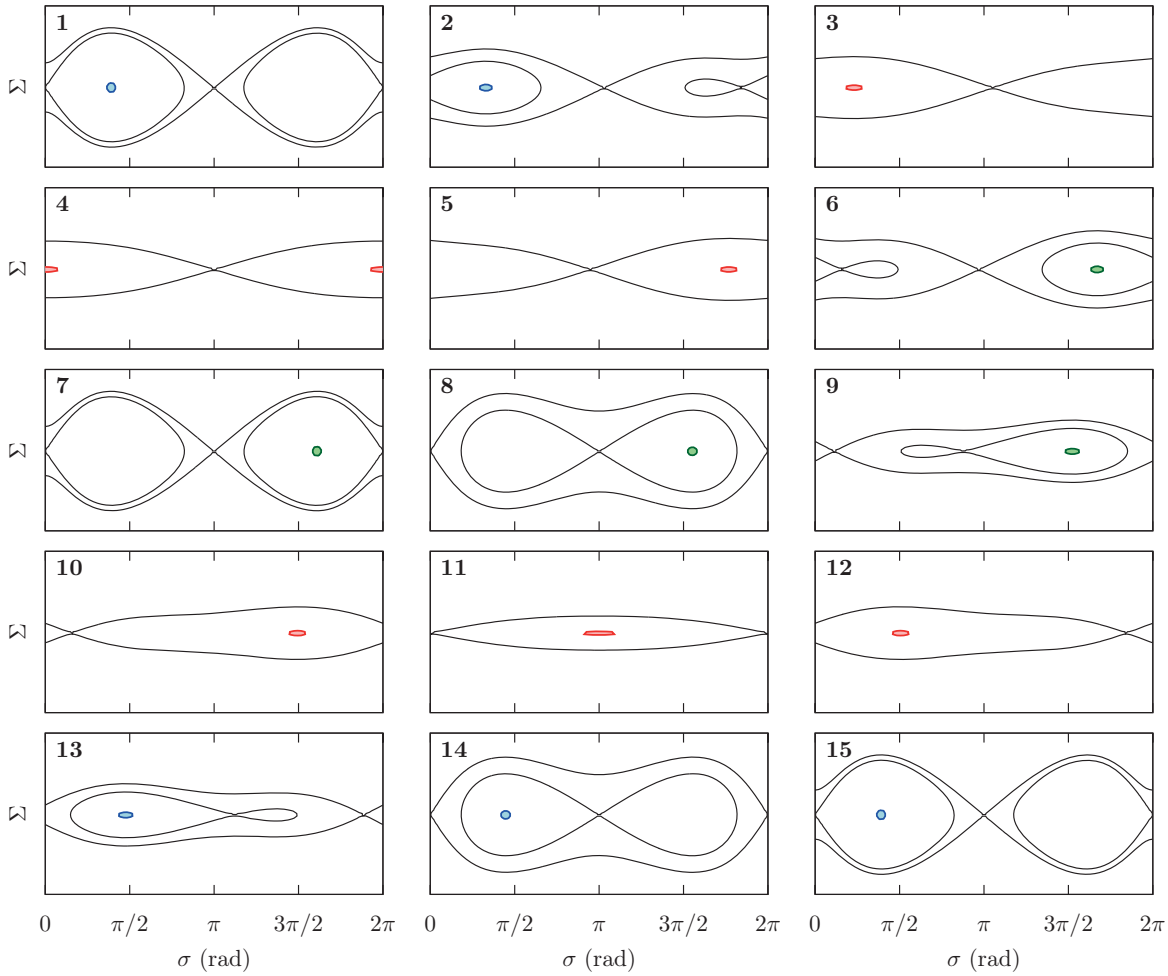

Figure 4.8 – Level curves of the semi-secular Hamiltonian $\mathcal{K}$ for (U, u) fixed according to 15 points of Fig. 4.7. For clarity, only the separatrices are shown. We recall that $\Sigma = \sqrt{\mu a}/k$ is the momentum conjugate to σ. When a separatrix disappears (as between the graphs 2 and 3), it means that the smallest resonance island has vanished, so all the level curves inside the resonance enclose the remaining equilibrium point. The semi-secular trajectory corresponding to the numerical integration of Fig. 4.7 is shown with the same colour code: blue for σ oscillating in the left island, green for the right one, and red when there is only one resonance island in the phase space. Since the secular parameter J is very close to 0, the semi-secular trajectory encircles tightly the resonance centre. The tiny area $|2\pi J|$ conserved is shown in mid-tones. One can note that between the graphs 1-7 and 8-14, the particle returns exactly to the same (ω, q) point (thus the same semi-secular geometry) but has changed resonance centre. On a secular timescale, the corresponding trajectory is a circulation of the resonance centre itself (see the evolution of σ in Fig. 4.7).

4.1.4 High-amplitude oscillations of the resonant angle σ

For a larger area $|2\pi J|$, that is, a higher amplitude of the semi-secular oscillations of σ, the inevitable separatrix crossing beyond some value of the perihelion distance produces important changes in the resonant secular dynamics (see Sect. 3.4.2). In other words, σ is constrained to circulate if the perihelion distance grows too much.

As shown in Fig. 4.9, this has the general effect of squeezing the secular trajectories towards Neptune, and even smooth out the equilibrium points if $|2\pi J|$ is large enough. Indeed, a high-amplitude oscillation of σ weakens the resonant part of the Hamiltonian function. This lets the non-resonant part dominate, and the latter has no equilibrium point for $a > 80$ AU other than the classic Kozai ones around $I = 63°$ and $117°$. In the upper grey regions of the graphs A and B, a secular model for circulating σ can be applied. However, for such a model the equilibrium points are rare and concentrated at small values of $\tilde{q}$, where the resonance is still close and effective (see Sect. 3.4.2 for examples). Moreover, the circulation of the resonant angle often triggers a diffusion of semi-major axis and the secular representation ceases to be relevant (the locking inside the resonance acts as a barrier against diffusion). In the lower grey region of the graph B, the particle is pushed out of the right resonance island, but since the left one has still a wide extent, a second capture can happen immediately and produce complex regular-by-parts trajectories. That transition can occur also in the $J = 0$ case, but only when the thick green line is crossed, that is at a much higher $\tilde{q}$. A large area $|2\pi J|$ restricts thus severely the possibility for a particle to reach high perihelion distances.

These considerations can be summed up by: deeper the resonance capture, larger the possible secular variations of the perihelion distance. However, the structures at low value of $\tilde{q}$, and in particular the usual equilibrium point at $\omega = 0$, can persist even for a large area $|2\pi J|$ (see the graph A of Fig. 4.9) since the resonance islands are pretty big.

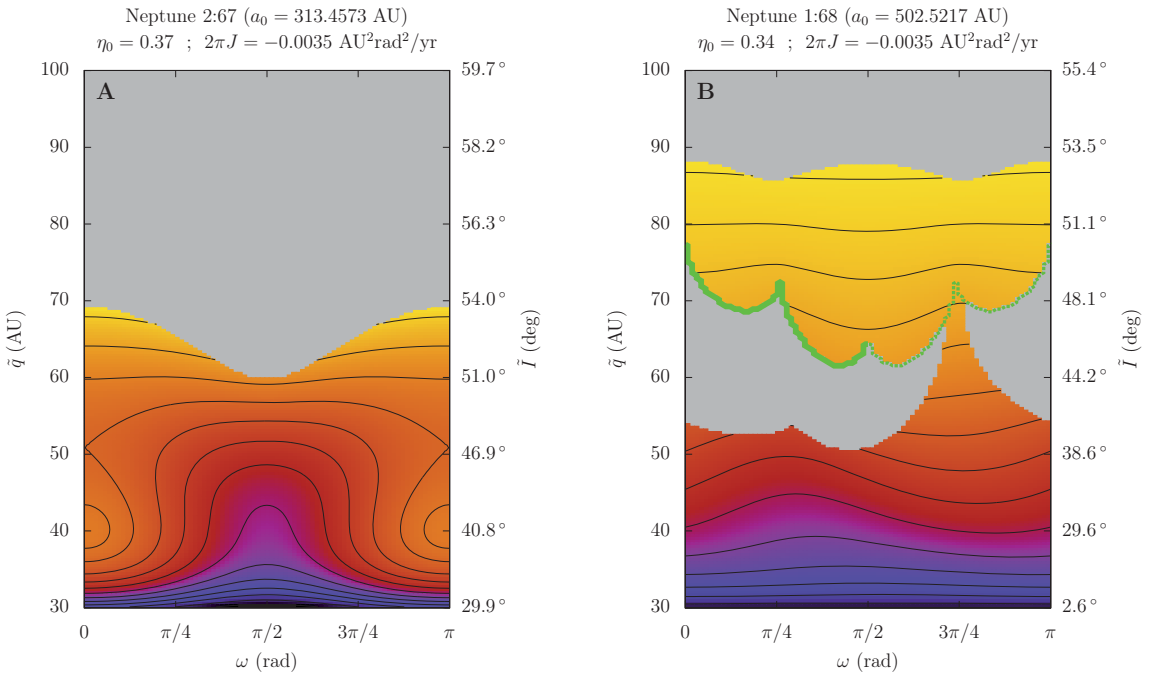

Figure 4.9 – Effect of a large area $|2\pi J|$. The resonances and corresponding a_0 are indicated above the graphs, as well as the parameters chosen. The grey colour denotes the regions where the semi-secular separatrices are too narrow to contain the area $|2\pi J|$, that is, where this secular model is not relevant. In the graph B ($1:k$ resonance), the particle is chosen to oscillate inside the right resonance island, and only one island remains beyond the green line. These phase portraits have to be compared to their counterpart with $J = 0$ in Fig. 4.3 and 4.6 (graphs A and D, respectively).

4.2 Application to observed resonant objects

Up to now, the application of the resonant secular model was made exclusively on distant resonances, for which the adiabatic approximation is more relevant. However, only a few trans-Neptunian objects are known with semi-major axes that large, and their orbital uncertainties are necessarily rather high since only a fraction of their orbits has been observed (orbital period $>$ 1000 years). In this section, we present the long-term evolution of the trans-Neptunian objects *known* to be in resonance, that is those for which the uncertainties of orbital elements are predominantly compatible with a resonant trapping. As presented for instance by Lykawka and Mukai (2007), they are quite numerous and most of them have small semi-major axes (because of the observational constraints). Fortunately, we will show that the adiabatic approximation is also viable for semi-major axes as small as 50 AU, even if the two timescales are not as strikingly separated as for $a > 100$ AU. For even closer objects, individual analyses would be required, not only to check the validity of the adiabatic approximation, but also the possible occurrence of secular resonances with the giant planets (Knezevic et al., 1991), which would also invalidate this model. Consequently, we focus here on the $\sim$40 currently known resonant trans-Neptunian objects with $a > 50$ AU.

We selected these objects from three reference classifications (Lykawka and Mukai, 2007; Gladman et al., 2008, 2012), retaining only the "securely classified" ones with a semi-major axis larger than 50 AU. Two recent observation reports were also added: Bannister et al. (2016) presents the discovery of $2015\,\mathrm{RR}_{245}$, which has a confirmed resonant classification; on the other hand, Sheppard et al. (2016) introduces some objects which are probably resonant or have been strongly affected by a mean-motion resonance with Neptune. This last classification is slightly different, but we chose to add these objects to this study to emphasise the link with recent results focussed on high-perihelion objects. Indeed, the secular model proved to be an efficient tool to reveal dynamical paths leading to high perihelion distances and large inclinations. The objects studied in this section are listed in Tab. 4.1.

In Sect. 4.2.1, we explain how suitable secular parameters can be obtained from known objects. Then, we selected the most representative phase portraits obtained. Most of the objects considered here have a quite ordinary secular dynamics (Sect. 4.2.2), but a subset of them evolve near or inside secular libration islands (Sect. 4.2.3) and one object follows a regular-by-part secular trajectory (Sect. 4.2.4).

4.2.1 Determination of the secular parameters

In Chp. 3, we presented the creation of the secular models. In the resonant case, the Hamiltonian is function of two dynamical variables $(\omega, \tilde{q})$ and depends on two free parameters (η_0, J). The problem is to compute these quantities for a given object, for which only the osculating coordinates are known. The standard procedure consists in filtering digitally the output of a medium-term numerical integration, thus removing the short-period component of the trajectory as we did in the semi-analytical theory.

Name		$k_p:k$	LY07	GL08	GL12	SH16	BA16	a_0	η_0	$-2\pi J$	ω	$\tilde{q}$
	$2001\,KG_{76}$	4:9	⋆	×				51.718	0.939	0.02	2.668	34.017
(42301)	$2001\,UR_{163}$	4:9	⋆	×				51.719	0.958	0.04	6.148	36.974
(95625)	$2002\,GX_{32}$	3:7	⋆	×				52.987	0.901	0.07	3.359	33.146
	$2002\,CZ_{248}$	3:7			⋆			52.987	0.919	0.026	5.252	32.413
(131696)	$2001\,XT_{254}$	3:7	⋆	×	⋆			52.988	0.946	0.04	3.294	35.910
(181867)	$1999\,CV_{118}$	3:7		×				52.988	0.949	0.04	2.650	37.493
(79978)	$1999\,CC_{158}$	5:12		×				53.991	0.904	0.017	1.841	39.096
(119878)	$2002\,CY_{224}$	5:12	⋆	×				53.991	0.896	0.011	2.689	35.275
(84522)	$2002\,TC_{302}$	2:5		×				55.474	0.784	0.13	1.585	39.002
(26375)	$1999\,DE_{9}$	2:5	⋆	×				55.478	0.897	0.18	2.884	32.283
(60621)	$2000\,FE_{8}$	2:5	⋆	×	⋆			55.479	0.909	0.05	2.739	33.109
(38084)	$1999\,HB_{12}$	2:5	⋆	×				55.480	0.890	0.105	1.052	32.615
	$2004\,KZ_{18}$	2:5			⋆			55.480	0.847	0.0015	0.136	34.310
	$2004\,EG_{96}$	2:5	⋆		⋆			55.481	0.871	0.045	0.185	32.110
	$2002\,GP_{32}$	2:5	⋆	×	⋆			55.481	0.907	0.0013	0.463	32.081
	$2000\,SR_{331}$	2:5	⋆	×				55.481	0.896	0.023	3.812	31.157
(143707)	$2003\,UY_{117}$	2:5	⋆	×				55.481	0.899	0.064	1.895	32.510
(135571)	$2002\,GG_{32}$	2:5	⋆	×				55.481	0.907	0.03	4.140	35.905
(69988)	$1998\,WA_{31}$	2:5	⋆	×				55.481	0.890	0.12	5.571	31.581
(119068)	$2001\,KC_{77}$	2:5	⋆	×				55.482	0.913	0.24	3.239	35.455
	$2004\,HO_{79}$	2:5			⋆			55.482	0.907	0.08	2.359	32.507
	$2001\,XQ_{254}$	2:5	⋆	×				55.484	0.894	0.19	0.189	31.089
	$2015\,GP_{50}$	2:5				×						
	$2012\,FH_{84}$	2:5				×						
(82075)	$2000\,YW_{134}$	3:8	⋆	×				57.920	0.909	0.00035	5.489	41.146
	$2004\,XR_{190}$	3:8				×						
	$2015\,FJ_{345}$	1:3				×		62.649	0.809	0.065	1.391	50.905
(136120)	$2003\,LG_{7}$	1:3	⋆	×				62.660	0.817	0.5	5.913	32.483
	$2015\,KH_{162}$	1:3				×						
	$2013\,FQ_{28}$	1:3				×						
(160148)	$2001\,KV_{76}$	2:7		×				69.430	0.835	0.076	4.098	34.421
(126619)	$2002\,CX_{154}$	3:11		×								
	$2014\,FC_{69}$	3:11				×						
	$2014\,FZ_{71}$	1:4				×		75.900	0.860	0.035	4.277	56.117
	$2015\,RR_{245}$	2:9					⋆	82.100	0.802	0.075	4.360	33.942
(26181)	$1996\,GQ_{21}$	2:11		×								
	$2008\,ST_{291}$	1:6				×		99.453	0.761	0.003	5.721	42.566
(184212)	$2004\,PB_{112}$	5:27		×				107.575	0.713	0.0055	0.158	35.392

Table 4.1 – List of the resonant trans-Neptunian objects with $a > 50$ AU. The resonance ratios $k_p:k$ are all with Neptune. The references used are abbreviated in LY07 (Lykawka and Mukai, 2007), GL08 (Gladman et al., 2008), GL12 (Gladman et al., 2012), SH16 (Sheppard et al., 2016) and BA16 (Bannister et al., 2016). A cross indicates that the object is classified as "resonant"; a star indicates that the article provides also the oscillation amplitude of the resonant angle with its uncertainty. In LY07 and GL12, the object is omitted if the classification is said "insecure". The right part of the table gives the characteristics of the resonant secular models obtained: a_0 is the reference semi-major axis chosen (AU) whereas η_0 (no unit) and $-2\pi J$ ($\mathrm{AU}^2\mathrm{rad}^2/\mathrm{yr}$) are the fixed parameters. Finally, ω (rad) and $\tilde{q}$ (AU) are the current secular argument of perihelion and reference perihelion distance of the object. Blank fields mean that the object was found non-resonant in the numerical integration starting from the nominal orbit given by AstDyS database. In the particular case of $2014\,FZ_{71}$, a secular model was developed although the nominal orbit solution was not resonant (see Sect. 4.2.4). In theory, the 1-sigma error bars would allow it also for $2015\,GP_{50}$, $2012\,FH_{84}$ and $2013\,FQ_{28}$.

The detailed procedure was introduced by Carpino et al. (1987) and implemented in the OrbFit Software Package[6]. For the resonant objects from Tab. 4.1, a numerical integration of 500 000 years was found more than enough to cover the semi-secular oscillations (related to the resonant angle). The numerical integrations were performed using the same software package, taking the nominal orbits given by AstDyS database[7] as initial conditions. The four giant planets were integrated consistently and the masses of the inner ones were added to the Sun. The invariable plane of the Solar System was taken as reference plane for the output. We used heliocentric coordinates, as this is the system on which is based the semi-analytical theory[8].

The secular values of (U, V, u) can be directly picked up from the filtered series, whereas the parameter J requires the computation of the area enclosed by the trajectory in the (Σ, σ) plane. Fig. 4.10 shows some examples of filtered output, with the graphical representation of the corresponding areas $2\pi J$. In the background, the level curves of the semi-secular Hamiltonian $\mathcal{K}$ with (U, u) fixed at their secular (that is filtered) current values are also plotted in order to assess the validity of the semi-analytical procedure. The filtered trajectories were always found to follow pretty well the level curves, showing that our simplified and averaged model captures the essence of the dynamics. The characteristics of the corresponding secular models are gathered in Tab. 4.1. The oscillation amplitudes of the resonant angles were generally found in very good agreement with the values given in Lykawka and Mukai (2007) and Gladman et al. (2012).

Please note that this method for getting the secular parameters of the observed bodies relies on the *nominal* orbit solutions. Consequently, the actual parameters could be a bit different, especially for the recently discovered objects. The corresponding changes concern mostly the parameter J which is sensitive to the initial conditions. For instance, a slight increase of the area $|2\pi J|$ leads to a wider coverage of the "grey" zones (on the sides of which separatrix crossings occur).

In our numerical integrations, some objects were found outside the expected resonances (blank lines in Tab. 4.1). Apart from two exceptions, this concerns small bodies reported by Sheppard et al. (2016) which are not classified as "resonant" from their current orbit but from their probable dynamical history. For these objects, a secular model *near* the resonance could still be developed (in which $2\pi J$ is the area under the curve), or the uncertainties of the nominal orbit could be taken into account to develop a secular model for a "potential" resonant orbit. This will be realised for $2014\,\mathrm{FZ}_{71}$.

[6] `http://adams.dm.unipi.it/orbfit/`

[7] `http://hamilton.dm.unipi.it/astdys/`

[8] Since the temporal series obtained are meant to be filtered, the short-period oscillations of the barycentre of the Solar System, usually removed by using barycentric coordinates, are not a problem.

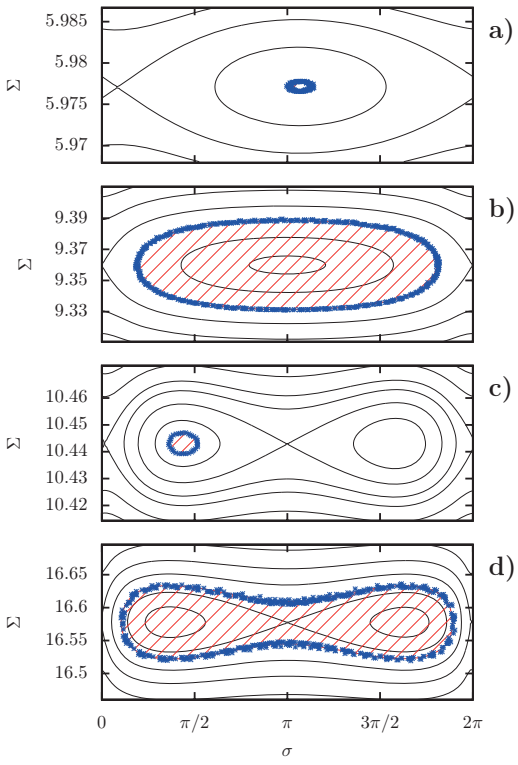

Figure 4.10 – Computation of the secular constant of motion J from the filtered numerical integrations. The examples shown are (from top to bottom): 82075, 119068, $2008\,\mathrm{ST}_{291}$ and 136120. See Tab 4.1 for the corresponding resonances. The axes are σ (rad) and Σ ($\mathrm{AU}^2\mathrm{rad/yr}$). The blue crosses come from the filtered output, whereas the red hatched area is equal to the quantity $-2\pi J$ used to construct the secular model. The black lines in the background are the level curves of $\mathcal{K}$ with (U, u) fixed. Various cases are shown: small (**a**,**c**) or large (**b**,**d**) area, single (**a**,**b**) or double (**c**,**d**) resonance island, simple (**a**,**b**), asymmetric (**c**) or horseshoe (**d**) oscillations.

4.2.2 Typical resonant secular evolutions

Most of the objects studied here are not very affected by their resonant relation with Neptune: this results in a "flat" secular evolution, with circulating ω and almost constant $\tilde{q}$. Such a secular behaviour is similar to what we would obtain for a non-resonant dynamics (where the only notable features are located at high inclinations). This indicates a small influence of the resonance on the long-term dynamics: indeed, the resonant link can never bring the small body away from its capture configuration, resulting in an unstable transient resonance[9]. This is confirmed for $2015\,\mathrm{RR}_{245}$ by the detailed dynamical study by Bannister et al. (2016).

Some examples of level curves of the secular Hamiltonian $\mathcal{F}$ are shown in Fig. 4.11. As before, the graphs are π-periodic in ω. Every object listed in Tab. 4.1 follows such kinds of trajectories, with the exception of the objects 135571, $2004\,\mathrm{KZ}_{18}$, $2008\,\mathrm{ST}_{291}$, 82075, $2015\,\mathrm{FJ}_{345}$ and $2014\,\mathrm{FZ}_{71}$, which we describe in Sects. 4.2.3 and 4.2.4. In order to check the validity of the adiabatic approximation, each graph features also a numerical integration of the two-degree-of-freedom semi-secular system. As required, the mean trajectory follows a level curve of the secular Hamiltonian. The extra oscillations due to the second degree of freedom are even almost undistinguishable, hidden in the curve

[9]This conclusion does not hold if the object was left on a distant resonant trajectory by the late migration of Neptune (Gomes et al., 2008). In that case, the constancy of the secular perihelion distance is a guarantee of stability, on the contrary.

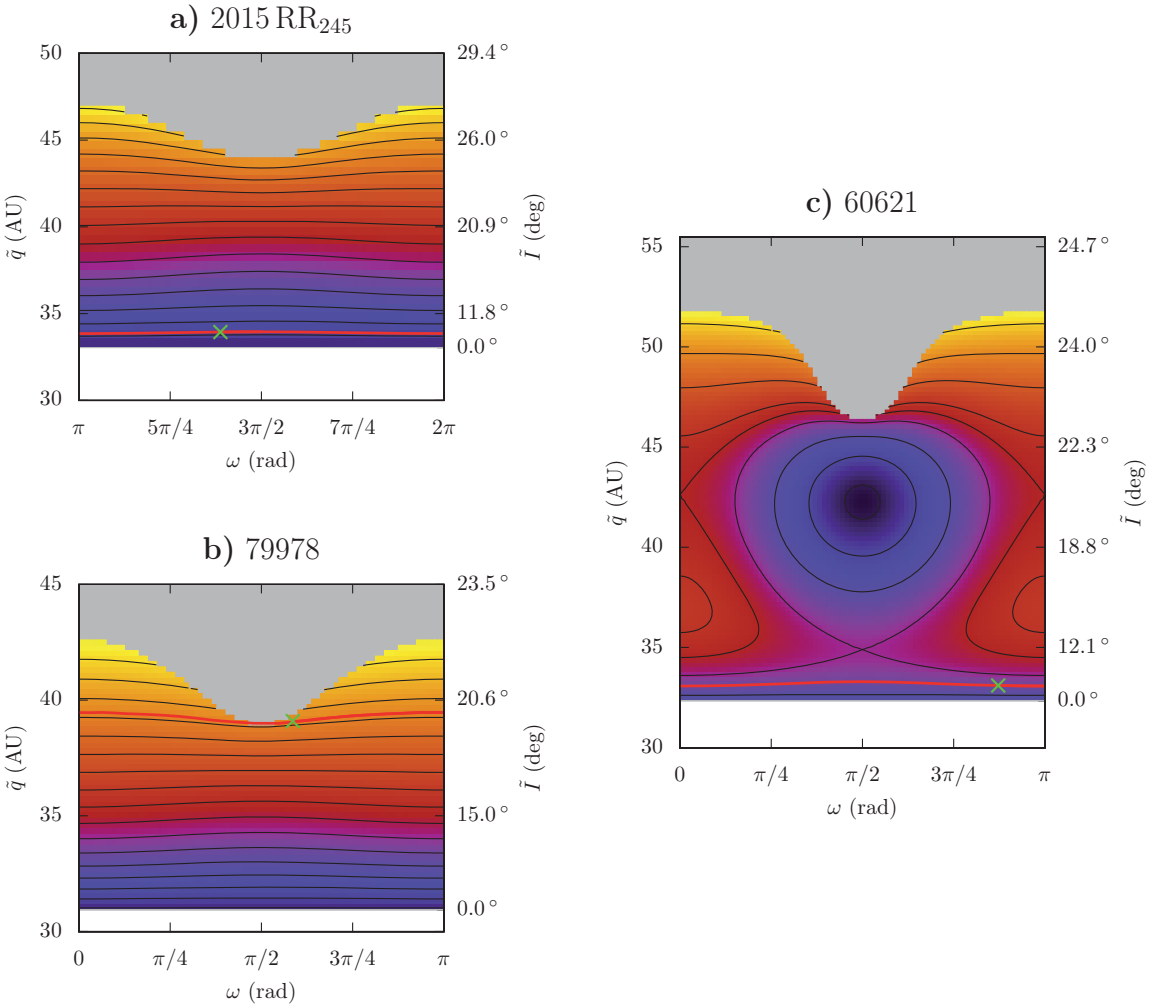

Figure 4.11 – Typical examples of phase portraits for the objects studied in this section. The colour shades represent the value of the secular Hamiltonian (dark/light for low/high), from which can be deduced the direction of motion along the level curves (black lines). The white zones are forbidden by the value of the parameter η_0 (it would require a cosine of inclination larger than 1), and the grey zones are forbidden by the value of the parameter J (the resonance island is too narrow to contain the signed area $2\pi J$). The green cross represents the current position of the object, and the red curve comes from a numerical integration of the two-degree-of-freedom semi-secular system. The names are written above the graphs (see Tab. 4.1 for the parameters of the models). On the graph **b**, the secular trajectory of 79978 forces periodically σ to circulate when the curve enters the grey zone (separatrix crossing). The numerical integration shows that this does not affect significantly the overall dynamics (red curve). The graph **c** shows that 60621 follows a "flat" trajectory even if the parameters of the model could allow interesting variations of orbital elements. The behaviour of the object $2004\,\mathrm{EG}_{96}$ (not shown) is very similar to that of 60621, but it follows a level curve much closer to the secular separatrix (lying just above the red curve). A small diffusion of its orbital elements (or a refinement of its orbital solution) could thus put it on a level curve leading to much higher perihelion distances.

width. Fig. 4.11**a** presents the most common case: the parameters of the secular model do not allow any peculiar geometry, and the specific level curve followed by the particle has nothing special either. In Fig. 4.11**b**, the particle is pushed outside of the resonance island in some portions of its trajectory. This does not affect the overall secular dynamics, however, since it re-enters the resonance with a similar parameter J. Finally, Fig. 4.11**c** presents a "missed" interesting case: the parameters of the secular model do allow important variations of the orbital elements but the particle is located on a flat level curve, outside of any libration island.

4.2.3 Objects affected by secular libration islands

The object 135571, presented in Fig. 4.12**a**, is the only one showing a *retrograde* circulation of ω. Indeed, it follows a level curve located *above* the two maxima of the secular Hamiltonian. It is also very close to the separatrix: a small chaotic diffusion (or a refinement of the orbital solution) could easily put it inside the secular libration island. The object $2004\,\mathrm{KZ}_{18}$, on the other hand, is clearly located in the island (Fig. 4.12**b**). This smooth quasi-periodic trajectory may not be "permanent", however, since it involves small perihelion distances. Indeed, the neighbouring resonances have large widths and a chaotic drift out of the resonance is a serious risk. The resonance captures of 135571 and $2004\,\mathrm{KZ}_{18}$ probably occurred in the lowest part of their secular trajectories (smallest perihelion distances). Since their dynamics is quasi-periodic, however, they will regularly return to their entrance configurations, leading to possible expulsions.

Figure 4.12**c** shows the case of $2008\,\mathrm{ST}_{291}$ which is associated with a much more distant resonance. The resonant angle σ oscillates in an asymmetric libration island (graph **c** of Fig. 4.10), which results in a secular Hamiltonian with level curves also asymmetric. $2008\,\mathrm{ST}_{291}$ is located inside a secular libration island, confining ω around a fixed value ($\sim 117°$) and producing large-amplitude oscillations of the perihelion distance. The object is on the descending part of the trajectory, implying that it has completed at least one cycle (period of about 115 Myrs). However, we note that $2008\,\mathrm{ST}_{291}$ has still uncertain orbital elements: Sheppard et al. (2016) reported clones evolving from $q \approx 35$ to 60 AU. These limits can be roughly measured in Fig. 4.12**c**, according to the position of the separatrix with respect to the object.

Finally we can also mention the object 82075, presented in Fig. 4.12**d**, which does not interact directly with a secular libration island but which is located on a level curve producing rather large variations of orbital elements (circulation of ω and oscillations of $\tilde{q}$ from about 38 to 44 AU). The minimum perihelion distance reached by 82075 seems quite high to be considered as a capture location. This led Lykawka and Mukai (2007) to classify it as a "detached" object.

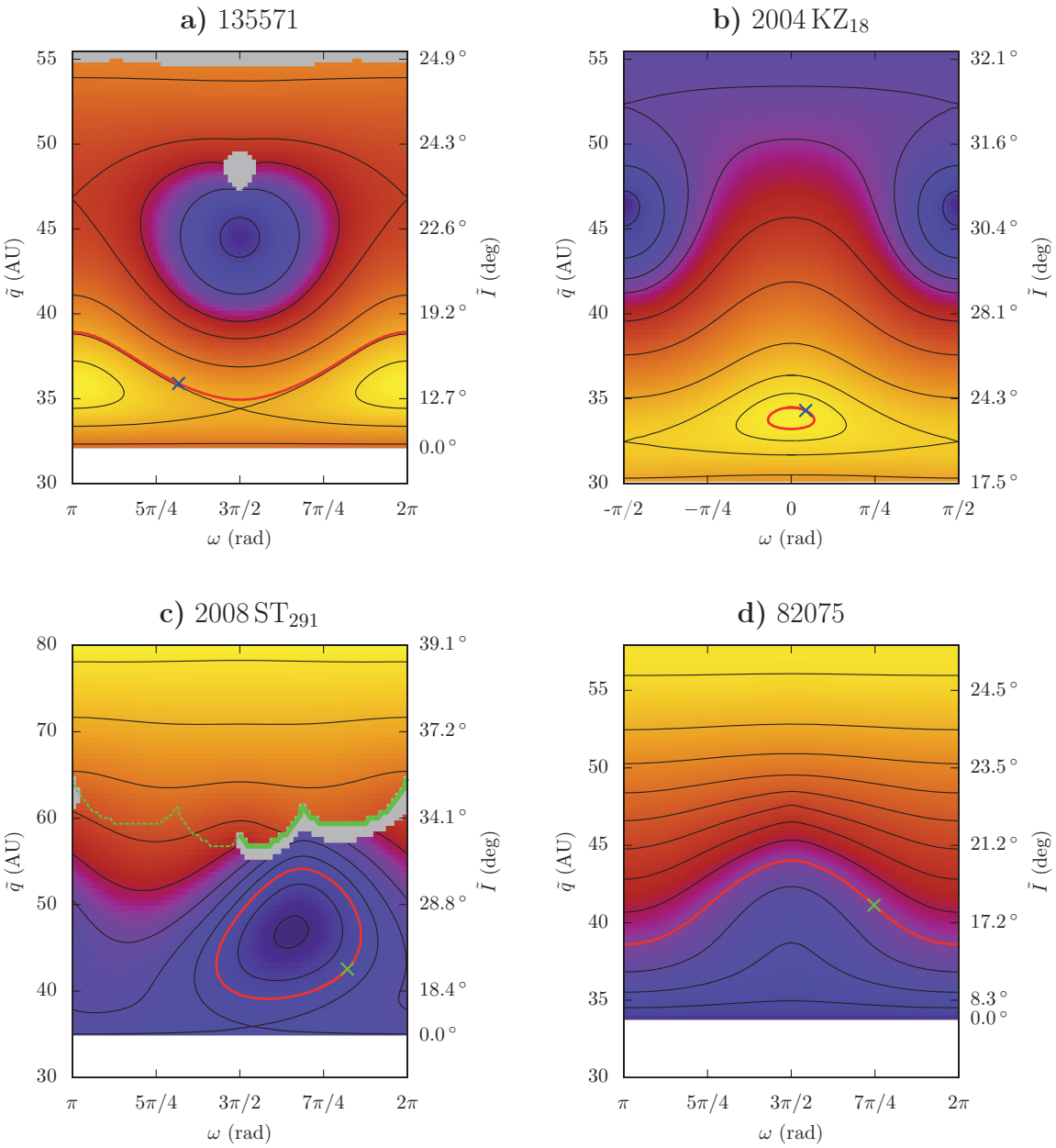

Figure 4.12 – Phase portraits of the objects affected by secular libration islands. On the graph **a**, the object 135571 is the only one found to have a retrograde circulation of ω. On the graph **b**, the secular evolution of $2004\,\mathrm{KZ}_{18}$ inside the mean-motion resonance makes ω oscillate around 0. On the graph **c**, there are two distinct regions according to the topology of the semi-secular phase-space, since the resonance of $2008\,\mathrm{ST}_{291}$ is of type $1:k$. Below the green line, the resonance island is doubled (as in Fig. 4.10**c**,**d**) resulting in asymmetric level curves. Above the green line, only one resonance island remains (as in Fig. 4.10**a**,**b**) and the level curves are symmetric. If the line is crossed, there can be either a discontinuity (thick green line) if the particle is located in the vanishing island, or a smooth transition (dotted green line) if it is located in the persisting island.

4.2.4 Regular-by-part secular dynamics

The object $2015\,\mathrm{FJ}_{345}$ presents the most interesting secular dynamics. Figure 4.13**a** shows that it is currently located in the single-island region of the 1:3 resonance (that is above the "green line"), but on a level curve coming from and leading to discontinuous transitions. Hence, its perihelion distance was probably raised from the double-island region (below the green line), starting much closer to Neptune, on a secular trajectory *leading to* the transition. The resonant secular model can be used to reconstruct a possible scenario: following the secular level curve of $2015\,\mathrm{FJ}_{345}$ backwards (toward the left), its intersection with the grey zone gives its location when it was ejected from the vanishing resonance island. At this point, the total area available in this island gives the parameter J to be used in a secular model describing the previous portion of the secular dynamics. Proceeding this way, we suppose that on a secular timescale, the separatrix crossings can be considered as instantaneous[10]. The area measured is small ($2\pi J \approx -0.0115$ AU^{2}rad^2/yr) since the separatrix crossing happened near the green line (blue spot in Fig. 4.13**a**). The corresponding previous secular trajectory is shown in Fig. 4.13**b**. Surprisingly, we find once again a trajectory coming from and leading to a transition, without any passage to smaller perihelion distances where the resonance capture with Neptune could have occurred. We use the same method to get the secular trajectory before this second transition (green spot in Fig. 4.13**b**). The level curves of the corresponding secular Hamiltonian are presented in Fig. 4.13**c**: we finally get a secular trajectory leading to much lower perihelion distances (at least below $\tilde{q} = 35$ AU, depending on the exact level curve followed by the particle), where the capture in resonance with Neptune could have occurred.

Since the overall trajectory is rather complicated, Fig. 4.14 sums up the three components by showing a numerical integration of the two-degree-of-freedom semi-secular system. We started from a position $(\omega, \tilde{q})$ on the level curve of Fig. 4.13**c**, as a potential position of capture in resonance with Neptune (black spot). Of course, the separatrix crossings are actually not instantaneous, so their exact outcomes depend on the phase at the time of transition (this holds especially for $2015\,\mathrm{FJ}_{345}$ which presents a substantial departure from the adiabatic approximation). Since the two separatrix crossings were found to be a bit sensitive to the initial phase chosen for σ and Σ, we tried different values distributed all along the level curve of the semi-secular Hamiltonian. The grey trajectories in Fig. 4.14 give an idea of the range of possible behaviours. Roughly half of the integrated trajectories were found to follow qualitatively the scenario from Fig. 4.13 (the red curve is one example of them). As predicted, the trajectory ends up near the observed position of $2015\,\mathrm{FJ}_{345}$, showing that this scenario is dynamically possible. It can be considered as the potential past trajectory producing the shortest path from the capture into resonance to the observed position of the body. The numerical integration from Fig. 4.14 gives also the timescale involved, which counts in tens of Myrs. In the

[10] As explained in Sects. 3.4.2 and 3.4.3, a chaotic extra change of J should be expected in the real case, depending on the exact phase of Σ and σ at the moment of the crossing. This change is expected to be small if the adiabatic approximation is well verified.

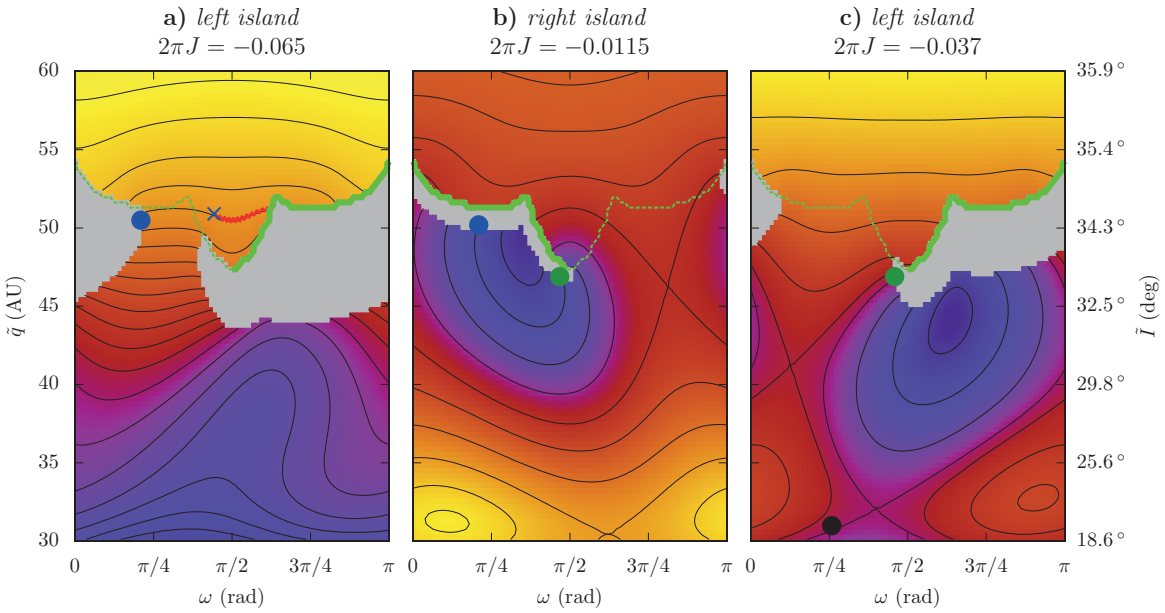

Figure 4.13 – Level curves of the secular Hamiltonian for the current and past evolution of the object 2015 FJ_{345}. Three smooth trajectories are considered, divided by separatrix crossings. The constant parameter η_0 is given in Tab. 4.1, whereas $2\pi J$ is given above the graphs ($AU^2 rad^2/yr$). The current orbital elements of 2015 FJ_{345} result in the leftmost phase portrait **a**. Contrary to previous graphs, the secondary oscillations of the semi-secular trajectory (red curve) are noticeable. The secular trajectory (mean curve), though, follows still pretty well the level curves given by the model. Starting from the current position of 2015 FJ_{345} (blue cross), the red curve is drawn until it reaches a change of the resonance topology (from a single to a double island), on the green line. Following the level curve toward the left (*past* evolution), the blue spot represents the position of the previous separatrix crossing undergone by 2015 FJ_{345}. The middle graph **b** shows the secular model for the past evolution of 2015 FJ_{345}. The blue spot represents its position at the transition to its current state (same as graph **a**). Following the level curve downwards (past evolution), the green spot shows the position of the previous separatrix crossing undergone by 2015 FJ_{345}. The rightmost graph **c** presents the secular model for the earlier evolution of 2015 FJ_{345}. The green spot shows its position at the transition to the next part of the trajectory (same as graph **b**). Following the level curve downwards (past evolution), the black spot is taken as initial condition for a numerical integration (see text and Fig. 4.14).

future, 2015 FJ_{345} is expected to go on with these types of transitions, possibly turning back to small perihelion distances. In particular, it is possible that several loops already occurred between its capture in resonance and its observed position. It could also stay in a resonant high-perihelion state for Gyrs if it has triggered a "high-perihelion trapping mechanism" (described in Sect. 4.4). The orbital uncertainties, though, prevent from any definitive conclusion. They should not affect our general conclusions, though: for instance, a slight change of orbital elements would leave 2015 FJ_{345} in the high-perihelion region and on a trajectory coming from a much lower perihelion distance. If ever it turns out that 2015 FJ_{345} is actually currently out of the resonance, the migration of Neptune could also be invoked (same type of trajectory, but in an earlier stage of the Solar System).

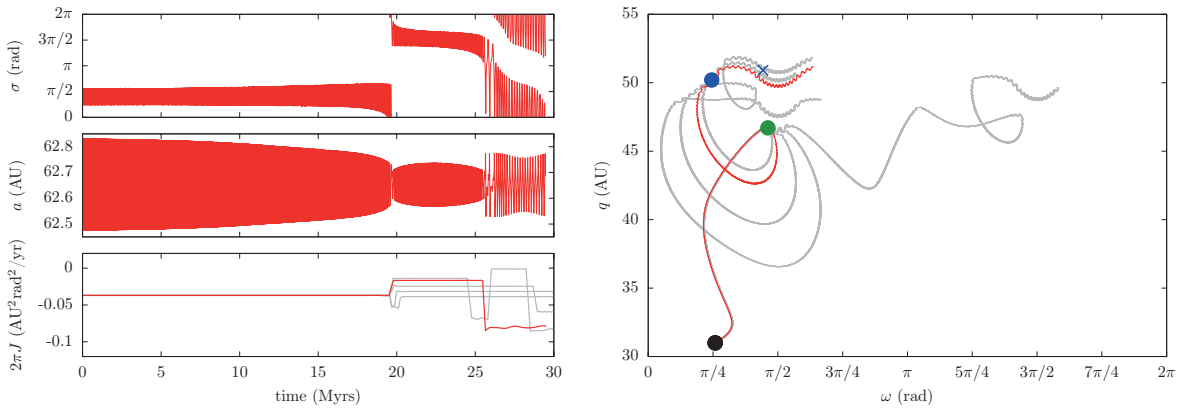

Figure 4.14 – Numerical integration of the two-degree-of-freedom semi-secular system. The initial conditions (origin of the time and black spot on the right) are taken according to the level curves plotted in Fig. 4.13**c**. On the right, the evolution of the couple (U, u) is drawn (with q instead of U, obtained by inverting Eq. 3.56). Several initial phases for (σ, Σ) were tried, leading to secular trajectories diverging at the first separatrix crossing (grey curves). Among them, the red trajectory is in agreement with our backward reconstruction: its second transition occurs on the blue spot, and it passes near the current position of $2015\,\mathrm{FJ}_{345}$ (to be compared with the level curves from Fig. 4.13). On the left, the evolution of the couple (σ, Σ) is represented for the red trajectory (with a instead of Σ). The two separatrix crossings, leading to a change of oscillation island, are easily noticeable. The bottom graph presents the evolution of the area $2\pi J$ for all the trajectories plotted on the right, showing the divergence at the first transition. Even if $2\pi J$ is plotted as a continuous line, please remember that its definition changes after each transition (different resonance island).

As discussed by Sheppard et al. (2016), such a mechanism is probably also responsible for the high perihelion distance of $2014\,\mathrm{FZ}_{71}$ even if this object is not found currently in resonance (according to its nominal orbit). Consequently, it could have been left in its current position at the end of Neptune's migration (Gomes et al., 2005b, 2008), or its resonant secular dynamics *itself* could have pushed it out of the resonance separatrices. We studied this last scenario by a close-to-resonance secular model (as used in Sect. 3.4.2), but no interaction at all with the resonance was detected (flat level curves). The migration of Neptune set apart, $2014\,\mathrm{FZ}_{71}$ is thus probably much closer to the resonance than its current best-fit orbit seems to indicate. Actually, its uncertainties are even *compatible* with a trapping in resonance (as already reported by Sheppard et al., 2016). As shown in Fig. 4.15, the semi-major axis of $2014\,\mathrm{FZ}_{71}$ can be slightly modified (at the 1-sigma level) to enter the resonance. If we change only the value of a, the minimum area $2\pi J$ in the case of resonance is equal to -0.035 AU^{2}rad^2/yr (red hatched region in Fig. 4.15). The corresponding resonant secular model is presented in Fig. 4.16**a**: we get a geometry very similar to what we obtained for $2015\,\mathrm{FJ}_{345}$, indicating that an analogous long-term resonant evolution probably occurred. Following the level curve toward the past, the second resonance island has an total area of -0.00205 AU^{2}rad^2/yr on the transition line, which gives the secular model represented in Fig. 4.16**b**. This time, we directly obtain a trajectory leading to much smaller perihelion distances (~ 38.5 AU), compatible with the numerical experiments by Sheppard

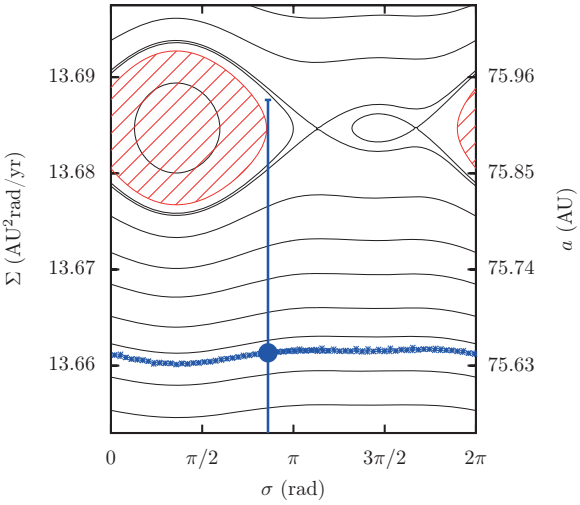

Figure 4.15 – Semi-secular phase portrait of $2014\,\mathrm{FZ}_{71}$. On the right axis, the values of a corresponding to Σ are shown. The blue crosses come from the filtered output of the full non-averaged numerical integration (same as Fig. 4.10), with the current position of $2014\,\mathrm{FZ}_{71}$ on the big spot. For comparison, the 1-sigma error bar of the (osculating) orbital solution is added. The uncertainty is compatible with the red hatched area inside the resonance, from which we get a possible value of the parameter J.

et al. (2016).

We did not try to obtain similar graphs for $2004\,\mathrm{XR}_{190}$ since its location out-of-resonance is securely assessed. Its current position is pretty well explained by an analogous resonant evolution, but occurring during the late migration of Neptune (Gomes, 2011).

In Fig. 4.16, one can note that the parameter η_0 puts a lower limit on the perihelion distances reachable by $2014\,\mathrm{FZ}_{71}$ (independently of the separatrix crossings encountered). This limit is equal to about 37 AU and corresponds to $\tilde{I} = 0$. This is quite high for a resonant capture (since a diffusion of a is necessary), but that argument was used by Sheppard et al. (2016) to state that $2014\,\mathrm{FZ}_{71}$ possibly originated in the Scattered Disc. Of course, the fixed value of η_0, or equivalently the approximate constancy[11] of $\sqrt{1-e^2}\cos I$ used by some authors (Gomes et al., 2008; Sheppard et al., 2016), gives only upper bounds for the variations in perihelion distance. Indeed, an object could very well be detached, but with a parameter η_0 allowing in principle any eccentricity and inclination. Consider for instance, a particle located on the highest level curve drawn on Fig. 4.13**c**.

[11]Strictly speaking, the quantity $\sqrt{1-e^2}\cos I$ is constant only in the non-resonant secular case (see Sect. 3.2). The analogous constant in the resonant case is $V = \sqrt{\mu a}\left(\sqrt{1-e^2}\cos I - k_p/k\right)$, but since the particle is trapped in resonance, a is never far from some given value.

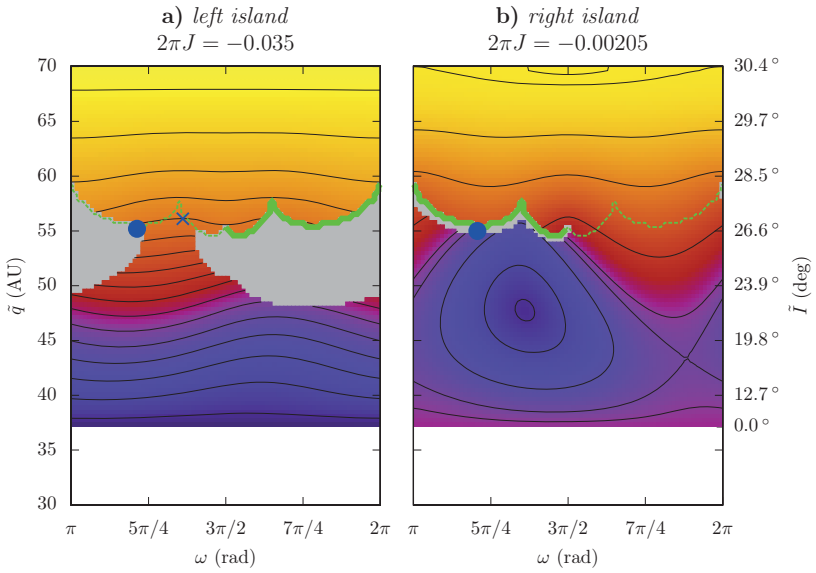

Figure 4.16 – Level curves of the secular Hamiltonian for the current and past evolution of the object $2014\,\mathrm{FZ}_{71}$. Two smooth trajectories are considered, divided by a separatrix crossing. The constant parameter η_0 is given in Tab. 4.1, whereas $2\pi J$ is given above the graphs ($\mathrm{AU}^2\mathrm{rad}^2/\mathrm{yr}$). The current orbital elements of $2014\,\mathrm{FZ}_{71}$ result in the left phase portrait **a**. Following the level curve toward the left (*past* evolution), the blue spot shows the position of the previous separatrix crossing undergone by $2014\,\mathrm{FZ}_{71}$. The right graph **b** presents the secular model for the past evolution of $2014\,\mathrm{FZ}_{71}$. The blue spot shows its position at the transition to its current state (same as graph **a**).

4.3 Application to distant objects

Because of evident observational constraints, the data for high-perihelion high-semi-major-axis trans-Neptunian objects is scarce and subject to large uncertainties. Hence, it is quite hard to determine if a particular observed object in that region presents a mean-motion resonance with one of the planets. Since the dynamics is chaotic in general, even a small change of semi-major axis can lead to very different long-term behaviours, with locking or not in a variety of mean-motion resonances. It is not rare, for example, that an object thought to be in resonance with Neptune for a given best-fit orbit, proved actually to be in a diffusive state when we add new observational constraints. For that reason, we can turn to a different approach to the problem: *if* a specific known object *were* in resonance with Neptune (now or in a close past or future), what *would* be its long term dynamics? In particular, would its current orbital elements allow some large variations of its perihelion distance q and/or confine its argument of perihelion ω? Independently of the uncertainty of its semi-major axis, its osculating variable $\eta = \sqrt{1-e^2}\cos I$ can indeed be used as parameter for a resonant secular model. We will see that such a general study, which is almost independent of the fit precision of the semi-major axis, can still be very informative.

Figure 4.17 presents the ranges of interest of η_0 (that is the interval allowing libration centres) for prograde orbits in resonances of types $k_p = 1, 2, 3, 4$ with Neptune. Here,

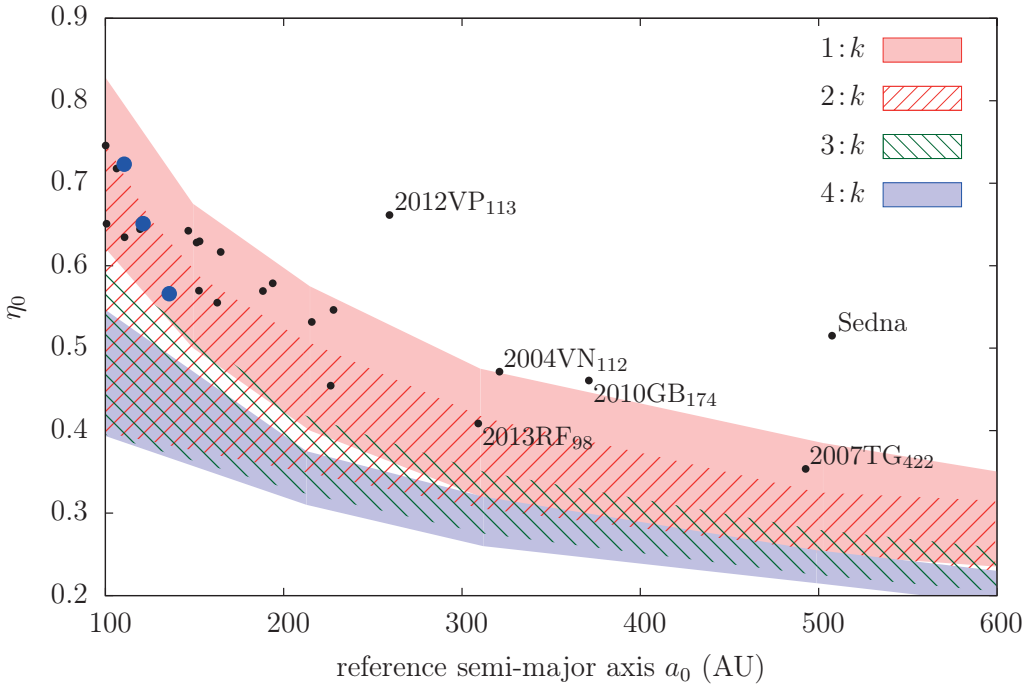

Figure 4.17 – Range of interest (that is the interval of η_0 allowing libration centres) for various types of mean-motion resonances with Neptune. It is calculated for $J = 0$ and the plot is restricted to prograde orbits ($\eta_0 > 0$). The black spots represent the position of 24 well-known small bodies with $a > 100$ AU and $q > 30$ AU according to AstDyS database, using a for a_0 and $\sqrt{1-e^2}\cos I$ for η_0. The trans-Neptunian object 2013 RF$_{98}$ is added from the JPL database. The names are shown for the bodies with $a > 250$ AU, and the blue points refer to those taken in example in the following (from left to right: 303775, 181902 and 2007 LH$_{38}$).

we restrict the study to small oscillations of σ, that is for $J \approx 0$ (as shown in Sect. 4.1, these trajectories are the most stable and present the most interesting variations of the orbital elements). The coloured ranges represented in Fig. 4.17 have been obtained by a systematic exploration and a fine tuning of η_0. As anticipated in Sect. 4.1.1, they follow definite laws with respect to the reference semi-major axes a_0 of the resonances (iso-curves of inclination and perihelion distance). The position of the known small bodies with $q > 30$ AU and $a > 100$ AU are added[12], showing in an evident way which ones could have a potentially interesting resonant relation with Neptune. The trans-Neptunian object 2013 RF$_{98}$ is also shown despite its very ill-determined orbit because it has been recently used in the article by Batygin and Brown (2016a).

First of all, we see that Sedna and 2012 VP$_{113}$ are completely out of every range of interest (they would require a much higher inclination or a much lower perihelion distance to enter the coloured zones). We can thus affirm that these two bodies *cannot* have had a perihelion near the planetary region and have been drifted away by the

[12]The orbital elements are taken from AstDyS database (`http://hamilton.dm.unipi.it/astdys`), except from 2013 RF$_{98}$ which comes from the JPL database.

secular interaction (resonant or non-resonant) with the known planets. Similar results were obtained by numerical means by Gomes et al. (2005b). As an illustration, Fig. 4.18 shows the secular behaviour that Sedna would have if it were in a resonance of type $2:k$ with Neptune with $J = 0$. Naturally, that graph corresponds to a specific resonance, but Fig. 4.17 certifies that *every other* resonance of the neighbourhood would produce such flat level curves. Moreover, numerical integrations show that for low inclinations and perihelion distances near Neptune, the resonances with $a_0 > 350$ AU are unstable: if an object happens to stay in such resonances, its perihelion distance should be *already* quite high to avoid any diffusion of semi-major axis[13]. Eventually, one can think of a more complex scenario for Sedna and $2012\,\mathrm{VP}_{113}$, including an initial resonant semi-major axis of 150-200 AU, followed by an excursion of perihelion, and finally a diffusion of a. However, this is also impossible because the semi-major axis cannot be affected by diffusion once the perihelion is so high, even if the particle is pushed out of the resonance (remember the empirical law of $q_{\min} = a/27.3 + 33.3$ AU by Gallardo et al., 2012). Such a mechanism is definitely not able to explain the current orbits of these two trans-Neptunian objects. We should think of other scenarios (as the interaction with an unknown external perturber) or different sources, as the Oort Cloud or a neighbour star in the birth cluster of the Sun (see in particular Jílková et al., 2015, and their other related works).

Contrary to Sedna and $2012\,\mathrm{VP}_{113}$, many objects are located well inside some range of interest, and sometimes even simultaneously for several types of resonance. In the following, we show various secular phase portraits that some of these small bodies would have if they were in resonance with Neptune. We chose only the trans-Neptunian objects compatible with a deep resonance, that is those for which the current value of the mean anomaly leads to a resonant angle σ near the equilibrium. We can get an estimation of the minimum area $|2\pi J|$ an object could have by assuming that its current secular semi-major axis is a_0 and considering the corresponding surface in the (Σ, σ) plane[14]. The next graphs are computed for specific resonances, but every neighbour resonance of the same type would produce a similar phase portrait (see Sect. 4.1). Each graph presents also the result of a numerical integration including the four giant planets. The secular variations of their orbital elements are given by the synthetic representation of Laskar (1990), supposed valid in the entire duration of the integrations. The initial conditions are taken from the best-fit orbits of AstDyS, excepted for the semi-major axes which are adjusted to produce the resonant captures. The required modifications are of the order of 2 AU, which is generally larger than the 3-σ uncertainty given by AstDyS. Hence, the trajectories shown are not supposed to represent the "real" motion

[13]In particular, we did not manage to lock $2007\,\mathrm{TG}_{422}$ in resonance in our numerical integrations (semi-major axis ≈ 493 AU) even by putting it exactly at the resonance centre. This is different for high inclinations, for which it is not rare to observe stable resonance captures with $a_0 > 500$ AU even for perihelion distances near Neptune. However, the probability to find a real body with that kind of orbit is likely very low.

[14]The same method was used in Sect. 4.2.4 for $2014\,\mathrm{FZ}_{71}$ (see Fig. 4.15) but it was limited to the uncertainty range of a.

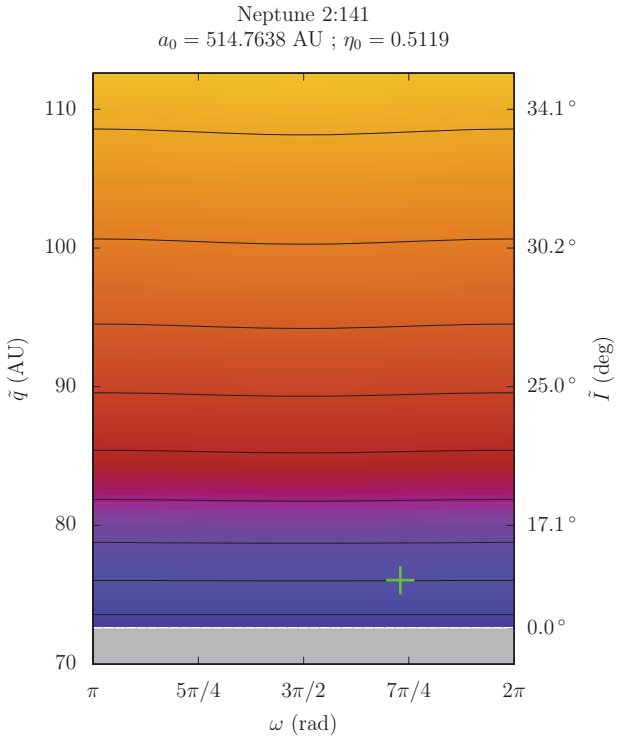

Figure 4.18 – Level curves of the secular Hamiltonian for the resonance $2:141$ with Neptune, which is located near the semi-major axis of Sedna. The value chosen for a_0 is indicated above the figure as well as the parameter η_0 corresponding to the elements of Sedna. This graph is plotted for $J = 0$ and the green cross shows the current position of Sedna in the plane (ω, q).

of these objects, but only to give an insight of what could be their secular dynamics in case of resonance.

The left graph of Fig. 4.19 presents the case of $2004VN_{112}$ which is located at the limit of the range of interest for $1:k$ resonances. Indeed, no equilibrium point remains and ω circulates. This kind of resonance would only result in oscillations of the perihelion of $2004VN_{112}$ from about 42 to 50 AU. The right graph of Fig. 4.19 shows the case of 303775 which is well inside the range of interest for $1:k$ resonances. Its current position would imply a reachable perihelion distance of 52 AU. We note that 303775 is also in the zone of interest for $2:k$ resonances, but its current mean anomaly would imply a large oscillation of the resonant angle leading to an unstable capture.

On Fig. 4.20, we see that resonances of types $1:k$ and $2:k$ would both decrease the perihelion distance of $2007LH_{38}$ towards Neptune, where the overlap with neighbour resonances leads eventually to a chaotic diffusion of the semi-major axis (not shown here). A very similar behaviour is observed for resonances near the nominal orbit of $2013RF_{98}$, but its very large uncertainties make very wide the range of possible resonances involved.

Finally, Fig. 4.21 shows that a resonance of type $2:k$ would result in small-amplitude oscillations of the perihelion of 181902 along with a circulation of ω. On the contrary, a resonance of type $1:k$ would raise its perihelion distance as far as 56 AU and possibly maintain it high on a billion-year timescale, depending on the next resonant behaviours adopted by the particle (see Sect. 3.4.3). In the next section, we will show that this

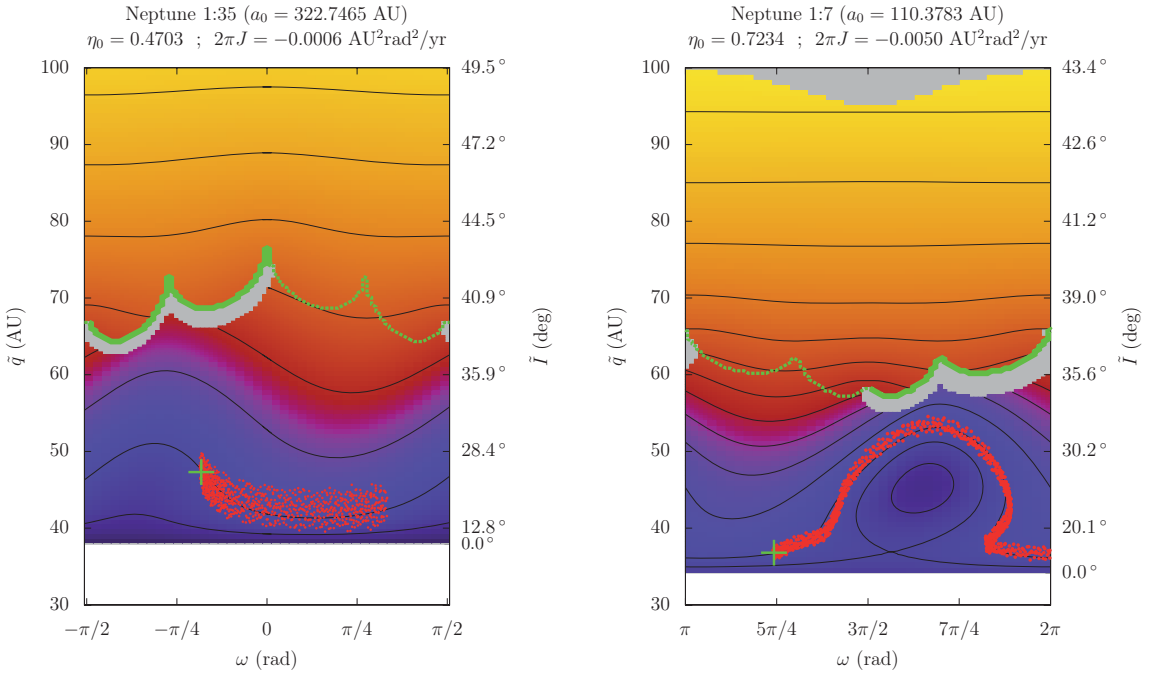

Figure 4.19 – Level curves of the secular Hamiltonian for two mean-motion resonances with Neptune located near the semi-major axes of the trans-Neptunian objects 2004VN$_{112}$ (left) and 303775 (right). The chosen values for a_0 are indicated above the figures as well as the parameters corresponding to the elements of these bodies. The green crosses show their current positions in the plane (ω, q) and the red dots are the results of numerical integrations: the presented time-spans are 350 Myrs on the left and 200 Myrs on the right. The secular evolutions on a larger timescale are found to be rather periodic.

is a common mechanism that can produce long-lived small bodies with high perihelion distances. Even if 181902 is not considered to follow that kind of dynamics, Fig. 4.21 shows that it is located in the required range of orbital elements, demonstrating that such a behaviour is not only a mathematical curiosity of the resonant secular model.

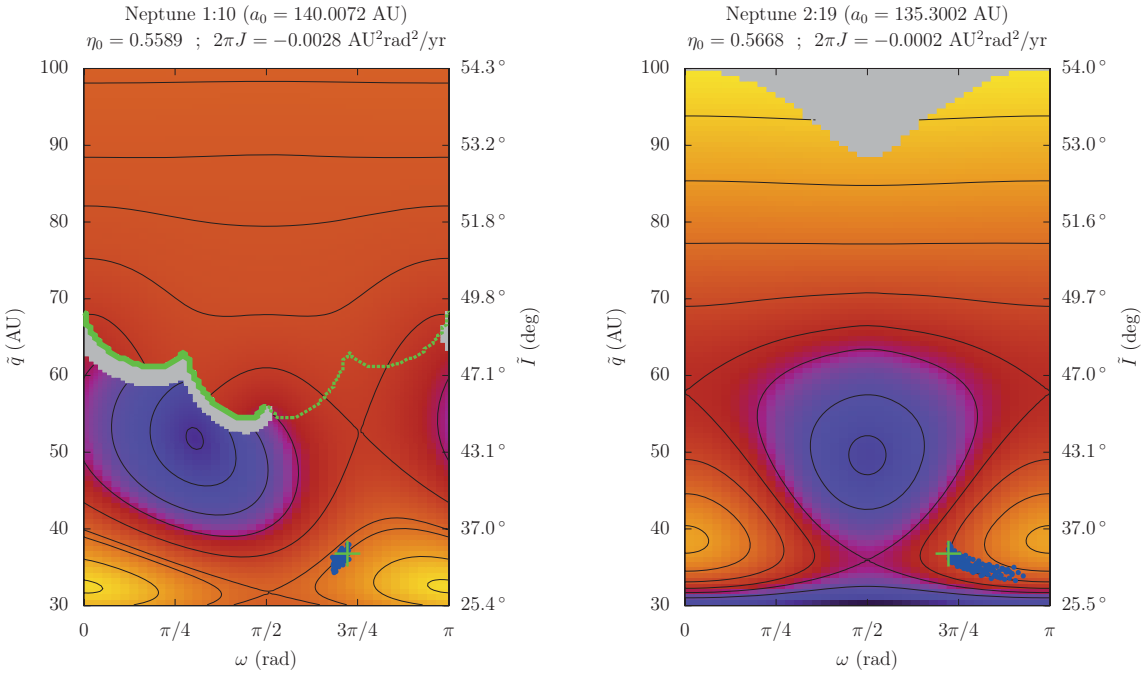

Figure 4.20 – Level curves of the secular Hamiltonian for two mean-motion resonances with Neptune located near the semi-major axis of the trans-Neptunian object 2007LH$_{38}$. The chosen values for a_0 are indicated above the figures as well as the parameters corresponding to the elements of 2007LH$_{38}$. The green crosses show its current position in the plane (ω, q) and the blue dots are the results of numerical integrations: the presented time-spans are 14 Myrs on the left and 28 Myrs on the right, after which 2007LH$_{38}$ is pushed outside of the resonances considered.

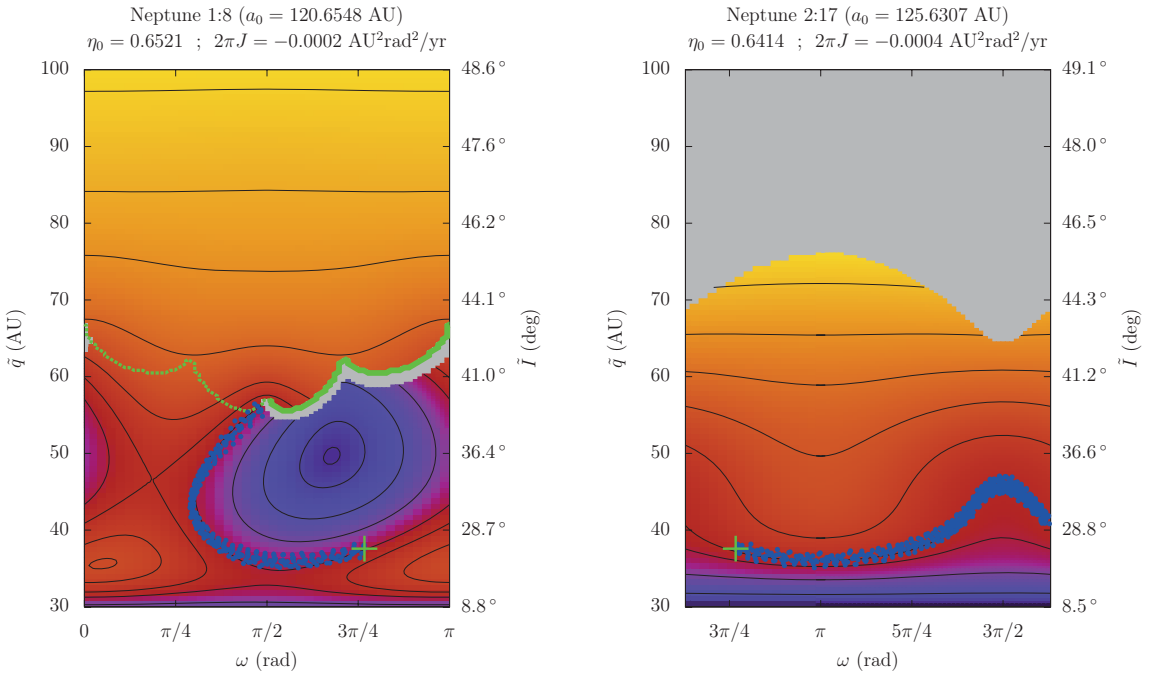

Figure 4.21 – Level curves of the secular Hamiltonian for two mean-motion resonances with Neptune located near the semi-major axis of the trans-Neptunian object 181902. The chosen values for a_0 are indicated above the figures as well as the parameters corresponding to the elements of 181902. The green crosses show its current position in the plane (ω, q) and the blue dots are the results of numerical integrations: the presented time-spans are 100 Myrs on the left and 30 Myrs on the right. On the left graph, the secular evolution leads the particle to the discontinuity line, where the occupied resonance island disappears. After the transition, the particle goes on switching secular behaviour (not shown here). On the right graph on the contrary, the secular evolution on a larger time-span is found to be rather periodic.

4.4 High-perihelion trapping mechanisms

The possibility of transferring Scattered Disc objects to high perihelion distances by resonant interactions with Neptune is well known from the work of Gomes et al. (2005b). Our resonant secular model is a suitable tool to further precise their results. In particular, they mention a possible trapping caused by the drop-off of the resonant terms in the disturbing function when the perihelion distance increases. Indeed, the particle becomes vulnerable to any other kind of perturbation, which destabilizes the resonant dynamics. We give an example of such mechanism in Fig. 4.22, where we chose on purpose a trajectory avoiding the discontinuity line (see Sect. 4.1.3). The secular dynamics is perfectly regular during the first loop, because the perihelion excursion is relatively modest. Then, when the resonant link with Neptune gets weaker, the perturbations induced by the varying small inclinations and eccentricities of the planets are strong enough to break the smooth resonant trajectory (at $t \approx 1$ Gyr): the secular parameter J makes unpredictable jumps and the particle is eventually pushed out of the resonance. Since the perihelion distance is very high, the semi-major axis is not subject to diffusion and so the particle remains trapped. The resonance is still very close, however, and the resonant angle switches chaotically from high-amplitude oscillations to circulation, but this has no notable effect on the orbital elements. Indeed, the probability to recover a secular trajectory leading to small values of q is extremely low (it would require a parameter $J \approx 0$).

Actually, that scenario was found to be relatively rare in our numerical experiments. However, we found another trapping mechanism coming directly from the conclusions drawn from Sect. 4.1. In that second scenario, the capture is not due to a drop-off of the resonant terms but simply to the crossing of the secular discontinuity line common to all resonances of type $1:k$. After the discontinuity, the particle can possibly remain in resonance but on a periodic trajectory avoiding any further crossing of the line in its discontinuous direction (see Sect. 4.1.3). In other words, the initial transition triggers an "irreversible" smooth behaviour, for which the return to the entrance configuration does not imply a new separatrix crossing. It will still be separatrix-grazing, but the natural evolution of the semi-secular phase space will immediately lead the particle away again. The trajectory adopted has a very wide area $|2\pi J|$, because the particle has been pushed outside of the vanishing island while the other one had a wide extent. Then, it simply becomes a horseshoe orbit when the second island reappears, avoiding any further separatrix crossing (the growing island appears *inside* the trajectory). As an illustration, one can imagine on Fig. 4.8 a trajectory remaining always inside the outer separatrix, but outside the inner one when it appears. Precisely, we saw in Sect. 4.1.4 that for a large parameter $|2\pi J|$, the secular level curves are very flat, without any large variations of the perihelion distance: this means that the particle reaches a permanent smooth high-perihelion evolution[15]. As shown by numerical simulations,

[15]Naturally, as the final trajectory relies on a high-amplitude oscillation of the resonant angle, the proximity of the separatrices can lead to an accidental extra transition. However, this proves to be very rare and only temporary, as seen in the next section.

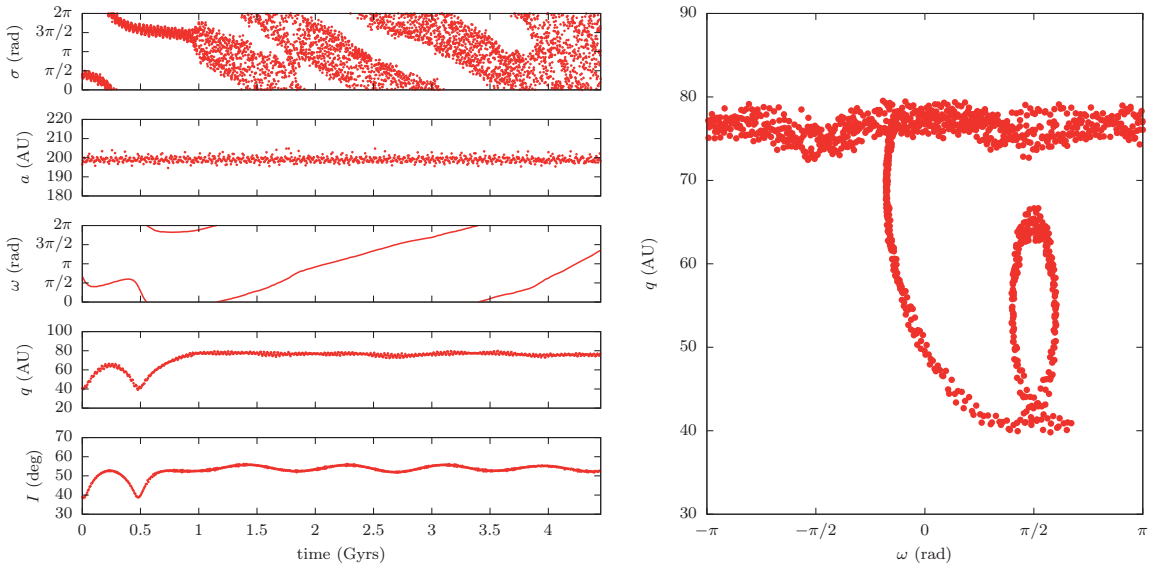

Figure 4.22 – Example of a particle initially trapped in the $1:17$ mean-motion resonance with Neptune. This numerical integration includes the four giant planets with the secular variations of their orbital elements. On the right, the same trajectory is plotted in the (ω, q) plane. It should be compared with Fig. 4.7 (neighbouring resonance and similar initial conditions), for which the circular and coplanar planetary orbits make the resonant dynamics much more stable, even at high perihelion distances.

that mechanism is rather frequent for the resonant particles attaining the discontinuity line. Naturally, it cannot involve resonances of type $2:k$ and further, because the corresponding secular trajectories are all periodic (there is no discontinuity line, see Sect. 4.1.1). To get specific examples, one can anticipate a bit and look at Figs. 4.25 to 4.27.

These two mechanisms imply that even a set of non-migrating planets can produce a permanent high-perihelion reservoir, continuously supplied with new objects which have a very low probability to come back to smaller perihelion distances during the lifetime of the Solar System. These objects are added to the primordial population of high-perihelion bodies, left on non-resonant orbits by the migration of Neptune (Gomes et al., 2005b).

Our secular model can be used to estimate the size and location of the high-perihelion reservoir produced by the second mechanism. For this purpose, we plotted the secular discontinuity line of all the resonances of type $1:k$ from $a_0 = 90$ to 600 AU in a grid of parameters η_0 in $[0;1]$ (prograde orbits). Since the crossings can happen at all values of ω, we retained only the average line, judged to be representative of a typical perihelion value for the capture (for example $\tilde{q} \approx 60$ AU and $\tilde{I} \approx 41°$ for the left graph of Fig. 4.21). The result is shown in Fig. 4.23, both for perihelion distance and inclination. We added the limits of the range of interest for $1:k$ resonances (same as Fig. 4.17), because such a trapping can occur only if there are secular level curves *lead-*

ing to the discontinuity line. Naturally, a separatrix crossing can happen much before the discontinuity line (see the graph B of Fig. 4.9), but at low perihelion distances the resonant dynamics is unstable for large values of $|2\pi J|$ and a separatrix crossing often triggers a diffusion of semi-major axis. Hence, in practice the high-perihelion trappings occur indeed near the secular discontinuity line. The reservoir is rather well delimited in the perihelion-inclination space because the position of the average discontinuity line follows more or less the range of interest: from Fig. 4.23, we can estimate its extension as roughly $q \in [55; 70]$ AU and $I \in [30; 50]^\circ$. This is consistent with the results of Gomes et al. (2005b), although their approach was rather different (they counted the numbers of objects ending up at $q > 40$ AU in their numerical simulations, whatever the mechanism that led them there). Naturally, these limits do not mean that an object cannot reach higher perihelion distances (see for instance the graph C of Fig. 4.6), but simply that an accumulation of objects should be observed there.

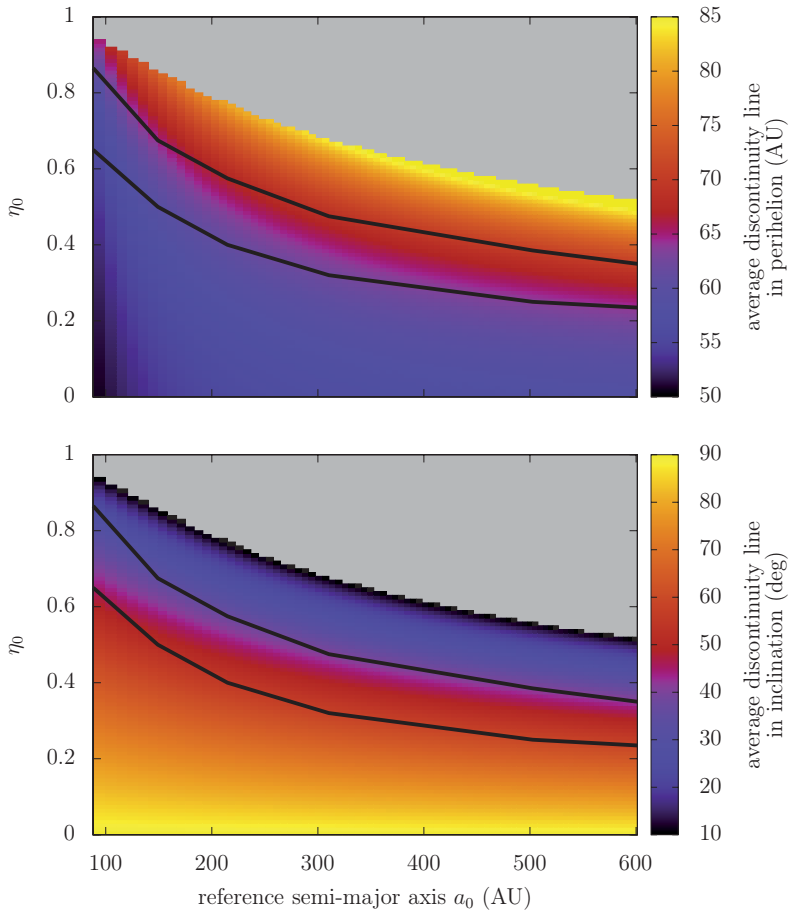

Figure 4.23 – Average position of the secular discontinuity line for all resonances of type $1 : k$ with Neptune from $1 : 5$ to $1 : 89$. In the grey region, there is no discontinuity line in the secular plots. The black lines delimit the "range of interest", that is the interval of η_0 allowing libration centres. A high-perihelion trapping is only possible between these lines, where secular level curves can lead the particle from low perihelion values to the discontinuity line.

4.5 Incoming objects from the Oort Cloud

The Oort Cloud is a well-known source of "new comets" and more generally of small bodies arriving in the planetary region with very eccentric orbits. There is an extensive literature about the flux of comets traversing the observable zone (near the orbit of the Earth) and the different ways to cross the Jupiter-Saturn barrier, but very little about the contribution of the Oort Cloud to the Scattered Disc. Actually, the combined effects of the planetary perturbations and of the galactic tides form an efficient mechanism that continuously replenish the Scattered Disc, which, in turn, contribute to feed the accumulation zone described in the previous section. The main effect of the galactic tides is a long-period oscillation of the perihelion distance, whereas the planets produce the well-known diffusion of semi-major axis. Since the galactic tides are only effective for $a > 1000$ AU, a typical scenario to create a Scattered Disc object from the Oort Cloud is to drive the perihelion distance a little beyond Neptune, where the planetary perturbations make the semi-major axis decrease below 1000 AU, turning off the action of the galactic tides. The particle becomes part of the Scattered Disc, where it can be possibly captured in a mean-motion resonance of type $1:k$ with Neptune and eventually end up in the accumulation zone.

The reservoir is actually pretty visible in the results by Fouchard et al. (2017) (see their Fig. 4), although they do not describe it in details. They simulated a precursor of Oort Cloud consisting in 10^7 objects with initial orbital elements such that $a \in [1100; 50\,000]$ AU, $q \in [15; 32]$ AU and $I \in [0; 20]^\circ$. In order to trace the high-perihelion trapping mechanism in their simulation, we picked up the objects arriving into the Scattered Disc (when their semi-major axes become smaller than 500 AU), and used it as initial conditions for a numerical integration until the date J2000. The corresponding initial times range from the formation of the Solar System until today. We used a more realistic planetary model than in Fouchard et al. (2017), including the four giant planets with the secular variations of their orbital elements. The particles reaching perihelion distances inside the planetary region were removed from the simulation. Technical details about that numerical integration are given in appendices C.4 and C.5. The final distribution of the sample is plotted in Fig. 4.24, centred on the region of interest in the scope of this work ($a \in [30, 500]$ AU). At first, we see that we should redefine the lower limit of the accumulation zone at $q \sim 50$ AU (instead of 55 AU from Sect. 4.4) because a significant amount of objects reach the discontinuity line below its average. Naturally, the reservoir is also delimited in semi-major axis, because extremely high-order resonances are unstable and associated with timescales much longer than the age of the Solar System. According to Fig. 4.24, the mean-motion resonances are efficient to drive the objects into the accumulation zone for $a \in [100; 300]$ AU.

Some examples of orbital evolutions coming from this simulation are shown in Figs. 4.25-4.28. The resonant relations with Neptune, necessary to explain the trapping process, are pretty obvious. Figure 4.25 presents a very common example of high-perihelion trapping by means of a resonance of type $1:k$ with Neptune. The resonance capture is deep (small area $|2\pi J|$) which allows to bring the perihelion to distances

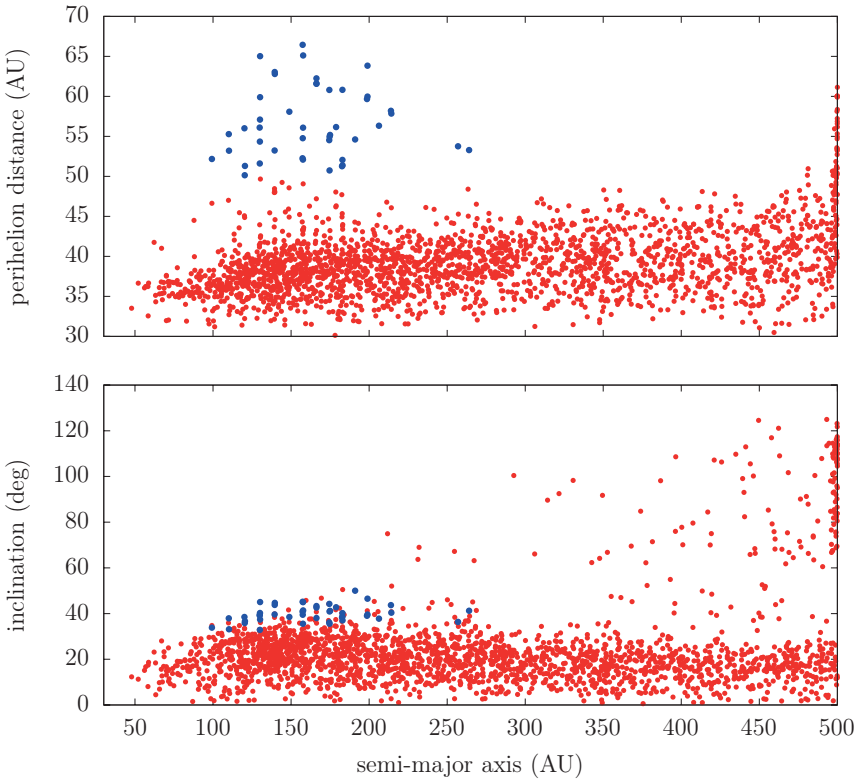

Figure 4.24 – Final state of the sample of particles transferred from the Oort Cloud to the Scattered Disc ($q > 30$ AU and $a < 500$ AU). The blue points are particles with perihelion distances larger than 50 AU and semi-major axes smaller than 450 AU. All of them are locked in mean-motion resonance with Neptune, including only one particle in a resonance of type $2:k$. The other ones are all locked in resonances of type $1:k$ and reached their current perihelion distances and inclinations billion years ago thanks to the trapping mechanism (the first one arrived 3 Gyrs ago and did not move ever since). For semi-major axes larger than 450 AU, the high-perihelion particles denote the beginning of the Oort Cloud (see Fouchard et al., 2017, for a wider scale).

where the diffusion of a is not a risk anymore. When the occupied resonance island shrinks and eventually disappears (thick green line), the particle adopts a dynamics with long-term stability: the resonant angle switches smoothly from high-amplitude oscillations inside the single island (beyond the line, in particular when $\omega \approx \pi/2 \mod \pi$) to horseshoe oscillations (below the line, in particular when $\omega \approx 0 \mod \pi$). This is the second mechanism described in Sect. 4.4.

Figure 4.26 shows that the trapping mechanism does not trigger always at the first attempt: in that particular case, the particle switches resonant configurations before finding the perfect entrance. That kind of "integrable by parts" trajectory was described in Sect. 3.4.3.

In Fig. 4.27, we see that the reservoir is not absolutely closed, because the slow diffusion of J can still occasion an extra transition *inside* one of the two resonance islands (instead of the more or less grazing horseshoe orbit). In that case, the new

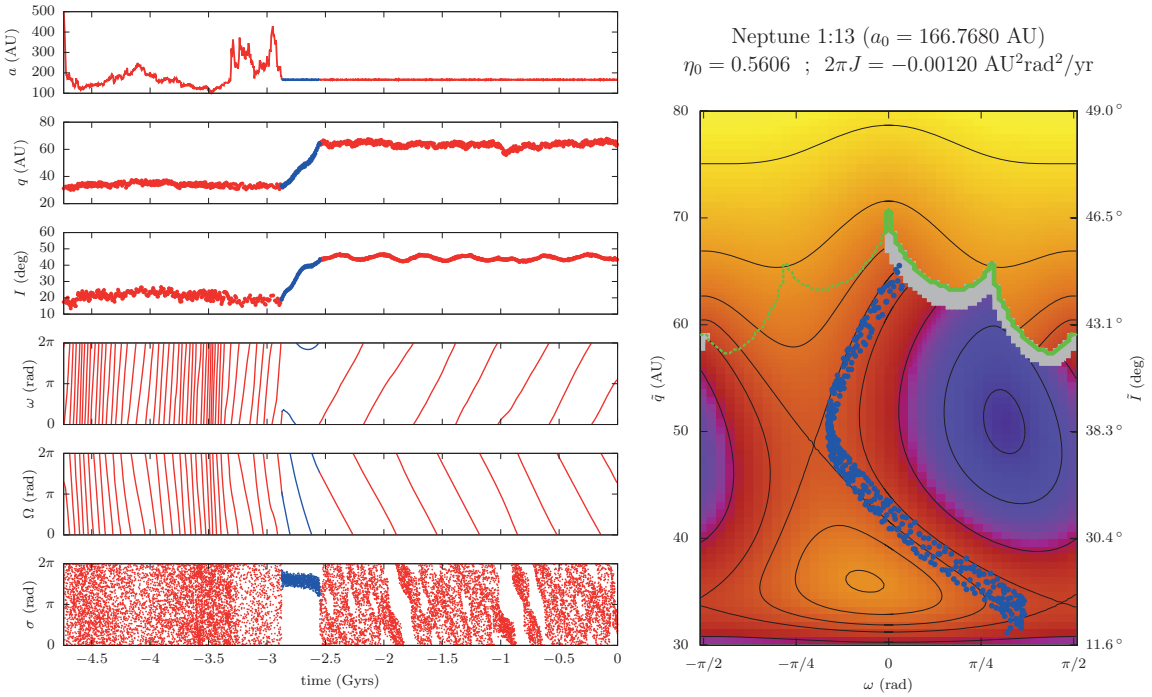

Figure 4.25 – Example of a particle coming from the Oort Cloud and captured in a resonance of type $1:k$ with Neptune. The origin of time is the date J2000. The resonant dynamics brings the particle toward the secular discontinuity line where it is trapped into the high-perihelion reservoir. On the right, the blue part of the trajectory is shown in the plane (ω, q) in front of the level curves given by the resonant secular model (the parameters used are indicated above the graph).

secular level curve may lead the particle back to smaller perihelion distances, but as long as the resonant link is not broken, this excursion is only temporary. In that specific example, the particle rejoins indeed the reservoir with a perihelion even higher than before. There is however a possibility of definitive escape from the reservoir if the perihelion distance decreases so much as to enter the chaotic region near Neptune, where the overlap of neighbouring resonances can break the quasi-integrable dynamics and trigger the diffusion of a. However, that kind of evolution seems to be rather exceptional.

Figure 4.28 presents the case of a resonant capture with inappropriate parameters: the area $|2\pi J|$ is rather high and the parameter η_0 is too close to the limit of the range of interest (see Fig. 4.17). Consequently, the particle is unable to reach the discontinuity line and trigger the trapping mechanism. It does not participate to the reservoir as described in Sect. 4.4, though Gomes et al. (2005b) would consider it as a High Perihelion Scattered Disc Object (HPSDO).

Finally, the particle presented in Fig. 4.29 is a kind of interloper: it is trapped in a resonance of type $2:k$ which indeed brings it into the range of orbital parameters specific to the reservoir, but its presence there is only temporary since there is no secular discontinuity line able to trigger the trapping mechanism. Such objects participate

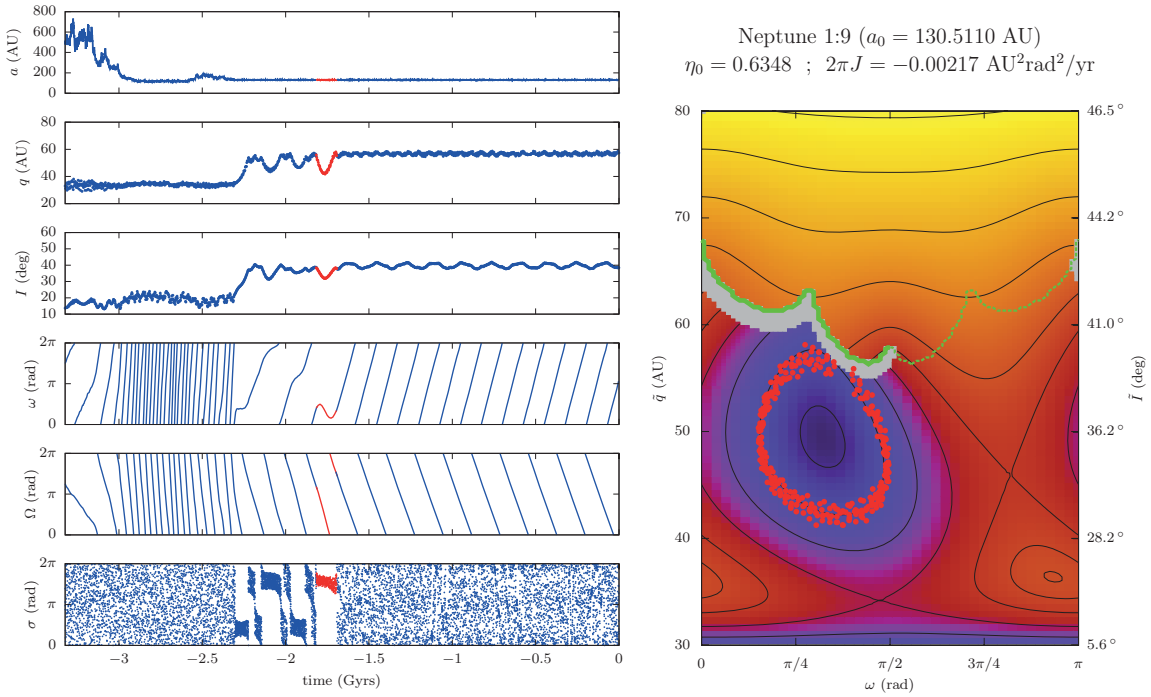

Figure 4.26 – Same as Fig. 4.25 for a particle which is not trapped immediately after the rise of its perihelion distance. Some extra separatrix crossings occur before reaching the long-term stability state specific to the accumulation zone. After the trapping, σ oscillates with a high amplitude around a circulating centre (even if the points seem to cover the entire range from 0 to 2π).

though to the accumulation (but to a lesser extent), because once trapped in resonance the time spent inside the accumulation zone can be pretty long.

We can estimate the current population contained in the reservoir by the fraction of blue points in Fig. 4.24: we get 42 objects, to be compared to the 263 627 initial conditions coming from the simulation by Fouchard et al. (2017), that is a fraction of 1.6/10 000. With respect to the 10^7 particles used in that simulation, we get a total fraction equal to 1/250 000 of the Oort Cloud objects.

There is no mention of irreversible trappings in Gomes et al. (2005b) other than the escape out-of-resonance due to Neptune's migration. According to them, every particle driven by a resonant secular dynamics is bound to recover its low-perihelion state after some amount of time. The fact that they did not observe such trappings is probably due to the narrowness of the dynamical path compared to the relatively low number of particles they simulated (10 000 for their largest sample). This could be also an indication that the distribution of the objects coming from the Oort Cloud is more suitable for the trappings to occur. Another possibility would be that the synthetic representation of the planetary motions used in our work is stable enough to allow the trappings, whereas the weak chaos produced in full N-body simulations (in particular the small variations of the planets semi-major axes) has a destabilising effect. Further numerical experiments should be conducted to get definite conclusions.

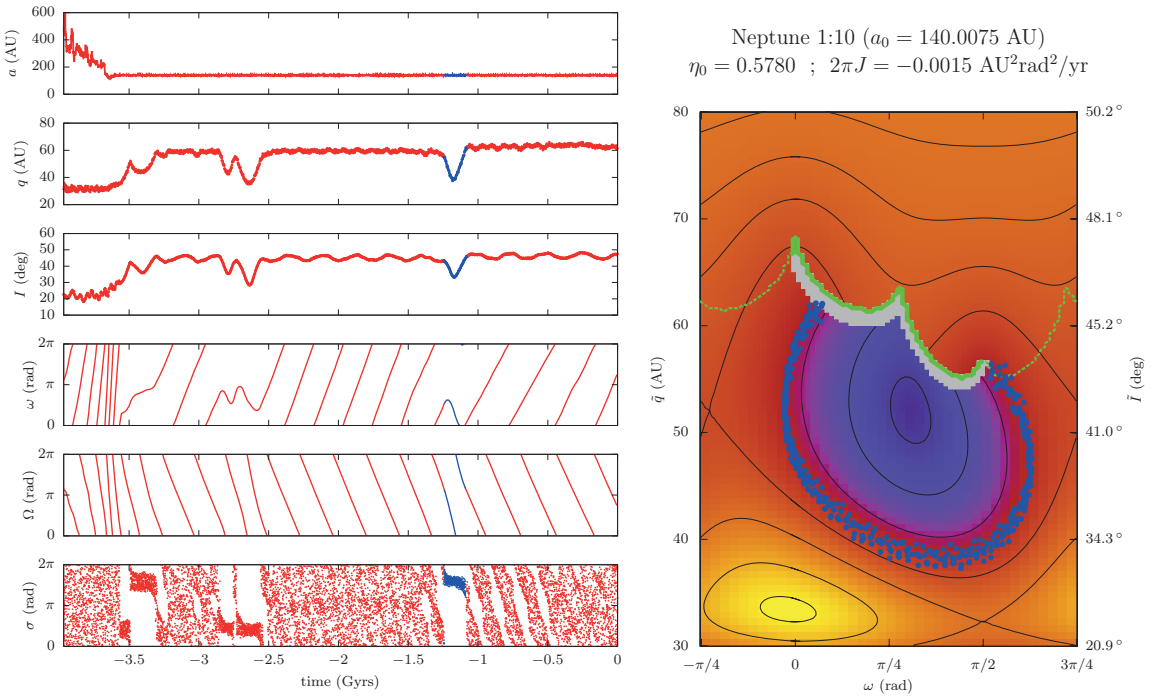

Figure 4.27 – Same as Fig. 4.25 for a particle incurring temporary escapes out of the reservoir. The time spent in the accumulation zone is though much longer than these random excursions.

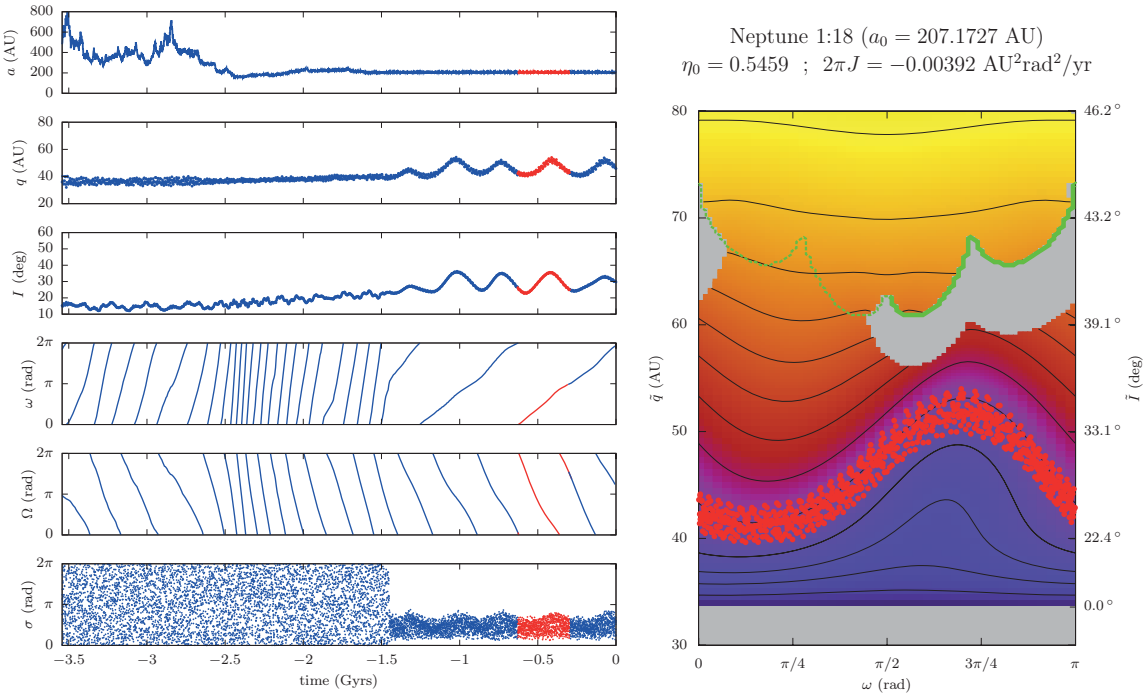

Figure 4.28 – Example of a particle coming from the Oort Cloud and captured in a resonance of type $1:k$ with Neptune, but with parameters making impossible the transfer to the high-perihelion accumulation zone.

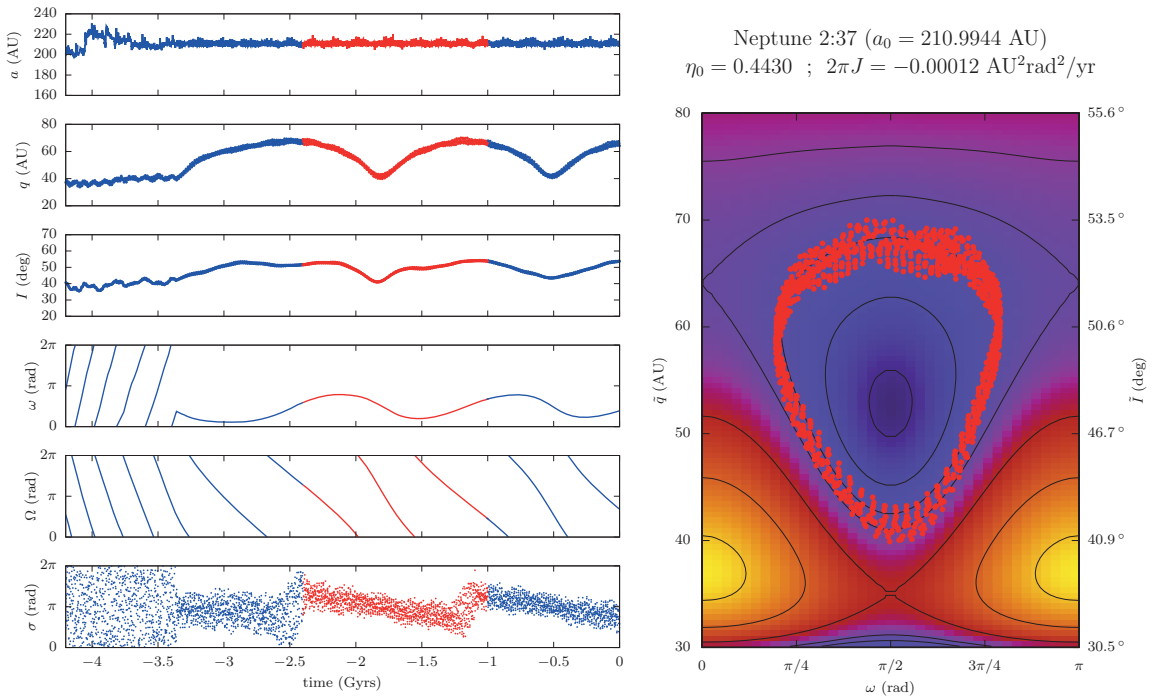

Figure 4.29 – Example of a particle coming from the Oort Cloud and captured in a resonance of type $2 : k$ with Neptune. The perihelion distance reaches high values but the periodic trajectory brings it back toward Neptune. (This numerical integration comes from another sample but the initial conditions are consistent with the distribution given by Fouchard et al. (2017) and used throughout this section).

Chapter 5

The breaking of symmetry: influence of an outer planet

Most of the results detailed in this chapter are more succinctly presented in Saillenfest et al. (2017b).

The hypothesis of a distant giant planet orbiting beyond Neptune is often proposed in the literature as accounting for otherwise mysterious features of the Solar System. Indeed, it could reproduce the observed orbital clustering of the distant trans-Neptunian objects (Batygin and Brown, 2016a), or the 6°-tilt of the solar equator with respect to the planetary invariable plane (Gomes et al., 2016; Bailey et al., 2016). In this chapter, we will not discuss the existence of such a planet, but focus on the rich dynamical system that it would create. We propose to study the effect of a distant perturber on the non-resonant secular dynamics of trans-Neptunian objects: the loss of symmetry implied by a massive body with significant eccentricity and inclination should disrupt the classic picture detailed in Sect. 3.2, so we aim at determining which features persist (if any) and how they transform under the perturbation.

In Sect. 5.1, we give a brief overview of our approach and how it places among previous studies. Then, Sect. 5.2 presents the planetary model used and the development of the secular Hamiltonian function, which is the starting point for the exploration of the dynamics. Section 5.3 details the dynamical features induced by a planar perturber on an arbitrarily inclined small body. This intermediate model makes the link between our study from Sect. 3.2 and the work by Beust (2016), mixing up the properties of both systems. Finally, we give an approach of the general case in Sect. 5.4, where we consider an eccentric and inclined distant planet but with a non-precessing argument of perihelion. Our observations and conclusions are outlined in Sect. 5.5.

5.1 Context

With no distant perturber, the non-resonant secular dynamics beyond Neptune is detailed in Sect. 3.2. Using coplanar and circular orbits for the known planets, the equi-

librium points and libration islands have well-determined locations and sizes in the space of orbital elements: for semi-major axes larger than 80 AU, the only equilibrium points are located at $\omega = \pi/2$ and $3\pi/2$ for an inclination I of about 63° or 117°. The perihelion distance at equilibrium is obtained through the constant parameter $C_K = (1 - e^2)\cos^2 I$. Moreover, we saw that the maximum variations of the perihelion distance, given by the width of the libration islands, cannot exceed 16.4 AU with that mechanism. For realistic values of the eccentricities and inclinations of the giant planets (non-zero but small), numerical integrations of the secular system show that these structures are almost unaltered: the weak interaction with these new degrees of freedom makes the equilibrium points become periodic orbits, tightly bounded around their nominal values (see for instance Fig. 3.4). One can note that the libration islands of ω divide the zones where ω circulates upwards from the zones where it circulates downwards. In the same way, the equilibrium point of Ω at $I = 90°$ divides the zones where Ω circulates upwards from the zones where it circulates downwards. This is summed up in Fig. 5.1.

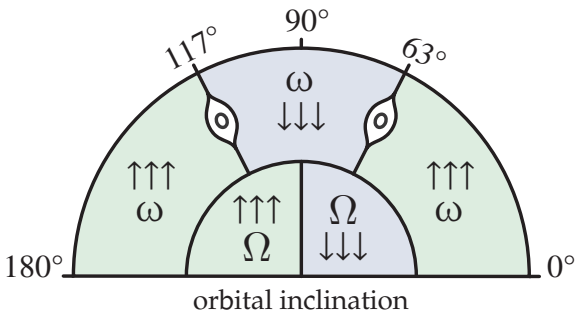

Figure 5.1 – Summary of the non-resonant secular dynamics beyond Neptune with no distant perturber. The angular scale represents the orbital inclination, from 0° to 180°. The classic libration islands for ω lie at $I \approx 63°$ and $I \approx 117°$ and they have a maximum width of 16.4 AU in perihelion distance. For $I = 90°$, any orbit is an equilibrium point for Ω (degeneracy). The different regimes are strictly hermetic: it is impossible for the particle to switch from one to another.

As pointed out by Batygin and Brown (2016a), the output of numerical simulations get much more significance when we understand the underlying dynamical processes. Their analytical computations about the effect of the distant planet, however, were limited to very low-order terms, and strong assumptions were used to get integrable models. These limitations were observed by Beust (2016), who subsequently studied the fully planar case. The corresponding secular system has only one degree of freedom so the dynamics is integrable: all the trajectories can be described by plotting the level curves of the secular Hamiltonian, with the semi-major axis as parameter. Let us write $\Delta\varpi$ the difference between the perihelion longitude of the particle and of the distant planet. Beust (2016) reported secular equilibrium points with libration zones around $\Delta\varpi = 0$ (at large perihelion distances) for non-crossing orbits, and $\Delta\varpi = \pi$ (at small perihelion distances) when the orbit of the particle crosses the trajectory of the distant planet. Then, he extended that model to introduce a mean-motion resonance between

the particle and the distant planet, keeping a single degree of freedom by using the adiabatic approximation. The level curves of the resonant secular Hamiltonian function present a large variety of equilibrium points distributed at no particular value of $\Delta\varpi$. Of course, these results hold only for a completely planar problem; besides, Beust (2016) used only the second-order term of the inner planetary perturbation (although the outer planet component was fully computed). When considering an arbitrarily inclined small body, such a truncated model cannot give rise to the Lidov-Kozai mechanism, whereas it has been shown that it can have important effects for trans-Neptunian objects (Gallardo et al., 2012).

Secular models for hierarchical systems in the general spatial case appear in the literature with works as early as Harrington (1968) for triple-star systems. Such models can be very efficient to capture the essence of the dynamics, so they are widely used and developed for systems with increasing complexity. We can mention for instance the recent work by Hamers et al. (2015) describing the evolution of two planets orbiting a binary star, and its generalisation by Hamers and Portegies Zwart (2016). In the planetary case, and in particular when one body is massless, such models are the natural generalisation of the work of Kozai (1962) so they are often said to raise an "eccentric-Kozai" mechanism, with two degrees of freedom (see for instance the review by Naoz, 2016). The non-zero eccentricity of the perturbing body makes possible a wide variety of trajectories, including striking orbital flips, during which the orbit of the small body switches suddenly from prograde to retrograde (see for instance Katz et al., 2011; Lithwick and Naoz, 2011; Naoz et al., 2013; Li et al., 2014b). In the context of the octupolar development of the secular system, Li et al. (2014a) studied the dynamics of a test-particle perturbed by an eccentric and inclined distant planet. In our case, the presence of an inner axis-symmetric component should mix the features of both models: a *classic* Kozai mechanism is produced by the known planets, while an *eccentric* Kozai mechanism is driven by the distant super-Earth. As before, we will restrict the study to orbits with a perihelion distance beyond Neptune, since they are much less chaotic and more likely to follow a secular dynamics. We will also focus on prograde orbits, since no retrograde object has been observed yet with a perihelion distance beyond Neptune.

5.2 Model and method

We use a set of N inner planets evolving on circular and coplanar orbits, along with an eccentric and inclined outer planet.

- The inner component of the perturbation stands for the currently known planets of the Solar System (which have indeed roughly circular and coplanar trajectories). We recall that the circular-coplanar approximation is justified by the very small eccentricity and inclination of the giant planets, especially when measured in their invariable plane. More generally, such a model can be seen as the dominant term

of an expansion in powers of the planetary eccentricities and inclinations (Thomas and Morbidelli, 1996).

- The mass of the outer planet is chosen to be ten earth-masses and its orbital elements at current epoch are given in Tab. 5.1. These values are within the best estimates obtained so far (Brown and Batygin, 2016) and consistent with those used in the literature.

Such a system is qualitatively similar to those studied by Innanen et al. (1997) or Takeda et al. (2008), namely a tight planetary system orbited by a distant star companion. They showed that due mutual interactions, the precession of the inner system of planets under the action of the inclined distant perturber is "rigid" (the mutual inclinations remain small, as well as the eccentricities). In our case, the perturber is much less massive than a star companion, but Bailey et al. (2016) and Gomes et al. (2016) showed that this mechanism could still be responsible for the tilt of the mean planetary plane of the Solar System with respect to the spin axis of the Sun.

Consistently with the notation used in the previous chapters, the orbital elements of the inner planets are written with a subscript i, whereas we use a prime for the outer one.

a'	e'	I'	ω'	Ω'
700 AU	0.6	30°	150°	113°

Table 5.1 – Current orbital elements of the distant planet used in this work. This "nominal" orbit is used for instance by Fienga et al. (2016).

5.2.1 Dynamics of the outer planet

Considering the distances involved, the inner planets are supposed negligibly affected by their distant companion. We thus neglect the effect of rigid precession described above (which is anyway relevant only in the inclined case, see Sect. 5.4). Arguments favouring this simplification are given by the Roy-Walker parameters ε^{23} and ε_{32} (Walker et al., 1980): whereas mutual parameters for the giant planets are of orders 10^{-4} to 10^{-6}, the effects of the distant planet on the internal system range from 10^{-9} (Neptune) to 10^{-11} (Jupiter). Conversely, the effects of the giant planets on their distant companion are of order 10^{-7} to 10^{-8}, so this is the next level of approximation to be taken into account, beyond strictly decoupled systems.

Hence, the long-term dynamics of the outer planet is accurately represented by a secular model as described in Sect. 3.2. Since it is far from every equilibrium point of both non-resonant and resonant secular Hamiltonians, this planet is a typical case of "decoupled" object with constant semi-major axis, eccentricity and inclination. Its long-term dynamics is thus accurately approximated by the leading-order term of the

development in the semi-major axes ratios (see Sect. 3.2.2). Up to this level of approximation, the constant precession rates of ω' and Ω' are:

$$\begin{cases} \dot{\omega}' = \delta^2 \dfrac{3}{8}\big(5\cos^2 I' - 1\big) \\ \dot{\Omega}' = -\delta^2 \dfrac{3}{4}\cos I' \end{cases} \quad \text{with} \quad \delta^2 = \sqrt{\frac{a'}{\mu}}\left(\frac{1}{a'(1-e'^2)}\right)^2 \sum_{i=1}^{N} \mu_i \left(\frac{a_i}{a'}\right)^2 \tag{5.1}$$

In these expressions, a_i is the constant semi-major axis of the ith planet, and μ and μ_i are the gravitational parameters of the Sun and of the ith planet, respectively. The elements with prime symbol are the ones of the distant planet, with the values from Tab. 5.1. By including Jupiter, Saturn, Uranus and Neptune (the masses of the terrestrial planets being added to the Sun), we obtain the following numerical values:

$$\dot{\omega}' = 0.201\,\text{rad/Gyr} \quad \text{and} \quad \dot{\Omega}' = -0.126\,\text{rad/Gyr} \tag{5.2}$$

They can be verified by unaveraged numerical simulations. In the rest of this work, we will refer to these two quantities as ν'_ω and ν'_Ω.

At some points, we will also consider a planar perturber, with orbital elements still given by Tab. 5.1 but with $I' = 0$. In that case, ω' and Ω' will be replaced by $\varpi' = \omega' + \Omega'$, with a precession rate of:

$$\dot{\varpi}' = \delta^2 \frac{3}{4} \approx 0.146\,\text{rad/Gyr} \tag{5.3}$$

We will refer to this last quantity as ν'_ϖ in the following[1].

5.2.2 Osculating dynamics of the small body

We consider the orbit of a small body perturbed by both the inner planets and the precessing outer super-Earth. In Delaunay heliocentric elements, the corresponding Hamiltonian function writes generically:

$$\begin{aligned} \mathcal{H}\Big(\{\Lambda_i\}, \Lambda', P'_\omega, P'_\Omega, L, G, H, \{\lambda_i\}, \lambda', \omega', \Omega', \ell, g, h\Big) = \\ \mathcal{H}_0\Big(\{\Lambda_i\}, \Lambda', P'_\omega, P'_\Omega, L\Big) + \varepsilon\mathcal{H}_1\Big(L, G, H, \{\lambda_i\}, \lambda', \omega', \Omega', \ell, g, h\Big) \end{aligned} \tag{5.4}$$

where the integrable part and the perturbation are respectively:

$$\begin{cases} \mathcal{H}_0 = -\dfrac{\mu^2}{2L^2} + \nu'_\omega P'_\omega + \nu'_\Omega P'_\Omega + \displaystyle\sum_{i=1}^{N} n_i\,\Lambda_i + n'\,\Lambda' \\ \varepsilon\mathcal{H}_1 = -\displaystyle\sum_{i=1}^{N} \mu_i \left(\frac{1}{|\mathbf{r}-\mathbf{r}_i|} - \mathbf{r}\cdot\frac{\mathbf{r}_i}{|\mathbf{r}_i|^3}\right) - \mu'\left(\frac{1}{|\mathbf{r}-\mathbf{r}'|} - \mathbf{r}\cdot\frac{\mathbf{r}'}{|\mathbf{r}'|^3}\right) \end{cases} \tag{5.5}$$

[1]This is the same expression as the Eq. 2 by Batygin and Brown (2016a), except that they give the associated period $2\pi/\nu'_\varpi$. Please note that there is a typo error in their expression (the inverse of a sum is *not* the sum of the inverses).

The vectors $\mathbf{r}$, $\mathbf{r}_i$ and $\mathbf{r}'$ are the heliocentric positions of the particle, of the ith inner planet, and of the outer one. The constants μ_i and μ' are the gravitational parameters of the planets, whereas $\{n_i\}$ and n' are their mean motions. The momenta $\{\Lambda_i\}$ and Λ' are conjugate to the mean longitudes $\{\lambda_i\}$ and λ' of the planets, and P'_ω and P'_Ω are conjugate to ω' and Ω'. They allow the definition of an autonomous system. We have then:

$$\begin{cases} \mathbf{r}_i \equiv \mathbf{r}_i(\lambda_i) \text{ for } i = 1, 2 \dots N \\ \mathbf{r}' \equiv \mathbf{r}'(\lambda', \omega', \Omega') \\ \mathbf{r} \equiv \mathbf{r}(L, G, H, \ell, g, h) \end{cases} \tag{5.6}$$

Finally, we recall that the Delaunay canonical coordinates (L, G, H, ℓ, g, h) are directly linked to the Keplerian elements $(a, e, I, \omega, \Omega, M)$ of the particle through (2.88).

The Hamiltonian system described by (5.4) has $N + 6$ degrees of freedom, but this number can be reduced using a geometric argument. Indeed, the perturbation involves ω' and Ω' only via the scalar product $\mathbf{r}\cdot\mathbf{r}'$ (this can be seen using a Legendre development of the inverse mutual distance, see Sect. 3.2.1). Computing this product in Keplerian elements and after some trigonometric manipulations, we get:

$$\begin{aligned} \frac{\mathbf{r}\cdot\mathbf{r}'}{r\,r'} &= \sin(\alpha)\sin(\alpha')\sin(I)\sin(I') \\ &+ \cos\left(\alpha - \alpha' + \Delta\Omega\right)\cos^2(I/2)\cos^2(I'/2) \\ &+ \cos\left(\alpha + \alpha' + \Delta\Omega\right)\cos^2(I/2)\sin^2(I'/2) \\ &+ \cos\left(\alpha + \alpha' - \Delta\Omega\right)\sin^2(I/2)\cos^2(I'/2) \\ &+ \cos\left(\alpha - \alpha' - \Delta\Omega\right)\sin^2(I/2)\sin^2(I'/2) \end{aligned} \tag{5.7}$$

where of course, the norms $r \equiv |\mathbf{r}|$ and $r' \equiv |\mathbf{r}'|$ are independent of ω' and Ω'. In that expression, the symbol α represents the sum of ω and the true anomaly (with a prime for the outer planet), and $\Delta\Omega = \Omega - \Omega'$. The longitudes of ascending nodes appear only through their difference, so it is possible to remove one degree of freedom by studying the system in a frame rotating with Ω'. This is realised by a linear transformation involving the Delaunay angle $h = \Omega$:

$$\begin{pmatrix} \delta h \\ \gamma \end{pmatrix} = \begin{pmatrix} 1 & -1 \\ 0 & 1 \end{pmatrix} \begin{pmatrix} h \\ \Omega' \end{pmatrix} \tag{5.8}$$

and applying its conjugate transposed to the momenta:

$$\begin{pmatrix} \tilde{H} \\ \Gamma \end{pmatrix} = \begin{pmatrix} 1 & 0 \\ 1 & 1 \end{pmatrix} \begin{pmatrix} H \\ P'_\Omega \end{pmatrix} \tag{5.9}$$

This change of coordinates allows the momentum associated to $\delta h = \Delta\Omega$ to be simply $\tilde{H} = H$ so we will omit the "tilde" sign in the following. In the new coordinates, the integrable part of the Hamiltonian function writes:

$$\mathcal{H}_0 = -\frac{\mu^2}{2L^2} + \nu'_\omega P'_\omega + \nu'_\Omega \Gamma - \nu'_\Omega H + \sum_{i=1}^{N} n_i\,\Lambda_i + n'\,\Lambda' \tag{5.10}$$

and the perturbation does not depend on γ. The momentum Γ being a constant of motion, we will discard the term $\nu'_\Omega \Gamma$ in the Hamiltonian (thus dropping one degree of freedom).

5.2.3 Secular model

The same method as in Sect. 3.2 will be used to switch to the secular coordinates: assuming that the particle is far from any mean-motion resonance with the planets, we can get rid of the short-period angles by a close-to-identity change of coordinates. At first order of the perturbation, the Hamiltonian function in the new coordinates (hereafter named *secular Hamiltonian*) is given by the average of $\mathcal{H}$ with respect to the fast independent angles ℓ and $\lambda_1, \lambda_2 ... \lambda_N, \lambda'$. Dropping the constant parts, it writes:

$$\mathcal{F}(P'_\omega, L, G, H, \omega', g, \delta h) = \nu'_\omega P'_\omega - \nu'_\Omega H + \mathcal{F}_1(L, G, H, \omega', g, \delta h) \tag{5.11}$$

where $\mathcal{F}_1$ is the numerically-computed average of $\varepsilon \mathcal{H}_1$. Even if we use the same symbols as before, we now manipulate the *secular coordinates*. As usual for non-resonant secular models, the semi-major axis of the particle (momentum L) becomes a parameter.

In the following, it is useful to have a normalized version of $\mathcal{F}$ which takes values of the order unity. This can be realised by adding a constant to $\mathcal{F}$ (dynamics unchanged) and multiplying it by a constant factor (change of time unit). For small bodies with a trajectory stretching between a_N and the orbit of the outer planet, judicious values of these constants are given by the development in the semi-major axes ratios :

$$\begin{aligned}
\mathcal{F} = {} & \nu'_\omega P'_\omega - \nu'_\Omega H \\
& - \frac{1}{a} \sum_{i=1}^{N} \mu_i - \frac{1}{a'} \mu' \\
& - \frac{1}{a} \sum_{i=1}^{N} \mu_i \left(\frac{a_i}{a} \right)^2 \frac{1}{8(1-e^2)^{3/2}} (3 \cos^2 I - 1) \\
& + \mathcal{O}\left(\sum_{i=1}^{N} \mu_i \left(\frac{a_i}{a} \right)^4 \right) + \mathcal{O}\left(\mu' \left(\frac{a}{a'} \right)^2 \right)
\end{aligned} \tag{5.12}$$

where computational details can be found in Laskar and Boué (2010) or in Sect. 3.2.1 for the inner component. The secular semi-major axis a being a constant of motion, the normalised version of the secular Hamiltonian is chosen to:

$$\overline{\mathcal{F}} = \frac{\mathcal{F} - C_{\text{offset}}}{C_{\text{scale}}} \tag{5.13}$$

where the constant coefficients C_{offset} and C_{scale} are:

$$\begin{cases} C_{\text{offset}} = -\dfrac{1}{a}\displaystyle\sum_{i=1}^{N}\mu_i - \dfrac{1}{a'}\mu' \\ C_{\text{scale}} = \dfrac{1}{4\,a}\displaystyle\sum_{i=1}^{N}\mu_i\left(\dfrac{a_i}{a}\right)^2 \end{cases} \tag{5.14}$$

By this choice of scaling factor C_{scale}, we suppose that the second-order term of the development for the inner planets is the leading term of the Hamiltonian. This holds for small semi-major axes (a little beyond a_N), but not for large ones, for which the second-order term of the development for the outer planet is more important. Moreover, the development (5.12) is valid only for trajectories entirely contained between the orbits of Neptune and of the outer planet, hence, the chosen coefficients have no clear dynamical meaning in the general case: they just allow to get a more "human-readable" value for the Hamiltonian function (say, not too far from unity).

As seen in the previous chapters, the numerical computation of the secular Hamiltonian is now a common procedure in celestial mechanics. For one-degree-of-freedom secular systems, the Hamiltonian value with respect to the coordinates gives an immediate qualitative description of the dynamics, since every possible trajectory is defined by a distinct level curve (Chps. 3 and 4). When two orbits cross, the resulting polar singularity of order 1 in the integral must be appropriately handled, but this is easily realised numerically so authors barely mention it anymore (see appendix B.5.1): *the averaged Hamiltonian always exists, and is a continuous function, even in the planet-crossing case; this is because an improper integral over a two-dimensional torus of a function with a polar singularity of order 1 is absolutely convergent* (quoted from Gronchi and Milani, 1998). Hence, for one-degree-of-freedom secular systems, the geometry of the phase portraits with respect to the parameters is obtained in a plain way even for crossing orbits. Of course, as pointed out by Thomas and Morbidelli (1996), the secular approximation does not automatically hold when two osculating orbits cross, because of the possibility of actual physical collision (or very close encounter). However, each branch of the generalised secular trajectory is perfectly valid, so the latter give at least the geometry of the solutions in a piecewise way. In addition, Gronchi and Milani (1998) stress that particles with repeated orbit crossings can still exhibit very smooth behaviours on a secular timescale. The system studied by Beust (2016) is even more critical, since it contains orbits which intersect *at all time*. Nevertheless, he reported system lifetimes larger than the age of the Solar System (before the accidental occurrence of a dramatically close encounter which does invalidate the secular representation), showing the significance of the generalised secular model.

The use of the numerically-computed secular system is less straightforward when there are several degrees of freedom: the complete equations of motion are required, and their calculation as well as their very mathematical definition are more problematic. Generically, any equation of motion can be obtained from $\mathcal{F}$ by inverting the partial

derivative and the integral symbols: the chain rule is used from Cartesian, through Keplerian, to Delaunay coordinates, and the result is numerically averaged over the short-period angles (we used that method, for instance, for the numerical integrations of the semi-secular system presented in Sect. 3.3). This amounts to consider the planets as massive interacting rings, forming what is called a "N-ring system" by Touma et al. (2009). The question to what extent this is equivalent to the time derivatives of the secular variables was extensively studied by Gronchi and Milani (1998) and Gronchi (2002). They demonstrated rigorously that this approach holds as long as the orbit of the small body does not cross any of the planetary orbits. During an orbit crossing, indeed, some of the partial derivatives are *not* defined (they present a polar singularity of order 2), even if the Hamiltonian itself is. However, they have a well-defined value arbitrarily close to the singularity on both sides, so in practice an orbit crossing results simply in a discontinuity of the "force" term in the equations of motion. Gronchi and Milani (1998) showed that a generalised solution passing through the discontinuity can be uniquely defined as the trajectory connecting the limits of the incoming and outgoing smooth solutions[2]. This generalised solution is necessarily non-smooth, but it is continuous. For a one-degree-of-freedom system, this corresponds to the usual level curves of the Hamiltonian, the crossings appearing as angular points. Please note that an orbit crossing does not imply necessarily a collision in the non-averaged system, neither a chaotic behaviour, since the bodies can be located in very distant points of their orbits when they cross. Figs. 5.2 and 5.3 present two examples of secular trajectories which are quasi-periodic even if they involve successive orbit crossings with the distant planet and/or Neptune. This stresses the necessity to correctly handle the crossings in this study, otherwise we could miss some equilibrium regions (any crossing orbit would appear chaotic).

Gronchi and Milani (2001) presented a practical algorithm to integrate numerically such a generalised secular trajectory: an integration step shall never pass through the discontinuity, so the idea is to stop the integration exactly at the crossing point (limit of the *left* smooth piece) and then restart it (*right* smooth piece) without computing the force at the transition point. Some integrators, as those using a Runge-Kutta-Gauss scheme, do not need the calculation of the force at the initial nor the final points of a given step. Such an integrator must be used, at least for these two particular steps[3]. To improve the stability of the numerical scheme even in the very neighbourhood of the transition, the discontinuous terms can be computed analytically using Kantorovich method with an appropriate intermediary function. For the sake of simplicity, we will not use it in this work. In return, the conservation of the Hamiltonian will always be

[2]There is actually one very specific case for which the generalised solution is not uniquely defined, namely when the crossing is exactly *tangential*. This can happen only if the mutual inclination of the asteroid and the planet is zero at the very moment of the orbit crossing. We will discard that case in this work, since it has negligible probability to occur for an initially arbitrarily inclined small body.

[3]Gronchi and Milani (2001) stress also the symplectic property of Runge-Kutta-Gauss integrators. The handling of the discontinuity, however, requires necessarily an adjustable integration step, which breaks the symplecticity of the overall scheme.

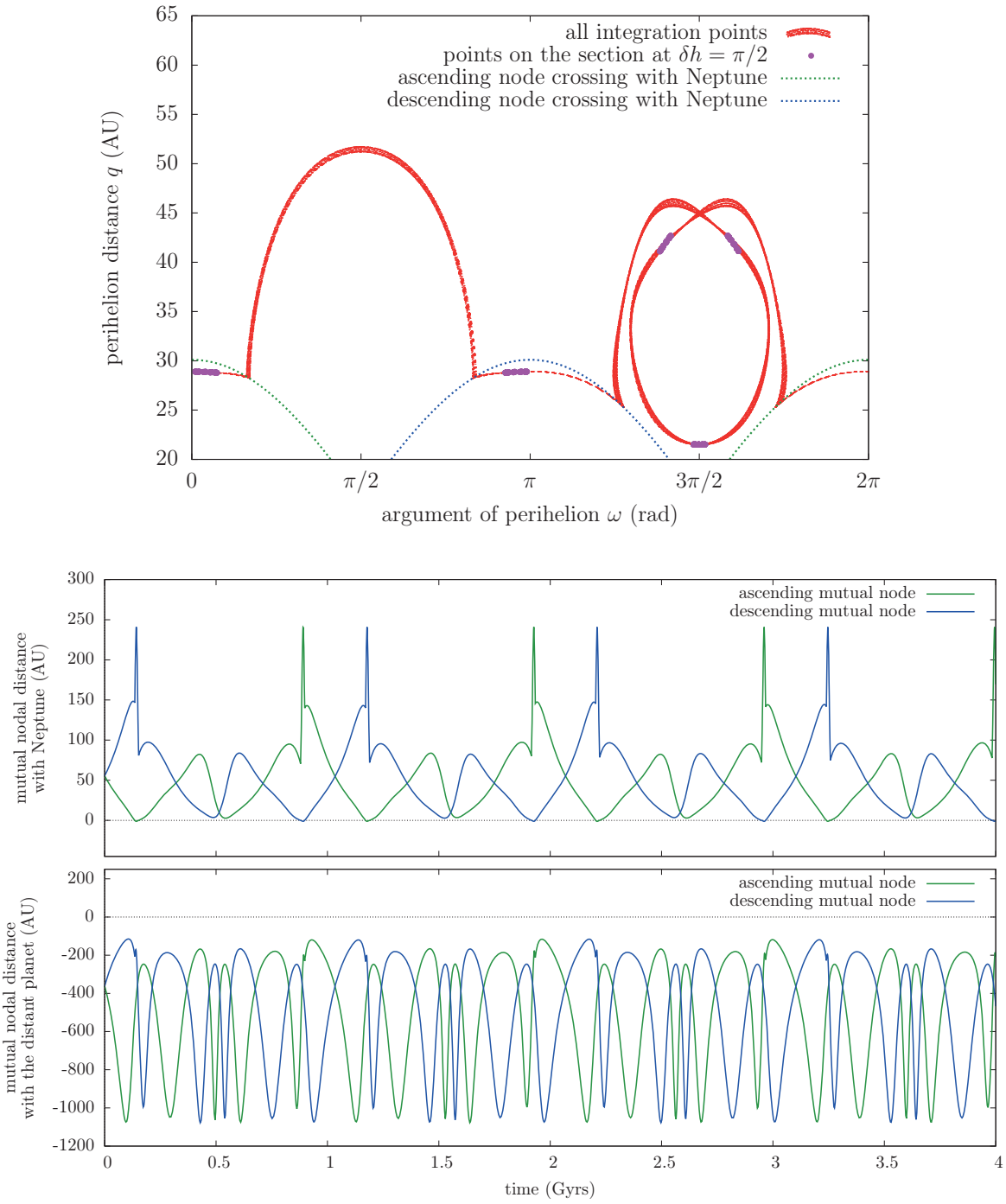

Figure 5.2 – Example of integrable secular trajectory incurring orbit crossings with Neptune. The distant perturber has a zero inclination and the fixed semi-major axis of the particle is $a = 150$ AU. This numerical integration is borrowed from Fig. 5.6**h**. On the top graph, the trajectory is projected on the plane (ω, q). Since the orbit of Neptune is circular with zero inclination, the positions of the crossings, obtained by setting Eq. (5.15) to zero, are simple functions of ω and q (green and blue curves). The trajectory forms an angle where the crossings take place. The two bottom graphs show the evolution of the mutual nodal distances with Neptune and the distant perturber. A crossing happens whenever one of them crosses the zero limit.

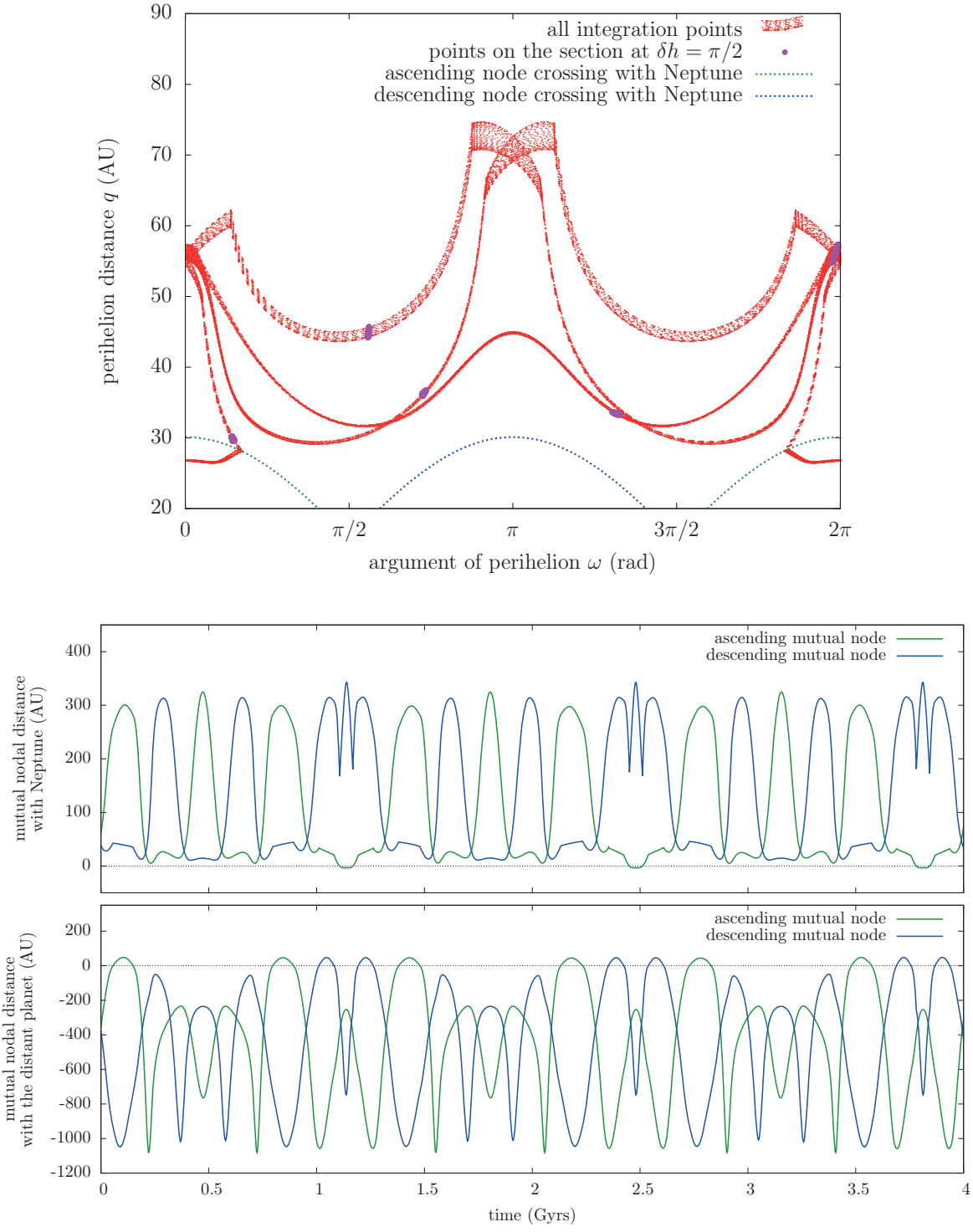

Figure 5.3 – Example of integrable secular trajectory incurring orbit crossings with Neptune and the distant perturber. The distant perturber has a zero inclination and the fixed semi-major axis of the particle is $a = 200$ AU. This numerical integration is borrowed from Fig. 5.7**d**. On the top graph, the crossings with the distant planet are not only functions of ω and q so they cannot be represented (contrary to Neptune). Still, they appear as angular points along the trajectory.

checked as a proxy of reliability of the numerical solutions (constancy of the normalised value at the 10^{-10} level). "Bad" behaviours were found very rare in our work and always avoidable by suitable integration steps. The detailed equations of motion of the averaged system are given in appendix B.3.2.

5.2.4 Computational details

When two orbits cross, the calculation of an integration step arriving exactly on the transition point deserves some comments. Gronchi and Milani (2001) present an iterative procedure using nested dichotomy methods, associated with a polynomial extrapolation to detect *a priori* when a crossing could occur. We preferred to use the method of Hénon (1982) which seems to be more straightforward: when a sub-step of the integrator is found to cross a discontinuity, the current step is immediately stopped and a unique, well-determined step is performed, arriving exactly on the desired point. This is made possible by a change of the independent variable used for the integration. In our case, two orbits cross when their mutual nodal distance vanishes, so the idea is to take this mutual nodal distance as a fictitious "time" and to make a single step leading it to zero. As detailed in appendix B.5.2, the mutual nodal distance of the small body with an arbitrary planet j (either the outer or an inner one) is given by:

$$\Delta_j^{\pm} = \frac{a(1-e^2)}{1 \pm e\cos\tilde{\omega}} - \frac{a_j(1-e_j^2)}{1 \pm e_j\cos\tilde{\omega}_j} \tag{5.15}$$

where $\pm$ stands for the ascending or descending mutual nodes. The angles $\tilde{\omega}$ and $\tilde{\omega}_j$ are the arguments of perihelion in the mutual reference frame, defined by the z-axis being parallel to the angular momentum of the planet and the x-axis pointing toward the ascending mutual node of the small body (that is where its orbit crosses the (x, y) plane from negative to positive z values). Please note that this reference frame is defined only for non-zero mutual inclinations, but it is anyway just a mathematical intermediate, used to define the orbit crossings. In terms of the Keplerian elements in the inertial frame, we get:

$$\begin{aligned}
\cos\tilde{\omega} &= \frac{\cos\omega(\sin I\cos I_j - \cos I\sin I_j\cos\Delta\Omega_j) + \sin\omega\sin I_j\sin\Delta\Omega_j}{\sqrt{1-(\cos I\cos I_j + \sin I\sin I_j\cos\Delta\Omega_j)^2}} \\
\cos\tilde{\omega}_j &= \frac{-\cos\omega_j(\sin I_j\cos I - \cos I_j\sin I\cos\Delta\Omega_j) + \sin\omega_j\sin I\sin\Delta\Omega_j}{\sqrt{1-(\cos I\cos I_j + \sin I\sin I_j\cos\Delta\Omega_j)^2}}
\end{aligned} \tag{5.16}$$

where $\Delta\Omega_j = \Omega - \Omega_j$. Naturally, the expression of $\Delta_j^{\pm}$ is greatly simplified for non-inclined planets on circular orbits (as the first N planets considered in this chapter). For any planet j, the time derivative of the mutual nodal distances can be computed in terms of the canonical coordinates by using the chain rule:

$$\frac{\mathrm{d}\Delta_j^{\pm}}{\mathrm{d}t} = \frac{\partial\Delta_j^{\pm}}{\partial g}\dot{g} + \frac{\partial\Delta_j^{\pm}}{\partial\delta h}\dot{\delta h} + \frac{\partial\Delta_j^{\pm}}{\partial G}\dot{G} + \frac{\partial\Delta_j^{\pm}}{\partial H}\dot{H} + \frac{\partial\Delta_j^{\pm}}{\partial\omega'}\dot{\omega}' \tag{5.17}$$

The expression of each term is given in appendix B.5.3. In practice, when a specific node crossing is detected, the corresponding mutual nodal distance (5.15) is taken as the new independent variable τ. Noting generically ρ its time derivative (5.17), the new equations of motion are obtained by dividing the Hamilton equations by ρ. The evolution of the physical time t must be added among the dynamical equations as:

$$\frac{\mathrm{d}t}{\mathrm{d}\tau} = \frac{1}{\rho} \tag{5.18}$$

Hence, the exact position on the node crossing is obtained by a single integration step $\Delta\tau$ leading τ to zero. The conventional variables are then recovered to pursue the integration. The drawback of this method is that, when switching to the variable τ, the integrator cannot make use of the previous integration steps[4] (for instance to build a first guess for predictor-corrector iterations). In the same way, the restart of the integration in the conventional variables is equivalent to begin from scratch again. We considered, though, that the consequent increase of computation time was compensated by dropping the possibly numerous iterations otherwise required to reach the node crossing to machine precision.

5.2.5 Preliminary remarks

Before presenting our results, some comments about their comparison to previous works can be useful. The strategy used in this chapter is similar to that of Li et al. (2014a), and in both studies, the eccentric Kozai mechanism is raised by an outer planet acting on a test-particle. However, the comparison should be realised with care, for two major reasons:

- On the one hand, Li et al. (2014a), as well as most works related to the eccentric Kozai mechanism, use a development of the Hamiltonian up to the octupolar term and the second order of the semi-major axis ratio. Of course, such a truncation is valid only for strictly hierarchical systems. They estimated this approximation to be valid for:
$$\frac{a}{a'}\frac{e'}{1-e'^2} < 0.1 \tag{5.19}$$
which amounts to $a < 75$ AU in our case, using the parameters in Tab. 5.1. In this article, this strong limitation is bypassed by using the full averaged Hamiltonian (obtained numerically), which is equivalent to a development containing an infinity of terms. We will consequently explore a parameter space which is well beyond the octupolar approximation.

- On the other hand, in our work the inner planets are the dominant part of the perturbation, especially for the small semi-major axes required in (5.19). Even

[4]Correcting coefficients could actually be computed but they would require to save a lot of information from the previous steps.

when the octupolar approximation could be valid, our results are thus strongly different from those obtained with models containing only the outer perturber.

In conclusion, the present study should be considered as an extension of the classic Kozai mechanism driven by inner planets to an additional external eccentric perturber, and not the contrary. Whereas numerous features of the eccentric Kozai mechanism are indeed revealed, they cannot be compared directly to previous works which use only the octupolar development[5].

5.3 Planar perturber

By imposing the perturber inclination to be zero, the dependence on ω' and Ω' from (5.7) becomes:

$$\begin{aligned}\frac{\mathbf{r}\cdot\mathbf{r}'}{r\,r'} &= \cos\left(\alpha - v' + \Omega - \varpi'\right)\cos^2(I/2) \\ &\quad + \cos\left(\alpha + v' - \Omega + \varpi'\right)\sin^2(I/2)\end{aligned} \tag{5.20}$$

where v' is the true anomaly of the distant planet. Since ϖ is the only meaningful angle for zero-inclination orbits, the term $\nu'_\omega P'_\omega + \nu'_\Omega P'_\Omega$ in the osculating Hamiltonian (5.5) is replaced by $\nu'_\varpi P'_\varpi$. The variable ϖ' acts just as Ω' from the general case, so the secular Hamiltonian for a planar perturber is simply:

$$\mathcal{F}(L,G,H,g,\delta h) = -\nu'_\varpi H + \mathcal{F}_1(L,G,H,g,\delta h) \tag{5.21}$$

where this time $\delta h = \Omega - \varpi'$. As before, the momentum L (or equivalently the semi-major axis a of the particle) is a free parameter. We are left with a two-degree-of-freedom system, non integrable in general, but which can be explored with Poincaré sections.

A Poincaré section can be used for the mapping of a two-degree-of-freedom Hamiltonian system in a two-dimensional surface spanned by one pair of conjugate coordinates. This surface is defined by a fixed value of a function of the coordinates, as well as a direction of crossing. Besides, each map is parametrised by the value of the Hamiltonian. In practice, the computation of such a map consists in integrating numerically the equations of motion in a large range of initial conditions (with same Hamiltonian value), and retaining only the points where the obtained trajectories cross the section in the chosen direction. The method of Hénon (1982) can be used once again, in order to get an integration point exactly on the surface. For two-degree-of-freedom systems, a Poincaré section allows to distinguish in a glance which trajectories are regular, as well as the size of the chaotic zones. Indeed, an integrable dynamics implies the existence of a second first integral (the first one being the Hamiltonian), so the corresponding trajectories evolve in a one-dimensional manifold. In practice, their section crossing

[5]We use here a broader definition of "classic" and "eccentric" Kozai mechanisms than Naoz et al. (2013) (right after their Eq. 26). Here, our definition holds for the non-truncated averaged Hamiltonian: it only indicates the orbit of the perturber, which is respectively circular or eccentric.

points accumulate on continuous lines (quasi-periodic trajectories) or finite-numbered fixed points (periodic trajectories). On the contrary, chaotic trajectories evolve in a two-dimensional manifold, so their section crossing points are area-filling. Since a point of the map defines one and only one solution, a chaotic trajectory cannot cross the section inside a region filled with an integrable flow. Thus, authors often speak of "stability islands embedded in a chaotic sea". This property implies the existence of "stable chaos" (so-called after Milani and Nobili, 1992), for which chaotic trajectories are tightly trapped between two integrable manifolds. In that case, the corresponding chaotic zone looks more like a moat than an open sea. At some points, we will also use the terms "sticky chaos" (introduced by Karney, 1983) in order to describe chaotic trajectories which behave temporarily as integrable ones (they "stick" to a nearby regular orbit). Such trajectories form denser accumulations of points in the sticky regions of the chaotic sea.

In all the following, the inner N planets considered are Jupiter, Saturn, Uranus and Neptune ($N = 4$), whereas the masses of the terrestrial planets are added to the Sun. The exploration of the parameter space is conducted as follows: for increasing values of the constant semi-major axis a, we present the most representative maps obtained when varying the value of the secular Hamiltonian $\overline{\mathcal{F}}$. The sections in both planes of conjugate coordinates are made simultaneously, so that we always present two maps for each value of $\overline{\mathcal{F}}$. In order to ease the interpretation, the momenta are replaced by non-canonical variables: we use the perihelion distance q instead of G, and H/L instead of H. Besides, the ranges of inclination spanned by the represented trajectories are given along with the chosen values of $\overline{\mathcal{F}}$. Some examples of parameters for real objects are given in Tab. 5.2.

name	a (AU)	q (AU)	H/L	ω (rad)	$\Omega - \varpi'$ (rad)	$\overline{\mathcal{F}}_1$	$\Omega - \Omega'$ (rad)	$\overline{\mathcal{F}}_2$
$2012\,VP_{113}$	255.9	80.54	0.6650	5.131	3.277	−1.561	5.895	−3.062
$2004\,VN_{112}$	316.4	47.32	0.4745	5.708	2.845	0.672	5.463	1.155
$2013\,RF_{98}$	349.2	36.09	0.3851	5.441	2.873	3.383	5.491	0.795
$2010\,GB_{174}$	367.1	48.79	0.4633	6.071	3.974	8.277	0.308	8.715
$2007\,TG_{422}$	476.5	35.57	0.3593	4.986	3.664	36.11	6.282	35.80
Sedna	493.1	76.03	0.5219	5.438	4.215	52.82	0.550	57.43

Table 5.2 – Heliocentric osculating elements at current time of the six objects with $a > 250$ AU used by Batygin and Brown (2016a). These elements are computed using AstDyS database (`http://hamilton.dm.unipi.it/astdys/`), where the value of ϖ' and Ω' are taken from Tab. 5.1. On the right, the corresponding value of the secular Hamiltonian is given using the osculating elements as an approximation of the secular ones. The two models considered here are written "1" for the planar perturber and "2" for the inclined perturber with $\nu'_\omega = 0$.

We use the following colour code for the points on the maps:

- *Black* – for integrable non-resonant trajectories. A fixed point on the maps corresponds to oscillations of the angle itself (by opposition to a resonant combination).

- *Blue* – for integrable trajectories driven by a resonance between the two degrees of freedom. A fixed point on the maps corresponds to oscillations of a linear combination of the two angles (which individually circulate[6]). Among them, *large green dots* are used to draw the $1:1$ resonances, in order to help the reader to distinguish the different features.

- *Red* – for chaotic trajectories, that is with unpredictable crossing points on the section spreading in a surface. This surface can be very large, or tightly packed between integrable curves.

Finally, please note that some regions of the maps are forbidden by the chosen value of the Hamiltonian: in our figures, such regions are represented in grey.

With no distant perturber, the equilibrium points and corresponding libration islands are well-known from Gallardo et al. (2012) and Sect. 3.2. If these equilibrium points persist in the perturbed problem, they are expected to become periodic orbits (mapped in discrete points on the sections), surrounded by quasi-periodic trajectories (mapped as curves).

Figure 5.4, computed for $a = 70$ AU, shows that the effect of the distant planet is almost unnoticeable for small semi-major axes. Indeed, the most notable features of the maps are driven by the inner planets: the classic equilibrium points at ω equal to $\pi/2$ and $3\pi/2$ are easily recognisable and the quantity $\sqrt{1-e^2}\cos I$ is almost conserved. In that particular case, the maps are very close to the trajectories in the physical space itself (which oscillates slightly around the lines on the sections). The only extra features due to the distant planet have a very little impact on the dynamics. They are namely:

a) The libration zones around ω equal to $\pi/2$ and $3\pi/2$ allow slightly larger oscillations of the perihelion distance.

b) The resonances $1:\pm1$ appear between the two angles (with respective resonant angles $\omega + \delta h$ and $\omega - \delta h$), but they have a very little effect on the dynamics.

c) The degeneracy of the $I = 90°$ line is removed: it splits into two fixed points at $\delta h = 0$ and π surrounded by thin libration islands. We recall that without eccentric perturber, the $H = 0$ line is entirely composed of equilibrium points for Ω.

One can note that the classic equilibrium points of ω at about $I = 63°$ divide the zones where ω circulates towards the right ($\dot{\omega} > 0$ below the islands) from the zones where it circulates towards the left ($\dot{\omega} < 0$ above the islands). In the same way, the equilibrium points of δh at about $I = 90°$ divide the zones where δh circulates towards

[6]Such a simple colour code can be a bit ambiguous, in particular for resonances between the oscillation frequency of one angle and the circulation frequency of the other: in our graphs, they will be represented in blue even if one angle oscillates. This should not mislead the reader, though, since further indications are given in the captions and in the text.

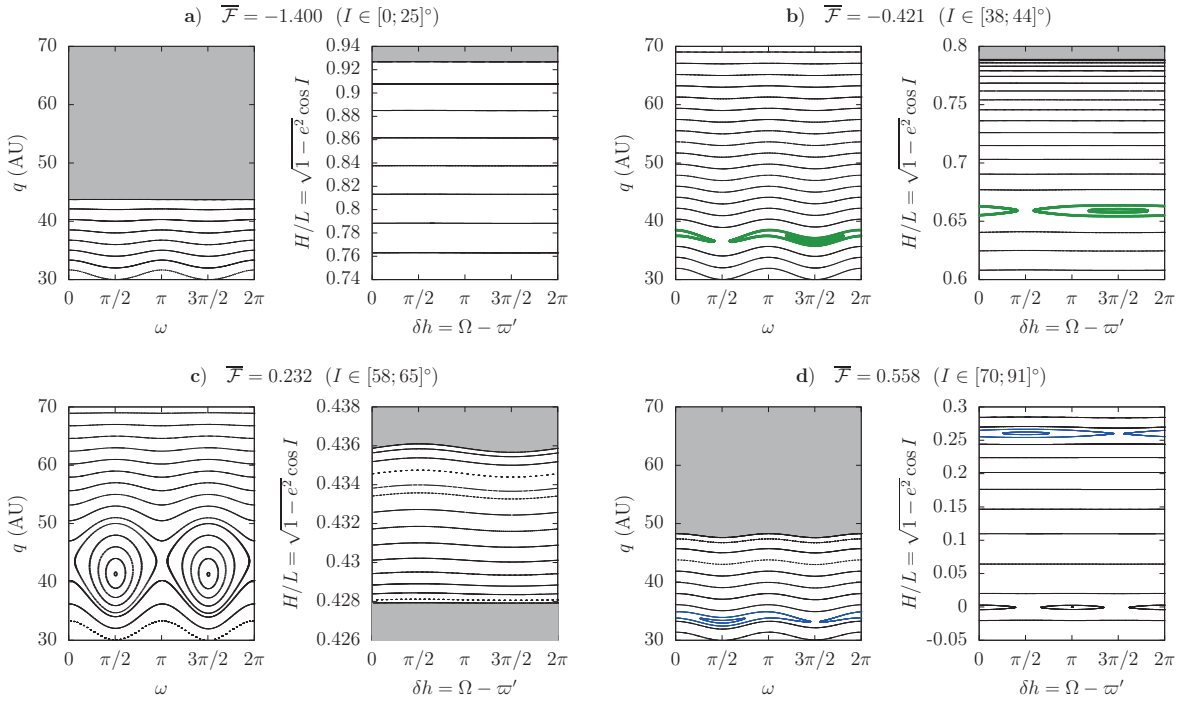

Figure 5.4 – Poincaré maps for a planar perturber. The constant semi-major axis of the particle is $a = 70$ AU. Each of the four panels (**a**,**b**,**c**,**d**) corresponds to a different value of the secular Hamiltonian. The range of inclination given for each panel is the range spanned by all the represented trajectories. Every section in the (ω, q) plane is made for $\delta h = \pi/2$ and $\dot{\delta h} < 0$. Every section in the $(\delta h, H)$ plane is made for $\omega = \pi/2$, with $\dot{\omega} > 0$ for (**a**,**b**) and $\dot{\omega} < 0$ for (**c**,**d**). The panels **b** and **d** feature the resonances $\omega + \delta h$ and $\omega - \delta h$, respectively. The panel **c** shows two fixed points for ω (at $I \approx 63^\circ$), and the panel **d** shows two fixed points for δh (at $I \approx 90^\circ$).

the right ($\dot{\delta h} > 0$ for $I > 90^\circ$) from the zones where it circulates towards the left ($\dot{\delta h} < 0$ for $I < 90^\circ$). The same situation was reported for the dynamics with no distant perturber (Fig. 5.1). It is important to keep it in mind all along this work, since the Poincaré sections are defined for a specific direction of crossing. Here, we mainly focus on prograde orbits, thus with $\dot{\delta h} < 0$, however, some sections feature also several trajectories with slightly negative momentum H, which consequently do not produce any point on the (ω, q) maps.

The confrontation with the results of Beust (2016) deserves some comments. In the fully planar case, ω and Ω are replaced by ϖ, and his figures are plotted in the $(\Delta\varpi, e)$ plane. Using our set of coordinates, $\Delta\varpi$ writes $\omega + \delta h$, so the equilibrium points reported by Beust (2016), corresponding to apsidal alignments or anti-alignments with the distant planet, are equivalent to the resonance $1:1$ (drawn in green) in our more general model[7]. This has a direct consequence: in the weakly perturbed system, apsidal

[7]For a more straightforward comparison with Beust (2016), we could have taken directly the angle $\Delta\varpi = \omega + \delta h$ as canonical coordinate. However, the other resonances would have become harder to interpret (for instance $\omega - \delta h$ turns to $2\omega - \Delta\varpi$), and we would have lost the property of the equilibrium points of ω and δh, dividing prograde from retrograde resonances.

confinement is only possible when ω and δh circulate in opposite directions, that is for inclinations below 63°, or lying between 90° and 117°. A direct link to the study of Beust (2016) is also given by the limits of the forbidden (grey) regions on the panels compatible with $I = 0°$. These limits are precisely given by $I = 0$, so they represent a specific level curve of the planar Hamiltonian function. This is not very informative in Fig. 5.4 since the limit is very flat (panel **a**). In the next figures, however, the positions and shapes of the libration zones will be clearly recognisable. To ease the comparison, we added in appendix B.4 the level curves of the Hamiltonian in the completely planar case (Fig. B.1). Each of these level curves could represent the limit of a forbidden region in a Poincaré section for the spatial case.

Beust (2016) reported no stable equilibrium point for small semi-major axes: there is actually one at $\Delta\varpi = 0$ (corresponding to an apsidal alignment with the distant planet), but located at non-zero inclinations. This can be seen on the panel **b** of Fig. 5.4, where the centre of the resonant trajectories corresponds to $\Delta\varpi = 0$, whereas the $\Delta\varpi = \pi$ point lies on the separatrix[8]. We note that $\Delta\varpi$ oscillates but ω and δh circulate in opposite directions.

For $a = 100$ AU, Fig. 5.5 shows that a chaotic zone shows up around the fixed points of ω (panels **c** and **d**). The libration islands for ω are besides very enlarged with respect to their maximum width of 16.4 AU without distant perturber. Various resonances appear between the two angles, including resonances between the circulation frequencies of ω and δh, resonances between the libration frequency of ω and the circulation frequency of δh, as well as secondary resonances. As usual for Poincaré sections, the maps show only the most obvious ones: a more careful analysis reveals a lot of complex high-order resonances hidden in the chaos. On the panel **b** of Fig. 5.5, there is a very thin island of apsidal alignment, barely noticeable, at high perihelion distances ($\Delta\varpi = 0$). Contrary to other resonances present in Figs. 5.4 and 5.5, its position is fixed even when we slightly change the Hamiltonian value: it always remains close to the circular orbit. This is the precursor of the $\Delta\varpi = 0$ equilibrium point reported by Beust (2016) in the planar case. For such a small semi-major axis, it is though limited to non-zero inclinations and a narrow range of Hamiltonian values.

For $a = 150$ AU, this equilibrium point is much more obvious (panels **b** and **d** of Fig. 5.6). We added extra panels to detail its evolution with inclination. On the panels **a** and **b**, remember that the limits of the grey zones correspond to the zero-inclination case. Knowing the position of the planar equilibrium points from Fig. B.1, we can determine whether they persist or not for inclined orbits. Indeed, the upper green points on the panel **b** come from very slightly inclined trajectories, and they enclose completely the zero-inclination limit (the small grey zone detached from the top). This implies that the $\Delta\varpi = 0$ equilibrium is transported continuously toward non-zero inclinations. For more inclined orbits, the fixed point switches from apsidal

[8]These sections are made respectively for δh and ω equal to $\pi/2$, so a fixed point at $3\pi/2$ means for both sections an equilibrium point of $\Delta\varpi = \omega + \delta h$ at 0.

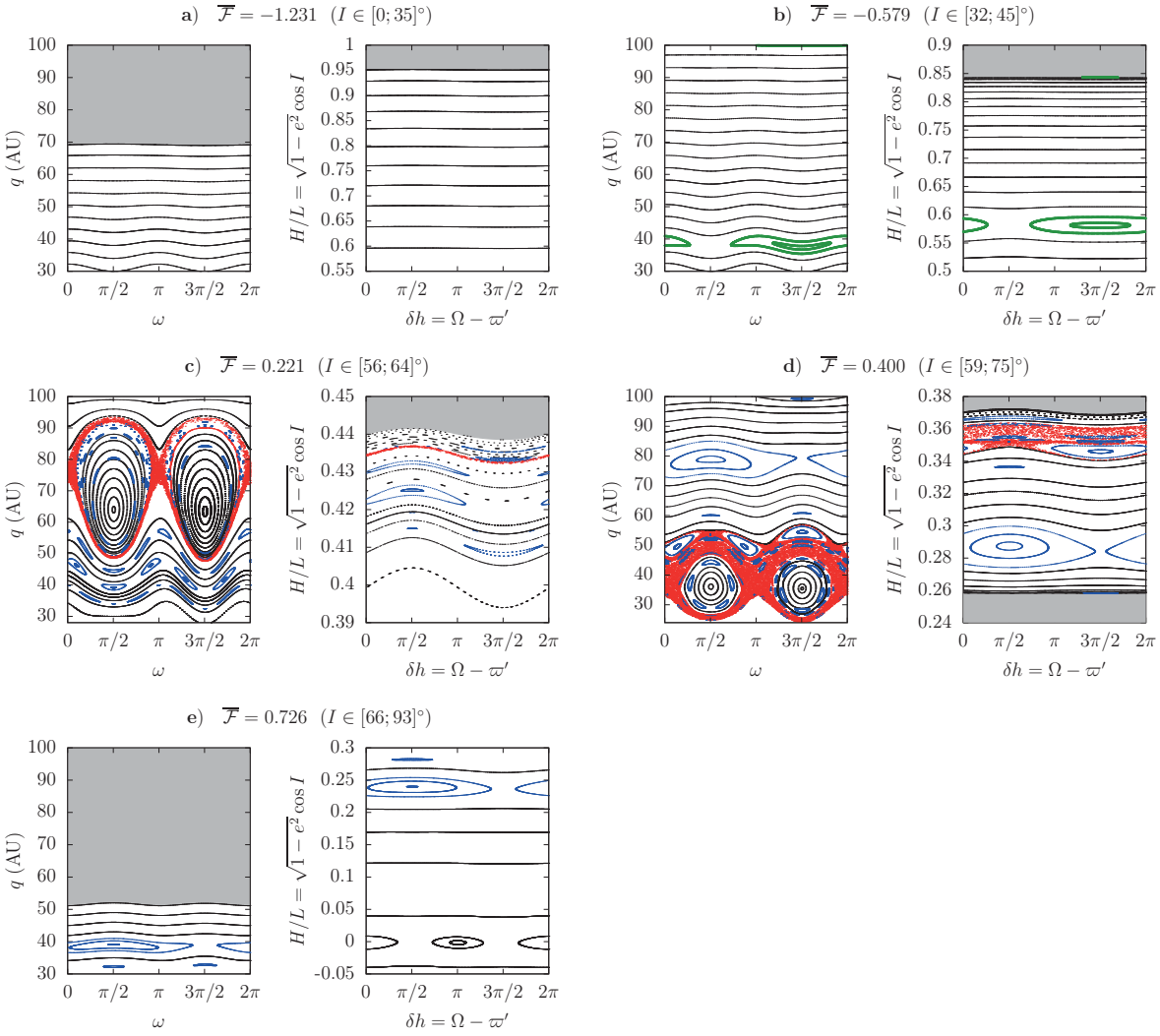

Figure 5.5 – Poincaré maps for a planar perturber (see text for details). The constant semi-major axis of the particle is $a = 100$ AU. Every section in the (ω, q) plane is made for $\delta h = \pi/2$ and $\dot{\delta h} < 0$. Every section in the $(\delta h, H)$ plane is made for $\omega = \pi/2$, with $\dot{\omega} > 0$ for (**a**,**b**,**c**) and $\dot{\omega} < 0$ for (**d**,**e**). Among other resonances, the panels **b** and **e** feature the resonances $\omega + \delta h$ and $\omega - \delta h$ (same as in Fig. 5.4). In the panels **c** and **d** numerous resonances are embedded in the chaotic sea (the corresponding resonant angles are given by the number of islands on the left and right graphs). The blue islands organised around the fixed points of ω are resonances between the libration frequency of ω and the circulation frequency of δh. A zoom-in view reveals secondary resonances as well.

alignment to anti-alignment in a small range of inclinations (panel **c** near the circular orbit). Moreover, the other $1:1$ resonance, already present for smaller semi-major axes, now stretches in a much wider region of the phase space (panel **c**), multiplying the possibilities of $\Delta\varpi$ oscillations. Hence, the claim of Beust (2016) that the non-resonant dynamics is able to produce both apsidal alignment and anti-alignment is widely generalised for inclined bodies. For semi-major axes as modest as $a = 150$ AU, though, the aligned case is clearly favoured. In the overall Fig. 5.6, we see that the possible excursion in inclination for a fixed Hamiltonian value is much wider than for smaller semi-major axes, making appear the classic ω fixed points on more numerous panels (**e**–**h**). However, the libration islands are quite "nibbled" by the surrounding chaotic sea, so they appear much thinner than in Fig. 5.5. The asymmetry of the two islands is due to the fixed value of δh used to build the map: the geometry of the two islands is inversed by taking $3\pi/2$ instead of $\pi/2$ (mirror symmetry). This dependence of the chosen section plane is another indicator of the stronger interaction between the two degrees of freedom.

For $a = 200$ AU (Fig. 5.7), the $\Delta\varpi$ libration island near the circular orbit becomes wider as the fixed point moves toward higher eccentricities (panels **b**,**c**,**d**). The evolution of its position and shape when varying a is thus generalised to non-zero inclinations. As before, it becomes a $\Delta\varpi = \pi$ libration island in some range of inclination (panel **c**). The other $\Delta\varpi = 0$ island, on the contrary, which was very large for $a = 150$ AU, is now surrounded by a chaotic zone (panels **b** and **c**). In some range of Hamiltonian values, it merges with the upper $1:1$ resonance and produces a very wide island (panel **d**). For slightly higher values of the Hamiltonian, however, this island turns to a chaotic zone (panel **e**), which announces the proximity of the classic libration zone for ω. Numerous orbits now intersect the trajectories of Neptune and/or the distant planet, especially in the chaotic regions. For trajectories with $I = 0$, we know from Beust (2016) that the intersecting orbits produce an equilibrium point at $\Delta\varpi = \pi$ (apsidal anti-alignment). This results in the detached grey zone in the panel **a**. It is surrounded by a thin quasi-periodic flow, showing that the libration island persists for very small inclinations (the green curve represented oscillates between $I = 0.1°$ and $0.5°$). For more inclined orbits, the chaos dominates but still sticking around the resonance. The chaos spreads also around the δh equilibrium points (panel **g**), allowing chaotic orbital flips between prograde and retrograde orbits. This is quite different from the regular orbits oscillating around $I = 90°$ (present also for smaller semi-major axes), since this time the orbit can stay retrograde for a long period of time, according to its wandering inside the chaotic zone. Very inclined and retrograde objects are actually observed in the distant Solar System[9], and their formation was studied in particular by Gomes et al. (2015) and Batygin and Brown (2016b). The latter pointed out that highly-inclined objects with small semi-major axes can still be explained by this mechanism, through a subsequent diffusion of semi-major axis due to the inner giant planets. Of course,

[9]On 2017-06-06, the JPL Small-Body Database Search Engine reports 8 non-cometary objects with $a > 150$ AU, $q > 5$ AU and $I > 50°$ (`https://ssd.jpl.nasa.gov/sbdb_query.cgi`).

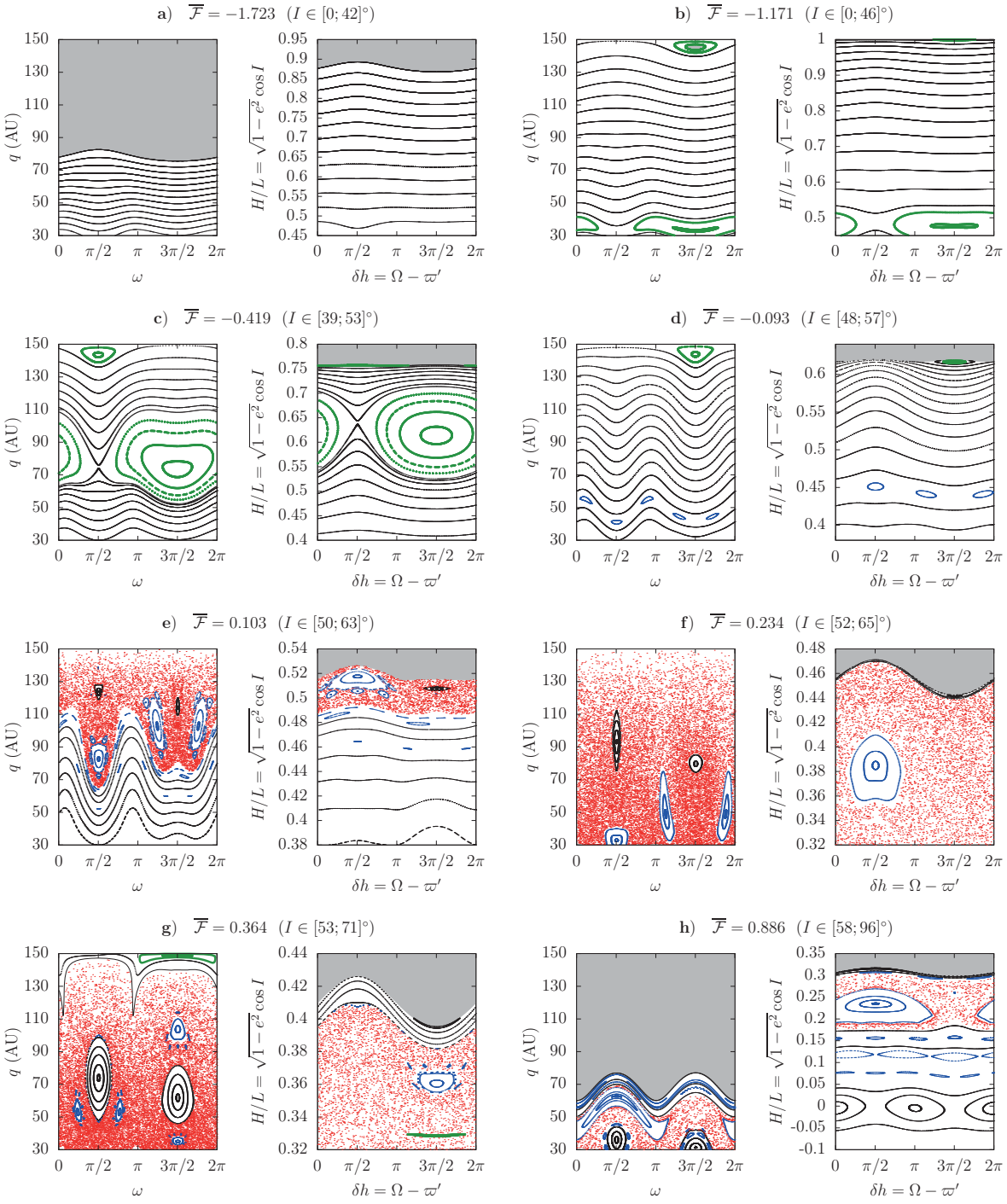

Figure 5.6 – Poincaré maps for a planar perturber. The constant semi-major axis of the particle is $a = 150$ AU. Every section in the (ω, q) plane is made for $\delta h = \pi/2$ and $\dot{\delta h} < 0$. Every section in the $(\delta h, H)$ plane is made for $\omega = \pi/2$, with $\dot{\omega} > 0$ for (**a**–**g**) and $\dot{\omega} < 0$ for **h**. In the panel **e**, the libration island of ω around $\pi/2$ appears only as a 1:1 resonance between the libration frequency of ω and the circulation frequency of δh (small black island at $\delta h = 3\pi/2$). We used black lines, though, to stress that ω itself oscillates around $\pi/2$, but please note that δh actually circulates, despite the closed black curves drawn on the right.

this last effect cannot appear in a secular model as ours. Finally, the most striking new features are the two forbidden regions at $\omega = 0$ and π on the panel **f**. They correspond to oscillations of *both* ω and δh around 0 or π, thus producing no points on these sections. In these regions, $\Delta\varpi$ oscillates also around 0 or π, leading to "frozen" aligned or anti-aligned orbits. The inclination of these trajectories oscillates around 90° (which is impossible to see in Fig. 5.7 because of the parameters chosen for the section), leading to a very particular geometry avoiding close orbital approaches. That kind of orbit is described more in detail below (Fig. 5.11). On the panel **e**, the different density of red points between the two chaotic zones has a purely numerical origin: orbits in the lowermost region are subject to repeated close encounters with either the outer or the internal planets, slowing down the computations. As a consequence, only a few points are obtained during a reasonable computing time.

For $a = 300$ AU, the only substantial stable features consists in resonances of apsidal alignment and anti-alignment (Fig. 5.8). The previous equilibrium points of ω (at $\pi/2$ and $3\pi/2$) and of δh (at 0 and π) persist only marginally on the panel **e**. Emerging from $I = 0$, the stable anti-aligned trajectories reach now moderate inclinations. For instance the resonant orbits on the panel **d** evolve between $I = 10°$ and 25°. On the panel **c**, note the presence of the two kinds of apsidal alignment: the very tiny green orbit at $q \approx 200$ AU is the residual of the island emerging from $I = 0$, whereas the bottom one is the usual 1:1 resonance present in every previous figure. Finally, the two forbidden zones on the panel **d** at $\omega = 0$ and π correspond also to apsidal alignments: they are filled with frozen orbits with both ω and δh oscillating around 0 or π, whereas I oscillates around 90° (same as for $a = 200$ AU, Fig. 5.7**f**). The variations in inclination allowed in the chaotic zones are very large, and orbital flips are allowed in almost every panel. The retrograde region of the phase space (not shown) is identical to the prograde one (mirror symmetry), with δh circulating in the opposite direction. Hence, the particles on chaotic trajectories can jump indifferently from prograde resonances ($\omega+\delta h$) to retrograde ones ($\omega-\delta h$). In the retrograde case, however, the resonance does not correspond to a particular orbital alignment. The complete orbital evolutions of the chaotic trajectories reveal transient states in every regime presented in Fig. 5.8, with sticky chaos. Fig. 5.9 presents a typical example (which contributes to fill with red dots the chaotic sea of Fig. 5.8**c**). We recognise apsidal alignments, apsidal anti-alignments, aligned frozen orbits with $I = 90°$, along with fast orbital flips (it takes some hundreds of Myrs to pass from 0° to 180°). Occasionally, the residuals of the classic equilibrium points make ω oscillate briefly around $\pi/2$ or $3\pi/2$. Such a behaviour is typical of what we obtain when integrating the known distant objects using the parameters given in Tab. 5.2 (using the first or the second secular model).

For completeness, we also present sections for $a = 500$ AU (Fig. 5.10). For such high semi-major axes, the phase space is filled with chaos, but the distant planet imposes strong constraints on the shape of the forbidden regions. Hence, even in the chaotic regime, the particle has no other possibility than following temporarily the various 1:1 resonances described throughout this section (similar to Fig. 5.9). Some very isolated

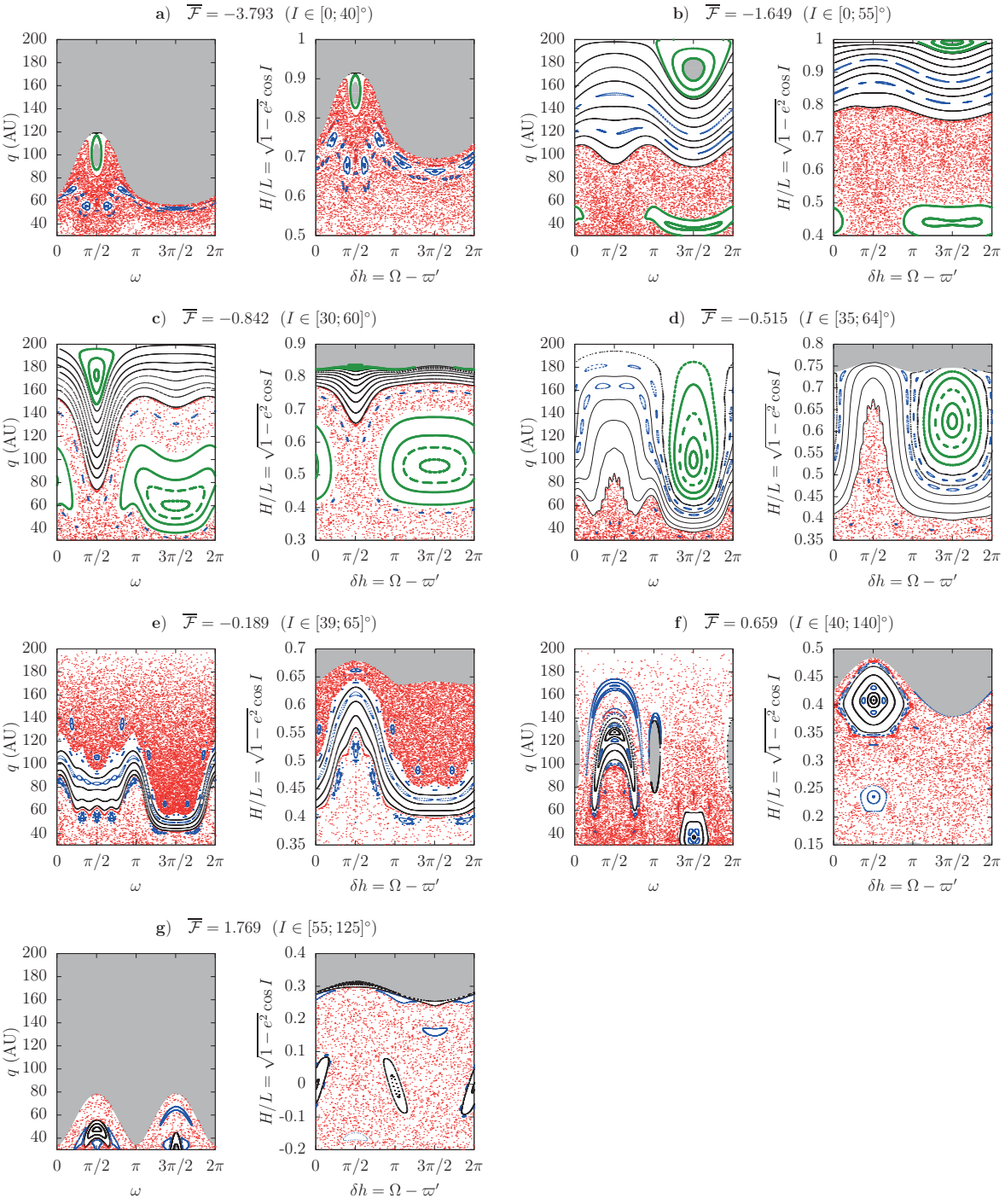

Figure 5.7 – Poincaré maps for a planar perturber. The constant semi-major axis of the particle is $a = 200$ AU. Every section in the (ω, q) plane is made for $\delta h = \pi/2$ and $\delta h < 0$. Every section in the $(\delta h, H)$ plane is made for $\omega = \pi/2$, with $\dot{\omega} > 0$ for (**a-e**) and $\dot{\omega} < 0$ for (**f**,**g**). On the panel **f**, the libration island of ω around $\pi/2$ appears only as a $1:1$ resonance between the circulation frequency of δh and the libration frequency of ω. We used black lines, though, to stress that ω itself oscillates around $\pi/2$ (but please note that δh actually circulates, despite the closed black curves drawn on the right).

regular trajectories persists, either as very high-order resonances hidden in the chaotic sea (panel **b** at $\Delta\varpi \approx 0$), or at very low inclinations (less than 1°). These latter, lying in the very vicinity of the forbidden regions, should persist for all values of the semi-major axis, since we retrieve the integrable model of Beust (2016). In the panel **c**, small stable regions in the resonances $\omega - \delta h$ and $\omega + \delta h$ are also visible.

We did not explore orbits with semi-major axes larger than the one of the distant planet. There exist probably other stable equilibrium points for trajectory entirely exterior to its orbit, but the problem becomes too significantly disconnected from the observed Solar System objects.

All the maps presented above are chosen at $\omega = \pi/2$ and $\delta h = \pi/2$, which does not allow to observe directly the equilibrium configurations with ω and δh both oscillating around 0 or π (they appear only as forbidden zones in Figs. 5.7**f** and 5.8**d**). In order to track that kind of behaviour, Fig. 5.11 shows the previous trajectories projected in sections chosen at $\omega = 0$ and $\delta h = 0$. These two equilibrium configurations appear from semi-major axes slightly smaller than 200 AU and become unstable beyond 300 AU. The aligned configuration is the last to vanish. The instability seems to be due to the oscillation of the perihelion: it goes through the inner planetary region for higher values of a, producing a complex pattern of orbit crossings. However, the signature of both configurations remains in the form of sticky chaos, producing in particular high-amplitude orbital flips for anti-aligned orbits (thin corridor available for $a = 300$ AU).

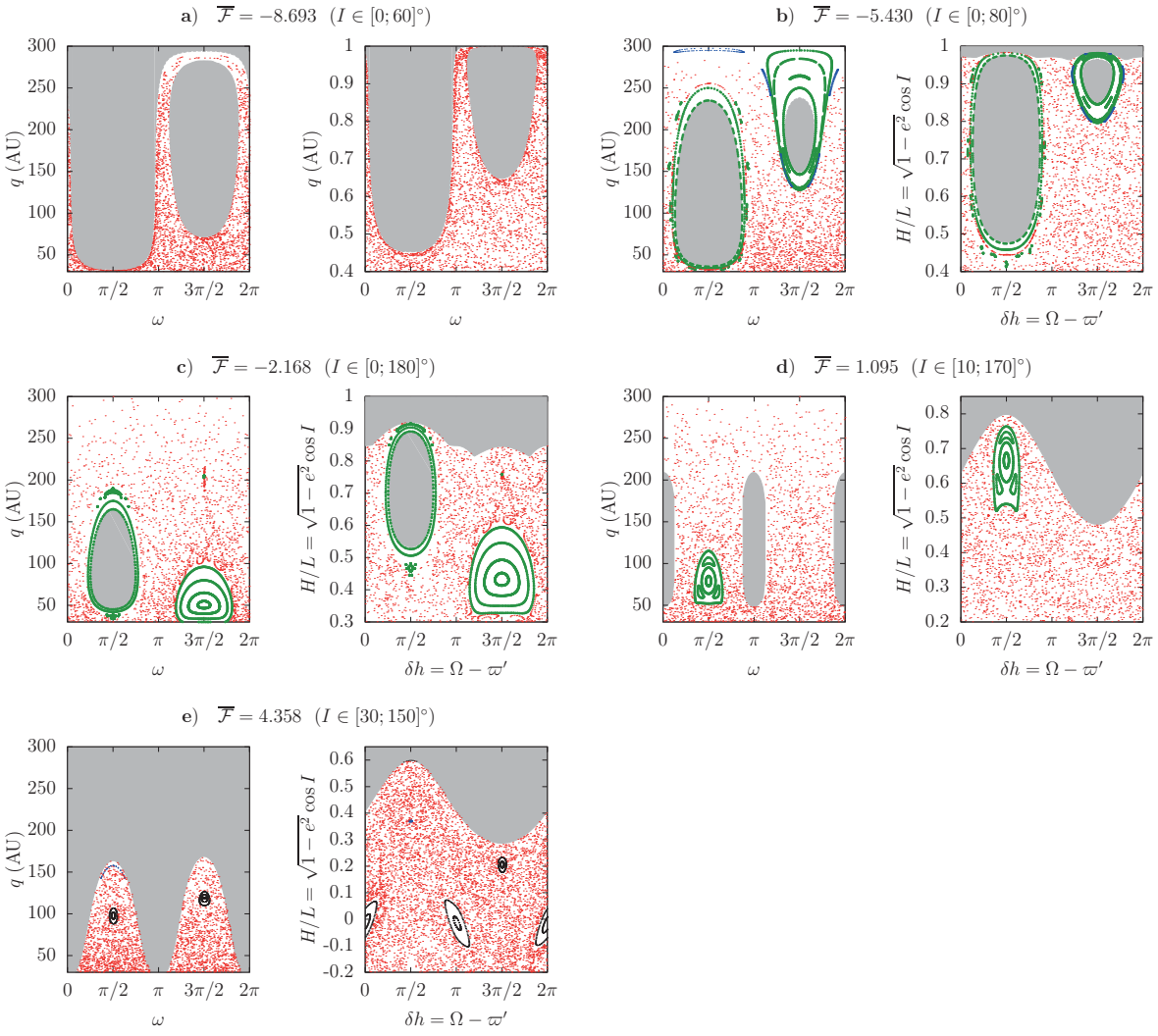

Figure 5.8 – Poincaré maps for a planar perturber. The constant semi-major axis of the particle is $a = 300$ AU. Every section in the (ω, q) plane is made for $\delta h = \pi/2$ and $\dot{\delta h} < 0$. Every section in the $(\delta h, H)$ plane is made for $\omega = \pi/2$, with $\dot{\omega} > 0$ for (**a-d**) and $\dot{\omega} < 0$ for **e**. The axes ranges are mainly focussed on prograde orbits ($H > 0$), but most of the chaotic orbits can flip (see the inclination ranges). On the panel **e**, the libration island of ω around $\pi/2$ appears only as a 1:1 resonance between the circulation frequency of δh and the libration frequency of ω (black island at $\delta h = 3\pi/2$). We used black lines, to stress that ω itself oscillates around $\pi/2$, but please note that δh actually circulates despite the closed black curves drawn on the right. On the panel **d** the two forbidden regions at $\omega = 0$ and π correspond to oscillations of both ω and δh around 0 or π, thus producing no points on these sections.

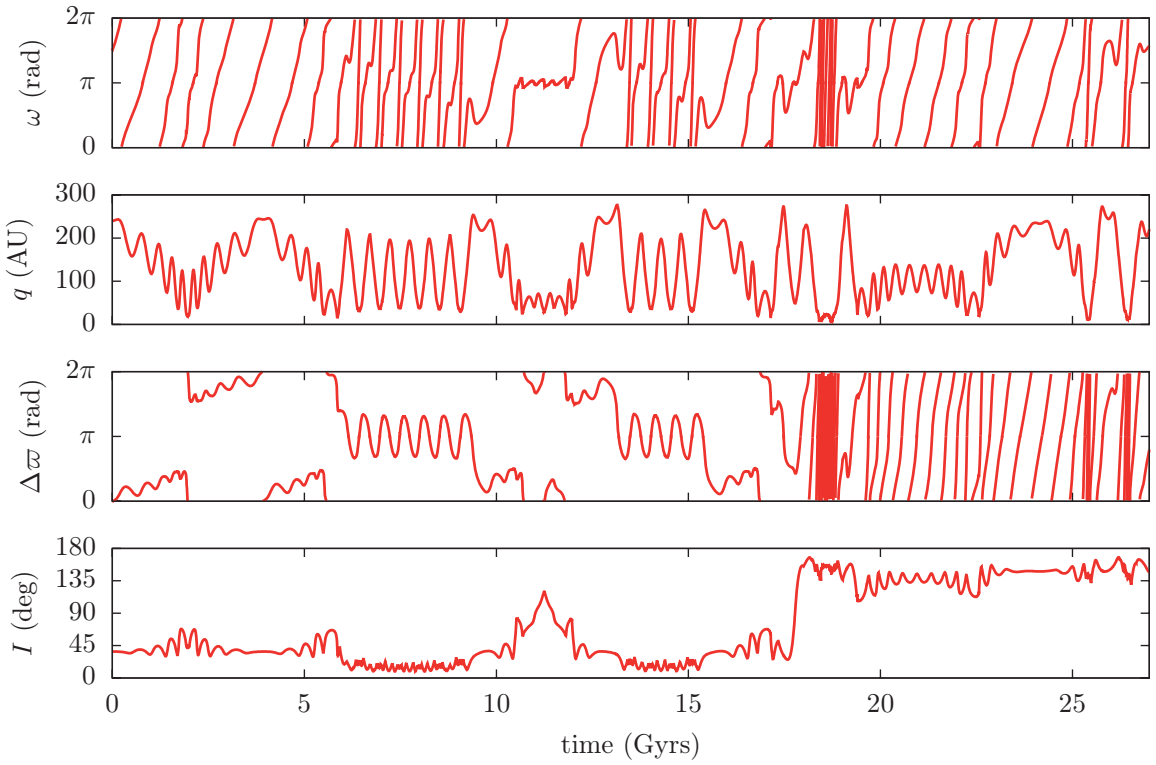

Figure 5.9 – Complete evolution of a chaotic trajectory with $a = 300$ AU. It contributes to the red dots on the maps **c** in Fig. 5.8. Firstly, the particle switches from apsidal alignment to anti-alignment (both with circulating ω and δh). Then it adopts a frozen aligned orbit ($\omega \approx \delta h \approx \pi$) with I oscillating around 90°, and after brief states in apsidal anti-alignment and alignment, it flips to a retrograde orbit. In the retrograde state, it sticks to the $\omega - \delta h$ resonance, symmetric to the prograde $\omega + \delta h$ one, but producing no particular alignment in the physical space. One can note that the apsidal anti-alignments are realised at very small inclinations, since the corresponding points on the Poincaré section lie near the limit of the forbidden zone (Fig. 5.8**c**), around the few regular trajectories.

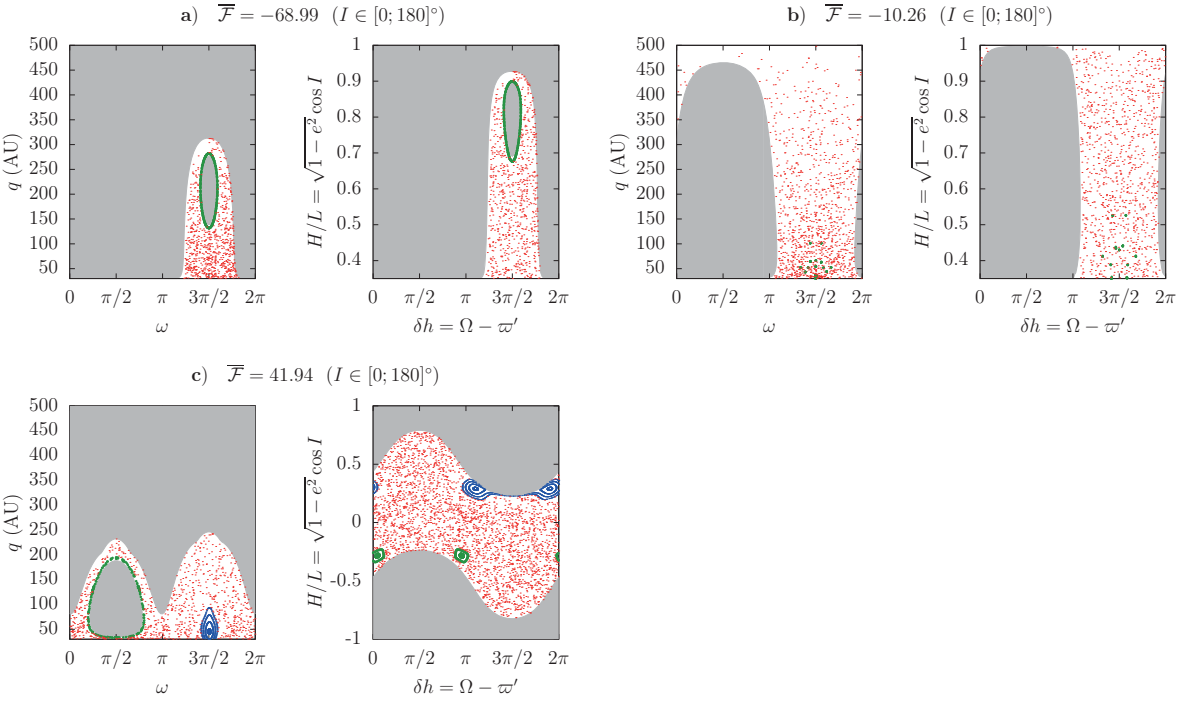

Figure 5.10 – Poincaré maps for a planar perturber. The constant semi-major axis of the particle is $a = 500$ AU. Every section in the (ω, q) plane is made for $\delta h = \pi/2$ and $\dot{\delta h} < 0$. Every section in the $(\delta h, H)$ plane is made for $\omega = \pi/2$, with $\dot{\omega} > 0$ for (**a**,**b**) and $\dot{\omega} < 0$ for **c**. The axes ranges are mainly focussed on prograde orbits ($H > 0$), but all of the chaotic orbits can flip (see the inclination ranges). On the panel **c**, a resonance $\omega - \delta h$ (leading to no particular orbital alignment) is visible for $I < 90^\circ$ in both the surfaces of section. It has a curious two-lobed geometry on the right. In the plane $(\delta h, H)$, a resonance $\Delta\varpi \approx \pi$ is also visible for $I > 90^\circ$ (it has two islands because ω and δh alternate between oscillation and circulation).

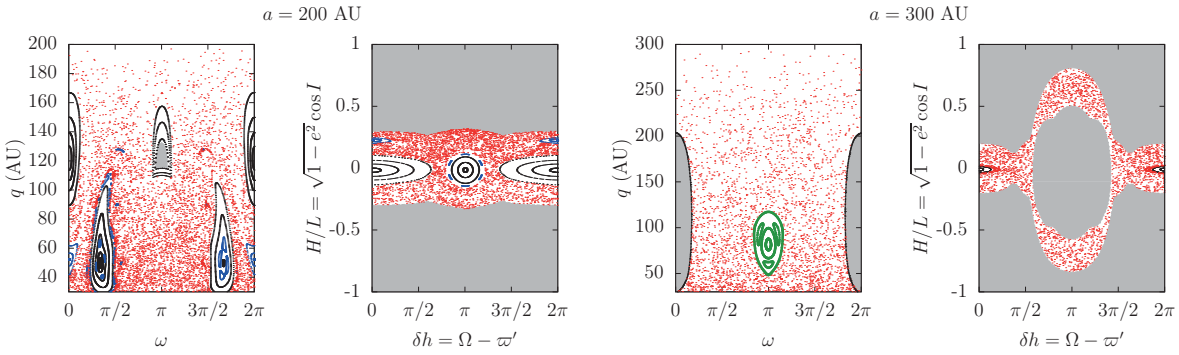

Figure 5.11 – Poincaré maps for a planar perturber. The sections in the (ω, q) plane are made for $\delta h = 0$ and $\dot{\delta h} < 0$. The sections in the $(\delta h, H)$ plane are made for $\omega = 0$, with $\dot{\omega} < 0$. The Hamiltonian value is the same as in Figs. 5.7**f** and 5.8**d**. For $a = 200$ AU, both the aligned and anti-aligned stable configurations are visible (as well as the classic equilibrium points of ω). For $a = 300$ AU, only the aligned one is stable, in a very small region. The section in the (ω, q) plane features also a resonance 1:1 with circulating ω and δh (same as Fig. 5.8**d**).

5.4 Toward a more general case

The complete system given by (5.11) has three degrees of freedom, with no possibility to further reduce it without loss of generality. Different strategies can be used to study the dynamics. The most direct one is to perform a series of numerical integrations, in order to compute Lyapunov exponents and stability maps. This would be loosing, however, the benefit of the secular model over the osculation system. Eventually, one can think of a more "mathematician-like" approach, consisting in the study of an intermediate system, less physically meaningful but still interesting dynamically speaking. This is the strategy adopted in the scope of this work, by adopting an unrealistic precession rate of $\nu'_\omega = 0$. This is a reasonable approximation for small bodies with moderate semi-major axes (say, less than 100 AU) far from the Kozai equilibrium points (inclination near 63° or 117°). Indeed the precession rates of such bodies are very fast compared to the outer planet, so that the variation of ω' can be considered as an adiabatic process (the orbit passes smoothly from one fixed value of ω' to the other, as long as no major change of topology occurs). However, we will not restrict the study to that region: in return, comparisons with the full secular system will be realised for typical trajectories all along the study.

With the arbitrary use of $\nu'_\omega = 0$, the secular system defined by (5.11) has only two degrees of freedom:

$$\mathcal{F}(G, H, g, \delta h) = -\nu'_\Omega H + \mathcal{F}_1(G, H, g, \delta h) \tag{5.22}$$

and two parameters (a and ω'). Once again, the dynamics can be explored using Poincaré sections. The second angle is this time $\delta h = \Omega - \Omega'$, so one must be careful when comparing with the results from Sect. 5.3. However, if ω' is fixed, Ω' behaves exactly like ϖ', so we can safely identify and link the features from the two cases (equilibrium points, resonances...). In the following, the constant ω' is chosen to its nominal current value given in Tab. 5.1.

Figure 5.12, computed for $a = 70$ AU, shows that even for small semi-major axes, the breaking of symmetry induced by the inclination of the distant perturber produces a richer dynamics, with numerous additional resonances. In the panel **b**, the two fixed points due to the resonance $\omega + \delta h$ correspond to an alignment between the apsidal line of the small body and the *nodes* line of the distant planet[10]. Hence, the orbital configuration is pretty different from what we obtain for a planar perturber (Fig. 5.4), although the same resonance is involved. Moreover, there are this time two fixed points (alignment and anti-alignment) instead of a single one. This holds also for the resonance $\omega - \delta h$ on the panel **d**. Numerical integrations of the full three-degree-of-freedom secular system reveal that all the libration islands present in Fig. 5.12 persist for a precessing ω'. These maps are thus representative of the complete system. Some resonances change critical argument (for instance, $\omega - 2\delta h$ turns to $\omega - 2\delta h + \omega'$), but not the 1:1 one. One

[10] On the contrary, apsidal alignment or anti-alignment would have resulted in fixed points on the sections at $\omega' \pm \pi/2$, where ω' is given in Tab. 5.1.

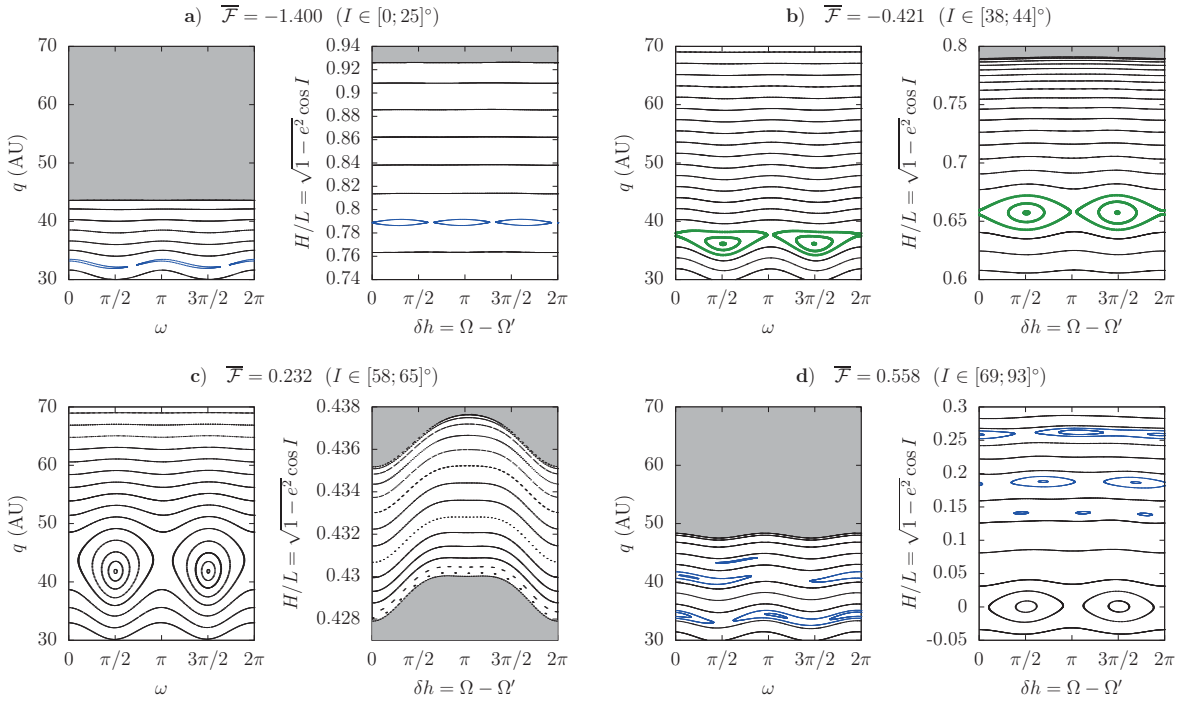

Figure 5.12 – Poincaré maps for an inclined perturber. The constant semi-major axis of the particle is $a = 70$ AU. Every section in the (ω, q) plane is made for $\delta h = \pi/2$ and $\dot{\delta h} < 0$. Every section in the $(\delta h, H)$ plane is made for $\omega = \pi/2$, with $\dot{\omega} > 0$ for (**a**,**b**) and $\dot{\omega} < 0$ for (**c**,**d**). The panel **a** features the resonance $2\omega + 3\delta h$. The panels **b** and **d** feature the resonances $\omega + \delta h$ and $\omega - \delta h$, respectively, with two different fixed points and horseshoe-type orbits. In the panel **d**, the resonances $\omega - 2\delta h$ and $\omega - 3\delta h$ are also visible.

can argue that a resonance with critical angle $\omega + \delta h = \varpi - \Omega'$ violates the D'Alembert rules, but as explained below, this resonance is not an artefact due to the fixity of ω'. Actually, the system departs from the three-body problem by its inner component, so one should not be surprised if some "unusual" resonances show up.

For $a = 100$ AU, a lot of resonances occupy the entire range of inclinations from 0° to 90° (Fig. 5.13). As seen in the panel **e**, the chaotic zone around the two fixed points of ω is much larger than for a planar perturber (Fig. 5.5), allowing large excursions of the perihelion distance. In the panel **a**, the resonance $\omega + 2\delta h$ is visible near the zero-inclination limit. It appears also in the panel **b**, near the circular orbit, taking the place of the island of apsidal alignment for a planar perturber (compare with Figs. 5.5 and 5.6). For a precessing ω', this resonance appears to become $\omega + 2\delta h - \omega' = \Delta\varpi + \Delta\Omega$, oscillating around π. Hence, the apsidal alignment $\Delta\varpi = 0$, reported by Beust (2016) and present for a planar perturber, does not persist (as such) if the perturber is itself inclined.

This is confirmed for larger semi-major axes, since Fig. 5.15, plotted for $a = 150$ AU, shows the same 1:2 resonance (panels **a** and **b**). In the panel **d**, only the right oscillation

island of ω is visible (at $q \approx 140$ AU); the other one is submerged by the chaotic sea. This asymmetry is due to the arbitrary fixed value of ω'. Still in the panel **d**, the red points form somewhat organised structures around the $3:1$ resonance, due to sticky chaos. Such trajectories evolve in a complex structure of secondary resonances: Fig. 5.14 presents an example of resonant trajectory in that region, and it is indeed very tortuous. The chaos spreads much faster than for a planar perturber, allowing flips between prograde and retrograde orbits (panel **f**) even for a as small as 150 AU (compare with Fig. 5.6 and 5.7).

For $a = 200$ AU, the chaos fills almost all the phase space (Fig. 5.17). The $\omega + 2\delta h$ resonance is still present near the zero-inclination limit (panel **a**) and the circular orbit (panel **b**). The classic equilibrium points for ω are almost entirely submerged by the chaotic sea: we found only one quasi-periodic orbit related to oscillations of ω, visible in the panel **e** (tiny blue points). Fig. 5.16 presents this trajectory in details and one can verify that it stays indeed near $I \approx 63°$. In that very perturbed case, the sizes of the stability islands do not give any idea of the variations of the orbital elements themselves. In that example, the excursion of the perihelion distance is actually very large, from about 30 to 180 AU. Eventually, the only feature still widely emerged in Fig. 5.17 is the $1:1$ resonance between ω and δh (panels **b** and **c**). The panel **d** is drawn for a Hamiltonian value slightly larger than for the panel **c**, showing the dissolution of the $1:1$ resonance in chaos. Once again, the finite number of points allows to distinguish structures in the chaotic region, and in particular the general shape of $1:1$ resonance island. Its signature thus persists, but in the form of sticky chaos. We found similar results in the case of a planar perturber (Fig. 5.7, panels **d**-**e**).

For semi-major axes larger than 200 AU, our simplified model becomes less relevant and its efficiency to describe the complete system is questionable. Moreover, the exploration of a very chaotic system by the means of Poincaré sections is cumbersome, since there is no guaranty that a stable volume of the phase space does not lie out of the chosen sections. The relevance of the model with $\nu'_\omega = 0$ can be assessed by tracking some well-chosen trajectories for increasing values of the semi-major axis. Figures 5.18 and 5.19 present numerical integrations of the complete three-degree-of-freedom system using initial conditions given by trajectories trapped in the $1:1$ resonance in the simplified model. The model with $\nu'_\omega = 0$ proves to be qualitatively relevant from $a = 70$ to 150 AU, since the orbital configuration is conserved (alignment between the apsidal line of the small body and the nodes line of the distant planet). The precession of ω' adds only extra periodic terms with small amplitudes. For larger semi-major axes, the forcing frequency results in jumps of ϖ from one node of the distant planet to the other ($\varpi - \Omega' = 0$ or π). In that example, these jumps produce an overall *apsidal* alignment, even if the *nodes* were concerned in the first place. This proves that a model with $\nu'_\omega = 0$ could be misleading for higher semi-major axes (an extended numerical analysis of the complete secular system would be required, loosing the vantage of a semi-analytical method).

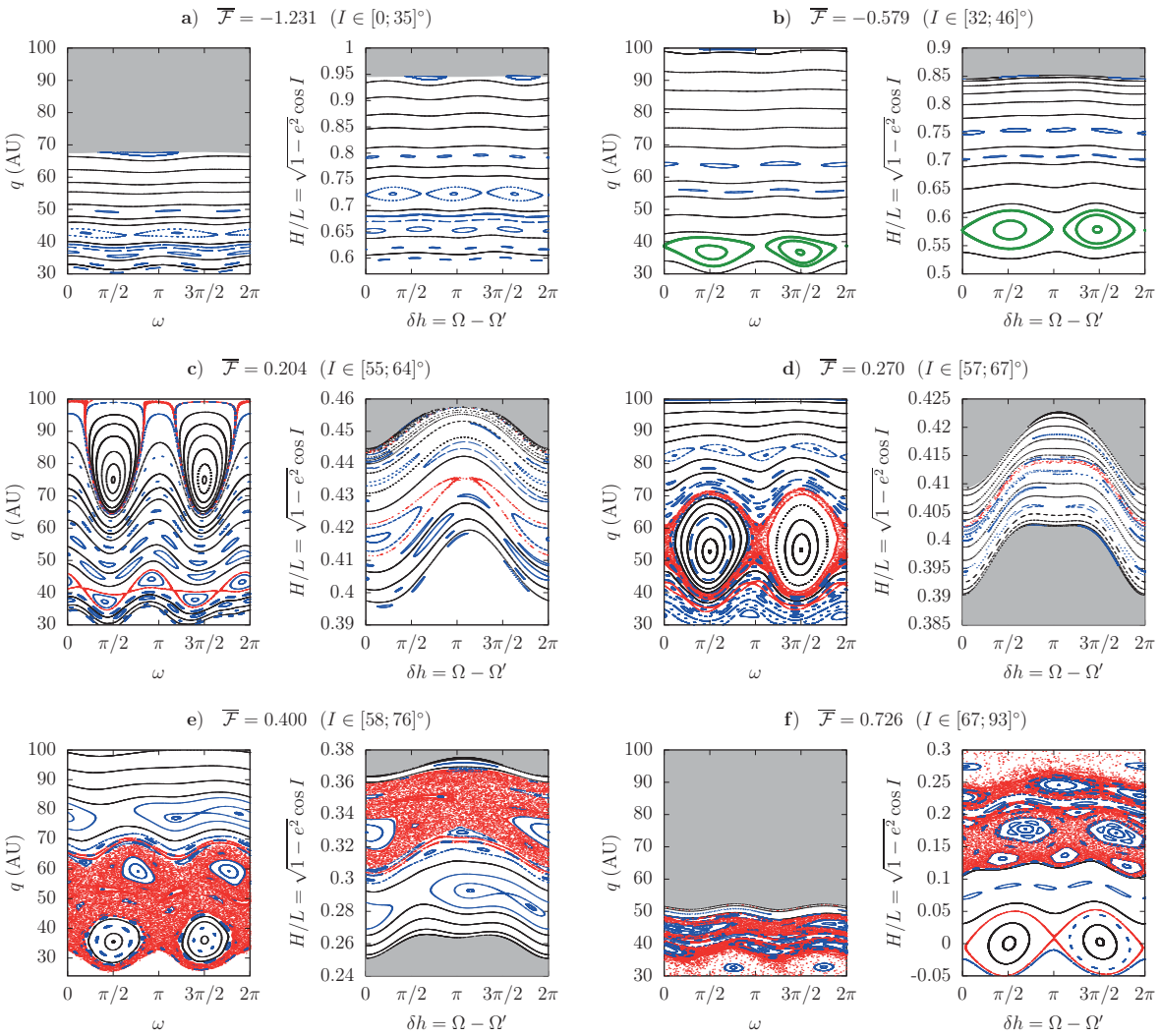

Figure 5.13 – Poincaré maps for an inclined perturber. The constant semi-major axis of the particle is $a = 100$ AU. Every section in the (ω, q) plane is made for $\delta h = \pi/2$ and $\dot{\delta h} < 0$. Every section in the $(\delta h, H)$ plane is made for $\omega = \pi/2$, with $\dot{\omega} > 0$ for (**a**,**b**,**c**) and $\dot{\omega} < 0$ for (**d**,**e**,**f**). The panels (**c**,**d**,**e**) show the shift of the fixed points for ω at $I \approx 63^\circ$ for nearby Hamiltonian values. The surrounding chaotic sea is very wide when the islands are near the semi-major axis of Neptune (panel **e**). Resonances between ω and δh are very numerous at all ranges of inclination. In the panels **e** and **f**, a zoom-in view reveals a very complex pattern of secondary resonances spreading in a fractal-like way.

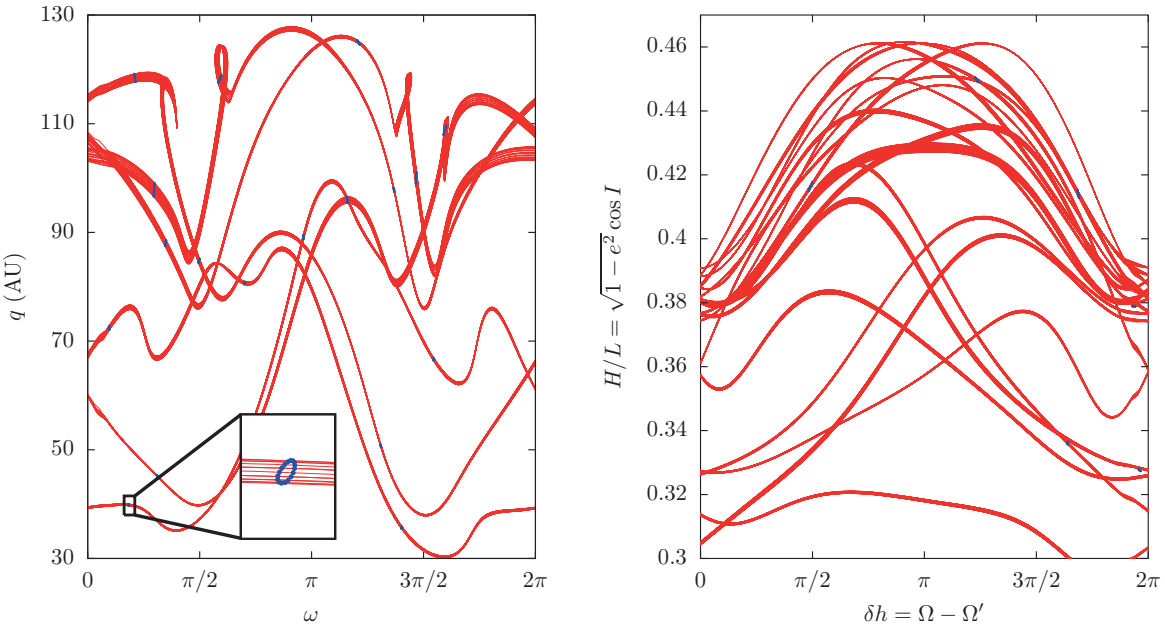

Figure 5.14 – Complete trajectory producing the blue spots in the panel **d** of Fig. 5.15 ($a = 150$ AU). This is a quasi-periodic orbit featuring the secondary resonance 6:1 between the circulation frequency of ω and the libration frequency of the resonant angle $3\omega + \delta h$. On each graph, blue points are added when the trajectory crosses the sections (same as Fig. 5.15). On the left, an enlargement shows the classic rounded shape formed by the section crossing points around the periodic trajectory. According to the resonance involved, the fixed points are 18 on the left and 6 on the right.

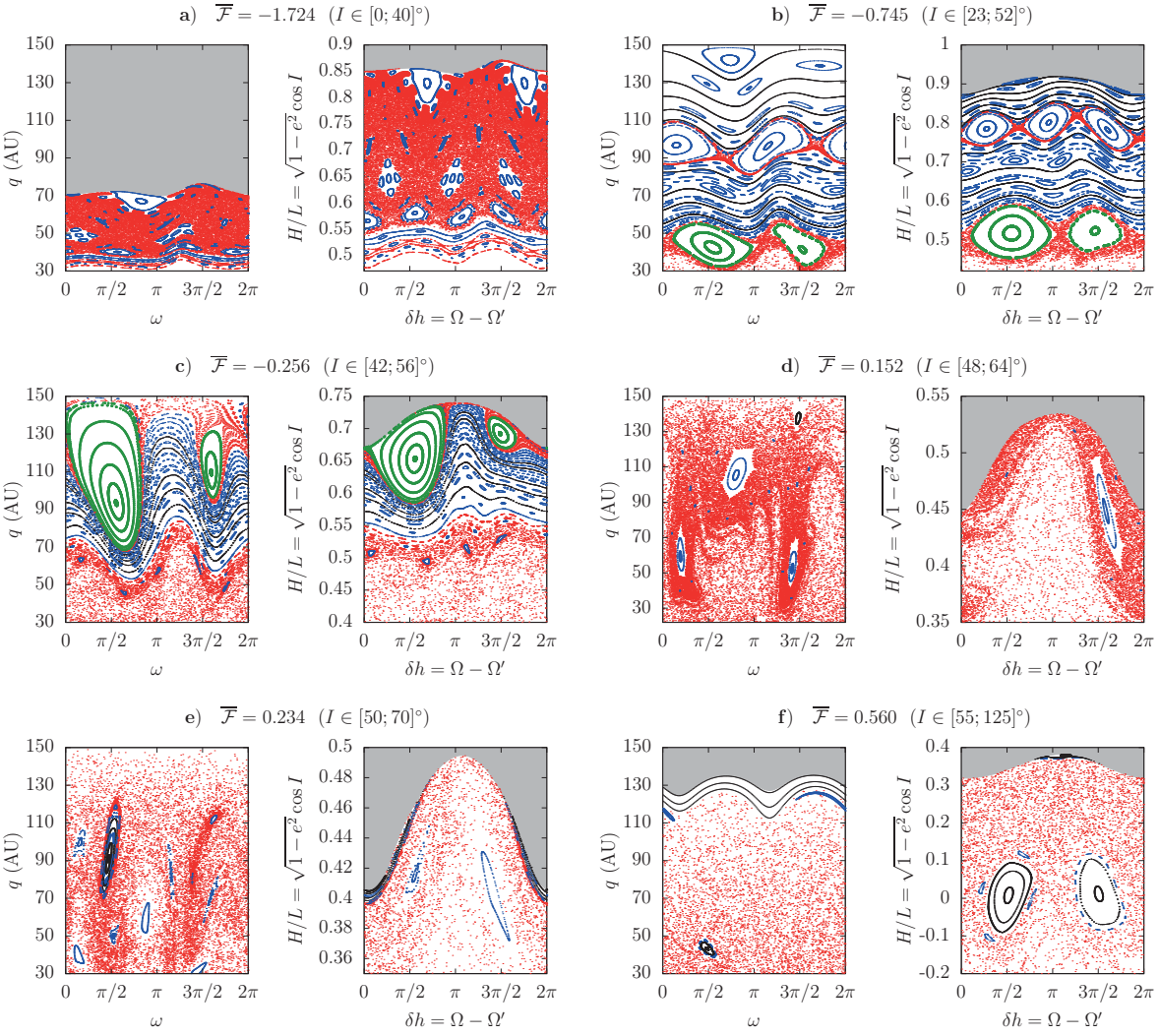

Figure 5.15 – Poincaré maps for an inclined perturber. The constant semi-major axis of the particle is $a = 150$ AU. Every section in the (ω, q) plane is made for $\delta h = \pi/2$ and $\dot{\delta h} < 0$. Every section in the $(\delta h, H)$ plane is made for $\omega = \pi/2$, with $\dot{\omega} > 0$ for (**a**,**b**,**c**,**d**,**e**) and $\dot{\omega} < 0$ for **f**.

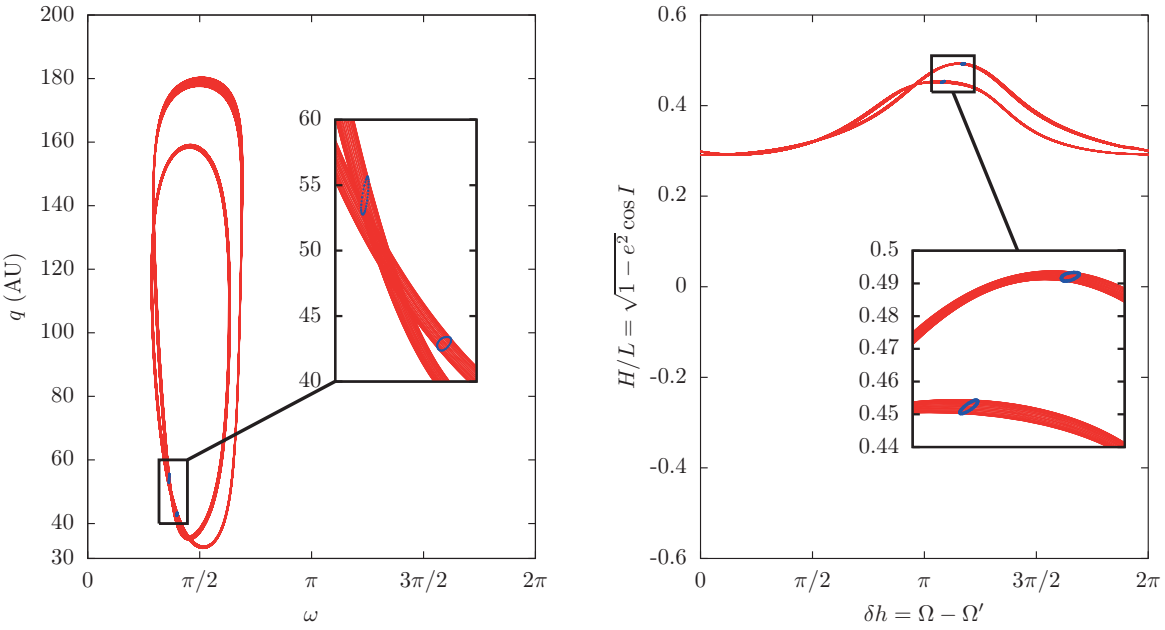

Figure 5.16 – Complete trajectory producing the tiny blue points in the panel **e** of Fig. 5.17 (a = 200 AU). This is a quasi-periodic orbit featuring the secondary resonance $2:1$ between $\dot{\delta h}$ and the libration frequency of the resonant angle $1:1$ between $\dot{\delta h}$ and the libration frequency of ω. On each graph, blue points are added when the trajectory crosses the sections (same as Fig. 5.17). Enlarged views show the classic rounded shapes formed by the section crossing points around the periodic trajectory. According to the resonance involved, the fixed points are 2 on both sides.

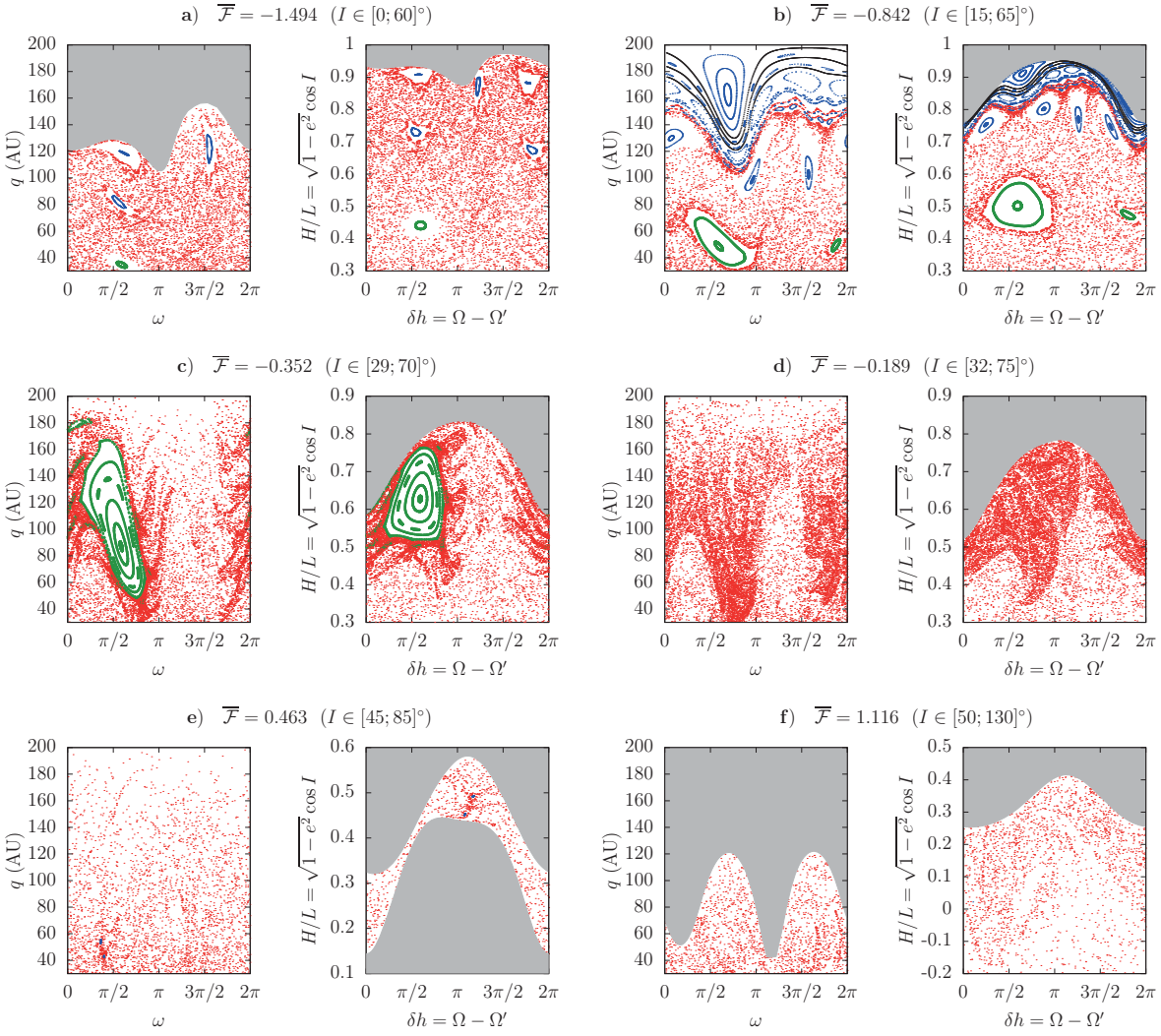

Figure 5.17 – Poincaré maps for an inclined perturber. The constant semi-major axis of the particle is $a = 200$ AU. Every section in the (ω, q) plane is made for $\delta h = \pi/2$ and $\dot{\delta h} < 0$. Every section in the $(\delta h, H)$ plane is made for $\omega = \pi/2$, with $\dot{\omega} > 0$ for (**a**,**b**,**c**,**d**) and $\dot{\omega} < 0$ for (**e**,**f**).

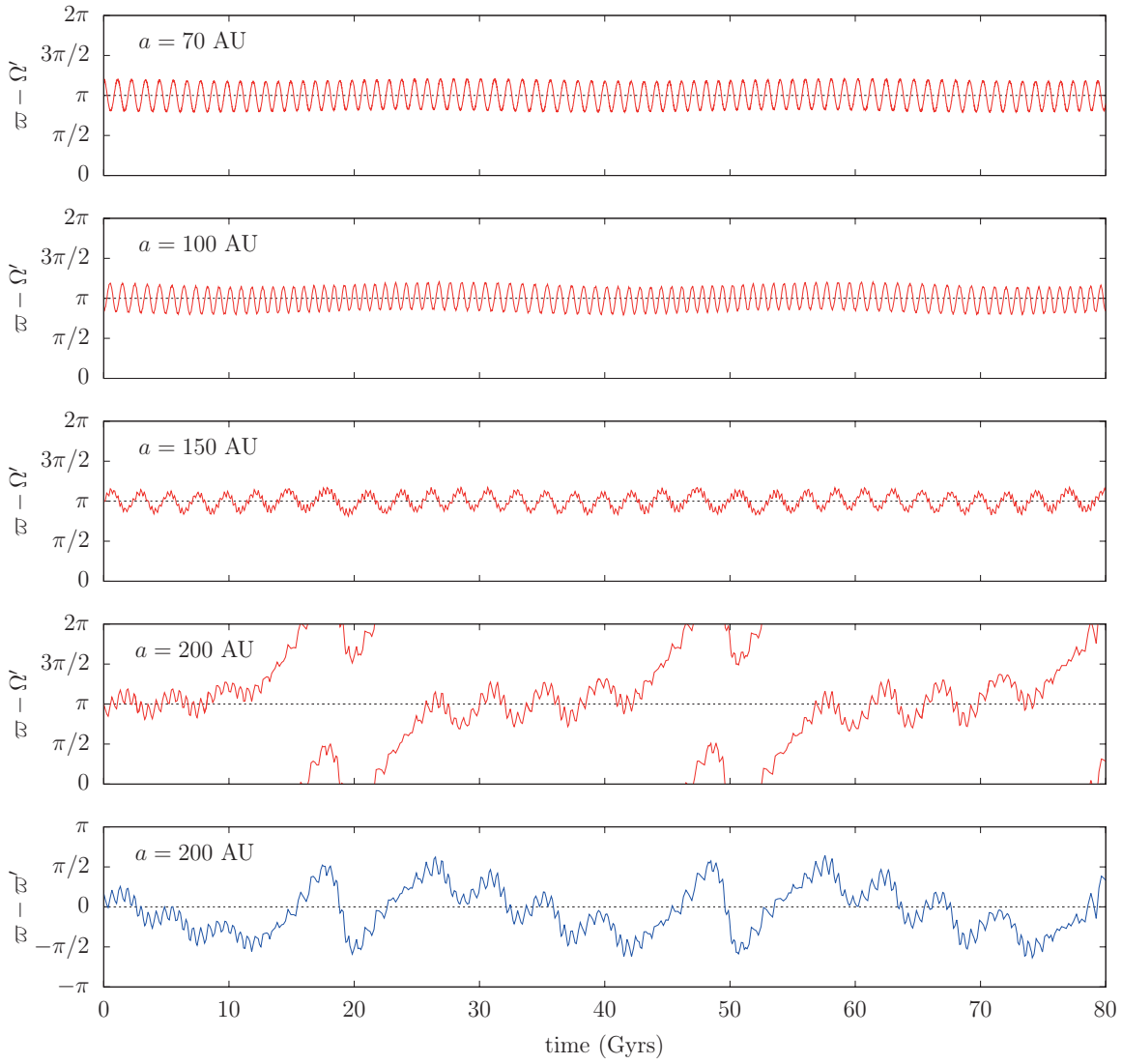

Figure 5.18 – Numerical integrations of the full three-degree-of-freedom secular system. The initial conditions are taken in the 1:1 resonance island of the simplified model (inside the left green trajectory in the panel **b** of Figs. 5.12, 5.13, 5.15 and 5.17). The time evolution of q and I are presented in Fig. 5.19. The new frequency is clearly visible (modulation on a ~ 31 Gyrs time span, which is the rotation period of ω'). The alignment persists for small semi-major axes ($\varpi - \Omega' \approx \pi$) but is broken beyond some value: for $a = 200$ AU, $\varpi - \Omega'$ jumps between 0 and π with the forcing frequency. The lowermost graph, presenting the same trajectory, shows that these jumps produce an overall apsidal alignment ($\Delta\varpi \approx 0$).

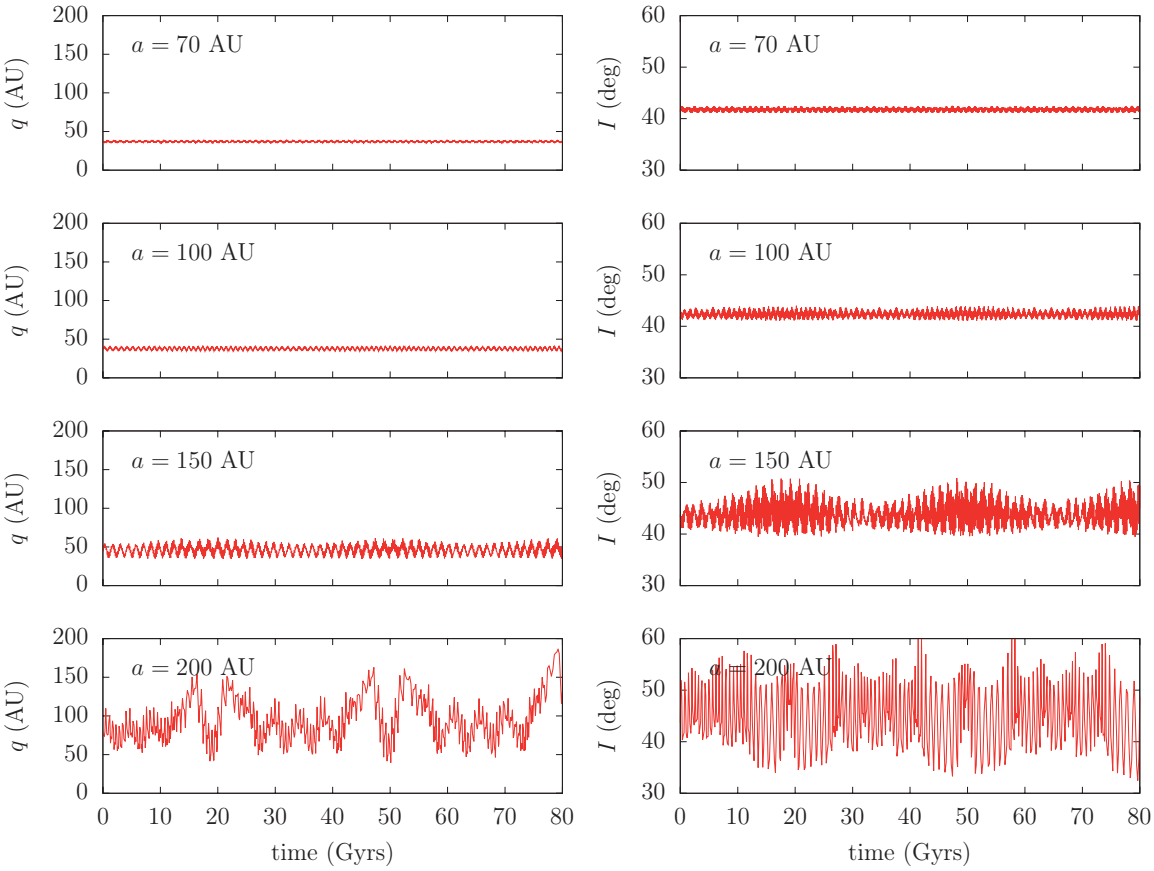

Figure 5.19 – Time evolution of the perihelion distance and of the inclination for the trajectories of Fig. 5.18.

5.5 Summary of the secular dynamics

For an eccentric planar perturber, the $\Delta\varpi$ resonances reported by Beust (2016) are smoothly transported toward non-zero inclinations, both in the aligned and anti-aligned configurations. They are created through ω and Ω circulating in opposite directions. Another island of apsidal alignment is highlighted, restricted to inclined orbits, and it has a pretty wide extension for $a > 150$ AU. Finally, very particular stable configurations exist from $a \approx 200$ to 300 AU, in which *both* ω and $\Omega - \varpi'$ oscillate around 0 or π, and I oscillates around 90°. These orbits are aligned or anti-aligned with the distant planet and perpendicular to the planetary plane. They are probably related to the high-inclination aligned population produced in the numerical experiments by Brown and Batygin (2016). For higher semi-major axes, these configurations lead the perihelion of the particle inside the inner planetary region, where the successive orbit crossings make them unstable. In addition, the classic equilibrium points of ω at $\pi/2$ and $3\pi/2$ (for $I \approx 63°$) are the source of a chaotic region, spreading all over the phase space when a increases. For $a > 300$ AU, the $\Delta\varpi$ resonances are the only remaining stable features, and the chaotic trajectories jump from one of them to the other. Hence, even if there are only small regular regions left beyond $a \sim 300$ AU, the signature of the apsidal alignments and anti-alignments largely remains in the form of sticky chaos. This contributes probably to a large extent to the aligned bodies coming from the simulations by Batygin and Brown (2016a).

The model with an inclined perturber with a fixed argument of perihelion, even if not strictly realistic, gives an idea of the secular dynamics in the general case. As expected, the chaos spreads faster than for a planar perturber. In the unsimplified secular system, the extra forcing frequency adds even more chaos in the system: in practice, the distant perturber can be neglected only for very small semi-major axes (say below 70 AU). For $a = 150$ AU already, only a small portion of the phase space is still filled with regular trajectories and large orbital flips become possible (switch between prograde and retrograde orbits). An inclined distant perturber should thus imply a substantial amount of retrograde objects with $a > 150$ AU, without even mentioning close encounters. Such objects are indeed observed, as reported by Batygin and Brown (2016b), even though none has been observed yet with a perihelion beyond the semi-major axis of Neptune. As before, the 1:1 resonance between the two degrees of freedom is the most persistent structure. For small semi-major axes (say below 150 AU), it results in an unusual alignment between the apsidal line of the small body and the nodes line of the distant planet. In a large sample, though, the signature of this configuration is probably unnoticeable, mixed up with the numerous other features.

Chapter 6

Discussion and future work

In this chapter, we summarise our approach, results and conclusions about the long-term orbital dynamics beyond Neptune. Some ideas of future work are also introduced in order to address complementary problems or issues directly raised by our results. In Sect. 6.1, the one-degree-of-freedom secular models developed throughout this work are recalled, along with their application field, their main vantages and their limits. Then, the exploration of the resonant model is exposed in Sect. 6.2 and its application to known objects is addressed in Sect. 6.3. Finally, the effects of an additional distant planet on the non-resonant dynamics are summed up in Sect. 6.4.

6.1 Secular models for the orbital dynamics beyond Neptune

At first, the dynamics beyond Neptune driven only by the known planets was studied. Considering an integrable (or quasi-integrable) short-term behaviour, the long-term dynamics can be efficiently described by a one-degree-of-freedom model with two free parameters. The approximations used are found to be relevant for semi-major axes larger than 50 AU. This method allows to visualise the long-term trajectories of the particles in the plane (ω, q), in which the notable features (equilibrium points, libration islands, separatrices) can be located. It can thus be used to explore all the possible trajectories allowed by the system. In particular, that method proves to be particularly suitable to detect large perihelion excursions.

Such a model is easily obtained when there is no mean-motion resonance in the system: the two parameters are then a and $C_K = (1 - e^2)\cos^2 I$. For a non-resonant dynamics, we showed that the maximum perihelion excursion possible is 16.4 AU, attainable on a Giga-year timescale for high semi-major axis and a very specific inclination (near 63° or 117°). A small body starting with a perihelion near the orbit of Neptune and in the required range of inclination can thus reach rather high perihelion distances from the planets, especially if it has undergone a prior diffusive process. That mechanism, though, cannot explain very large perihelion distances as the ones revealed by

numerical integrations.

When there is a mean-motion resonance between the body and one of the planets, the adiabatic invariance theory allows to construct a "resonant secular model". The two fixed parameters are then η_0 (a surrogate of C_K) and the area $2\pi J$ enclosed by the resonant canonical coordinates. The only obstruction to a fully integrable representation comes then from a possible extreme narrowing of the resonance island, which can make circulate the resonant angle (separatrix crossing). In such a case, the secular representation is possible only by parts, each of them with a different parameter J. Such transitions can happen frequently for the resonances of type $1:k$, even for enclosed areas equal to zero, because of the pure disappearance of the occupied resonance island. For a specific trajectory, these repeated changes of behaviour are an evident source of long-term chaos and make somehow questionable the use of a secular model. It remains though very effective as a general tool, to locate the secular equilibrium points and distinguish in a glance the regular trajectories from the "segmented" ones.

6.2 The long-term resonant dynamics

Using the resonant secular model, it was straightforward to bring out trajectories with very large perihelion variations (for instance from 30 to 80 AU). Such extreme values were usually considered too high to be reached by the means of perturbations from the known planets. Moreover, that kind of trajectory is not restricted to high-inclination regimes as in the non-resonant case: a low perihelion trajectory lying near the ecliptic can be smoothly turned into a high-perihelion and high-inclination orbit. The general geometry of the phase portraits depends very little on the resonance order (that is on the reference semi-major axis a_0 of the resonance $k_p:k$) but it is function of its coefficient k_p. Indeed, the very same level curves can be obtained for very different values of a_0 providing that the parameter η_0 is modified accordingly (smaller η_0 for higher a_0). The resonances with $k_p = 1$ are the only ones to present wide regions with two resonance islands. For prograde orbits of this type, there is a clear limit in perihelion distance beyond which there remains only one resonance island. We refer to that limit as the "secular discontinuity line".

The resonant secular model highlights a dynamical path from low inclinations and a perihelion near Neptune to a quasi-integrable high-perihelion state with long-term stability. That mechanism is directly linked to the secular discontinuity line, so it is specific to resonances with $k_p = 1$. Indeed, the crossing of the secular discontinuity line can trigger a very stable resonant behaviour, where the particle alternates smoothly from high-amplitude oscillations inside the single island (when beyond the line) to horseshoe oscillations (when below it). In that way, there is no more discontinuity and J can be conserved indefinitely. As the final area $|2\pi J|$ is large, q is almost constant and ω circulates. Thanks to the large value of q, the final orbit is stable despite the high-amplitude oscillations of the resonant angle (no diffusion of semi-major axis). The very long-term stability of that "reservoir" implies that its population should be increasing

since the formation of the planetary system. We estimated its size by the means of the semi-analytical model: it lies approximately in $a \in [100; 300]$ AU, $q \in [50; 70]$ AU and $I \in [30; 50]^\circ$ (with circulating angles ω and Ω). Indeed, it happens to be the end-state of an appreciable number of objects in numerical simulations of trans-Neptunian objects.

Along this study, we considered only resonances of "type eccentricity", because they are the most frequent for the observed and simulated trans-Neptunian objects. For highly inclined objects, however, other types of resonances could be considered (types "inclination" of "mixed"). Similar secular models, also based on the adiabatic approximation, could be developed and used to explore the long-term dynamics driven by such resonances. This could be interesting not only for trans-Neptunian objects, but also for mutually-interacting satellite systems.

6.3 Application to known objects

The application to the known resonant trans-Neptunian objects is also very informative, since it gives a precise idea of what type of trajectory they can follow. This allows us to distinguish which orbits can have been created by a resonant link with Neptune on its current orbit, and which ones have a more complex history (involving the planetary migration or another source of perturbation). According to the secular model, most of the known resonant objects experience virtually no change of perihelion distance, indicating a small influence of the resonance on their long-term dynamics. Indeed, the resonant link can never bring them away from their capture configurations, resulting in unstable transient resonances. On the other hand, four objects are located near notable features of the phase portraits:

- Locked in the 2:5 resonance, 135571 evolves very close to secular libration islands and shows a retrograde (or possibly oscillatory) evolution of ω.
- In the same resonance, $2004\,\mathrm{KZ}_{18}$ is located near the centre of a libration island at $\omega = 0$ (a perfect secular evolution would produce very small oscillations of ω around 0).
- The object 82075 (3 : 8 resonance) shows oscillations of the perihelion distance from 38 to 44 AU (with circulating ω).
- In the more distant 1 : 6 resonance, $2008\,\mathrm{ST}_{291}$ evolves in a wide asymmetric libration island centred at $\omega \approx 117^\mathrm{o}$, resulting in oscillations of q from 39 to 55 AU.

The cases of $2015\,\mathrm{FJ}_{345}$ and $2014\,\mathrm{FZ}_{71}$ are more complicated, since they follow secular trajectories leading to separatrix crossings. Following the level curves backwards, possible scenarios can be retraced from their capture into resonance to their current positions. They require one or more resonant transitions (passage from one resonance island to the other) and originate at much smaller perihelion distances.

As already stated in previous studies, a resonant interaction with Neptune is found unable to explain the current orbits of Sedna and $2012\,VP_{113}$. However, the majority of the observed objects (resonant or not) with $a > 100$ AU and $q > 30$ AU, are located inside the range of parameters that would allow strong variations of their orbital elements in case of mean-motion resonance. This is however unable to explain an accumulation of objects as the one invoked recently to postulate the existence of a ninth planet in the Solar System. Indeed, for small perihelion distances (say < 40 AU), the equilibrium points are all located at $\omega = 0 \mod \pi$ whatever the resonance considered: this could not favour $\omega = 0$ against π, or produce any preferential location for Ω. Such features, if they are really significant in the observed distribution of the trans-Neptunian objects, would require an asymmetric perturbation. It could be an additional eccentric distant planet (Batygin and Brown, 2016a) or the memory of a captured population from another star (Jílková et al., 2015). In the first case, one-degree-of-freedom secular models cannot be obtain for the distant trans-Neptunian objects. In the second case, they can be used to describe the current dynamics of these objects, now that the perturber has gone.

6.4 Secular dynamics with a distant perturber

In the presence of an external ten-earth-mass perturber having a substantial eccentricity, a secular model can still be defined, but it has at least two degrees of freedom. Indeed, the secular non-resonant dynamics is analogous to an "eccentric-Kozai" mechanism but with both an inner component (the four giant planets) and an outer one (the eccentric distant perturber). By the means of Poincaré sections, the cases of a non-inclined or inclined outer planet were successively studied, making the connection with previous works. In the inclined case, the problem was reduced to two degrees of freedom by assuming a non-precessing argument of perihelion for the perturbing body. A special attention was given to prograde orbits with perihelion distances beyond Neptune. Classically, the equilibrium points of ω at $I \approx 63^\circ$ or 117° divide the regions where ω circulates toward the right and toward the left. The analogous limit for Ω is $I = 90^\circ$. This puts some constraints on the regions sensible to a confinement of ϖ in the weakly perturbed case, only possible when ω and Ω circulate in opposite directions ($I \in [0; 63]^\circ$ or $I \in [90; 117]^\circ$).

The size of the external perturbation is typically ruled by the semi-major axis of the small body: the classic integrable picture is still valid below about 70 AU, but it is progressively destroyed when we get closer to the external perturber. In particular, for $a > 150$ AU, large-amplitude orbital flips become possible, and for $a > 200$ AU, the Kozai libration islands at $\omega = \pi/2$ and $3\pi/2$ are totally submerged by the chaotic sea. Numerous secular resonances are highlighted. The most large and persistent ones are associated to apsidal alignments or anti-alignments with the orbit of the distant perturber. A non-resonant secular dynamics produces two kinds of stable aligned or anti-aligned orbits: the ones with a small inclination (for which ω and Ω circulate in

opposite directions), and the ones with an inclination near 90° (for which ω and Ω are both fixed to 0 or π, producing "frozen" orbits).

Despite the existence of numerous stable orbits, the secular dynamics at high semi-major axes is largely dominated by chaos. We conclude that even in the secular system, which is free from any diffusion of semi-major axis, the orbital alignment of distant objects (as well as any organised structure beyond $a \sim 200$ AU) induced by a distant perturber are almost only produced through a collective behaviour of chaotic trajectories, each of them spending more time in preferred locations of the phase space but still wandering "everywhere". In particular, this is the case of the six objects with $a > 250$ AU analysed by Batygin and Brown (2016a) and gathered in Tab. 5.2. Hence, the fact that the seemingly clustered objects do not remain efficiently shepherded in long-term numerical simulations is not a sufficient argument to rule out the hypothesis of an external perturber in the Solar System, neither the discovery of distant bodies *out* of the accumulation regions. For instance, the recently discovered trans-Neptunian object $2015\,\mathrm{GT}_{50}$ (Bannister et al., 2017) is neither aligned nor anti-aligned: according to the MPC database, in this case $\Delta\varpi \approx 272°$ using for the distant perturber the data of Tab. 5.1. Here, the only viable approach is to deal with distributions, which should be peaked or not around preferential configurations. Whereas it would be simple (in theory) to confirm the existence of a distant planet by direct observation, to exclude it requires the analysis of a large observational sample, pretty hard to obtain.

This study was limited to secular orbits away from mean-motion resonances with the planets. Mean-motion resonances are a well-known source of orbital confinements, and they are likely to allow a lot of stable configurations. However, particles with slowly diffusing semi-major axes, even with successive transient captures in various mean-motion resonances, would present in overall the signature of a *non-resonant* secular dynamics (see for instance Fig. 3.5). Hence, in order to allow specific confinements, such resonance trappings must be long enough. Since a long-term resonant interaction with Neptune cannot confine ω in a manner that fits the orbital distribution of the observed distant objects, the mean-motion resonances involved should be with the hypothetical distant planet. An averaged model in the resonant case could also be developed (by taking advantage of the separation between the timescales involved), but the corresponding Poincaré maps are expected to be extremely rich and probably difficult to interpret.

Appendix A

The frequency analysis

Most of the work presented in this chapter was realised for my Master thesis, however, the program developed in this occasion was reused during my Ph.D. in a published paper (Renner et al., 2016), so I summarise it here.

The frequency analysis method of J. Laskar was first introduced in Laskar (1988, 1990). Section A.1 recalls the basics of it and details some theoretical and practical aspects about its implementation. See Laskar (2005) for thorough details and proofs about its application to quasi-periodic trajectories. Section A.2 presents the use of the frequency analysis in the context of the orbital dynamics of Atlas, a natural satellite of Saturn.

A.1 Theoretical context and method

In Sect. 2.2.5, we introduced the action-angle coordinates. Let us consider a Hamiltonian system with n degrees of freedom, represented by the Hamiltonian function $\mathcal{H}$. If it is integrable (and under certain conditions), we are assured that action-angle coordinates $(J, \theta) \in \mathbb{R}^n \times \mathbb{T}^n$ exist, but we do not known the change of coordinates leading to them (this is all the difficulty of analytical theories). However, the action-angle coordinates are *intrinsic* to the system, such that even if the system is written in other coordinates, the latter still evolve with the *proper frequencies* $\{\omega_j\}_{j=1,2...n}$ (which are the constant circulation frequencies of the angles $\{\theta_j\}_{j=1,2...n}$). The proper frequencies are not uniquely defined: any integer combination of some $\{\omega_j\}$ can be chosen also as a proper frequency.

Let $f(t)$ be a real function of the time, representing any dynamical variable describing the system. The previous property allows to write it as a multidimensional Fourier series of θ:

$$f(t) = \sum_{\mathbf{h} \in \mathbb{Z}^n} a_h \exp i\, \mathbf{h} \cdot \theta(t) \qquad , \quad a_h \in \mathbb{C} \tag{A.1}$$

By developing the scalar products $\mathbf{h} \cdot \theta(t)$, we get a series of the form:

$$f(t) = \sum_{k \in \mathbb{N}} A_k \exp i\nu_k t \qquad , \quad A_k \in \mathbb{C} \tag{A.2}$$

in which the $\{\nu_k\}$ are integer combinations of the proper frequencies $\{\omega_j\}_{j=1,2...n}$. Now, let us suppose that we know a solution $f(t)$ of the dynamics (for instance, coming from a numerical integration). Then, the *frequency analysis* of J. Laskar, presented below, allows to determine numerically the amplitudes $\{A_k\}$ along with the corresponding frequencies $\{\nu_k\}$ of the Fourier development of $f(t)$. By identifying each ν_k as an integer combination of fixed frequencies, we finally get the proper frequencies of the system. If the system is not degenerated, that is if:

$$\det\left(\frac{\partial\omega(J)}{\partial J}\right) = \det\left(\frac{\partial^2\mathcal{H}(J)}{\partial J^2}\right) \neq 0 \tag{A.3}$$

then the application $J \mapsto \omega(J)$ is a diffeomorphism, so the system can be described equivalently by its proper frequencies ω or by the actions J (see Arnold, 1989). The dynamics is thus entirely characterised. Numerically-computed series of the type (A.1) form a so-called *synthetic representation*: they have the form and the regularity of an analytical theory, but all the coefficients and frequencies were obtained numerically.

If the system is not integrable, of course, a Fourier series of the form (A.1) is not defined anymore. If the system is not too far from being integrable, though, a frequency analysis could still provide a set of frequencies and amplitudes but they would result only in an approximation of the real dynamics, more or less accurate according to the degree of chaos. In practice, such frequencies are not constant (they are not "proper"), and their rates of variation allow to quantify the degree of stability of the system (see Laskar, 1990).

A.1.1 Fine analysis

We aim at reconstructing numerically a quasi-periodic function $f(t)$ from a series of its values on the interval[1] $[0, T]$. It consists thus in determining the different frequencies contained in f and the corresponding complex amplitudes. Let us consider a general quasi-periodic function of the form:

$$f(t) = \sum_{k=1}^{N} A_k\, \mathrm{e}_k(t) \qquad \text{where} \quad A_k \in \mathbb{C} \;\text{ and }\; \mathrm{e}_k(t) \equiv \exp(i\nu_k t) \tag{A.4}$$

Its Fourier series on $[0, T]$ is defined by:

$$\hat{f}(t) = \sum_{n=-\infty}^{+\infty} \langle f, v_n\rangle\, v_n(t) \qquad \text{with} \;\; v_n(t) = \exp(i\, n\nu_0\, t) \;\text{ and }\; \nu_0 = \frac{2\pi}{T} \tag{A.5}$$

$\hat{f}(t)$ is thus the projection of $f(t)$ on the vector space generated by the vectors $\{v_n\}_{n\in\mathbb{Z}}$, with the scalar product:

$$\langle f, g\rangle = \frac{1}{T}\int_0^T f(t)\overline{g(t)}\,\mathrm{d}t \tag{A.6}$$

[1] Laskar (2005) defines this interval as $[-T, T]$, which is only a matter of convention.

In practice, the integral will be computed numerically by the method of Hardy (see appendix C.6), considering that $f(t)$ is stored with a small-enough step size to neglect the numerical errors and the *aliasing*[2]. One can note that if the frequencies $\{\nu_k\}_{k=1,2..N}$ are not integer multiples of ν_0, then $\hat{f}(t)$ will be a very poor representation of $f(t)$, in which the frequencies are only obtained at the ν_0 level of precision. Actually, we can obtain a much better precision of the frequencies by studying the variations of the "amplitude function" defined by:

$$\mathcal{A}(\nu) = \big\langle f\,,\, \exp(i\nu t)\big\rangle \tag{A.7}$$

Indeed, if $f(t)$ is made of only one oscillating term, we get:

$$\Big|\mathcal{A}(\nu)\Big| = \Big|\big\langle A_1 \exp(i\nu_1 t)\,,\, \exp(i\nu t)\big\rangle\Big| = \left|A_1 \frac{\sin\big[(\nu_1-\nu)T/2\big]}{(\nu_1-\nu)T/2}\right| \tag{A.8}$$

This function reaches its maximum when ν is equal to the exact value of ν_1, and we have besides the equality $\mathcal{A}(\nu_1) = A_1$ (Fig. A.1**a**). The determination of ν_1 simply amounts to find the maximum of the function $|\mathcal{A}(\nu)|$. Practically, a preliminary Fast Fourier Transform allows to locate roughly the maximum, then an algorithm using a quadratic interpolation can be used for the fine search (see appendix C.7).

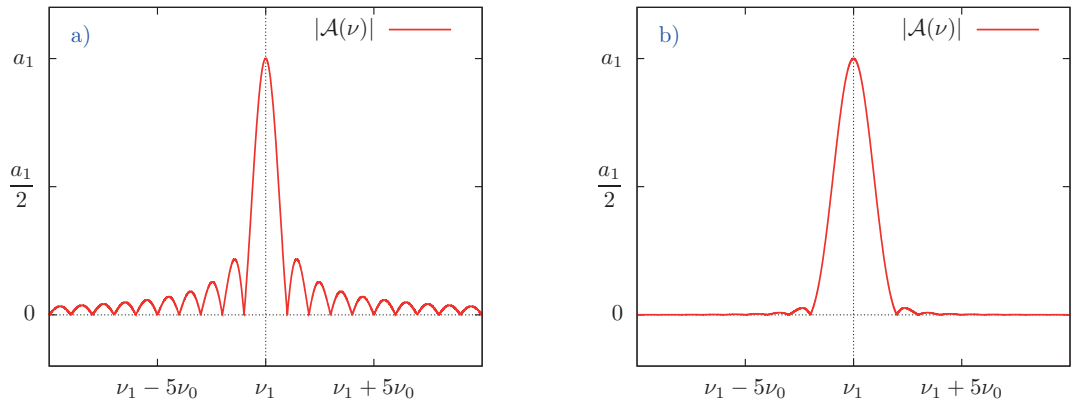

Figure A.1 – Norm of the amplitude function in the case of only one sinusoidal term: **a)** without the Hanning window; **b)** with the Hanning window.

In the more realistic case in which $f(t)$ is the sum of several (possibly numerous) terms, a local maximum is associated to each frequency ν_k. The addition of one term causes a distortion of the peaks associated to the other terms: this changes their heights and theirs exact positions, which are not centred anymore at the $\{\nu_k\}$ (Fig. A.2**a**). Fortunately, the distortion is weak for well-separated frequencies, and we can limit its effect by adding a weight function to the scalar product.

[2]The temporal sampling of $f(t)$ puts a cut-off frequency $\nu_{cut} = \pi/\Delta t$: any frequency larger than ν_{cut} cannot be determined correctly, and this comes from a pure lack of knowledge about the function.

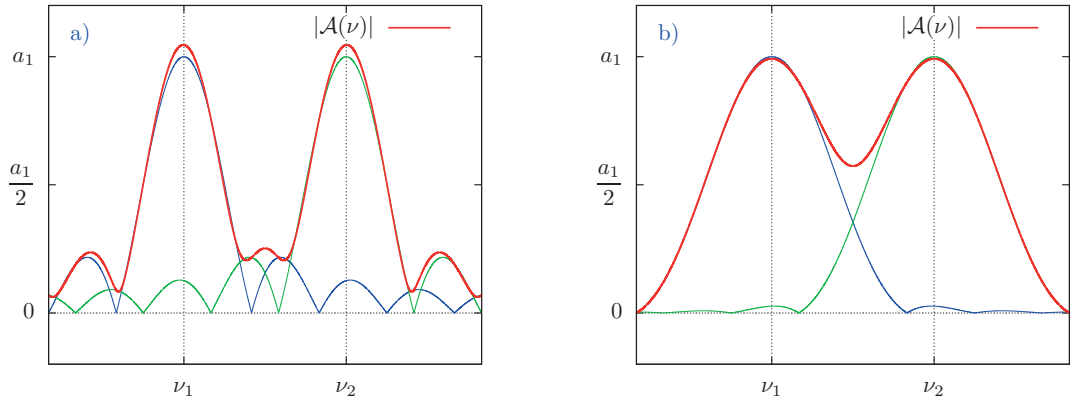

Figure A.2 – Norm of the amplitude function in the case of two sinusoidal terms: **a)** without the Hanning window; **b)** with the Hanning window. The curves obtained for the two terms taken separately are drawn in blue and green.

A.1.2 Weight function for the scalar product

In order to minimise the mutual perturbations between the various terms, it is possible to reduce the oscillations of $\mathcal{A}(\nu)$ around its maxima. This can be realised by a new definition of the scalar product. In the equation (A.6), we introduced implicitly a weight $\chi(t) = 1$, which results in a decrease of $|\mathcal{A}(\nu)|$ as the inverse of the distance to the maximum (Fig. A.1**a**). This decrease can be accelerated by using the Hanning window[3], which writes:

$$\chi(t) = 1 - \cos(\nu_0\, t) \tag{A.9}$$

The scalar product becomes then:

$$\langle f, g\rangle = \frac{1}{T}\int_0^T f(t)\overline{g(t)}\chi(t)\,\mathrm{d}t \tag{A.10}$$

This new scalar product results in a decrease of the oscillations of $|\mathcal{A}(\nu)|$ as the inverse *cubed* of the distance to the maximum (Fig. A.1**b**). The different terms are consequently much less distorted by each other (Fig. A.2**b**). In return, the Hanning window doubles the width of the central peak[4].

The use of the Hanning window allows to detect the maxima of $|\mathcal{A}(\nu)|$ with a precision of about $1.2\,\nu_0\sqrt{\varepsilon}$, in which ε is the machine precision (see appendix C.7). However, these maxima still do not correspond exactly to the values of the frequencies $\{\nu_k\}$: in Fig. A.2, we note a slight shift of the maxima of the red curve with respect to the terms taken separately. Of course, Fig. A.2 presents the worst case in which the two terms have the same amplitude, the same phase, and neighbour frequencies

[3]See Laskar (2005) for the types of function which can be used as window in this context.

[4]We consider that two maxima are indistinguishable if their separation is smaller than $\Delta\nu = 2\,\nu_0$. Even if some methods can be used to bypass this limitation (see Sect. A.1.4), this comes from a lack of information on the function $f(t)$, namely a too small tabulation interval $[0, T]$.

($\Delta\nu = 2.5\,\nu_0$). Actually, terms of very distant frequencies (with respect to ν_0) virtually do not interact with each other, and in the same way, high-amplitude terms are not distorted by small-amplitude ones. Hence, it is enough to subtract from the signal the already-determined terms to make fully appear the remaining ones.

A.1.3 Basis of orthonormal functions

Once the frequencies $\{\nu_k\}$ are obtained, the reconstruction of $f(t)$ as a quasi-periodic series is simply its projection on the vector subspace formed by the vectors $\{\mathrm{e}_k = \exp(i\nu_k t)\}$. However, contrary to its Fourier series, these basis vectors are not necessarily orthogonal. In order to perform the projection, we must define a basis of orthogonal vectors $\{u_k\}$, for which the projection of f on u_k is equivalent to the scalar product $\langle f, u_k\rangle$. As pointed out for instance by Laskar et al. (1992), this can be realised using Gram-Schmidt orthonormalisation algorithm:

$$\begin{cases} u_1 = \mathrm{e}_1 \\ u_2 = \dfrac{\mathrm{e}_2 - \langle \mathrm{e}_2, u_1\rangle\, u_1}{\|\mathrm{e}_2 - \langle \mathrm{e}_2, u_1\rangle\, u_1\|} \\ \quad \vdots \\ u_N = \dfrac{\mathrm{e}_N - \displaystyle\sum_{k=1}^{N-1} \langle \mathrm{e}_N, u_k\rangle\, u_k}{\left\|\mathrm{e}_N - \displaystyle\sum_{k=1}^{N-1} \langle \mathrm{e}_N, u_k\rangle\, u_k\right\|} \end{cases} \tag{A.11}$$

that is:

$$\begin{pmatrix} u_1 \\ u_2 \\ \vdots \\ u_N \end{pmatrix} = \begin{pmatrix} a_{1,1} & 0 & \cdots & 0 \\ a_{2,1} & a_{2,2} & \cdots & 0 \\ \vdots & \vdots & \ddots & \vdots \\ a_{N,1} & a_{N,2} & \cdots & a_{N,N} \end{pmatrix} \begin{pmatrix} \mathrm{e}_1 \\ \mathrm{e}_2 \\ \vdots \\ \mathrm{e}_N \end{pmatrix} \tag{A.12}$$

where the coefficients a_{ij} are obtained line by line, by recursion. Writing:

$$W_{ik} = \sum_{m=1}^{k} \overline{a_{km}}\, \langle \mathrm{e}_i, \mathrm{e}_m\rangle \tag{A.13}$$

the recursion formula is:

$$\begin{cases} a_{1,1} = 1 \\ \\ a_{ii} = \dfrac{1}{\left\| \mathrm{e}_i - \sum\limits_{n=1}^{i-1} \left(\sum\limits_{k=n}^{i-1} a_{kn} W_{ik} \right) \mathrm{e}_n \right\|} \\ \\ a_{ij} = \dfrac{- \sum\limits_{k=j}^{i-1} a_{kj} W_{ik}}{\left\| \mathrm{e}_i - \sum\limits_{n=1}^{i-1} \left(\sum\limits_{k=n}^{i-1} a_{kn} W_{ik} \right) \mathrm{e}_n \right\|} \quad \forall\, j < i \\ \\ a_{ij} = 0 \quad \forall\, j > i \end{cases} \tag{A.14}$$

In order to project the function f on the basis $\{u_k\}$, *every* basis vector should be known. Hence, the amplitudes $\{A_k\}$ can be computed only when we known *all* the frequencies. This is problematic for subtracting a term from the signal: since some frequencies have not been obtained yet, it is impossible to know its correct amplitude. The solution is to proceed by successive approximations: after the determination of each new frequency, f is projected onto the subspace generated by the only vectors known so far. The amplitudes are then corrected step by step.

Let us write $A_k^{(n)}$ the nth estimate of A_k; $f^{(n)}$ the residual function after the nth step (n terms have been subtracted); and $\mathcal{A}^{(n)}(\nu) = \left\langle f^{(n)}, \exp(i\nu t) \right\rangle$ the amplitude function applied to $f^{(n)}$. Then, the procedure can be summarised by:

First term:

a) maximum of $|\mathcal{A}(\nu)| \rightsquigarrow$ value of $\nu_1 \rightsquigarrow$ computation of a_{11} $(= 1)$

b) projection of f onto the subspace generated by $u_1 \rightsquigarrow$ first approximation of A_1:

$$P(f)_{\{u_1\}} = \langle f, u_1 \rangle\, u_1 = \Big(\langle f, u_1 \rangle\, a_{11} \Big) \mathrm{e}_1 = A_1^{(1)}\, \mathrm{e}_1$$

c) The first term is removed from the signal: $f^{(1)} = f - A_1^{(1)} \mathrm{e}_1$

Second term:

a) maximum of $|\mathcal{A}^{(1)}(\nu)| \rightsquigarrow$ value of $\nu_2 \rightsquigarrow$ computation of a_{21} and a_{22}

b) projection of f onto the subspace generated by u_1 and $u_2 \rightsquigarrow$ approximation of A_1 and A_2:

$$\begin{aligned} P(f)_{\{u_1,u_2\}} =& \langle f, u_1 \rangle\, u_1 + \langle f, u_2 \rangle\, u_2 = \Big(\langle f, u_1 \rangle\, a_{11} + \langle f, u_2 \rangle\, a_{21} \Big) \mathrm{e}_1 + \Big(\langle f, u_2 \rangle\, a_{22} \Big) \mathrm{e}_2 \\ =& A_1^{(2)}\, \mathrm{e}_1 + A_2^{(1)}\, \mathrm{e}_2 \end{aligned}$$

c) The two terms are removed from the signal: $f^{(2)} = f - A_1^{(2)}\mathrm{e}_1 - A_2^{(1)}\mathrm{e}_2$

Generalisation:

a) maximum of $|\mathcal{A}^{(n-1)}(\nu)| \rightsquigarrow$ value of $\nu_n \rightsquigarrow$ computation of the line n of the matrix

b) projection of f onto the subspace generated by $\{u_1, u_2 ... u_n\} \rightsquigarrow$ new estimate of the amplitudes:

$$\begin{cases} A_k^{(n-k+1)} = A_k^{(n-k)} + \langle f, u_n \rangle \, a_{nk} \quad \forall \; k < n \\ A_n^{(1)} = \langle f, u_n \rangle \, a_{nn} \end{cases} \tag{A.15}$$

c) All the terms determined are removed from the signal:

$$f^{(n)} = f - \sum_{k=1}^{n} A_k^{(n-k+1)} \mathrm{e}_k \tag{A.16}$$

Table A.1 presents the example of a function composed of five terms. The successive approximations of the amplitudes are shown step by step until all terms have been obtained. We note that the precision estimate of the frequencies ($1.2\,\nu_0\sqrt{\varepsilon} \approx 10^{-10}$, see Sect. A.1.2) is overcome by a factor 10.

1st term obtained	
ν_1	8.999999999990624
$A_1^{(1)}$	10.000000004736222

2nd term obtained	
ν_2	7.000000000047539
$A_1^{(2)}$	10.000000000510646
$A_2^{(1)}$	8.000000002849145

3rd term obtained	
ν_3	4.999999999995975
$A_1^{(3)}$	10.000000000040544
$A_2^{(2)}$	8.000000000208155
$A_3^{(1)}$	5.000000001150417

4th term obtained	
ν_4	2.999999999993570
$A_1^{(4)}$	10.000000000000327
$A_2^{(3)}$	8.000000000020115
$A_3^{(2)}$	5.000000000094020
$A_4^{(1)}$	2.000000000528189

5th term obtained	
ν_5	1.000000000010531
$A_1^{(5)}$	10.000000000000000
$A_2^{(4)}$	8.000000000000007
$A_3^{(3)}$	5.000000000000000
$A_4^{(2)}$	1.999999999999990
$A_5^{(1)}$	1.000000000000002

Table A.1 – Frequency analysis of a function composed of five terms (series of 62401 points with a time-step of 0.03). The true frequencies are $\{9, 7, 5, 3, 1\}$, the respective amplitudes are $\{10, 8, 5, 2, 1\}$ and the phases are all 0.

In the case of a series containing an unknown number of terms (which may be infinite), we need a criterion to stop the search for new frequencies. Several conditions can be considered:

- A given number of terms is reached.
- The amplitude of the new term obtained is negligible (according to the required precision).
- The standard deviation of the residual function $f^{(n)}(t)$ is below some threshold, or does not decrease significantly.
- The new frequency detected is very close to some frequency already determined: this can mean either that the two peaks cannot be dissociated, or that one term has been badly determined (that last case is studied in Sect. A.1.4).

Note on discrete computations Until now, we always considered integrals as continuous, by supposing that the discretisation errors were below the machine precision; moreover, one can note that some simple integrals involved in the algorithm can be computed analytically. However, if the step-size is not small enough to allow the continuous approximation, one should not mix numerical (discrete) integrals and analytical expressions: the frequencies and amplitudes would by surprisingly less precise. That effect is probably due to the scalar product, which is *defined as discrete* (since the function $f(t)$ is not known in a continuous way). Hence, the use of analytical expressions would be equivalent to change of scalar product along the computation.

A.1.4 Re-determination of the frequencies

In Sect. A.1.2, we saw that the frequencies cannot be determined exactly because of the mutual distortions of the maxima in the amplitude function (even if the Hanning window allowed to limit this phenomenon). In order to bypass this limitation, Champenois (1994) presented an iterative method: when a second term has been subtracted from the signal, it consists in re-injecting the first one and re-determining it. Indeed, the corresponding peak will be much less distorted than previously, so it will be much closer to the value of the real frequency. By iterations, the algorithm converges then toward much more precise values of the two frequencies, and even allows (to some extent) to distinguish two very neighbour peaks in the amplitude function, separated than less than $\Delta\nu = 2\,\nu_0$. The method is of course generalisable to more than two frequencies, and various implementations are possible. The strategy used by Lainey et al. (2006) seems quite satisfactory. It can be summed up by:

- A term is immediately re-injected if it is detected a second time (indeed, since the frequencies are not recovered exactly, there remain residual peaks in the amplitude function).
- If a term is detected two times in a row, all the terms determined so far are re-injected and re-determined one by one.

- The iterations stop when the re-determined frequencies do not change significantly: it is thus impossible to improve the precision. As a last step, the complete set of frequencies can possibly be re-determined once again, in order to assess the convergence for each of them.

An illustration of this algorithm is presented in Tab. A.2, column "frequency".

A.1.5 Optimisation of the algorithm

When it comes to re-determining a term, the whole orthonormalisation process (Sect. A.1.3) becomes computationally intensive: indeed, the orthonormal vectors being defined by recursion, the modification of only one term requires the computation of the corresponding vector, but also of all the following ones. In this section, we present a way to simplify this method.

In Sect. A.1.1, we saw that if the tabulated function $f(t)$ is made of only one term with frequency ν_1, the corresponding amplitude A_1 is simply given by $\mathcal{A}(\nu_1)$. This is also the case if the vectors $\{\mathrm{e}_k\}$ are intrinsically orthogonal[5]. Precisely, in order to re-determine some term, the latter is re-injected into the *residual* function, which is thus not far from being indeed composed of only one term. Hence, the method presented in Sect. A.1.4, along with improving the frequency values, improves also their respective amplitudes. In order to study this process more rigorously, let us consider a function composed of two terms:

$$f(t) = A_1\,\mathrm{e}_1(t) + A_2\,\mathrm{e}_2(t) \tag{A.17}$$

For now, we suppose that the two frequencies are obtained exactly at the first shot. The orthonormalisation process gives then the following amplitudes (see Sect. A.1.3):

$$\begin{aligned}
\text{first step: } &\Big\{ A_1^{(1)} = \langle f, \mathrm{e}_1 \rangle \\
\text{second step: } &\begin{cases} A_2^{(1)} = \langle f, u_2 \rangle\, a_{22} = \dfrac{\langle f, \mathrm{e}_2 \rangle - \langle f, \mathrm{e}_1 \rangle\, \mathrm{e}_{12}}{\| \mathrm{e}_2 - \mathrm{e}_{21}\, \mathrm{e}_1 \|^2} \\ A_1^{(2)} = A_1^{(1)} + \langle f, u_2 \rangle\, a_{21} = \langle f, \mathrm{e}_1 \rangle - \dfrac{\langle f, \mathrm{e}_2 \rangle - \langle f, \mathrm{e}_1 \rangle\, \mathrm{e}_{12}}{\| \mathrm{e}_2 - \mathrm{e}_{21}\, \mathrm{e}_1 \|^2}\ \mathrm{e}_{21} \end{cases}
\end{aligned} \tag{A.18}$$

in which we write $\mathrm{e}_{12} \equiv \langle \mathrm{e}_1, \mathrm{e}_2 \rangle \in \mathbb{C}$. Let us compare these results with the values given directly by $\mathcal{A}(\nu)$, but re-injecting and re-determining the first term:

$$\begin{aligned}
\text{first step: } &\Big\{ A_1^{(1)} = \langle f, \mathrm{e}_1 \rangle \\
\text{second step: } &\Big\{ A_2^{(1)} = \langle f - A_1^{(1)}\, \mathrm{e}_1\ ,\ \mathrm{e}_2 \rangle = \langle f, \mathrm{e}_2 \rangle - \langle f, \mathrm{e}_1 \rangle\, \mathrm{e}_{12} \\
\text{re-determination: } &\Big\{ A_1^{(2)} = \langle f - A_2^{(1)}\, \mathrm{e}_2\ ,\ \mathrm{e}_1 \rangle = \langle f, \mathrm{e}_1 \rangle - \Big(\langle f, \mathrm{e}_2 \rangle - \langle f, \mathrm{e}_1 \rangle\, \mathrm{e}_{12} \Big) \mathrm{e}_{21}
\end{aligned} \tag{A.19}$$

[5]The vectors $\{\mathrm{e}_k\}$ are orthogonal if they correspond to very different frequencies (infinitely different), if the width T of the interval is very large (infinitely large), or if the frequencies ν_k are integer multiples of $\nu_0 = 2\pi/T$.

We note that (A.18) and (A.19) are equal apart from a real factor, which can be expressed as:

$$\begin{aligned}\frac{1}{\|\mathrm{e}_2 - \mathrm{e}_{21}\,\mathrm{e}_1\|^2} &= \frac{1}{\langle \mathrm{e}_2 - \mathrm{e}_{21}\,\mathrm{e}_1 \ , \ \mathrm{e}_2 - \mathrm{e}_{21}\,\mathrm{e}_1 \rangle} \\ &= \frac{1}{1 - |\mathrm{e}_{21}|^2} \\ &= 1 + |\mathrm{e}_{21}|^2 + |\mathrm{e}_{21}|^4 + |\mathrm{e}_{21}|^6 + ...\end{aligned} \tag{A.20}$$

If the two terms are nearly orthogonal, this factor is thus close to 1. Moreover, once the first term has been re-determined, we can apply the same process to the second term and repeat it iteratively. This gives the following chain:

$$\begin{aligned}
A_2^{(1)} &= \langle f - A_1^{(1)}\,\mathrm{e}_1 \ , \ \mathrm{e}_2 \rangle = \langle f, \mathrm{e}_2 \rangle - \langle f, \mathrm{e}_1 \rangle\,\mathrm{e}_{12} \\
A_1^{(2)} &= \langle f - A_2^{(1)}\,\mathrm{e}_2 \ , \ \mathrm{e}_1 \rangle = \langle f, \mathrm{e}_1 \rangle - \Big(\langle f, \mathrm{e}_2 \rangle - \langle f, \mathrm{e}_1 \rangle\,\mathrm{e}_{12} \Big) \mathrm{e}_{21} \\
A_2^{(2)} &= \langle f - A_1^{(2)}\,\mathrm{e}_1 \ , \ \mathrm{e}_2 \rangle = \Big(\langle f, \mathrm{e}_2 \rangle - \langle f, \mathrm{e}_1 \rangle\,\mathrm{e}_{12} \Big) \left(1 + |\mathrm{e}_{21}|^2 \right) \\
A_1^{(3)} &= \langle f - A_2^{(2)}\,\mathrm{e}_2 \ , \ \mathrm{e}_1 \rangle = \langle f, \mathrm{e}_1 \rangle - \Big(\langle f, \mathrm{e}_2 \rangle - \langle f, \mathrm{e}_1 \rangle\,\mathrm{e}_{12} \Big) \mathrm{e}_{21} \left(1 + |\mathrm{e}_{21}|^2 \right) \\
A_2^{(3)} &= \langle f - A_1^{(3)}\,\mathrm{e}_1 \ , \ \mathrm{e}_2 \rangle = \Big(\langle f, \mathrm{e}_2 \rangle - \langle f, \mathrm{e}_1 \rangle\,\mathrm{e}_{12} \Big) \left(1 + |\mathrm{e}_{21}|^2 + |\mathrm{e}_{21}|^4 \right) \\
A_1^{(4)} &= \langle f - A_2^{(3)}\,\mathrm{e}_2 \ , \ \mathrm{e}_1 \rangle = \langle f, \mathrm{e}_1 \rangle - \Big(\langle f, \mathrm{e}_2 \rangle - \langle f, \mathrm{e}_1 \rangle\,\mathrm{e}_{12} \Big) \mathrm{e}_{21} \left(1 + |\mathrm{e}_{21}|^2 + |\mathrm{e}_{21}|^4 \right) \\
&\ \ \vdots
\end{aligned} \tag{A.21}$$

The effect of the re-determination is obvious here (and it can be proved by recursion): it simply adds a correction of higher order in $|\mathrm{e}_{21}|^2$. The amplitudes converge thus rapidly toward the values given by the orthonormalisation process (and of course, the convergence is faster if the terms are nearly orthogonal). This is generalised to more than two frequencies, so we conclude that the successive re-determination of the terms is equivalent to projecting f using the orthonormal basis.

In the above calculation, we supposed that the two frequencies were obtained immediately at the maximum precision. In practice, the re-determination of one term, along with the refinement of its amplitude, improves also its frequency (this was the first purpose of the re-determination). In this context, we consider that the repeated modification of the orthonormal basis is an unnecessary intensive part of the algorithm, since the re-determination process already realises it indirectly. As a precaution, it is still possible to compute the orthonormal basis only once the "final" improvements of the terms have been obtained, in order to suppress the potential imperfections of the amplitudes that could subsist.

The whole procedure is illustrated in Tab. A.2, using the same five-term function as in Tab. A.1: at each iteration, all the terms are re-injected and re-determined one by one. Hence, the amplitudes are rapidly as good as using the orthonormal basis, and the frequencies are clearly improved as well.

Re-determination of the 2nd term ($\nu_2 = 7$, $A_2 = 8$)		
iteration	frequency	amplitude
1	7.000000000047539	8.000000002849147
2	7.000000000003888	8.000000000000002
3	6.999999999999364	7.999999999999999
4	7.000000000000049	8.000000000000000

Table A.2 – Refinement of the frequencies and amplitudes by re-determination. The function contains the same five terms as in Tab. A.1, but only the second one is shown here. From Tab. A.1, the final result using the orthonormal basis is: $\nu_2 = 7.000000000047539$ and $A_2 = 8.000000000000007$.

A.2 Application to the orbital dynamics of Atlas

Atlas is a natural satellite of Saturn (the closest one to the outer edge of the "A" ring). Its orbital dynamics is very rich because of the perturbations by other satellites, as Prometheus and Pandora, but also Janus, Epimetheus and Mimas. The *Cassini* spacecraft provided very accurate images of these various satellites, allowing detailed dynamical studies. In our paper Renner et al. (2016), it is shown that the orbital dynamics of Atlas is mainly driven by its 53:54 mean-motion resonance with Prometheus. Since they have comparable eccentricities, the two resonant combinations (which are respectively Corotation and Lindblad eccentricity resonances):

$$\begin{aligned} \sigma_C &= 54\lambda_P - 53\lambda_A - \varpi_P \\ \sigma_L &= 54\lambda_P - 53\lambda_A - \varpi_A \end{aligned} \tag{A.22}$$

have comparable strengths on the dynamics of Atlas (same order of magnitude in the disturbing function). This gives rise to a chaotic dynamics with a Lyapunov time of ~ 10 years, to be compared to the orbital periods (~ 14 hours). In that work, the frequency analysis allows to track the proper frequencies from simplified integrable models to the real chaotic case, in which the proper frequencies are not defined anymore. In the full system, the frequency analysis still provides some frequencies and amplitudes (for well-chosen tabulation intervals $[0, T]$), which can be compared to their counterparts in the integrable models. The addition of Pandora as a perturbing body does not change significantly the measured frequencies and their rates of variation, showing that the motion of Atlas is indeed dominated by its interaction with Prometheus. The reader can find the full article by Renner et al. (2016) at:

`https://doi.org/10.3847/0004-6256/151/5/122`

It is also available in free access at:

`https://arxiv.org/abs/1602.01967`

Appendix B

Computational details

In this chapter, we give some details about long analytical computations which would have bother the reader interested by new results.

B.1 General proofs

B.1.1 Generalisation of a transformation applied to the positions

We present here the complete proof of the canonical nature of the first change of coordinates given in Sect. 2.2.4. It amounts to show that for $(\mathbf{Q},\mathbf{q}) \in \mathbb{R}^N \times \mathbb{R}^N$, a function of the form:

$$F(\mathbf{Q},\mathbf{q}) = (\mathrm{D}f(\mathbf{q})^{-1})^{\mathrm{T}}\,\mathbf{Q} \tag{B.1}$$

verifies automatically:

$$\mathrm{D}_{\mathbf{q}}F\,(\mathrm{D}_{\mathbf{Q}}F)^{\mathrm{T}} = \mathrm{D}_{\mathbf{Q}}F\,(\mathrm{D}_{\mathbf{q}}F)^{\mathrm{T}} \tag{B.2}$$

This is equivalent to show that the matrix $\mathcal{M} = \mathrm{D}_{\mathbf{q}}F\,(\mathrm{D}_{\mathbf{Q}}F)^{\mathrm{T}}$ is symmetric, that is $\mathcal{M}_{ij} = \mathcal{M}_{ji}$. Let us use the notation $\mathcal{A} = (\mathrm{D}f^{-1})^{\mathrm{T}}$. We have thus $\mathrm{D}_{\mathbf{Q}}F = \mathcal{A}$ and:

$$\mathrm{D}_{\mathbf{q}}F = \mathrm{D}_{\mathbf{q}}\begin{pmatrix}\sum_k \mathcal{A}_{1k}Q_k\\ \sum_k \mathcal{A}_{2k}Q_k\\ \sum_k \mathcal{A}_{3k}Q_k\\ \vdots\end{pmatrix} = \begin{pmatrix}\sum_k \frac{\partial \mathcal{A}_{1k}}{\partial q_1}Q_k & \sum_k \frac{\partial \mathcal{A}_{1k}}{\partial q_2}Q_k & \sum_k \frac{\partial \mathcal{A}_{1k}}{\partial q_3}Q_k & \cdots\\ \sum_k \frac{\partial \mathcal{A}_{2k}}{\partial q_1}Q_k & \sum_k \frac{\partial \mathcal{A}_{2k}}{\partial q_2}Q_k & \sum_k \frac{\partial \mathcal{A}_{2k}}{\partial q_3}Q_k & \cdots\\ \sum_k \frac{\partial \mathcal{A}_{3k}}{\partial q_1}Q_k & \sum_k \frac{\partial \mathcal{A}_{3k}}{\partial q_2}Q_k & \sum_k \frac{\partial \mathcal{A}_{3k}}{\partial q_3}Q_k & \cdots\\ \vdots & \vdots & \vdots & \ddots\end{pmatrix} \tag{B.3}$$

The column n of the matrix $\mathrm{D}_{\mathbf{q}}F$ is thus equal to the vector $\partial\mathcal{A}/\partial q_n\,\mathbf{Q}$. Then, we can use the following matrix identity:

$$\frac{\partial M^{-1}}{\partial x} = -M^{-1}\frac{\partial M}{\partial x}M^{-1} \tag{B.4}$$

which gives, from the definition of $\mathcal{A}$:

$$\frac{\partial \mathcal{A}}{\partial q_n} = -(\mathrm{D}f^{-1})^{\mathrm{T}}\left(\frac{\partial \mathrm{D}f}{\partial q_n}\right)^{\mathrm{T}}(\mathrm{D}f^{-1})^{\mathrm{T}} = -\mathcal{A}\left(\frac{\partial \mathrm{D}f}{\partial q_n}\right)^{\mathrm{T}}\mathcal{A} \tag{B.5}$$

By computing the products and using $(\mathrm{D}f)_{\ell m} = \partial f_\ell / \partial q_m$, one component of this matrix writes:

$$\left(\frac{\partial \mathcal{A}}{\partial q_n}\right)_{ik} = -\sum_{\ell,m} \frac{\partial^2 f_\ell}{\partial q_m \partial q_n} \mathcal{A}_{im} \mathcal{A}_{\ell k} \tag{B.6}$$

By multiplication by $\mathbf{Q}$, this gives the components of the matrix $\mathrm{D}_{\mathbf{q}} F$:

$$(\mathrm{D}_{\mathbf{q}} F)_{in} = -\sum_{k,\ell,m} \frac{\partial^2 f_\ell}{\partial q_m \partial q_n} \mathcal{A}_{im} \mathcal{A}_{\ell k} Q_k \tag{B.7}$$

By multiplication by $\mathcal{A}^{\mathrm{T}}$, we finally obtain the components of the matrix $\mathcal{M}$:

$$\mathcal{M}_{ij} = -\sum_{k,\ell,m,n} \frac{\partial^2 f_\ell}{\partial q_m \partial q_n} \mathcal{A}_{im} \mathcal{A}_{jn} \mathcal{A}_{\ell k} Q_k \tag{B.8}$$

which are equal by permutation of i and j (since the indexes m and n are mute). This closes the proof.

B.2 Analytical non-resonant secular model

B.2.1 Analytical integral of the odd Legendre polynomials

The following proof is required to compute the analytical form of the non-resonant secular model (Sect. 3.2.1). We want to show that for $k \in \mathbb{N}$:

$$I_k = \int_0^{2\pi} (\alpha \cos\lambda + \beta \sin\lambda)^{2k+1} \,\mathrm{d}\lambda = 0 \tag{B.9}$$

where $\alpha, \beta \in \mathbb{R}$. It is immediate to verify this result for $k = 0$. Then, if it holds for the index k, we have:

$$\begin{aligned} I_{k+1} &= \int_0^{2\pi} (\alpha \cos\lambda + \beta \sin\lambda)^{2(k+1)+1} \,\mathrm{d}\lambda \\ &= \int_0^{2\pi} (\alpha \cos\lambda + \beta \sin\lambda)(\alpha \cos\lambda + \beta \sin\lambda)^{2k+2} \,\mathrm{d}\lambda \end{aligned} \tag{B.10}$$

which can be integrated by parts:

$$\begin{aligned} I_{k+1} = &\Big[(\alpha \sin\lambda - \beta \cos\lambda)(\alpha \cos\lambda + \beta \sin\lambda)^{2k+2}\Big]_0^{2\pi} \\ &- \int_0^{2\pi} (\alpha \sin\lambda - \beta \cos\lambda)(2k+2)(\alpha \cos\lambda + \beta \sin\lambda)^{2k+1}(-\alpha \sin\lambda + \beta \cos\lambda) \,\mathrm{d}\lambda \end{aligned} \tag{B.11}$$

The first part is zero, hence, regrouping the terms:

$$\begin{aligned} I_{k+1} &= (2k+2)\int_0^{2\pi} \left[\alpha^2+\beta^2-(\alpha\cos\lambda+\beta\sin\lambda)^2\right](\alpha\cos\lambda+\beta\sin\lambda)^{2k+1}\,\mathrm{d}\lambda \\ &= (2k+2)\Big[(\alpha^2+\beta^2)I_k - I_{k+1}\Big] \end{aligned} \tag{B.12}$$

By factorising every I_{k+1} in the left-hand side, we finally get:

$$I_{k+1} = \frac{2k+2}{2k+3}(\alpha^2+\beta^2)I_k = 0 \tag{B.13}$$

which ends the proof.

B.2.2 Analytical integral of the even Legendre polynomials

The following proof is required to compute the analytical form of the non-resonant secular model (Sect. 3.2.1). We want to show that for $k > 0$:

$$\begin{aligned} J_k &= \int_0^{2\pi} (\alpha\cos\lambda+\beta\sin\lambda)^{2k}\,\mathrm{d}\lambda = \frac{1\times3\times5\times\ldots\times(2k-1)}{2\times4\times6\times\ldots\times2k}(\alpha^2+\beta^2)^k \\ &= \frac{2k-1}{2k}(\alpha^2+\beta^2)J_{k-1} \end{aligned} \tag{B.14}$$

where $\alpha, \beta \in \mathbb{R}$. It is immediate to verify this result for $k = 1$. Then, if it holds for the index k, we have:

$$\begin{aligned} J_{k+1} &= \int_0^{2\pi} (\alpha\cos\lambda+\beta\sin\lambda)^{2(k+1)}\,\mathrm{d}\lambda \\ &= \int_0^{2\pi} (\alpha\cos\lambda+\beta\sin\lambda)(\alpha\cos\lambda+\beta\sin\lambda)^{2k+1}\,\mathrm{d}\lambda \end{aligned} \tag{B.15}$$

which can be integrated by parts:

$$\begin{aligned} J_{k+1} = &\Big[(\alpha\sin\lambda-\beta\cos\lambda)(\alpha\cos\lambda+\beta\sin\lambda)^{2k+1}\Big]_0^{2\pi} \\ &- \int_0^{2\pi} (\alpha\sin\lambda-\beta\cos\lambda)(2k+1)(\alpha\cos\lambda+\beta\sin\lambda)^{2k}(-\alpha\sin\lambda+\beta\cos\lambda)\,\mathrm{d}\lambda \end{aligned} \tag{B.16}$$

The first part is zero, hence, regrouping the terms:

$$\begin{aligned} J_{k+1} &= (2k+1)\int_0^{2\pi} \left[\alpha^2+\beta^2-(\alpha\cos\lambda+\beta\sin\lambda)^2\right](\alpha\cos\lambda+\beta\sin\lambda)^{2k}\,\mathrm{d}\lambda \\ &= (2k+1)\Big[(\alpha^2+\beta^2)J_k - J_{k+1}\Big] \end{aligned} \tag{B.17}$$

By factorizing every J_{k+1} in the left-hand side, we finally get:

$$J_{k+1} = \frac{2(k+1)-1}{2(k+1)}(\alpha^2+\beta^2)J_k \tag{B.18}$$

which ends the proof.

B.2.3 First terms of the development

By expanding the inverse of the mutual distances in Legendre polynomials, an analytical expression of the non-resonant secular Hamiltonian can be obtained. The general form of the result is presented in equations (3.26) and (3.27), and the first terms are the followings:

$n=1$
$\alpha_1 = 1/8$
$P_1^0(x) = 1$ $Q_1^0(x) = -1 + 3\,x^2$

$n=2$
$\alpha_2 = 9/1024$
$P_2^0(x) = 2 + 3\,x^2$ $Q_2^0(x) = 3 - 30\,x^2 + 35\,x^4$
$P_2^1(x) = 10$ $Q_2^1(x) = -1 + 7\,x^2$

$n=3$
$\alpha_3 = 25/65536$
$P_3^0(x) = 2\,(8 + 40\,x^2 + 15\,x^4)$ $Q_3^0(x) = -5 + 105\,x^2 - 315\,x^4 + 231\,x^6$
$P_3^1(x) = 210\,(2 + x^2)$ $Q_3^1(x) = 1 - 18\,x^2 + 33\,x^4$
$P_3^2(x) = 63$ $Q_3^2(x) = -1 + 11\,x^2$

$n=4$
$\alpha_4 = 245/33554432$
$P_4^0(x) = 5\,(16 + 168\,x^2 + 210\,x^4 + 35\,x^6)$ $Q_4^0(x) = 35 - 1260\,x^2 + 6930\,x^4 - 12012\,x^6 + 6435\,x^8$
$P_4^1(x) = 630\,(48 + 80\,x^2 + 15\,x^4)$ $Q_4^1(x) = -1 + 33\,x^2 - 143\,x^4 + 143\,x^6$
$P_4^2(x) = 1386\,(10 + 3\,x^2)$ $Q_4^2(x) = 1 - 26\,x^2 + 65\,x^4$
$P_4^3(x) = 858$ $Q_4^3(x) = -1 + 15\,x^2$

$n=5$
$\alpha_5 = 567/4294967296$
$P_5^0(x) = 14\,(128 + 2304\,x^2 + 6048\,x^4 + 3360\,x^6 + 315\,x^8)$ $Q_5^0(x) = -63 + 3465\,x^2 - 30030\,x^4 + 90090\,x^6 - 109395\,x^8 + 46189\,x^{10}$
$P_5^1(x) = 9240\,(32 + 112\,x^2 + 70\,x^4 + 7\,x^6)$ $Q_5^1(x) = 7 - 364\,x^2 + 2730\,x^4 - 6188\,x^6 + 4199\,x^8$
$P_5^2(x) = 240240\,(8 + 8\,x^2 + x^4)$ $Q_5^2(x) = -1 + 45\,x^2 - 255\,x^4 + 323\,x^6$
$P_5^3(x) = 8580\,(14 + 3\,x^2)$ $Q_5^3(x) = 3 - 102\,x^2 + 323\,x^4$
$P_5^4(x) = 12155$ $Q_5^4(x) = -1 + 19\,x^2$

$n = 6$
$\alpha_6 = 7623/549755813888$
$P_6^0(x) = 14\,(256 + 7040\,x^2 + 31690\,x^4 + 36960\,x^6 + 11550\,x^8 + 693\,x^{10})$ $Q_6^0(x) = 231 - 18018\,x^2 + 225225\,x^4 - 1021020\,x^6 + 2078505\,x^8 - 1939938\,x^{10} + 676039\,x^{12}$
$P_6^1(x) = 60060\,(128 + 768\,x^2 + 1008\,x^4 + 336\,x^2 + 21\,x^8)$ $Q_6^1(x) = -3 + 225\,x^2 - 2550\,x^4 + 9690\,x^6 - 14535\,x^8 + 7429\,x^{10}$
$P_6^2(x) = 90090\,(80 + 168\,x^2 + 70\,x^4 + 5\,x^6)$ $Q_6^2(x) = 5 - 340\,x^2 + 3230\,x^4 - 9044\,x^6 + 7429\,x^8$
$P_6^3(x) = 12155\,(224 + 160\,x^2 + 15\,x^4)$ $Q_6^3(x) = -5 + 285\,x^2 - 1995\,x^4 + 3059\,x^6$
$P_6^4(x) = 230945\,(6 + x^2)$ $Q_6^4(x) = 1 - 42\,x^2 + 161\,x^4$
$P_6^5(x) = 29393$ $Q_6^5(x) = -1 + 23\,x^2$

$n = 7$
$\alpha_7 = 5577/70368744177664$
$P_7^0(x) = 264\,(1024 + 39936\,x^2 + 274560\,x^4 + 549120\,x^6 + 360360\,x^8 + 72072\,x^{10} + 3003\,x^{12})$ $Q_7^0(x) = -429 + 45045\,x^2 - 765765\,x^4 + 4849845\,x^6 - 14549535\,x^8 + 22309287\,x^{10} - 16900975\,x^{12} + 5014575\,x^{14}$
$P_7^1(x) = 180180\,(768 + 7040\,x^2 + 15840\,x^4 + 11088\,x^6 + 2310\,x^8 + 99\,x^10)$ $Q_7^1(x) = 33 - 3366\,x^2 + 53295\,x^4 - 298452\,x^6 + 735471\,x^8 - 817190\,x^{10} + 334305\,x^{12}$
$P_7^2(x) = 8423415\,(1280 + 4608\,x^2 + 4032\,x^4 + 960\,x^6 + 45\,x^8)$ $Q_7^2(x) = -1 + 95\,x^2 - 1330\,x^4 + 6118\,x^6 - 10925\,x^8 + 6555\,x^{10}$
$P_7^3(x) = 35565530\,(192 + 288\,x^2 + 90\,x^4 + 5\,x^6)$ $Q_7^3(x) = 1 - 84\,x^2 + 966\,x^4 - 3220\,x^6 + 3105\,x^8$
$P_7^4(x) = 19399380\,(72 + 40\,x^2 + 3\,x^4)$ $Q_7^4(x) = -1 + 69\,x^2 - 575\,x^4 + 1035\,x^6$
$P_7^5(x) = 4056234\,(22 + 3\,x^2)$ $Q_7^5(x) = (-1 + 5\,x^2)\,(-1 + 45\,x^2)$
$P_7^6(x) = 1300075$ $Q_7^6(x) = -1 + 27\,x^2$

$n = 8$
$\alpha_8 = 96525/72057594037927936$
$P_8^0(x) = 429\,(2048 + 107520\,x^2 + 1048320\,x^4 + 3203200\,x^6 + 3603600\,x^8 + 1513512\,x^{10} + 210210\,x^{12} + 6435\,x^{14})$ $Q_8^0(x) = 6435 - 875160\,x^2 + 19399380\,x^4 - 162954792\,x^6 + 669278610\,x^8 - 1487285800\,x^{10}$ $+1825305300\,x^{12} - 1163381400\,x^{14} + 300540195\,x^{16}$
$P_8^1(x) = 510510\,(4096 + 53248\,x^2 + 183040\,x^4 + 219648\,x^6 + 96096\,x^8 + 13728\,x^{10} + 429\,x^{12})$ $Q_8^1(x) = -143 + 19019\,x^2 - 399399\,x^4 + 3062059\,x^6 - 10935925\,x^8 + 19684665\,x^{10} - 17298645\,x^{12} + 5892945\,x^{14}$
$P_8^2(x) = 176534358\,(512 + 2816\,x^2 + 4224\,x^4 + 2112\,x^6 + 330\,x^8 + 11\,x^{10})$ $Q_8^2(x) = 11 - 1386\,x^2 + 26565\,x^4 - 177100\,x^6 + 512325\,x^8 - 660330\,x^{10} + 310155\,x^{12}$
$P_8^3(x) = 25219194\,(1792 + 4608\,x^2 + 3024\,x^4 + 560\,x^6 + 21\,x^8)$ $Q_8^3(x) = -21 + 2415\,x^2 - 40250\,x^4 + 217350\,x^6 - 450225\,x^8 + 310155\,x^{10}$
$P_8^4(x) = 87885070\,(528 + 616\,x^2 + 154\,x^4 + 7\,x^6)$ $Q_8^4(x) = 7 - 700\,x^2 + 9450\,x^4 - 36540\,x^6 + 40455\,x^8$
$P_8^5(x) = 47322730\,(176 + 80\,x^2 + 5\,x^4)$ $Q_8^5(x) = -5 + 405\,x^2 - 3915\,x^4 + 8091\,x^6$
$P_8^6(x) = 23401350\,(26 + 3\,x^2)$ $Q_8^6(x) = 3 - 174\,x^2 + 899\,x^4$
$P_8^7(x) = 19389690$ $Q_8^7(x) = -1 + 31\,x^2$

B.3 Equations of motion in the averaged coordinates

B.3.1 Non-resonant case

In this section, we detail the equations of motion for the secular system in the non-resonant case. The Hamiltonian function $\mathcal{F}(L,G,H,g)$ is given by (3.13) and (3.28). Dropping the constant parts and making apparent the required averages, it writes:

$$\begin{aligned}\mathcal{F} &= -\frac{1}{(2\pi)^{N+1}}\int_0^{2\pi}\!\!\int_0^{2\pi}\!\!\dots\int_0^{2\pi}\sum_{i=1}^{N}\frac{\mu_i}{|\mathbf{r}-\mathbf{r}_i|}\;\mathrm{d}\lambda_1\mathrm{d}\lambda_2\dots\mathrm{d}\lambda_N\,\mathrm{d}\ell \\ &= -\frac{1}{4\pi^2}\int_0^{2\pi}\left(\sum_{i=1}^{N}\int_0^{2\pi}\frac{\mu_i}{|\mathbf{r}-\mathbf{r}_i|}\,\mathrm{d}\lambda_i\right)\mathrm{d}\ell\end{aligned} \tag{B.19}$$

Since the variables λ_i are mute, we can gather each integral of the summation into a single integral, realised over a *common* variable $\lambda^\star$:

$$\mathcal{F} = -\frac{1}{4\pi^2}\int_0^{2\pi}\!\!\int_0^{2\pi}\left(\sum_{i=1}^{N}\frac{\mu_i}{|\mathbf{r}-\mathbf{r}_i|}\right)\mathrm{d}\lambda^\star\,\mathrm{d}\ell \tag{B.20}$$

Finally, it is more convenient to perform the integral over the true anomaly ν instead of the mean anomaly $\ell = M$. By using (2.26), we get:

$$\mathcal{F} = -\frac{1}{4\pi^2}\int_0^{2\pi}\!\!\int_0^{2\pi}\left(\sum_{i=1}^{N}\frac{\mu_i}{|\mathbf{r}-\mathbf{r}_i|}\right)\frac{(1-e^2)^{3/2}}{(1+e\cos\nu)^2}\,\mathrm{d}\lambda^\star\,\mathrm{d}\nu \tag{B.21}$$

Since (B.21) is written in terms of the Keplerian elements:

$$a = \frac{L^2}{\mu} \quad ; \quad e = \sqrt{1-\frac{G^2}{L^2}} \quad ; \quad I = \operatorname{acos}\frac{H}{G} \quad ; \quad \omega = g \quad ; \quad \Omega = h \tag{B.22}$$

its partial derivatives are computed using the chain rule:

$$\begin{cases}\dfrac{\partial\mathcal{F}}{\partial G} = \dfrac{\partial\mathcal{F}}{\partial e}\dfrac{\partial e}{\partial G} + \dfrac{\partial\mathcal{F}}{\partial I}\dfrac{\partial I}{\partial G} \\ \dfrac{\partial\mathcal{F}}{\partial H} = \dfrac{\partial\mathcal{F}}{\partial I}\dfrac{\partial I}{\partial H}\end{cases} \quad ; \quad \begin{cases}\dfrac{\partial\mathcal{F}}{\partial g} = \dfrac{\partial\mathcal{F}}{\partial\omega} \\ \dfrac{\partial\mathcal{F}}{\partial h} = 0\end{cases} \tag{B.23}$$

From (B.22), the required partial derivatives of the Keplerian elements write:

$$\frac{\partial e}{\partial G} = -\frac{G}{\mu a e} \quad ; \quad \frac{\partial I}{\partial G} = \frac{\cos I}{G\sin I} \quad ; \quad \frac{\partial I}{\partial H} = \frac{-1}{G\sin I} \tag{B.24}$$

The computation of the dynamical equations (B.23) requires the partial derivatives of $\mathcal{F}$ with respect to the Keplerian elements. This is realised by inverting the integrals

and partial derivatives symbols (this holds as long as there is no crossing between the orbits considered). Injecting the explicit expression of $\mathcal{F}$ (B.21) in the dynamical equations (B.23), we get:

$$\frac{\partial \mathcal{F}}{\partial G} = \frac{1}{4\pi^2}\int_0^{2\pi}\int_0^{2\pi}\left[\left(\sum_{i=1}^{N}\mu_i\frac{\mathbf{r}-\mathbf{r}_i}{|\mathbf{r}-\mathbf{r}_i|^3}\right)\cdot\left(\frac{\partial \mathbf{r}}{\partial e}\frac{\partial e}{\partial G}+\frac{\partial \mathbf{r}}{\partial I}\frac{\partial I}{\partial G}\right)\frac{(1-e^2)^{3/2}}{(1+e\cos\nu)^2}\right.$$
$$\left.+\left(\sum_{i=1}^{N}\frac{\mu_i}{|\mathbf{r}-\mathbf{r}_i|}\right)\frac{\sqrt{1-e^2}}{(1+e\cos\nu)^2}\left(3e+\frac{2(1-e^2)\cos\nu}{1+e\cos\nu}\right)\frac{\partial e}{\partial G}\right]\mathrm{d}\lambda^\star\,\mathrm{d}\nu$$

$$\frac{\partial \mathcal{F}}{\partial H} = \frac{1}{4\pi^2}\int_0^{2\pi}\int_0^{2\pi}\left(\sum_{i=1}^{N}\mu_i\frac{\mathbf{r}-\mathbf{r}_i}{|\mathbf{r}-\mathbf{r}_i|^3}\right)\cdot\frac{\partial \mathbf{r}}{\partial I}\frac{\partial I}{\partial H}\frac{(1-e^2)^{3/2}}{(1+e\cos\nu)^2}\,\mathrm{d}\lambda^\star\,\mathrm{d}\nu$$

$$\frac{\partial \mathcal{F}}{\partial g} = \frac{1}{4\pi^2}\int_0^{2\pi}\int_0^{2\pi}\left(\sum_{i=1}^{N}\mu_i\frac{\mathbf{r}-\mathbf{r}_i}{|\mathbf{r}-\mathbf{r}_i|^3}\right)\cdot\frac{\partial \mathbf{r}}{\partial \omega}\frac{(1-e^2)^{3/2}}{(1+e\cos\nu)^2}\,\mathrm{d}\lambda^\star\,\mathrm{d}\nu$$

$$\frac{\partial \mathcal{F}}{\partial h} = 0$$

The partial derivative of $\mathcal{F}$ with respect to h is zero because of the average (see Sect. 3.2.1), but the integrand takes non-zero values.

At this point, the partial derivatives of $\mathbf{r}$ with respect to the Keplerian elements are the only ones which have not been explicitly written in this section. Using the notation $\mathbf{r} = r\,\mathbf{n}$ with:

$$r = \frac{a(1-e^2)}{1+e\cos\nu} \quad \text{and} \quad \mathbf{n} = \begin{pmatrix}\cos(\omega+\nu)\cos\Omega - \sin(\omega+\nu)\sin\Omega\cos I\\ \cos(\omega+\nu)\sin\Omega + \sin(\omega+\nu)\cos\Omega\cos I\\ \sin(\omega+\nu)\sin I\end{pmatrix} \tag{B.25}$$

we give them all for completeness (some of them are used in the following sections):

$$\frac{\partial \mathbf{r}}{\partial a} = \frac{r}{a}\,\mathbf{n} \tag{B.26}$$

$$\frac{\partial \mathbf{r}}{\partial e} = -\frac{r\cos\nu + 2ae}{1+e\cos\nu}\,\mathbf{n} \tag{B.27}$$

$$\frac{\partial \mathbf{r}}{\partial I} = r\begin{pmatrix}\sin(\omega+\nu)\sin\Omega\sin I\\ -\sin(\omega+\nu)\cos\Omega\sin I\\ \sin(\omega+\nu)\cos I\end{pmatrix} \tag{B.28}$$

$$\frac{\partial \mathbf{r}}{\partial \omega} = r \begin{pmatrix} -\sin(\omega+\nu)\cos\Omega - \cos(\omega+\nu)\sin\Omega\cos I \\ -\sin(\omega+\nu)\sin\Omega + \cos(\omega+\nu)\cos\Omega\cos I \\ \cos(\omega+\nu)\sin I \end{pmatrix} \tag{B.29}$$

$$\frac{\partial \mathbf{r}}{\partial \Omega} = r \begin{pmatrix} -\cos(\omega+\nu)\sin\Omega - \sin(\omega+\nu)\cos\Omega\cos I \\ \cos(\omega+\nu)\cos\Omega - \sin(\omega+\nu)\sin\Omega\cos I \\ 0 \end{pmatrix} \tag{B.30}$$

$$\frac{\partial \mathbf{r}}{\partial \nu} = \frac{re\sin\nu}{1+e\cos\nu}\,\mathbf{n} + r \begin{pmatrix} -\sin(\omega+\nu)\cos\Omega - \cos(\omega+\nu)\sin\Omega\cos I \\ -\sin(\omega+\nu)\sin\Omega + \cos(\omega+\nu)\cos\Omega\cos I \\ \cos(\omega+\nu)\sin I \end{pmatrix} \tag{B.31}$$

B.3.2 Non-resonant case with a distant perturber

In this section, we detail the equations of motion for the secular system in the non-resonant case, with the presence of an additional planet with non-zero eccentricity and inclination (Chp. 5). The equations are quite generic: this perturber is not necessarily "distant". The Hamiltonian function $\mathcal{F}(P'_\omega, L, G, H, \omega', g, \delta h)$ is given by (5.11). Making apparent the required averages, its explicit form is $\mathcal{F} = \mathcal{F}_0 + \mathcal{F}_P + \mathcal{F}_S$ with:

$$\begin{cases} \mathcal{F}_0 = \nu'_\omega P'_\omega - \nu'_\Omega H \\ \mathcal{F}_P = -\dfrac{1}{4\pi^2}\displaystyle\int_0^{2\pi}\!\!\int_0^{2\pi} \left(\sum_{i=1}^{N} \frac{\mu_i}{|\mathbf{r}-\mathbf{r}_i|}\right) \frac{(1-e^2)^{3/2}}{(1+e\cos\nu)^2}\,\mathrm{d}\lambda^\star\,\mathrm{d}\nu \\ \mathcal{F}_S = -\dfrac{1}{4\pi^2}\displaystyle\int_0^{2\pi}\!\!\int_0^{2\pi} \frac{\mu'}{|\mathbf{r}-\mathbf{r}'|}\,\frac{(1-e'^2)^{3/2}}{(1+e'\cos\nu')^2}\,\frac{(1-e^2)^{3/2}}{(1+e\cos\nu)^2}\,\mathrm{d}\nu'\,\mathrm{d}\nu \end{cases} \tag{B.32}$$

In the expression of the planar component $\mathcal{F}_P$, the mean longitudes of all the planets i are gathered in the mute variable $\lambda^\star$, resulting in a single integral (see Sect. B.3.1). In the spatial component $\mathcal{F}_S$, both the integrals are realised over the true anomalies, resulting in the two coefficients depending on e, ν, e' and ν'. The canonical coordinates used are the same as in Sect. B.3.1, except that δh is the *relative* ascending node instead of simply $h = \Omega$. However, since Ω appears only in $\mathcal{F}_S$ and only through $\delta h = \Omega - \Omega'$, the partial derivative of $\mathcal{F}$ with respect to δh is equal to its partial derivative with respect to Ω.

Since $\lambda^\star$, ν' and ν are all mute variables, the components $\mathcal{F}_P$ and $\mathcal{F}_S$ can actually be gathered into a single double integral using the *common* angle $\nu^\star$:

$$\begin{aligned} \mathcal{F}_{PS} &= \mathcal{F}_P + \mathcal{F}_S \\ &= -\frac{1}{4\pi^2}\int_0^{2\pi}\!\!\int_0^{2\pi} \left(\frac{\mu'}{|\mathbf{r}-\mathbf{r}'|}\,\frac{(1-e'^2)^{3/2}}{(1+e'\cos\nu^\star)^2} + \sum_{i=1}^{N}\frac{\mu_i}{|\mathbf{r}-\mathbf{r}_i|}\right)\frac{(1-e^2)^{3/2}}{(1+e\cos\nu)^2}\,\mathrm{d}\nu^\star\,\mathrm{d}\nu \end{aligned} \tag{B.33}$$

The average may seem a bit confusing in that form, since $\nu^\star$ has a different meaning for each planet. However, it is better handled numerically because it requires the computation of only one double average.

The dynamical equations are computed using the chain rule:

$$\left\{\begin{array}{l}\dfrac{\partial\mathcal{F}}{\partial G}=\dfrac{\partial\mathcal{F}_{PS}}{\partial e}\dfrac{\partial e}{\partial G}+\dfrac{\partial\mathcal{F}_{PS}}{\partial I}\dfrac{\partial I}{\partial G}\\ \dfrac{\partial\mathcal{F}}{\partial H}=-\nu_\Omega+\dfrac{\partial\mathcal{F}_{PS}}{\partial I}\dfrac{\partial I}{\partial H}\end{array}\right.\quad;\quad\left\{\begin{array}{l}\dfrac{\partial\mathcal{F}}{\partial g}=\dfrac{\partial\mathcal{F}_{PS}}{\partial\omega}\\ \dfrac{\partial\mathcal{F}}{\partial\delta h}=\dfrac{\partial\mathcal{F}_S}{\partial\Omega}\end{array}\right. \tag{B.34}$$

where the derivatives of the Keplerian elements with respect to the canonical coordinates can be taken from (B.24).

The computation of the dynamical equations (B.34) requires the partial derivatives of $\mathcal{F}_S$ and $\mathcal{F}_{PS}$ with respect to the Keplerian elements. This is realised by inverting the integrals and partial derivatives symbols (this holds as long as there is no crossing between the orbits considered). Injecting the explicit expression of $\mathcal{F}$ (B.32-B.33) in the dynamical equations (B.34), we get:

$$\begin{aligned}\frac{\partial\mathcal{F}}{\partial G}=\frac{1}{4\pi^2}\int_0^{2\pi}\!\!\int_0^{2\pi}\Bigg[&\left(\mu'\frac{\mathbf{r}-\mathbf{r}'}{|\mathbf{r}-\mathbf{r}'|^3}\,\frac{(1-e'^2)^{3/2}}{(1+e'\cos\nu^\star)^2}+\sum_{i=1}^{N}\mu_i\frac{\mathbf{r}-\mathbf{r}_i}{|\mathbf{r}-\mathbf{r}_i|^3}\right)\cdot\left(\frac{\partial\mathbf{r}}{\partial e}\frac{\partial e}{\partial G}+\frac{\partial\mathbf{r}}{\partial I}\frac{\partial I}{\partial G}\right)\frac{(1-e^2)^{3/2}}{(1+e\cos\nu)^2}\\&+\left(\frac{\mu'}{|\mathbf{r}-\mathbf{r}'|}\,\frac{(1-e'^2)^{3/2}}{(1+e'\cos\nu^\star)^2}+\sum_{i=1}^{N}\frac{\mu_i}{|\mathbf{r}-\mathbf{r}_i|}\right)\frac{\sqrt{1-e^2}}{(1+e\cos\nu)^2}\left(3e+\frac{2(1-e^2)\cos\nu}{1+e\cos\nu}\right)\frac{\partial e}{\partial G}\Bigg]\mathrm{d}\nu^\star\,\mathrm{d}\nu\end{aligned}$$

$$\frac{\partial\mathcal{F}}{\partial H}=\frac{1}{4\pi^2}\int_0^{2\pi}\!\!\int_0^{2\pi}\left(\mu'\frac{\mathbf{r}-\mathbf{r}'}{|\mathbf{r}-\mathbf{r}'|^3}\,\frac{(1-e'^2)^{3/2}}{(1+e'\cos\nu^\star)^2}+\sum_{i=1}^{N}\mu_i\frac{\mathbf{r}-\mathbf{r}_i}{|\mathbf{r}-\mathbf{r}_i|^3}\right)\cdot\frac{\partial\mathbf{r}}{\partial I}\frac{\partial I}{\partial H}\frac{(1-e^2)^{3/2}}{(1+e\cos\nu)^2}\,\mathrm{d}\nu^\star\,\mathrm{d}\nu$$

$$\frac{\partial\mathcal{F}}{\partial g}=\frac{1}{4\pi^2}\int_0^{2\pi}\!\!\int_0^{2\pi}\left(\mu'\frac{\mathbf{r}-\mathbf{r}'}{|\mathbf{r}-\mathbf{r}'|^3}\,\frac{(1-e'^2)^{3/2}}{(1+e'\cos\nu^\star)^2}+\sum_{i=1}^{N}\mu_i\frac{\mathbf{r}-\mathbf{r}_i}{|\mathbf{r}-\mathbf{r}_i|^3}\right)\cdot\frac{\partial\mathbf{r}}{\partial\omega}\frac{(1-e^2)^{3/2}}{(1+e\cos\nu)^2}\,\mathrm{d}\nu^\star\,\mathrm{d}\nu$$

$$\frac{\partial\mathcal{F}}{\partial\delta h}=\frac{1}{4\pi^2}\int_0^{2\pi}\!\!\int_0^{2\pi}\mu'\frac{\mathbf{r}-\mathbf{r}'}{|\mathbf{r}-\mathbf{r}'|^3}\cdot\frac{\partial\mathbf{r}}{\partial\Omega}\,\frac{(1-e'^2)^{3/2}}{(1+e'\cos\nu')^2}\,\frac{(1-e^2)^{3/2}}{(1+e\cos\nu)^2}\,\mathrm{d}\nu'\,\mathrm{d}\nu$$

At this point, the partial derivatives of $\mathbf{r}$ with respect to the Keplerian elements are the only ones which have not been explicitly written in this section. They can be found in Sect. B.3.1, equations (B.26-B.31).

B.3.3 Case of a single resonance

In this section, we detail the equations of motion for the semi-secular system in the resonant case. The Hamiltonian function $\mathcal{K}(\Sigma, U, V, \sigma, u)$ is given by (3.57) and (3.58). Making apparent the required averages, its explicit form is $\mathcal{K} = \mathcal{K}_0 + \mathcal{K}_N + \mathcal{K}_R$ with:

$$\begin{cases} \mathcal{K}_0 = -\dfrac{\mu}{2a} - n_p \dfrac{k_p}{k}\sqrt{\mu\, a} \\ \mathcal{K}_N = -\dfrac{1}{4\pi^2}\displaystyle\int_0^{2\pi}\!\!\int_0^{2\pi} \left(\sum_{i\neq p} \frac{\mu_i}{|\mathbf{r}-\mathbf{r}_i|}\right) \frac{(1-e^2)^{3/2}}{(1+e\cos\nu)^2}\,\mathrm{d}\lambda^\star\,\mathrm{d}\nu \\ \mathcal{K}_R = -\dfrac{1}{2\pi k}\displaystyle\int_0^{2\pi k} \mu_p \left(\frac{1}{|\mathbf{r}-\mathbf{r}_p|} - \mathbf{r}\cdot\frac{\mathbf{r}_p}{|\mathbf{r}_p|^3}\right)\mathrm{d}\lambda_p \end{cases} \tag{B.35}$$

In the expression of the non-resonant part $\mathcal{K}_N$, the mean longitudes of all the planets $i \neq p$ are gathered in the mute variable $\lambda^\star$, resulting in a single integral (see Sect. B.3.1). Moreover, the integral over γ is realised through the true anomaly ν, since:

- a turn of γ equivalent to k_p turns of λ
- the integrand of $\mathcal{K}_N$ is 2π-periodic in λ so one turn is enough
- the integral over λ can be turned into an integral over ν by using (2.26)

In the expression of the resonant part $\mathcal{K}_R$, the integral over γ is realised through k turns of λ_p. We note, however, that $\mathbf{r}$ depends also on λ_p *via* the resonant angle σ (3.41). Indeed, in $\mathcal{K}_R$ the mean anomaly of the particle has to be replaced by:

$$M(\sigma, \lambda_p, \omega, \Omega) = \frac{1}{k}\sigma + \frac{k_p}{k}(\lambda_p - \omega - \Omega) \tag{B.36}$$

and its true anomaly ν accordingly. Since (B.35) is written in terms of the Keplerian elements:

$$\begin{cases} a = \dfrac{(k\Sigma)^2}{\mu} \\ e = \sqrt{1 - \left(\dfrac{U + k_p\Sigma}{k\Sigma}\right)^2} \\ I = \operatorname{acos}\left(\dfrac{V + k_p\Sigma}{U + k_p\Sigma}\right) \end{cases} \quad ; \quad \begin{cases} \omega = u \\ \Omega = v \\ \nu = f(\Sigma, U, \sigma, u, v) \end{cases} \tag{B.37}$$

its partial derivatives are computed using the chain rule:

$$\begin{cases} \dfrac{\partial \mathcal{K}}{\partial \Sigma} = \dfrac{\partial \mathcal{K}}{\partial a}\dfrac{\partial a}{\partial \Sigma} + \dfrac{\partial \mathcal{K}}{\partial e}\dfrac{\partial e}{\partial \Sigma} + \dfrac{\partial \mathcal{K}}{\partial I}\dfrac{\partial I}{\partial \Sigma} + \dfrac{\partial \mathcal{K}_R}{\partial \nu}\dfrac{\partial \nu}{\partial \Sigma} \\ \dfrac{\partial \mathcal{K}}{\partial U} = \dfrac{\partial \mathcal{K}}{\partial e}\dfrac{\partial e}{\partial U} + \dfrac{\partial \mathcal{K}}{\partial I}\dfrac{\partial I}{\partial U} + \dfrac{\partial \mathcal{K}_R}{\partial \nu}\dfrac{\partial \nu}{\partial U} \\ \dfrac{\partial \mathcal{K}}{\partial V} = \dfrac{\partial \mathcal{K}}{\partial I}\dfrac{\partial I}{\partial V} \end{cases} \quad ; \quad \begin{cases} \dfrac{\partial \mathcal{K}}{\partial \sigma} = \dfrac{\partial \mathcal{K}_R}{\partial \nu}\dfrac{\partial \nu}{\partial \sigma} \\ \dfrac{\partial \mathcal{K}}{\partial u} = \dfrac{\partial \mathcal{K}}{\partial \omega} + \dfrac{\partial \mathcal{K}_R}{\partial \nu}\dfrac{\partial \nu}{\partial \omega} \\ \dfrac{\partial \mathcal{K}}{\partial v} = 0 \end{cases} \tag{B.38}$$

Most of the partial derivatives of the Keplerian elements are not too complicated (only the non-zero ones are shown here):

$$\begin{cases} \dfrac{\partial a}{\partial \Sigma} = \dfrac{2k^2\Sigma}{\mu} \\ \dfrac{\partial e}{\partial \Sigma} = \dfrac{\sqrt{1-e^2}}{e}\dfrac{U}{k\Sigma^2} \\ \dfrac{\partial I}{\partial \Sigma} = \dfrac{\cos I - 1}{\sin I}\dfrac{k_p}{U + k_p\Sigma} \end{cases} \quad ; \quad \begin{cases} \dfrac{\partial e}{\partial U} = -\dfrac{\sqrt{1-e^2}}{e}\dfrac{1}{k\Sigma} \\ \dfrac{\partial I}{\partial U} = \dfrac{\cos I}{\sin I}\dfrac{1}{U + k_p\Sigma} \\ \dfrac{\partial I}{\partial V} = \dfrac{-1}{\sin I}\dfrac{1}{U + k_p\Sigma} \end{cases} \tag{B.39}$$

but the true anomaly ν appearing in $\mathcal{K}_R$ requires a specific treatment. Indeed, it is function of both of the angles (σ, u, v) and the momenta (Σ, U), because its value from the mean anomaly (B.36) depends on the eccentricity e through Kepler's equation. The partial derivatives of the true anomaly with respect to the angles are obtained straightforwardly:

$$\begin{cases} \dfrac{\partial \nu}{\partial \sigma} = \dfrac{\partial \nu}{\partial M}\dfrac{\partial M}{\partial \sigma} = \dfrac{1}{k}\dfrac{(1 + e\cos\nu)^2}{(1-e^2)^{3/2}} \\ \dfrac{\partial \nu}{\partial \omega} = \dfrac{\partial \nu}{\partial M}\dfrac{\partial M}{\partial \omega} = -\dfrac{k_p}{k}\dfrac{(1 + e\cos\nu)^2}{(1-e^2)^{3/2}} \\ \dfrac{\partial \nu}{\partial \Omega} = \dfrac{\partial \nu}{\partial M}\dfrac{\partial M}{\partial \Omega} = -\dfrac{k_p}{k}\dfrac{(1 + e\cos\nu)^2}{(1-e^2)^{3/2}} \end{cases} \tag{B.40}$$

Its partial derivatives with respect to the momenta are more subtle. The dependence of ν on the eccentricity can be made apparent by considering it as a three-stage nested function, passing through the eccentric anomaly E:

$$\nu \equiv \nu\Big(e, E\big(e, M(\sigma, \lambda_p, \omega, \Omega)\big)\Big) \tag{B.41}$$

Hence, the required derivatives can be computed as:

$$\frac{\partial \nu}{\partial \Sigma} = \frac{\mathrm{d}\nu}{\mathrm{d}e}\frac{\partial e}{\partial \Sigma} \quad ; \quad \frac{\partial \nu}{\partial U} = \frac{\mathrm{d}\nu}{\mathrm{d}e}\frac{\partial e}{\partial U} \tag{B.42}$$

using (B.39). It remains only to compute the total derivative of ν with respect to the eccentricity:

$$\frac{\mathrm{d}\nu}{\mathrm{d}e} = \frac{\partial \nu}{\partial e} + \frac{\partial \nu}{\partial E}\frac{\partial E}{\partial e} \tag{B.43}$$

Two partial derivatives are obtained from the relation (2.21) between the real and eccentric anomalies:

$$\frac{\partial \nu}{\partial e} = \frac{\sin E}{\sqrt{1-e^2}(1-e\cos E)} \quad ; \quad \frac{\partial \nu}{\partial E} = \frac{\sqrt{1-e^2}}{1-e\cos E} \tag{B.44}$$

The last one can be computed from Kepler's equation, considering the eccentric anomaly E as a function of M and e:

$$M = E - e\sin E \implies 0 = \partial E - e\cos E\,\partial E - \sin E\,\partial e \tag{B.45}$$

which leads finally to:

$$\frac{\partial E}{\partial e} = \frac{\sin E}{1-e\cos E} \tag{B.46}$$

Gathering (B.44) and (B.46) together, the total derivative of ν (B.43) is finally:

$$\frac{\mathrm{d}\nu}{\mathrm{d}e} = \frac{2-e^2-e\cos E}{\sqrt{1-e^2}(1-e\cos E)^2}\sin E \tag{B.47}$$

Now that we know all the partial derivatives of the Keplerian elements with respect to the canonical coordinates $(\Sigma, U, V, \sigma, u, v)$, the computation of the dynamical equations (B.38) requires the partial derivatives of $\mathcal{K}$ with respect to the Keplerian elements. This is realised by inverting the integrals and partial derivatives symbols (this holds as long as there is no crossing between the orbits considered). Injecting the explicit expression of $\mathcal{K}$ (B.35) in the dynamical equations (B.38), we get:

$$\begin{cases}
\dfrac{\partial \mathcal{K}_0}{\partial \Sigma} = \dfrac{\mu}{a\Sigma} - n_p k_p \\
\dfrac{\partial \mathcal{K}_N}{\partial \Sigma} = \dfrac{1}{4\pi^2}\displaystyle\int_0^{2\pi}\!\!\int_0^{2\pi} \left[\left(\sum_{i\neq p} \mu_i \frac{\mathbf{r}-\mathbf{r}_i}{|\mathbf{r}-\mathbf{r}_i|^3} \right) \cdot \left(\frac{\partial \mathbf{r}}{\partial a}\frac{\partial a}{\partial \Sigma} + \frac{\partial \mathbf{r}}{\partial e}\frac{\partial e}{\partial \Sigma} + \frac{\partial \mathbf{r}}{\partial I}\frac{\partial I}{\partial \Sigma} \right) \frac{(1-e^2)^{3/2}}{(1+e\cos\nu)^2} \right. \\
\qquad\qquad \left. + \left(\sum_{i\neq p} \frac{\mu_i}{|\mathbf{r}-\mathbf{r}_i|} \right) \frac{\sqrt{1-e^2}}{(1+e\cos\nu)^2} \left(3e + \frac{2(1-e^2)\cos\nu}{1+e\cos\nu} \right) \frac{\partial e}{\partial \Sigma} \right] \mathrm{d}\lambda^\star\,\mathrm{d}\nu \\
\dfrac{\partial \mathcal{K}_R}{\partial \Sigma} = \dfrac{1}{2\pi k}\displaystyle\int_0^{2\pi k} \mu_p \left(\frac{\mathbf{r}-\mathbf{r}_p}{|\mathbf{r}-\mathbf{r}_p|^3} + \frac{\mathbf{r}_p}{|\mathbf{r}_p|^3} \right) \cdot \left(\frac{\partial \mathbf{r}}{\partial a}\frac{\partial a}{\partial \Sigma} + \left(\frac{\partial \mathbf{r}}{\partial e} + \frac{\partial \mathbf{r}}{\partial \nu}\frac{\mathrm{d}\nu}{\mathrm{d}e} \right) \frac{\partial e}{\partial \Sigma} + \frac{\partial \mathbf{r}}{\partial I}\frac{\partial I}{\partial \Sigma} \right) \mathrm{d}\lambda_p
\end{cases}$$

$$\begin{cases}
\dfrac{\partial \mathcal{K}_0}{\partial U} = 0 \\
\dfrac{\partial \mathcal{K}_N}{\partial U} = \dfrac{1}{4\pi^2}\displaystyle\int_0^{2\pi}\!\!\int_0^{2\pi} \left[\left(\sum_{i\neq p} \mu_i \frac{\mathbf{r}-\mathbf{r}_i}{|\mathbf{r}-\mathbf{r}_i|^3} \right) \cdot \left(\frac{\partial \mathbf{r}}{\partial e}\frac{\partial e}{\partial U} + \frac{\partial \mathbf{r}}{\partial I}\frac{\partial I}{\partial U} \right) \frac{(1-e^2)^{3/2}}{(1+e\cos\nu)^2} \right. \\
\qquad\qquad \left. + \left(\sum_{i\neq p} \frac{\mu_i}{|\mathbf{r}-\mathbf{r}_i|} \right) \frac{\sqrt{1-e^2}}{(1+e\cos\nu)^2} \left(3e + \frac{2(1-e^2)\cos\nu}{1+e\cos\nu} \right) \frac{\partial e}{\partial U} \right] \mathrm{d}\lambda^\star\,\mathrm{d}\nu \\
\dfrac{\partial \mathcal{K}_R}{\partial U} = \dfrac{1}{2\pi k}\displaystyle\int_0^{2\pi k} \mu_p \left(\frac{\mathbf{r}-\mathbf{r}_p}{|\mathbf{r}-\mathbf{r}_p|^3} + \frac{\mathbf{r}_p}{|\mathbf{r}_p|^3} \right) \cdot \left(\left(\frac{\partial \mathbf{r}}{\partial e} + \frac{\partial \mathbf{r}}{\partial \nu}\frac{\mathrm{d}\nu}{\mathrm{d}e} \right) \frac{\partial e}{\partial U} + \frac{\partial \mathbf{r}}{\partial I}\frac{\partial I}{\partial U} \right) \mathrm{d}\lambda_p
\end{cases}$$

$$\begin{cases} \dfrac{\partial \mathcal{K}_0}{\partial V} = 0 \\ \dfrac{\partial \mathcal{K}_N}{\partial V} = \dfrac{1}{4\pi^2}\displaystyle\int_0^{2\pi}\int_0^{2\pi} \left(\sum_{i\neq p} \mu_i \frac{\mathbf{r}-\mathbf{r}_i}{|\mathbf{r}-\mathbf{r}_i|^3}\right) \cdot \frac{\partial \mathbf{r}}{\partial I}\frac{\partial I}{\partial V}\frac{(1-e^2)^{3/2}}{(1+e\cos\nu)^2}\,\mathrm{d}\lambda^\star\,\mathrm{d}\nu \\ \dfrac{\partial \mathcal{K}_R}{\partial V} = \dfrac{1}{2\pi k}\displaystyle\int_0^{2\pi k} \mu_p \left(\frac{\mathbf{r}-\mathbf{r}_p}{|\mathbf{r}-\mathbf{r}_p|^3} + \frac{\mathbf{r}_p}{|\mathbf{r}_p|^3}\right) \cdot \frac{\partial \mathbf{r}}{\partial I}\frac{\partial I}{\partial V}\,\mathrm{d}\lambda_p \end{cases}$$

$$\begin{cases} \dfrac{\partial \mathcal{K}_0}{\partial \sigma} = 0 \\ \dfrac{\partial \mathcal{K}_N}{\partial \sigma} = 0 \\ \dfrac{\partial \mathcal{K}_R}{\partial \sigma} = \dfrac{1}{2\pi k}\displaystyle\int_0^{2\pi k} \mu_p \left(\frac{\mathbf{r}-\mathbf{r}_p}{|\mathbf{r}-\mathbf{r}_p|^3} + \frac{\mathbf{r}_p}{|\mathbf{r}_p|^3}\right) \cdot \frac{\partial \mathbf{r}}{\partial \nu}\frac{\partial \nu}{\partial \sigma}\,\mathrm{d}\lambda_p \end{cases}$$

$$\begin{cases} \dfrac{\partial \mathcal{K}_0}{\partial u} = 0 \\ \dfrac{\partial \mathcal{K}_N}{\partial u} = \dfrac{1}{4\pi^2}\displaystyle\int_0^{2\pi}\int_0^{2\pi} \left(\sum_{i\neq p} \mu_i \frac{\mathbf{r}-\mathbf{r}_i}{|\mathbf{r}-\mathbf{r}_i|^3}\right) \cdot \frac{\partial \mathbf{r}}{\partial \omega}\frac{(1-e^2)^{3/2}}{(1+e\cos\nu)^2}\,\mathrm{d}\lambda^\star\,\mathrm{d}\nu \\ \dfrac{\partial \mathcal{K}_R}{\partial u} = \dfrac{1}{2\pi k}\displaystyle\int_0^{2\pi k} \mu_p \left(\frac{\mathbf{r}-\mathbf{r}_p}{|\mathbf{r}-\mathbf{r}_p|^3} + \frac{\mathbf{r}_p}{|\mathbf{r}_p|^3}\right) \cdot \left(\frac{\partial \mathbf{r}}{\partial \omega} + \frac{\partial \mathbf{r}}{\partial \nu}\frac{\partial \nu}{\partial \omega}\right)\,\mathrm{d}\lambda_p \end{cases}$$

$$\begin{cases} \dfrac{\partial \mathcal{K}_0}{\partial v} = 0 \\ \dfrac{\partial \mathcal{K}_N}{\partial v} = 0 \\ \dfrac{\partial \mathcal{K}_R}{\partial v} = 0 \end{cases}$$

The partial derivative of $\mathcal{K}_N$ with respect to v is zero because of the average (see Sect. 3.3.3), but the integrand takes non-zero values.

At this point, the partial derivatives of $\mathbf{r}$ with respect to the Keplerian elements are the only ones which have not been explicitly written in this section. They can be found in Sect. B.3.1, equations (B.26-B.31).

B.4 Secular Hamiltonian with a distant perturber in the fully planar case

Figure B.1 presents the level curves of the secular Hamiltonian in the case of a zero-inclination eccentric perturber and a zero-inclination trans-Neptunian object. If we consider an arbitrarily inclined trans-Neptunian object, on the contrary, each of these lines corresponds to the limit of a forbidden region in the Poincaré sections (Sect. 5.3).

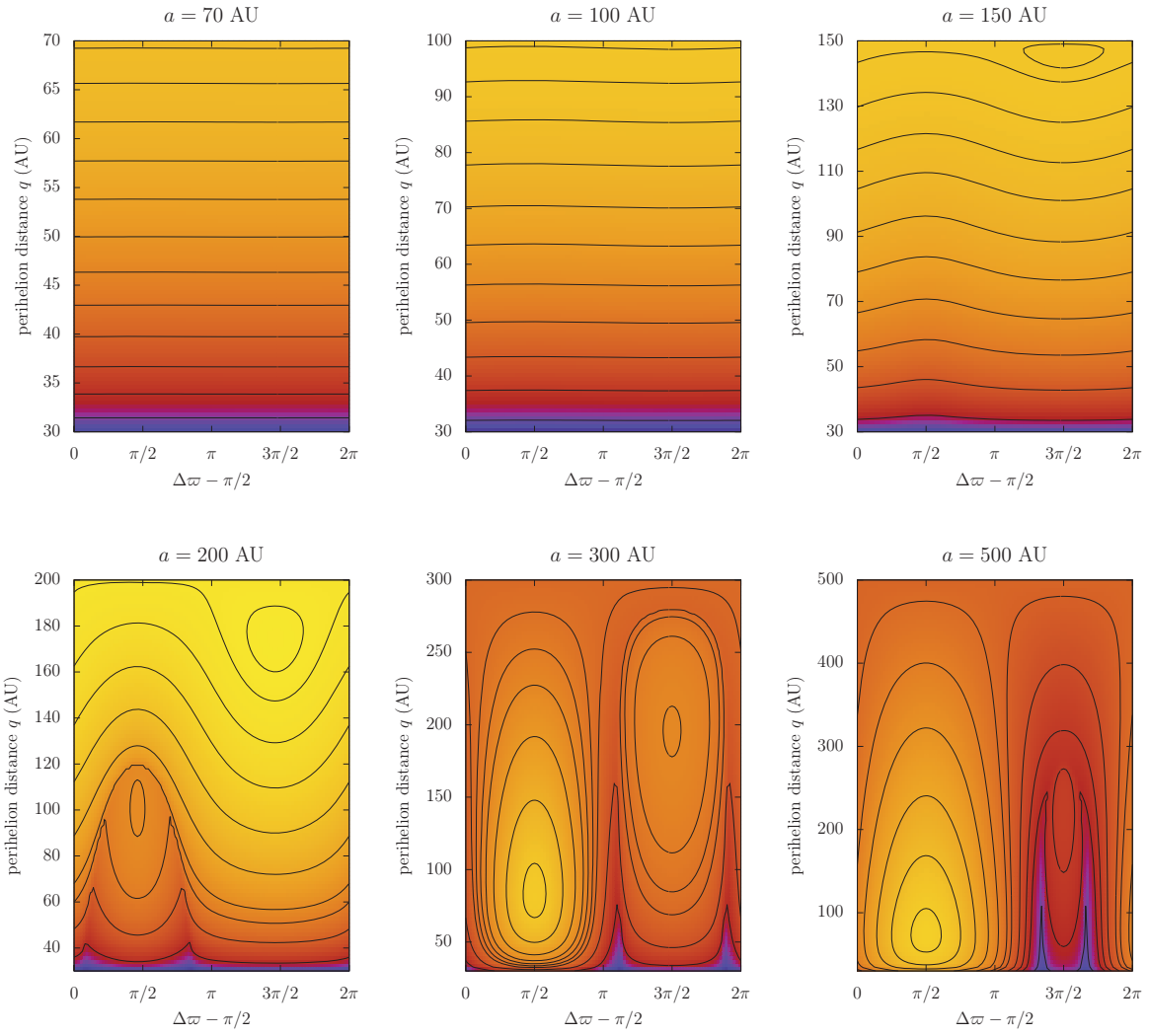

Figure B.1 – Level curves of the secular Hamiltonian in the fully planar case (same as Beust, 2016). The perturbations of both the internal planets and the distant one are completely taken into account (numerical average). In order to ease the comparison with the Poincaré sections throughout Chp. 5, we use the perihelion distance q instead of e, and $\Delta\varpi - \pi/2$ instead of $\Delta\varpi$.

B.5 Numerical treatment of the singularities

B.5.1 Splitting of the integral at node crossings

The computation of the secular (or semi-secular) Hamiltonian requires the numerical averaging of the inverse of the mutual distance between two bodies on Keplerian orbits. Here, the two bodies are called generically the "particle" and the "planet" (the latter with primed elements). The integrand is singular if the two orbits cross, but the double average is still well defined (Gronchi and Milani, 1999). However, the numerical computation can fail if the singularity is not explicitly taken into account. In practice, it is enough to split the integral where the crossing occurs and sum the segments.

If one of the two orbits lie in the reference plane, a necessary condition for a crossing to occur is that the second body is at one of its nodes (true anomaly equal to $-\omega$ or $-\omega+\pi$). This is the case for the planets considered in Chp. 3 or for the inner planets used in Chp. 5. By default, the double integral can always be split at these two points, whether a crossing happens or not.

The value of the true anomaly of the particle at a potential crossing point is less trivial if the planet has an eccentric and inclined orbit, as for the outer planet considered in Chp. 5. Let us introduce an intermediary reference frame $(\tilde{x},\tilde{y},\tilde{z})$, in which the $\tilde{z}$-axis is perpendicular to the orbital plane of the planet (in the direction of its angular momentum). For now, the $\tilde{x}$- and $\tilde{y}$-axes can be chosen arbitrarily in the orbital plane of the planet, so we will use the simplest possibility, in which the $\tilde{x}$-axis points toward the ascending node of the planet. In that reference frame, the instantaneous position of the particle can be written in terms of its conventional coordinates (x,y,z):

$$\begin{pmatrix}\tilde{x}\\ \tilde{y}\\ \tilde{z}\end{pmatrix} = R_1(-I')R_3(-\Omega')\begin{pmatrix}x\\ y\\ z\end{pmatrix} \tag{B.48}$$

with as usual:

$$\begin{pmatrix}x\\ y\\ z\end{pmatrix} = \frac{a\,(1-e^2)}{1+e\cos\nu}\begin{pmatrix}\cos(\omega+\nu)\cos\Omega-\sin(\omega+\nu)\sin\Omega\cos I\\ \cos(\omega+\nu)\sin\Omega+\sin(\omega+\nu)\cos\Omega\cos I\\ \sin(\omega+\nu)\sin I\end{pmatrix} \tag{B.49}$$

from Eqs. 2.28 and 2.29. The explicit computation of the two rotations appearing in (B.48) gives:

$$\begin{pmatrix}\tilde{x}\\ \tilde{y}\\ \tilde{z}\end{pmatrix} = \frac{a\,(1-e^2)}{1+e\cos\nu}\begin{pmatrix}\cos\alpha\cos\Delta\Omega-\sin\alpha\sin\Delta\Omega\cos I\\ \sin\alpha\sin I\sin I'+(\cos\alpha\sin\Delta\Omega+\sin\alpha\cos\Delta\Omega\cos I)\cos I'\\ \sin\alpha\sin I\cos I'-(\cos\alpha\sin\Delta\Omega+\sin\alpha\cos\Delta\Omega\cos I)\sin I'\end{pmatrix} \tag{B.50}$$

where $\alpha=\omega+\nu$ and $\Delta\Omega=\Omega-\Omega'$. An orbit crossing can only happen at one of the two points where the particle crosses the orbital plane of the planet, which means at

$\tilde{z} = 0$. The corresponding two values of the true anomaly ν of the particle are thus given by the two solutions of:

$$\tan(\omega + \nu) = \frac{\sin \Delta\Omega \, \sin I'}{\sin I \cos I' - \cos \Delta\Omega \, \cos I \sin I'} \tag{B.51}$$

As before, the double integral can always be split at these two points, whether a crossing happens or not. This prevents from the more complicated tests of actual orbit crossings presented in Sect. B.5.2.

B.5.2 The mutual nodal distances

As far as only the *value* of the secular Hamiltonian is required, the simple method presented in Sect. B.5.1 can be used to split the integral in smooth segments easily handled numerically. On the contrary, if the *partial derivatives* of the secular Hamiltonian are required (for instance to perform a numerical integration in the secular coordinates, as in Chp. 5), we need a way to verify if an orbit crossing is reached or has been encountered inside a given time-step. Indeed, contrary to the Hamiltonian itself, some of the partial derivatives are not defined at orbit crossings, so a special care should be taken. Convenient quantities were introduced by Gronchi (2002) in order to measure the proximity to orbit crossings: the ascending and descending *mutual nodal distances*. As we will see, they can be positive or negative according to the mutual positions of the two Keplerian orbits, and one of them is equal to zero if a crossing occurs.

Let us introduce the *mutual reference frame* $(\tilde{x}, \tilde{y}, \tilde{z})$, in which the $\tilde{z}$-axis is perpendicular to the orbital plane of the planet (in the direction of its angular momentum), and the $\tilde{x}$-axis points in the direction of the *mutual ascending node* of the particle, that is, the point where it crosses the orbital plane of the planet from negative to positive $\tilde{z}$ values. Then, we define the *mutual arguments of perihelion* $\tilde{\omega}$ and $\tilde{\omega}'$ as the angles between the $\tilde{x}$-axis and the directions of the respective perihelia (measured along the two orbits in the same direction as their true anomaly). The two mutual nodal distances are defined as:

$$\Delta^{\pm} = \frac{a(1-e^2)}{1 \pm e\cos\tilde{\omega}} - \frac{a'(1-e'^2)}{1 \pm e'\cos\tilde{\omega}'} \tag{B.52}$$

where $\pm$ stands for the ascending or descending mutual nodes. This distance is negative if the node of the particle is located inside the orbit of the planet, positive if it is located outside it, and zero at the exact crossing. The computation of $\tilde{\omega}$ and $\tilde{\omega}'$ is realised as follows: let $\mathbf{n}$ and $\mathbf{n}'$ be unit vectors pointing in the directions of the angular momenta of the two bodies. In the conventional reference frame, they can be written in terms of their orbital elements as:

$$\mathbf{n} = \begin{pmatrix} \sin\Omega \sin I \\ -\cos\Omega \sin I \\ \cos I \end{pmatrix} \quad ; \quad \mathbf{n}' = \begin{pmatrix} \sin\Omega' \sin I' \\ -\cos\Omega' \sin I' \\ \cos I' \end{pmatrix} \tag{B.53}$$

(see Sect. 2.1.3). The vector $\mathbf{n}'$ gives directly the direction of the $\tilde{z}$-axis. On the other hand, the $\tilde{x}$-axis is perpendicular to both $\mathbf{n}$ and $\mathbf{n}'$ and it points in direction of the mutual ascending node of the particle, so it is directed by the unit vector:

$$\mathbf{m} = \frac{\mathbf{n}' \times \mathbf{n}}{|\mathbf{n}' \times \mathbf{n}|} \tag{B.54}$$

Setting the true anomaly to zero in (2.28), the directions of the two perihelia write:

$$\mathbf{p} = \begin{pmatrix} \cos\omega\cos\Omega - \sin\omega\sin\Omega\cos I \\ \cos\omega\sin\Omega + \sin\omega\cos\Omega\cos I \\ \sin\omega\sin I \end{pmatrix} \quad ; \quad \mathbf{p}' = \begin{pmatrix} \cos\omega'\cos\Omega' - \sin\omega'\sin\Omega'\cos I' \\ \cos\omega'\sin\Omega' + \sin\omega'\cos\Omega'\cos I' \\ \sin\omega'\sin I' \end{pmatrix} \tag{B.55}$$

in the conventional reference frame. The cosines of the mutual arguments of perihelion are thus simply given by $\cos\tilde{\omega} = \mathbf{m}\cdot\mathbf{p}$ and $\cos\tilde{\omega}' = \mathbf{m}\cdot\mathbf{p}'$. Their explicit calculation from (B.53-B.55) gives the formulas used in Chp. 5, namely:

$$\begin{cases} \cos\tilde{\omega} = \dfrac{\cos\omega(\sin I\cos I' - \cos I\sin I'\cos\Delta\Omega) + \sin\omega\sin I'\sin\Delta\Omega}{\sqrt{1-(\cos I\cos I' + \sin I\sin I'\cos\Delta\Omega)^2}} \\ \cos\tilde{\omega}' = \dfrac{-\cos\omega'(\sin I'\cos I - \cos I'\sin I\cos\Delta\Omega) + \sin\omega'\sin I\sin\Delta\Omega}{\sqrt{1-(\cos I\cos I' + \sin I\sin I'\cos\Delta\Omega)^2}} \end{cases} \tag{B.56}$$

where $\Delta\Omega = \Omega - \Omega'$. In the case of a planet following a zero-inclination orbit (as the distant planet considered in Sect. 5.3), we have of course $\tilde{\omega} = \omega$, and $\tilde{\omega}'$ is simplified into:

$$\cos\tilde{\omega}' = \cos(\Omega - \varpi') \tag{B.57}$$

Finally, if the planet has a circular zero-inclination orbit (as the planets considered in Chp. 3 or the inner planets used in Chp. 5), the mutual nodal distances (B.52) turn simply to:

$$\Delta^{\pm} = \frac{a(1-e^2)}{1 \pm e\cos\omega} - a' \tag{B.58}$$

One can note that the mutual nodes are not defined if the mutual inclination of the two orbits is equal to zero. This was not a problem in the scope of this work, but this led Gronchi and Tardioli (2013) to define another way to describe the "distance" between two orbits, which is more general and more regular than its description in terms of orbital elements.

B.5.3 Equations with a nodal distance as time variable

As stated in Sect. 5.2.3, the orbit crossings occurring in the numerical integration of the secular system can be handled by a change of the independent ("time") variable during the integration. Indeed, taking the mutual nodal distance (Δ^+ or Δ^- accordingly) as the new independent variable, it is straightforward to make an integration step

arriving at the *exact* crossing point, which is then used to restart the integration after the singularity. This method was introduced by Hénon (1982) in a more general way. In this section, we detail the computation of the time derivative of the mutual nodal distance, which is necessary to obtain the equations of motion in the new coordinates (see Sect. 5.2.3). Using the chain rule, it writes generically:

$$\frac{\mathrm{d}\Delta^{\pm}}{\mathrm{d}t} = \frac{\partial\Delta^{\pm}}{\partial g}\dot{g} + \frac{\partial\Delta^{\pm}}{\partial\delta h}\dot{\delta h} + \frac{\partial\Delta^{\pm}}{\partial G}\dot{G} + \frac{\partial\Delta^{\pm}}{\partial H}\dot{H} + \frac{\partial\Delta^{\pm}}{\partial\omega'}\dot{\omega'} \tag{B.59}$$

where $\{\dot{g}, \dot{\delta h}, \dot{G}, \dot{H}, \dot{\omega'}\}$ are obtained from the partial derivatives of the secular Hamiltonian $\mathcal{F}(P'_\omega, L, G, H, \omega', g, \delta h)$ detailed in the appendix B.3.2. Hence, it only remains to compute the partial derivatives of the mutual nodal distance with respect to the coordinates $\{g, \delta h, G, H, \omega'\}$.

Case of a circular zero-inclination planet: From (B.58) and the expression of the Keplerian elements in terms of the canonical coordinates (B.22), we get:

$$\begin{cases} \dfrac{\partial\Delta^{\pm}}{\partial g} = \dfrac{\partial\Delta^{\pm}}{\partial\omega}\dfrac{\partial\omega}{\partial g} = \pm\dfrac{ae(1-e^2)}{(1\pm e\cos\omega)^2}\sin\omega \\ \dfrac{\partial\Delta^{\pm}}{\partial\delta h} = 0 \\ \dfrac{\partial\Delta^{\pm}}{\partial G} = \dfrac{\partial\Delta^{\pm}}{\partial e}\dfrac{\partial e}{\partial G} = \dfrac{-a}{1\pm e\cos\omega}\left[2e \pm \dfrac{(1-e^2)}{1\pm e\cos\omega}\cos\omega\right]\dfrac{\partial e}{\partial G} \\ \dfrac{\partial\Delta^{\pm}}{\partial H} = 0 \\ \dfrac{\partial\Delta^{\pm}}{\partial\omega'} = 0 \end{cases} \tag{B.60}$$

where the partial derivative $\partial e/\partial G$ is detailed in (B.24).

Case of an eccentric zero-inclination planet: In that case, the canonical coordinate δh is equal to $\Omega - \varpi'$ and ω' is suppressed from the equations (see Sect. 5.3). From (B.52) and (B.57), we get:

$$\begin{cases} \dfrac{\partial\Delta^{\pm}}{\partial g} = \dfrac{\partial\Delta^{\pm}}{\partial\omega}\dfrac{\partial\omega}{\partial g} = \pm\dfrac{ae(1-e^2)}{(1\pm e\cos\omega)^2}\sin\omega \\ \dfrac{\partial\Delta^{\pm}}{\partial\delta h} = \dfrac{\partial\Delta^{\pm}}{\partial\tilde{\omega}'}\dfrac{\partial\tilde{\omega}'}{\partial\delta h} = \mp\dfrac{a'e'(1-e'^2)}{(1\pm e'\cos\delta h)^2}\sin\delta h \\ \dfrac{\partial\Delta^{\pm}}{\partial G} = \dfrac{\partial\Delta^{\pm}}{\partial e}\dfrac{\partial e}{\partial G} = \dfrac{-a}{1\pm e\cos\omega}\left[2e \pm \dfrac{(1-e^2)}{1\pm e\cos\omega}\cos\omega\right]\dfrac{\partial e}{\partial G} \\ \dfrac{\partial\Delta^{\pm}}{\partial H} = 0 \end{cases} \tag{B.61}$$

where the partial derivative $\partial e/\partial G$ is detailed in (B.24).

Case of an eccentric inclined planet: In that case, the canonical coordinate δh is equal to $\Omega - \Omega'$ (see Sect. 5.2.2). From (B.52) and (B.56), we get:

$$\left\{\begin{array}{l} \dfrac{\partial\Delta^\pm}{\partial g} = \dfrac{\partial\Delta^\pm}{\partial\cos\tilde\omega}\dfrac{\partial\cos\tilde\omega}{\partial\omega} \\ \dfrac{\partial\Delta^\pm}{\partial\delta h} = \dfrac{\partial\Delta^\pm}{\partial\cos\tilde\omega}\dfrac{\partial\cos\tilde\omega}{\partial\delta h} + \dfrac{\partial\Delta^\pm}{\partial\cos\tilde\omega'}\dfrac{\partial\cos\tilde\omega'}{\partial\delta h} \\ \dfrac{\partial\Delta^\pm}{\partial G} = \dfrac{\partial\Delta^\pm}{\partial e}\dfrac{\partial e}{\partial G} + \dfrac{\partial\Delta^\pm}{\partial\cos\tilde\omega}\dfrac{\partial\cos\tilde\omega}{\partial I}\dfrac{\partial I}{\partial G} + \dfrac{\partial\Delta^\pm}{\partial\cos\tilde\omega'}\dfrac{\partial\cos\tilde\omega'}{\partial I}\dfrac{\partial I}{\partial G} \\ \dfrac{\partial\Delta^\pm}{\partial H} = \dfrac{\partial\Delta^\pm}{\partial\cos\tilde\omega}\dfrac{\partial\cos\tilde\omega}{\partial I}\dfrac{\partial I}{\partial H} + \dfrac{\partial\Delta^\pm}{\partial\cos\tilde\omega'}\dfrac{\partial\cos\tilde\omega'}{\partial I}\dfrac{\partial I}{\partial H} \\ \dfrac{\partial\Delta^\pm}{\partial\omega'} = \dfrac{\partial\Delta^\pm}{\partial\cos\tilde\omega'}\dfrac{\partial\cos\tilde\omega'}{\partial\omega'} \end{array}\right. \tag{B.62}$$

where the partial derivatives $\partial e/\partial G$, $\partial I/\partial G$ and $\partial I/\partial H$ are detailed in (B.24). Some of the other derivatives appearing in that expression are computed using (B.52):

$$\begin{array}{l} \dfrac{\partial\Delta^\pm}{\partial\cos\tilde\omega} = \mp\dfrac{ae(1-e^2)}{(1\pm e\cos\tilde\omega)^2} \quad ; \quad \dfrac{\partial\Delta^\pm}{\partial\cos\tilde\omega'} = \pm\dfrac{a'e'(1-e'^2)}{(1\pm e'\cos\tilde\omega')^2} \\ \dfrac{\partial\Delta^\pm}{\partial e} = \dfrac{-a}{1\pm e\cos\tilde\omega}\left[2e \pm \dfrac{(1-e^2)}{1\pm e\cos\tilde\omega}\cos\tilde\omega\right] \end{array} \tag{B.63}$$

Finally, the last required expressions are obtained from (B.56). Indeed, writing:

$$\cos\tilde\omega = \frac{\alpha}{\sqrt{\beta}} \quad \text{and} \quad \cos\tilde\omega' = \frac{\alpha'}{\sqrt{\beta}} \tag{B.64}$$

with:

$$\left\{\begin{array}{l} \alpha = \cos\omega(\sin I\cos I' - \cos I\sin I'\cos\delta h) + \sin\omega\sin I'\sin\delta h \\ \alpha' = -\cos\omega'(\sin I'\cos I - \cos I'\sin I\cos\delta h) + \sin\omega'\sin I\sin\delta h \\ \beta = 1 - (\cos I\cos I' + \sin I\sin I'\cos\delta h)^2 \end{array}\right. \tag{B.65}$$

these partial derivatives are:

$$\begin{array}{ll} \dfrac{\partial\cos\tilde\omega}{\partial\omega} = \dfrac{1}{\sqrt{\beta}}\dfrac{\partial\alpha}{\partial\omega} & ; \quad \dfrac{\partial\cos\tilde\omega'}{\partial\omega'} = \dfrac{1}{\sqrt{\beta}}\dfrac{\partial\alpha'}{\partial\omega'} \\ \dfrac{\partial\cos\tilde\omega}{\partial\delta h} = \dfrac{1}{\sqrt{\beta}}\left(\dfrac{\partial\alpha}{\partial\delta h} - \dfrac{\alpha}{2\beta}\dfrac{\partial\beta}{\partial\delta h}\right) & ; \quad \dfrac{\partial\cos\tilde\omega'}{\partial\delta h} = \dfrac{1}{\sqrt{\beta}}\left(\dfrac{\partial\alpha'}{\partial\delta h} - \dfrac{\alpha'}{2\beta}\dfrac{\partial\beta}{\partial\delta h}\right) \\ \dfrac{\partial\cos\tilde\omega}{\partial I} = \dfrac{1}{\sqrt{\beta}}\left(\dfrac{\partial\alpha}{\partial I} - \dfrac{\alpha}{2\beta}\dfrac{\partial\beta}{\partial I}\right) & ; \quad \dfrac{\partial\cos\tilde\omega'}{\partial I} = \dfrac{1}{\sqrt{\beta}}\left(\dfrac{\partial\alpha'}{\partial I} - \dfrac{\alpha'}{2\beta}\dfrac{\partial\beta}{\partial I}\right) \end{array} \tag{B.66}$$

It simply remains to use the expression of α to obtain:

$$\left\{\begin{array}{l} \dfrac{\partial\alpha}{\partial\omega} = -\sin\omega(\sin I\cos I' - \cos I\sin I'\cos\delta h) + \cos\omega\sin I'\sin\delta h \\ \dfrac{\partial\alpha}{\partial\delta h} = (\sin\omega\cos\delta h + \cos\omega\cos I\sin\delta h)\sin I' \\ \dfrac{\partial\alpha}{\partial I} = \cos\omega(\cos I\cos I' + \sin I\sin I'\cos\delta h) \end{array}\right. \tag{B.67}$$

as well as for α':

$$\begin{cases} \dfrac{\partial \alpha'}{\partial \omega'} = \sin\omega'(\sin I' \cos I - \cos I' \sin I \cos \delta h) + \cos\omega' \sin I \sin \delta h \\ \dfrac{\partial \alpha'}{\partial \delta h} = (\sin\omega' \cos \delta h - \cos\omega' \cos I' \sin \delta h) \sin I \\ \dfrac{\partial \alpha'}{\partial I} = \cos\omega'(\sin I' \sin I + \cos I' \cos I \cos \delta h) + \sin\omega' \cos I \sin \delta h \end{cases} \tag{B.68}$$

and for β:

$$\begin{cases} \dfrac{\partial \beta}{\partial \delta h} = 2(\cos I \cos I' + \sin I \sin I' \cos \delta h) \sin I \sin I' \sin \delta h \\ \dfrac{\partial \beta}{\partial I} = 2(\cos I \cos I' + \sin I \sin I' \cos \delta h)(\sin I \cos I' - \cos I \sin I' \cos \delta h) \end{cases} \tag{B.69}$$

This closes the computation of the time derivative of the mutual nodal distance.

Appendix C

Some numerical methods used

In this chapter, we detail some of the numerical algorithm implemented and tested throughout this work. The methods presented here usually come from reference works and they were adapted to the problem under study. We will not introduce routines which have been picked from libraries and used with only minor modifications: QUADPACK for the computation of integrals (Piessens et al., 1983); LAPACK for linear algebra; Numerical Recipes (Press et al., 2007) for maximisation/minimisation routines and root computations.

C.1 Resolution of Kepler's equation

Numerical studies involving the Keplerian elements often require the computation of the real anomaly ν as a function of the mean anomaly M. In order to do so, an intermediate step through the eccentric anomaly E is required (see Sect. 2.1.1). The difficulty comes from the passage from M to E, since Kepler's equation $M = E - e\sin E$ is implicit. The numerical method used should involve the smallest computational cost possible, because this operation can be required very frequently (as, for instance, at every step of a numerical integration). A vast panel of iterative methods were developed and a comparative study can be found in Danby and Burkardt (1983). The strategy used in this work is a variant of the best compromise reported by Danby (1987). Noting:

$$f(E) = E - e\sin(E) - M \tag{C.1}$$

each iterative step $E_{k+1} = E_k + \delta_k$ leading to the root of $f(E)$ for a given value of M requires the computation of:

$$\begin{aligned}
\delta_{\mathrm{N}} &= -\frac{f(E_k)}{f'(E_k)} && \longrightarrow \text{ Newton's method} \\
\delta_{\mathrm{H}} &= -\frac{f(E_k)}{f'(E_k) + \frac{1}{2}\delta_N f''(E_k)} && \longrightarrow \text{ Halley's method} \\
\delta_k &= -\frac{f(E_k)}{f'(E_k) + \frac{1}{2}\delta_H f''(E_k) + \frac{1}{6}\delta_H^2 f'''(E_k)} && \longrightarrow \text{ higher order}
\end{aligned} \tag{C.2}$$

Using the initial guess:

$$E_0 = \begin{cases} M + e^2(\sqrt[3]{6M} - M) & \text{if} \quad M < 1.14 \\ M + 0.85e & \text{otherwise} \end{cases} \tag{C.3}$$

we get a convergence to machine precision in one or two iterations almost everywhere in the (M, e) space. As shown in Fig. C.1, some small regions require up to three iterations, but never more than that. One can note that the threshold for M used in (C.3) is slightly different from Danby (1987) in order to speed up the convergence near pericentre. The difference comes from our more restrictive convergence criterion (which is only set to 10^{-12} in Danby, 1987).

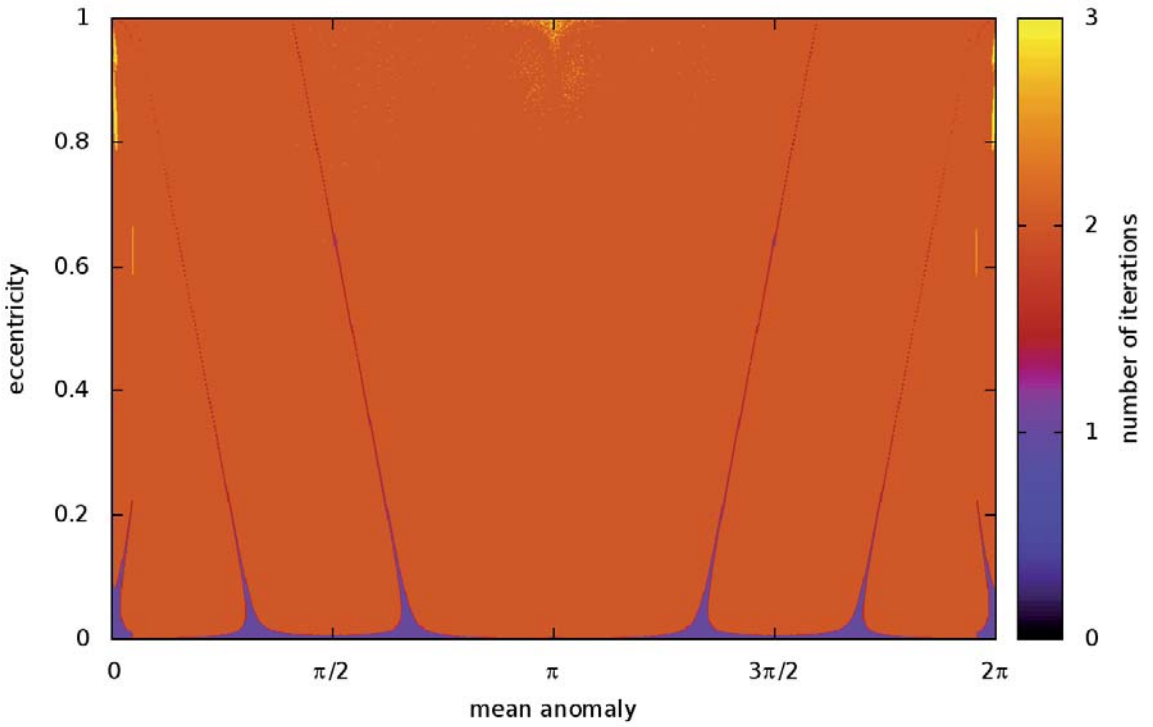

Figure C.1 – Number of iterations required to obtain the convergence of Kepler's equation below $|f(E)| = 5 \times 10^{-16}$ in double precision. The line $e = 0$ has a zero number of iterations since in that case $E = M$. The slight modification of the method presented by Danby (1987) allows to reduce the yellow zones near $M = 0$ and $M = 2\pi$.

Other methods should be used for hyperbolic orbits (see for instance Burkardt and Danby, 1983; Serafin, 1998) with a special attention to "pathological" cases (Serafin, 2002). The exact parabolic case has an explicit solution, as detailed by Duriez (1990).

C.2 Two-body propagator

Since the two-body problem is integrable analytically, the vector state at an arbitrary instant t can be computed exactly from an initial condition. Whereas it is straightforward to obtain it in Keplerian elements (see Sect. 2.1.2), in practice, we often need it directly in Cartesian coordinates centred on the second body. Fortunately, this can be achieved without calculating the full transformation toward and from Keplerian elements, by using Gauss' functions $f(t)$ and $g(t)$. The method presented here is taken from Danby (1988), page 162.

Let $\mathbf{r}_0$ and $\mathbf{v}_0$ be the initial Cartesian position and velocity of the body, with $C = \|\mathbf{r}_0 \times \mathbf{v}_0\| \neq 0$. The state of this body at any time t can be written in the form:

$$\begin{cases} \mathbf{r}(t) = f(t)\mathbf{r}_0 + g(t)\mathbf{v}_0 \\ \mathbf{v}(t) = f'(t)\mathbf{r}_0 + g'(t)\mathbf{v}_0 \end{cases} \tag{C.4}$$

where the prime symbol represents the time derivative. In particular, in coordinates (X, Y, Z) for which the Z-axis is perpendicular to the orbital plane, we have:

$$\begin{pmatrix} X(t) \\ Y(t) \\ Z(t) \end{pmatrix} = f(t) \begin{pmatrix} X_0 \\ Y_0 \\ 0 \end{pmatrix} + g(t) \begin{pmatrix} \dot{X}_0 \\ \dot{Y}_0 \\ 0 \end{pmatrix} \tag{C.5}$$

which is easily inverted to give:

$$\begin{cases} f(t) = \dfrac{1}{C}\left[X(t)\dot{Y}_0 - Y(t)\dot{X}_0\right] \\ g(t) = \dfrac{1}{C}\left[Y(t)X_0 - X(t)Y_0\right] \end{cases} \tag{C.6}$$

with $C = X_0\dot{Y}_0 - Y_0\dot{X}_0$. In the elliptic case, the explicit expression of $X(t)$ and $Y(t)$ can be obtained from Sect. 2.1.1 in function of the eccentric anomaly E:

$$\begin{cases} X(t) = a(\cos E - e) \\ Y(t) = a\sqrt{1-e^2}\sin E \end{cases} \tag{C.7}$$

Taking its time derivative and using the relation (2.26) between E and the mean anomaly M, we have also:

$$\begin{cases} \dot{X}(t) = -a\dot{E}\sin E = -\dfrac{na^2}{r}\sin E \\ \dot{Y}(t) = a\sqrt{1-e^2}\,\dot{E}\cos E = \dfrac{na^2}{r}\sqrt{1-e^2}\cos E \end{cases} \tag{C.8}$$

Using $C = na^2\sqrt{1-e^2}$, we get the expression of the Gauss' functions:

$$\begin{cases} f(t) = \dfrac{a}{r_0}(\cos\Delta E - 1) + 1 \\ g(t) = \Delta t + \dfrac{1}{n}(\sin\Delta E - \Delta E) \end{cases} \tag{C.9}$$

which allow to get $\mathbf{r}(t)$. Finally their derivatives, required to compute $\mathbf{v}(t)$, are:

$$\begin{cases} f'(t) = -\dfrac{na^2}{r_0}\dfrac{\sin\Delta E}{r(t)} \\ g'(t) = a\dfrac{\cos\Delta E - 1}{r(t)} + 1 \end{cases} \tag{C.10}$$

where $r(t)$ is computed from the already-obtained vector $\mathbf{r}(t)$. These functions are general, suitable also for an arbitrarily oriented reference frame (it amounts to apply a constant rotation to the left and right-hand sides of Eq. C.4). Please note that we expressed them only with respect to $\Delta t = t - t_0$ and $\Delta E = E - E_0$.

The detailed procedure to compute Gauss' functions is thus the following. At first, the semi-major axis of the orbit is obtained from the energy integral:

$$\frac{1}{2}\mathbf{v}_0^2 - \frac{\mu}{r_0} = -\frac{\mu}{2a} \tag{C.11}$$

which gives also the mean-motion $n = \sqrt{\mu/a^3}$. At this point, it only remains to compute ΔE in order to apply $f(t)$ and $g(t)$. This is realised using the relations:

$$\begin{cases} k_0 \equiv e\cos E_0 = 1 - \dfrac{r_0}{a} \\ h_0 \equiv e\sin E_0 = \dfrac{\mathbf{r}_0 \cdot \mathbf{v}_0}{na^2} \end{cases} \tag{C.12}$$

which are necessary for the resolution of Kepler's equation in the "difference form". The latter writes:

$$\begin{cases} M_0 = E_0 - e\sin E_0 \\ M = E - e\sin E \end{cases} \implies \Delta M = \Delta E - e(\sin E - \sin E_0) \tag{C.13}$$

that is:

$$n\Delta t - h_0 = \Delta E - k_0\sin\Delta E - h_0\cos\Delta E \tag{C.14}$$

This last equation is solved for ΔE by an iterative method analogous to the one presented for the conventional equation of Kepler (Sect. C.1).

Finally, it should be noted that for small values of ΔE, the cancellation errors in the expression of g (C.9), when subtraction the very close quantity $\sin\Delta E$, can be avoided by using the equivalent relation:

$$g(t) = \frac{1}{n}\Big[(1-k_0)\sin\Delta E + h_0(1-\cos\Delta E)\Big] \tag{C.15}$$

and replacing any occurrence of $1 - \cos\Delta E$ in (C.9), (C.10) and (C.15) by:

$$1 - \cos\Delta E = 2\sin^2\frac{\Delta E}{2} \tag{C.16}$$

A similar procedure can be applied to parabolic or hyperbolic orbits, see Danby (1988) for more details.

C.3 Cubic splines interpolation

In this section, we detail the interpolation method used to speed up the computation of the two-degree-of-freedom semi-secular Hamiltonian $\mathcal{K}$ for (U, u) fixed (Sects. 3.3.3 and 3.3.4). The function to be interpolated here has thus two dimensions (σ and Σ). The regularity condition of Hamiltonian functions (at least $\mathcal{C}^2$) makes natural the choice of cubic splines, since they impose the continuity of the two first derivatives on the grid points. After the introduction of the one-dimensional case (Sect. C.3.1), we discuss the generalisation to two dimensions (Sect. C.3.2).

C.3.1 One-dimensional case

Let us begin with the case of $N+1$ couples $\{x_k, f_k\}$ for $k = 1, 2...N+1$. Each point (x_k, f_k) is linked to the point (x_{k+1}, f_{k+1}) by the cubic polynomial:

$$P_k(x) = a_k + b_k(x - x_k) + c_k(x - x_k)^2 + d_k(x - x_k)^3 \tag{C.17}$$

with the following conditions of continuity:

$$\begin{cases} P_k(x_k) = f_k \\ P'_k(x_k) = P'_{k-1}(x_k) \\ P''_k(x_k) = P''_{k-1}(x_k) \\ P_k(x_{k+1}) = f_{k+1} \end{cases} \tag{C.18}$$

Writing $\Delta_k = x_{k+1} - x_k$, the latter lead to the subsystem:

$$\begin{cases} a_k = f_k \\ b_{k-1} + 2c_{k-1}\Delta_{k-1} + 3d_{k-1}\Delta_{k-1}^2 - b_k = 0 \\ c_{k-1} + 3d_{k-1}\Delta_{k-1} - c_k = 0 \\ b_k\Delta_k + c_k\Delta_k^2 + d_k\Delta_k^3 = f_{k+1} - f_k \end{cases} \tag{C.19}$$

which mixes the coefficients of P_k and P_{k-1}. Since all the $\{a_k\}$ are directly known, we remove them from the system. The subsystem (C.19) can be written as the matrix product:

$$\begin{pmatrix} 1 & 2\Delta_{k-1} & 3\Delta_{k-1}^2 & -1 & 0 & 0 \\ 0 & 1 & 3\Delta_{k-1} & 0 & -1 & 0 \\ 0 & & 0 & \Delta_k & \Delta_k^2 & \Delta_k^3 \end{pmatrix} \begin{pmatrix} b_{k-1} \\ c_{k-1} \\ d_{k-1} \\ b_k \\ c_k \\ d_k \end{pmatrix} = \begin{pmatrix} 0 \\ 0 \\ f_{k+1} - f_k \end{pmatrix} \tag{C.20}$$

There are N splines in total, each a them with 3 unknown coefficients, so we need $3N$ linear equations to close the system. For the first spline P_1, the two continuity equations

with the polynomial $k-1$ are not possible. This gives two arbitrary conditions to be added in the system, and they are usually chosen symmetrically for P_1 and P_N.

The general system can be written in terms of matrix blocks. Let us define the block $\mathbf{A}_k$ by:

$$\mathbf{A}_k = \begin{pmatrix} -1 & 0 & 0 \\ 0 & -1 & 0 \\ \Delta_k & \Delta_k^2 & \Delta_k^3 \\ 1 & 2\Delta_k & 3\Delta_k^2 \\ 0 & 1 & 3\Delta_k \end{pmatrix} \quad \text{for} \quad k = 2, 3 \ldots N-1 \tag{C.21}$$

At the borders, $\mathbf{A}_k$ has two lines less:

$$\mathbf{A}_1 = \begin{pmatrix} \Delta_1 & \Delta_1^2 & \Delta_1^3 \\ 1 & 2\Delta_1 & 3\Delta_1^2 \\ 0 & 1 & 3\Delta_1 \end{pmatrix} \quad \text{and} \quad \mathbf{A}_N = \begin{pmatrix} -1 & 0 & 0 \\ 0 & -1 & 0 \\ \Delta_N & \Delta_N^2 & \Delta_N^3 \end{pmatrix} \tag{C.22}$$

The general system to be inverted writes then:

$$\begin{pmatrix}
x & x & x & x & x & x & x & x & x & . & . & . & x & & x & & x & x & x & x \\
a & a & a & & & & & & & & & & & & & & & & & \\
a & \mathbf{A}_1 & a & a & a & a & & & & & & & & & & & & & & \\
a & a & a & a & a & a & & & & & & & & & & & & & & \\
 & & & a & \mathbf{A}_2 & a & & & & & & & & & & & & & & \\
 & & & a & a & a & a & a & a & & & & & & & & & & \\
 & & & a & a & a & a & a & a & & & & & & & & & & \\
 & & & & & & a & \mathbf{A}_3 & a & & & & & & & & & & & \\
 & & & & & & a & a & a & & & & & & & & & & & \\
 & & & & & & a & a & a & . & & & & & & & & & & \\
 & & & & & & & & & . & . & & & & & & & & & \\
 & & & & & & & & & & . & . & & & & & & & & \\
 & & & & & & & & & & & . & a & a & a & & & & & \\
 & & & & & & & & & & & & a & a & a & & & & & \\
 & & & & & & & & & & & & a & \mathbf{A}_{N-1} & a & & & & & \\
 & & & & & & & & & & & & a & a & a & a & a & a & & \\
 & & & & & & & & & & & & a & a & a & a & \mathbf{A}_N & a & & \\
 & & & & & & & & & & & & & & & a & a & a & & \\
y & y & y & y & y & y & y & y & y & . & . & . & y & y & y & y & y & y & y & y
\end{pmatrix}
\begin{pmatrix} b_1 \\ c_1 \\ d_1 \\ b_2 \\ c_2 \\ d_2 \\ b_3 \\ c_3 \\ d_3 \\ \vdots \\ b_{N-1} \\ c_{N-1} \\ d_{N-1} \\ b_N \\ c_N \\ d_N \end{pmatrix}
=
\begin{pmatrix} X \\ f_2 - f_1 \\ 0 \\ 0 \\ f_3 - f_2 \\ 0 \\ 0 \\ f_4 - f_3 \\ 0 \\ 0 \\ \vdots \\ 0 \\ 0 \\ f_N - f_{N-1} \\ 0 \\ 0 \\ f_{N+1} - f_N \\ Y \end{pmatrix} \tag{C.23}$$

where a signifies an entry of a $\mathbf{A}_k$ block, x and y mean arbitrary conditions for the borders, and blank fields are zero. The two border conditions are a matter of choice. For instance, we can choose to fix the values of the derivatives in x_1 and x_{N+1} to $X, Y \in \mathbb{R}$:

$$\begin{cases} b_1 = X \\ b_N + 2\,c_N\Delta_N + 3\,d_N\Delta_N^2 = Y \end{cases} \tag{C.24}$$

or we can choose to fix the values of the second derivatives:

$$\begin{cases} 2\,c_1 = X \\ 2\,c_N + 6\,d_N\Delta_N = Y \end{cases} \tag{C.25}$$

Of course, these conditions can be mixed according to the case under study. Finally, it simply remains to inverse the system (C.23) to get all the coefficients of the cubic

splines (for instance, using the LAPACK library). In order to avoid border effects, one must ensure that the abscissa in which we want to compute the value of the function is sufficiently far from the boundaries of the interpolation.

The above resolution presents the most general case, where the points $\{x_k\}$ are arbitrarily spaced. If they are equispaced, on the contrary, the uniform step Δ can be used as unit of length, which greatly simplifies the overall method[1]. Indeed, all the blocks $\mathbf{A}_k$ ($k = 2, 3...N-1$) are equal and the matrix to be inversed contains only integer coefficients. If successive interpolations have to be performed using the same number of equispaced points and the same type of border conditions, the LU decomposition of the matrix can be computed once for all and reused all along the program. In that way, the resolution of (C.23) is even faster than a matrix multiplication[2].

C.3.2 Two-dimensional case

For a two-dimensional function $\{x_k, y_k, f_k\}$, it seems natural to generalise the method presented in Sect. C.3.1 by using two-dimensional cubic polynomials, with 16 coefficients each. In a regular grid, by imposing the first and second partial derivatives to be equal at the grid points, and setting arbitrarily the cross derivative on the borders, plus the cross derivative and the partial first derivatives at the four corners, we get indeed a closed linear system. However, numerical experiments showed that such a system has an approximate rank deficiency (non-zero but small determinant), and that this situation gets worst when we increase the number of points. Hence, the numerical resolution becomes rapidly inefficient. The exact origin of this rank deficiency is still mysterious to me...

Two other (less satisfactory) strategies can be used to compute a two-dimensional cubic interpolation. The first one, used for instance in image processing, consists in imposing not only the value of the function at the corners of each cell, but also its two partial derivatives and its cross derivative. Each cell is thus decoupled from the others and the resolution becomes trivial. However, the computation of the three derivatives at each grid point is computationally expensive in our case. Moreover, we note that the resulting function is only $\mathcal{C}^1$. The second strategy, which is the one retained for this work, consists in considering the two-dimensional interpolation as two sets of one-dimensional cubic-spline interpolations. Let us consider a grid of the form:

$$\{x_i, y_j, f_{ij}\} \quad , \quad i = 1, 2...N \quad , \quad j = 1, 2...M \tag{C.26}$$

Each grid line (x-direction) is interpolated by one-dimensional splines, and the coefficients for each line j are saved. Then, the value of f at an arbitrary point (x, y) is obtained by a two-step procedure:

[1] If Δ is taken as unit of length, please note that the border values X and Y should be multiplied by Δ (for the derivatives) or Δ^2 (for the second derivatives).

[2] The successive inversions of the linear system are faster if the LU decomposition is stored instead of the inverse matrix. Indeed the unknown vector is obtained by "back-substitution", rather than by the (possibly very numerous) sums of products required by the matrix multiplication by the inverse.

1. compute f at every point $\{x, y_j\}$ for $j = 1, 2...M$ using the saved one-dimensional splines

2. use these values to perform another one-dimensional interpolation in the y-direction, which finally gives f at the point (x, y)

One can note that the x and y axes can be exchanged, in particular when the derivatives of the splines are required (the above procedure allows to compute only the y-derivative of f). The efficiency of this method may seem questionable, since a linear system of type (C.23) has to be inversed for each call of the interpolated function. However, the use of a regular grid allows to inverse the system by back substitution, which is extremely fast (see Sect. C.3.1).

In our case, the function which has to be interpolated is the semi-secular Hamiltonian $\mathcal{K}(\Sigma, U, V, \sigma, u)$ seen as a function of σ and Σ only (see Sects. 3.3.3 and 3.3.4). Its interpolation in a 30×30 grid covering the overall resonance island proves to be drastically faster than the direct computation of its value and partial derivatives, otherwise necessary for the numerical integrations. Such a grid resolution is found to be more than enough considering the required precision.

C.4 The trans-Neptunian tree

In this section, we detail the algorithm used to integrate numerically a large sample of Scattered Disc objects with initial conditions ranging from early stages of the Solar System until today. The sample considered in this work comes from the simulation of an Oort Cloud precursor by Fouchard et al. (2017): during that simulation, any object that got a semi-major axis smaller than 500 AU together with a perihelion distance beyond Neptune became part of the "Scattered Disc sample". From the 10^7 simulated particles, 263 627 of them were removed and put in this sample. Since they are not affected anymore by the galactic tides, our goal is to follow their evolution in detail, driven only by the perturbations of the planets, using a planetary model more accurate than in Fouchard et al. (2017). Our results are presented in Sect. 4.5.

The use of a synthetic representation for the motion of the planets allows to get directly their positions at a given time, without the need of long backward integrations and heavy data files (the positions of the planets should have been stored at every time-step during 5 Gyrs). The direct numerical integration of the planets together with the massless particles is also judged inefficient, because the time-step would be restricted according to the fastest planet in the system (a few years for Jupiter), whereas the trans-Neptunian objects considered here have orbital periods of several thousand years. Consequently, we used the synthetic representation of Laskar (1990), supposed valid on a billion-year timescale. As discussed in Sect. 4.5, even if the orbits of the giant planets are rather stable from the late planetary migration, such a model could be not strictly realistic.

The second difficulty comes from the different times of the initial conditions contained in the sample. Even if the planets are modelled by a synthetic representation, the computation of their positions is by far the most expensive part of the algorithm (because of the sines and cosines). Hence, in order to get reasonable computation times, a large number of particle should be integrated at the same time. At a given time-step, the algorithm must thus determine which bodies are "active" (they must be propagated), and which ones are still in the "waiting-list" because the integration has not reached yet their time of initial conditions. If a time-step goes past the time of a new initial condition, the corresponding particle is propagated using a two-body motion around the barycentre of the Solar System in order to match the exact time reached by the numerical integration[3]. It is then added to the active particles.

The particles reaching perihelion distances inside the planetary region or semi-major axes larger than 2000 AU are removed from the simulation. In particular, if at a given time all the active particles are removed, the time t reached by the numerical integration is directly advanced to the earliest initial condition contained in the waiting-list (this is allowed thanks to the use of a synthetic representation for the planets). The action of removing particles adds a new technical problem: if the particles are sorted in a array by their time of initial conditions, the removal of one of them requires to shift all the remaining particles by one index. Considering the large number of particles and the high rate of ejection, this would be pretty inefficient. That problem was treated by sorting the particles in a Binary Search Tree according to their time of initial conditions. In a Binary Search Tree, each element contains two pointers (*left* and *right*) pointing towards elements which have a lower and higher value, respectively, than its own value. Hence, the portion of the tree hanging to its left pointer contains only elements with values lower than its own value, and the portion of the tree hanging to its right pointer contains only elements with values higher than its own value. Such a structure allows very fast operations as searching, adding or removing elements, which are implemented using very elegant recursive algorithms. For instance, let us consider a given element of the Binary Search Tree: if its time of initial conditions is *below* the current integration time, then it is "active", so it must be propagated in the next time-step. Since this is also the case for every element hanging to its left pointer, we only have to repeat the test to the right portion of the tree. On the contrary, if the time of initial conditions of the element is *above* the current integration time, then it is "waiting" and this is also the case for every element hanging to its right pointer, so we only have to repeat the test to the left portion of the tree.

Figure C.2 illustrates the operations of adding an element (realised before the numerical integration) and deleting an element (realised if a particle is removed from the integration). If a new element has an already present number, in principle it could be

[3]The integration is realised with a symplectic integrator of type $ABAC_3$ (Laskar and Robutel, 2001). In barycentric coordinates, a fixed time-step of 10 years was found to be a good compromise (see Sect. C.5). Accordingly, the two-body propagations are used for a fraction of time-step, that is only for some years. Considering the large orbital periods of the particles, the resulting change of the sample distribution is negligible.

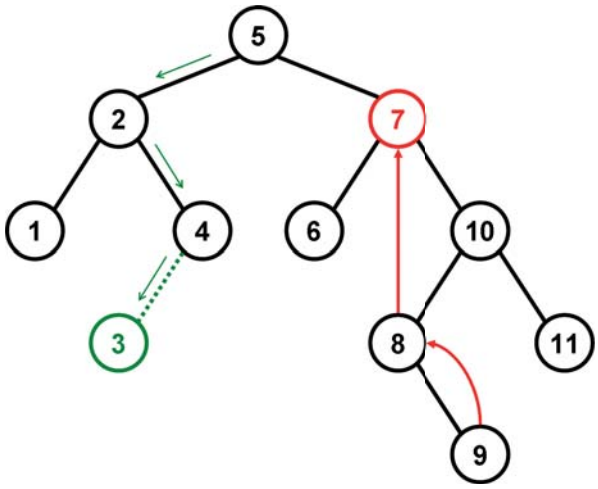

added: **3** as a new-born child
deleted: **7** replaced by **8** (itself replaced by **9** and its possible progeny)

Figure C.2 – Elementary operations which can be applied to a Binary Search Tree. In our application, the integers are replaced by the times of initial conditions. A new element does not modify the tree structure: it is added as a new-born child, that is instead of a "leaf" (*NULL* child). An element to be deleted is: *i*) simply suppressed if it has no child; *ii*) replaced by its child and its progeny if it has only one; *iii*) replaced by the minimum element of its right progeny (or the maximum element of its left progeny), which is suppressed according to *i* or *ii*.

added arbitrarily to the left or to the right portion of the tree. In our case, an object having a time of initial condition *equal* to the time t reached by the integration must be propagated. Hence we use the convention of adding elements with already present numbers to the left portion of the tree, along with the elements with lower values (which must also be propagated).

In order to achieve reasonable computation times, the program is also parallelized such that at each time-step, the active particles are propagated in parallel. Indeed, each portion of a Binary Search Tree can be considered as independent and treated by a different processor. Hence, each processor propagate only the active objects contained in its respective tree portion (the tree must though be *balanced* in order to fairly divide the tasks between processors). Thanks to the Binary Search Tree structure, the identification of the active particles, performed by each processor in its portion or tree, is very fast. Using that algorithm, a good compromise was obtained by splitting the sample of 263 627 objects into sub-samples of 20 000 particles. Each of them required about 5 days of computation to complete 5 Gyrs of integration.

An alternative to the Binary Search Tree would have consisted in an ordered linked-list, keeping at any time-step a pointer to the first element of the "waiting" portion of the list. This would avoid to browse the list at each time-step, but with the drawback to be less easily parallelized, since each element of a linked-list cannot be considered as independent (contrary to the branch of a binary tree).

C.5 Integrators for massive billion-year simulations

In this section, we discuss the choice of numerical integrator for computing the trajectory of several hundred thousand particles over a 5-Gyr timescale. Various numerical integrators can be found in the literature, including the widely used MERCURY package by Chambers (1999). However, the particular type of orbits studied here (always beyond the planets and possibly very distant from them), as well as the particular form of the planetary trajectories used (a synthetic representation, see Sect. C.4), could allow a more efficient specific treatment. In the following, we detail some of the integrators implemented and tested during this study. Their efficiency is discussed in Sect. C.5.4 as compared to classic methods (as the non-symplectic integrator by Everhart 1985 and its improved version by Rein and Spiegel 2015).

First of all, whatever the integrator used, the integration in barycentric coordinates turns out to be several orders of magnitude faster than in heliocentric coordinates. Indeed, the motion of distant small Solar System bodies consists in a slightly perturbed two-body problem with respect to the barycentre of the Solar System, gathering the mass of the Sun and the planets (Todorovic-Juchniewicz, 1981; Kaib et al., 2011). If heliocentric coordinates are used for the numerical integration, the short-period oscillations of the "force" term, due to the displacement of the Sun around the barycentre of the Solar System, make necessary the use of a very small time-step (a fraction of period of Jupiter). Consequently, this cancels the benefit of the synthetic representation over the direct integration of the planets. On the other hand, if barycentric coordinates are used for the numerical integration, the same precision is reached with a much larger time-step (a fraction of period of the small body), leading to a much faster algorithm. As an example, Fig. C.3 compares the final orbital energy for the same orbits integrated in heliocentric and barycentric coordinates. While the results are equally bad for small perihelion distances (because of close encounters), the supremacy of the barycentric coordinates is obvious for more distant trajectories. Using a non-symplectic integrator with adjustable time-step (not shown), the final results in the two sets of coordinates are equivalent, because the step size is adjusted to reach the precision requested. However, the integration in heliocentric coordinates is more than ten times slower since it realises much more numerous smaller time-steps. Barycentric coordinates lead thus in any case to a much more efficient algorithm. One can note that the analytical and semi-analytical theories developed through this work are intrinsically heliocentric: in order to allow their comparison to the numerical results, it is enough to write the *output* of the numerical integrations in heliocentric coordinates, even if they are realised in barycentric ones[4].

[4]In some additional experiments, we performed also a few integrations in which the planets were included consistently. In that case, the natural choice is to use Jacobi coordinates (see for instance Milani and Gronchi, 2010): the most distant body included is the test-particle, so its coordinates are indeed barycentric. Moreover, the equations in Jacobi coordinates take the form required by the integrators by Laskar and Robutel (2001).

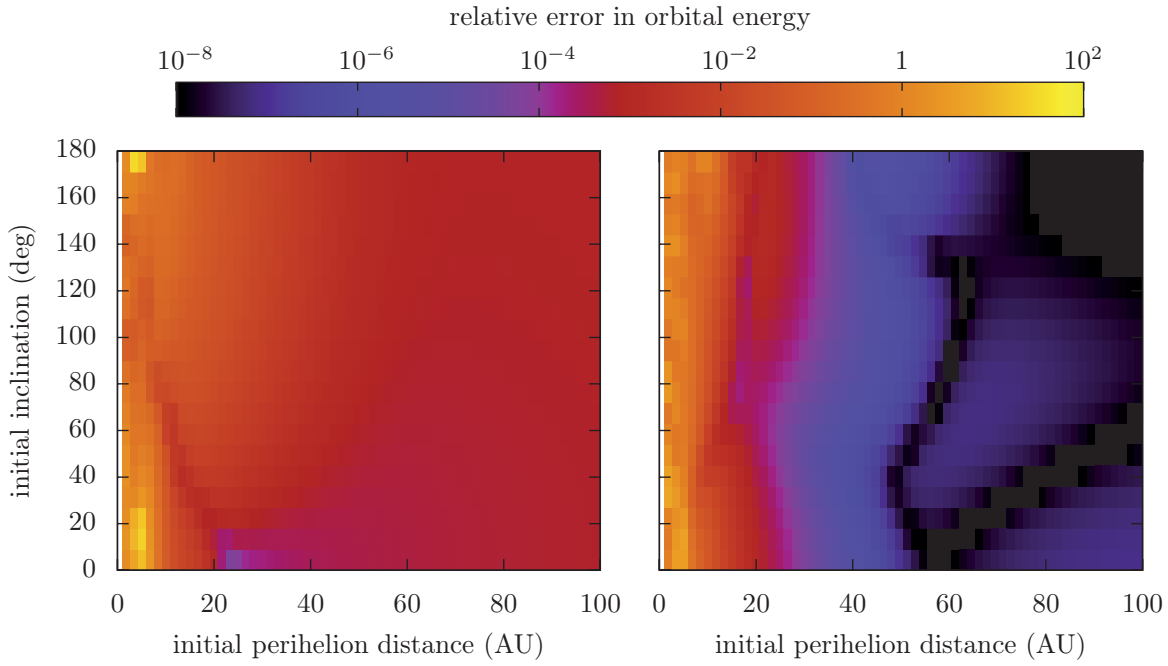

Figure C.3 – Comparison of numerical integrations in heliocentric (left graph) and barycentric (right graph) coordinates. The results are plotted in the plane of the initial barycentric values of the perihelion distance q and the inclination I. The other initial barycentric orbital elements are for all orbits: $a = 800$ AU, $\omega = 54°$, $\Omega = 0°$ and $M = 180°$. We used in both case the symplectic integrator $ABAC_3$ by Laskar and Robutel (2001) with a constant time-step of 10 years (see Sect. C.5.1). The numerical integrations are all performed over 2500 time-steps, that is slightly more than one orbit. The colour shade represents the relative error of the final value of $1/a$, as compared to a reference numerical integration (integrator by Rein and Spiegel, 2015, with strong tolerance factor).

Generically, there are two types of integrators: implicit (in which each time-step requires to solve a system of non-linear equations) and explicit (in which the state after one step is an explicit function of the current state). Of course, implicit integrators are more difficult to implement and lead to heavier computational costs[5]. However, they are much easier to develop theoretically and they are generally more stable numerically than explicit schemes. Then, there are two kinds of problems in which a numerical solution is needed, associated to different kinds of integrators:

1. The calculation of given trajectories with a high accuracy, in which the (algorithm-dependent) deviation from the "exact" solution *must* be negligible.

2. The long-term computation of fictitious objects, for which we are interested in the *qualitative* behaviour of the population, but not in the exactness of every individual trajectory (which is anyway impossible to obtained over long durations).

[5]The resolution of the system of non-linear equations requires an iterative procedure, for instance a Newton-type method with a convergence criterion. The first guess is generally computed by interpolation from the previous steps.

The first case is the typical problem of ephemerides calculations, in which the purely numerical errors are (or should be) very small compared to the uncertainties coming from the initial conditions. Long-term predictions are thus meaningless because of the chaotic divergence of nearby trajectories. In such a case, the precision takes precedence over the computation time, and since the integrations are performed on relatively short timescales, fundamental algorithm-dependent errors (such as energy drifts) stay anyway at a negligible level. For this purpose, two integrators are widely used in celestial mechanics: the implicit method of Everhart (1985), actually quite messy (so one should prefer the revised version by Rein and Spiegel, 2015), and the Bulirsch-Stoer algorithm (Hairer et al., 2008).

The second case, on the contrary, deals with general properties of the dynamical system such as its long-term stability. For instance, the precise position of a given object is not important, in contrast to the qualitative evolution of its orbit. In such a case (which is the one of this work), we must ensure that the fundamental properties of the system are reproduced by the integrator, so that the general behaviour *of the sample* stays close to the real one. We are dealing here with Hamiltonian systems, so their basic features are the conservation of the Hamiltonian value, the time-reversibility of the equations, and the conservation of the symplectic structure of the equations (each time-step should be canonical, that is area-preserving in the phase space). Unfortunately, numerical integrators *cannot* conserve exactly the Hamiltonian value generically while being symplectic (Zhong and Marsden, 1988). However, the symplecticity ensures that the energy undergoes no irreversible drift, so that the numerical solutions always stay in the vicinity of the real trajectories (or say, in the dynamical region of the phase space that they occupy). For instance, the periodic trajectory of a pendulum can become quasi-periodic (or even chaotic for improperly large time-steps), but it will never be damped or accelerated, as it would inevitably occur for non-symplectic methods (until it asymptotically stops, or makes complete cycles around its axis). This property of symplectic integrators can be summed up by: "instead of giving the approximate solution of an exact system of differential equations, symplectic integrators provide the exact solution of an approximate system". At this point, please note that this approximate system is *defined* by the time-step of the integrator, so that a change of step size during the integration would be equivalent to a change of dynamical system! This would of course break the conservation properties of the overall algorithm (see for instance Yoshida, 1993; Breiter, 1999), even if some tricks can be used to reduce the discontinuities due to variable steps or changes of numerical scheme (Kaib et al., 2011).

Implicit symplectic and time-reversible integrators can be obtained quite straightforwardly. For instance, these properties are shared by all the implicit Runge-Kutta scheme of even order using the coefficients of the Gaussian quadrature (see Hairer et al., 2008). On the other hand, explicit symplectic integrators can only by applied to a particular form of Hamiltonian systems, namely when the Hamiltonian function can be written as the sum of "sub-Hamiltonians" which are each integrable individually (Breiter, 1999). The most common case of application is when it has the form $\mathcal{H} = \mathcal{A} + \varepsilon\mathcal{B}$, for which we can take advantage of the smallness of $\varepsilon \ll 1$. In the

following, we briefly introduce the explicit symplectic and time-reversible integrators of Laskar and Robutel (2001) and we detail their application to our problem, with and without the use of time-regularisation methods.

C.5.1 Explicit symplectic integrators

From Sect. 2.2, we know that the time derivative of a function f of the coordinates writes:

$$\frac{\mathrm{d}f}{\mathrm{d}t} = \{f, \mathcal{H}\} = -L_{\mathcal{H}} f \tag{C.27}$$

where $L_{\mathcal{H}} = \{\mathcal{H}, .\}$ is the linear operator associated to the Poisson brackets[6]. The function f evaluated along the solution of the dynamical system, as seen as a function of t, can be written as:

$$f(t) = \exp(-tL_{\mathcal{H}}) f(0) = \sum_{n=0}^{\infty} \frac{t^n}{n!} (-L_{\mathcal{H}})^n f(0) \tag{C.28}$$

For instance, f can be one component of the state vector. The basic principle of a symplectic integrator is to approximate the operator $\exp(-tL_{\mathcal{H}})$ by the one coming from an integrable Hamiltonian system, say $\exp(-tL_{\mathcal{K}})$, mimicking the original one. This method relies heavily on the Campbell-Baker-Hausdorff formula for several non-commuting operators (Yoshida, 1993). For two non-commuting operators X and Y, it states that:

$$\exp X \exp Y = \exp Z \tag{C.29}$$

for some unknown operator Z. Since X and Y do not commute, we have of course $Z \neq X + Y$. In our case, though, it is enough to know that Z exists (whatever its expression) to guarantee that an integrator composed of several sub-steps of integrable Hamiltonians is symplectic. In particular, if we consider several Hamiltonian functions $\{\mathcal{X}_i\}$, the operator:

$$S(h) = \exp(-a_1 h L_{\mathcal{X}_1}) \exp(-a_2 h L_{\mathcal{X}_2}) \exp(-a_3 h L_{\mathcal{X}_3}) \ldots \quad \text{with } a_1, a_2, a_3 ... \in \mathbb{R} \tag{C.30}$$

can be written as $\exp(-hL_{\mathcal{K}})$ for some unknown Hamiltonian $\mathcal{K}$. If the dynamical systems defined by the $\{\mathcal{X}_i\}$ are all integrable analytically, then the operator S (which can be considered as one step h of a symplectic integrator) has an exact analytical expression. The difference between two integrators comes thus from the choice of the Hamiltonians $\{\mathcal{X}_i\}$ and the corresponding coefficients $\{a_i\}$, designed to make S as close as possible to the original operator $\exp(-hL_{\mathcal{H}})$.

Let us consider that the Hamiltonian $\mathcal{H}$ can be written as:

$$\mathcal{H} = \mathcal{A} + \varepsilon \mathcal{B} \tag{C.31}$$

[6]Laskar and Robutel (2001) define the Poisson brackets as the opposite of the one used in this work. One must be careful of the corresponding minus signs when comparing the two versions.

with no assumption yet on the smallness of the coefficient ε. If $\mathcal{A}$ and $\mathcal{B}$ taken separately are both integrable analytically, generic integrators with n stages can be obtained by the operator:

$$S_n(h) = \exp(-a_1 h L_{\mathcal{A}}) \exp(-b_1 h L_{\varepsilon\mathcal{B}}) ... \exp(-a_n h L_{\mathcal{A}}) \exp(-b_n h L_{\varepsilon\mathcal{B}}) \tag{C.32}$$

Indeed, one step h of the real system writes:

$$\exp(-hL_{\mathcal{H}}) = 1 - h\{\mathcal{H}, .\} + \frac{h^2}{2}\{\mathcal{H}, \{\mathcal{H}, .\}\} + \mathcal{O}(h^3) \tag{C.33}$$

that is, using the expression of $\mathcal{H}$:

$$\begin{aligned}\exp(-hL_{\mathcal{H}}) = 1 &- h\{\mathcal{A}, .\} - \varepsilon h\{\mathcal{B}, .\} \\ &+ \frac{h^2}{2}\{\mathcal{A}, \{\mathcal{A}, .\}\} + \varepsilon\frac{h^2}{2}\{\mathcal{A}, \{\mathcal{B}, .\}\} + \varepsilon\frac{h^2}{2}\{\mathcal{B}, \{\mathcal{A}, .\}\} + \varepsilon^2\frac{h^2}{2}\{\mathcal{B}, \{\mathcal{B}, .\}\} \\ &+ \mathcal{O}(h^3)\end{aligned} \tag{C.34}$$

If we consider for instance a two-stage integrator

$$S_2(h) = \exp(-a_1 h L_{\mathcal{A}}) \exp(-b_1 h L_{\varepsilon\mathcal{B}}) \exp(-a_2 h L_{\mathcal{A}}) \exp(-b_2 h L_{\varepsilon\mathcal{B}}) \tag{C.35}$$

the analogous expansion for the approximate Hamiltonian $\mathcal{K}$ is:

$$\begin{aligned}\exp(-hL_{\mathcal{K}}) = &\left(1 - a_1 h\{\mathcal{A}, .\} + \frac{(a_1 h)^2}{2}\{\mathcal{A}, \{\mathcal{A}, .\}\} + \mathcal{O}(h^3)\right) \\ &\times \left(1 - b_1\varepsilon h\{\mathcal{B}, .\} + \frac{(b_1 h)^2}{2}\varepsilon^2\{\mathcal{B}, \{\mathcal{B}, .\}\} + \mathcal{O}(h^3)\right) \\ &\times \left(1 - a_2 h\{\mathcal{A}, .\} + \frac{(a_2 h)^2}{2}\{\mathcal{A}, \{\mathcal{A}, .\}\} + \mathcal{O}(h^3)\right) \\ &\times \left(1 - b_2\varepsilon h\{\mathcal{B}, .\} + \frac{(b_2 h)^2}{2}\varepsilon^2\{\mathcal{B}, \{\mathcal{B}, .\}\} + \mathcal{O}(h^3)\right)\end{aligned} \tag{C.36}$$

that is:

$$\begin{aligned}\exp(-hL_{\mathcal{K}}) = 1 &- \left(a_1 + a_2\right) h\{\mathcal{A}, .\} - \left(b_1 + b_2\right) \varepsilon h\{\mathcal{B}, .\} \\ &+ \left(\frac{a_1^2}{2} + \frac{a_2^2}{2} + a_1 a_2\right) h^2\{\mathcal{A}, \{\mathcal{A}, .\}\} \\ &+ \left(a_1 b_1 + a_1 b_2 + a_2 b_2\right) \varepsilon h^2\{\mathcal{A}, \{\mathcal{B}, .\}\} + b_1 a_2\, \varepsilon h^2\{\mathcal{B}, \{\mathcal{A}, .\}\} \\ &+ \left(\frac{b_1^2}{2} + \frac{b_2^2}{2} + b_1 b_2\right) h^2\varepsilon^2\{\mathcal{B}, \{\mathcal{B}, .\}\} \\ &+ \mathcal{O}(h^3)\end{aligned} \tag{C.37}$$

By comparison to (C.34), a second-order symplectic integrator should thus verify:

$$\begin{cases} a_1 + a_2 = 1 \\ b_1 + b_2 = 1 \\ a_1 b_1 + a_1 b_2 + a_2 b_2 = \dfrac{1}{2} \\ b_1 a_2 = \dfrac{1}{2} \end{cases} \tag{C.38}$$

in which we removed the two redundant equations. The resolution of this system gives $(a_1, b_1, a_2, b_2) = (1/2, 1, 1/2, 0)$, which leads to the classic *leapfrog* integrator. It involves only positive sub-steps, and Suzuki (1991) showed that this property is only possible for integrators of order 2 or less. The problem with negative sub-steps is that while the resulting step is equal to h, the covered distance (in absolute value) increases rapidly with the order, leading to an unstable integrator. This is probably why the leapfrog (which is also time-reversible because $b_2 = 0$) is so widely used despite its low order.

In that context, Laskar and Robutel (2001) looked for a family of integrators being:

1. explicit
2. symplectic
3. symmetric, which leads to $S(h)^{-1} = S(-h)$, that is, time-reversibility
4. containing only positive sub-steps

Their idea is that, whereas it is impossible to fulfil all these properties for integrators of order larger than 2 in h, we can still take advantage of the smallness of ε to achieve a much higher precision than the leapfrog. This is realised by the reproduction by $\exp(-hL_{\mathcal{K}})$ of not *all* the terms in h^3 and higher orders, but only those of lowest order in ε. They showed that such integrators S exist with orders $h^p\varepsilon + h^2\varepsilon^2$ for all $p \in \mathbb{N}$ (for instance, $p = 2$ for the leapfrog). Furthermore, if the system with Hamiltonian:

$$\mathcal{C} = \{\{\mathcal{A}, \mathcal{B}\}, \mathcal{B}\} \tag{C.39}$$

is also integrable, the following integrator obtained from S:

$$S_c(h) = \exp(c\, h^3 \varepsilon^2 L_{\mathcal{C}})\, S(h)\, \exp(c\, h^3 \varepsilon^2 L_{\mathcal{C}}) \tag{C.40}$$

fulfils also all the required properties, and with the suitable choice of coefficient c, it has a remainder of order $h^p\varepsilon + h^4\varepsilon^2$.

In the following, we will use integrators with $p = 6$, namely the ABA_3 (using the terminology from Laskar and Robutel, 2001), and its version $ABAC_3$ with the two corrector steps using $\mathcal{C}$. As in Laskar and Robutel (2001) or Breiter et al. (2007), these integrators prove to be the best compromise in terms of complexity and accuracy: in our applications, they give almost the same precision as integrators of types $ABA_4/ABAC_4$ and higher, with less computational effort. We note that similar results are obtained using integrators of type BAB_3 and $BABC_3$ (which also have $p = 6$).

C.5.2 Mixed-variable schemes

From Sect. 3, the equations of motion of a massless particle in the barycentric (inertial) reference frame are:

$$\ddot{\mathbf{x}} = -\mu \frac{\mathbf{x} - \mathbf{x}_\odot}{|\mathbf{x} - \mathbf{x}_\odot|^3} - \sum_{i=1}^{N} \mu_i \frac{\mathbf{x} - \mathbf{x}_i}{|\mathbf{x} - \mathbf{x}_i|^3} \tag{C.41}$$

in which $\{\mathbf{x}_i\}$ are the barycentric positions of the planets, and $\mathbf{x}_\odot$ is the barycentric position of the Sun. Since the synthetic representation used in this work gives the *heliocentric* positions of the planets $\{\mathbf{r}_i\}$ as function of the time, the barycentric position of the Sun is obtained from the definition of the barycentre:

$$\begin{aligned} \sum_{i=1}^{N} \mu_i \, \mathbf{x}_i + \mu \, \mathbf{x}_\odot = \mathbf{0} &\iff \sum_{i=1}^{N} \mu_i \, \mathbf{r}_i + \mu_{\text{tot}} \, \mathbf{x}_\odot = \mathbf{0} \quad \text{where} \quad \mu_{\text{tot}} = \mu + \sum_{i=1}^{N} \mu_i \\ &\iff \mathbf{x}_\odot(t) = -\frac{1}{\mu_{\text{tot}}} \sum_{i=1}^{N} \mu_i \, \mathbf{r}_i(t) \end{aligned} \tag{C.42}$$

from which we get also the barycentric position of each planet i: $\mathbf{x}_i = \mathbf{x}_\odot + \mathbf{r}_i$. The Hamiltonian reproducing the equations of motion (C.41) can be chosen as:

$$\mathcal{H}(\mathbf{X}, T, \mathbf{x}, t) = \frac{1}{2}\mathbf{X}^2 - \frac{\mu}{|\mathbf{x} - \mathbf{x}_\odot|} - \sum_{i=1}^{N} \frac{\mu_i}{|\mathbf{x} - \mathbf{x}_i|} + T \tag{C.43}$$

where $\mathbf{X} = \dot{\mathbf{x}}$ is the momentum conjugate to the position $\mathbf{x}$ and T is the momentum conjugate to the time t (in order to get an autonomous system). The initial value of T is arbitrary: it only fixes the constant value of $\mathcal{H}$ (see Sect. 2.2.1).

For trajectories entirely beyond Neptune, we know that the solutions are perturbed two-body orbits around the barycentre of the Solar System, so we define the splitting $\mathcal{H} = \mathcal{A} + \varepsilon\mathcal{B}$ by adding and subtracting $\mu_{\text{tot}}/|\mathbf{x}|$:

$$\begin{cases} \mathcal{A} = \dfrac{1}{2}\mathbf{X}^2 - \dfrac{\mu_{\text{tot}}}{|\mathbf{x}|} + T \\ \varepsilon\mathcal{B} = \dfrac{\mu_{\text{tot}}}{|\mathbf{x}|} - \dfrac{\mu}{|\mathbf{x} - \mathbf{x}_\odot|} - \displaystyle\sum_{i=1}^{N} \frac{\mu_i}{|\mathbf{x} - \mathbf{x}_i|} \end{cases} \tag{C.44}$$

Since the position of the barycentre of the Solar System almost coincides with the centre of the Sun, the Hamiltonian $\varepsilon\mathcal{B}$ is indeed a small quantity. In order to apply the integrators by Laskar and Robutel (2001) to our dynamical system, we must compute the explicit expression of the propagation over one step h of the systems defined by the Hamiltonians $\mathcal{A}$, $\varepsilon\mathcal{B}$ and $\mathcal{C} = \{\{\mathcal{A}, \mathcal{B}\}, \mathcal{B}\}$ taken separately. Writing τ the time variable (to prevent the confusion with the canonical coordinate t), the propagation using $\mathcal{A}$ is

straightforward:

$$\begin{cases} \mathbf{X}(\tau), \mathbf{x}(\tau) \xrightarrow{\text{two-body propagator}} \mathbf{X}(\tau+h), \mathbf{x}(\tau+h) \\ \dfrac{\mathrm{d}t}{\mathrm{d}\tau} = \dfrac{\partial \mathcal{A}}{\partial T} = 1 \implies t(\tau+h) = t(\tau) + h \\ \dfrac{\mathrm{d}T}{\mathrm{d}\tau} = -\dfrac{\partial \mathcal{A}}{\partial t} = 0 \implies T(\tau+h) = T(\tau) \end{cases} \tag{C.45}$$

in which the two-body propagator consists of Gauss' f and g functions presented in Sect. C.2. Since they involve (to some extent) the Keplerian elements of the particle, the integrator is said to use *mixed variables*. The propagation using the Hamiltonian $\varepsilon\mathcal{B}$ is also easily computed:

$$\begin{cases} \dfrac{\mathrm{d}\mathbf{x}}{\mathrm{d}\tau} = \dfrac{\partial \varepsilon\mathcal{B}}{\partial \mathbf{X}} = 0 \implies \mathbf{x}(\tau+h) = \mathbf{x}(\tau) \\ \dfrac{\mathrm{d}t}{\mathrm{d}\tau} = \dfrac{\partial \varepsilon\mathcal{B}}{\partial T} = 0 \implies t(\tau+h) = t(\tau) \\ \dfrac{\mathrm{d}\mathbf{X}}{\mathrm{d}\tau} = -\dfrac{\partial \varepsilon\mathcal{B}}{\partial \mathbf{x}} = \mu_{\mathrm{tot}} \dfrac{\mathbf{x}}{|\mathbf{x}|^3} - \mu \dfrac{\mathbf{x}-\mathbf{x}_\odot}{|\mathbf{x}-\mathbf{x}_\odot|^3} - \displaystyle\sum_{i=1}^{N} \mu_i \dfrac{\mathbf{x}-\mathbf{x}_i}{|\mathbf{x}-\mathbf{x}_i|^3} \\ \qquad \implies \mathbf{X}(\tau+h) = \mathbf{X}(\tau) + h \left(\mu_{\mathrm{tot}} \dfrac{\mathbf{x}}{|\mathbf{x}|^3} - \mu \dfrac{\mathbf{x}-\mathbf{x}_\odot}{|\mathbf{x}-\mathbf{x}_\odot|^3} - \displaystyle\sum_{i=1}^{N} \mu_i \dfrac{\mathbf{x}-\mathbf{x}_i}{|\mathbf{x}-\mathbf{x}_i|^3} \right) \\ \dfrac{\mathrm{d}T}{\mathrm{d}\tau} = -\dfrac{\partial \varepsilon\mathcal{B}}{\partial t} = \mu \dfrac{\mathbf{x}-\mathbf{x}_\odot}{|\mathbf{x}-\mathbf{x}_\odot|^3} \cdot \dot{\mathbf{x}}_\odot + \displaystyle\sum_{i=1}^{N} \mu_i \dfrac{\mathbf{x}-\mathbf{x}_i}{|\mathbf{x}-\mathbf{x}_i|^3} \cdot \dot{\mathbf{x}}_i \\ \qquad \implies T(\tau+h) = T(\tau) + h \left(\mu \dfrac{\mathbf{x}-\mathbf{x}_\odot}{|\mathbf{x}-\mathbf{x}_\odot|^3} \cdot \dot{\mathbf{x}}_\odot + \displaystyle\sum_{i=1}^{N} \mu_i \dfrac{\mathbf{x}-\mathbf{x}_i}{|\mathbf{x}-\mathbf{x}_i|^3} \cdot \dot{\mathbf{x}}_i \right) \end{cases} \tag{C.46}$$

One can note that the propagation of T is only required for checking the conservation of the Hamiltonian value, otherwise it can be ignored (so the time-consuming partial derivatives of the planets positions are not required either). Finally, the application of the two corrector steps involves the Hamiltonian:

$$\mathcal{C} = \{\{\mathcal{A}, \varepsilon\mathcal{B}\}, \varepsilon\mathcal{B}\} = \frac{\partial \varepsilon\mathcal{B}}{\partial \mathbf{x}} \cdot \frac{\partial \varepsilon\mathcal{B}}{\partial \mathbf{x}} = \left(\mu_{\mathrm{tot}} \frac{\mathbf{x}}{|\mathbf{x}|^3} - \mu \frac{\mathbf{x}-\mathbf{x}_\odot}{|\mathbf{x}-\mathbf{x}_\odot|^3} - \sum_{i=1}^{N} \mu_i \frac{\mathbf{x}-\mathbf{x}_i}{|\mathbf{x}-\mathbf{x}_i|^3} \right)^2 \tag{C.47}$$

that we will write schematically $\mathcal{C} = \mathbf{F} \cdot \mathbf{F}$ with:

$$\mathbf{F} = \begin{pmatrix} F_1(\mathbf{x}, \mathbf{t}) \\ F_2(\mathbf{x}, \mathbf{t}) \\ F_3(\mathbf{x}, \mathbf{t}) \end{pmatrix} = \mu_{\mathrm{tot}} \frac{\mathbf{x}}{|\mathbf{x}|^3} - \mu \frac{\mathbf{x}-\mathbf{x}_\odot}{|\mathbf{x}-\mathbf{x}_\odot|^3} - \sum_{i=1}^{N} \mu_i \frac{\mathbf{x}-\mathbf{x}_i}{|\mathbf{x}-\mathbf{x}_i|^3} \tag{C.48}$$

The propagation using the Hamiltonian $\mathcal{C}$ can thus be written as:

$$\begin{cases} \dfrac{\mathrm{d}\mathbf{x}}{\mathrm{d}\tau} = \dfrac{\partial \mathcal{C}}{\partial \mathbf{X}} = 0 \implies \mathbf{x}(\tau + h) = \mathbf{x}(\tau) \\ \dfrac{\mathrm{d}t}{\mathrm{d}\tau} = \dfrac{\partial \mathcal{C}}{\partial T} = 0 \implies t(\tau + h) = t(\tau) \\ \dfrac{\mathrm{d}\mathbf{X}}{\mathrm{d}\tau} = -\dfrac{\partial \mathcal{C}}{\partial \mathbf{x}} = -2\,(\mathrm{D}\mathbf{F})^{\mathrm{T}}\mathbf{F} \implies \mathbf{X}(\tau + h) = \mathbf{X}(\tau) + h\left(-2\,(\mathrm{D}\mathbf{F})^{\mathrm{T}}\mathbf{F}\right) \\ \dfrac{\mathrm{d}T}{\mathrm{d}\tau} = -\dfrac{\partial \mathcal{C}}{\partial t} = -2\,\dfrac{\partial \mathbf{F}}{\partial t}\cdot\mathbf{F} \implies T(\tau + h) = T(\tau) + h\left(-2\,\dfrac{\partial \mathbf{F}}{\partial t}\cdot\mathbf{F}\right) \end{cases} \tag{C.49}$$

Noting $\mathbf{x} = (x_1, x_2, x_3)^{\mathrm{T}}$, the matrix $(\mathrm{D}\mathbf{F})^{\mathrm{T}}$ is defined as:

$$\begin{aligned} (\mathrm{D}\mathbf{F})^{\mathrm{T}} &= \begin{pmatrix} \partial F_1/\partial x_1 & \partial F_2/\partial x_1 & \partial F_3/\partial x_1 \\ \partial F_1/\partial x_2 & \partial F_2/\partial x_2 & \partial F_3/\partial x_2 \\ \partial F_1/\partial x_3 & \partial F_2/\partial x_3 & \partial F_3/\partial x_3 \end{pmatrix} \\ &= \frac{\mu_{\mathrm{tot}}}{|\mathbf{x}|^3}\left[\mathbb{1} - 3\frac{\mathbf{x}}{|\mathbf{x}|^2}\mathbf{x}^{\mathrm{T}}\right] - \frac{\mu}{|\mathbf{x} - \mathbf{x}_\odot|^3}\left[\mathbb{1} - 3\frac{\mathbf{x} - \mathbf{x}_\odot}{|\mathbf{x} - \mathbf{x}_\odot|^2}(\mathbf{x} - \mathbf{x}_\odot)^{\mathrm{T}}\right] \\ &\quad - \sum_{i=1}^{N} \frac{\mu_i}{|\mathbf{x} - \mathbf{x}_i|^3}\left[\mathbb{1} - 3\frac{\mathbf{x} - \mathbf{x}_i}{|\mathbf{x} - \mathbf{x}_i|^2}(\mathbf{x} - \mathbf{x}_i)^{\mathrm{T}}\right] \end{aligned} \tag{C.50}$$

where $\mathbb{1}$ is the 3×3 identity matrix. Finally, we have:

$$\begin{aligned} \frac{\partial \mathbf{F}}{\partial t} &= \frac{\mu}{|\mathbf{x} - \mathbf{x}_\odot|^3}\left[\dot{\mathbf{x}}_\odot - 3\frac{\mathbf{x} - \mathbf{x}_\odot}{|\mathbf{x} - \mathbf{x}_\odot|^2}(\mathbf{x} - \mathbf{x}_\odot)\cdot\dot{\mathbf{x}}_\odot\right] \\ &\quad + \sum_{i=1}^{N} \frac{\mu_i}{|\mathbf{x} - \mathbf{x}_i|^3}\left[\dot{\mathbf{x}}_i - 3\frac{\mathbf{x} - \mathbf{x}_i}{|\mathbf{x} - \mathbf{x}_i|^2}(\mathbf{x} - \mathbf{x}_i)\cdot\dot{\mathbf{x}}_i\right] \end{aligned} \tag{C.51}$$

which is only required to check the conservation of the Hamiltonian value.

Using that kind of algorithm, one can note that if ε tends to 0, the motion is an *exact* two-body propagation around the barycentre of the Solar System. The validity of the above formulas can be assessed by checking the behaviour of the error with respect to the step h used. Fig. C.4 shows the maximum error of the Hamiltonian value for a fictitious particle integrated during about one orbital period. In some range of step size, the terms in $h^2\varepsilon^2$ dominate (slope equal to h^2), but they are correctly removed by the use of the corrector, pushing back the error in the $h^4\varepsilon^2$ terms (slope equal to h^4).

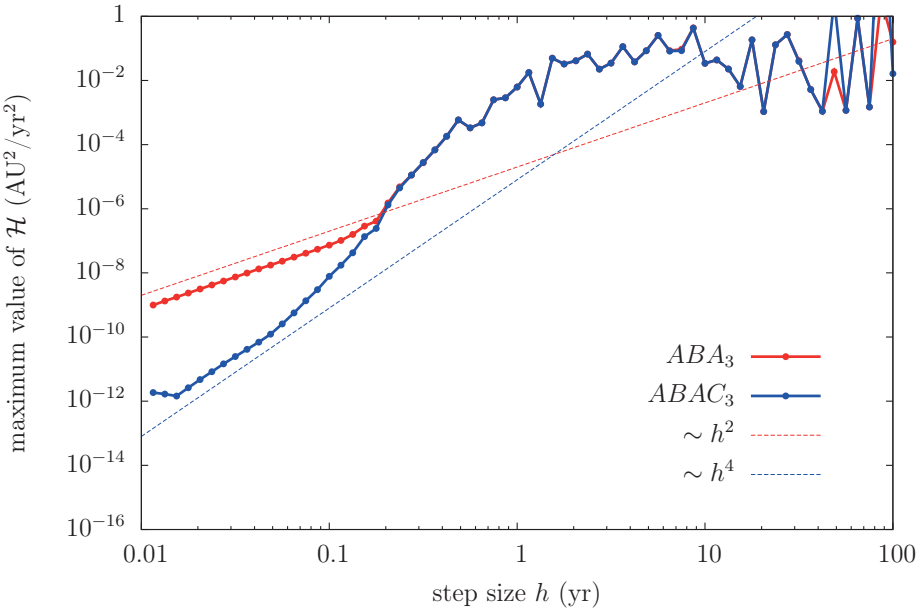

Figure C.4 – Maximum variation of the Hamiltonian value for a fictitious particle integrated over 200 years using the algorithm described in this section. The barycentric initial conditions are $(a, q, I, \omega, \Omega, M) = (33 \text{ AU}, 2 \text{ AU}, 0, 0, 0, \pi)$ at time J2000. The dynamics of the four giant planets are given by the synthetic representation by Laskar (1990) and the masses of the inner planets are added to the mass of the Sun. The initial value of T is chosen such that $\mathcal{H} = 0$. The same integrator is used without corrector (red curve) and with corrector (blue curve).

C.5.3 The regularisation by Kustaanheimo and Stiefel

The constant step size is often seen as a strong drawback of symplectic integrators. In contrast, conventional integrators are designed to adapt the time resolution according to the rate of change of the "force" in order to achieve a given accuracy of the new state vector. This limitation of symplectic integrators can be bypassed to some extent by regularisation methods (the development of which depends on the problem under consideration). Such methods consist in replacing the time variable t by a fictitious time τ which, while increasing with a constant step, will naturally realise more numerous steps in regions where the force changes rapidly with respect to t. In the case of a perturbed two-body problem, a judicious choice seems to be to increase the number of steps near perihelion, that is, when the particle goes (possibly much) faster. This could hold especially in our case, since the perturbations apply mostly near perihelion, when the particle is closer to the planetary region. Such a regularisation can be achieved by using the Kustaanheimo-Stiefel (KS) coordinates. The most important feature in our case is the change of time variable (see Sect. 2.2.2), but the KS coordinates have also the interesting property of turning the two-body problem into an harmonic oscillator, which is much easier to propagate than in conventional coordinates (Sect. C.2). In this section, we recall briefly the construction of a symplectic integrator using the KS regularisation, as described for instance by Breiter (1999).

First of all, let us define the coefficient $\alpha \in \mathbb{R}_+$ which has the dimension of length. Its choice, somehow arbitrary, is discussed later. Let $(\mathbf{X}, T, \mathbf{x}, t)$ be our first set of canonical coordinates, with Hamiltonian (C.43). The canonical transformation from the KS coordinates:

$$(\mathbf{U}, U^\star, \mathbf{u}, u^\star) \in \mathbb{R}^4 \times \mathbb{R} \times \mathbb{R}^4 \times \mathbb{R} \longmapsto (\mathbf{X}, T, \mathbf{x}, t) \in \mathbb{R}^3 \times \mathbb{R} \times \mathbb{R}^3 \times \mathbb{R} \tag{C.52}$$

is defined by:

$$\begin{pmatrix} x_1 \\ x_2 \\ x_3 \end{pmatrix} = \frac{1}{\alpha} \begin{pmatrix} u_0^2 + u_1^2 - u_2^2 - u_3^2 \\ 2(u_1 u_2 + u_0 u_3) \\ 2(u_1 u_3 - u_0 u_2) \end{pmatrix} \tag{C.53}$$

and:

$$\begin{pmatrix} X_1 \\ X_2 \\ X_3 \end{pmatrix} = \frac{\alpha}{2\mathbf{u}^2} \begin{pmatrix} U_0 u_0 + U_1 u_1 - U_2 u_2 - U_3 u_3 \\ U_0 u_3 + U_1 u_2 + U_2 u_1 + U_3 u_0 \\ -U_0 u_2 + U_1 u_3 - U_2 u_0 + U_3 u_1 \end{pmatrix} \tag{C.54}$$

whereas the time variables remain unchanged: $(T, t) = (U^\star, u^\star)$. We note that the relation (C.53) gives the remarkable property:

$$r \equiv |\mathbf{x}| = \frac{1}{\alpha} \mathbf{u}^2 \tag{C.55}$$

Since the transformation drops one dimension ($\mathbf{u} \in \mathbb{R}^4$ but $\mathbf{x} \in \mathbb{R}^3$), its inverse contains some arbitrariness. We will use the conventions from Breiter (1999) and Breiter et al. (2007), setting:

$$\begin{pmatrix} u_0 \\ u_1 \\ u_2 \\ u_3 \end{pmatrix} = \begin{cases} \sqrt{\dfrac{\alpha}{2(r + x_1)}} \begin{pmatrix} 0 \\ r + x_1 \\ x_2 \\ x_3 \end{pmatrix} & \text{if } x_1 \geqslant 0 \\ \sqrt{\dfrac{\alpha}{2(r - x_1)}} \begin{pmatrix} -x_3 \\ x_2 \\ r - x_1 \\ 0 \end{pmatrix} & \text{if } x_1 < 0 \end{cases} \tag{C.56}$$

and enforcing the link:

$$U_0 u_1 - U_1 u_0 - U_2 u_3 + U_3 u_2 = 0 \tag{C.57}$$

Adding the latter as a additional line of the matrix (C.54), the inverse transformation for the momenta is:

$$\begin{pmatrix} U_0 \\ U_1 \\ U_2 \\ U_3 \end{pmatrix} = L\,\mathbf{X} \quad \text{where} \quad L \equiv \frac{2}{\alpha} \begin{pmatrix} u_0 & u_3 & -u_2 \\ u_1 & u_2 & u_3 \\ -u_2 & u_1 & -u_0 \\ -u_3 & u_0 & u_1 \end{pmatrix} \tag{C.58}$$

We now need to express the Hamiltonian (C.43) in the new coordinates. From (C.54) and using the convention (C.57), we get:

$$\mathbf{X}^2 = \frac{\alpha^2}{4}\frac{\mathbf{U}^2}{\mathbf{u}^2} \tag{C.59}$$

The Hamiltonian $\mathcal{A}$ expressed in the new coordinates is thus:

$$\mathcal{A} = \frac{\alpha^2}{8}\frac{\mathbf{U}^2}{\mathbf{u}^2} - \alpha\frac{\mu_{\text{tot}}}{\mathbf{u}^2} + U^\star \tag{C.60}$$

Then, the perturbation $\varepsilon\mathcal{B}$ is expressed as in (C.44), but where $\mathbf{x}$ is seen as a function of $\mathbf{u}$ using (C.53). Let us now change the scale of time, introducing the fictitious time τ such that:

$$\frac{\mathrm{d}\tau}{\mathrm{d}t} = \frac{\alpha}{4r} = \frac{\alpha^2}{4\mathbf{u}^2} \tag{C.61}$$

At this point, the meaning of the parameter α becomes apparent. Indeed, the definition of the fictitious time should be compared to the relation (2.26) between the eccentric and mean anomalies:

$$\mathrm{d}E = \frac{a}{r}\mathrm{d}M \tag{C.62}$$

Using the fact that $\mathrm{d}M = n\mathrm{d}t$ where n is the mean motion, the analogous expression using the fictitious time is:

$$\mathrm{d}E = \frac{4a}{\alpha}\, n\mathrm{d}\tau \tag{C.63}$$

Since we consider a perturbed two-body problem, we will choose the constant parameter $\alpha = 4a$ (where a is the *initial* osculating semi-major axis of the orbit), leading to the equality $\mathrm{d}E = n\mathrm{d}\tau$ at the initial instant. In the new coordinates, the fictitious time τ has really the dimension of a time, and the orbital period is the same in t or in τ. These properties would be verified at all time for a zero perturbation.

Since the scaling (C.61) is not constant along the trajectories (it depends on the position), we must use the general time-regularisation transformation introduced in Sect. 2.2.2. The pair of canonical coordinates (T, t) is already contained in the definition of $\mathcal{H}$, so the new Hamiltonian is given by:

$$\mathcal{M} = \frac{\mathrm{d}t}{\mathrm{d}\tau}\mathcal{H} \tag{C.64}$$

Dropping the constant term, it writes $\mathcal{M} = \mathcal{M}_0 + \varepsilon\mathcal{M}_1$ with:

$$\begin{cases} \mathcal{M}_0 = \dfrac{1}{2}\mathbf{U}^2 + \dfrac{4\mathbf{u}^2}{\alpha^2}U^\star \\ \varepsilon\mathcal{M}_1 = -\dfrac{4\mathbf{u}^2}{\alpha^2}\gamma(\mathbf{u}, u^\star) \end{cases} \tag{C.65}$$

where we used the notation:

$$\gamma(\mathbf{u}, u^\star) = \frac{\mu}{|\mathbf{x} - \mathbf{x}_\odot|} + \sum_{i=1}^{N}\frac{\mu_i}{|\mathbf{x} - \mathbf{x}_i|} \tag{C.66}$$

In this expression, $\mathbf{x}$ is seen as a function of $\mathbf{u}$ using (C.53), whereas $\mathbf{x}_\odot$ and $\{\mathbf{x}_i\}$ are functions of $u^\star = t$ given by the synthetic representation.

From Sect. 2.2.2, we know that this system is equivalent to the initial one *provided that* the constant value of $\mathcal{H}$ is zero. This is easily achieved by choosing the initial value of $U^\star$ accordingly (which so far was arbitrary). At all time, $U^\star$ is thus equal to the opposite of the two-body-problem energy, minus the planetary perturbations (C.44), that is:

$$U^\star = T = -\left(\frac{1}{2}\mathbf{X}^2 - \frac{\mu_{\rm tot}}{|\mathbf{x}|}\right) - \varepsilon\mathcal{B} \tag{C.67}$$

We note that it is positive for a (sufficiently slightly) perturbed elliptic orbit, and negative for an hyperbolic one.

As in Sect. C.5.2, the Hamiltonian (C.65) contains an integrable part and a perturbation, and this perturbation, taken individually, is also integrable. We can thus apply the integrator by Laskar and Robutel (2001) detailed in Sect. C.5.1. For this purpose, we must first compute the explicit expression of the propagation over one step h of the systems defined by the Hamiltonians $\mathcal{M}_0$, $\varepsilon\mathcal{M}_1$ and $\mathcal{N} = \{\{\mathcal{M}_0, \varepsilon\mathcal{M}_1\}, \varepsilon\mathcal{M}_1\}$ taken separately. The equations of motion generated by the unperturbed two-body Hamiltonian $\mathcal{M}_0$ are:

$$\begin{cases} \dfrac{\mathrm{d}\mathbf{u}}{\mathrm{d}\tau} = \dfrac{\partial\mathcal{M}_0}{\partial\mathbf{U}} = \mathbf{U} \\ \dfrac{\mathrm{d}u^\star}{\mathrm{d}\tau} = \dfrac{\partial\mathcal{M}_0}{\partial U^\star} = \dfrac{4\mathbf{u}^2}{\alpha^2} \\ \dfrac{\mathrm{d}\mathbf{U}}{\mathrm{d}\tau} = -\dfrac{\partial\mathcal{M}_0}{\partial\mathbf{u}} = -\dfrac{8}{\alpha^2}U^\star\mathbf{u} \\ \dfrac{\mathrm{d}U^\star}{\mathrm{d}\tau} = -\dfrac{\partial\mathcal{M}_0}{\partial u^\star} = 0 \end{cases} \tag{C.68}$$

The last equation implies that $U^\star$ is constant along the propagation, which gives a very simple form to the coupled equations governing the evolution of $\mathbf{u}$ and $\mathbf{U}$:

$$\ddot{\mathbf{u}} = -\frac{8U^\star}{\alpha^2}\mathbf{u} \tag{C.69}$$

This is the dynamical equation of a harmonic oscillator, which has a very simple analytical solution. The type of the solution depends on the sign of $U^\star$ and we saw that it is positive in the elliptic case. The solution of (C.69) oscillates thus with the constant frequency[7]:

$$\omega = \sqrt{\frac{8U^\star}{\alpha^2}} \tag{C.70}$$

With $\mathbf{u}(\tau)$ and $\mathbf{U}(\tau)$ as initial conditions, by looking for a general solution composed

[7]One can note that if the perturbation tends to zero, the value of $U^\star$ is simply $\mu_{\rm tot}/(2a)$, so from our choice of the constant parameter $\alpha = 4a$, this leads to $\omega = n/2$. Consequently, one pulsation of the KS harmonic oscillator corresponds to two orbital periods of the two-body problem.

of a cosine and a sine terms, the propagation from τ to $\tau+h$ using $\mathcal{M}_0$ is finally:

$$\left\{\begin{array}{l}\mathbf{u}(\tau+h)=\mathbf{u}(\tau)\cos(\omega h)+\mathbf{U}(\tau)\dfrac{\sin(\omega h)}{\omega}\\ u^\star(\tau+h)=u^\star(\tau)+\dfrac{4}{\alpha^2}\displaystyle\int_\tau^{\tau+h}\mathbf{u}(s)^2\mathrm{d}s\\ \qquad=u^\star(\tau)+\dfrac{2}{\alpha^2}\left(\mathbf{u}(\tau)^2+\dfrac{\mathbf{U}(\tau)^2}{\omega^2}\right)h-\dfrac{2}{\alpha^2\omega^2}\Big(\mathbf{u}(\tau+h)\cdot\mathbf{U}(\tau+h)-\mathbf{u}(\tau)\cdot\mathbf{U}(\tau)\Big)\\ \mathbf{U}(\tau+h)=-\mathbf{u}(\tau)\,\omega\sin(\omega h)+\mathbf{U}(\tau)\cos(\omega h)\\ U^\star(\tau+h)=U^\star(\tau)\end{array}\right. \tag{C.71}$$

in which the quantity $\mathbf{u}^2+\mathbf{U}^2/\omega^2$ in invariant along the propagation. Analogous formulas can be obtained in the hyperbolic case (see Breiter et al., 2007). One can note that they are much more straightforward than the two-body propagation required in conventional coordinates (Sect. C.5.2).

On the other hand, the propagation using the Hamiltonian $\varepsilon\mathcal{M}_1$ writes:

$$\left\{\begin{array}{l}\dfrac{\mathrm{d}\mathbf{u}}{\mathrm{d}\tau}=\dfrac{\partial\varepsilon\mathcal{M}_1}{\partial\mathbf{U}}=\mathbf{0}\implies\mathbf{u}(\tau+h)=\mathbf{u}(\tau)\\ \dfrac{\mathrm{d}u^\star}{\mathrm{d}\tau}=\dfrac{\partial\varepsilon\mathcal{M}_1}{\partial U^\star}=0\implies u^\star(\tau+h)=u^\star(\tau)\\ \dfrac{\mathrm{d}\mathbf{U}}{\mathrm{d}\tau}=-\dfrac{\partial\varepsilon\mathcal{M}_1}{\partial\mathbf{u}}=\dfrac{8}{\alpha^2}\left(\gamma\,\mathbf{u}-\dfrac{1}{2}\mathbf{u}^2L\,\mathbf{w}\right)\\ \qquad\implies\mathbf{U}(\tau+h)=\mathbf{U}(\tau)+h\dfrac{8}{\alpha^2}\left(\gamma\,\mathbf{u}-\dfrac{1}{2}\mathbf{u}^2L\,\mathbf{w}\right)\\ \dfrac{\mathrm{d}U^\star}{\mathrm{d}\tau}=-\dfrac{\partial\varepsilon\mathcal{M}_1}{\partial u^\star}=\dfrac{4\mathbf{u}^2}{\alpha^2}\dfrac{\partial\gamma}{\partial u^\star}\implies U^\star(\tau+h)=U^\star(\tau)+h\left(\dfrac{4\mathbf{u}^2}{\alpha^2}\dfrac{\partial\gamma}{\partial u^\star}\right)\end{array}\right. \tag{C.72}$$

in which the matrix $L(\mathbf{u})$ is defined in (C.58) and the function $\gamma(\mathbf{u},u^\star)$ is defined in (C.66). We have in particular the relations:

$$\left\{\begin{array}{l}\dfrac{\partial\gamma}{\partial\mathbf{u}}=-L\,\mathbf{w}\\ \dfrac{\partial\gamma}{\partial u^\star}=\mu\dfrac{\mathbf{x}-\mathbf{x}_\odot}{|\mathbf{x}-\mathbf{x}_\odot|^3}\cdot\dot{\mathbf{x}}_\odot+\displaystyle\sum_{i=1}^N\mu_i\dfrac{\mathbf{x}-\mathbf{x}_i}{|\mathbf{x}-\mathbf{x}_i|^3}\cdot\dot{\mathbf{x}}_i\end{array}\right. \tag{C.73}$$

where:

$$\mathbf{w}(\mathbf{u},u^\star)=\begin{pmatrix}w_1\\w_2\\w_3\end{pmatrix}=\mu\frac{\mathbf{x}-\mathbf{x}_\odot}{|\mathbf{x}-\mathbf{x}_\odot|^3}+\sum_{i=1}^N\mu_i\frac{\mathbf{x}-\mathbf{x}_i}{|\mathbf{x}-\mathbf{x}_i|^3} \tag{C.74}$$

Finally the application of the two corrector steps involves the Hamiltonian:

$$\mathcal{N}=\{\{\mathcal{M}_0,\varepsilon\mathcal{M}_1\},\varepsilon\mathcal{M}_1\}=\frac{\partial\varepsilon\mathcal{M}_1}{\partial\mathbf{u}}\cdot\frac{\partial\varepsilon\mathcal{M}_1}{\partial\mathbf{u}}=\frac{64}{\alpha^4}\left(\frac{1}{2}\mathbf{u}^2L\,\mathbf{w}-\gamma\,\mathbf{u}\right)^2 \tag{C.75}$$

that we will write schematically:

$$\mathcal{N} = \frac{64}{\alpha^4}\,\mathbf{F}\cdot\mathbf{F} \tag{C.76}$$

with:

$$\mathbf{F}(\mathbf{u},u^\star) = \begin{pmatrix} F_0(\mathbf{u},u^\star) \\ F_1(\mathbf{u},u^\star) \\ F_2(\mathbf{u},u^\star) \\ F_3(\mathbf{u},u^\star) \end{pmatrix} = \frac{1}{2}\mathbf{u}^2 L(\mathbf{u})\,\mathbf{w}(\mathbf{u},u^\star) - \gamma(\mathbf{u},u^\star)\,\mathbf{u} \tag{C.77}$$

The propagation using the Hamiltonian $\mathcal{N}$ can thus be written as:

$$\left\{\begin{array}{l} \dfrac{\mathrm{d}\mathbf{u}}{\mathrm{d}\tau} = \dfrac{\partial\mathcal{N}}{\partial\mathbf{U}} = 0 \implies \mathbf{u}(\tau+h) = \mathbf{u}(\tau) \\ \dfrac{\mathrm{d}u^\star}{\mathrm{d}\tau} = \dfrac{\partial\mathcal{N}}{\partial U^\star} = 0 \implies u^\star(\tau+h) = u^\star(\tau) \\ \dfrac{\mathrm{d}\mathbf{U}}{\mathrm{d}\tau} = -\dfrac{\partial\mathcal{N}}{\partial\mathbf{u}} = -\dfrac{128}{\alpha^4}\,(\mathrm{D}\mathbf{F})^{\mathrm{T}}\mathbf{F} \implies \mathbf{U}(\tau+h) = \mathbf{U}(\tau) + h\left(-\dfrac{128}{\alpha^4}\,(\mathrm{D}\mathbf{F})^{\mathrm{T}}\mathbf{F}\right) \\ \dfrac{\mathrm{d}U^\star}{\mathrm{d}\tau} = -\dfrac{\partial\mathcal{N}}{\partial u^\star} = -\dfrac{128}{\alpha^4}\,\dfrac{\partial\mathbf{F}}{\partial u^\star}\cdot\mathbf{F} \implies U^\star(\tau+h) = U^\star(\tau) + h\left(-\dfrac{128}{\alpha^4}\,\dfrac{\partial\mathbf{F}}{\partial u^\star}\cdot\mathbf{F}\right) \end{array}\right. \tag{C.78}$$

The matrix $(\mathrm{D}\mathbf{F})^{\mathrm{T}}$ is defined as:

$$\begin{aligned} (\mathrm{D}\mathbf{F})^{\mathrm{T}} &= \begin{pmatrix} \partial F_0/\partial u_0 & \partial F_1/\partial u_0 & \partial F_2/\partial u_0 & \partial F_3/\partial u_0 \\ \partial F_0/\partial u_1 & \partial F_1/\partial u_1 & \partial F_2/\partial u_1 & \partial F_3/\partial u_1 \\ \partial F_0/\partial u_2 & \partial F_1/\partial u_2 & \partial F_2/\partial u_2 & \partial F_3/\partial u_2 \\ \partial F_0/\partial u_3 & \partial F_1/\partial u_3 & \partial F_2/\partial u_3 & \partial F_3/\partial u_3 \end{pmatrix} \\ &= \frac{1}{2}\mathbf{u}^2\left(M + LDL^{\mathrm{T}}\right) - \gamma\,\mathbb{1}_4 + \mathbf{u}(L\mathbf{w})^{\mathrm{T}} + (L\mathbf{w})\mathbf{u}^{\mathrm{T}} \end{aligned} \tag{C.79}$$

where $\mathbb{1}_4$ is the 4×4 identity matrix. We have besides used the following matrices:

$$M(\mathbf{w}) = \frac{2}{\alpha}\begin{pmatrix} w_1 & 0 & -w_3 & w_2 \\ 0 & w_1 & w_2 & w_3 \\ -w_3 & w_2 & -w_1 & 0 \\ w_2 & w_3 & 0 & -w_1 \end{pmatrix} \tag{C.80}$$

and:

$$D = \frac{\mu}{|\mathbf{x}-\mathbf{x}_\odot|^3}\left[\mathbb{1}_3 - 3\frac{\mathbf{x}-\mathbf{x}_\odot}{|\mathbf{x}-\mathbf{x}_\odot|^2}(\mathbf{x}-\mathbf{x}_\odot)^{\mathrm{T}}\right] + \sum_{i=1}^{N}\frac{\mu_i}{|\mathbf{x}-\mathbf{x}_i|^3}\left[\mathbb{1}_3 - 3\frac{\mathbf{x}-\mathbf{x}_i}{|\mathbf{x}-\mathbf{x}_i|^2}(\mathbf{x}-\mathbf{x}_i)^{\mathrm{T}}\right] \tag{C.81}$$

where $\mathbb{1}_3$ is the 3×3 identity matrix. Finally, the last partial derivative involved in the propagation (C.78) is:

$$\frac{\partial\mathbf{F}}{\partial u^\star} = \frac{1}{2}\mathbf{u}^2 L\frac{\partial\mathbf{w}}{\partial u^\star} - \frac{\partial\gamma}{\partial u^\star}\mathbf{u} \tag{C.82}$$

using (C.73) and:

$$\begin{aligned}\frac{\partial \mathbf{w}}{\partial u^\star} = &\frac{\mu}{|\mathbf{x}-\mathbf{x}_\odot|^3}\left(-\dot{\mathbf{x}}_\odot + 3\frac{\mathbf{x}-\mathbf{x}_\odot}{|\mathbf{x}-\mathbf{x}_\odot|^2}(\mathbf{x}-\mathbf{x}_\odot)\cdot\dot{\mathbf{x}}_\odot\right)\\ &+\sum_{i=1}^{N}\frac{\mu_i}{|\mathbf{x}-\mathbf{x}_i|^3}\left(-\dot{\mathbf{x}}_i + 3\frac{\mathbf{x}-\mathbf{x}_i}{|\mathbf{x}-\mathbf{x}_i|^2}(\mathbf{x}-\mathbf{x}_i)\cdot\dot{\mathbf{x}}_i\right)\end{aligned} \tag{C.83}$$

As before, we note that if ε tends to 0, this algorithm gives the motion of an *exact* two-body propagation around the barycentre of the Solar System. The validity of the above formulas (especially the complex corrector steps) can be assessed by checking the behaviour of the error with respect to the step h used. Fig. C.5 shows the maximum error of the value of $\mathcal{H}$ for a fictitious particle integrated during about one orbital period. In some range of step size, the terms in $h^2\varepsilon^2$ dominate (slope equal to h^2), but they are correctly removed by the use of the corrector, pushing back the error in the $h^4\varepsilon^2$ terms (slope equal to h^4). Contrary to Fig. C.4, the step size h refers now to the fictitious time τ (however, since the semi-major axis of the particle does not vary much over the time span considered, the number of steps per orbit is roughly the same).

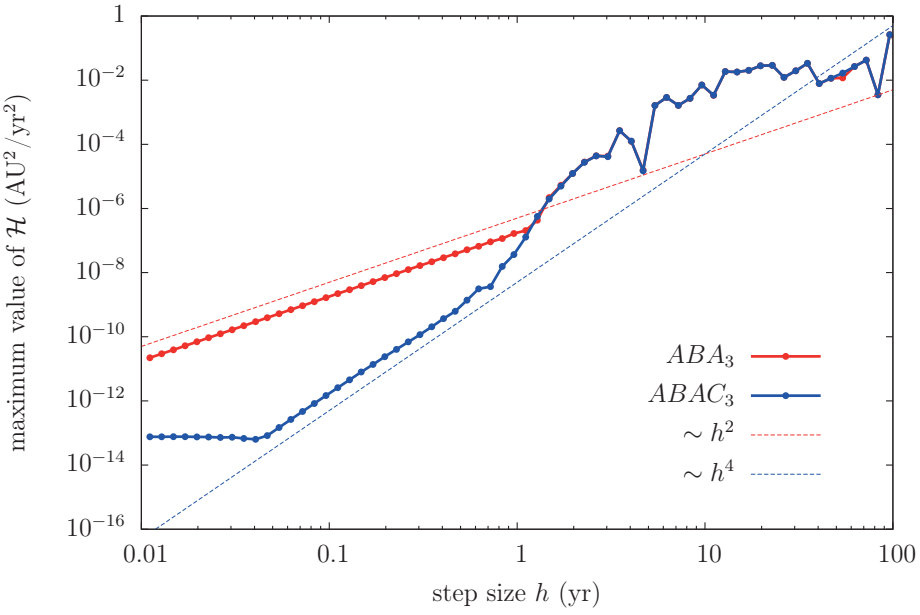

Figure C.5 – Maximum variation of the value of $\mathcal{H}$ for a fictitious particle integrated over 200 years using the algorithm described in this section (KS barycentric coordinates). The initial conditions and planetary model are the same as in Fig. C.4. The theoretical value of $\mathcal{H}$ is zero. The same integrator is used without corrector (red curve) and with corrector (blue curve).

C.5.4 Efficiency of the algorithms

First of all, we note that the computation of a single step h is a bit faster in the mixed-variable integrator (Sect. C.5.2) than in the KS one (Sect. C.5.3), even if it requires the two-body propagation[8]. Indeed, the use of KS coordinates makes necessary the computation of the partial derivatives with respect to the physical time $u^\star = t$, whereas in conventional coordinates they are only needed to check the Hamiltonian conservation (and thus removed after the experimental phase). These partial derivatives are quite time-consuming in our case, since the synthetic representation involves trigonometric functions. However, at a given precision the KS integrator is much faster, since it requires a much smaller number of steps: Fig. C.6 presents the comparison of speed versus accuracy of the two methods, showing that for the same computing time the integrations using the KS coordinates are more accurate by several orders of magnitude.

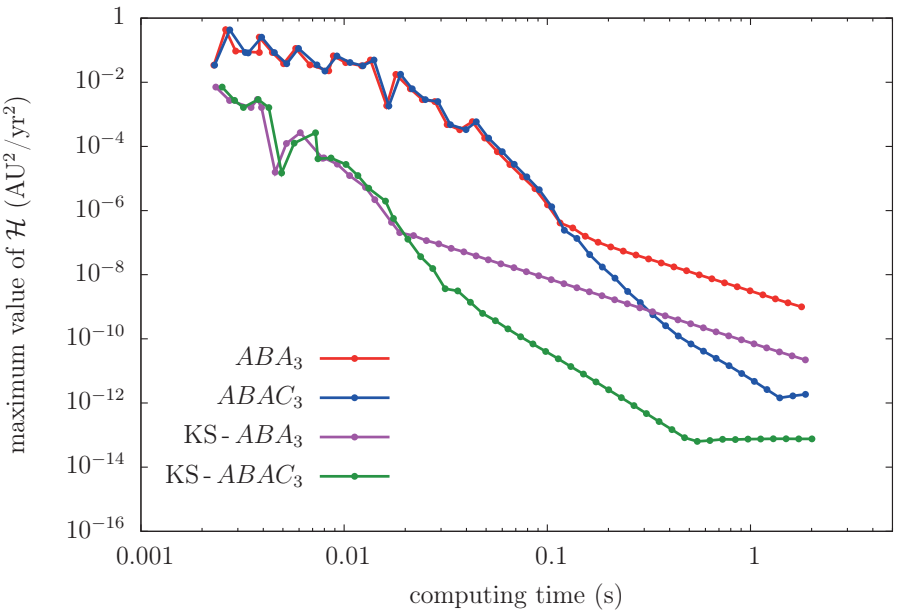

Figure C.6 – Same integrations as in Figs. C.4 and C.5, but using the computation time in the x-axis. For a given integrator, the computation time is directly proportional to the time-step used. Since the integration span is relatively small, the additional time required by the corrector steps is barely visible (the curves with correctors are slightly shifted toward the right).

Let us now turn to the comparison of long-term numerical integrations. Please remember that our goal in Sect. 4.5 is to propagate a large sample of objects, in order to track the qualitative long-term evolution of their orbits (by contrast to getting accurate individual positions over time). Moreover, we are mainly interested in distant trajectories, with perihelion located (possibly much) beyond Neptune. Since any particle

[8]For instance, using the corrector and with the smallest time-step represented in Figs. C.4 and C.5, the computing times using the same processor are in average 1.31 s and 1.22 s, using respectively the KS and conventional coordinates (without energy checking). These two integrations involve the same number of steps.

reaching a perihelion distance smaller than the semi-major axis of Neptune is removed from the simulation, there is no possibility of close encounter (except for very particular cases that we can dismiss). Consequently, we deal here with the very slightly perturbed case, as for all the models developed and discussed throughout this work, so the orbital evolution only results from the long-term accumulation of perturbations, resonant or not. In the following, we compare numerical integrations of particles with an initial semi-major axis $a = 800$ AU and an initial inclination $I = 0°$. Several initial perihelion distances are considered, from a purely quasi-periodic trajectory ($q = 100$ AU) to chaotic diffusion ($q = 50$ AU). Such a high semi-major axis has been chosen for the corresponding high sensibility to chaos (Gallardo et al., 2012) and the inefficiency of the captures into mean-motion resonances.

Figs. C.7 and C.8 show that surprisingly, for large perihelion distances the KS integrator is largely outclassed by the mixed-variable one. It even needs a higher number of steps *per orbit* in order to follow qualitatively well the smooth quasi-integrable trajectory. For such long integration spans, the KS scheme seems to behave as a non-symplectic integrator: the solution does converge toward the real trajectory when decreasing the step size, but in an unordered way. By comparison, the mixed-variable integrator follows qualitatively well the dynamics even for large steps, and the decrease of the step size only reduces the oscillations around the real trajectory. In the two cases, we note that the use the corrector steps somehow stabilises the numerical solution. Here, the nature of the perturbation is secular by essence, that is very small in magnitude but accumulating on a long timescale, *all along* the orbit of the particle. This is probably why the KS integrator, even for a quite eccentric orbit, turns out to be not as competitive as we could have expected: the large increase of the (physical) time-step near aphelion seems to keep it from accurately account for the secular accumulation of perturbations. Contrarily, the mixed-variable symplectic integrator does spend a lot of steps near aphelion, but thus it reproduces well the secular perturbations by the planets (for instance, the orbital period of Neptune is always resolved by the steps).

Fig. C.9 shows the slightly chaotic case, for which the rate of semi-major axis diffusion can be checked using a reference numerical integration. Using the mixed-variable integrator, the green and red curves (step sizes of 10 and 3 years) are now noticeably distinct, but still qualitatively equivalent in regards to the rate of diffusion. The same conclusion as above holds for the KS integrator. Finally, Fig. C.10 shows the frankly chaotic case, in which all the trajectories seem more or less acceptable. The very accurate integrator by Rein and Spiegel (2015) gives itself diverging results according to the exact precision parameter chosen: we reach the intrinsic uncertainty of chaotic trajectories treated by finite-precision arithmetic. Results on such long timescales are necessarily different from one integration to another, even when considering only the round-off errors. Hence, these trajectories should be considered only as possible outcomes in that region of initial conditions, and they cannot be used to study the validity of the integrators.

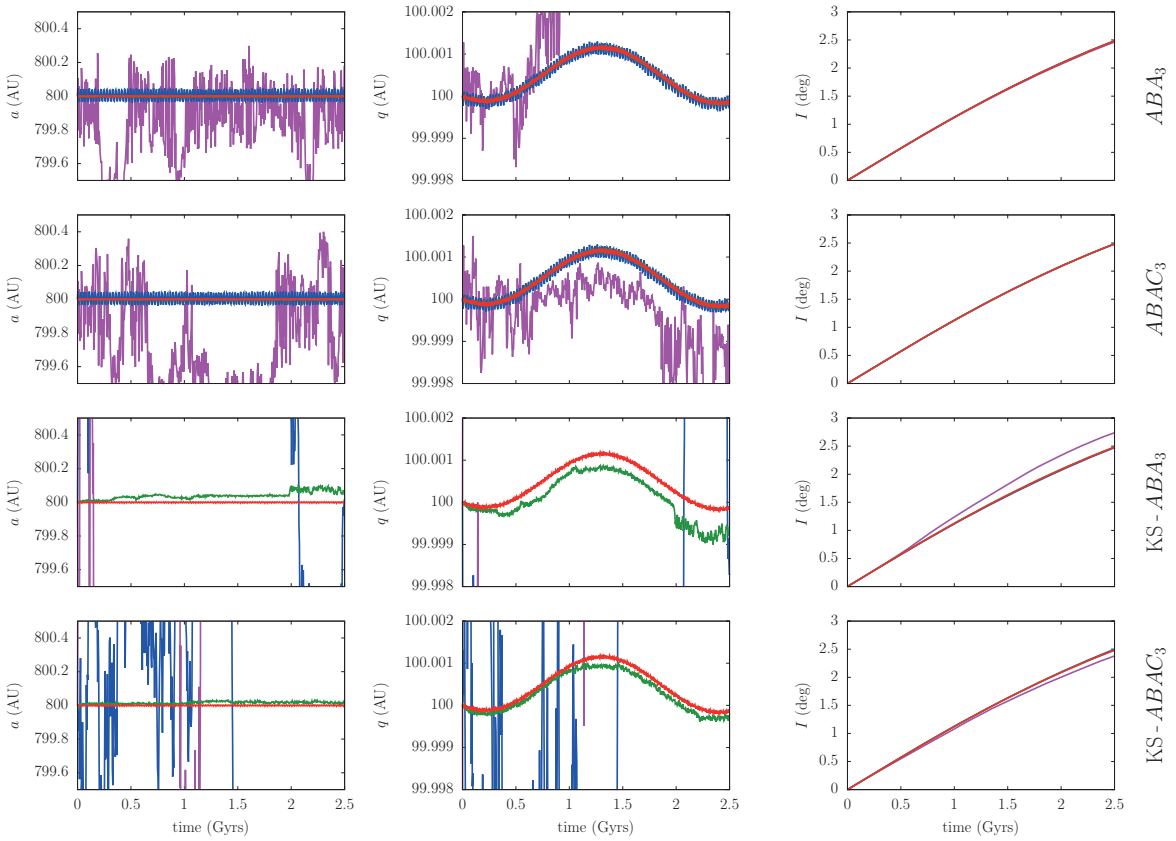

Figure C.7 – Long-term numerical integration using four types of integrators (written on the right). The elements represented are barycentric. The colour code represents the time-step used: it is equal to 100 yrs (magenta), 32 yrs (blue), 10 yrs (green) and 3 yrs (red). In the conventional coordinates the step is realised in the real time t (two top rows), whereas in the KS coordinates it is realised in the fictitious time τ (two bottom rows). In the two top rows, the green curve is hidden below the red one. In the two bottom rows, the semi-major axis of the magenta curve diffuses in the interval ± 100 AU (out of the graphs), and the blue one in ± 10 AU. The computing time of these integrations were: $ABA_3 : (16, 50, 151, 463)$ min, $ABAC_3 : (18, 56, 178, 538)$ min, KS - $ABA_3 : (14, 42, 127, 383)$ min and KS - $ABAC_3 : (15, 49, 149, 453)$ min. In the conventional coordinates, the Hamiltonian value was computed (thus the overall higher durations than in the KS ones). For a given step size, its conservation is roughly equivalent for the four integrators.

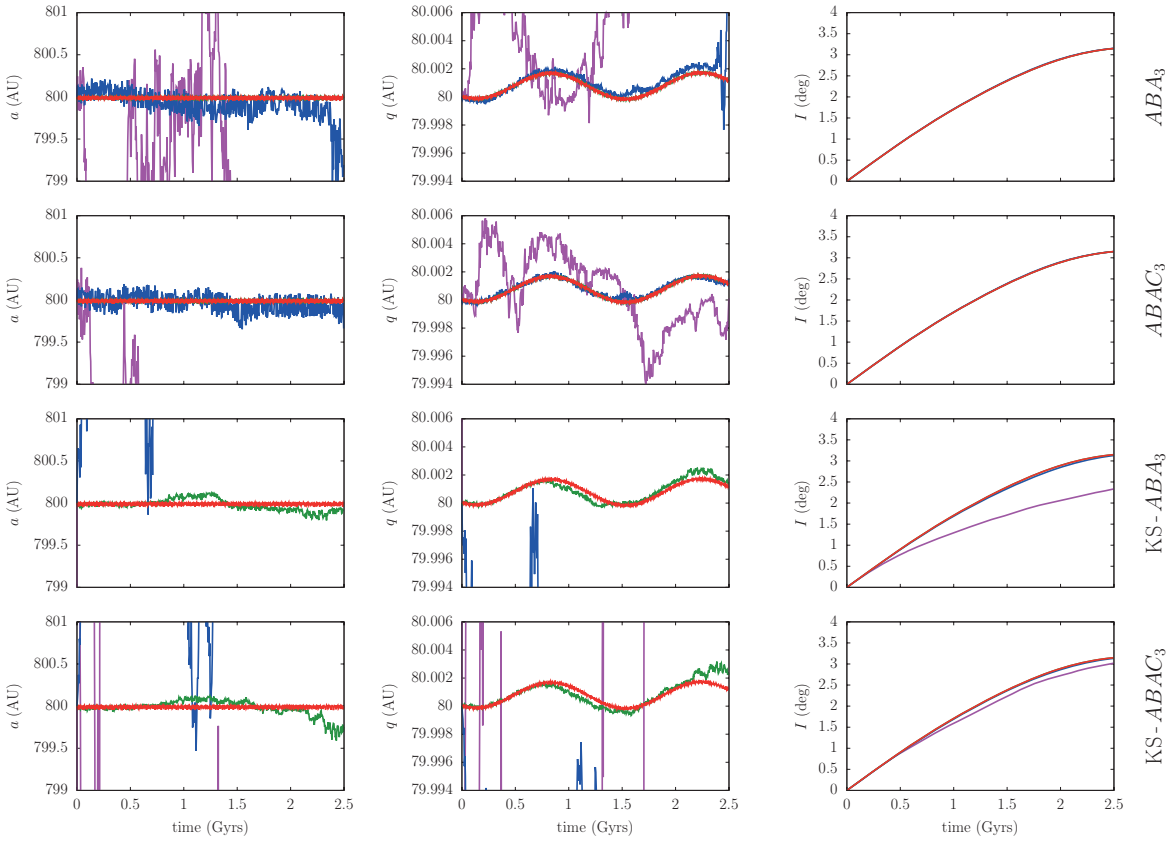

Figure C.8 – Same as Fig. C.7 but with an initial perihelion distance equal to 80 AU. The orbit is closer to the chaotic zone but the real trajectory is still quasi-integrable (as shown by a long but very accurate integration using the non-symplectic integrator by Rein and Spiegel, 2015). In the two top rows, the green curve is hidden below the red one. The computing times are very similar as in Fig. C.7. In the two top rows, the semi-major axis of the magenta curve diffuses in the interval ±4 AU (out of the graphs). In the two bottom rows, the semi-major axis of the magenta curve diffuses in the interval ±800 AU, and the blue one in ±25 AU.

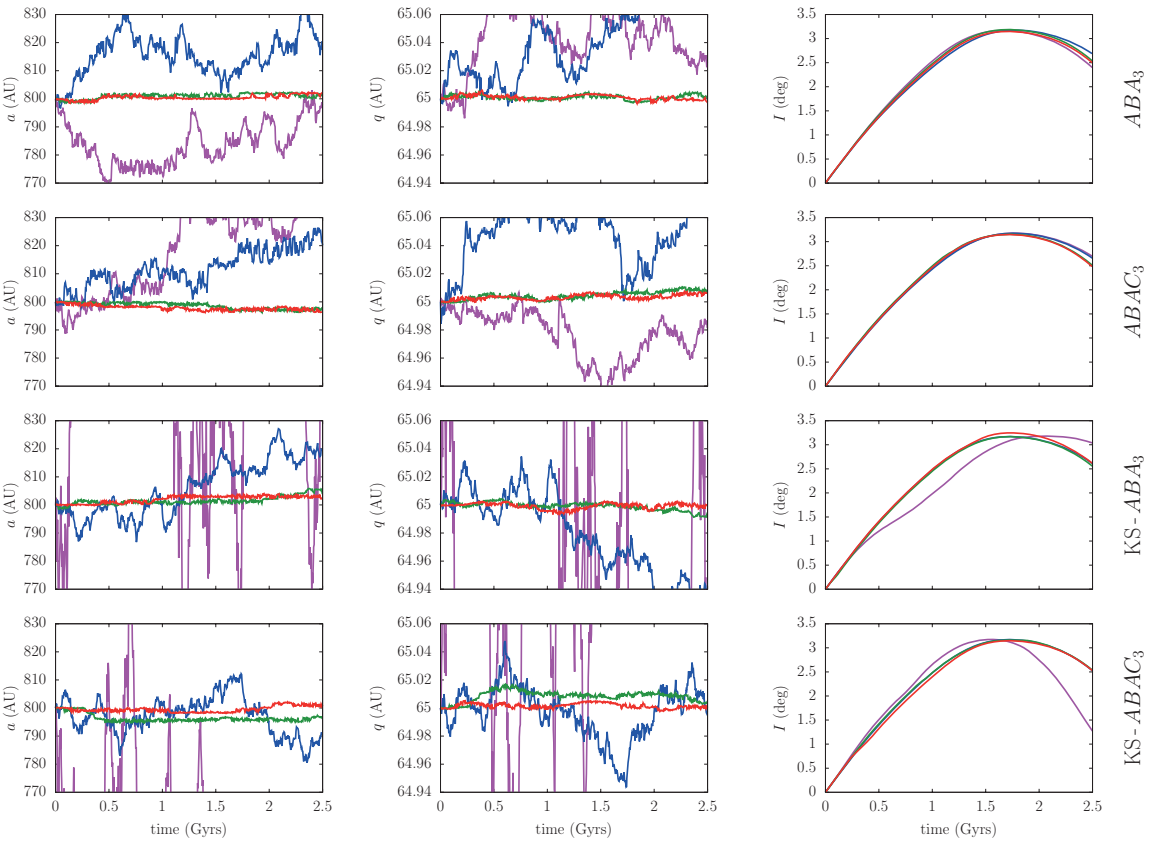

Figure C.9 – Same as Fig. C.7 but with an initial perihelion distance equal to 65 AU. The real trajectory diffuses slowly similarly as the red and green trajectories given by ABA_3 and $ABAC_3$ (as shown by a very long but very accurate integration using the non-symplectic integrator by Rein and Spiegel, 2015). In the two bottom rows, the semi-major axis of the magenta curve diffuses in the interval ± 400 AU (out of the plot).

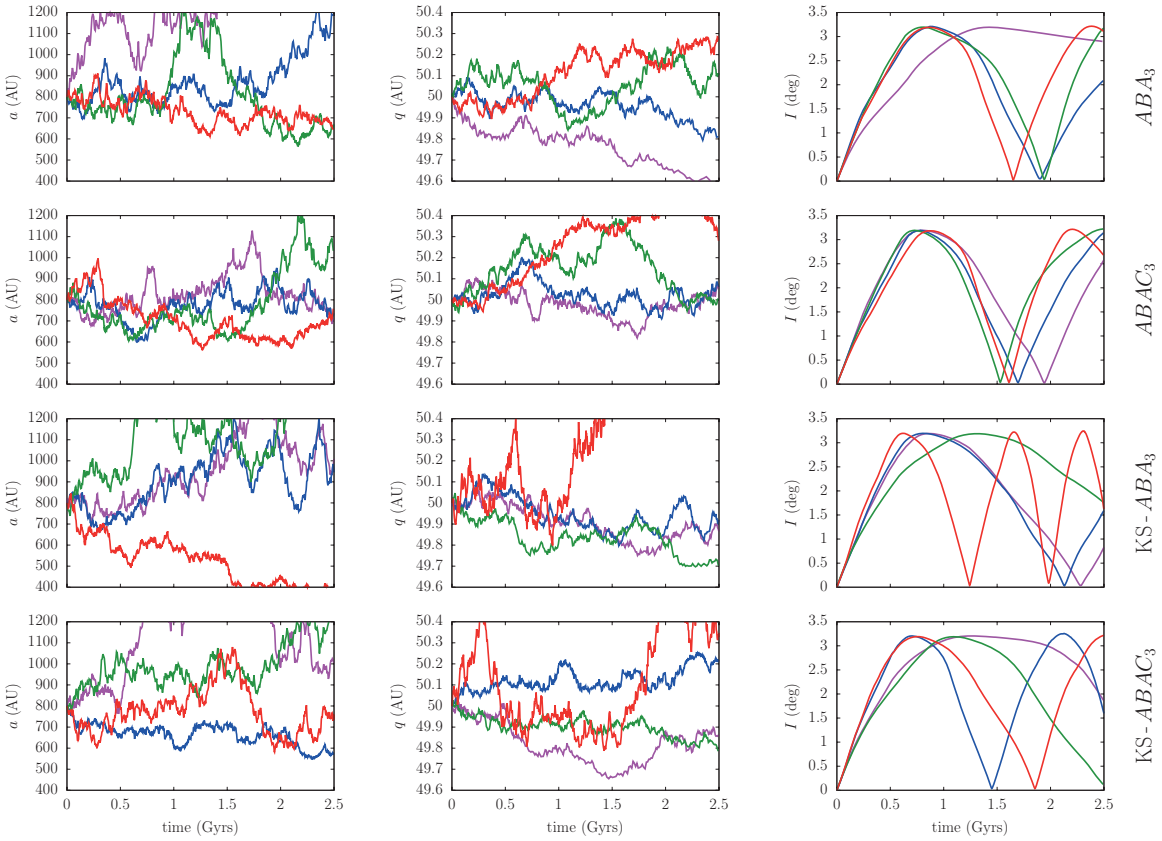

Figure C.10 – Same as Fig. C.7 but with an initial perihelion distance equal to 50 AU. We recall the colour code according to the time-step: 100 yrs (magenta), 32 yrs (blue), 10 yrs (green) and 3 yrs (red). The trajectory obtained from the non-symplectic integrator by Rein and Spiegel (2015) presents the same rate of diffusion as all these orbits, but the behaviour of the inclination is best reproduced by $ABAC_3$.

From these experimentations, the long-term evolution of distant bodies seems to be best reproduced by the mixed-variable integrator $ABAC_3$, for which we retain a time-step of 10 years as optimum choice. This leads to long but not prohibitive computation times for the whole sample (see Sect. C.4). Moreover, the fact that the orbits of Neptune and Uranus are well resolved by the step size is probably necessary to properly account for the possible captures into mean-motion resonances.

Nevertheless, the particularity of KS integrators to resolve more accurately the passages at perihelion rather than at aphelion *is* an incredible advantage over symplectic schemes using purely Cartesian coordinates (as for the decomposition $\mathcal{A}$=kinetic energy/$\varepsilon\mathcal{B}$=potential): indeed, the sharp variation of the Cartesian coordinates at perihelion for highly eccentric orbits are badly reproduced if the time-step is large, leading to large errors even in the non-perturbed case. However, this does not hold for mixed-variable symplectic schemes as the one presented in Sect. C.5.2, since the two-body component is solved analytically. Moreover, since the fictitious time τ is proportional to $\sqrt{a}E$, the use of the KS integrator requires implicitly that the semi-major axis of the orbit does not change much during the integration. For instance, if a decreases a lot along the integration, the constant step of τ becomes a very large portion of the whole orbit, leading to inaccurate results. Since the region of the Solar System studied here is particularly subject to chaotic diffusion, the KS coordinates prove to be rather unsuitable.

C.5.5 Notes on other methods

Some other integration algorithms were also experimented, as the generalisation of the hybrid method of Chambers (1999) to the whole Solar System. In a few words, it consists in applying a gauge to the Hamiltonian functions $\mathcal{A}$ and $\varepsilon\mathcal{B}$, such that some "amount" of $\varepsilon\mathcal{B}$ can be transferred to $\mathcal{A}$ when needed. In practice, this is realised by redefining the splitting (C.44) as:

$$\left\{\begin{array}{l} \mathcal{A} = \dfrac{1}{2}\mathbf{X}^2 - \dfrac{\mu_{\rm tot}}{|\mathbf{x}|} + T + (1-\kappa)\left(\dfrac{\mu_{\rm tot}}{|\mathbf{x}|} - \dfrac{\mu}{|\mathbf{x}-\mathbf{x}_\odot|} - \displaystyle\sum_{i=1}^{N}\dfrac{\mu_i}{|\mathbf{x}-\mathbf{x}_i|}\right) \\ \varepsilon\mathcal{B} = \kappa\left(\dfrac{\mu_{\rm tot}}{|\mathbf{x}|} - \dfrac{\mu}{|\mathbf{x}-\mathbf{x}_\odot|} - \displaystyle\sum_{i=1}^{N}\dfrac{\mu_i}{|\mathbf{x}-\mathbf{x}_i|}\right) \end{array}\right. \tag{C.84}$$

where κ is a $\mathcal{C}^2$ function of the coordinates, taking values between 0 and 1. This allows to ensure that $\varepsilon\mathcal{B}$ remains at all time a small quantity compared to $\mathcal{A}$, but still conserving the overall symplecticity of the integrator. Whenever some amount of $\varepsilon\mathcal{B}$ is transferred to $\mathcal{A}$, the latter becomes non integrable, so the sub-steps of the symplectic scheme are realised using another numerical integrator (as the Bulirsch-Stoer). Please note that the function κ should be absolutely flat when the perturbation is small enough (that is where it is equal to 1), such that its partial derivatives with respect to the position are zero, making the Hamiltonian $\mathcal{A}$ integrable again analytically. That method was

initially designed by Chambers (1999) to deal with close encounters, but our idea was to apply it more generally when the barycentric distance of the body gets smaller than a given quantity. Our results were not fully satisfactory: even if in some cases, good accuracies were achieved using very large time-steps (50 or 100 years), the computing times were only moderately lower than for the standard mixed-variable integrator with a step of 10 years. Moreover, the fact that none of the planetary orbits are resolved beyond some distance threshold (where $\kappa = 1$) could yield to the same problem as the KS coordinates, discussed above.

C.6 Hardy's discrete integration

Hardy's integration method is a particular application of the Newton-Cotes formulas (Press et al., 2007). It consists in an integration by parts in which polynomial interpolations are realised. The value obtained for each part is thus computed analytically. In Hardy's method, the intervals are made of seven points, so the polynomial used are of order 6. The method is thus *exact* for the integration of polynomials of order $\leqslant 6$.

Let us consider a function $f(t)$ tabulated on $[a, b]$ by $N + 1$ equidistant points $\{t_k, f_k\}_{k=0,1..N}$ separated by an interval Δt. We impose that N is a multiple of 6, so that:

$$\int_a^b f(t)\,\mathrm{d}t = \sum_{n=0}^{N/6-1} \int_{t_{6n}}^{t_{6n+6}} f(t)\,\mathrm{d}t = \sum_{n=0}^{N/6-1} \int_{t_{6n}}^{t_{6n+6}} P_6^{(n)}(t)\,\mathrm{d}t + \mathcal{O}\left(\mathrm{M}\left[\frac{\Delta t}{6}\right]^9\right) \quad \text{(C.85)}$$

in which $P_6^{(n)}(t)$ is the polynomial of order 6 obtained by the interpolation of $f(t)$ at the points $\{t_{6n}, t_{6n+1}, ..., t_{6n+6}\}$ and M is the upper bound of $f^{(8)}(t)$ on $[a, b]$. See Isaacson and Keller (1966) for more details. Using Lagrange's interpolation, the computation of the coefficients of $P_6^{(n)}(t)$ is straightforward. It leads to the following expression of the sub-integral:

$$\begin{aligned}\int_{t_{6n}}^{t_{6n+6}} P_6^{(n)}(t)\,\mathrm{d}t = \frac{\Delta t}{140}\Big(&41f_{6n} + 216f_{6n+1} + 27f_{6n+2} + 272f_{6n+3} \\ &+ 27f_{6n+4} + 216f_{6n+5} + 41f_{6n+6}\Big)\end{aligned} \quad \text{(C.86)}$$

We finally get the value of the whole integral between a and b by the summation over n.

C.7 Maximisation by quadratic interpolation

Starting from a first guess, we look for the exact position of the maximum of a real function $g(x)$. The first step consists in bracketing the maximum, that is to find a triplet of points $\{a, b, c\}$ such that $b \in]a, c[$ with $g(b)$ larger than both $g(a)$ and $g(c)$. In that case, $g(x)$ has necessarily a maximum on $]a, c[$, provided, of course, that it does

not diverge on this interval. Once such points $\{a, b, c\}$ are known, the function $g(x)$ is approximated by the (unique) polynomial of order 2 which has the same values as g in a, b and c. In this way, the abscissa of the maximum is easy to compute:

$$x_{max} = b + \frac{1}{2}\frac{\big[g(a) - g(b)\big](c-b)^2 - \big[g(c) - g(b)\big](a-b)^2}{\big[g(a) - g(b)\big](c-b) - \big[g(c) - g(b)\big](a-b)} \tag{C.87}$$

A correct choice for $\{a, b, c\}$ ensures that it is indeed a maximum (not a minimum), and that the denominator is not zero (the three points are not aligned). Then, the procedure can be iterated: if $x_{max} \in]b, c[$ or $x_{max} \in]a, b[$ respectively, the value of b becomes the new a or the new c, and x_{max} becomes the new central point b. The iterations can be stopped when $|c - a|$ is smaller than the required precision. Be careful, though, that the precision is limited by the shape of the function in the neighbourhood of its maximum. Indeed, even if the *value* of the maximum $g(x_{max})$ is obtained at machine precision, this is never the case of its abscissa x_{max} (for instance, think of a function very "flat" around x_{max}). An estimate of the limit of precision can be obtained by a Taylor expansion of g around its maximum:

$$g(x) \approx g(x_{max}) + \frac{(x - x_{max})^2}{2} g''(x_{max}) \tag{C.88}$$

in which here, x_{max} is the true position of the maximum. Writing ε the machine precision, the convergence is obtained when the new position x is such that:

$$\left|\frac{g(x) - g(x_{max})}{g(x_{max})}\right| < \varepsilon \tag{C.89}$$

The maximum precision reachable for the position of the maximum is then:

$$\frac{(x - x_{max})^2}{2}|g''(x_{max})| < \varepsilon\,|g(x_{max})| \iff |x - x_{max}| < \sqrt{\frac{2\,\varepsilon\,|g(x_{max})|}{|g''(x_{max})|}} = \varepsilon_x \tag{C.90}$$

In our case, we aim at maximising the amplitude function $\mathcal{A}(\nu) = \langle f, \mathrm{e}^{i\nu t}\rangle$ for which a first guess is given by a Fast Fourier Transform (Sect. A.1.1). The FFT gives a very rough representation of $\mathcal{A}(\nu)$, so the initial bracketing should be realised with some care (see Fig. C.11). The precision reachable can be estimated using (C.90) and supposing that the maxima of $\mathcal{A}(\nu)$ are separated enough to consider that it behaves locally as a one-term function. Indeed, using the Hanning window, Eq. A.8 rewrites:

$$g(\nu) = |\mathcal{A}(\nu)| = \left|\frac{A_1\,\pi^2}{\pi^2 - \big[(\nu_1 - \nu)T/2\big]^2}\frac{\sin\big[(\nu_1 - \nu)T/2\big]}{(\nu_1 - \nu)T/2}\right| \tag{C.91}$$

By computing the derivatives of g expressed at its maximum ν_1, we finally get:

$$\varepsilon_\nu = \sqrt{\frac{24\,\varepsilon}{(1 - 6/\pi^2)\,T^2}} = \frac{\nu_0}{\pi}\sqrt{\frac{6\,\varepsilon}{1 - 6/\pi^2}} \approx 1.245\,\nu_0\,\sqrt{\varepsilon} \tag{C.92}$$

Since the frequencies are not always well separated, the peaks can appear slightly larger so one should take a safety margin (for instance $2\,\nu_0\,\sqrt{\varepsilon}$). In practice, the maximum precision is reached when the three points used for the quadratic interpolation become horizontally aligned at the working precision, leading to a zero denominator in (C.87).

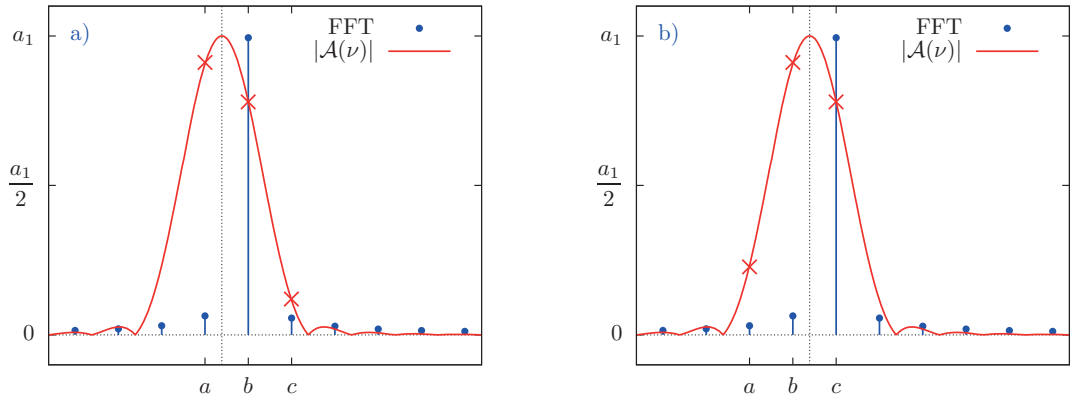

Figure C.11 – Bracketing of the maximum of the amplitude function $\mathcal{A}(\nu)$ starting from a FFT: **a)** bad bracketing because $g(b) < g(a)$; **b)** suitable bracketing.

Bibliography

V. I. Arnold. *Mathematical Methods of Classical Mechanics*. Springer-Verlag, graduate texts in mathematics edition, 1989.

E. Bailey, K. Batygin, and M. E. Brown. Solar Obliquity Induced by Planet Nine. *Astronomical Journal*, 152, October 2016.

M. T. Bannister, M. Alexandersen, S. D. Benecchi, Y.-T. Chen, A. Delsanti, W. C. Fraser, B. J. Gladman, M. Granvik, W. M. Grundy, A. Guilbert-Lepoutre, S. D. J. Gwyn, W.-H. Ip, M. Jakubik, R. L. Jones, N. Kaib, J. J. Kavelaars, P. Lacerda, S. Lawler, M. J. Lehner, H. W. Lin, P. S. Lykawka, M. Marsset, R. Murray-Clay, K. S. Noll, A. Parker, J.-M. Petit, R. E. Pike, P. Rousselot, M. E. Schwamb, C. Shankman, P. Veres, P. Vernazza, K. Volk, S.-Y. Wang, and R. Weryk. OSSOS. IV. Discovery of a Dwarf Planet Candidate in the 9:2 Resonance with Neptune. *Astronomical Journal*, 152, December 2016.

M. T. Bannister, J. J. Kavelaars, B. J. Gladman, J.-M. Petit, T. Burdullis, S. D. J. Gwyn, Y.-T. Chen, M. Alexandersen, and M. Schwamb. Minor Planet Electronic Circular 2017-M22. *Minor Planet Center*, 2017.

K. Batygin and M. E. Brown. Evidence for a Distant Giant Planet in the Solar System. *Astronomical Journal*, 151, January 2016a.

K. Batygin and M. E. Brown. Generation of Highly Inclined Trans-Neptunian Objects by Planet Nine. *Astrophysical Journal Letters*, 833, December 2016b.

C. Beaugé and F. Roig. A Semianalytical Model for the Motion of the Trojan Asteroids: Proper Elements and Families. *Icarus*, 153, October 2001.

H. Beust. Orbital clustering of distant Kuiper belt objects by hypothetical Planet 9. Secular or resonant? *Astronomy & Astrophysics*, 590, May 2016.

P. I. O. Brasil, R. S. Gomes, and J. S. Soares. Dynamical formation of detached trans-Neptunian objects close to the 2:5 and 1:3 mean motion resonances with Neptune. *Astronomy & Astrophysics*, 564, April 2014.

S. Breiter. Explicit Symplectic Integrator for Highly Eccentric Orbits. *Celestial Mechanics and Dynamical Astronomy*, 71, 1999.

S. Breiter, M. Fouchard, R. Ratajczak, and W. Borczyk. Two fast integrators for the Galactic tide effects in the Oort Cloud. *Monthly Notices of the Royal Astronomical Society*, 377, May 2007.

D. Brouwer and G. M. Clemence. *Methods of celestial mechanics*. Academic Press, New York, 1961.

M. E. Brown and K. Batygin. Observational Constraints on the Orbit and Location of Planet Nine in the Outer Solar System. *Astrophysical Journal Letters*, 824, June 2016.

T. M. Burkardt and J. M. A. Danby. The solutions of Kepler's equation. II. *Celestial Mechanics*, 31, November 1983.

M. Carpino, A. Milani, and A. M. Nobili. Long-term numerical integrations and synthetic theories for the motion of the outer planets. *Astronomy & Astrophysics*, 181, July 1987.

J. E. Chambers. A hybrid symplectic integrator that permits close encounters between massive bodies. *Monthly Notices of the Royal Astronomical Society*, 304, April 1999.

S Champenois. *Dynamique de la résonance entre Mimas et Téthys*. PhD thesis, Observatoire de Paris, 1994.

J. M. A. Danby. The Solution of Kepler's Equations - Part Three. *Celestial Mechanics*, 40, September 1987.

J. M. A. Danby. *Fundamentals of celestial mechanics*. Macmillan, New York, 1988.

J. M. A. Danby and T. M. Burkardt. The solution of Kepler's equation. I. *Celestial Mechanics*, 31, October 1983.

L. Duriez. Le problème des deux corps revisité. In D. Benest and C. Froeschle, editors, *Modern Methods in Celestial Mechanics*, 1990.

K. M. Ellis and C. D. Murray. The Disturbing Function in Solar System Dynamics. *Icarus*, 147, September 2000.

E. Everhart. An efficient integrator that uses Gauss-Radau spacings. In A. Carusi and G. B. Valsecchi, editors, *Dynamics of Comets: Their Origin and Evolution*, 1985.

A. Fienga, J. Laskar, H. Manche, and M. Gastineau. Constraints on the location of a possible 9th planet derived from the Cassini data. *Astronomy & Astrophysics*, 587, March 2016.

L. Floría. A Simple Derivation of the Hyperbolic Delaunay Variables. *Astronomical Journal*, 110, August 1995.

M. Fouchard, C. Froeschlé, G. Valsecchi, and H. Rickman. Long-term effects of the Galactic tide on cometary dynamics. *Celestial Mechanics and Dynamical Astronomy*, 95, May 2006.

M. Fouchard, H. Rickman, Ch. Froeschlé, and G.B. Valsecchi. On the present shape of the Oort cloud and the flux of "new" comets. *Icarus*, 292, August 2017.

T. Gallardo. The occurrence of high-order resonances and Kozai mechanism in the scattered disk. *Icarus*, 181, March 2006a.

T. Gallardo. Atlas of the mean motion resonances in the Solar System. *Icarus*, 184, September 2006b.

T. Gallardo, G. Hugo, and P. Pais. Survey of Kozai dynamics beyond Neptune. *Icarus*, 220, August 2012.

B. Gladman, B. G. Marsden, and C. Vanlaerhoven. Nomenclature in the Outer Solar System. In M. A. Barucci, H. Boehnhardt, D. P. Cruikshank, A. Morbidelli, and R. Dotson, editors, *The Solar System Beyond Neptune*, 2008.

B. Gladman, S. M. Lawler, J.-M. Petit, J. Kavelaars, R. L. Jones, J. W. Parker, C. Van Laerhoven, P. Nicholson, P. Rousselot, A. Bieryla, and M. L. N. Ashby. The Resonant Trans-Neptunian Populations. *Astronomical Journal*, 144, July 2012.

R. Gomes, H. F. Levison, K. Tsiganis, and A. Morbidelli. Origin of the cataclysmic Late Heavy Bombardment period of the terrestrial planets. *Nature*, 435, May 2005a.

R. Gomes, R. Deienno, and A. Morbidelli. The inclination of the planetary system relative to the solar equator may be explained by the presence of Planet 9. *Astronomical Journal*, 153, December 2016.

R. S. Gomes. The origin of TNO 2004 XR $_{190}$ as a primordial scattered object. *Icarus*, 215, October 2011.

R. S. Gomes, T. Gallardo, J. A. Fernández, and A. Brunini. On The Origin of The High-Perihelion Scattered Disk: The Role of The Kozai Mechanism And Mean Motion Resonances. *Celestial Mechanics and Dynamical Astronomy*, 91, January 2005b.

R. S. Gomes, J. A. Fernández, T. Gallardo, and A. Brunini. The Scattered Disk: Origins, Dynamics, and End States. In M. A. Barucci, H. Boehnhardt, D. P. Cruikshank, A. Morbidelli, and R. Dotson, editors, *The Solar System Beyond Neptune*, 2008.

R. S. Gomes, J. S. Soares, and R. Brasser. The observation of large semi-major axis Centaurs: Testing for the signature of a planetary-mass solar companion. *Icarus*, 258, September 2015.

G. F. Gronchi. Generalized Averaging Principle and the Secular Evolution of Planet Crossing Orbits. *Celestial Mechanics and Dynamical Astronomy*, 83, May 2002.

G. F. Gronchi and A. Milani. Averaging on Earth-Crossing Orbits. *Celestial Mechanics and Dynamical Astronomy*, 71, 1998.

G. F. Gronchi and A. Milani. The stable Kozai state for asteroids and comets. With arbitrary semimajor axis and inclination. *Astronomy & Astrophysics*, 341, January 1999.

G. F. Gronchi and A. Milani. Proper Elements for Earth-Crossing Asteroids. *Icarus*, 152, July 2001.

G. F. Gronchi and C. Tardioli. The evolution of the orbit distance in the double averaged restricted 3-body problem with crossing singularities. *Discrete and Continuous Dynamical Systems*, 18, 2013.

E. Hairer, S. P. Nørsett, and G. Wanner. *Solving Ordinay Differential Equation I, second revised edition*. Springer-Verlag, Berlin Heidelberg, 2008.

A. S. Hamers and S. F. Portegies Zwart. Secular dynamics of hierarchical multiple systems composed of nested binaries, with an arbitrary number of bodies and arbitrary hierarchical structure. First applications to multiplanet and multistar systems. *Monthly Notices of the Royal Astronomical Society*, 459, July 2016.

A. S. Hamers, H. B. Perets, F. Antonini, and S. F. Portegies Zwart. Secular dynamics of hierarchical quadruple systems: the case of a triple system orbited by a fourth body. *Monthly Notices of the Royal Astronomical Society*, 449, June 2015.

R. S. Harrington. Dynamical evolution of triple stars. *Astronomical Journal*, 73, April 1968.

M. Hénon. Exploration numérique du probleme restreint - IV. Masses égales, orbites non périodiques. *Bulletin Astronomique*, 3, 1966.

M. Hénon. On the numerical computation of Poincaré maps. *Physica D Nonlinear Phenomena*, 5, September 1982.

J. Henrard. A semi-numerical perturbation method for separable Hamiltonian systems. *Celestial Mechanics and Dynamical Astronomy*, 49, March 1990.

J. Henrard. *Dynamics Reported – Expositions in Dynamical Systems*, volume 2. Springer Berlin Heidelberg, 1993.

K. A. Innanen, J. Q. Zheng, S. Mikkola, and M. J. Valtonen. The Kozai Mechanism and the Stability of Planetary Orbits in Binary Star Systems. *Astronomical Journal*, 113, May 1997.

E. Isaacson and H. B. Keller. *Analysis of numerical methods*. Dover Publications, 1966.

L. Jílková, S. Portegies Zwart, T. Pijloo, and M. Hammer. How Sedna and family were captured in a close encounter with a solar sibling. *Monthly Notices of the Royal Astronomical Society*, 453, November 2015.

N. A. Kaib, T. Quinn, and R. Brasser. Decreasing Computing Time with Symplectic Correctors in Adaptive Timestepping Routines. *Astronomical Journal*, 141, January 2011.

C. F. F. Karney. Long-time correlations in the stochastic regime. *Physica D Nonlinear Phenomena*, 8, September 1983.

B. Katz, S. Dong, and R. Malhotra. Long-Term Cycling of Kozai-Lidov Cycles: Extreme Eccentricities and Inclinations Excited by a Distant Eccentric Perturber. *Physical Review Letters*, 107(18), October 2011.

Z. Knezevic, A. Milani, P. Farinella, Ch. Froeschle, and C. Froeschle. Secular resonances from 2 to 50 AU. *Icarus*, 93, October 1991.

Y. Kozai. Secular perturbations of asteroids with high inclination and eccentricity. *Astronomical Journal*, 67, November 1962.

Y. Kozai. Secular perturbations of resonant asteroids. *Celestial Mechanics*, 36, May 1985.

V. Lainey, L. Duriez, and A. Vienne. Synthetic representation of the Galilean satellites' orbital motions from L1 ephemerides. *Astronomy & Astrophysics*, 456, 2006.

J. Laskar. Secular evolution of the solar system over 10 million years. *Astronomy & Astrophysics*, 198, June 1988.

J. Laskar. A numerical experiment on the chaotic behaviour of the solar system. *Nature*, 338, March 1989.

J. Laskar. The chaotic motion of the solar system - A numerical estimate of the size of the chaotic zones. *Icarus*, 88, December 1990.

J. Laskar. Frequency map analysis and quasiperiodic decompositions. In D. Benest, C. Froeschle, and E. Lega, editors, *Hamiltonian Systems and Fourier Analysis: New Prospects for Gravitational Dynamics*. Cambridge Scientific Publishers, 2005.

J. Laskar and G. Boué. Explicit expansion of the three-body disturbing function for arbitrary eccentricities and inclinations. *Astronomy & Astrophysics*, 522, November 2010.

J. Laskar and P. Robutel. High order symplectic integrators for perturbed Hamiltonian systems. *Celestial Mechanics and Dynamical Astronomy*, 80, July 2001.

J. Laskar, C. Froeschlé, and A. Celletti. The measure of chaos by the numerical analysis of the fundamental frequencies. Application to the standard mapping. *Physica D*, 56, May 1992.

A. Lemaître. Resonances: Models and Captures. In J. Souchay and R. Dvorak, editors, *Lecture Notes in Physics, Berlin Springer Verlag*, volume 790, March 2010.

A. Lemaître and A. Morbidelli. Proper elements for highly inclined asteroidal orbits. *Celestial Mechanics and Dynamical Astronomy*, 60, September 1994.

G. Li, S. Naoz, M. Holman, and A. Loeb. Chaos in the Test Particle Eccentric Kozai-Lidov Mechanism. *Astrophysical Journal*, 791, August 2014a.

G. Li, S. Naoz, B. Kocsis, and A. Loeb. Eccentricity Growth and Orbit Flip in Near-coplanar Hierarchical Three-body Systems. *Astrophysical Journal*, 785, April 2014b.

M. L. Lidov. The evolution of orbits of artificial satellites of planets under the action of gravitational perturbations of external bodies. *Planetary and Space Science*, 9, October 1962.

Y. Lithwick and S. Naoz. The Eccentric Kozai Mechanism for a Test Particle. *Astrophysical Journal*, 742, December 2011.

P. S. Lykawka and T. Mukai. Dynamical classification of trans-neptunian objects: Probing their origin, evolution, and interrelation. *Icarus*, 189, July 2007.

S. Mikkola and P. Wiegert. Regularizing Time Transformations in Symplectic and Composite Integration. *Celestial Mechanics and Dynamical Astronomy*, 82, April 2002.

A. Milani and S. Baccili. Dynamics of Earth-crossing asteroids: the protected Toro orbits. *Celestial Mechanics and Dynamical Astronomy*, 71, May 1998.

A. Milani and G. F. Gronchi. *Theory of Orbit Determination*. Cambridge University Press, 2010.

A. Milani and A. M. Nobili. An example of stable chaos in the Solar System. *Nature*, 357, June 1992.

M. Moons and A. Morbidelli. Secular resonances inside mean-motion commensurabilities: the 4/1, 3/1, 5/2 and 7/3 cases. *Icarus*, 114, March 1995.

M. Moons, A. Morbidelli, and F. Migliorini. Dynamical Structure of the 2/1 Commensurability with Jupiter and the Origin of the Resonant Asteroids. *Icarus*, 135, October 1998.

A. Morbidelli. Asteroid Secular Resonant Proper Elements. *Icarus*, 105, September 1993.

A. Morbidelli. *Modern celestial mechanics: aspects of solar system dynamics*. London: Taylor & Francis, 2002.

A. Morbidelli and H. F. Levison. Scenario for the Origin of the Orbits of the Trans-Neptunian Objects 2000 CR_{105} and 2003 VB_{12} (Sedna). *Astronomical Journal*, 128, November 2004.

C. D. Murray and S. F. Dermott. *Solar System Dynamics*. Cambridge University Press, 1999.

S. Naoz. The Eccentric Kozai-Lidov Effect and Its Applications. *Annual Review of Astronomy and Astrophysics*, 54, September 2016.

S. Naoz, W. M. Farr, Y. Lithwick, F. A. Rasio, and J. Teyssandier. Secular dynamics in hierarchical three-body systems. *Monthly Notices of the Royal Astronomical Society*, 431, May 2013.

A. Neishtadt. On the change in the adiabatic invariant on crossing a separatrix in systems with two degrees of freedom. *Journal of Applied Mathematics and Mechanics*, 51, 1987.

R. Piessens, E. de Doncker-Kapenga, and C. W. Ueberhuber. *Quadpack. A subroutine package for automatic integration*. Springer Series in Computational Mathematics, 1983.

W. H. Press, S. A. Teukolsky, W. T. Vetterling, and B. P. Flannery. *Numerical Recipes: The Art of Scientific Computing, third edition*. Cambridge University Press, 2007.

H. Rein and D. S. Spiegel. IAS15: a fast, adaptive, high-order integrator for gravitational dynamics, accurate to machine precision over a billion orbits. *Monthly Notices of the Royal Astronomical Society*, 446, January 2015.

S. Renner, N. J. Cooper, M. El Moutamid, B. Sicardy, A. Vienne, C. D. Murray, and M. Saillenfest. Origin of the Chaotic Motion of the Saturnian Satellite Atlas. *Astronomical Journal*, 151, May 2016.

F. Roig, A. Simula, S. Ferraz-Mello, and M. Tsuchida. The high-eccentricity asymmetric expansion of the disturbing function for non-planar resonant problems. *Astronomy & Astrophysics*, 329, January 1998.

M. Saillenfest and G. Lari. The long-term evolution of known resonant transneptunian objects. *Astronomy & Astrophysics*, accepted, 2017. doi: 10.1051/0004-6361/201730525.

M. Saillenfest, M. Fouchard, G. Tommei, and G.B. Valsecchi. Long-term dynamics beyond Neptune: secular models to study the regular motions. *Celestial Mechanics and Dynamical Astronomy*, 126, November 2016.

M. Saillenfest, M. Fouchard, G. Tommei, and G.B. Valsecchi. Study and application of the resonant secular dynamics beyond Neptune. *Celestial Mechanics and Dynamical Astronomy*, 127, April 2017a.

M. Saillenfest, M. Fouchard, G. Tommei, and G.B. Valsecchi. Non-resonant secular dynamics of trans-Neptunian objects perturbed by a distant super-Earth. *Celestial Mechanics and Dynamical Astronomy*, accepted, 2017b. doi: 10.1007/s10569-017-9775-7.

R. A. Serafin. Bounds on the Solution to Kepler's equation:II. Universal and Optimal Starting Points. *Celestial Mechanics and Dynamical Astronomy*, 70, February 1998.

R. A. Serafin. 'On Solving Kepler's Equation For Nearly Rectilinear Hyperbolic Orbits'. *Celestial Mechanics and Dynamical Astronomy*, 82:363–373, April 2002.

S. S. Sheppard, C. Trujillo, and D. J. Tholen. Beyond the Kuiper Belt Edge: New High Perihelion Trans-Neptunian Objects with Moderate Semimajor Axes and Eccentricities. *Astrophysical Journal Letters*, 825, July 2016.

M. Suzuki. General theory of fractal path integrals with applications to many-body theories and statistical physics. *Journal of Mathematical Physics*, 32, February 1991.

G. Takeda, R. Kita, and F. A. Rasio. Planetary Systems in Binaries. I. Dynamical Classification. *Astrophysical Journal*, 683, August 2008.

F. Thomas and A. Morbidelli. The Kozai Resonance in the Outer Solar System and the Dynamics of Long-Period Comets. *Celestial Mechanics and Dynamical Astronomy*, 64, September 1996.

B. Todorovic-Juchniewicz. When we may and Need to Use Barycentric Orbit of a Comet. *Acta Astronomica*, 31, 1981.

J. R. Touma, S. Tremaine, and M. V. Kazandjian. Gauss's method for secular dynamics, softened. *Monthly Notices of the Royal Astronomical Society*, 394, April 2009.

K. Tsiganis, R. Gomes, A. Morbidelli, and H. F. Levison. Origin of the orbital architecture of the giant planets of the Solar System. *Nature*, 435, May 2005.

I. W. Walker, A. G. Emslie, and A. E. Roy. Stability criteria in many-body systems. I - an empirical stability criterion for co-rotational three-body systems. *Celestial Mechanics*, 22, November 1980.

K. J. Walsh, A. Morbidelli, S. N. Raymond, D. P. O'Brien, and A. M. Mandell. A low mass for Mars from Jupiter's early gas-driven migration. *Nature*, 475, July 2011.

J. Wisdom. A perturbative treatment of motion near the 3/1 commensurability. *Icarus*, 63, August 1985.

H. Yoshida. Recent Progress in the Theory and Application of Symplectic Integrators. *Celestial Mechanics and Dynamical Astronomy*, 56, March 1993.

G. Zhong and J. E. Marsden. Lie-Poisson Hamilton-Jacobi theory and Lie-Poisson integrators. *Physics Letters A*, 133, November 1988.

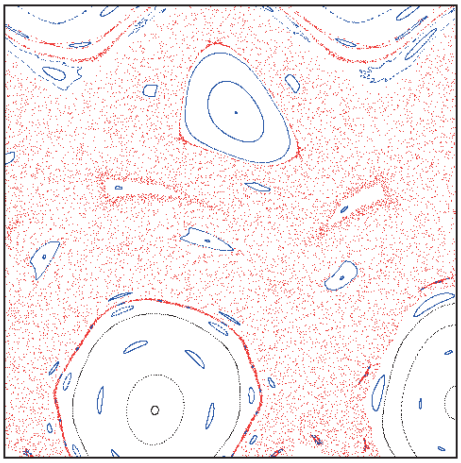

Secular theories and orbital dynamics beyond Neptune The dynamical structure of the trans-Neptunian region is still far from being fully understood, especially concerning high-perihelion objects. The major part of this work is focussed on the development of secular models, used to describe the orbital dynamics of trans-Neptunian objects both in the non-resonant and resonant cases. One-degree-of-freedom systems can be obtained, which allows to represent any trajectory by a level curve of the Hamiltonian. Such a formalism is very efficient to explore the parameter space. It reveals pathways to high perihelion distances, as well as "trapping mechanisms", able to maintain the objects on very distant orbits for billions of years. The application of the resonant secular model to the known objects is also very informative, since it shows graphically which observed orbits require a complex scenario (as the planetary migration or an external perturber), and which ones can be explained by the influence of the known planets.

The last part of this work is devoted to the extension of the non-resonant secular model to the case of an external massive perturber. If it has a substantial eccentricity and/or inclination, it introduces one or two more degrees of freedom in the system, so the secular dynamics is non integrable in general. In that case, the analysis can be realised by Poincaré sections, which allows to distinguish the chaotic regions of the phase space from the regular ones.